Advances in Science, Technology & Innovation
IEREK Interdisciplinary Series for Sustainable Development

Hesham M. El-Askary · Saro Lee · Essam Heggy
Biswajeet Pradhan *Editors*

Advances in Remote Sensing and Geo Informatics Applications

Proceedings of the 1st Springer Conference of the Arabian Journal of Geosciences (CAJG-1), Tunisia 2018

IEREK RESEARCH & KNOWLEDGE ENRICHMENT

Springer

Advances in Science, Technology & Innovation

IEREK Interdisciplinary Series for Sustainable Development

Editorial Board Members

Hassan Abdalla
Md. Abdul Mannan
Chaham Alalouch
Sahar Attia
Sofia Natalia Boemi
Hocine Bougdah
Emmanuel Bozonnet
Luciano De Bonis
Dean Hawkes
Stella Kostopoulou
Yasser Mahgoub
Saleh Mesbah Elkaffas
Nabil Mohareb
Iman O. Gawad
Mieke Oostra
Gloria Pignatta
Anna Laura Pisello
Federica Rosso
Biswajeet Pradhan

Series editor

Mourad Amer

Advances in Science, Technology & Innovation (ASTI) is a series of peer-reviewed books based on the best studies on emerging research that redefines existing disciplinary boundaries in science, technology and innovation (STI) in order to develop integrated concepts for sustainable development. The series is mainly based on the best research papers from various IEREK and other international conferences, and is intended to promote the creation and development of viable solutions for a sustainable future and a positive societal transformation with the help of integrated and innovative science-based approaches. Offering interdisciplinary coverage, the series presents innovative approaches and highlights how they can best support both the economic and sustainable development for the welfare of all societies. In particular, the series includes conceptual and empirical contributions from different interrelated fields of science, technology and innovation that focus on providing practical solutions to ensure food, water and energy security. It also presents new case studies offering concrete examples of how to resolve sustainable urbanization and environmental issues. The series is addressed to professionals in research and teaching, consultancies and industry, and government and international organizations. Published in collaboration with IEREK, the ASTI series will acquaint readers with essential new studies in STI for sustainable development.

More information about this series at http://www.springer.com/series/15883

Hesham M. El-Askary
Saro Lee • Essam Heggy
Biswajeet Pradhan
Editors

Advances in Remote Sensing and Geo Informatics Applications

Proceedings of the 1st Springer Conference of the Arabian Journal of Geosciences (CAJG-1), Tunisia 2018

Springer

Editors
Hesham M. El-Askary
Schmid College of Science and Technology
Chapman University
Orange, CA, USA

Saro Lee
Korea Institute of Geoscience and Mineral Resources
Daejeon, Korea (Republic of)

Essam Heggy
University of Southern California
Los Angeles, CA, USA

and

Jet Propulsion Laboratory
Caltech
Pasadena, CA, USA

Biswajeet Pradhan
University of Technology Sydney
Sydney, NSW, Australia

ISSN 2522-8714 ISSN 2522-8722 (electronic)
Advances in Science, Technology & Innovation
IEREK Interdisciplinary Series for Sustainable Development
ISBN 978-3-030-01439-1 ISBN 978-3-030-01440-7 (eBook)
https://doi.org/10.1007/978-3-030-01440-7

Library of Congress Control Number: 2018958355

© Springer Nature Switzerland AG 2019
This work is subject to copyright. All rights are reserved by the Publisher, whether the whole or part of the material is concerned, specifically the rights of translation, reprinting, reuse of illustrations, recitation, broadcasting, reproduction on microfilms or in any other physical way, and transmission or information storage and retrieval, electronic adaptation, computer software, or by similar or dissimilar methodology now known or hereafter developed.
The use of general descriptive names, registered names, trademarks, service marks, etc. in this publication does not imply, even in the absence of a specific statement, that such names are exempt from the relevant protective laws and regulations and therefore free for general use.
The publisher, the authors and the editors are safe to assume that the advice and information in this book are believed to be true and accurate at the date of publication. Neither the publisher nor the authors or the editors give a warranty, express or implied, with respect to the material contained herein or for any errors or omissions that may have been made. The publisher remains neutral with regard to jurisdictional claims in published maps and institutional affiliations.

This Springer imprint is published by the registered company Springer Nature Switzerland AG
The registered company address is: Gewerbestrasse 11, 6330 Cham, Switzerland

Preface

Remote sensing observations can close gaps due to information scarcity by complementing ground-based sparse data. Spatial, spectral, temporal, and radiometric characteristics of satellites sensors are most suitable for features identification. The local to global nature and broad spatial scale of remote sensing with the wide range of spectral coverage are essential characteristics, which make satellites an ideal platform for mapping, observation, monitoring, assessing, and providing necessary mitigation measures and control for different related Earth systems processes.

This proceedings volume is based on the best papers accepted for presentation during the 1st Springer Conference of the Arabian Journal of Geosciences (CAJG-1), Tunisia 2018. The book compiles a wide range of topics addressing various issues by experienced researchers mainly from different research institutes in the Mediterranean, MENA region, North America, and Asia.

Main topics include Geoinformatics Applications, Land Use Land Cover Mapping and Change Detection, Emerging Remote Sensing Applications, Rock Formations Soil Lithology Mapping, Vegetation Mapping Impact Assessment, Natural Hazards Mapping and Assessment, Ground Water Mapping and Assessment, Coastal Management Marine Environment, and Atmospheric Sensing.

This volume sheds light on the usage of different remote sensing technologies, mapping the techniques in a geographic information system environment along with some advanced signal processing and deep learning approaches. New emerging sensing platforms addressing groundwater and natural hazards are also discussed along with patterns, mechanisms, and impacts of climate at different spatial domains. Some various case studies are also included where some state-of-the-art tools and algorithms are implemented to analyze some emerging Earth processes and environmental variabilities.

Orange, USA — Hesham M. El-Askary
Daejeon, Korea (Republic of) — Saro Lee
Pasadena, USA — Essam Heggy
Sydney, Australia — Biswajeet Pradhan
July 2018

Acknowledgements

Our appreciation is extended to the authors of the papers for their hard and diligent work and producing high-quality contributions. We would like to thank the reviewers of the papers for their in-depth reviews and great efforts in improving the quality of the papers. Also, thanks are extended to Amjad Kallel who supervised and handled the evaluation process, to Sahbi Moalla who handled the submission and evaluation system for the ten conference proceedings volumes, and the publishing staff of Springer headed by Nabil Khélifi, Senior Editor for their efforts and contributions in completing this conference proceedings volume. All the above-mentioned efforts were very important in making this book a success.

About the 1st Springer Conference of the Arabian Journal of Geosciences (CAJG-1), Tunisia 2018

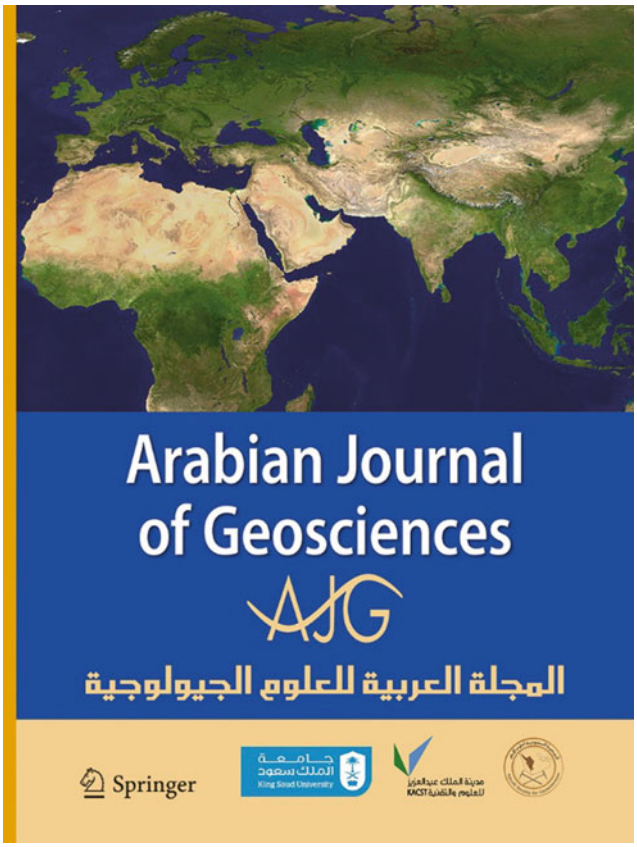

The *Arabian Journal of Geosciences* (AJG) is a Springer journal publishing original articles on the entire range of Earth sciences in partnership with the Saudi Society for Geosciences. The journal focuses on, but not limited to, research themes which have regional significance to the Middle East, the Euro-Mediterranean, Africa, and Asia. The journal receives on average 2000 submissions a year and accepts around 500 papers for publication in its 24 annual issues (acceptance rate 25%). It enjoys the participation of an editorial team of 100 international associate editors who generously help in evaluating and selecting the best papers.

In 2008, Prof. Abdullah Al-Amri, in close partnership with Springer, founded the Arabian Journal of Geosciences (AJGS). In this year, the journal celebrates its tenth anniversary. On this occasion and to mark this event, the Founder and Editor-in-Chief of the AJGS Prof. Al-Amri organized in close collaboration with Springer the 1st Conference of the Arabian Journal of Geosciences (1st CAJG) in Hammamet, Tunisia, from November 12 to 15, 2018 (www.cajg.org).

The conference was an occasion to endorse the journal's long-held reputation for bringing together leading authors from the Middle East, the Euro-Mediterranean, Africa, and Asia who work at the wide-ranging fields of Earth sciences. The conference covered all crosscutting themes of Geosciences and focused principally on the following ten tracks:

- Track 1. Climate, paleoclimate, and paleoenvironmental changes
- Track 2. Geoinformatics, remote sensing, geodesy
- Track 3. Geoenvironmental engineering, geomechanics and geotechnics, geohazards
- Track 4. Geography, geoecology, geoarcheology, geotourism
- Track 5. Geophysics, seismology
- Track 6. Hydrology, hydrogeology, hydrochemistry
- Track 7. Mineralogy, geochemistry, petrology, and volcanology
- Track 8. Petroleum engineering and petroleum geochemistry
- Track 9. Sedimentology, stratigraphy, paleontology, geomorphology, pedology
- Track 10. Structural/petroleum/mining geology, geodynamics, marine geology

The dynamic four-day conference provided more than 450 attendees with opportunities to share their latest unpublished findings and learn the newest geoscience studies. The event also allowed attendees to meet and discuss with the journal's editors and reviewers.

More than 950 short contributing papers to the conference were submitted by authors from more than 70 countries. After a pre-conference peer review process by more than 500 reviewers, 700 papers were accepted. These papers were published as chapters in the conference proceedings by Springer.

The conference proceedings consist of ten edited volumes, each edited by the following group of Arabian Journal of Geosciences (AJGS) editors and other guest editors:

Volume 1. Patterns and Mechanisms of Climate, Paleoclimate, and Paleoenvironmental Changes from Low-Latitude Regions

Zhihua Zhang (AJGS Editor): Beijing Normal University, Beijing, China
Nabil Khélifi (AJGS Editor): Earth Sciences Editorial Department, Springer, Heidelberg, Germany
Abdelkader Mezghani (Guest Editor): Norwegian Meteorological Institute, Norway
Essam Heggy (Guest Editor): University of Southern California and Jet Propulsion Laboratory, Caltech, USA

Volume 2. Advances in Remote Sensing and Geo Informatics Applications

Hesham M. El-Askary (Guest Editor): Schmid College of Science and Technology at Chapman University, USA
Saro Lee (AJGS Editor): Korea Institute of Geoscience and Mineral Resources, Daejeon, South Korea
Essam Heggy (Guest Editor): University of Southern California and Jet Propulsion Laboratory, Caltech, USA
Biswajeet Pradhan (AJGS Editor): University of Technology Sydney, Sydney, Australia

Volume 3. Recent Advances in Geo-Environmental Engineering, Geomechanics and Geotechnics, and Geohazards

Amjad Kallel (AJGS Editor): ENIS, University of Sfax, Tunisia
Zeynal Abiddin Erguler (AJGS Editor): Dumlupinar University, Kutahya, Turkey
Zhen-Dong Cui (AJGS Editor): China University of Mining and Technology, Xuzhou, Jiangsu, China
Ali Karrech (AJGS Editor): The University of Western Australia, Australia
Murat Karakus (AJGS Editor): University of Adelaide, Australia

Pinnaduwa Kulatilake (AJGS Editor): Department of Materials Science and Engineering, The University of Arizona, USA
Sanjay Kumar Shukla (AJGS Editor): School of Engineering, Edith Cowan University, Perth, Australia

Volume 4. Exploring the Nexus of Geoecology, Geography, Geoarcheology, and Geotourism: Advances and Applications for Sustainable Development in Environmental Sciences and Agroforestry Research

Haroun Chenchouni (AJGS Editor): University of Tebessa, Algeria
Ezzoura Errami (Guest Editor): Chouaïb Doukkali University, El Jadida, Morocco
Fernando Rocha (Guest Editor): University of Aveiro, Portugal
Luisa Sabato (AJGS Editor): Università degli Studi di Bari "Aldo Moro", Bari, Italy

Volume 5. On Significant Applications of Geophysical Methods

Narasimman Sundararajan (AJGS Editor): Sultan Qaboos University, Muscat, Oman
Mehdi Eshagh (AJGS Editor): University West, Trollhättan, Sweden
Hakim Saibi (AJGS Editor): United Arab Emirates University, Al-Ain, Abu Dhabi, UAE
Mustapha Meghraoui (AJGS Editor): Université de Strasbourg, Strasbourg, France
Mansour Al-Garni (AJGS Editor): King Abdulaziz University, Jeddah, Saudi Arabia
Bernard Giroux (AJGS Editor): Centre Eau Terre Environnement, Québec, Canada

Volume 6. Advances in Sustainable and Environmental Hydrology, Hydrogeology, Hydrochemistry and Water Resources

Helder I. Chaminé (AJGS Editor): School of Engineering—ISEP, Polytechnic of Porto, Portugal
Maurizio Barbieri (AJGS Editor): University of Rome La Sapienza, Italy
Ozgur Kisi (AJGS Editor): Ilila State University, Tbilisi, Georgia
Mingjie Chen (AJGS Editor): Sultan Qaboos University, Muscat, Oman
Broder J. Merkel (AJGS Editor): TU Bergakademie Freiberg, Freiberg, Germany

Volume 7. Petrogenesis and Exploration of the Earth's Interior

Domenico Doronzo (AJGS Editor): Consejo Superior de Investigaciones Cientificas, Spain
Emanuela Schingaro (AJGS Editor): Università degli Studi di Bari Aldo Moro—UniBa, Italy
John S. Armstrong-Altrin (AJGS Editor): The National Autonomous University of Mexico, Mexico
Basem Zoheir (Guest Editor): Benha University, Egypt and University of Kiel, Germany

Volume 8. Advances in Petroleum Engineering and Petroleum Geochemistry

Santanu Banerjee (AJGS Editor): Indian Institute of Technology Bombay, Mumbai, India
Reza Barati (AJGS Editor): The University of Kansas, Lawrence, KS, USA
Shirish Patil (Guest Editor): Saudi Aramco and King Fahd University of Petroleum and Minerals, Dhahran, Saudi Arabia

Volume 9. Paleobiodiversity and Tectono-sedimentary Records in the Mediterranean Tethys and Related Eastern Areas

Mabrouk Boughdiri (AJGS Editor): University of Carthage, Amilcar, Tunisia
Beatriz Bádenas (AJGS Editor): University of Zaragoza, Zaragoza, Spain
Paul Selden (AJGS Editor): University of Kansas, Lawrence, Kansas, USA
Etienne Jaillard (Guest Editor): Université Grenoble Alpes, France
Peter Bengtson (AJGS Editor): Universität Heidelberg, Heidelberg, Germany
Bruno R. C. Granier (AJGS Editor): Université de Bretagne Occidentale, Brest, France

Volume 10. The Structural Geology Contribution to the Africa-Eurasia Geology: Basement and Reservoir Structure, Ore Mineralisation and Tectonic Modelling

Federico Rossetti (Guest Editor): Università Roma Tre, Roma, Italy
Ana Crespo Blanc (Guest Editor): University of Granada, Spain
Federica Riguzzi (Guest Editor): National Institute of Geophysics and Volcanology, Roma, Italy
Estelle Leroux (Guest Editor): IFREMER, Unité Géosciences Marines, Plouzané, France
Kosmas Pavlopoulos (Guest Editor): Paris Sorbonne University Abu Dhabi, Abu Dhabi, UAE
Olivier Bellier (Guest Editor): CEREGE, Aix-en-Provence, France
Vasilios Kapsimalis (Guest Editor): Institute of Oceanography, Hellenic Centre for Marine Research, Anavyssos, Greece

About the Conference Steering Committee

General Chair

Abdullah Al-Amri: Founder and Editor-in-Chief of AJGS, King Saud University, Saudi Arabia

Conference Supervisor

Nabil Khélifi: Senior Publishing Editor, Springer Middle East and North African Program Springer, a part of Springer Nature, Heidelberg, Germany

Scientific Committee Chair

François Roure: Guest of Editorial Board of AJGS, IFP—Energies Nouvelles, France

Walter D. Mooney: Guest of Editorial Board of AJGS, US Geological Survey Western Region, USA

Local Organization Chair

Mabrouk Boughdiri: Associate Editor of AJGS, University of Carthage, Bizerte, Tunisia

Evaluation Chair

Amjad Kallel: Assistant Editor of AJGS, ENIS, University of Sfax, Tunisia

Publication Chair

Biswajeet Pradhan: Associate Editor of AJGS, University of Technology Sydney, Sydney, Australia

Essam Heggy: Guest of Editorial Board of AJGS, University of Southern California and Jet Propulsion Laboratory, Caltech, USA

Program Chair

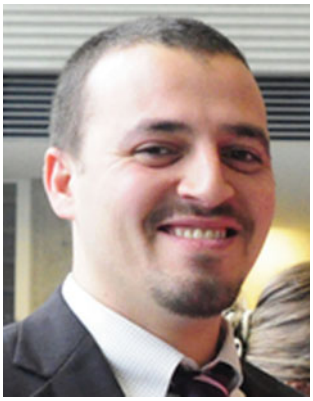

Hakim Saibi: Associate Editor/Assistant Editor of AJGS, United Arab Emirates University, Al-Ain, Abu Dhabi, UAE

Domenico Doronzo: Associate Editor/Assistant Editor of AJGS, Consejo Superior de Investigaciones Cientificas, Spain

Communication Chair

Mohamed Ksibi: Guest of Editorial Board of AJGS, ISBS, University of Sfax, Tunisia

English Language Advisory Committee

Abdelmajid Dammak: ENIS, University of Sfax, Tunisia
Chokri Khalaf: FMS, University of Sfax, Tunisia
Dhouha Mabrouk: FLSHS, University of Sfax, Tunisia
Mohamed Elbahi: ENIS, University of Sfax, Tunisia
Sami Shami: ENIS, University of Sfax, Tunisia
Yasmine Basha: FLSHS, University of Sfax, Tunisia

Conference Manager

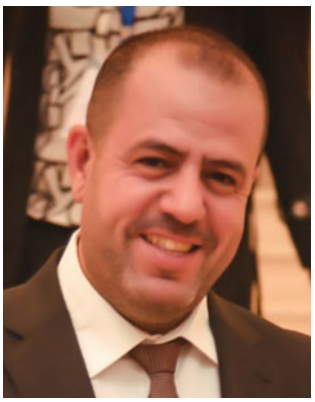

Mohamed Sahbi Moalla: Coordinator of AJGS, ISET, University of Sfax, Tunisia

Contents

About the Editors

Prof. Hesham M. El-Askary received his Ph.D. in Computational Sciences and Informatics from George Mason University in 2004. He is the 2015 recipient of the Chapman University's elite Senior Wang-Fradkin Professorship award. In 2016, he was named as the regional coordinator on a $3 million Euro grant from the European Union's (EU) Horizon 2020. The three-year project, known as GEO-CRADLE, deals with coordinating and integrating state-of-the-art Earth Observation Activities in the regions of North Africa, Middle East and Balkans and Developing Links with GEO-related initiatives toward GEOSS. Through this work, he with the research team were able to deliver the first analytical solar Atlas of Egypt that is now considered to be the official document of the government for solar investment. This work was recently presented at Planet Earth Institute at the Royal Society in London during a seminar that discussed the future of solar energy in Africa. His research interests include dust storms monitoring and detection using different remote sensing technologies as well as studying other extreme events. He is also involved in studying air pollution problems over mega cities due to natural and man-made effects as well as climate change and its impacts on sea level rise and coral reefs for coastal areas. In his research Prof. El-Askary uses earth observations to study the impact of sever dust storms anomalous chlorophyll outbreaks in the marine environment, hurricanes intensification as well as transport of microbes' causing Kawasaki disease outbreaks. Recently, Prof. El-Askary has been focusing on using Earth observations for water resources management and precision agriculture along the sustainable development goals. Prof. El-Askary has published over a 100 refereed research publications, conferences full paper, and book chapters in these research areas. Dr. El-Askary's research has been supported by National Science Foundation, NASA, United States Department of Agriculture and European Union. Dr. El-Askary has received the Saudi Arabia award hosted by the Arab Administrative Development Organization (ARADO) affiliated with the League of Arab states for the best published article in Environmental Management among 150 articles in 2006. He is also a member of the Institute of Electrical and Electronics Engineers (IEEE), AGU, EGU, COSPAR, and Phi Beta Delta Honor Society.

Dr. Saro Lee completed his B.Sc. in Geology (1991), M.Sc. in GIS-based geological hazard mapping (1993) and a Ph.D. in landslide susceptibility mapping using GIS (2000) at Yonsei University in Seoul (Korea). He is currently a Principal Researcher at the Geological Research Division of Korea Institute of Geoscience and Mineral Resources (KIGAM). He is also a Professor at the University of Science and Technology (UST) in Daejeon (South Korea). He started his professional career in 1995 as a researcher at KIGAM. He spent many years as a part-time lecturer in many universities. He carried out many international cooperative research projects in the fields of mineral potential and geological hazard in Brazil, Bhutan, Cambodia, China, Indonesia, Malaysia, Philippines, Thailand, and Vietnam. He also managed several times the Korea International Cooperation Agency (KOICA) International Training Program and gave lectures in the fields of Mineral Exploration and GIS/RS for participants from many countries. His research interest includes geospatial predictive mapping with GIS and RS such as landslide susceptibility, ground subsidence hazard, groundwater potential, mineral potential, and habitat mapping. He has co-authored more than 100 research articles in refereed journals and is an ISI highly cited researcher (ca. 5000 citations, h-index 37). In 2015, Dr. Lee joined the AJGS as an Associate Editor responsible for evaluating submissions in Environmental, Geotechnical and Applied Sciences.

Dr. Essam Heggy is a Research Scientist at the Microwave Systems, Sensors and Imaging Lab (MiXIL), at the Viterbi School of Engineering at the University of Southern California and affiliate of the Rosetta project at the Jet Propulsion Laboratory. Heggy obtained both his M.Sc. and Ph.D. respectively in 1999 and 2002 with distinguished honors from the Paris VI University in France (UPMC-Sorbonne). His research focuses on understanding the water evolution in Earth's arid environments as well as planetary surfaces using radar surface and subsurface characterization methods. His research particularly focuses on understanding volatile evolution in the North African Sahara and Arabian Peninsula, as well as Mars, the Moon, Jovian Icy satellites, and Near-Earth Objects. His work involves probing structural, hydrological, and volcanic elements in terrestrial and planetary environments using different types of radar imaging and sounding techniques as well as measuring the electromagnetic properties of rocks in the radar frequency range. He is currently a member of the science team of the MARSIS instrument aboard the Mars Express orbiter (2003–present), the Mini-SAR experiment aboard Chandrayaan-1, the Mini-RF experiment onboard the Lunar Reconnaissance Orbiter (2008–present), the CONSERT radar experiment aboard the Rosetta mission (2004–present), and the WISDOM GPR onboard ExoMars 2020 Rover (2008–Present). He also edited a special JGR-Planets (AGU) volume on terrestrial and planetary radars. He is on the founding editorial board of the Journal of Arctic Geoscience ARKTOS

(Springer), Geosciences (MDPI), National Geographic and co-chaired several sessions in international conferences and workshops on terrestrial and planetary radar subsurface imaging including AGU, LPSC, and IEEE meetings.

Dr. Biswajeet Pradhan received B.Sc. with honors from Berhampur University (India), M.Sc. from the Indian Institute of Technology (IIT) in Bombay (India), and M.Tech. in Civil Engineering from the IIT in Kanpur (India) and Dresden University of Technology (Germany). He received Ph.D. in GIS and Geomatics Engineering from the University Putra Malaysia. From 2008 to 2010, he was a recipient of the Alexander von Humboldt Research Fellowship from Germany. In 2011, he received his Habilitation in Remote Sensing from Dresden University of Technology (Germany). Since March 2015, he is serving as the Humboldt Ambassador Scientist for the Alexander Von Humboldt Foundation (Germany). He is also the recipient of the prestigious German Academic Exchange Research (DAAD) Fellowship Award, Saxony State Fellowship from 1999 to 2002, Keith Atherton Research Award, and Georg Forster Research Award from German Government. He is currently Faculty Member of Department of Civil Engineering, University Putra Malaysia. He has more than 16 years of teaching, research, consultancy, and industrial experience. Out of his more than 450 articles, more than 276 have been published in science citation index (SCI/SCIE) technical journals. He has written two books in GIS data compression and disaster management and edited three volumes, and written 12 book chapters. He has recently submitted two new books for publication with Springer. He specializes in Remote Sensing, GIS application, and soft computing techniques in natural hazard and environmental problems. His published work has been widely cited by his peers with more than 4800 citations in SCOPUS database allowing him to reach an h-index of 47. He has completed 20 research projects. Most recently, he has been selected as a 2016 Web of Science High Cited Researcher. Dr. Pradhan is a member of many professional bodies such as Committee of Space Research (COSPAR), Senior Member of IEEE, United Nations Outer Space Research Programme (UNOOSA), and many more. He sits as a board member of many national programs in Malaysia and Southeast Asia. He is a regular reviewer for many international bodies alike Dutch Research Council, European Science Foundation, Austrian Science Foundation, Research Council UK (RCUK), and many more. He has been also active with teaching and supervising of many Ph.D., MSc., and undergraduate students. Dr. Pradhan has widely traveled abroad visiting more than 55 countries to present his research findings (e.g., Germany, USA, Netherlands, UK, Switzerland, Turkey, South Korea, Japan, Indonesia, Thailand, and many more). In 2013, Dr. Pradhan joined the AJGS as an Associate Editor responsible for evaluating submissions in the fields of Environmental, Geoinformatics, and Geotechnical Sciences.

Part I
Keynote

Strong Interactions Indicated Between Dust Aerosols and Precipitation Related Clouds in the Nile Delta

Hesham M. El-Askary, Wenzhao Li, Maram El-Nadry, M. Awad, and Alaa R. Mostafa

Abstract

Atmospheric aerosol particles affect the formation of precipitation through influencing on microphysical properties of water and ice clouds. In early May of 2018, we observed the coincident of strong dust and rain events in the Nile Delta area. We also used Hybrid-Single Particle Lagrangian Integrated Trajectory (HYSPLIT) model, NMMB/BSC-dust model and NOAA-18 Cloud Height product to validate this same movement of dust and clouds that induced precipitation. In addition, Niño 3.4 index with historical rain and dust anomalous events during 1980–2017 were analyzed to reveal the relationship between these events and global climate system. The results revealed an obvious matching in both intensity and movement for both dust and precipitation events in early May 2018. Extreme precipitation anomalies during 1990–1999 occurred in company with positive Niño indices and less dust events.

Keywords

Precipitation • Dust • Nile delta • Climate change • AERONET

1 Introduction

The mass of aerosols in the atmosphere accounts for only one billionth of the total mass of the atmosphere. However, aerosols have important effects on global energy and water cycle, particularly through its interactions with clouds [2, 4]. The increase in aerosols leads to an increase in cloud droplet particle concentration and a decrease in cloud droplet radius, which changes the radiation characteristics of the cloud, leading to an increase in cloud albedo, known as the Twomey effect [8]. Meanwhile, it also adjusts the liquid water content and cloud thickness, reduces precipitation efficiency and increases cloud life time, called the Albrecht effect [1]. As the main cloud system of precipitation, convective cloud systems are the main carriers for the exchange of water vapor, trace gases and aerosols in the troposphere and are more sensitive to atmospheric aerosols. By studying the interaction between clouds and aerosols, it helps to gain a better knowledge the interactions between aerosols and climate.

In this research, we observed and studied strong dust events and precipitation coincided in the Nile Delta during early May of 2018. Strong interactions between these two factors are implied; analysis also reveals their relation with climate changes.

2 Data and Methods

Aerosol optical depth (AOD) observations and analysis data during May 2018 were obtained from AERONET Cairo station. TRMM precipitation data for the Nile delta were studied for the same period. The combination of Integrated Multi-satellite Retrievals for GPM (IMERG) rain rate, MODIS Terra AOD and VIIRS SNPP True Color images were displayed for North Africa during May 3rd to 6th. In addition, the HYSPLIT air parcels trajectory analysis for Cairo station were compared with the movement of dust event (simulation from NMMB/BSC-Dust model) and precipitation-induced cloud (NOAA-18 cloud height product). Furthermore, the normalized AOD and rain anomalies (Z-score calculated from MERRA-2 dataset) for this region were calculated and compared with Niño 3.4 index during 1980–2017.

H. M. El-Askary (✉) · W. Li
Chapman University, Orange, CA 92866, USA
e-mail: elaskary@chapman.edu

H. M. El-Askary · M. El-Nadry · M. Awad · A. R. Mostafa
Department of Environmental Sciences, Faculty of Science, Alexandria University, Moharem Bek, Alexandria, 21522, Egypt

© Springer Nature Switzerland AG 2019

H. M. El-Askary et al. (eds.), *Advances in Remote Sensing and Geo Informatics Applications*, Advances in Science, Technology & Innovation, https://doi.org/10.1007/978-3-030-01440-7_1

3 Results

The events of dust and precipitation in Nile Delta are presented in the Fig. 1a. The severe dust event (AOD > 3, coarse) reached Cairo on May 3rd and May 4th, with following events on 10th, 22nd of the same month. Simultaneously, the precipitation also occurred in the same region on May 3rd, 4th, 6th, 10th and 23rd. On the right side of Fig. 1a, strong dust events coincided with precipitation in the black squared region, with high AOD value. The path of the cloud movement (middle Fig. 1b) and dust (right Fig. 1b) matches the output of HYSPLIT trajectory model. The relationship between climate change between dust and precipitation anomalies is shown in Fig. 1c. It is worth noting that during the period of 1990 to 1999, the severe precipitation anomalies (Z-score > 3) coincided with positive Niño 3.4 index and negative dust AOD anomalies, indicating Nile Delta tends to have more rains during the El Niño years.

4 Discussion

Dust aerosols, with larger size and optical thickness, can change the radiation balance of the earth-atmosphere system through absorbing and scattering of solar radiation. Meanwhile, they can also alter the cloud microphysics and precipitation processes as cloud condensation nuclei (CCN) and atmospheric ice nuclei (IN) [5, 6]. Dust aerosol has an important contribution to the formation of ice clouds and the transition of vapor phase in clouds revealed in recent studies. Research also showed that the air masses form could freeze in −5 to −9 °C, which demonstrated that dust aerosols could be used as effective IN for the cloud process [7]. A recent study proved that Large amounts of aerosol particles in the atmosphere can increase the lifespan of large storm clouds by delaying rainfall, making clouds larger and extending their life span, and generating more extreme storms when the rain finally comes [3]. However, dust aerosols' positive impact on precipitation does not reflect on Fig. 1c, where it indicates the negative relationship between dust and precipitation anomalies as to the Niño indices. This may be explained by its difference in scales (regional versus global) and dust-related impact on the cloud (microphysics reactions vs radiative effects).

5 Conclusion

In this research, with the help of data resources from both in situ (AERONET) and remote sensing (NOAA-18, MODIS TERRA and TRMM) observations, as well as modeling (HYSPLIT and NMMB/BSC-dust) and reanalysis data (MERRA-2), we observed and studied the interactions between dust aerosols and precipitation taking place during early May 2018. We also analyzed their relationship to global climate indices (Niño 3.4), showing that extreme precipitation events in Nile Delta only occurred in positive Niño years and mostly coincided with less dust activities. It is noteworthy that even the positive effect exists between dust aerosols associated with raining in regional system such as Nile Delta, the complexity of global climate system could bring more uncertainties in explaining precipitation changes. Addressing more detailed mechanisms for interpreting the effects of dust aerosols in radiation flux, microphysical interaction and sensitivity to climate change will be investigated in future research.

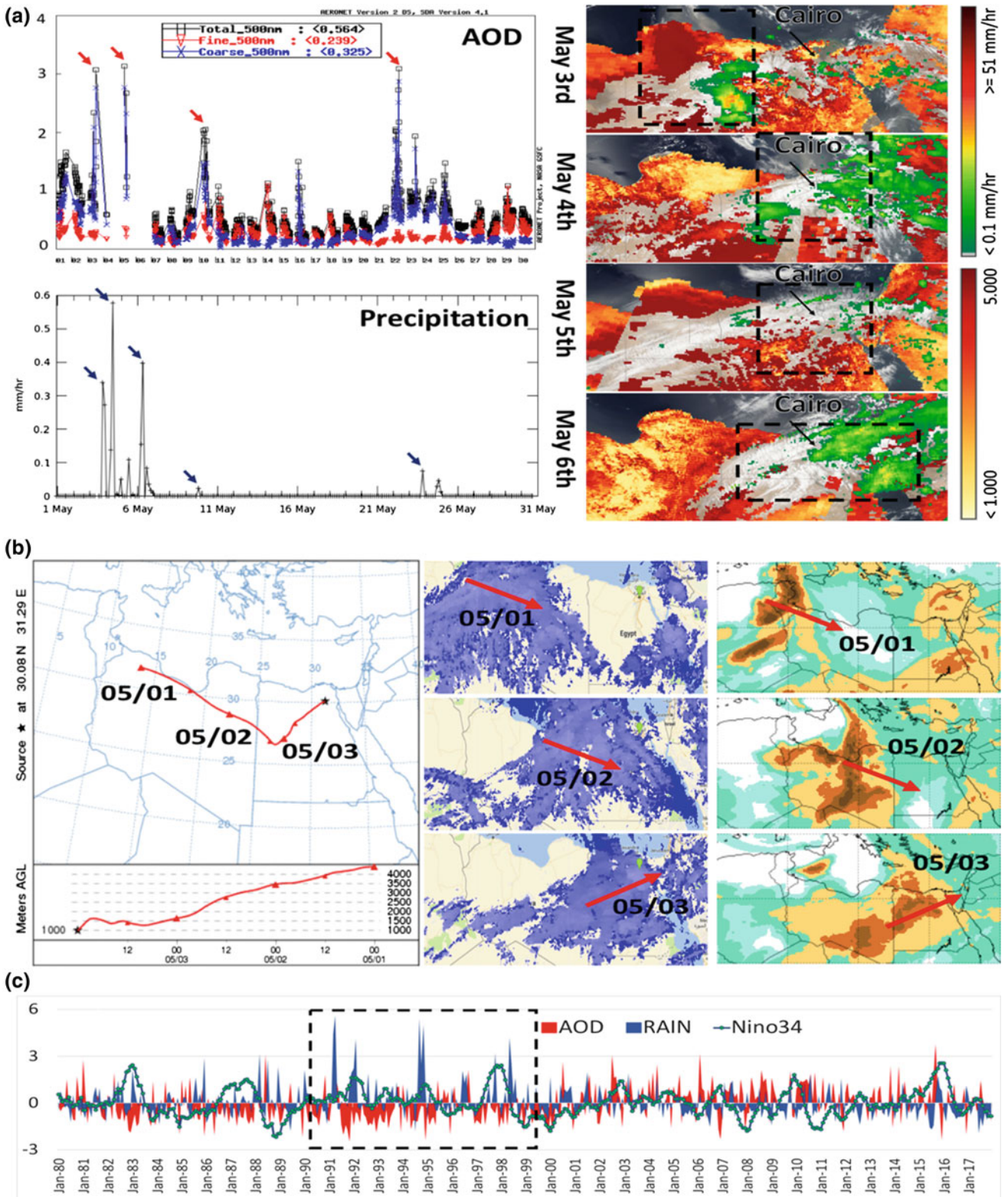

Fig. 1 **a** Aerosol records of AERONET Cairo station, and TRMM records of the same region (Left); MODIS TERRA AOD and IMERG Rain Rate in North Africa during May 3rd–6th (right). **b** 3-day HYSPLIT air parcels trajectory of for Nile Delta (left); Cloud movement of during May 1st–3rd (middle); Dust movement of NMMB/BSC model of same period (right). **c** Niño 3.4 index, MERRA-2 Dust AOD and Rain Z-score during 1980–2017

References

1. Albrecht, B.A.: Aerosols, cloud microphysics, and fractional cloudiness. Science **245**, 1227–1230 (1989)
2. Breon, F.-M.: Aerosol effect on cloud droplet size monitored from satellite. Science **295**, 834–838 (2002)
3. Chakraborty, S., Fu, R., Massie, S.T., Stephens, G.: Relative influence of meteorological conditions and aerosols on the lifetime of mesoscale convective systems. Proc. Natl. Acad. Sci. **113**, 7426–7431 (2016)
4. DeMott, P.J., Sassen, K., Poellot, M.R., et al: African dust aerosols as atmospheric ice nuclei: African dust aerosols as ice nuclei. Geophys. Res. Lett. **30** (2003)
5. El-Askary, H., Li, J., Li, W., et al.: Impacts of aerosols on the retreat of the sierra nevada glaciers in California. Aerosol. Air Qual. Res. **18**, 1317–1330 (2018)
6. Graf, H.-F.: Atmospheric science: the complex interaction of aerosols and clouds. Science **303**, 1309–1311 (2004)
7. Sassen, K.: Indirect climate forcing over the western US from Asian dust storms: indirect climate forcing from Asian dust storms. Geophys. Res. Lett. **29** 103-1–103-4 (2002)
8. Twomey, S.: The influence of pollution on the shortwave albedo of clouds. J. Atmospheric Sci. **34**, 1149–1152 (1977)

Exploring Desert Aquifers and Polar Ice Sheets and Their Responses to Climate Evolution: OASIS Mission Concept

Essam Heggy, Paul A. Rosen, Richard Beatty, Tony Freeman, Young Gim and The OASIS Team

Abstract

The Orbiting Arid Subsurface and Ice Sheet Sounder (OASIS) mission concept is a single instrument, small-size, venture-class mission directly aimed at exploring the signatures of climate change in both cold and warm deserts regions on Earth: the polar ice sheets and the hyper-arid deserts (Fig. 1). OASIS has two well-defined science objectives. The first is to determine the thickness, inner structure, and basal boundary conditions of Earth's ice sheets to understand their dynamics and improve models of current and future ice sheet response to climate change and, hence, to better constrain ice sheet contribution to sea level rise. The second objective is to perform detailed mapping of the spatial distribution of shallow (<100 m deep) aquifers in North Africa and the Arabian Peninisula to understand groundwater dynamic in fossil aquifers to assess their current response to climatic stresses and paleoclimatic conditions that formed them. These two mission objectives are achieved using a sounding radar operating at 45 MHz center frequency with 10 MHz bandwidth. The proposed OASIS radar would be able to map only the upper water table of fossil aquifer systems. This proceeding has been updated from the proceeding published in IEEE-IGARSS (2013).

Keywords

Climate change • Groundwater • Polar Ice Sheets • Radar Sounding • Sea-level rise

1 Mission Concept

The OASIS mission concept can achieve the two above-mentioned objectives by orbiting the Earth for 18 months in low Earth sun-synchronous orbit, which decays gradually as the mission progresses achieving unprecedented systematic, dense coverage, with orbit track spacing ranging from 5 km at the equator to several hundred meters when closest to the poles. The mission concept is optimized for these measurements, and can take advantage of reduced solar activity at the end of 2016 and by operating in the 4 am early morning hours to open a window through the Earth's ionosphere for the low-frequency radar waves. Our preliminary analysis shows that an 18-month mission could be achieved near solar minimum even with a high-drag spacecraft with no propulsion. However, our concept includes a butane propulsion system that would provide orbit adjustment and reboost to meet mission lifetime requirements and avoid the higher drag and environmental effects at lower orbits. The OASIS payload could be hosted on a 50 kg/50 W-payload class spacecraft bus (as shown in Fig. 2) that can be launched by Pegasus XL.

2 Science Objectives

OASIS is the first mission concept to directly explore the signatures of climate change in the subsurface of two of the least well understood desertic regions on earth: The polar ice sheet and the hyper-arid deserts. OASIS has seven science objectives that address key questions on ice sheets dynamics,

Essam Heggy: Presenting Author

E. Heggy (✉)
Viterbi School of Engineering, University of Southern California, 3737 Watt Way, Los Angeles, CA, USA
e-mail: heggy@usc.edu

E. Heggy
Jet Propulsion Laboratory, Caltech, 3737 Watt Way, Pasadena, CA, USA

P. A. Rosen · R. Beatty · T. Freeman · Y. Gim
The OASIS Team
NASA's Jet Propulsion Laboratory, Caltech, 3737 Watt Way, Pasadena, CA, USA

© Springer Nature Switzerland AG 2019

H. M. El-Askary et al. (eds.), *Advances in Remote Sensing and Geo Informatics Applications*, Advances in Science, Technology & Innovation, https://doi.org/10.1007/978-3-030-01440-7_2

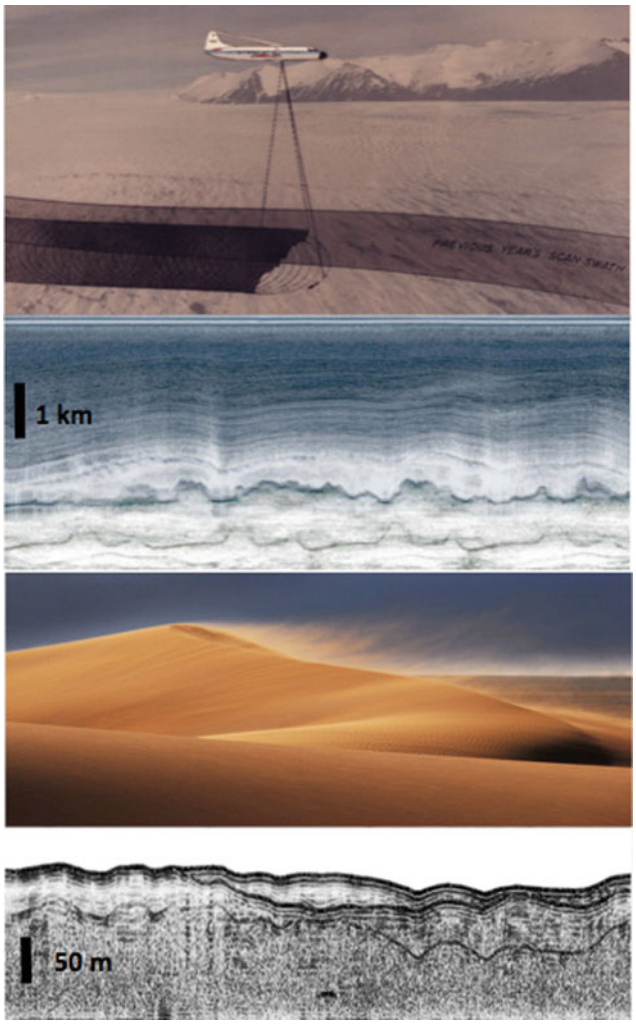

Fig. 1 Low-frequency airborne radar subsurface mapping of the bed topography of the Antarctic ice sheets 2.5 km deep (top two) and of the aeolian dunes bottoms few tens of meters deep in the Kuwait desert (bottom two). OASIS will provide similar data from orbit for large regions that exceed airborne coverage capabilities

and desert hydrology and paleoclimate questions. These objectives are met by OASIS observations over Antarctica, Greenland, North African Sahara, and the Arabian Peninsula. The primary data to be acquired are radar profiles that show reflections from the surface, internal layers, and the basal interface where signal losses are not greater than the available radar dynamic range. These data are normally viewed as a "2D-radargram" as shown in Fig. 1, with one axis in the along-track direction and the other axis in time delay, essentially a 10 m vertical resolution cross section.

Our science objectives can be classified under two categories: **(1) Ice Sheets Science Objectives**: (A) Measure the ice thickness, stratigraphy, and basal characteristics of the polar ice sheets, including large-scale topography, roughness, and hydraulic gradients. (B) Identify regions of past flow reorganization, and constrain age-depth structure within the ice sheets. (C) Reassess current state and discharge rates of polar ice sheets. (D) Integrate ice thickness, basal characteristics and internal stratigraphy within ice flow models to assess catchment-scale sensitivity of ice sheets and their potential contribution to sea level rise. **(2) Desert Hydrology Science Objectives**: (A) Measure the depth of the water table in shallow aquifers and its spatial variability. (B) Identify hydraulic gradients and geologic structures conducive to, or hindering, the recharge, flow, and discharge of groundwater. (C) Combine OASIS observations with the available in situ geophysical datasets for the Saharan aquifers to provide insights into their hydrogeologic evolution. The outcome of the mission would provide the science community with the first comprehensive and well-positioned map products of ice sheet thickness and basal topography, as well as the first detailed regional maps of the shallow aquifers in the North African Sahara and the Arabian Peninsula deserts.

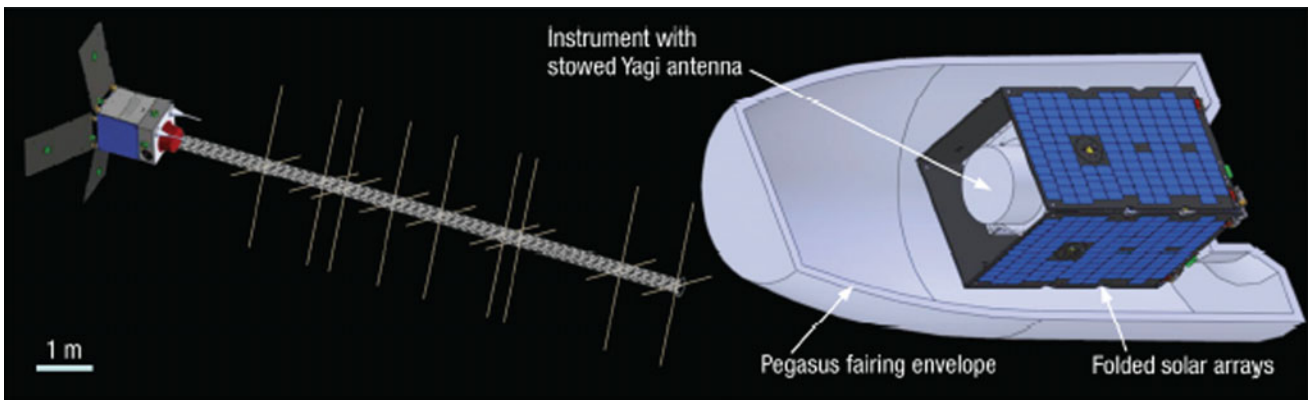

Fig. 2 OASIS Sounding radar and its 11-m deployable Yagi antenna integrated on a 50 kg payload bus and its accommodation onboard the Pegasus XL fairing envelope

3 The Low Frequency Sounding Radar

The factors that influence our radar design are: (1) the surface SNR that allow deep penetration in ice and desert; (2) the range-bandwidth of the radar that addresses the science resolution requirements of 10 m (in the subsurface), (3) low off-nadir surface scattering, constrained by interaction of the radar wave with the ionosphere; and (4) radar signal polarization that also derives from ionospheric propagation constraints. The radar parameters summarized in Table 1, are the result of a number of trade studies, including instrument and mission design parameters, to achieve a robust design: (1) *Center Frequency*: We chose a center frequency of 45 MHz, approximately 10 times higher than the Earth's night-time maximum plasma frequency, to be as low as possible for subsurface penetration without suffering excessive Earth ionospheric delay, dispersion and loss. (2) *Spatial Resolution*: To meet the vertical resolution requirement of 10 m in ice and dry sand, we have designed the radar electronics subsystems to have a 10-MHz bandwidth. To achieve the 1 km along-track resolution requirement and reduce the data volume, we will use a MARSIS-type on-board processing design of summing radar pulses in the frequency domain to a scale over which the nadir signal is coherent, i.e., the Fresnel Zone. This is also within the coherence scale length for the ionosphere at 45 MHz. (3) *Polarization*: To avoid Faraday rotation effects on linearly polarized waves, we will transmit a circularly polarized waveform and receive the opposite sense polarization. We have also investigated the degree of distortion in a circularly transmitted wave when Earth magnetic field is perpendicular to the propagation direction. The maximum distortion from circularity occurs near the geomagnetic equatorial regions and its magnitude is less than 1.5°; consequently, there will be little loss in the received power due to a circular to elliptic polarization change.

Four factors affect the science returns and influence our mission and instrument design: (1) penetration depth variability, (2) the effects of propagation through the ionosphere, (3) the ability to resolve subsurface features from clutter, and (4) the effect of electromagnetic interference on the surface SNR.

4 Compelling Nature of the Mission Concept

Understanding the impact of climate change on sea level and groundwater resources has a direct effect on human populations around the world. ***For Ice Sheets***: Glaciers and ice sheets modulate global sea level by storing water deposited as snow on the surface and by discharging water back into the ocean through melting and iceberg calving. Only recently have we recognized that the size of this frozen reservoir can change quickly, as demonstrated by the rapid thinning of several Glaciers in Greenland and Antarctica [2–5]. Current glaciological dynamical models have been unable to predict these events, due in part to major gaps in our knowledge of ice sheet properties. A fundamental goal of OASIS is to substantially improve our knowledge of ice sheet thickness and basal topography. Improved knowledge of these boundary conditions will better quantify current ice flux and enhance our ability to predict future ice sheet contributions to

Table 1 Summary of the OASIS radar characteristics as compared to MARSIS and SHARAD

Specification	OASIS	MARSIS	SHARAD
DC power (Watt)	64	50	25
Antenna length (m)	10	40	10
Antenna type	Cross Yagi	Dipole	Dipole
Polarization of transmitted wave	Circular	Linear	Linear
Center frequency (MHz)	45	1–5	20
Bandwidth (MHz)	10	1	10
Peak radiated power (Watt)	100	5	10
Exciter type	Chirp	Chirp	Chirp
PRF (Hz)	1200	127	700
ADC bits	12	8	8
Sampling scheme	Direct	Down conversion	Direct
FFT length	1024	512	None
On-board process	Doppler tillering/Pre-summing	Doppler filtering/Pre-summing	Pre-summing
Vertical resolution (m)	10	100	10
Spatial resolution (km)	1	3	0.3
Data rale (kbps)	582	15–30	2200

sea level. ***Desert Environments***: Hyper-arid environments represent ~10% of the Earth's surface, but are poorly studied with regard to climate change. Yet water scarcity and quality, drastic changes in rainfall, flash floods, high rates of aquifer depletion, and accelerated desertification are all signs that suggest substantial large-scale climatic variability in those areas [6], and the variability can be correlated to global change [1]. With this mission's proposed ability to map and characterize groundwater depth and hydraulic heads on a large scale and at high resolution in desert environments, OASIS will improve current understanding of Earth's paleo-environment in terms of geographic variations in precipitation over extended epochs, groundwater inventories, dynamics and improved models of the evolution of Earth's water cycle. 5. Aknowledgements: This proceeding has been published in the 2013 IEEE-IGARSS proceedings and the preface of the Euro-Mediterranean Journal for Environmental Integration, it is added to this volume to support the discussion on future groundwater remote sensing experiments for arid areas held at the CAJG conference. The purpose is to have manuscripts associated to large-scale groundwater mapping techniques associated to groundwater case studies performed in arid areas.

Acknowledgements This proceeding has been published in the 2013 IEEE-IGARSS proceedings and the preface of the Euro-Mediterranean Journal for Environmental Integration, it is added to this volume to support the discussion on future groundwater remote sensing experiments for arid areas held at the CAJG conference. The purpose is to have manuscripts associated to large-scale groundwater mapping techniques associated to groundwater case studies performed in arid areas.

References

1. Maliva, R., Missimer, T.: Arid Lands Water Evaluation and Management. Springer, New York, USA. https://doi.org/10.1007/978-3-642-29104-3 (2012)
2. Rignot, E.: Changes in ice dynamics and mass balance of the Antarctic ice sheet. Phil. Trans R. Soc. A **364**(1844), 1637–1655 https://doi.org/10.1098/rsta.2006.1793. Royal-Society Discussion Meeting on Evolution of the Antarctic Ice Sheet, London, England, 17–18 Oct 2005 (2006)
3. Rott, H., Rack, W., Skvarca, P., De Angelis, H.: Northern Larsen Ice Shelf, Antarctica: further retreat after collapse. Ann. Glaciol. **34**, 277–282 (2002). https://doi.org/10.3189/172756402781817716
4. Scambos, T., Bohlander, J., Shuman, C., Skvarca, P.: Glacier acceleration and thinning after ice shelf collapse in the Larsen B embayment. Antarctica. Geophys. Res. Lett. **31**(18), 1–4 (2004). https://doi.org/10.1029/2004GL020670
5. Thomas, R., Frederick, E., Li, J., Krabill, W., Manizade, S., Paden, J., Sonntag, J., Swift, R., Yungel, J.: Accelerating ice loss from the fastest Greenland and Antarctic glaciers. Geophys. Res. Lett. **38** (L10502), 1–6 (2011)
6. Wagner, W.: Ground Water in the Arab Middle East. Springer, Heidelberg, Germany. https://doi.org/10.1007/978-3-642-19351-4 (2011)

Artificial Intelligence and Spatial Modelling in Natural Hazards and Environmental Applications

Biswajeet Pradhan

Abstract

Modeling and predicting geohazards is extremely difficult due to their complex behavior in the real-world. In fact, several aspects of these environmental applications are considered in computer-based modeling to accurately estimating real-world phenomena. Till date, none of the proposed methods have reached to zero uncertainties or errors to recognize the entire disaster's events. Globally, many people have lost their lives due to various types of natural hazards. Therefore, it is important to detect, monitor and predict them to protect the inhabitants against the potential natural hazards that threaten human lives and properties. Recently, artificial intelligent (AI) methods have received a great deal of attraction due to their precision to model the complex problems such as natural hazards. AI can see different aspects of a complex problem with sufficient iteration and details. In recent years, implementation of AI models coupled with geospatial information systems (GIS) are the most efficient and accurate approach to model natural disasters i.e. flooding, earthquake, landslides, forest fire and drought rather than other existing methods. This gives an insight into the ability of applied AI models in some natural hazards applications.

Keywords

Artificial intelligence • Geospatial information systems • Geohazard • Modelling

1 Introduction

Complex systems like natural hazard modeling require a set of reasoning mechanism to address spatial information in database management systems [1]. There are always challenges with the amount of uncertainty for natural systems with a high dynamic that requires intelligent decision-making provision as well as geographic information systems (GIS). Recently, many geoscientists have commenced non-parametric techniques with the help of artificial intelligence (AI) that can explain and model environmental issues [2, 3].

Given the intrinsic nature of the natural geospatial phenomenon, it is logical for such a modeling to be carried out in a geographical information system platform. Over the past ten years, AI has led to many practical problems. Many of these developments in AI are essentially generally applicable to the GIS domain [3, 4].

Artificial Intelligent (AI) models empower geospatial ecosystem by providing near real-time human level perception; integrate into analytical workflows and driving data exploration and visualization the entire process of creating scalable insights from large amounts of data. Such machines will be able to 'understand' geospatial information themselves with deep learning methods, able to self-obtain geospatial information from their surroundings as per required to do their jobs, all processing them in real-time. This is truly an extraordinary age in the computing sense. With efficient computing performance, machines are well suited to solving simple tasks using fixed programming rules, however, when problems get complicated, machines have trouble understanding specific situations, and adapting to new situations. Therefore, artificial intelligence aims to improve machines ability to solve complex problems like a human can do [4–6].

In this paper, some state-of-the-art latest models which are commonly used for solving natural problems using artificial intelligence and geographical information systems

B. Pradhan (✉)
Faculty of Engineering and IT, Centre for Advanced Modelling and Geospatial Information Systems (CAMGIS), University of Technology, Sydney, Ultimo, NSW 2007, Australia
e-mail: Biswajeet.Pradhan@uts.edu.au

© Springer Nature Switzerland AG 2019

H. M. El-Askary et al. (eds.), *Advances in Remote Sensing and Geo Informatics Applications*, Advances in Science, Technology & Innovation, https://doi.org/10.1007/978-3-030-01440-7_3

were reviewed. The author summarized the related discussions of AI and GIS and identified the steps and directions for research on natural hazards and environmental applications.

2 Methods

Nowadays, AI has been studied as a collection of advanced programming techniques. The essence of intelligence by building computer systems and using these insights to solve real-world issues such as natural hazard forecasting, environmental modeling, and risk simulation. From this perspective, the AI seeks to develop systems that try to imitate human intelligence without claiming that the relevant processes are perceived. Technically speaking, AI is a branch of computer science whose purpose is to simulate the process of thinking human beings [4].

AI can develop a multicriteria technology for building expert systems in the real world. It computes, learn and ask questions about whether a machine can properly consider its reason and what to consider as a trial [3]. AI replicates the human brain, can do many tasks efficiently and makes machines smarter, thus performing complex tasks with easier instructions given by the analyst. It also can learn from data without the need for having prior knowledge about that data and who collected them and how they were captured. AI has the potential of combining data from different sources and extracting knowledge that is useful for making rapid yet effective decisions [7].

AI has various sub-branches and advanced algorithms used in natural hazard modeling [8], for instance: Machine Learning (ML) refers to the techniques involved in dealing with vast data in the most intelligent fashion to derive actionable insights. Statistics is that branch of mathematics which utilizes data, either of the entire population or a sample drawn from the population to carry out the analysis and present inferences. Data Mining deals with searching specific information and ML solely concentrates on performing a given task. Deep Learning (DL) is associated with a machine learning algorithm e.g. Neural Network (NN) which uses the concept of a human brain to facilitate the modeling of arbitrary functions.

3 Results

The AI Methods applied to natural hazards and environmental modelling are: Artificial Neural Networks (ANN), Fuzzy Logic (FL), Adaptive Network-based Fuzzy Inference System (ANFIS), Support Vector Machine (SVM), Decision Tree (DT), Random Forest (RF), Logistic regression (LR), Bagging and Boosting methods and many others.

In natural hazard and environmental studies, traditional AI methods such as SVM, ANN, and DT have been widely used, however, new AI methods such as Recurrent Neural Networks (RNN), and Convolutional Neural Networks (CNN), or the ensemble of these models are rarely applied. Implementation of AI using GIS platform for natural hazards and environmental disasters offers a perfect system to increase accuracy and efficiency (see Fig. 1).

In a very recent paper by [9], they applied ANN techniques for urban earthquake vulnerability Assessment [9]. Kernel Logistic Regression (KLR) and Alternating Decision

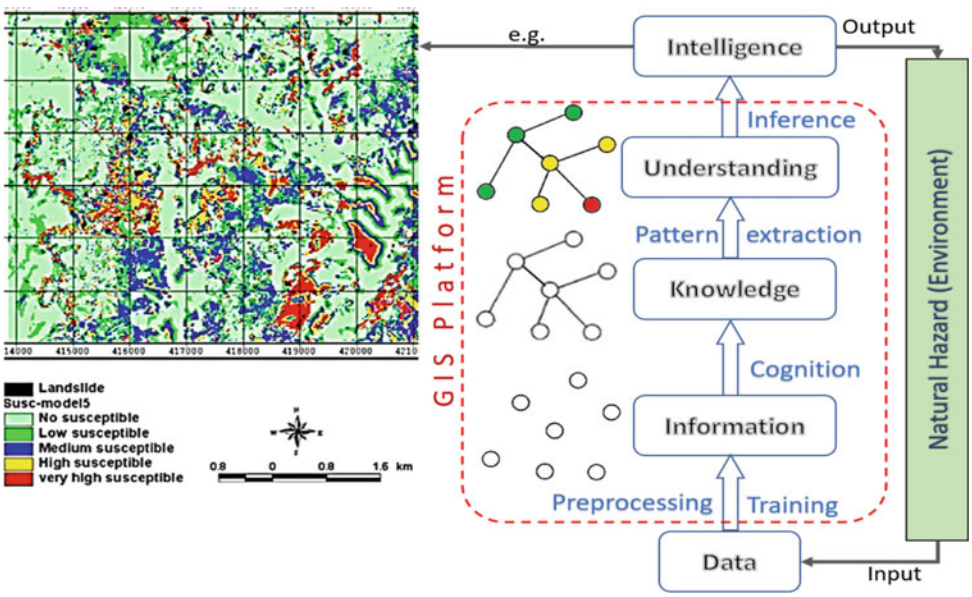

Fig. 1 The process of converting raw data to decision-making through the various levels of the artificial intelligent geospatial modeling system

Tree (ADT) were applied in landslide susceptibility mapping at China with high accuracy [7]. Different kernel types of SVM ensemble with LR have been investigated over several study areas to model the flood susceptibility to achieve the most calibrated flooding scenario [10, 11]. A hybrid AI method is proposed for the modeling of forest fire probability. In this approach, a Neural Fuzzy inference system (NF) was used to model the forest fire susceptibility [12].

4 Conclusion

AI is gaining immense popularity in many fields of natural hazard applications using remote sensing and GIS platforms. Compared with other traditional methods, AI can achieve higher accuracy and efficiency in most environmental applications. One of the main reasons for this rise in using AI is because of big data and computing performance become more powerful approaches.

As these frontier technologies continue to transform industries, I wonder what it hides for geospatial community. The geospatial framework has a vast amount of data hence, AI can help automate the extraction of information from these visual data-sets, something that was not possible before.

Integrating GIS and AI in natural hazard applications proposes a potential machine to cut the cost of spatial analyses by dropping the amount of data interpreted in time. This procedure consequences the output from a small area that can be transferred to a larger area accurately without extra time or re-data collection.

However, the potential of AI using GIS in geo-hazards domain has not yet been fully accomplished. On the one hand, both disciplines are divided into analytical topics; however, most GIS applications are desirable to carry out AI-guided tools using the standard commercial GIS package.

References

1. Ozesmi, S.L., Ozesmi, U.: An artificial neural network approach to spatial habitat modelling with interspecific interaction. Ecol. Model. **116**, 15–31 (1999)
2. Wang, Y., Rizos, C., Ge, L., Anner, M., Dwyer, M.: Distributed artificial intelligence in GIS—geolet: a distributed geo-spatial information retriever. J. Spat. Sci. **50**(2), 37–50 (2005)
3. Voženílek, V.: Artificial intelligence and GIS: mutual meeting and passing. In: INCOS'09. International Conference on Intelligent Networking and Collaborative Systems, 2009, pp. 279–284. IEEE (2009)
4. Al-Bastaki, Y.A.L.: GIS image compression and restoration: a neural network approach. Inf. Technol. J. **5**(1), 88–93 (2006)
5. Beres, M., Foresti, L., Tapia, R., Kanevski, M.: Frost risk mapping using neural networks and GIS decision models. Geophys. Res. Abstracts **10** (2008)
6. Sezer, E.A., Pradhan, B., Gokceoglu, C.: Manifestation of an adaptive neuro-fuzzy model on landslide susceptibility mapping: Klang valley, Malaysia. Expert Syst. Appl. **38**(7), 8208–8219 (2011)
7. Hong, H., Pradhan, B., Xu, C., Bui, D.T.: Spatial prediction of landslide hazard at the Yihuang area (China) using two-class kernel logistic regression, alternating decision tree and support vector machines. Catena **133**, 266–281 (2015)
8. Bui, D.T., Tuan, T.A., Klempe, H., Pradhan, B., Revhaug, I.: Spatial prediction models for shallow landslide hazards: a comparative assessment of the efficacy of support vector machines, artificial neural networks, kernel logistic regression, and logistic model tree. Landslides **13**(2), 361–378 (2016)
9. Alizadeh, M., Ngah, I., Hashim, M., Pradhan, B., Pour, A.B.: A hybrid analytic network process and artificial neural network (ANP-ANN) model for urban earthquake vulnerability assessment. Remote Sens. **10**(6) (2018)
10. Tehrany, M.S., Pradhan, B., Mansor, S., Ahmad, N.: Flood susceptibility assessment using GIS-based support vector machine model with different kernel types. Catena **125**, 91–101 (2015)
11. Mojaddadi, H., Pradhan, B., Nampak, H., Ahmad, N., Ghazali, A. H.B.: Ensemble machine-learning-based geospatial approach for flood risk assessment using multi-sensor remote-sensing data and GIS. Geomatics Nat. Hazards Risk **8**(2), 1080–1102 (2017)
12. Bui, D.T., Bui, Q.T., Nguyen, Q.P., Pradhan, B., Nampak, H., Trinh, P.T.: A hybrid artificial intelligence approach using GIS-based neural-fuzzy inference system and particle swarm optimization for forest fire susceptibility modeling at a tropical area. Agricult. Forest Meteorol. **233**, 32–44 (2017)

Part II
Geoinformatics and Applications

Visualization of Subsurface Data Using Three-Dimensional Cartograms

Ziqiang Li and Saman A. Aryana

Abstract

A three-dimensional cartogram is a thematic 3D map on which the volume of each region is linearly proportional to an extensive property enclosed within. This work formulated a 3D cartogram using a linear diffusion process. The 3D cartogram algorithm may be applied to a uniform Cartesian grid such that the distribution of the property of interest, such as the hydrocarbon pore volume in each cell, is equalized throughout the transformed domain. The spatial distortion of the grid cells serves as the qualitative indicator of this property, and the color may be used to visualize the spatial distribution of another property, such as permeability. Such a 3D cartogram on which a second property is mapped is a two-variable 3D cartogram.

Keywords

Two-Variable 3D cartograms • Diffusion • Topology-preserving cartograms

1 Introduction

A map is a graphic representation of an environment [1]. Maps are often divided into two subclasses: reference maps and thematic maps [2]. Maps created with the intent to demonstrate certain features and concepts are thematic, such as those that are designed to show the spatial distribution of a statistic. A value-by-area map, also known as a cartogram, is a quantitative thematic map that converts a measure of a non-negative distribution to an area on the map [3]. On a cartogram, the size of a region is linearly proportional to its statistical property. To date, several cartogram algorithms have been proposed [4–9].

This work presented a three-dimensional (3D) grid visualization technique that visualizes two quantities both in situ and simultaneously by utilizing spatial distortion and chromatic overlay. Maps created using such techniques are referred to as two-variable 3D cartograms [2]. On such maps, spatial distortion can be achieved through 3D diffusion cartogram transformation—a conceptually simple cartogram algorithm based on the elementary physics idea of linear diffusion [8, 9] —while color information can be embedded into the geometry through volumetric coloring and shading (versus area shading on a 2D two-variable map). Two-variable 3D cartograms are readable, topology-preserving and may be made interactive [9].

2 Formulation

2.1 Diffusion-Based Homogenization

Mathematically, a diffusion-based cartogram transformation in a domain Ω is a homeomorphism $\mathcal{T}: \Omega \rightarrow \Omega$ whose Jacobian is proportional to a given non-negative intensive property distribution $f(\mathbf{r})$:

$$\frac{\partial \mathcal{T}}{\partial \mathbf{r}} = \frac{f(\mathbf{r})}{\bar{f}}, \tag{1}$$

where $\bar{f}$ is the average intensity in Ω. The idea behind the diffusion cartogram method is to let an intensive property "flow" from high-valued areas into low-valued areas until homogenization is achieved, during which the movements of region borders are calculated. Linear diffusion conveniently satisfies the requirement on the Jacobian. The governing equation of linear diffusion is

$$\frac{\partial f}{\partial t} - \nabla^2 f = 0. \tag{2}$$

Z. Li · S. A. Aryana (✉)
University of Wyoming, Laramie, WY 82072, USA
e-mail: saryana@uwyo.edu

© Springer Nature Switzerland AG 2019

H. M. El-Askary et al. (eds.), *Advances in Remote Sensing and Geo Informatics Applications*,
Advances in Science, Technology & Innovation, https://doi.org/10.1007/978-3-030-01440-7_4

2.2 Diffusion Cartogram Transformation in 3D

Let Ω be a cuboid domain $[0, L_x] \times [0, L_y] \times [0, L_z]$ with Neumann boundary condition. The basis of the general solution is the cosine basis. Thus, the general solution is

$$f(\mathbf{r}, t) = \frac{8}{L_x L_y L_z} \sum_{(l,m,n)} \hat{f}_{lmn} \cos k_{xl} x \cos k_{ym} y \cos k_{zn} z \exp\left\{-|\mathbf{k}_{lmn}|^2 t\right\}, \tag{3}$$

where the Fourier coefficients are defined for non-negative l, m and n indices as

$$\hat{f}_{lmn} = \frac{(\delta_{l0}+1)(\delta_{m0}+1)(\delta_{n0}+1)}{8} \iiint_{\Omega} f(\mathbf{r}, 0) \cos k_{xl} x \cos k_{ym} y \cos k_{zn} z dV, \tag{4}$$

and the wave vectors $\mathbf{k}_{lmn}$ are defined as $(k_{xl}, k_{ym}, k_{zn}) = \pi(l/L_x, m/L_y, n/L_z)$. According to the standard treatment of diffusion [8], the expression for the velocity field in terms of the distribution is

$$\frac{d\mathbf{x}}{dt} = \mathbf{v} = -\frac{\nabla f}{f} = -\frac{1}{f}\left(\frac{\partial f}{\partial x}, \frac{\partial f}{\partial y}, \frac{\partial f}{\partial z}\right), \tag{5}$$

Consequently, the diffusion cartogram transformation maps a point $\mathbf{r}_0$ to $\mathcal{T}(\mathbf{r}_0)$ by

$$\mathcal{T} : \Omega \to \Omega, \mathbf{r}_0 \mapsto \mathbf{r}_0 + \int_0^{\infty} \mathbf{v}(\mathbf{r}_t, t) dt, \tag{6}$$

where $\mathbf{r}_t$ is the cumulative displacement of said point at time t. Distributions of properties in real-world models are usually heterogeneous. As such, the discrete version of the continuous formulation is used upon real-world models. Appropriate spatial discretization scheme, time-stepping

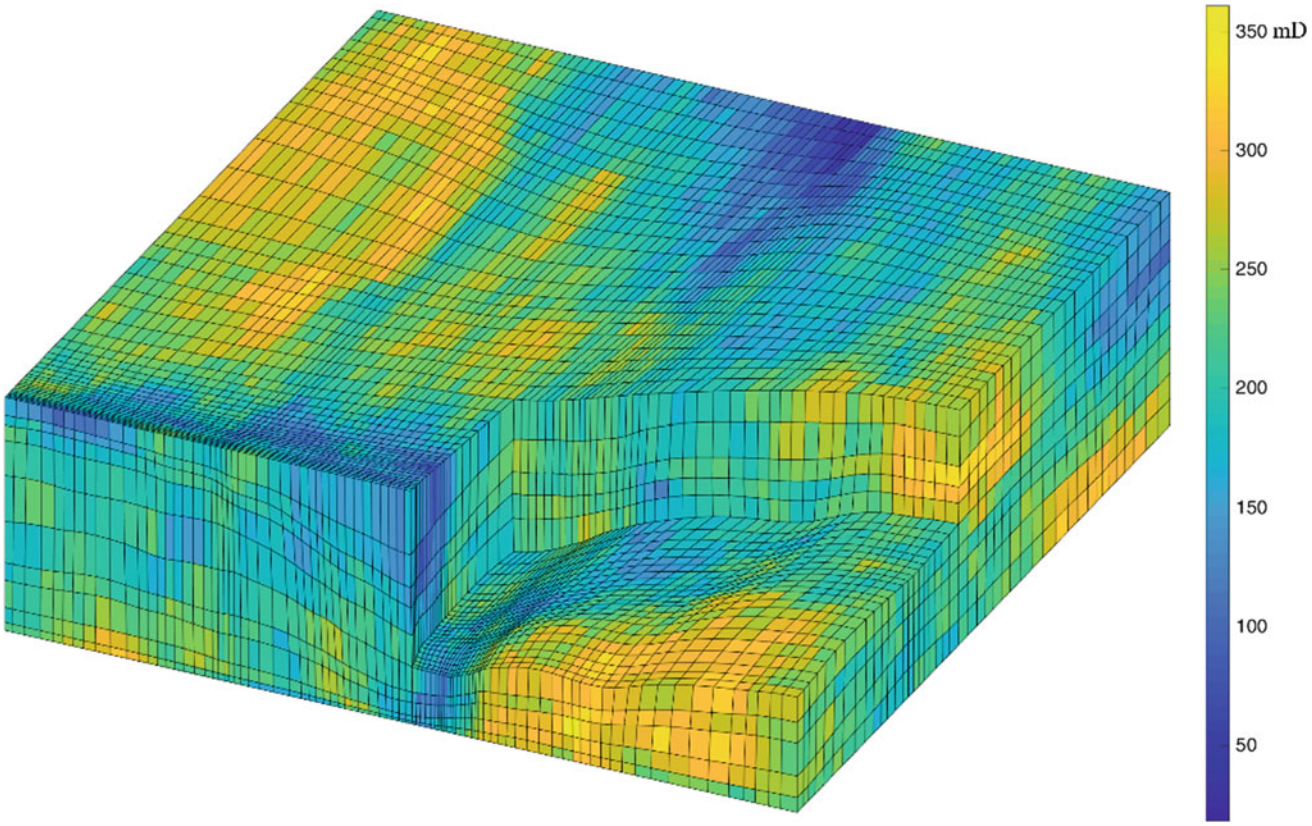

Fig. 1 3D cartogram applied to HCPV distribution on a uniform Cartesian grid, with colors indicating permeability distribution. The color bar shows the scale of permeability in millidarcies (mD). The partial cross-section in one corner shows some transformation of the interior cells

behavior and halting conditions are crucial to numerical implementations [8, 9]. Tissot's indicatrix, a quantitative indicator of distortion for planar cartograms, will be adapted for the 3D cartogram using ellipsoids in place of ellipses for visualization of the presence and the degree of distortion [10].

3 Results

Given a synthetic subsurface model of a uniform Cartesian grid with 38,720 grid cells (88 × 44 × 10 division) along with its hydrocarbon pore volume (HCPV) and permeability distribution, we would like to visualize both statistics on a single 3D map. To this end, a two-value 3D cartogram of the subsurface model is generated. The entire grid is transformed by equalizing its HCPV through a 3D diffusion cartogram transformation and the transformed grid cells are colored to convey permeability information (see Fig. 1).

4 Discussion

HCPV and permeability distribution of the subsurface model shown in Fig. 1 are visualized through spatial distortion and coloring. The 3D cartogram of the subsurface model is distorted because HCPV values are non-uniform in the non-transformed domain. Diffusion cartogram transforms the volumes of the grid cells to be proportional to their HCPV content. Recent advances in visualization techniques, such as the immersive 3D Cave Automatic Virtual Environments (CAVE) and interactive embedded 3D graphs in digital formats such as the Portable Document Format (PDF) [9], have expanded our ability to interpret and interact with 3D spatially related data. These technologies enable the use of 3D two-value cartograms to explore models of the subsurface interactively and convey the spatial distribution of properties more robustly. Any physical property, its uncertainty, as well as any statistic that is expressed on a positive scale may be homogenized using the diffusion cartogram. Additional data may be superimposed on the resulting cartogram via colors. Application examples include aquifers, petroleum reservoirs, subsurface mineral deposits, and groundwater contamination.

5 Conclusions

Two-value cartogram in 3D enables the visualization of two distributions in a single map. A 3D cartogram is formulated using a linear diffusion process. The two-value cartogram is applied to a synthetic subsurface model to homogenize the HCPV content of the cells. Other information, i.e., permeability, is shown using coloring, thereby integrating the geometry and color in a single two-value cartogram.

Acknowledgements This work has been made possible through financial support from the Carbon Management Institute at the University of Wyoming. The corresponding author thanks Director Coddington for the lively discussions.

References

1. Robinson, A.H., Petchenik, B.B.: The Nature of Maps: essays toward Understanding Maps and Mapping. University of Chicago Press, Chicago (1976)
2. Dent, B.D.: Cartography: thematic Map Design, 5th edn. McGraw-Hill Higher Education, New York (1999)
3. Tobler, W.: Thirty five years of computer cartograms. Ann. Assoc. Am. Geogr. **94**(1), 58–73 (2004)
4. Raisz, E.: The rectangular statistical cartogram. Geogr. Rev. **24**(2), 292–296 (1934)
5. Dougenik, J.A., Chrisman, N.R., Niemeyer, D.R.: An algorithm to construct continuous area cartograms. The Professional Geographer **37**(1), 75–81 (1985)
6. Alam, M.J., Kobourov, S.G., Veeramoni, S.: Quantitative measures for cartogram generation techniques. Comput. Graphics Forum **34**(3), 351–360 (2015)
7. Nusrat, S., Kobourov, S.: The state of the art in cartograms. Comput. Graphics Forum **35**(3), 619–642 (2016)
8. Gastner, M.T., Newman, M.E.J.: Diffusion-based method for producing density-equalizing maps. Proc. Natl. Acad. Sci. **101** (20), 7499–7504 (2004)
9. Li, Z., Aryana, S.A.: Diffusion-based cartogram on spheres. Cartography Geog. Inf. Sci. (2017)
10. Gastner, M.T., Seguy, V., More, P.: Fast flow-based algorithm for creating density-equalizing map projections. Proc. Natl. Acad. Sci. **115**(10), E2156–E2164 (2018)

GIS Contribution to the Implementation of an EOSID Process Followed in Case of an Engine Failure After the Take-off of a Boeing 737-500 Aircraft from Tabarka-Aïn Draham International Airport (NW of Tunisia)

Mohamed Hafedh Hamza, Meriem Saddour, Hanen Mokrani, and Raouf Khelif

Abstract

The present work was prepared in collaboration with the Tunisian Air Company (Tunis Air) for the creation of a GIS application used for the implementation of an EOSID (Engine Out Standard Instrument Departures) process. The study area is Tabarka-Ain Draham International Airport (NW of Tunisia) and the chosen aircraft is the Boeing 737-500. This study presented the procedure to be followed in case of engine failure after takeoff which consists of changes of trajectory made in order to avoid obstacles. This would allow the aircraft to bypass the penalizing obstacles, thus eliminating the need to reduce the maximum take-off weight. The usefulness of GIS is observed in its proposed solutions: the presentation of the terrain in 3 dimensions, the presentation of the simulation of the flight as well as the possible paths to follow. This work will be very useful for aeronautical companies in the field of aviation safety.

Keywords

Aircraft • EOSID • GIS • Tunis Air • Tabarka-Aïn Draham International Airport

1 Introduction

The Engine Out Standard Instrument Departure (EOSID) is an alternative lateral trajectory, optimized to avoid obstacles, used in case of engine failure [1]. The present work is the result of collaboration between the Section of Geomatics, Earth and Planning of the Faculty of Science of Tunis (Tunisia) and the Navigation and Infrastructure department of the Tunisian National Airline Tunis Air (IATA code: TU, ICAO code: TAR) which was founded in 1948 (2,991,841 passengers in 2016). The goal of this work was to implement a GIS-based EOSID security process used in case of engine failure occurring after takeoff of a Boeing 737-500 aircraft from runway 27 located at the airport of Tabarka-Aïn Draham International Airport (NW of Tunisia). The GIS technique used in this study was an effective tool making the data analyses easier to handle and provide high capabilities of handling large spatial data [2]. With GIS, aeronautical organizations can: Create, visualize, analyze, and disseminate critical data from Aeronautical Information Systems (AIS).

2 Materials and Methods

2.1 Study Area

Tabarka-Ain Draham International Airport (IATA code: TBJ, ICAO code: DTKA) is located fifteen kilometers east of the coastal town of Tabarka (northeastern Tunisia), near the Algerian border, between sea and mountains. It serves the entire north-west of Tunisia and was put into operation in 1992. Covering an area of 240 ha, it received 43,000 passengers in 2016 (Fig. 1).

M. H. Hamza (✉)
Department of Geography and Geographic Information Systems, Faculty of Arts, King Abdulaziz University, Jeddah, Kingdom of Saudi Arabia
e-mail: mhhamza@kau.edu.sa

M. H. Hamza · M. Saddour · H. Mokrani
Section of Geomatics, Earth and Planning, Department of Geology, Faculty of Science of Tunis, Tunis, Tunisia

R. Khelif
Navigation and Infrastructure Department, Tunis Air, Tunis, Tunisia

© Springer Nature Switzerland AG 2019

H. M. El-Askary et al. (eds.), *Advances in Remote Sensing and Geo Informatics Applications*, Advances in Science, Technology & Innovation, https://doi.org/10.1007/978-3-030-01440-7_5

Fig. 1 Study area

2.2 Methodology

EOSID (Engine Out Standard Instrument Departure) process was used in this study. Each EOSID is designed for a specific aircraft family and runway. It consists in a rescue trajectory, used in some cases of engine failure. Using an EOSID is not an obligation, particularly for some non-mountainous landscapes where the takeoff performance is not limited by obstacle clearance [3]. The present study is related to the case of engine failure that occurred after takeoff of a Boeing 737-500 aircraft from runway 27 of the studied airport.

2.3 Organization Chart

The organization chart is presented in Fig. 2.

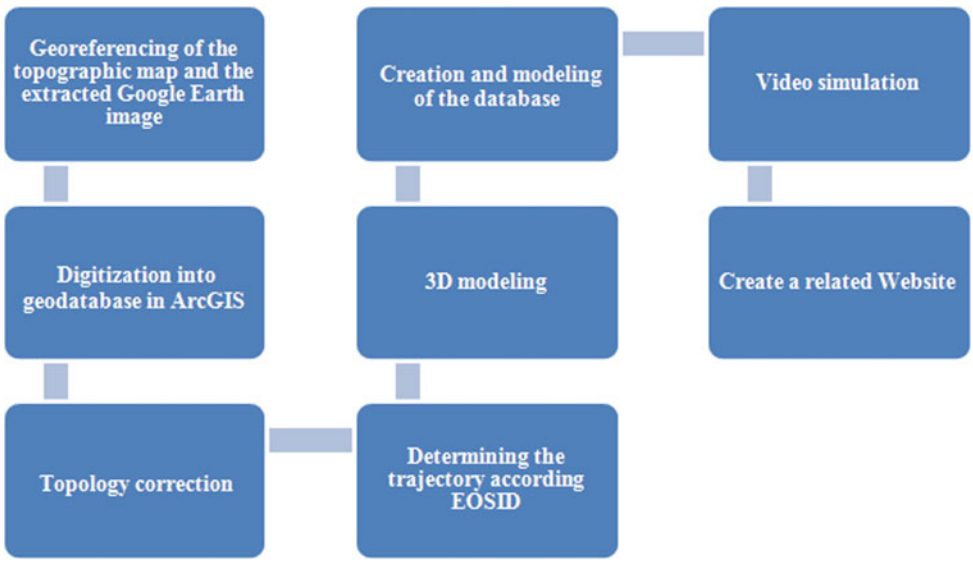

Fig. 2 Organization chart

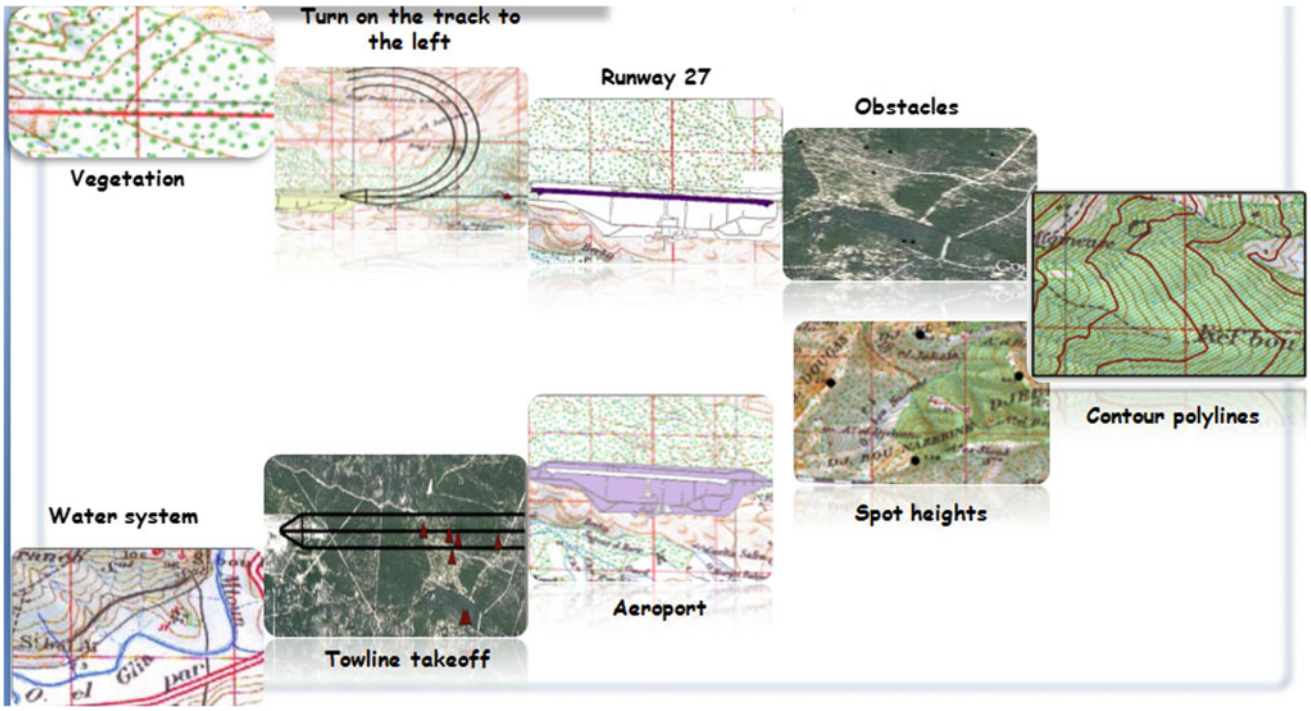

Fig. 3 Used data

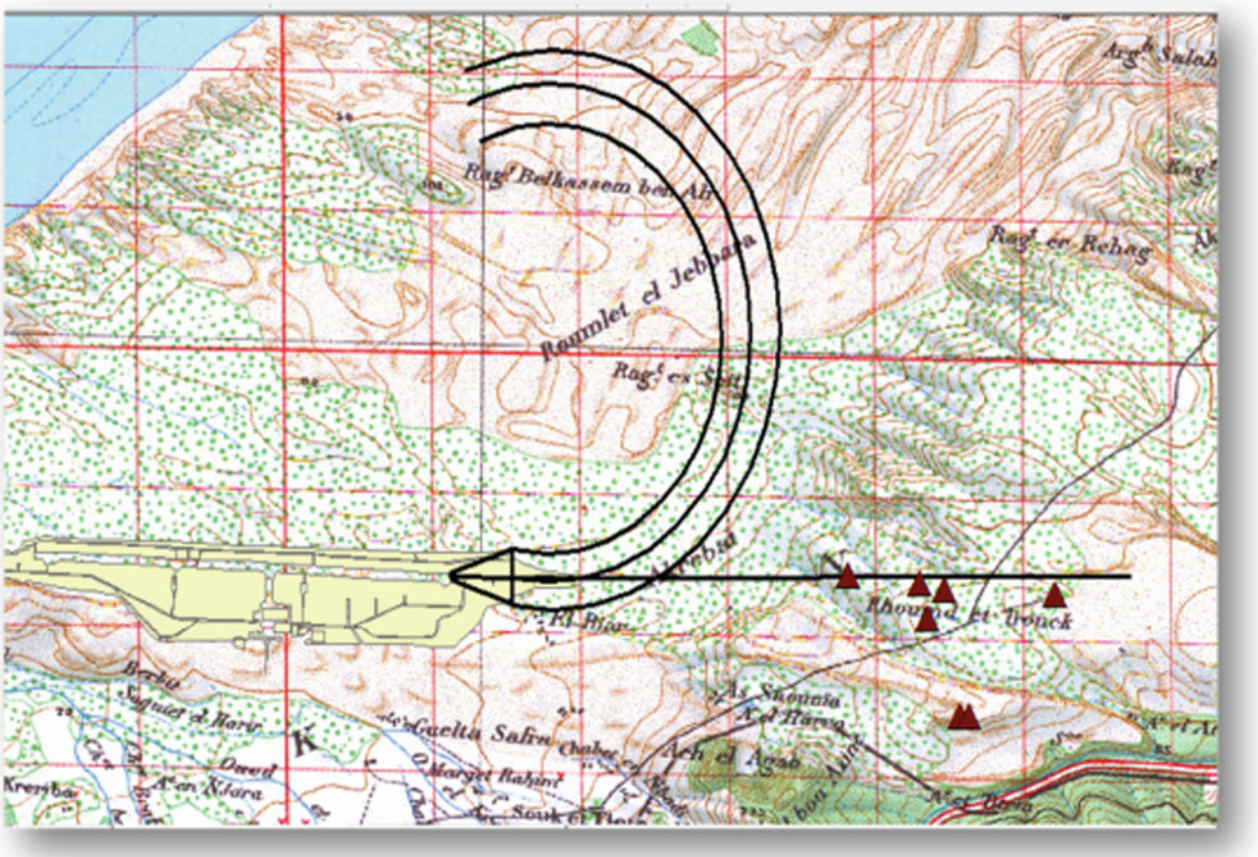

Fig. 4 Trajectory of the left turn used in the case of EOSID

2.4 Used Data and Software

Figure 3 shows the used data in this study. The used data were integrated into a geo-database file which was connected and integrated into ArcGIS. PowerAMC was used for database management, Google Earth Pro for 3D data and Adobe Dreamweaver for the creation of website integrating the obtained results.

3 Results

The following parameters were extracted based on charts related to the Boeing 737-500: Maximum takeoff weight MTOW = 74,850 kg, Runway weight limitation = 71,500 kg, Second segment takeoff climb weight limitation = 62,000 kg, Obstacle weight limitation = 50,300 kg.

EOSID process seems to be the best procedure in the case of the runway 27. By comparing the limitations presented by each of the two gaps (left and right), we retained the EOSID procedure with a left turn (Fig. 4).

4 Discussion

We were able to achieve a theoretical plan which would be followed in case of an engine failure. ArcGIS was used to represent the followed trajectory and create a Digital Elevation Model for the study area. The chosen EOSID process was presented into a 3-dimension format and a video simulation was created using the ArcGIS Animation function. That can help visualize perspective changes, geographic movements, and temporal changes. The final step of the study was to create a website related to the EOSID process using Adobe Dreamweaver software. The present work represented only the beginning of a project, which could be further developed in the near future.

5 Conclusion

The present study related to the procedure followed in case of engine failure after takeoff as well as the video simulation of the procedure, is very interesting for the Tunis Air aeronautical company, since it is strongly related to the safety of the flight and the travelers. Thanks to GIS, we were able to achieve a theoretical plan which would be followed in case of an engine failure. This work is just the beginning of a project, which could be further developed in the future.

References

1. International Civil Aviation Organization ICAO: Safety Management Manual (SMM), 2nd edn (2009)
2. Hamza, M.H., Added, A., Rodríguez, R., Abdeljaoued, S., Ben Mammou, A.: A GIS-based DRASTIC vulnerability and net recharge reassessment in an aquifer of a semi-arid region (Metline-Ras Jebel-Raf Raf aquifer, Northern Tunisia). J. Environ. Manage. **84**, 12–19, July 2007. https://doi.org/10.1016/j.jenvman.2006.04.004, edited by Elsevier
3. Talgorn, B., Laporte, S., Bes, C., Segonds, S.: One Engine Out Takeoff Trajectory Optimization Conference: 10th AIAA Aviation Technology, Integration, and Operations (ATIO) Conference (2010). https://doi.org/10.2514/6.2010-9013

On Geo-informatics Ecosystem Framework for Energy Resources Management in the Frontier Sedimentary Basins

Nimmagadda L. Shastri, Said Hanafy, and Sharaf Eldin Mahmoud

Abstract

Data heterogeneity and multidimensionality are major challenges when dealing with the integration of exploration data sources in the frontier basins. We took advantage of the fact that the geology and geophysics (G & G) do not have boundaries either with the continents or their associated countries. Frontier basins may have generated enormous digital-data on geological structures and reservoirs in areas where the continents and their tectonic plates drifted. The digital data are indeed in Big Data scale, characterized by volumes and varieties in spatial dimensions that may have emerged in the form of conceptualization and contextualization attributes. The frontier basin research thus needs knowledge-based ecosystems, with entities, dimensions and their logical data models interpreted in geo-informatics focus. An integrated framework is proposed, generating a multidimensional metadata structure for meta-knowledge. The meta-knowledge derivable from metadata models can immensely be useful in interpreting the connectivity between G & G events and assessing the hydrocarbon potential of frontier basins. The metadata models are made so flexible as to be extended and implemented in worldwide super basins.

Keywords

Geo-informatics • Frontier basins • Ecosystem • Energy resources • Big data

1 Introduction

There are many sedimentary basins with thousands of sq. km areal extents in both onshore and offshore areas, especially in places where the tectonic plates drifted millions of years ago. The petroleum potential of these basins is unknown, because of the little information we have to ascertain the existence of basins and sizes of petroleum systems including the connectivity between their elements and processes. The digital ecosystem is an emerging concept [4, 5] to establish connectivity among petroleum systems in the Middle Eastern sub-basins that share common elements and processes. In the present context, information systems and technologies, application programs, databases, Internet and software systems manage applications of geo-informatics to investigate different petroleum systems and their linked onshore and offshore oil & gas fields. The storage, processing, interpretation, dissemination of knowledge are several depictions of geo-informatics in spatial-temporal dimensions from which new opportunity areas of total petroleum system (TPS) and associated frontier potential can be investigated.

In spite of several decades of exploration, the limits of petroleum systems are unknown or unaccounted, especially in the frontier basins. With the advent of new database technologies in geo-informatics scenarios, it is now possible to organize and implement large size data models and simplify them in exploration industries, especially in areas, where thousands of wells and 2D/3D seismic vintages exist in geographic dimensions. "Ecosystem and embedded ecosystems" are the recent focus [5] in sedimentary basin environments, where no geological boundaries exist. A robust and holistic approach, with ontology-based data warehouse modelling, data mining, visualization and data interpretation [4, 6] are proposed for managing larger domains of sedimentary basins in the Arabian Peninsula, especially where a frontier potential exists.

N. L. Shastri (✉)
School of Management, Information Systems,
Curtin University, Perth, Australia
e-mail: shastri.nimmagadda@curtin.edu.au

S. Hanafy
Tharwa Petroleum, Cairo, Egypt

S. E. Mahmoud
Geophysics Department, Cairo University, Giza, Egypt

© Springer Nature Switzerland AG 2019

H. M. El-Askary et al. (eds.), *Advances in Remote Sensing and Geo Informatics Applications*,
Advances in Science, Technology & Innovation, https://doi.org/10.1007/978-3-030-01440-7_6

1.1 Geo-informatics and Petroleum Ontologies

Wherever multiple petroleum systems exist in sedimentary basins (Fig. 1), petroleum ontologies [5] are known to examine and characterize the semantics of data sources, as per diverse contextual domains. The total volume of African and Arabian basins' data [3, 6] makes it hard to find specific geological episodes of petroleum systems in each release of heterogeneous datasets. Data search is popular through keywords and/or acronyms. Searching zones of geological interest in frontier basins can be achieved through computing algorithms and matching strings [4, 7].

Multidimensional warehouse repositories match with objectives of machine learning that supports the cognitive geological interpretation [5, 7]. *Inclusiveness*, *uniqueness*, *cogency*, *veracity* and *reliability* properties of artefacts are assured while organizing data and building data structures as per company standards and protocols. Much of the value of petroleum resources comes from an interconnected network of related multidimensional data warehouse repositories in the frontier basins. The criteria for data integration approaches to address the current problems include: (a) substantiating the uniqueness in common concepts (b) characterizing data integration in several formats (c) agreeing to conflicting tenacities of different data sources (d) data unanimity, and (e) presentation of interpretable generic data views. So the future scope of data integration systems is in frontier basins, since they are in Big Data scale. To manage the volume and variety of data (including geographical and periodical extents, with hundreds of trillion bytes of data in the Middle Eastern contexts), large size DB systems are necessary to leverage, store and present multidimensional oil and gas data events in various logical and physical schemas [5, 7].

2 Description of Ontologies in Frontier Basins

The recent increase in demand for hydrocarbons, declining production even from mature basins, and high oil prices force the international explorers to explore new petroleum resources in frontier basins. Geology of frontier basins is poorly understood, making prospectivity and exploration challenging to assess and venture in years to come. In addition, the data in multiple basins are scattered, unusable for data integration, due to format differences and survey-permits held by multiple stakeholders. Mining the data facts and enhancing value in knowledge-based domains in different producing onshore and offshore sedimentary basins are the current focus. Ontologies describe the data semantics to make up the connectivity and data integration. Syntactic and schematic heterogeneities existing in between different data dimensions and associated attributes address the description of taxonomies or ontologies, where conceptualized and contextualized dimensions are logically brought into a unified metadata. Such knowledge-based associations [5] are put together among several domains of petroleum systems at frontier basin scale [3, 4, 6] to ease the data integration process in the warehouse (Fig. 2). In this context, the concept of the ecosystem is emerging within the generic total petroleum system (TPS), existing in petroleum provinces of the Arabian Peninsula.

The exploration business deals with *structure* and *reservoir* data. The carbonate reservoirs (especially of Jurassic age) report hydrocarbon potential and production on commercial scale in Middle Eastern onshore and offshore petroleum systems. Exploration data in these regions exhibit an intense heterogeneity, unique classification and architectural

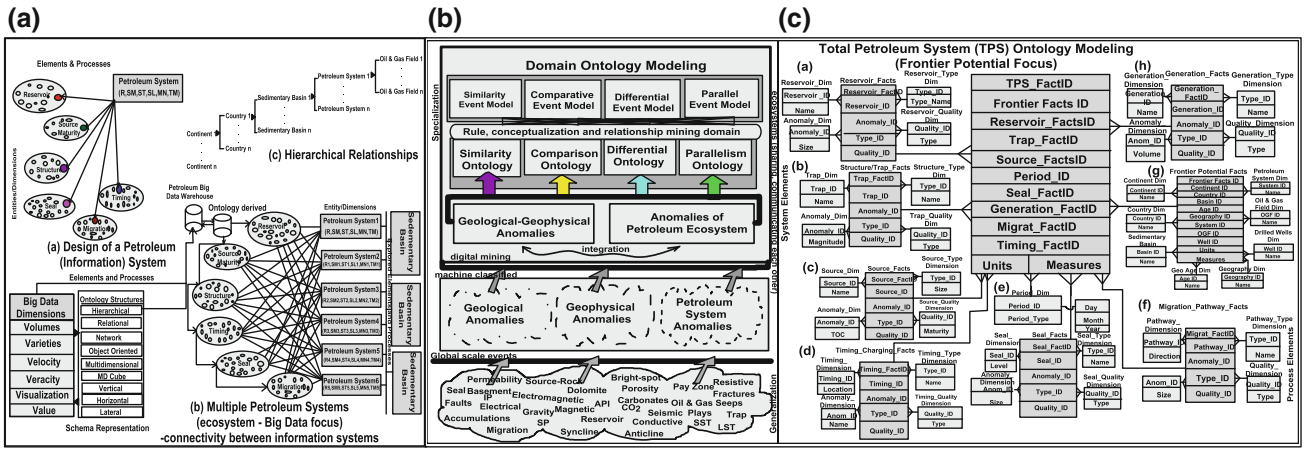

Fig. 1 **a** Domain ontology modelling, **b** generic TPS data schemas—frontier potential modelling—connecting basins and systems

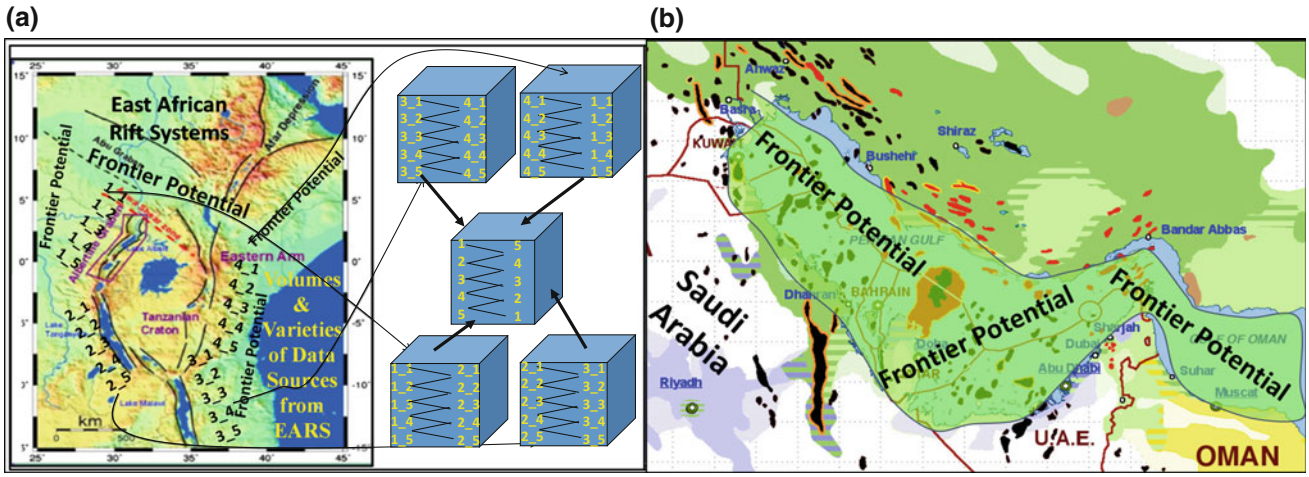

Fig. 2 Examples of East African and Middle Eastern frontier potential basins

relationships [5]. Either similarity or dissimilarity observed in elements and processes is unique in petroleum systems of Asia, Australia, Middle East and African continents [1, 2, 6]. Capturing and integrating petroleum data in warehouse schemas can overcome the existing data integration limitations. This alternate approach describes ontologies, which do not necessarily rely on keywords or similarity metrics. Further, the petroleum ontology framework promotes the use and reuse of ontologies in various data models, simplifying user queries [5, 7]. The fine-grained multidimensional data structuring is interoperable and adaptable in warehouse metadata models. It can efficiently simplify the data mining and interpretation artefacts. The metadata models in larger sedimentary basins support the data mining and interpretation of data views, connecting the global geological knowledge to cognitive data patterns of local basins.

3 Conclusion and Future Perspectives

For knowledge representations in multiple domains, the Big Data systems play decisive roles in establishing several links among heterogeneous exploration data. Sustainable management of natural resources in frontier basins is a serious business issue. We have proposed new information system and technology remedies in investigating the resources on the continental scale. Models and integrated frameworks associated with the TPS and frontier potential benefit the fields of geo-informatics. The spatial-temporal dimensions have large significance in analyzing the models and implementing them in various geographic contexts. On the continental scale, the framework can successfully offer and deploy the geo-informatics solutions in the Eurasian-African, Australasian and West African-East Latin American sedimentary basins, where there is a frontier potential and an immense scope of energy resource development and management.

References

1. Bastia, R.: Expanding exploration frontiers of India. In: 8th Biennial International Conference & Exposition on Petroleum Geophysics, p. 419, SPG, Hyderabad, India (2010)
2. Brooks, J.: Classic Petroleum Provinces, Geological Society Special Publication, vol. 50, pp. 1–8, http://sp.lyellcollection.org/ (1990)
3. Corti, G.: Evolution and characteristics of continental rifting: analog modelling-inspired view and comparison with examples from the East African Rift System. Tectonophysics **522–523**, 1–33 (2012)
4. Nimmagadda, S.L., Dreher, H.V.: Big-data integration methodologies for effective management and data mining of petroleum digital ecosystems. In: 7th IEEE International Conference on Digital Ecosystems and Technologies (DEST), Menlo Park, CA, USA (2013)
5. Nimmagadda, S.L., Dreher, H.V., Nawaz, M., Laiq, K., Ahmed, M.: On data integration workflows for an effective management of multidimensional petroleum digital ecosystems in Arabian gulf basins. In: 4th IEEE International Conference (DEST), Dubai, UAE (2010)
6. Schumacher, D., Clavareau, L.: Hydrocarbon exploration survey strategies for frontier basins and other under-explored areas, search and discovery Article #80503. In: AAPG pages, International Conference & Exhibition, Australia (2016)
7. Wand, Y.: An ontological analysis of the relationship construct in conceptual modelling. ACM Trans. Database Syst. **24**(4), 494–528 (2000)

Comparative GIS-Based Automated Landform Classifications: Application of Jenness and Shary Methods to the Jebel Chaambi Area (West-Central Tunisia)

Meriem Labiadh, Ibtissem Amri, and Mohamed Chedly Rabiaa

Abstract

Two landform classifications (Jenness and Shary methods) using spatial statistics and image processing algorithms were performed for the first time in Tunisia. They were applied to the J. Chaambi area (West-central Tunisia). Attempting to highlight geo-morphometric properties of 30 m resolution Digital Elevation Models (DEM), the Jenness classification leads to define ten classes using the 'Topographical Position Index' as performed by the module in Arcgis 10.2. The Shary classification is based on a combination of five slope curvature signs producing twelve main landform categories. Plains characterize the main landform type in the first classification; however, convex and concave saddles correspond to the second. The window of perception, in both classification cases, has a major influence on the representation of results. Indeed, the scale effect on classification should be tested by applying both methods to the same area but at different scales.

Keywords

Landform • Classification • DEM • TPI • Curvature • J. Chaambi

1 Introduction

Landform classification is an important tool for investigations related to geographical distribution and pedological resource mapping for soil management and valorization. Several methods were developed to automate the extraction of landforms from Digital Elevation Models (DEMs) e.g. [2, 6] and many algorithms and software programs serve to calculate the terrain derivatives [3, 5].

The J. Chaambi area is the highest-elevation relief in Tunisia (1544 m). Its landforms express a variety of geomorphic processes and related external geodynamic history, all being worth of a wise identification. This study tried to fill the gap of cartographical and geomorphological data of this region and helped identify the places to be protected from soil erosion for a better territory development and rural planning.

2 Materials and Methods

Jenness and Shary methods are two automated classifications applied using the Digital Elevation Model (DEM) provided by NASA and gathered by the Shuttle Radar Topography Mission (30 m SRTM). Arcgis 10.2 and SAGA-GIS software algorithms (System for Automated Geoscientific Analysis) were employed as technical tools.

The Jenness classification procedure is based on Topographic Position Index (TPI) and uses the DEMs as the unique input layer. Practically, TPI is the difference between a cell elevation value and the elevation average of its neighborhood. Hence, positive and negative values correspond to a higher (ridges) and lower cell elevation (valleys), respectively; while null values refer to close elevations as in flat or mid-slope areas [7]. The TPI expresses relative elevation as a fraction of local relief:

tpi <scalefactor> = int((dem - focalmean(dem, annulus, irad, orad)) + 0.5)

M. Labiadh · I. Amri
Faculty of Sciences of Bizerte, University of Carthage, 7021 Zarzouna, Bizerte, Tunisia

M. Labiadh (✉) · I. Amri · M. C. Rabiaa
Research Unit 02UR10-01, Geomatics of Geosystems, Campus Universitaire, 2010 Manouba, Tunisia
e-mail: labiadh.meriem@gmail.com

M. C. Rabiaa
Faculty of Arts and Humanities of Manouba, University of Manouba, Manouba, Tunisia

© Springer Nature Switzerland AG 2019

H. M. El-Askary et al. (eds.), *Advances in Remote Sensing and Geo Informatics Applications*, Advances in Science, Technology & Innovation, https://doi.org/10.1007/978-3-030-01440-7_7

scalefactor = outer radius in map units, irad = inner radius of annulus in cells, orad = outer radius of annulus in cells.

For Shary classification, landform categories are identified after morphometric calculations using GIS functions. The process of the landscape conversion into landform categories was based on the slope shape (curvature). Mathematically, a curvature is a second spatial derivative of the terrain parameters. The second derivatives of DEM and other morphometric variables are obtained following a methodology proposed by [1]. This methodology consists in moving a 3 × 3 window across a DEM and then calculating the values for the window central cell. For example the difference curvature, E (m^{-1}): E = ½ (kv − kh), is the half-difference of vertical (kv) and horizontal (kh) curvatures [6]. Comparing two accumulation mechanisms of gravity-driven, E shows to what extent the relative deceleration of flows is higher than flow convergence at a given point of the topographic surface.

3 Results

Our results are mostly shown through maps. For example, Jenness classification (Fig. 1) shows that class 5 covers most of the landform area (plains). On the field, it corresponds to a vast system of staggered glacis and terraces, particularly developed in the south of the Chaambi relief, characterized by homogenous calcareous accumulations. It corresponds also to a well-individualized plain especially around Garet En Naam. In the southeast of Chaambi relief at Bled Dogra and Ouled Hanadra, the plains are covered with alluvium provided from a dense and a well-incised gully network. Class 7 (upper slope) coincides with the alluvial fans of the Chaambi piedmont as well as to several bump-shaped small hills. Both hillsides of the J. Chaambi exhibit a series of incised stream (class 1) within the upper Cretaceous limestone, caused by gully erosion. Spatially, class 1 is generally associated to class 10 which is represented by ridges. Steep slopes exceeding 30% are observed. These steep slopes favor the runoff and are the main cause of erosion of marly formations (Santonian).

The Shary classification shows complex landscapes with a wide intricacy of landforms. Convex saddles are assumed to be indicative of upper slope positions and concave saddles are related to lower-water-receiving surfaces associated to backslopes. This classification explicitly assumes that land surface morphology form is directly related to surface processes (erosion) and relative landform position. In our case, the aggregation of the twelve landform classes of J. Chaambi area into hills, saddles and depressions shows that saddles occupy 74.21% of the study area. The combination of horizontal and vertical curvature signs made it possible to obtain a relative dissipation, accumulation and transit map.

4 Discussion

For landform classifications, several approaches were developed, including those, which use manual delineations on maps, aerial photographs or satellite image. Semi-automatic to automatic methods aim to reduce potential subjectivity of interpretation in manual ones. For a previous Tunisian case study, our work [4] delimited

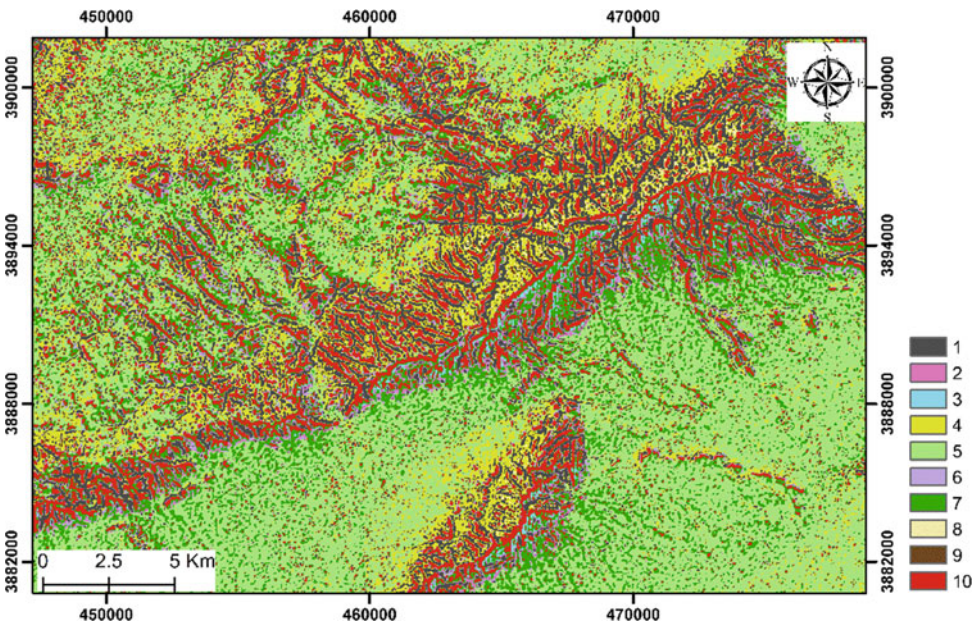

Fig. 1 Jenness landform classification. 1: Canyons, deeply incised streams; 2: Midslope drainages, shallow valleys; 3: Upland drainages; 4: U-shaped valleys; 5: Plains; 6: Open slopes; 7: Upper slopes; 8: Local ridges, hills in valleys; 9: Midslope, ridges, small hills in plains; 10: Mountain tops, high ridges

landforms in the "Tunisian Dorsale" range (Abdeladim watershed) using landscape segmentation as based on direct field observations. Our previous method is considered here as time consuming and applicable only to small areas.

Jenness developed an algorithm using TPI for automatic classification of landforms that provides easier and repeatable methods leading to classify the landscape into position and landform categories. TPI is derived by applying geometrical and topological analyses using local statistics. Nevertheless, the application of this classification on the relief of the Chaambi shows that certain classes (midslope, upland drainage, local ridges and mall hills in plain) seem to be missing. These classes can be clustered in order to facilitate the visualization and/or the analysis of the concerned relief. Indeed, a reduced number of landform classes may lead to easier decipherable data and more objective result interpretations. Furthermore, the landform geometry is not fully taken into account in the Jenness classification, which leads to the use of Shary classification. Wilson [8] confirmed that the Shary classification is a complete system of classification by curvature, applicable on local and regional contexts. Recently, Florinsky [1] asserts that the Shary classification is promising as it focuses on the landform-process relationships.

5 Conclusion

The landform pattern of the Tunisian relief of J. Chaambi was described here for the first time by means of GIS-based automated landform classifications. The results obtained are in a good agreement with direct field observations. For the studied J. Chaambi area, Jenness classification based on Topographic Position Index (TPI) generates 10 landform types where plains and upper slopes are mostly represented. This method is easy and fast with a simple user interface and allows us to better correlate the relief classes with the geological setting of the study area. The Shary classification consisted of two steps: the computation of secondary terrain attributes (five types of curvatures) and automated landform classification. This method highlights 12 landforms where convex and concave saddles occupy 70.22% of the study area. Despite its complexity, the Shary classification has the advantage of linking landforms and related processes such as accumulation, transit and dissipation. We consider future improvements to refine landform classification of J. Chaambi with the availability of a higher DEM resolution and the use of ArcGIS geo-morphometry toolbox. This may provide additional functions for true multi-scale land surface analysis and classification.

References

1. Florinsky, I.V.: Digital Terrain Analysis in Soil Science and Geology, 2nd edn. Academic Press, Amsterdam (2016)
2. Iwahashi, J., Pike, R.: Automated classifications of topography from DEMs by an unsupervised nested-means algorithm and a three-part geometric signature. Geomorphology **86**(3–4), 409–440 (2007)
3. Jenness, J.: Topographic Position Index Extension for ArcView 3.x. Jenness Enterprises (2005)
4. Richard, J.F., Allouch-Khébour, F., Labiadh, M., Morschel, J., Riahi, O., Temple-Boyer, E.: L'eau et le paysage dans la Dorsale Tunisienne. UMR LISAH. IRD Tunis, Institut de Recherche pour le Développement (2005)
5. Rigol-Sanchez, J.P., Stuart, N., Pulido-Bosch, A.: ArcGeomorphometry a toolbox for geomorphometric characterisation of DEMs in the ArcGIS environment. Comput. Geosci. **85**, 155–163 (2015)
6. Shary, P.A.: Land surface in gravity points classification by a complete system of curvatures. Math. Geol. **27**, 373–390 (1995)
7. Weiss, A.: Topographic position and landforms analysis. In: Poster Presentation, ESRI Users Conference, vol. 200, San Diego (2001)
8. Wilson, J.P.: Digital terrain modeling. Geomorphology **137**(1), 107–121 (2012)

A GIS-Based Spatially Distributed Crop Water Demand Modelling for Pullambadi Canal Command Area in Lower Cauvery Basin, Tamil Nadu, India

Subbarayan Saravanan, J. Jacinth Jennifer, D. Abijith, and Leelambar Singh

Abstract

The assessment of irrigation demand is an important component for an effective water management in the canal command area. The rapid increase in the water scarcity on recent years have been a boon to the farmers who require water for irrigation purposes. Effective water management technique is the utmost required system to schedule the water for irrigation purposes so as to overcome the issues due to water scarcity. But there exist serious issues related to the water management system; they include the availability of real time information on the agricultural land in the command area of the canal, its area, the crop variety and the water demand for each crop. These data cannot be availed that easily as many irrigation schemes are vast and cover about hundreds and sometimes thousands of square miles and have vast numbers of farms; their scale severely limits the effectiveness of the data collection. The present study focused on assessment of the irrigation and agriculture potential for Pullambadi Irrigation project using Geospatial Techniques. The daily weather parameters, the land use/land cover of the region were collected as they serve to be the primary requirements. The study incorporated the data availed from satellite imageries and other possible sources and the water requirement for the years 2015 and 2016 were computed. As per the obtained results, the canal command area required 1069.96 and 965.1 Mm^3 for the years 2015 and 2016, respectively.

Keywords

Crop water requirement • Evapotranspiration • Irrigation • Remote sensing and geographic information system

S. Saravanan (✉) · J. Jacinth Jennifer · D. Abijith · L. Singh
National Institute of Technology,
Tiruchirappalli, Tamil Nadu, India
e-mail: ssaravanan@nitt.edu

1 Introduction

India is a highly populated country which hosts 18% of the world population, perhaps with only 2.4% of world geographical area along with 4% of world's renewable water resource. The increase in population highly stresses food production and water consumption resulting in a very difficult situation to be faced under the present drastic climatic change. At present, the agricultural sector consumes about 83% of total water use and it is likely to fall by 10–20% by 2025 to fulfill the intense hike for domestic and industrial needs. This situation imposes the need for some management schemes to improve the utilization of water resources. The efficacy of the scheme should be capable to achieve more crop per drop of water to satisfy the food demand for the increasing population of the country. Numerous research works have been carried out to compute the water demand in the agricultural sector [1–3]. The research works have incorporated the soil type, climatic condition and water distribution system. The aforesaid factors rely on an extensive spatial distribution thus making it complex to understand; this has paved way for the intrusion of Geographical Information System (GIS) and other technologies to this field. The aim of this paper was to explore the possible use of GIS in the field of irrigation water management. The objective of this study was to bring out a schedule of water supply to the Pullambadi canal command area throughout the year in order to carry out efficient irrigation practice.

2 Study Area Description

Pullambadi is a panchayat town in Tiruchirappalli District of Tamil Nadu, India. The total Population of the region is above 10,000. Agriculture is the main occupation and Paddy is main crop grown in this region. Pullambadi Canal, which is one of the biggest irrigation projects in Tamil Nadu, passes through the town. It lies in 10° 58'N, 78° 55'E.

© Springer Nature Switzerland AG 2019

H. M. El-Askary et al. (eds.), *Advances in Remote Sensing and Geo Informatics Applications*,
Advances in Science, Technology & Innovation, https://doi.org/10.1007/978-3-030-01440-7_8

Pullambadi canal irrigates 8831 acres and its indirect potential is 13,283 acres through tanks and has the total irrigation capacity of 22,114 acres. The Pullambadi canal is one of the major tributaries of river Cauvery. The Pullambadi canal is a seasonal and not a perennial canal. The tanks act as a buffer for the farmers during the water distress times.

3 Materials and Methods

The study adopts the Remote Sensing and GIS techniques, exploiting the Landsat-8 satellite imagery of the study area which were acquired as month-wise data over the period June to August for Kuruvai and over August to October for Samba, for the years 2015 and 2016. The required weather data for the study were obtained from the Indian Meteorological Department. The land use/land cover of the command area was mapped using the satellite imagery and the prominent crops cultivated in the area were studied. The site visits provided additional information about the agricultural practice of the region.

The crop water requirement, the crop period and the consumptive use of the crops were computed by calculating the crop coefficient and the actual evapotranspiration of the crop. Spatially distributed evapotranspiration was computed using the Hargreaves and Samani model. The available soil moisture for each time step was computed using a simple water balance equation. The crop water requirement served well to schedule the water supply to the Pullambadi canal.

4 Results and Discussion

The study was carried out for the years 2015 and 2016. The data considered for the study include, land use/land cover, minimum and maximum temperature, wind, pressure, humidity and rainfall. The crop coefficient map (Fig. 1a) was obtained by exploiting the crop information obtained from the land use/land cover map. The spatially distributed evapotranspiration was modelled using the Hargreaves and Samani model adopted the data such as: minimum and maximum temperature, wind, pressure, humidity and rainfall. The crop coefficient values and the modelled evapotranspiration values provided the actual evapotranspiration and the spatially varying soil moisture (Fig. 1b) thereby allowing for the consumptive use of the study area.

The Pullambadi canal command area required 1069.90 Mm^3 in the year 2015 and 965.1 Mm^3 in the year 2016. With respect to the monsoon rainfall and the prominent water loss, the water requirement varies throughout the year. The month-wise water requirement is displayed in Table 1.

5 Conclusion

This study primarily focused on discussing the present water issue of Tamil Nadu. There exists a prominent drought and water demand in the Indian states is on the steady increase. In order to cater for their need and bring out a prominent solution, the Pullambadi Canal command area, Lower

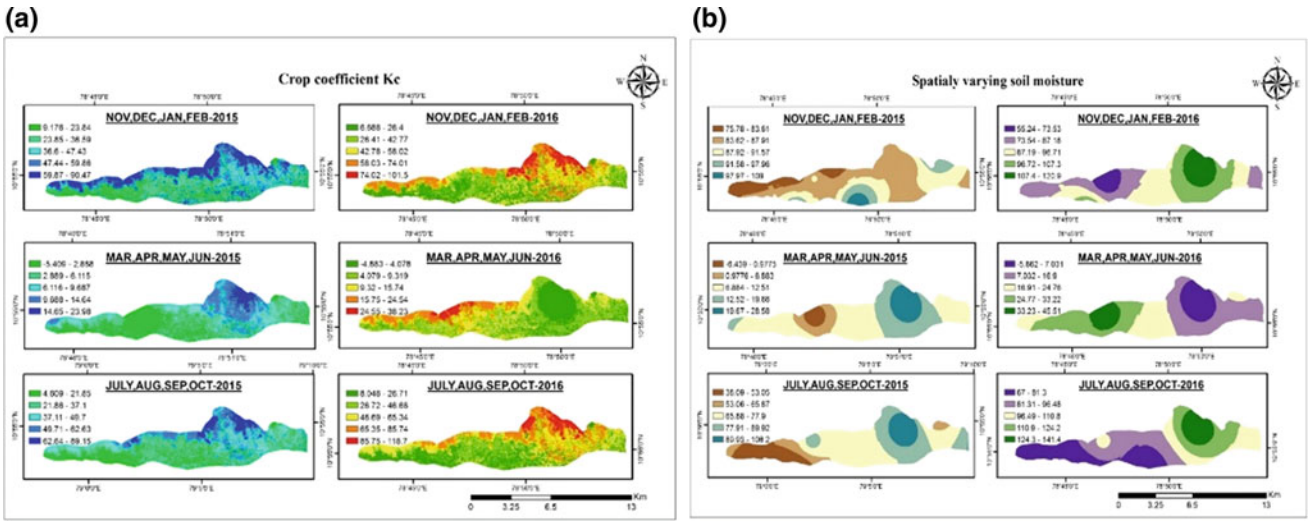

Fig. 1 **a** Crop coefficient and **b** Spatially varying soil moisture of the Pullambadi canal command area

Table 1 Water scheduling for each crop

Crop	Area (m^2)	Month	Water req (2015) Mm^3	Water req (2016) Mm^3
Kuruvai	25,260,000 m^2	Mar	50.85	45.86
		Apr	62.33	56.22
		May	36.1	32.55
		June	14.76	13.31
Samba	47,085,000 m^2	Mar	106.71	96.25
		Apr	130.81	118
		May	75.73	68.31
		June	30.98	27.94
Sugarcane	58,430,000 m^2	Mar	117.6	106.1
		Apr	144.14	130
		May	83.45	75.26
		June	34.13	30.8
Banana	28,095,000 m^2	Mar	56.54	51
		Apr	69.3	62.51
		May	40.12	36.19
		June	16.41	14.8
		Total water req.	1069.96 Mm^3	965.1 Mm^3

Cauvery River Basin, Tamil Nadu, India was chosen as the study area. A monthly based simple water balance was generated for the determination of spatially varying irrigation water requirement. The prominent crops being Kuruvai, Samba, Sugarcane and Banana, the sugarcane cultivation requires more water compared to the other crops. This is because sugarcane cultivation covers the major portion of the region, and its crop period is longer, which means a higher consumptive use. Also, from the field survey, the average values of water conveyance loss were estimated to be 26% in the main canal and 13% in secondary canals. From these analyses, it was revealed that 8.9×10^5 m^3 of water was deficient in Pullambadi command area during the study period.

References

1. PMP Atlas for Cauvery and other East Flowing river basins, Final Report, Central Water commission and Indian Meteorological Department (2015)
2. Sachan, S., Chandola, V.K., Lohani, A.K.: Probability analysis of rainfall and crop water requirement using CROPWAT model for crop planning in a canal command of upper Bhima Basin of Maharashtra. Int. J. Agric. Environ. Biotechnol. **9**(1), 123–135 (2016)
3. Sadeghi, S.H., Zabihi, M., Vafakhah, M., Hazbavi, Z.: Spatiotemporal mapping of rainfall erosivity index for different return periods in Iran. Nat. Hazards **87**, 35–56 (2017)

Solar Power Plant Site Location Suitability Analysis Using GIS Weighted Average Raster Overlay [Lebanon]

Amal Iaaly, Oussama Jadayel, Nabil Karame, and Nachaat Khayat

Abstract

After the civil war, the electricity sector in Lebanon faced numerous challenges due to the lack of maintenance and funding. Rationing hours increased dramatically and consequently, citizens diverted toward the private sector in order to compensate for this electricity shortage. The majority of the produced electricity is based on burning fuel leading to an extensive pollution. To overcome both the environmental and electrical shortage dilemmas, this paper studied the feasibility of solar energy as a complementary solution. North Lebanon district is the adopted case study. The suitable zone to establish a solar plant is selected scientifically using Geographic Information System (GIS) while taking into account all the restrictions and criteria. The raster analysis overlay method using weighted average sum was implemented. The study succeeded in selecting one appropriate region that can compensate for the North region power deficit.

Keywords

GIS • Solar energy • Weighted sum raster overlay • Lebanon • Electricity

1 Introduction

Electricity is a crucial part of individuals' lives, and people have always taken it for granted until they recognized its worth. Problems in electricity generation and distribution in Lebanon have become more frequent. These problems cover not only the inefficient supply of electricity, but also the unpredictable faults in the system, the overly expensive bills, the unsystematic expansion of the network, the inadequate distribution, as well as the damage to the ecosystem and environment caused by the traditional generation and production methods. In Lebanon, a serious deficit between power demand and generation is increasing as a result of the continuous increment in the demand versus a decreasing supply rate. In a recent study, it has been reported that the demand for electrical power has increased from 2450 MW in 2010 to 3280 MW in 2015 [1] even though Electricity du Liban (EDL) has a maximum production capacity of about 2260 MW (90% of what is produced from thermal power plants) [2, 3]. This value is due to the aging of the plants and the fact that some of them existed since 1970 (Jieh thermal power plant was put into service in 1970, while Zouk thermal power plant was put into service in the 1980's) and the newest one is now fifteen years old [2].

To compensate for this shortage and due to the huge international concern about the environment, Lebanon has begun to show interest in renewable energy. Solar energy, which consists of the heat and the radiant light coming from the sun, is a major source of renewable energy. The process of producing electricity from solar energy is still young in Lebanon. In 2002, and with the aid of the United Nation Development Program (UNDP), the Lebanese Center for Energy Conservation (LCEC) was introduced. The LCEC became the leading independent institution concerned with renewable energy. Since then, many solar power projects were initiated and most of them were directed towards heating water or energizing road lights [4]. In 2011, the Lebanese Government approved of the initiation of the "Beirut River Solar Snake" project. This project consists of covering the Beirut River in Borj Hammoud by 3600 solar panels along 325 m. It is estimated that this solar field will ensure 1655 MWh yearly, the sufficient need of approximately a thousand houses in the region. The project will eventually extend the solar field to reach 7 km along the river, producing 10 MW of electricity, which is enough to energize more than ten thousand houses [5]. In 2014, the parliament approved of a law giving electricity production

A. Iaaly (✉) · O. Jadayel · N. Khayat
University of Balamand, Balamand, Al Kurah, Lebanon
e-mail: amal.iaaly@balamand.edu.lb

N. Karame
Lebanese University, Tripoli, Lebanon

© Springer Nature Switzerland AG 2019

H. M. El-Askary et al. (eds.), *Advances in Remote Sensing and Geo Informatics Applications*,
Advances in Science, Technology & Innovation, https://doi.org/10.1007/978-3-030-01440-7_9

licenses based upon the recommendation of the Ministry of Energy and Water. However, due to both geographical and environmental restrictions, the biggest challenge in Lebanon is to find a suitable location to install solar fields [5]. Geographical Information System (GIS) represents a powerful tool to find the optimal location using the weighted average overlay raster analysis method based on the restrictions criteria [6].

2 Methodology

Through the use of GIS, the authors focused on finding the most appropriate location for a Solar Power Station (SPS) in North Lebanon region based on various criteria. In the course of this study, a set of criteria were identified from the available literature. These are:

C1: Open terrain with less than 5% slope.
C2: Away from urban areas.
C3: Away from forests.
C4: Away from natural reserves.
C5: Near other power stations.
C6: Near main roads.

Moreover, a solar power plant requires a large area. The area demand of such project ranges between 1 and 2 km^2. This area would be storing approximately 50–100 MW of installed electric capacity [7]. Hence, in order to find the optimal location using GIS, a systematic process was followed:

Step 1-Data collection: Location and attribute data regarding all the transformers, stations, substations, and power plants feeding the North region were gathered using a field survey. A field tour was necessary in order to find the exact location of each station/substation and power plant that feeds the North area.

Step 2-GIS base map development: Various maps such as the distribution of urban areas, the Digital Elevation Model (DEM), the road network, and the forests are needed in vector formats. These are obtained from the Council for Development and Reconstruction (CDR) taken from the National Physical Master Plan for Lebanese Territory (NPMPLT 2005 updated in 2009). Urban Areas, roads, and forests were updated to account for the urban expansion during the last ten years using satellite images from ArcGIS online base map taken in 2016 Accuracy 50 cm. As for the protected areas, the data were retrieved from the Ministry of Environment.

Step 3-Slope Analysis: Criterion C1 requires the conversion of the DEM into a raster slope map in order to identify flat regions.

Step 4-The construction of the Euclidean distances raster: Criteria C 2, 3, 4, 5 and 6 require the construction of raster Euclidian distance maps based on a straight-line distance.

Step 5-Weighted Average Raster Maps creation: The input criteria layers are in different numbering systems with different ranges; therefore, in order to combine them in a single analysis, each cell for each criterion must be reclassified into a common preference scale such as 1–10, with 10 being the most favorable. The preference values should not only be assigned relative to each other within the layer but also should have the same rate between the layers. Accordingly, if a location for one criterion is assigned a preference of 5, it will have the same influence on the phenomenon as a 5 in a second criterion. For example, the slopes are reclassified on a 1–10 scale, and the one with the least slope being the most favorable is assigned the higher scale of value 10. As the slopes become steeper, they are assigned decreasing values, with the steepest slopes being assigned a 1. We followed the same reclassification process using the 1–10 scale for the other criteria. Figure 1 represents an example of such a map for the proximity to existing power stations.

Step 6-Overlay Analysis: The Weighted Overlay is considered the most used approach for overlay analysis to solve multi-criteria problems such as site selection and suitability models. Using the raster calculator, all the weighted average raster map representing the criteria were summed with equal weight. The output gave a weighted map with values ranging from 22 to 56 where the highest values generally indicate that a location is more suitable.

3 Results

The values in the weighted average raster layer generated in step 6 were subdivided into 10 classes. All the classes lower than 5 were grouped in order to reflect regions that are not favorable to establish an SPS based on the various criteria identified earlier. The other classes ranging from 6 to 10 represent a possible location for SPS. The classified layer was converted into a vector format and values greater than five were queried representing optimal SPS locations. The vector layer was overlaid over the cadastral map of North Lebanon region in order to identify the name of the villages most suitable for SPS. A total of twenty sites were identified with areas ranging from 2 to 122 km^2. These sites are

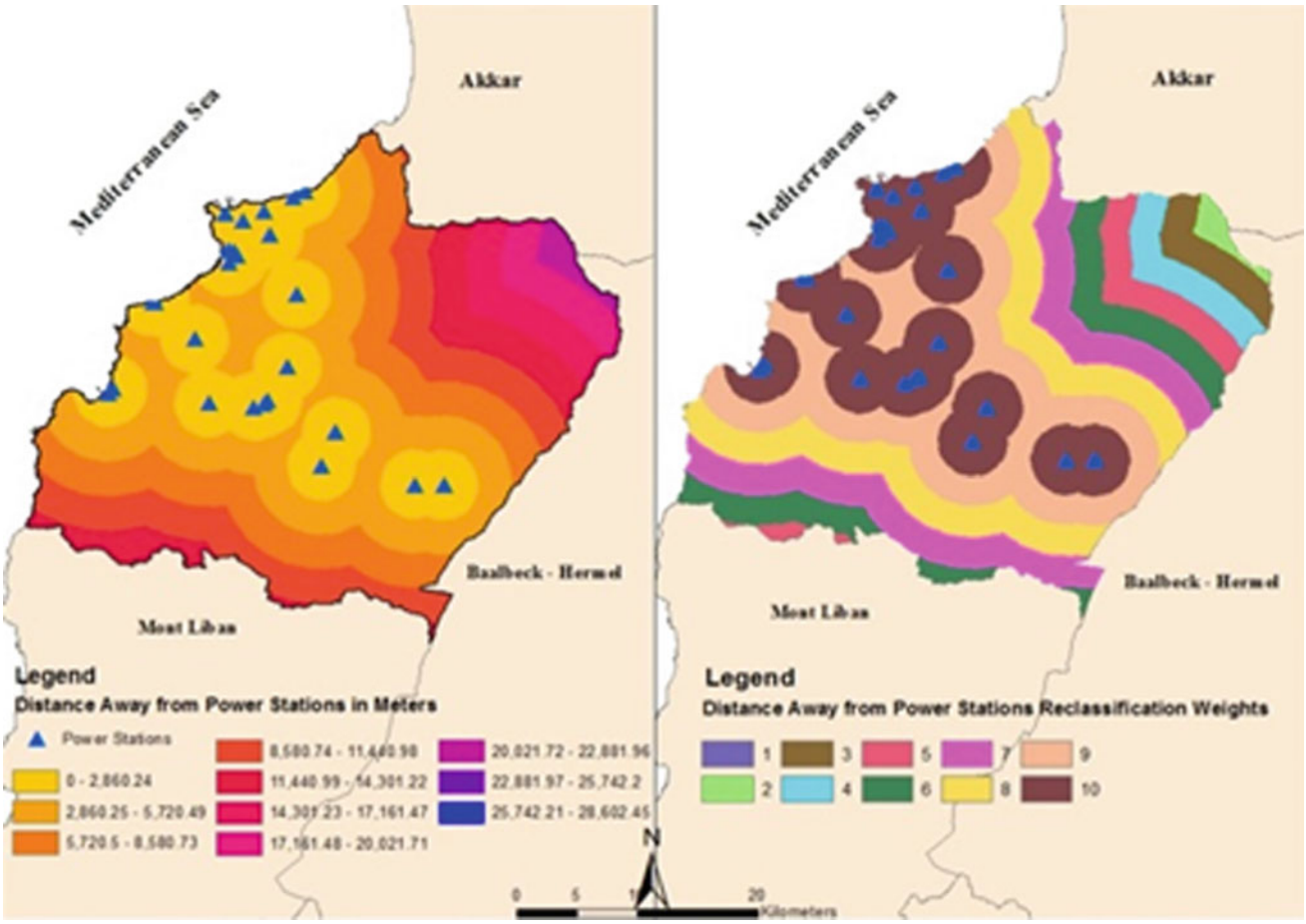

Fig. 1 Euclidean distance map for the existing power stations and their reclassifications

distributed among various administrative districts in North Lebanon Region which are Akkar, Batroun, Bcharee, Minnieh-Dennieh, and Zgharta.

4 Discussion

Even though GIS was a helpful scheme in determining the suitable locations, further analyses need to be performed in order to minimize the site suitability options. Hence, the total electricity demand and deficiency of the North region was calculated. It was found that an area of 2.5 km^2 is sufficient to nourish the power demand deficiency of Kadisha (the local power generating authority). By filtering the sites by their areas, an optimal site was identified located between the villages of Kfarhabou, Rachaaien, and Acheich with an area of 2.5 km^2 (Fig. 2). This area can generate 150 MW of electricity taking into account a 2200 KWh annual average of insolation, and 25% efficiency for the power plant. This number is equal to 50% of the total power demand in the North. Currently, Kadisha can feed 65% of the total North power demand (300 MW). Thus, this SPS can compensate Kadisha's power deficiency and alleviate the current power crisis in the North and supply clean green renewable energy.

5 Conclusion

In the course of this study, the problems of electricity in Lebanon were analyzed and presented. The shortage of supply and heavy emissions of carbon dioxide were the main motives of this study. Therefore, solar operating power plants are a must to deal with these issues as they will compensate for the shortage in supply and drastically reduce the carbon dioxide emissions and heavy pollution. However, finding a suitable location was considered a challenge since such projects require a lot of space and it is constrained by numerous conditions and restrictions. For this reason, the need for GIS was necessary. As a conclusion, the site location analysis of the project revealed very optimistic results where a total sum of all

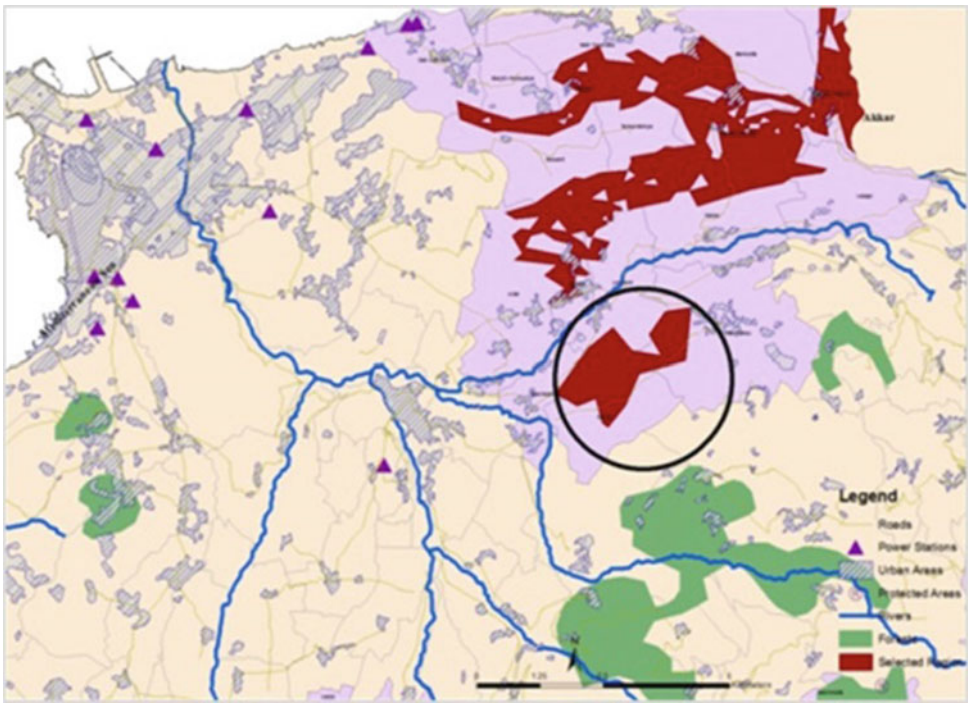

Fig. 2 Solar power plant suitable location in North Lebanon

the suitable sites in the North is found to be around 80 km^2. An area of 2.5 km^2 can cover up to 50% of the North power demand and a perfect location was found between the villages of Kfarhabou, Rachaaien, and Acheich.

References

1. Fardoun, F., Ibrahim, O., Younes, R., Louahlia-Gualous, H.: Electricity of Lebanon: problems and recommendations. Energy Procedia **19**, 310–320 (2012)
2. Electricity du Liban: EDL power structure (2004). Technical report (2004)
3. Electricity du Liban: Lebanon electricity consumption (2015). Technical report (2015)
4. Lebanese Center for Energy Conservation: The 500 solar water heaters implementation grant by the Chinese government. Technical report (2006)
5. Haddad, R.: The ambitious solar project promises more electricity for Lebanon. Technical report, Al-Monitor: The pulse of the Middle East (2015)
6. Brewer, J., Ames, D., Solan, D., Lee, R., Carlisle, J.: Using GIS analytics and social preference data to evaluate utility-scale solar power site suitability. Renew. Energ. **81**, 825–836 (2015)
7. Fadel, R., Hammond, G., Harajli, H., Jones, C., Kabakian, V., Winnett, A.: The Lebanese electricity system in the context of sustainable development. Energ. Policy **38**(2), 751–761 (2010)

Producing a Three Dimensional Model for the University of Baghdad Campus Using GIS Environment

Zahraa E. Hussein, Layla K. Abbas, Mohammed R. Falih, and Wasan M. Mohammed

Abstract

It is known that the creation of a 3D map has become a necessity for some applications especially in managing of city planning. In this paper, Geographic information system tools were used to create the 3D model; these provide the best visual interpretation of spatial data that supports a project designer in terms of planning and decision processes. This paper presented a simple strategy to create a 3D model for the University of Baghdad, Aljadrya Campus using GIS tools that would be integrated with a SketchUp software. A certain number of reference control stations were created and distributed within the whole study area using GNSS static technique, which is required for a georeferencing process. The methodology of this study also includes an assessment procedure regarding the positional accuracy and length by measuring arbitrary buildings and points in the field work of this study. Then, the resulting 3D model may be employed for clearly planning, creating new buildings and updating specified networks. Moreover, it may be used for getting positioning coordinates and length that have an accuracy level of less than 10 cm in addition to the ability to utilize it by new students for exact inference of locations. It is worth mentioning that the whole work of this study was uploaded to the GIS website online for use as an open source data.

Keywords

GIS tools • 3D model creation • Positional accuracy • Length accuracy

1 Introduction

Recently, GIS has become the most active and popular technology in terms of viewing, analyzing, and managing spatial information than others. In addition to its ease of use, it has a great ability for data analysis, which is one of the reasons for gaining popularity. The 3D Maps can be used for inference and future vision as well as for use in many projects with simulating reality [1]. There are several studies which are closely connected to our topic like [2], that proposed a method to integrate a 3D modeling software with geo information techniques. This research aimed to develop 3D GIS database in terms of reconstruction of terrain, buildings and other features related to a certain city model. Suan Sak campus of Chiang Mai University was selected as a study area in this paper. The sources of this paper based on digital photogrammetry and high-resolution satellite images which have been processed based on the image analysis technique. The findings show that the integrated technique for 3D GIS database development is undeniably fast and reliable. Reference [3] published another research that explains a simple procedure to generate 3D GIS model for Al al-Bayt University campus, a similar idea as this study. This 3D model helps users to access spatial data to support design, planning and data management. The results of the study suggested an effective method to improve data management such as maps, plans, usage of services and facilities. In addition, the workflow in this study consists of sharing the spatial data using GIS online, service, supports work productivity of customers to use apps for the desktop, browsers, smartphones, and tablets. Thus, the data of ArcGIS online became public, and anyone can download the maps and the geographical data [4]. The ArcGIS Online is also capable of controlling how to share the maps, apps, and data. Such information can be shared publicly, with specific groups, or simply be kept completely private [5].

Z. E. Hussein · L. K. Abbas · M. R. Falih (✉) · W. M. Mohammed
University of Baghdad, Baghdad, 10001, Iraq
e-mail: engmohammedrahman@gmail.com

© Springer Nature Switzerland AG 2019

H. M. El-Askary et al. (eds.), *Advances in Remote Sensing and Geo Informatics Applications*,
Advances in Science, Technology & Innovation, https://doi.org/10.1007/978-3-030-01440-7_10

2 Methodology

The overall work steps to create **3D GIS model** are summarized as follows:

2.1 Field Work

The field work included three steps. Firstly, a reconnaissance stage of the University of Baghdad was performed, Aljadrya Campus for updating all its spatial information, and then observing objects that are hard to recognize from the imagery source. In the second stage, four reference control points were determined and distributed in corner edges of the study area. GNSS static technique was used to measure the reference control points with a high accuracy level (millimeters) using Topcon GR5 receivers. It is worth mentioning that the GNSS surveying mechanism regarding this study depends on specific properties such as the period of observation that reached up to two hours in the base receiver and half an hour for the rover receiver. Additionally, GNSS raw data were processed using International GNSS service (IGS), then the four reference control points (GNSS stations) were adjusted based on the Traverse network model. Sequentially, many of the check points were measured using Total Station device to evaluate the accuracy of positions. This step was implemented in the third stage and depends on the reference control points coordinates mentioned above.

2.2 Data Source and Processes Using GIS Tools

A high resolution satellite image (10 cm), obtained from Bing satellite and which spatial resolution was changed by resampling raster until reaching the required resolution, was used to digitize all objects within the study area. Additionally, the SketchUp software was used to design a 3d model for some distinctive buildings such as University Tower, Gate and playgrounds. Regarding the processing step, ArcGIS (version 10.x) was utilized for input and processing spatial data. Initially, the satellite image of the study area was uploaded to GIS environment and corrected using a geo-referencing procedure and projected to a real coordinates system (WGS84). As known in the contemporary GIS, the geospatial data were organized in one of geo-databases that includes all feature classes like point, polygon and polyline. After creating the different types of feature classes. All objects of the study area were digitized depending on their shapes. Moreover, a specified information related to the study area objects like height, area and site of departments were input in their attribute table. All the previous steps were prepared to create a two-dimensional map in Arc map of GIS, Fig. 1a. Next, the 3D model was built up in Arc scene depending on the height of buildings of the study area in order to create the 3D map related to the University of Baghdad Campus, Fig. 1b. Accordingly, the 3D model creation from the 2D map consists of three steps. Preparation of the previously-mentioned building heights in the field work stage, considered as the first step. In the second

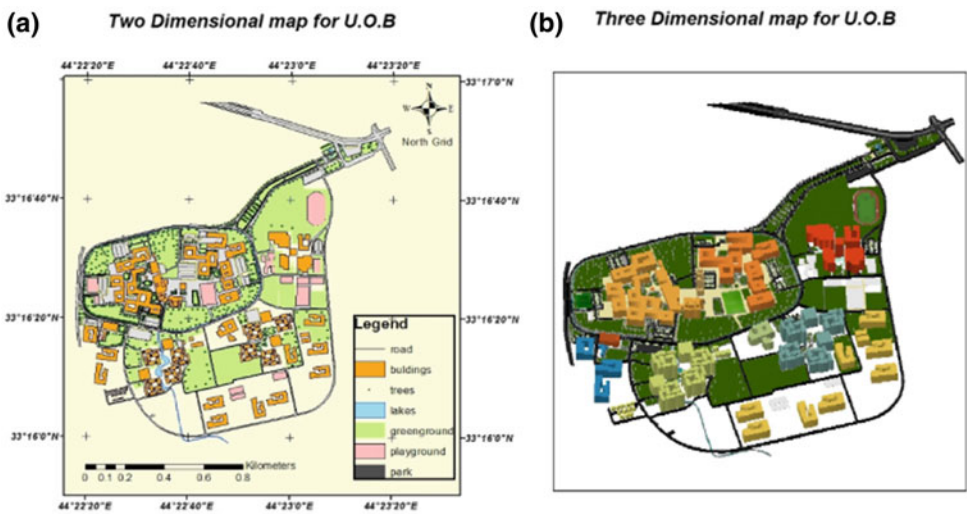

Fig. 1 The 2D map (**a**), and the 3D map (**b**) of University of Baghdad in the GIS

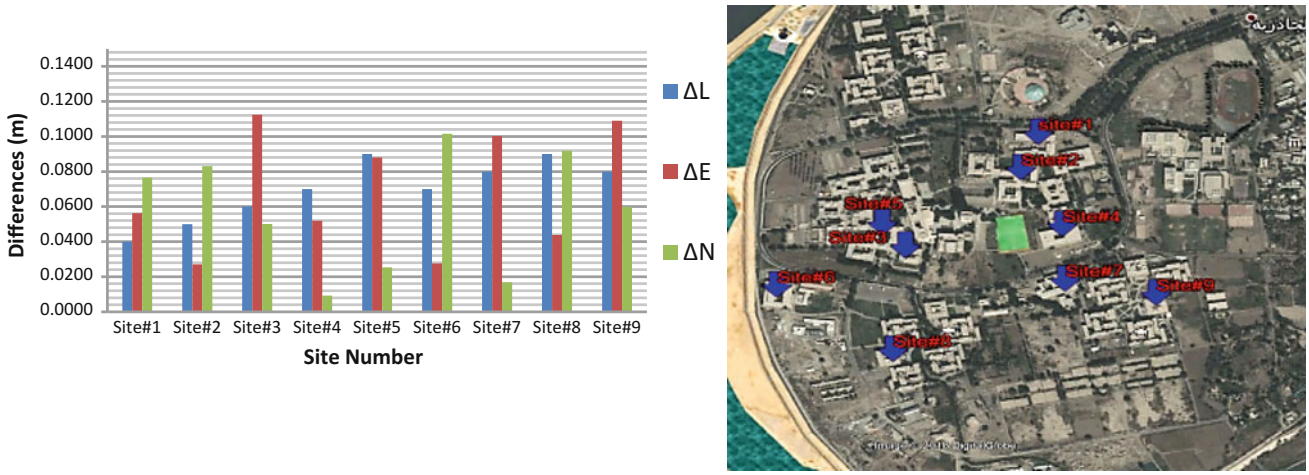

Fig. 2 The differences values between the field measurements and the GIS 3D model

step, a new layer of buildings was created and converted to collada extension for designing a 3D model in the SketchUp software. Then, the designed 3D model is inserted on the GIS Arc scene.

2.3 Measurements Accuracy Evaluation

In this stage, several sites of the University Campus were arbitrarily selected to measure a certain length and position that can be recognized in the satellite image such as the length of a building and its corners. Then, the measurement values of the fieldwork were compared with their corresponding length and position values in the 3D model using the root mean square error **(RMSE)** to assess the differences between them. The RMSE value of the length differences **(ΔL)** is equal to **7.2 cm**, while the positional differences in both of the east **(ΔE)** and the north **(ΔN)** directions are **7.6** and **6.5 cm**, respectively. Thus, the overall mentioned differences can be summarized in Fig. 2.

2.4 Sharing the Studied Model with GIS Online

The methodology of this study includes sharing the 3D map on GIS online in certain steps. After creating an account on the GIS online website, the main steps of the GIS online sharing can be summarized in Fig. 3.

3 Conclusion

This paper presents a simple mechanism to create the 3D model using GIS for the selected study area that represents the University of Baghdad. This study took into consideration for the high accuracy level of the created 3D model using a high resolution satellite image (10 cm) and the highly accurate GNSS static technique measurements (sub millimeters). Accordingly, the positional and length accuracy of the studied model reaches about a sub centimeter using the RMSE value to evaluate the differences between the real measurements and the corresponding 3D model

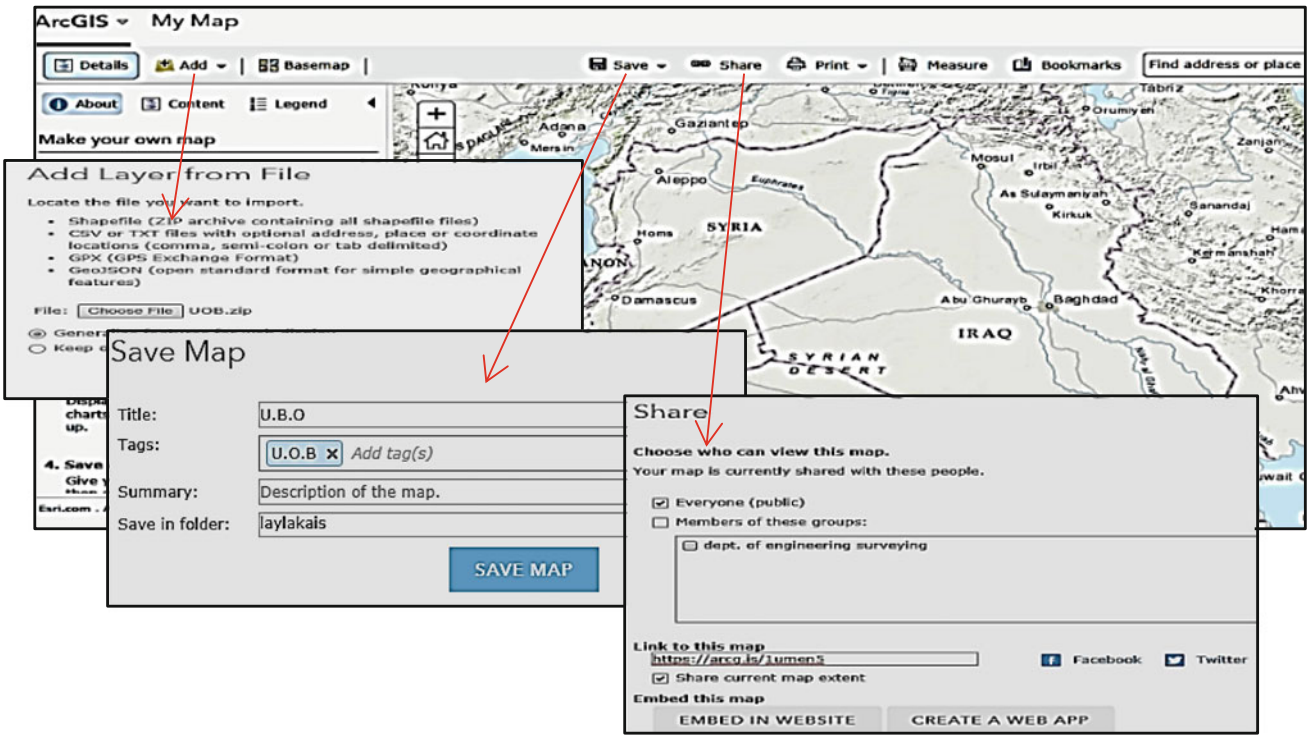

Fig. 3 Summary of sharing data using GIS online

computations. For more advantages, the overall works regarding the 3D model creation were uploaded to the website belong to the GIS online. This paper offers more support for planners and designers of urban projects and may offer an inference map for any strangers at the University of Baghdad.

References

1. Pulighe, G., Baiocchi, V., Lupia, F.: Horizontal accuracy assessment of very high resolution google earth images in the city of Rome, Italy. Int. J. Digital Earth **9**(4) (2016)
2. Malumpong, C., Chen, X.: Interoperable three-dimensional GIS City modeling with geo-informatics techniques and 3D modeling software. In: The International Archives of the Photogrammetry, Remote Sensing and Spatial Information Sciences (2008)
3. Al-Rawabdeh, A., Al-Ansari, N., Attya, H., Knutsson, S.: GIS Applications for Building 3D Campus, utilities and implementation mapping aspects for university planning purposes. J. Civil Eng. Archit. **8**(1), 19–28 (2014)
4. Tang, T., Zhao, J., Coleman, D.J.: Design of a GIS-enabled online discussion forum for participatory planning. In: Proceedings of the 4th Annual Public Participation GIS Conference, Cleveland State University, Cleveland, Ohio, USA (2005)
5. Boulos, M.K.: Web GIS in practice III: creating a simple interactive map of England's strategic health authorities using Google Maps API, Google Earth KML, and MSN Virtual Earth Map Control. Int. J. Health Geog. **4**(2005)

Seasonal Hydrological Loading from GPS Observed Data Across Contiguous United States Using Integrated Apache Hadoop Framework

Pece V. Gorsevski, Yuning Fu, Kurt S. Panter, Jeffrey Snyder, and Asanga M. Ramanayake

Abstract

The study examined the relationship between seasonal vertical loading deformation and seasonal hydrological loading from precipitation specified as rain and snow. The vertical loading deformation is characterized by time-series estimated from continuous Global Positioning System (GPS) network across the contiguous United States for a timeframe of 48 months (January 1st, 2013 to December 31st, 2016). The data processing used custom-built R scripts and spatial libraries that were integrated with Hive framework which is a data warehouse extension of Apache Hadoop that is used as a database query interface. The relationships of vertical displacement were explored by visualization techniques such as spatial maps and wavelet coherence plots.

Keywords

Vertical loading deformation • GPS • Hadoop • Wavelet • Crustal deformation

1 Introduction

Assessment of vertical displacement of the Earth's crust is achieved by different techniques including high-precision surveying, implementation of differential Interferometric Synthetic Aperture Radar (InSAR), use of continuous GPS stations, aerial digital photogrammetry and laser scanning [1–3]. Specifically, the advantages of GPS include continuous coverage of high sampling rates that generate hourly, daily, weekly, or monthly solutions; high observational precision in horizontal and vertical components; long-term stability; potential for detection of rapid displacements and horizontal strain components; and an expanding global coverage of observation stations within Global Navigation Satellite System (GNSS) that integrates different systems such as the United States (US) GPS, Russia's GLONASS, China's BeiDou, and the European Union (EU) Galileo.

This paper explored the relationship between time-series data collected from the US GPS network stations and estimated precipitation. The data processing workflow implemented (1) a system with multi-node Hadoop cluster (a total of three computers) for parallel processing of data; (2) development of custom-built R scripts for spatial integration with GRASS GIS; and (3) visualization and analysis of relationships between vertical displacement from GPS and hydrological loading from precipitation.

2 Study Area and Methodology

The study used data for the continental United States (US) for 48 months between January 1st, 2013 and December 31st, 2016. The crustal vertical deformation is characterized by time-series estimated from GPS network from a total of 4347 stations. The GPS time series used in this study was GPS daily solution. The data were processed by GIPSY OASIS-II software and stored by the Nevada Geodetic Laboratory (NGL) at the University of Nevada, Reno and published on their File Transfer Protocol (FTP) server [4]. The monthly precipitation data that matched the GPS time-series dataset were acquired from the PRISM climate group [5].

The processing of the time-series data was implemented by Apache Hadoop. The Hadoop Distributed File System (HDFS) is the main component for storing the data while the processing framework implements MapReduce model which reduces the complexity of the problem into parallelized distributed solution across the cluster [6]. The MapReduce is a programming model which consists of two main elements:

P. V. Gorsevski (✉) · Y. Fu · K. S. Panter · J. Snyder
A. M. Ramanayake
School of Earth, Environment and Society, Bowling Green State University, Bowling Green, OH 43403, USA
e-mail: peterg@bgsu.edu

© Springer Nature Switzerland AG 2019

H. M. El-Askary et al. (eds.), *Advances in Remote Sensing and Geo Informatics Applications*, Advances in Science, Technology & Innovation, https://doi.org/10.1007/978-3-030-01440-7_11

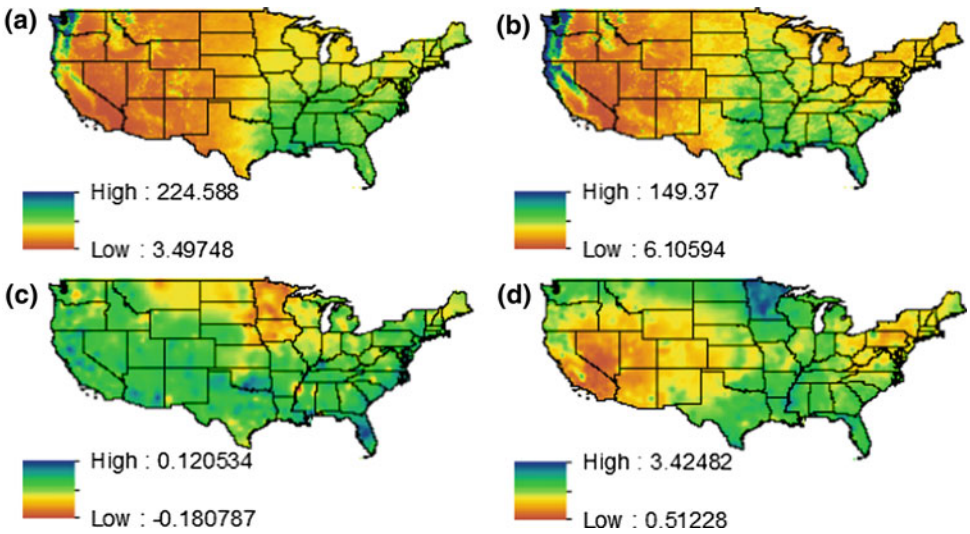

Fig. 1 Precipitation maps (mm) of **a** monthly average and **b** standard deviation (not detrended), and GPS maps (mm) of **c** monthly average and **d** standard deviation (detrended)

(1) a mapper used for spliting data for parallel processing across the cluster; and (2) a reducer which partitions and combines the data into a single value or a set of values. The Apache Hive extension is a high-level MapReduce framework which was used in this research for reducing the GPS data to monthly averages.

The regularized spline with tension interpolation method was used to convert the GPS point datasets into continuous raster datasets using spatial libraries in R in conjunction with GRASS GIS. The interpolated data represented the vertical crustal deformation from the GPS dataset. The hydrological loading from the precipitation datasets were downloaded as monthly rasters. Both datasets were detrended before wavelet coherence analysis was implemented.

3 Results and Discussion

The spatial distribution of monthly precipitation varies across the US (Fig. 1). The precipitation is higher in the east and lower in the west, except for the northwest which receives the highest precipitation. Also, the standard deviation map of the precipitation shows that the southeast and the northwest have the highest variability. The average GPS displacement map shows that below average values are mostly concentrated in the northern central region. This region was covered by glaciers more than 10,000 year ago and still undergoes isostatic rebound. However, the standard deviation map of GPS displacement shows that the western region associated with the mountains has the least variation, which could be due to different geologic rock types (i.e., GPS seasonal deformation dominated by surface mass loading). For instance, this region has a much higher proportion of bedrock exposed (i.e., less sediment cover) and, perhaps, a lower density of vegetation due to climate and elevation. Interestingly, that the northeastern region also shows lower variability but has more mountains. This region was also covered by glaciers like the north central area.

Locally weighted scatterplot smoothing (LOWESS) curves for the monthly time-series were generated from standardized mean values (Fig. 2). Although the monthly distributions of the values were highly variable, the curves depict (a) the seasonal patterns of precipitation and (b) GPS displacement. Results from individual monthly Pearson's comparisons between the precipitation and the GPS displacement suggested that some months were highly correlated (i.e., $r = 0.6$, December 2014).

The wavelet coherence is similar to correlation measurement where the value of 1 (red color) represents high correlation and a value of 0 (blue color) represents no correlation (Fig. 3a). For example, the highest correlation between the time-series that is represented in red color is centered between 0.25 and 2 periods (months). The high correlation is also shown in the average (global) coherence plot (Fig. 3b) which suggests that high correlation is associated with periods 4, 6, 8 and 12. This analysis indicates that there is seasonal, semi-annual, and annual correlation between precipitation and GPS displacement.

The phase is represented by arrows (Fig. 3a) indicating the leading/lagging of the two time-series. A zero phase difference means synchronized time-series that move together. When arrows point to the east or west the time series

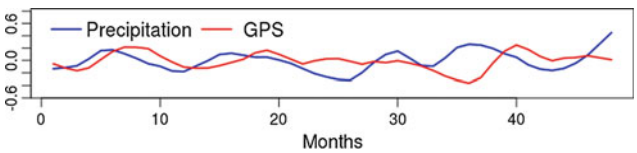

Fig. 2 LOWESS curves from monthly precipitation and GPS displacement from entire US

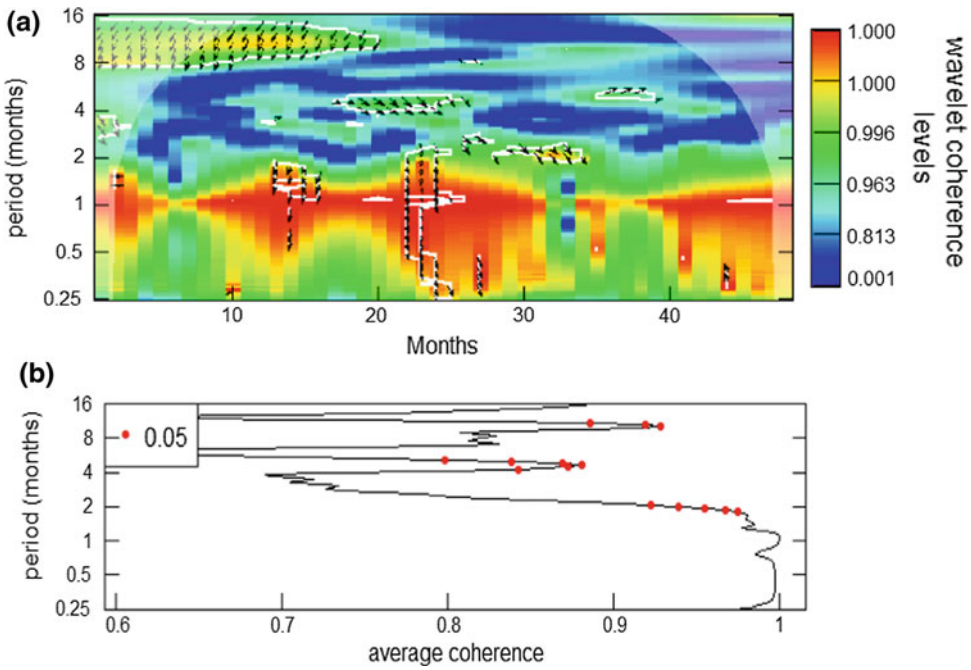

Fig. 3 Wavelet coherence (**a**) and average coherence (**b**) between average monthly precipitation and average GPS displacement

are positively or negatively correlated. On the other hand, arrows pointing southward means that the first time series leads the second, whereas arrows pointing northward shows the opposite. Most of the arrows are pointing southward which means that precipitation preceded the vertical displacement.

4 Conclusions

The wavelet coherence analysis shows that vertical displacement is influenced by seasonal hydrologic loading using mean estimates. The analysis demonstrates that seasonal, semi-annual, and annual correlation occur between precipitation and GPS displacement even at a large US regional scale. The leading time-series is the precipitation which represents the hydrological loading that influences the behavior of the seasonal ground deformation. Also, the implementation of this integrated Hadoop framework shows the potential for processing large regional scale datasets that could be supplemented with additional heterogeneous sources of spatio-temporal data.

References

1. Liwei, L., Lingyun, J., Xiaodong, Y.: Present-day crustal deformation around Kalpin block, Xinjiang, China, observed by InSAR. Geod. Geodyn. **5**, 23–28 (2014)
2. Fabris, M., Achilli, V., Menin, A.: Estimation of subsidence in Po Delta area (Northern Italy) by integration of GPS data, high-precision leveling and archival orthometric elevations. Int. J. Geosci. **05**, 571 (2014)
3. Fu, Y., Freymueller, J.T., Jensen, T.: Seasonal hydrological loading in southern Alaska observed by GPS and GRACE. Geophys. Res. Lett. **39**, L15310 (2012)
4. The National Aeronautics and Space Administration (NASA), Jet Propulsion Laboratory (JPL), https://www.jpl.nasa.gov. Accessed 10 Feb 2018
5. Parameter-elevation Regressions on Independent Slopes Model (PRISM) Climate group, http://prism.oregonstate.edu. Accessed 23 Apr 2018
6. Apache Hadoop, http://hadoop.apache.org. Accessed 03 May 2018

Characterization of Periodic Signals and Noises of Geocenter Motion from Space Geodesy Techniques Data

Bachir Gourine

Abstract

The purpose of this work was to characterize the signals and noises of Geocenter variations time series obtained from different space geodesy techniques as Global Positioning System (GPS), Doppler Orbitography and Radiopositioning Integrated on Satellite (DORIS), and Satellite Laser Ranging (SLR). The methodology proposed is based on the estimation of periodic signals by performing the frequency analysis using FAMOUS software (Frequency Analysis Mapping On Unusual Sampling) and evaluation of noises level and type by Allan variance technique. The available data covers 13 years (from 1993 to 2006) of weekly series of Geocenter residuals components, according to ITRF2000. The results obtained are more accurate according to GPS and SLR of about 2–8 mm than DORIS of about 8–42 mm. The estimated seasonal signals amplitudes are of about of few mm per technique with centimetre level for Z Geocenter coordinate of DORIS. The Geocenter motion derived from the SLR technique is more accurate and close to the geodynamic models. The noise analysis shows a dominant white noise in the SLR and DORIS solutions at level of 0.6–1 mm and 10–40 mm, respectively. However, the GPS solution is characterized by a flicker noise at the millimetre level, relating to mismodelling systematic errors.

Keywords

Geocenter motion • Frequency analysis • Noise estimation • Space geodesy techniques

1 Introduction

Space Geodesy provides for different applications in earth sciences, a Terrestrial Reference Frame (TRF) in which the Earth system parameters are expressed: Rotation of the Earth, Gravity field, tectonic Plates, Geocenter motion. This latter is considered as the motion of the center-of-mass (CM) of the total Earth system with respect to the center-of-figure (CF) of the solid Earth surface [9]. It reflects the global scale mass redistribution and the interaction between the solid Earth and mass loading. It can be tracked and observed by space geodetic positioning techniques such as Satellite Laser Ranging (SLR), Doppler Orbitography and Radiopositioning Integrated on Satellite (DORIS), and global positioning system (GPS). The SLR technique is considered as a perfect technique for the Geocenter recovery. However, SLR-derived Geocenter coordinates are mainly affected by the inhomogeneous distribution of the SLR stations. Besides, the GPS and DORIS techniques have well distributed and dense networks, but complicated surface force modelling, tropospheric delay modelling/estimation, and transmitter/receiver phase center calibrations, etc. create many complications for the Geocenter motion determination, in case of GPS. For DORIS, the satellites tracked present significant challenges to precise orbit determination, so noisier and less stable results w.r.t. than the other techniques [7]. The objective of this paper was to examine the contribution of each individual technique at the Geocenter assessment and to check their reliability and precision. The analysis methodology proposed is based on (i) the frequency analysis of time series of Geocenter components by Famous (Frequency Analysis Mapping On Unusual Sampling) Software [8], in order to extract seasonal signals, (ii) the study of the noise affecting these series, by Allan variance method to assess their stability (type and level of noise) [3], and (iii) the results comparison of SLR, DORIS and GPS solutions with geodynamic models.

B. Gourine (✉)
Department of Space Geodesy, Centre of Space Techniques, 31200 Arzew, Algeria
e-mail: bgourine@cts.asal.dz

© Springer Nature Switzerland AG 2019

H. M. El-Askary et al. (eds.), *Advances in Remote Sensing and Geo Informatics Applications*, Advances in Science, Technology & Innovation, https://doi.org/10.1007/978-3-030-01440-7_12

2 Methodology and Data Used

The methodology is based on the extraction and analysis of periodic signals of time series and the study of noise that affects them. A program called ANASCO (Statistical and Spectral Analysis of Time Series of Sites in Co-location) developed by [5] and FAMOUS program (Frequency Analysis Mapping On Unusual Sampling) developed by [8], were performed for Statistical and Spectral Analyses of Geocenter variations time series and noise estimation using Allan variance. Two parameters characterize the noise: the type and level of noise [3] and [6]. The data processed through this study are the weekly series of the Helmert translations parameters between the reference frames of each technique (GPS, SLR and DORIS) and ITRF2000. The period of the data is about 13 years (1993–2006), except for the GPS data which begin in 1996, Fig. 1. The results of the statistical analysis performed by ANASCO program showed that the translations (movement of Geocentre) were well estimated by the SLR technique (with an average of about 0.5 mm, and an accuracy of about 4–8 mm) and by GPS (in average of 6.4 mm with an accuracy of 2–8 mm). For DORIS technique, the determination of these parameters (in average of 0.2 mm) was less accurate (of about 8–42 mm). Indeed, the estimated values were high especially for TZ component. Although the SLR technique is dedicated for an "exact" determination of the Geocenter, GPS technique allows a more accurate estimation, thanks to the density and geographical distribution of the IGS stations network.

3 Results and Analysis

The Geocenter variations are due mainly to the redistribution of masses in the atmosphere, oceans and hydrologic reservoirs, in addition to earthquakes and tectonic plates. They have two main periodic components: annual and semi-annual terms.

Table 1 gives the values of the amplitudes and phases and their standard deviations of annual and semi-annual signals for solutions of DORIS, SLR and GPS techniques and two geodynamic models of [1] and [2]. The signal parameters, as amplitude A and phase φ, are defined from: $y = A \cdot cos(\omega (t - t_0) + \varphi)$, where t_0 is 1st January of the reference year indicated in the table. Some periodic signals have not been estimated by FAMOUS, they are mentioned as dashes in the table.

The results in Table 1 show an agreement at the millimetre level for the amplitudes of different solutions. The annual term is estimated in all components of Geocenter according to the three techniques. The amplitudes of the TZ component are important, particularly for DORIS solution. In fact, according to Gobinddass' et al. study [4], this bias is due to modelling errors of the solar radiation pressure on satellites TOPEX/Poseidon and SPOT, even if Chen et al. [1] give an annual range close to that of SLR technique at 0.5 mm. We note also a good agreement at the millimetre level (and even better than mm) of SLR amplitudes with those of geodynamic models. This is due to the fact that these models are based on laser data of LAGEOS satellites. However, the semi-annual term was not found in the components TX of SLR, TY of GPS and TZ according to DORIS and GPS techniques. For the phases, the agreements are less convincing. The results of geodynamic models used were carried out on five years of data only, versus 13 years in our case. Moreover, these geodynamic models have no real predictive feature. A comparison between seasonal signals of different space geodesy techniques with both geodynamic models, based on correlation factor was performed. It revealed a good agreement in terms of amplitude and phase for SLR and GPS techniques, respectively. Figure 2 illustrates the evaluation of stability of Geocenter motion, according to space techniques based on Allan variance computation. The GPS results show the existence of flicker noise while the SLR and DORIS results exhibit a dominant white noise. In terms of stability, the results of GPS and SLR are most accurate, with about 0.2–1 mm, and

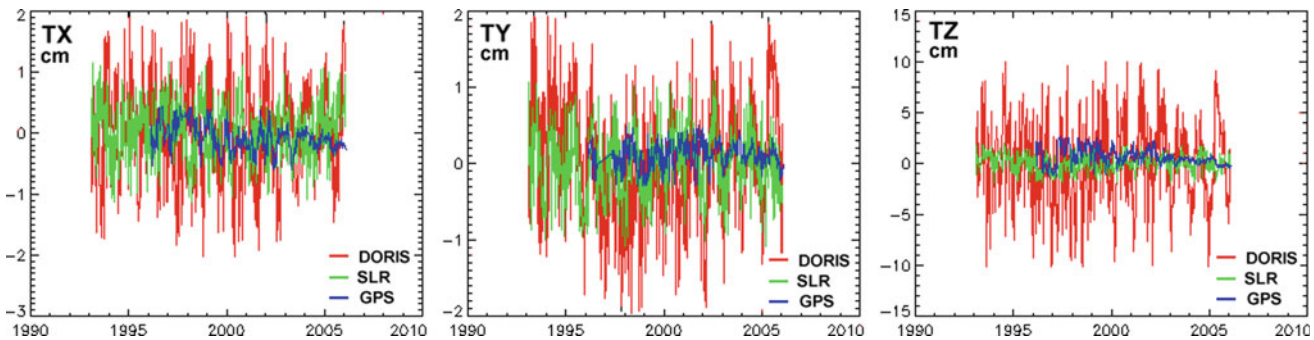

Fig. 1 Time series of the geocentre motion (*TX*, *TY*, *TZ*) according to GPS, SLR and DORIS techniques

Table 1 Comparison of Geocenter seasonal signals between DORIS, SLR and GPS, and with geodynamic models. Amplitude A is in mm and phase φ in degrees

	DORIS		SLR		GPS		Dong et al. [2]		Chen et al. [1]	
Parameter and period	A σA	φ $\sigma\varphi$	A σA	φ $\sigma\varphi$	A σA	φ $\sigma\varphi$	A	φ	A	φ
TX 1 yr	6.4 ±0.4	354 ±6.6	2.7 ±0.4	154 ±9.4	1.5 ±0.2	122 ±10.6	4.2	224	2.4	244
TX ½ yr	2.5 ±0.4	80 ±16.4	–	–	1.1 ±0.2	340 ±15.4	0.8	210	0.7	1
TY 1 yr	5.3 ±0.5	247 ±7.9	3.4 ±0.4	217 ±6.3	0.8 ±0.3	21 ±34.7	3.2	339	2.0	270
TY ½ yr	1.6 ±0.6	60 ±24.2	0.8 ±0.2	1 ±30	–	–	0.4	206	0.9	41
TZ 1 yr	28.7 ±2.1	168 ±7.3	4.6 ±0.7	132 ±8.9	3.7 ±0.7	195 ±18.5	3.5	235	4.1	228
TZ ½ yr	–	–	1.7 ±0.6	203 ±26.2	–	–	1.1	133	0.5	58
Reference year	1993		1993		1996		1990		1990	

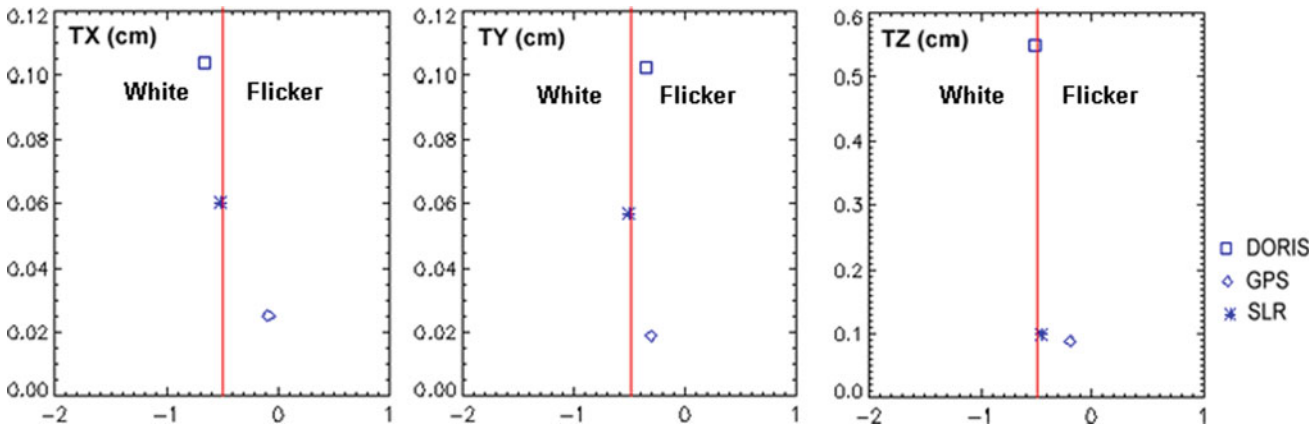

Fig. 2 Distribution of the type of noise (x-axis) and noise level (y-axis) for Geocentre motion according to GPS, SLR and DORIS techniques

0.6–1 mm, respectively. However, the DORIS results are less accurate with 10–40 mm of precision.

4 Conclusion

In this paper, we presented the results of the time series analysis of Geocenter variations derived from space geodetic techniques (SLR, GPS and DORIS), for the characterization of signals and noises of these time series. The proposed analysis methodology was based on frequency analysis and noise study. An average RMS of about 2–8 mm was obtained for Geocenter variation components according to GPS and SLR techniques. The frequency analysis was performed by FAMOUS program for the estimation of annual and semi-annual terms of Geocenter motion where the results of SLR solution are in good agreements with geodynamic models. This confirms the reliability of this technique in Geocenter determination. In terms of noise, the flicker noise was detected in GPS solution, while a dominant white noise characterizes the SLR, DORIS time series. In terms of stability, the results of GPS and SLR are the most accurate for Geocenter motion. Finally, using recent data will be of great interest to improve the Geocenter motion analysis.

References

1. Chen, J.L., Wilson, C.R., Eanes, R.J., Nerem, R.S.: Geophysical interpretation of observed geocentre variations. J. Geophys. Res. **104**(B2), 2683–2690 (1999)
2. Dong, D., Dickey, J.O., Chao, Y., Cheng, K.: Geocentre variations caused by atmosphere, ocean and surface ground water. Geophys. Res. Lett. **24**(15), 1867–1870 (1997)
3. Feissel-Vernier, M., de Viron, O., Lebail, K.: Stability of VLBI, SLR, DORIS, and GPS positioning. Earth Planets Space **59**, 475–497 (2007)
4. Gobinddass, M.L., Willis, P., de Viron, O., Sibthorpe, A., Ries, J. C., Zelensky, N.P., Bar-Sever, Y.E., Diament, M., Ferland, R.: Systematic biases in DORIS-derived geocentre time series related to solar pressure mis-modeling. J. Geodesy **83**(9), 849–858 (2009)
5. Gourine, B.: Combinaison des données spatiales de positionnement en vue de l'optimisation des réseaux géodésiques: Modélisation, Filtrage, Traitement et Analyse (in French). Ph.D. thesis of USTO-MB, Oran, Algeria (2011)
6. Gourine, B.: Use of Starlette and LAGEOS-1&-2 laser measurements for determination and analysis of stations coordinates and EOP time series. C.R. Geosci. **344**, 319–333 (2012)
7. Krzysztof, S.: Limitations, challenges, and prospects of different space geodetic techniques used for the determination of the Geocenter motion. In: International Workshop on the Inter-Comparison of Space and Ground Gravity and Geometric Spatial Measurements, Strasbourg, France (2017)
8. Mignard, F.: User Guide of FAMOUS Software. Internal Report of OCA-France (2005)
9. Wu, X., Ray, J., Van Dam, T.: Geocenter motion and its geodetic and geophysical implications. J. Geodyn. **58**, 44–61 (2012)

Geo-Informatics for Optimal Design of Desalination Plants Using Renewable Energy Sources: The DESiRES Platform Paradigm

Eftichios Koutroulis, George Petrakis, Dionissios Hristopulos, Achilles Tripolitsiotis, Nabila Halouani, Arij Ben Naceur, and Panagiotis Partsinevelos

Abstract

This work described the operational capabilities of a platform developed to assist decision makers to determine the optimal location and configuration of desalination plants to be powered by renewable energy sources. The platform, called DESiRES, operates under an open source geographical information system interface. Interoperability with geostatictical and optimization design algorithm modules was achieved via the location based information provided by the geographical module. The current stage of DESiRES platform development (i.e., study areas, data used, etc.) was presented along with the basic platform functionalities, showing a great potential for design and assessment of desalination in the Mediterranean region.

Keywords

Geographic information systems • Desalination plant design • Renewable energy sources • Decision making

1 Introduction

The Mediterranean region is one of the most water-scarce regions in the world [1]. In order to confront such a severe water-scarcity problem, desalination technology is a potential option, since it provides reliable, high-quality sources of water, which are produced under direct local control, thus reducing the need for importing and transferring water from other regions, and reducing the vulnerability to external factors [2]. Considering that the energy cost accounts for about half of the overall desalination plant cost [3] and that the operation of a desalination plant may have negative environmental impact (i.e. through greenhouse gas emissions when fossil fuels and/or nuclear power are used, significant water consumption for cooling the conventional electric energy production units etc.), it is evident that by using Renewable Energy Sources (RES) for power-supplying desalination plants provides an environmentally friendly and economically sustainable solution to water scarcity issues in the Mediterranean region.

Under the framework of the ERANET-MED funded project entitled "DES^{2}iRES" an Internet-based, web-Geographical Information System (web-GIS) is being developed to provide policy-makers and stakeholders in the Mediterranean region with a user-friendly tool for the optimal design and sizing of RES-powered desalination plants.

In the following Section the architecture of the DESiRES platform was given along with its functionality. Section 3 presented the current status of the three main DESiRES modules emphasizing in the geo-information provided and this short paper which ended with a discussion (Sect. 4) of the main problems encountered and with the future plans (Sect. 5) for platform validation and extension to other Mediterranean regions.

2 Architecture and Functionality

The DESiRES platform integrates novel algorithms for the optimal design and sizing of desalination plants, the implementation of geostatistical analysis to exploit in situ and remotely-sensed data, and GIS visualization tools to provide answers to critical policy drive questions such as: Is it feasible to construct an RES-powered desalination plant? If yes, what is the optimal location? If not, why? Can existing desalination plants be upgraded to be powered by RES? What kind of technology should be used?

E. Koutroulis · G. Petrakis · D. Hristopulos · P. Partsinevelos (✉)
Technical University of Crete, University Campus,
Akrotiri, 73100 Chania, Greece
e-mail: ppartsi@mred.tuc.gr

A. Tripolitsiotis
Space Geomatica P.C, Xanthoudidou 10A,
73134 Chania Crete, Greece

N. Halouani · A. B. Naceur
Faculty of Sciences of Tunis, University of Tunis El Manar,
Tunis, 2092, Tunisia

© Springer Nature Switzerland AG 2019

H. M. El-Askary et al. (eds.), *Advances in Remote Sensing and Geo Informatics Applications*,
Advances in Science, Technology & Innovation, https://doi.org/10.1007/978-3-030-01440-7_13

The DESiRES platform consists of three distinct but interoperable modules (Fig. 1):

1. **GIS module**: This module contains the database of all information needed included among others: historical meteorological records for solar irradiance, ambient temperature, wind speed, wave height, and the operational characteristics of devices to be used for the optimal design of the desalination plant. The GIS-module also provides the graphical user interface not only for area-of-interest selection but also for the manual inclusion of data from the user.
2. **Geo-statistical module**: Upon the selection of the location where the desalination plant is to be constructed by the user and the desired RES and/or industrial configuration, the geo-statistical tool retrieves, by the GIS-module, the coordinates of this location. Then, it processes the meteorological records available in the platform database. The objective was to generate hourly values for a typical year, for each of the meteorological variables studied. The typical year was determined from statistical analysis of the available data for a number of years. In case of inadequate data, a time-series of at least one year of hourly data was generated. The output of the geostatistical module is fed to the optimization module.
3. **Optimization module**: This module receives input by both the GIS (location and operational characteristics) and the geostatistical (annual hourly values for necessary meteorological parameters) module. Then, processing, using a modified version of the algorithm originally presented in [4], is carried out and the results are automatically sent to the user by email and/or the GIS interface.

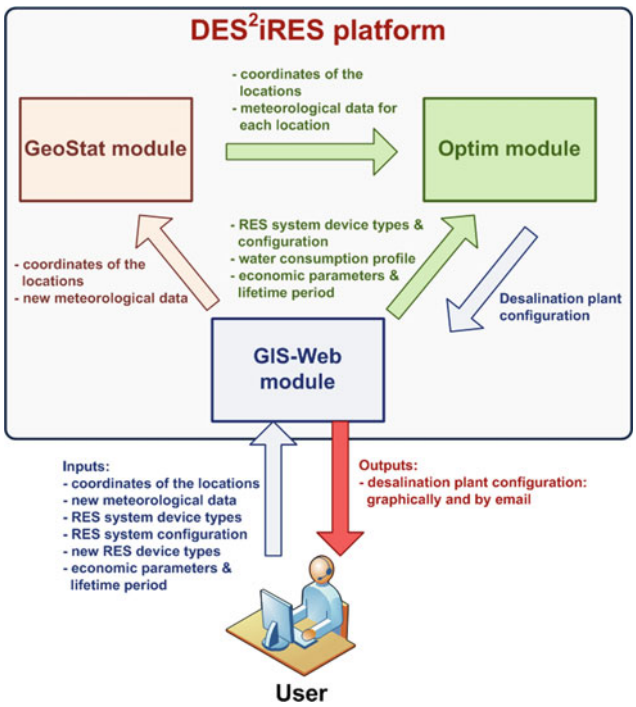

Fig. 1 The software architecture of the DESiRES platform

3 The DESIRES Geo-Information Platform

At the moment the DESiRES is being implemented for two case study areas: one in Greece and one in Tunisia. For these areas the availability of in situ meteorological data has been investigated through free but also commercial databases. Currently, records from 12 stations in Crete, Greece and 10 stations in Tunisia along with land use and spatial planning geo-information have been incorporated in the DESiRES platform (Fig. 2).

4 Discussion

The technical success of the DESiRES platform lies upon the availability of historical meteorological data records to allow the calculation of the typical meteorological year, the spatial density of available meteorological stations to enable efficient implementation of spatio-temporal geo-statistical algorithms, and the computational time of the optimization algorithm.

The success of the platform will be measured by the number of users and entities who will use the platform and incorporate it into their every-day operations. The platform design aims to provide ease of use, attractive user-interface, complete and accurate geo-information, and modularity as well as adaptability to changing requirements, specifications and needs in order to maximize its appeal.

In this stage of DESiRES development we have identified problems related to availability of free meteorological data, the presence of data gaps, sometimes extending over substantial time periods, in meteorological records, and most importantly the short-length of the available records (even in commercial meteorological data products) that prevent the accurate estimation of the typical meteorological year.

5 Conclusion

This work presented the concept and current status as well as problems encountered for the development of a web-based platform for optimal design of desalination plants powered

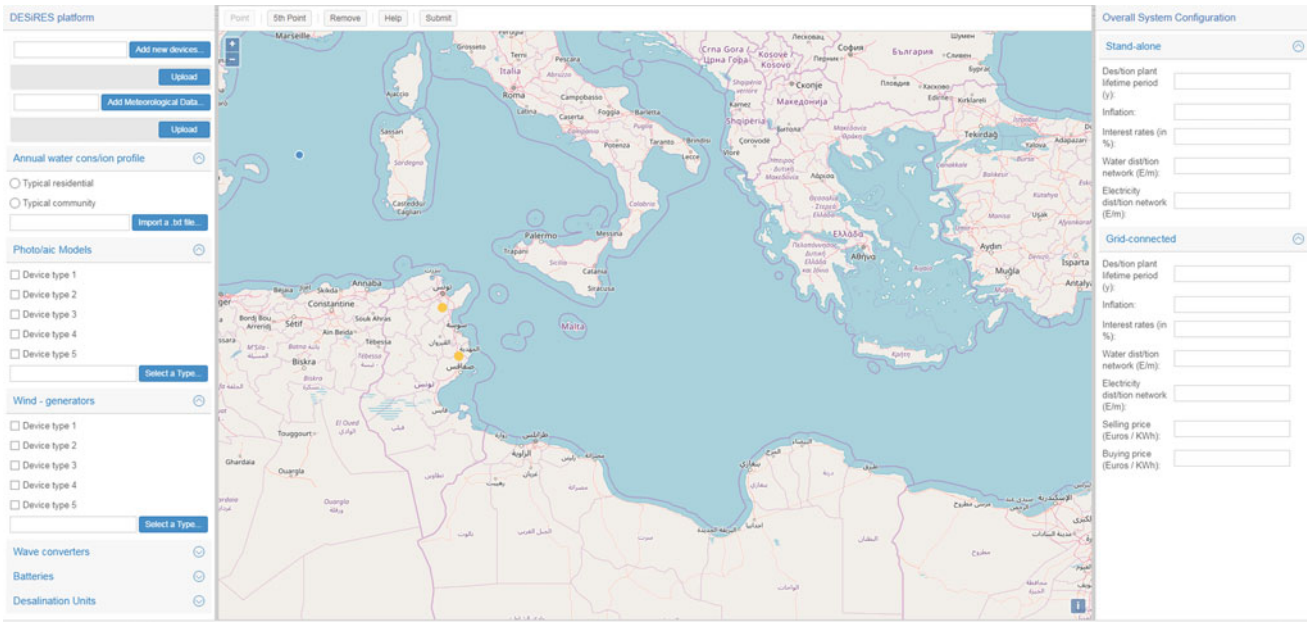

Fig. 2 The DESiRES platform interface. The yellow dots indicate areas of interest as selected by the user

with renewable energy sources. The DESiRES platform is a fully functioning demonstration project that further seeks for data providers and users who will assess its operational capabilities and functionalities. DESiRES integrates technological, scientific and industrial knowledge along with societal and political particularities to optimize the location and configuration of desalination plants in the Mediterranean region through a cost effective combination of available RES technologies.

Acknowledgements The research presented in this manuscript was funded by the project DESIRES:DESign of DESalination systems based on optimal usage of multiple Renewable Energy Sources, ERANETMED NEXUS-14-049, co-financed by the European Commission's 7th Framework Programme.

References

1. Simonet, S.: Adapting to Climate Change in the Water Sector in the Mediterranean: situation and Prospects. Pan Bleu (2011)
2. Cooley, H.: Seawater desalination: Panacea or Hype? Actionbioscience, April 2010 [Online]. Available: http://www.actionbioscience.org/environment/cooley.html. Accessed Feb 2015
3. Herndon, A.: Energy makes up half of desalination plant costs: Study. Bloomberg, 1 May 2013 [Online]. Available: https://www.bloomberg.com/news/articles/2013-05-01/energy-makes-up-half-of-desalination-plant-costs-study. Accessed Feb 2015
4. Koutroulis, E., Kolokotsa, D., Potirakis, A., Kalaitzakis, K.: Methodology for optimal sizing of stand-alone photovoltaic/wind-generator systems using genetic algorithms. Sol. Energy **80** (9), 1072–1088 (2006)

Combination of Simple Additive Weighting (SAW) and Hierarchical Analysis Process (HAP) Methods for the Determination of Construction Suitability Zones in the Eastern Part of the Jijel Region (North East Algeria)

Karim Remoum and Azzedine Bouzenoune

Abstract

The objective of this study was to propose concepts allowing the establishment of an interactive system of decision support adapted to the conduct of territorial processes relative to the challenges of the different phases of decision making. To support effectively the problem of Territorial Planning which consists in the search for a surface satisfying at best some criteria among a set of variants, Geographical Information Systems (GIS) and existing geotechnical data were analyzed and aggregated using MultiCriteria Decision Support (AMCD), namely the Simple Additive Weighting method (SAW) and the Analytic Hierarchy Process method (AHP). The combination of the two methods allowed us to make a concordance map to select the best suitable sites.

Keywords

Geographic information system (GIS) • Simple additive weighting (SAW) • Hierarchical analysis process (AHP) • Multi-criteria decision analysis (AMCD) • ArcGis

1 Introduction

The growing population and industrial development of the Jijel region is a challenge for the local authorities. They have to resort to new techniques for spatial planning. Indeed, it is important that all the parameters involved in the planning of this region are taken into account for effective sustainable implications. It seems appropriate to use a multidisciplinary approach which makes it possible to propose a decision support tool for the identification of areas suitable for the construction and implementation of works of great, vital importance.

The Geographic Information System (GIS) and the Multicriteria Assessment (EMC) are particularly useful for identifying sites suitable for this type of development. The integration of GIS and multicriteria analysis methods is a privileged and essential way to render GIS genuine decision support systems [1, 2]. This approach has already been applied by several authors for the choice of a given site [3, 4].

The objective of this study was to develop a model for the selection of areas suitable for construction, particularly vital works from a geographic information system (GIS) and multi-criteria assessment in order to guide decision-makers in reviving this sector for spatial planning for sustainable development.

The study area is characterized by a large depression located in the eastern part of Jijel, bordered to the south, east and west by a group of mountains whose absolute altitude is from 300 to 1000 m. The overall area of this basin is approximately 244 km^2.

2 Materials and Methods

The materials consist of data and software. The applied approach in this study requires a compilation of cartographic data (topographic map at the 1:25,000 scale, geological map at the 1:50,000 scale) and alphanumerical data relating to geotechnical surveys. The collection of these data enabled the establishment of a Space Reference database. ArcGIS 10.2.2 software was used for data processing.

The data used in this study can be grouped into three main data sources such as basic topographic maps, a lithological map and geotechnical studies data. From these three data sources, six factors were chosen for the achievement of the different layers in ArcGIS. These are soil, slope, flood susceptibility, swelling potential, liquefaction potential, and depth of groundwater. Many steps have been completed in

K. Remoum (✉) · A. Bouzenoune
Laboratory of Geological Engineering, University Mohammed Seddik Ben Yahia of Jijel, Ouled Aissa, 18000 Jijel, Algeria
e-mail: karimremoum@univ-jijel.dz

A. Bouzenoune
e-mail: bouzenoune@univ-jijel.dz

© Springer Nature Switzerland AG 2019

H. M. El-Askary et al. (eds.), *Advances in Remote Sensing and Geo Informatics Applications*,
Advances in Science, Technology & Innovation, https://doi.org/10.1007/978-3-030-01440-7_14

the GIS to obtain the final layers required in this study. In GIS, each criterion was classified into classes, and each class received a relevance rating based on experts and previous literature in this area.

After having prepared all the criteria within ArcGIS, and in order to obtain suitable sites for construction in the eastern part of Jijel, both methods were adopted to calculate the weights of the criteria and the production of the final map of construction suitability index using the "Map Algebra" spatial extension tool in the GIS.

3 Results

In the SAW method, the final map of suitability for construction was divided, using the method of equal intervals in five classes: very low, low, medium, high and very high; these different classes covered areas occupying 40.06 km^2 (16.17%), 23.66 km^2 (9.55%), 27.71 km^2 (11.18%), 64.76 km^2 (26.46 km^2) and 91.56 km^2 (36.96%), respectively. Similarly, the final map of suitability for construction established by AHP was divided into five classes, very low, low, medium, high and very high, covering areas of 40.06 km^2 (16.17%), 8.21 km^2 (3.31%), 38.22 km^2 (15.43%), 15.51 km^2 (6.26%) and 145.75 km^2 (58.83%), respectively.

In order to combine the maps obtained from the two methods (SAW and AHP), each map was classified into five categories. The five categories were numbered as follows: very low (1), low (2), medium (3), high (4), and very high (5). The final maps were seized into the GIS for eventual processing by the spatial analysis tool "Map Algebra". The results of this process included the number of pixels for each class and the number of raster category combinations for SAW and AHP, as well as the percentages of correspondents for each category, are shown in Table 1.

4 Discussion

The combined number of categories for SAW and AHP [(1, 1), (2, 2), (3, 3), (4, 4) and (5, 5)] was considered to be the number of the corresponding pixels resulting from the two methods. The different combinations of categories [(5, 4), (3, 2), (4, 3)] were not considered as concordant.

The percentage of raster values for the corresponding and non-corresponding categories is shown in Fig. 1. The final comparison map resulting from the combination of the two maps using the two methods was reclassified, then the categories with the same number of corresponding raster were merged to produce the category of concordant and non corresponding areas (Fig. 2). The percentage of corresponding pixels in the comparison map is 70% (in green), while the percentage of non corresponding pixels is 30% (yellow).

5 Conclusion

GIS combined with multi-criteria analysis provide land management opportunities that integrate all the parameters related to sustainable management. These techniques were applied to the eastern part of the Jijel region for the modeling of spaces suitable for the construction and implementation of vital works. The aptitude maps obtained by the SAW and AHP method were intended to guide development actors. They highlighted five categories: very low, low, medium, high and very high. The final map resulting from the combination of the two suitability maps for building reveals two categories: concordance areas with a percentage of pixels of 70% and a non-concordance area that represents 30% of the pixels. The concordance zone between the two maps helps guide decision-makers in choosing suitable sites for vital consideration works.

Table 1 The results of combining two maps resulting from (SAW) and (AHP) methods

Raster value	Count	Raster category (AHP)	Raster category (SAW)	Corresponding pixels ratios	Classification
1	3577	3 (M)	3 (M)	9, 19	Concordant
2	14,382	5 (VH)	5 (VH)	36, 96	Concordant
3	6293	1 (VL)	1 (VL)	16, 17	Concordant
4	8511	5 (VH)	4 (H)	21, 87	Concordant
5	1289	2 (L)	2 (L)	3, 31	Non-concordant
6	2427	3 (M)	2 (L)	6, 24	Non-concordant
7	775	4 (H)	3 (M)	1, 99	Non-concordant
8	1661	4 (H)	4 (H)	4, 27	Concordant

VL Very low, *L* Low, *M* Moderate, *H* High, *VH* Very high

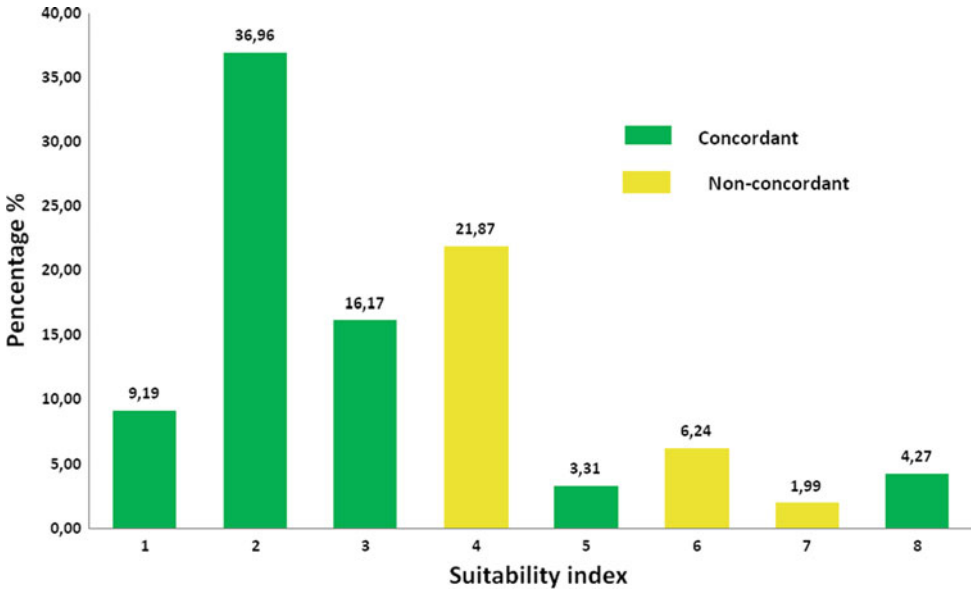

Fig. 1 The percentages of raster values of the classes of the comparison map

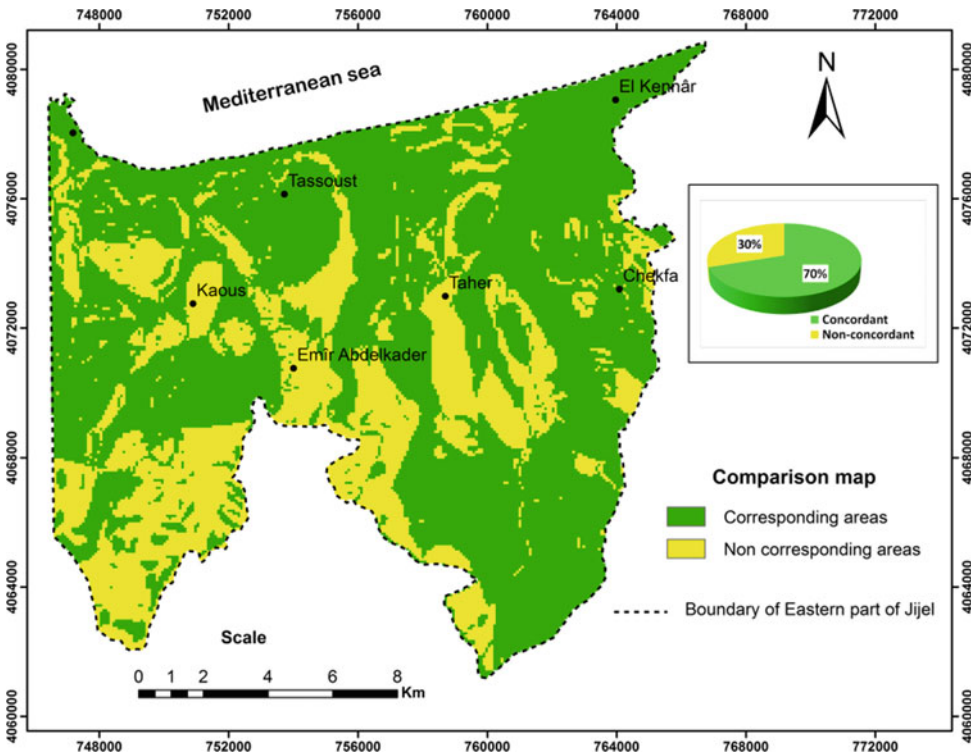

Fig. 2 Comparison map of concordant and non-concordant areas between AHP and SAW methods and its percentages

References

1. Malczewski, J.: GIS and Multicriteria Decision Analysis. Wiley, New York (1999)
2. Malczewski, J., Rinner, C.: Multicriteria decision analysis in geographic information science. Earth Sci. Geog. (2015)
3. Rozos, D., Bathrellos, G.D., Skilodimou, H.D.: Comparison of the implementation of rock engineering system and analytic hierarchy process methods, upon landslide susceptibility mapping, using GIS: a case study from the Eastern Achaia County of Peloponnesus. Greece. Environ. Earth Sci. **63**, 49–63 (2011)
4. Bathrellos, G.D., Gaki-Papanastassiou, K., Skilodimou, H.D., Papanastassiou, D., Chousianitis, K.G.: Potential suitability for urban planning and industry development using natural hazard maps and geological-geomorphological parameters. Environ. Earth Sci. **66**, 537–548 (2012)

Building Segmentation of Aerial Images in Urban Areas with Deep Convolutional Neural Networks

Yaning Yi, Zhijie Zhang, and Wanchang Zhang

Abstract

Building segmentation of aerial images in urban areas is of great importance for many applications, such as navigation, change detection, areal monitoring and urban planning. However, due to the uncertainties involved in images, a detailed and effective solution is still critical for further applications. In this paper, we proposed a novel deep convolutional neural network for building segmentation of aerial images in urban areas, which was based on the down-sampling-then-up-sampling architecture. The suggested network is similar to that of the FCN, but with ours differs as it takes into account the multi-scale features using Atrous Spatial Pyramid Pooling. Additionally, motivated by the recent published works, the depth-wise separable convolution was also adopted to replace the standard convolution in our proposed method, which largely reduced the training parameters. To evaluate the performance of our proposed method, a very high resolution aerial image dataset (0.075 m) was used to train and test the images. In addition, two state-of-the-art methods named FCN-8s and SegNet were also compared with our method for performance evaluations. The experiments demonstrated that our method outperformed the state-of-the-art methods greatly both in terms of qualitative and quantitative performance.

Keywords

Convolutional neural networks • Building segmentation • Aerial image • Depth-wise separable convolution • Atrous convolution

1 Introduction

Building segmentation of aerial images in urban areas is of great importance for many applications, such as navigation, change detection, areal monitoring and urban planning. In recent years, with the rapid technical development of image processing and computer vision, many deep-learning methods have been proposed and largely improved the performance of building segmentation compared to the traditional methods. However, due to the uncertainties involved in the images, detailed and effective solutions are still critical for further applications.

For building segmentation, traditional methods are mainly based on edge-detection and classification or segmentation techniques, which need a lot of manual involvement, such as the design of feature descriptors, the selection of optimal parameters and the choice of classifier. In the recent years, with the development of computer vision technology, deep-learning approaches have been considered as a very important method not only in building segmentation [1], but also in other object extractions [2]. Many methods have been proposed for building segmentation since the appearance of convolutional neural networks (CNN) and fully convolutional neural networks (FCN) [3–5].

In this paper, we proposed a novel deep convolutional neural network for building segmentation of aerial images in urban areas, which was based on the down-sampling-then-up-sampling architecture, in the same way as the FCN, but differing in the fact that the multi-scale features took into account the use of Atrous Spatial Pyramid Pooling (ASPP). In addition, to reduce the training parameters, we adopted

Y. Yi · W. Zhang (✉)
Key Laboratory of Digital Earth Science, Institute of Remote Sensing and Digital Earth, Chinese Academy of Sciences, Beijing, 100094, China
e-mail: zhangwc@radi.ac.cn

Y. Yi
e-mail: yiyn@radi.ac.cn

Y. Yi
University of Chinese Academy of Sciences, Beijing, 100049, China

Z. Zhang
Center for Environmental Science and Engineering, University of Connecticut, Storrs, CT 06269-4148, USA
e-mail: zhijie.zhang@uconn.edu

© Springer Nature Switzerland AG 2019

H. M. El-Askary et al. (eds.), *Advances in Remote Sensing and Geo Informatics Applications*, Advances in Science, Technology & Innovation, https://doi.org/10.1007/978-3-030-01440-7_15

the depth-wise separable convolution [6] to replace the standard convolution.

2 Methodology

2.1 The Proposed Method

As shown in Fig. 1, our proposed network consists of two parts: (1) a convolution network with ASPP was used to extract the feature maps from images and (2) the feature maps were up-sampled back to the original input resolution. For the convolution network, the minimum feature map size is 16 × 16. Different from the FCN, we added the ASPP after the block 5. The Atrous rates were 4, 8, 12, 16, respectively. Subsequently, a concatenate layer was added to fuse the multi-scale feature maps followed by a 1 × 1 convolutional layer. In terms of up-sampling, to get a finer result, low-level features were considered by the skip connections which concatenated the feature maps obtained from the up-sampling. The up-sampling factors were 2, 4, 8, 16 for blocks 2, 3, 4, 7, respectively. At the end of the network, a 1 × 1 convolutional layer followed by a soft-max classifier was appended to obtain probability maps. It should be noted that all 3 × 3 convolutional layers were applied in the depth-wise separable convolution, which factorized a standard convolution into a depth-wise convolution followed by a pointwise convolution. The depth-wise separable convolution compressed our network parameters to less than 2.6 million (52 × smaller than FCN-8s [3], which had 134.32 million parameters, 12 × smaller than SegNet [7], which had 31.82 million parameters). Due to the limitation of computation capability, we did not compare the speed of different methods. The time complexity was left for future investigations.

2.2 Experimental Setup

In this paper, we used the aerial images with a spatial resolution of 0.075 m downloaded from the Internet (https://data.linz.govt.nz) for the experiments. The aerial images have been converted into orthophotos, and then they were divided into two parts with 80% for training and 20% for validation, respectively. To evaluate the performance, an aerial image with the size of 8000 × 8000, not considered in training, was used to test the method. A total of 38,143 training patches with the size of 256 × 256 in the experiments were prepared. Similarly, the ground truth dataset with consistent size was generated.

The networks that included FCN-8s, SegNet and our proposed method were implemented in Keras using Tensorflow as backend. A single NVIDIA GeForce GTX 1080Ti GPU was used to train and test the networks. During training, due to the limitation of computing capability, we set the batch size at 4, while the initial learning rate of 0.001 was set. The Adam was taken as an optimizer of the parameters.

3 Results and Discussion

For a better evaluation of the performance of our method, we presented the qualitative and quantitative comparison results of those two methods and ours in Fig. 2 and Table 1. For a qualitative comparison, the results of FCN-8s and SegNet were inaccurate and incomplete as seen in Fig. 2. In addition, some backgrounds were misclassified as buildings. However, our method produced more accurate and smooth segmentation results, which proved the feasibility of our proposed method when compared to the others.

For a quantitative comparison, five commonly used metrics, i.e., precision, recall, F1, overall accuracy and

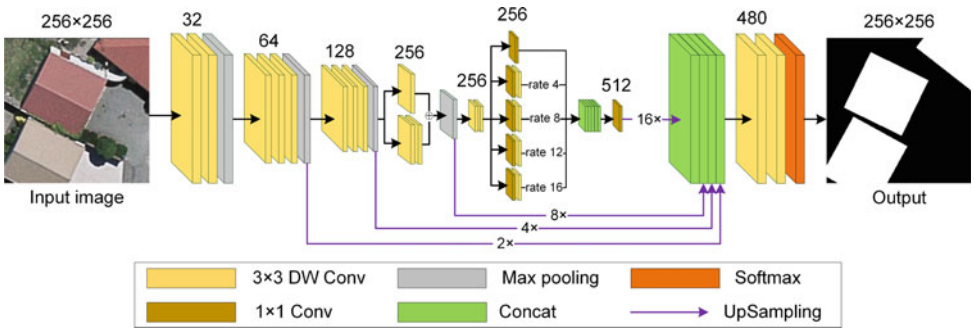

Fig. 1 Illustration of our proposed network. The depth-wise separable convolution (DW Conv) was used to replace standard convolution. The number of kernels for eight convolution blocks was [32, 64, 128, 256, 256, 256, 512, 480]

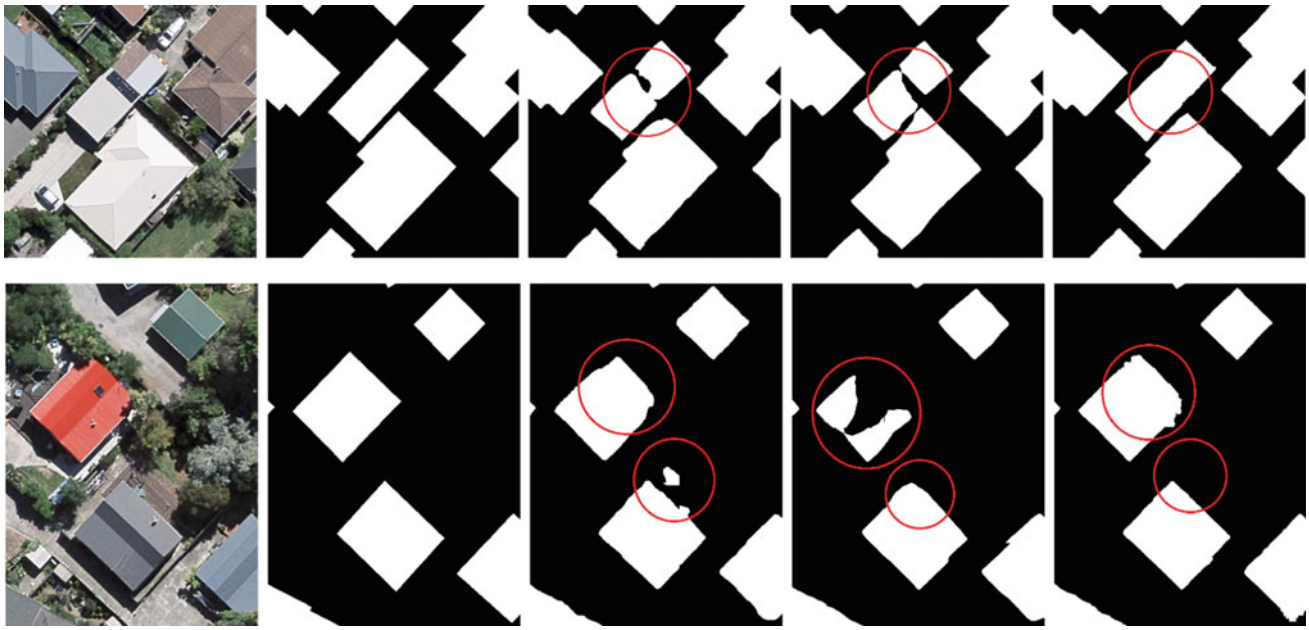

Fig. 2 Quantitative comparison of segmentation results. White indicates the buildings, while black indicates the background. From left to right: original aerial image, ground truth, results of FCN-8s, results of SegNet and results of ours, respectively

Table 1 Quantitative comparison with deep networks, where the values in bold were the best

Method	Precision	Recall	F1	Overall accuracy	Kappa coefficient
FCN-8s	0.8921	0.9306	0.9109	0.9470	0.8733
SegNet	0.8714	0.9411	0.9049	0.9424	0.8637
Ours	**0.9084**	**0.9482**	**0.9279**	**0.9571**	**0.8973**

Kappa coefficient, were used to evaluate the performance of the different networks. Table 1 shows that our proposed method achieved the best results on the five metrics. Especially, the Kappa coefficient of our method was more than 2% higher than that of FCN-8s and SegNet. The comparison results show that our method had better performance in building segmentation.

4 Conclusions

In this paper, a novel deep convolutional neural network was proposed to perform building segmentation of aerial images in urban areas. Different from previous studies, we took the multi-scale features of images into account by using ASPP, and replaced the standard convolution by the depth-wise separable convolution, which drastically reduced the training parameters. The experiments showed that our method outperformed the state-of-the-art methods greatly in terms of both qualitative and quantitative performances. For future work, we will try to optimize the segmentation results by using the elevation information such as the digital surface model.

Acknowledgements This study was financially supported by the National Key Research and Development Program of China (Grant No. 2016YFB0502502 and No. 2016YFA0602302).

References

1. Volpi, M., Tuia, D.: Dense semantic labeling of subdecimeter resolution images with convolutional neural networks. IEEE Trans. Geosci. Remote Sens. **55**(2), 881–893 (2017)
2. Miao, Z., Fu, K., Sun, H., Sun, X., Yan, M.: Automatic water-body segmentation from high-resolution satellite images via deep networks. IEEE Geosci. Remote Sens. Lett. (99), 1–5 (2018)
3. Long, J., Shelhamer, E., Darrell, T.: Fully convolutional networks for semantic segmentation. In: IEEE Conference on Computer

Vision and Pattern Recognition (CVPR), pp. 3431–3440. IEEE, Boston, MA, USA (2015)
4. Li, J., Ding, W., Li, H., Liu, C.: Semantic segmentation for high-resolution aerial imagery using multi-skip network and Markov random fields. In: 2017 IEEE International Conference on Unmanned Systems (ICUS), pp. 12–17. IEEE, Beijing, China (2017)
5. Marmanis, D., Wegner, J.D., Galliani, S., Schindler, K., Datcu, M., Stilla, U.: Semantic segmentation of aerial images with an ensemble of CNNS. ISPRS Annal. Photogrammetry Remote Sens. Spat. Inf. Sci. **3**(3), 473–480 (2016)
6. Chollet, F.: Xception: deep learning with depthwise separable convolutions. In: 2017 IEEE Conference on Computer Vision and Pattern Recognition (CVPR), pp. 1800–1807. IEEE, Honolulu, HI, USA (2017)
7. Badrinarayanan, V., Kendall, A., Cipolla, R.: SegNet: a deep convolutional encoder-decoder architecture for image segmentation. IEEE Trans. Pattern Anal. Mach. Intell. **39**(12), 2481–2495 (2017)

A Hybrid Approach to Super Resolution Mapping for Water-Spread Area and Capacity Estimation of Reservoir Using Satellite Image (India)

Heltin Genitha Cyril Amala Dhason and Indhumathi Muthaia

Abstract

For proper monitoring and scheduling of the supply of drinking water in reservoirs, it is necessary to carry out the capacity surveys. Remote sensing techniques can be used to estimate the capacity of the reservoirs in an inexpensive and less laborious way. In this paper, a super resolution mapping based on hybrid approach was developed and applied to Landsat OLI image of the Puzhal reservoir, Chennai city, southern India and the reservoir water-spread area was estimated. The estimated water-spread was used to find the capacity of the reservoir using Trapezoidal formula. The hybrid approach uses New Fuzzy Cluster Centroid (NFCC) algorithm for sub-pixel mapping and multi-objective genetic algorithm for super resolution mapping. The super resolution mapping is an advanced classification technique which accurately maps the location of classes within a pixel. The capacity determined from the image processing technique is compared with that estimated from the field survey data with a meagre 1.35% error. Hence, it is observed that the super resolution mapping is a prominent methodology to estimate the water-spread area of the reservoir which in turn increases the accuracy of the estimation capacity of the reservoir.

Keywords

Sub-pixel mapping • Super resolution mapping • Satellite image • Water-spread area

1 Introduction

Chennai city largely depends only on the rain water stored in lakes and reservoir situated in its periphery as there are no perennial rivers. Many researchers have carried out works relating to capacity estimation of reservoirs using remote sensing techniques, which is time and cost effective. The remote sensing techniques used are per-pixel classification (Maximum Likelihood Classifier, Minimum Likelihood Classifier, Bayesian Classifier, Normalized Difference Water Index etc.), sub-pixel Classification (Linear Spectral Unmixing, Fuzzy C means etc.) and super resolution mapping (Hopfield Neural Network). These works show that the remote sensing based capacity survey is economical and time effective.

For water-spread area estimation, the super resolution mapping technique was used. For super resolution mapping, a linear optimization solution using the spatial dependence within and between a coarse pixel was proposed by Verhoeye [3]. Other approaches include the pixel swapping algorithm [2], Hopfield Neural Network [1] and the Particle Swarm Optimization (PSO) algorithm [4]. In this work, super resolution mapping technique was used to determine the water-spread area of the reservoir. Then, the capacity of the reservoir was determined by the water-spread area of the reservoir

2 Methodology

In this paper, the multi-spectral image of the reservoir is soft classified using NFCC for unsupervised classification algorithm. The output fraction image was given as input to super resolution mapping (multi-objective genetic algorithm) to determine the water-spread area of the reservoir. Then, from the water-spread area, the volume of the reservoir was calculated using trapezoidal formula. Finally the capacity of the reservoir estimated using the remote sensing approach was

H. G. C. A. Dhason (✉)
Department of Information Technology, St. Joseph's College of Engineering, Chennai, India
e-mail: heltingenitha@stjosephs.ac.in

I. Muthaia
Department of Civil Engineering, St. Joseph's College of Engineering, Chennai, India

© Springer Nature Switzerland AG 2019

H. M. El-Askary et al. (eds.), *Advances in Remote Sensing and Geo Informatics Applications*, Advances in Science, Technology & Innovation, https://doi.org/10.1007/978-3-030-01440-7_16

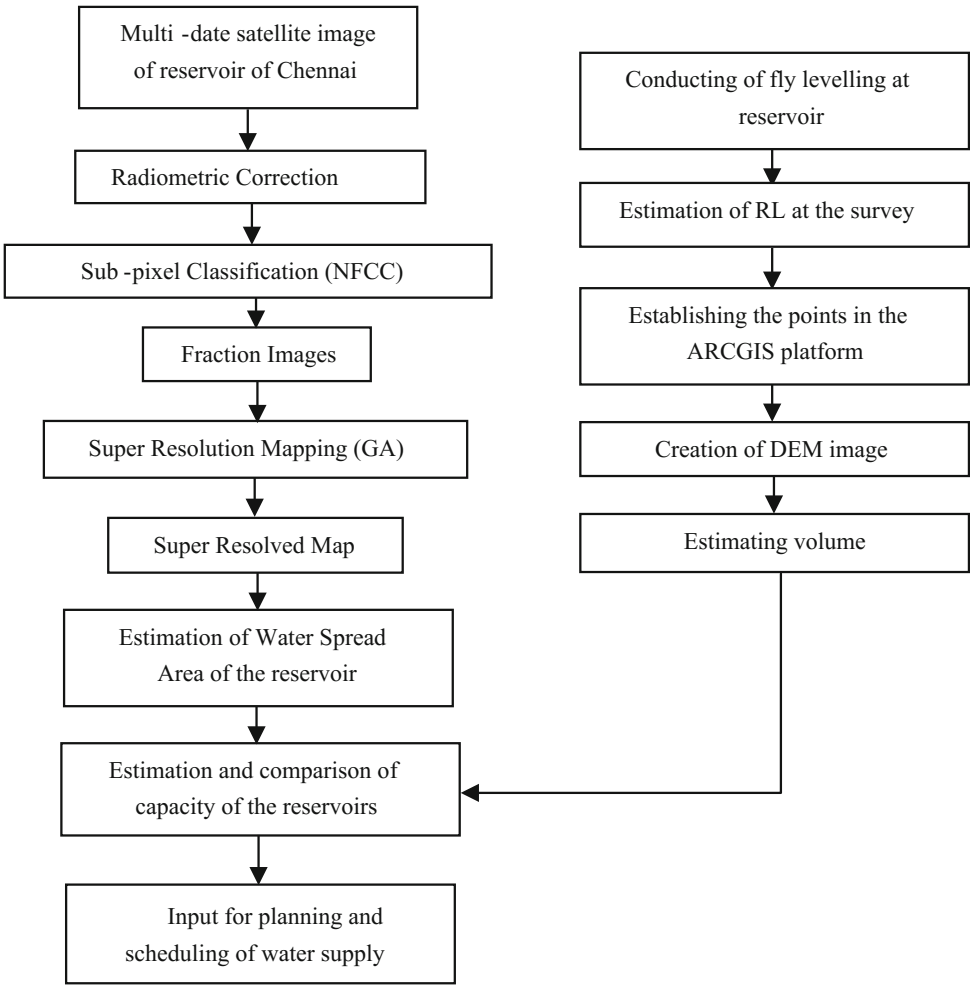

Fig. 1 Methodology to estimate the water-spread area and volume of the reservoir

compared with the capacity estimated using the field survey data. Figure 1 shows the methodology to estimate the water-spread area and capacity of the reservoirs using the super resolution approach.

2.1 Sub-pixel Classification: New Fuzzy Cluster Centroid for Unsupervised Classification Algorithm

The New Fuzzy Cluster Centroid for Unsupervised Classification algorithm is a sub-pixel classification algorithm used to identify the proportion of classes within the pixel. The new objective function (Eq. 1) is formulated by adding the new term with the distance between the pixels and cluster centers in the spectral domain. This new term is articulated by multiplying the Lagrange's multiplier with the membership values of the pixel for a particular class and then subtracted by one. The NFCC objective function is minimized as follows

$$J_{New} = \sum_{i=1}^{c}\sum_{j=1}^{n} m_{ij}^{f}\left\|x_j - c_i\right\|^2 + \sum_{j=1}^{n}\varepsilon_j\sum_{i=1}^{c}\left(m_{ij}-1\right) \quad (1)$$

where, with respect to membership grade m_{ij}, c_i the cluster center, n is the number of data points, c is the number of clusters, f is a fuzzifier (=2).

2.2 Super Resolution Mapping: Multi-objective Genetic Algorithm

The steps for genetic algorithm include: reading the proportion image; resolving the pixels into sub-pixels; extracting all the population for that pixel; evaluating the fitness function (Eq. 2); performing selection, cross-over and mutation operation without disrupting the proportions. The fitness function was calculated using the following formula.

$$\text{Fitness Function} = \text{K1} * \text{Max}(\text{Spatial Dependence}) + \text{K2} * \text{Max}(\text{Spatial Attraction}) \quad (2)$$

where, K1 and K2 are the weights. The spatial dependence refers to the proximity of the sub-pixels which is the summation of a_i for every sub-pixel. For a sub pixel, the average matrix (a_i) is calculated as

$$a_i = \sum_{j=1}^{N} \frac{n_{ij}}{N} \tag{3}$$

where, n_{ij} is the spatial distribution of the sub-pixels, N is the total surrounding sub-pixels.

Spatial attraction uses the fraction values from the surrounding pixels to compute the spatial distribution of the sub-pixels for each class component. The spatial attraction is calculated using

$$Spatial\,Attraction(c, p_{ij}) = \sum_{m=1}^{n} \frac{F_c(P_m)}{d(p_{ij}, P_m)} \tag{4}$$

where, p_{ij} is the sub-pixel for pixel P_{rs}, P_m is neighbouring pixel for pixel P_{rs}, $F_c(P_m)$ is the proportion of the mth neighbour for every class c, $d(p_{ij}, P_m)$ is the Euclidian distance between p_{ij} and P_m.

2.3 Capacity Estimation: Trapezoidal Formula

The water-spread area estimated using the super resolution mapping approach is given as input to Trapezoidal formula and the capacity of the reservoir is estimated. The capacity (C) between two successive reservoir water levels was calculated by trapezoidal formula (Eq. 5).

$$C = (H1 - H2) * \left(A1 + A2 + \sqrt{A1 * A2}\right)/3 \tag{5}$$

where, C is the capacity between two successive water levels, H1 and H2 are the two water levels. A1 and A2 are the water-spread areas at the reservoir at different water levels. Cumulative capacity of the reservoir is obtained by summing up the capacity of the reservoir at different water levels 1 and 2.

3 Results and Discussion

Experiments were carried out using multi-date (before monsoon and after monsoon) Landsat 8 (Bands 1–8) image of resolution 30 m for Puzhal Reservoir for the period 2014–2017. Sub-pixel (NFCC for unsupervised classification algorithm) and super resolution mapping (multi-objective genetic algorithm) approaches were applied to the Landsat 8 FCC image of the Puzhal reservoir to compute the water-spread area of the reservoir and then the capacity of the reservoir was estimated using the Trapezoidal formula (Fig. 2). In contrast, the field survey of the reservoir was carried out for a better understanding of reservoir volume estimation process. The elevations for the required coordinates of the reservoirs were calculated by fly levelling which is one of the direct levelling methods of an object. From the field survey data, the projected map and the Digital Elevation Model of the reservoir was prepared (Fig. 3). The results obtained from remote sensing approach were compared with the field survey data (Table 1).

There are various factors affecting the performance of evaluating the capacity of the reservoir. In this paper all the factors were taken into account to accurately estimate the capacity of the reservoir using the super resolution mapping of satellite images. The topography of the reservoir was also

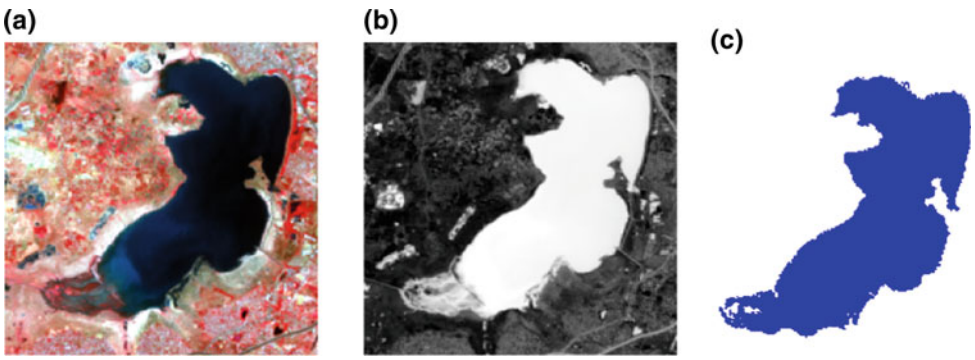

Fig. 2 **a** Landsat 8 FCC image, **b** proportion image of water class using NFFCC for unsupervised classification algorithm, **c** super resolved map using hybrid genetic algorithm

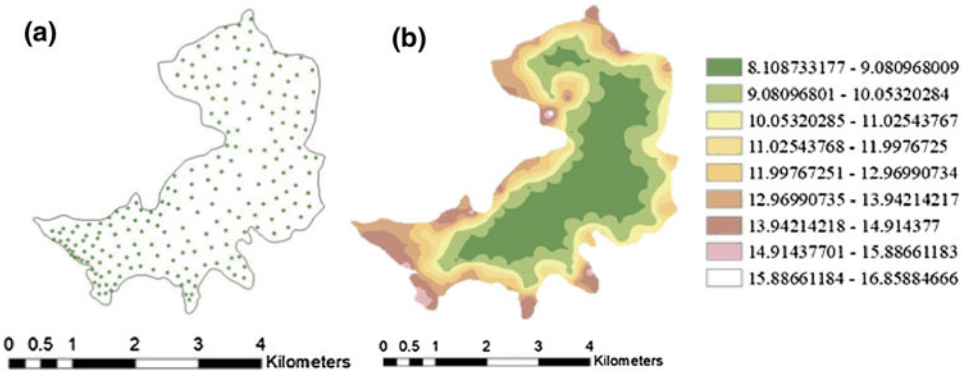

Fig. 3 Puzhal reservoir (**a**), Projected map (**b**) and surveyed points (**b**) Digital elevation model

Table 1 Comparison of capacity of the reservoir from remote sensing approach and field survey data

Sl. no	Date	Water level (m)	Capacity from super resolution mapping (Mcft)	Capacity from field survey (Mcft)	Error %
1	17-3-2014	45.30	2260	2229	1.37
2	05-6-2014	40.52	1463	1440	1.57
3	24-6-2015	34.86	738	729	1.21
4	25-5-2016	41.95	1688	1663	1.48
5	25-3-2017	33.48	602	595	1.16

obtained from the reservoir authorities and it was also considered for capacity estimation.

4 Conclusion

In this work, the super-resolution mapping approach was applied to satellite image to estimate the water-spread area of the Puzhal reservoir and the volume was estimated. Since, the super-resolution mapping approach enhances the spatial resolution of the satellite image, the water-spread area was accurately estimated, in turn the capacity of the reservoirs was also precisely estimated.

References

1. Nguyen, Q., Atkinson, P.M., Lewis, H.G.: Super-resolution mapping using Hopfield neural network with panchromatic imagery. Int. J. Remote Sens. **32**(21), 6149–6176 (2011)
2. Thornton, M.W., Atkinson, P.M., Holland, D.A.: Super resolution mapping of rural land cover features from fine spatial resolution satellite sensor imagery. Int. J. Remote Sens. **27**, 473–491 (2006)
3. Verhoeye, J., Wulf, R.D.: Land cover mapping at sub-pixel scales using linear optimization techniques. Remote Sens. Environ. **79**, 96–104 (2002)
4. Wang, Q., Wang, L., Liu, D.: Particle swarm optimization-based sub-pixel mapping for remote-sensing imagery. Int. J. Remote Sens. **33**, 6480–6496 (2012)

Multi-source System for Accurate Urban Extension Detection

Hassna Kilani, Hichem Ben Abdallah, Takoua Abdellatif, and Rabah Attia

Abstract

This paper proposed a novel observation system that is based on multi sources of collected data for urban extension detection. In addition to the satellite image processing, the evolution of unmanned aerial vehicle (UAV) technology created a practical data source for image classification and mapping. For the detected data analysis, storage and processing, a big data framework for urban extension detection was presented. In this Framework, Deep Learning (DL) algorithms were used for the classification and the analysis of multi source images.

Keywords

Very high resolution (VHR) images • UAV • Deep-learning • Urban extension • U-net architecture

1 Introduction

In the process of urban development, urban spatial structure and morphology structure are constantly changing. Advanced spatial information technology, remote sensing (RS) and geographic information systems (GIS) integration technology were used to monitor and simulate the dynamic evolution of urban spatial patterns [1, 2].

In particular, we were interested in urban extension detection mainly non-authorized extension. Our goal was also to obtain centimeter-level resolution and accuracy products that can be generated even with low-cost cameras (a few-hundred euros). To this end, as a low-cost alternative to the classical cartography based on satellites as a data source, we used UAV platforms as an efficient source of data as it is the case for many disciplines such as inspection, surveillance, mapping and 3D modeling [3–5]. For geomatics applications, the first experiences were carried out by Przybilla and Wester-Ebbinghaus [6]. Over the previous years, UAV-based applications have been widely used in the geomatics domain [7].

On the other hand, urban observation programs continuously provide data with different spatial, spectral and temporal characteristics. A need to scale and improve image-processing quality has become an emerging challenge. In order to handle the massive streams of imagery, advanced preprocessing and mining tools such as object detection and localization were required. Neural networks have shown promising results in object classification and detection compared to traditional methods [8, 9]. Big data infrastructures are needed for massive data storage and real time processing. In our proposed system, we used the Deep Learning for accurate urban detection and we built a Big Data framework to handle the scalability of collected data and achieve a real-time processing.

In this paper, we were motivated by the need to collect multi-source data from Satellites and UAVs for urban extension detection and propose a system architecture for massive and real-time data analysis and storage. The First part described the proposed multi-source system. In the second part, the deep learning was compared to the classical methods for remote sensing and UAV image processing. The paper was concluded by a description of our ongoing work on urban extension detection.

2 Multi-source Systems for Urban Extension

In the field of remote sensing image analysis, different sources of data entities carrying complementary information about the observed area generally provide efficient data analysis [10]. In our work, we considered data originating

H. Kilani (✉) · H. B. Abdallah · T. Abdellatif · R. Attia
SERCOM Laboratory, Tunisia Polytechnic School, La Marsa, Tunisia
e-mail: hasna.kilani@ept.rnu.tn

H. B. Abdallah
Centre de Recherche Militaire CRM, L'Aouina, Tunisia

© Springer Nature Switzerland AG 2019

H. M. El-Askary et al. (eds.), *Advances in Remote Sensing and Geo Informatics Applications*, Advances in Science, Technology & Innovation, https://doi.org/10.1007/978-3-030-01440-7_17

from either UAVs or satellites. The two data sources are complementary. Indeed, satellites allow collecting a wide range of images on large surfaces. UAVs are used for well-defined regions to have more precise information about urban properties. They are also less expensive and practical to use for rapid observations.

Figure 1 presents the urban surveillance system that we considered in our project.

We can distinguish two layers:

- A data sensing layer: it comprises satellites and UAV engines connected to base stations.
- A data processing and storage platform: we consider a message broker that classifies input data following a set of topics [11]. A set of services are connected to the broker to be notified about received and analyzed events such as the detection of a new non-authorized building. These services, for instance, can use SMS or emails for authority notifications. Since storing historical images is very important for urban extension prevention analytics and for surveys, our designed platform also contains a big Data storage to archive all detected images [12].

3 Deep Learning Image Classification

In the current literature, the support vector machine (SVM) [13, 14] has been viewed as an efficient and stable method for hyper-spectral classification tasks, especially for the small training sample sizes. Some SVM extensions in the hyper-spectral image classification were presented to improve the classification performance.

Neural networks (NN), such as multilayer perceptron (MLP) and radial basis function (RBF) neural networks, have already been investigated for classification of remote sensing data. In [15], the authors proposed a semi-supervised neural network framework for large-scale HSI classification. Actually, in remote sensing classification tasks, the SVM is superior to the traditional NN in terms of classification accuracy as well as computational cost. However, a deeper NN architecture [16] whose performance is competitive to SVM is considered as a powerful model for classification. For this reason, we adopted DL for either satellite or UAV images processing. The building detection was performed based on U-Net architecture [17] using multispectral satellite images.

Regarding DL deployment processes, they can be either embedded in the UAVs or set on the server side. As introduced in our previous work [10], a heterogeneous deployment is appropriate in the present case since it depends on multiple factors such as the network bandwidth, latency, remaining battery charge and emergency level of the information to carry out a fast and better decision-making.

4 Conclusion and On-going Work

In this paper, we presented the multi-source system for urban extension detection. The Deep-learning was tested on an embedded system (raspberry pi) for image classification. A first version of the Big Data platform was already developed using Kafka as message broker and MangoDB as noSQL database.

The performance analysis of the proposed system, was primarily evaluated for satellite image based on U-Net

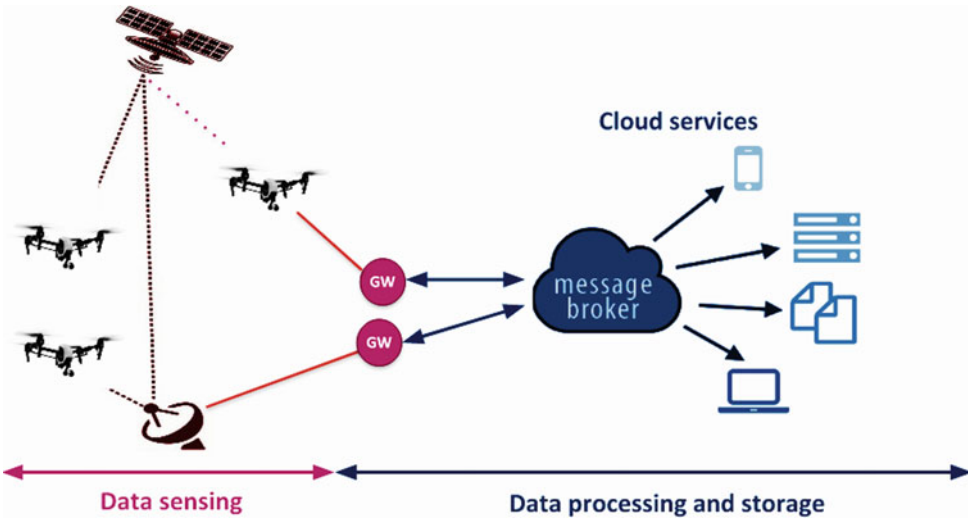

Fig. 1 Architecture of the multi-source urban surveillance system

architecture. Then a UAV embedded DL processing would be proceeded. We are planning to consider different scenarios and different system configurations with variant configuration parameters (image detection frequency, nature of observed urban regions, and UAV properties like speed and heights), etc.

Acknowledgements This work was conducted in collaboration with National Mapping and Remote Sensing Center (CNCT), in the context of the national project PRF on "Urban extension detection 2015–2018".

References

1. Fernandez Galarreta, J., Kerle, N., Gerke, M.: UAV-based urban structural damage assessment using object-based image analysis and semantic reasoning. Nat. Hazards Earth Syst. Sci. **15**, 1087–1101 (2015). https://doi.org/10.5194/nhess-15-1087-2015
2. Fabio, R., Luigi, B., Francesco, N.: UAV photogrammetry for mapping and 3d modelling: current status and future perspectives. In: Conference on Unmanned Aerial Vehicle in Geomatics, Zurich, Switzerland (2011)
3. Jason, D.R., Levente, J.K., Hendrik, F.H: Drone-based reconstruction for 3D geospatial data processing. In: IEEE 3rd WF-IoT, Reston, VA, USA (2016)
4. Colomina, I., Blázquez, M., Molina, P., Parés, M.E, Wis, M.: Towards a new paradigm for high-resolution low-cost photogrammetry and remote sensing. Int. Arch. Photogrammetry, Remote Sens. Spat. Info. (2008)
5. Eisenbeiss, H.: UAV photogrammetry. Dissertation ETH No. 18515, Institute of Geodesy and Photogrammetry, ETH Zurich, Switzerland, Mitteilungen 105 (2009)
6. Przybilla, H.-J., Wester-Ebbinghaus, W.: Bildflug mit ferngelenktem Kleinflugzeug. Bildmessung und Luftbildwesen. Zeitschrift fuer Photogrammetrie und Fernerkundung. Herbert Wichman Verlag, Karlsruhe, Germany
7. Jae-Neung, L., Keun-Chang, K.: A trends analysis of image processing in unmanned aerial vehicle. Int. Sci. Index, Comput. Info. Eng. (2014)
8. Dalton, L., Hsiuhan, L.Y., Andrew, R., et al: Domain-adapted convolutional networks for satellite image classification: a large-scale interactive learning workflow. IEEE J. Sel. Top. Appl. Earth Observations Remote Sens. (2018)
9. Pascal, K., Jan Dirk, W., Aurelien, L., Martin, J., Thomas, H., Konrad, S.: Learning aerial image segmentation from online maps. IEEE Trans. Geosci. Remote Sens. (2017)
10. Luis, GC., Devis, T., Gabriele, M.: Multimodal classification of remote sensing images: a review and future directions. Proc. IEEE (2015)
11. BenAbdallah, H., Abdelatif, T., Chekir, F.: Hydle: a deployment framework for efficient IoT surveillance systems. In: 27th International Conference on Enabling Technologies: Infrastructure for Collaborative Enterprises (Accepted Paper) (2018)
12. Naser, H.M., Tarik, T., Osama, A.: Low-altitude unmanned aerial vehicles-based internet of things services: comprehensive survey and future perspectives. IEEE Internet Things J. (2016)
13. Modiri, M., Salehabadi, A., Mohebbi, M., Hashemi, A.M., Masumi, M.: Classification of urban feature from unmanned aerial vehicle images using GASVM integration and multi-scale segmentation. Int. Arch. Photogrammetry, Remote Sens. Spat. Info. Sci. (2015)
14. Xicheng, T., Yang, S., Wenting, X.: Remote sensing image classification based on SVM and object semantic. In: Geo-Informatics in Resource Management and Sustainable Ecosystem. Communications in Computer and Information Science, vol. 398. Springer, Berlin, Heidelberg (2013)
15. Ratle, F., Camps-Valls, G., Weston, J.: Semisupervised neural networks for efficient hyperspectral image classification. IEEE Trans. Geosci. Remote Sens. (2010)
16. Hinton, G.E., Salakhutdinov, R.R.: Reducing the dimensionality of data with neural networks. Science (2006)
17. Vladimir, I., Sergey, M., Vladimir, O.: Satellite Imagery Feature Detection Using Deep Convolutional Neural Network: A Kaggle Competition (2017). arXiv:1706.06169

3D Reconstruction of Residential Areas with SfM Photogrammetry

Murat Yakar and Yusuf Dogan

Abstract

Photogrammetry is the use of two dimensional (2D) images to provide measurement data. Photogrammetry uses a procedure referred to as "Structure from Motion" (SfM) to solve feature positions within a defined coordinate system. SfM photogrammetry offers the possibility of fast, automated and low-cost 3D data acquisition. The aim of this study was to investigate some applications of 3D reconstruction of residential areas generated by SfM photogrammetry. 3 different sites were reconstructed by 3 different methods using a UAV system. Each method was examined according to its advantages and drawbacks in the light of the SfM photogrammetry.

Keywords

SfM • Photogrammetry • UAV • Residential • 3D reconstruction

1 Introduction

Photogrammetry is the use of two dimensional (2D) images to provide measurement data. Measurement data includes positions of objects and relationships between objects. Photogrammetry uses a procedure referred to as "Structure from Motion" (SfM) to solve feature positions within a defined coordinate system. SfM refers to a set of algorithms from computer vision sciences that assist photogrammetry by automatically detecting and matching features across multiple images, then triangulating positions. The term is a bit of a catch-phrase and within the science of photogrammetry and there are alternate terms such as "multi-view photogrammetry" [1]. SfM photogrammetry offers the possibility of fast, automated and low-cost acquisition of 3D data [2]. Therefore SfM photogrammetry is quite useful and flexible to generate 3D reconstruction of a place like residential areas [3, 4].

The aim of this study was to investigate some applications of 3D reconstruction of residential areas generated by SfM photogrammetry.

2 Materials and Methods

We detected 3 settlement areas (a village, a university campus and a cultural heritage site) to generate 3D reconstructions. Unmanned Aerial Vehicle (UAV) equipped with a non-metric digital camera were used for the acquisition of 3D data of residential areas. Different methods were applied in each study area.

The study on the 15 ha archaeological site was carried out by setting up GCPs. Oblique images that were taken to generate a high quality 3D model using a UAV flight planner application.

The study on the 19 ha village settlement was achieved without GCP and vertical images that were taken using a UAV. A flight plan was created to take overlapping photographs.

The other study on the 250 ha university campus area was carried out without GCP but a RTK integrated UAV acquired images with high accurate and precise coordinates.

After those field study acquired data were processed using a software programmed with an SfM algorithm. The processing results are point cloud, Digital Terrain Model (DTM), Digital Surface Model (DSM), Digital Elevation Model (DEM) and orthophoto.

3 Results

Products of the studies have been generated with different methods. Therefore they have different accuracy and precision. 3D model of archeological site and campus area

M. Yakar (✉) · Y. Dogan
Mersin University, 33190 Ciftlikkoy, Turkey
e-mail: myakar@mersin.edu.tr

© Springer Nature Switzerland AG 2019

H. M. El-Askary et al. (eds.), *Advances in Remote Sensing and Geo Informatics Applications*,
Advances in Science, Technology & Innovation, https://doi.org/10.1007/978-3-030-01440-7_18

Table 1 Average camera location error of campus site (X-Longitude, Y-Latitude, Z-Altitude)

X error (m)	Y error (m)	Z error (m)	XY error (m)	Total error (m)
0.477305	0.801804	2.45519	0.933118	2.62654

Table 2 Average camera location error of village site (X-Longitude, Y-Latitude, Z-Altitude)

X error (m)	Y error (m)	Z error (m)	XY error (m)	Total error (m)
1.10959	0.964221	0.431713	1.47	1.53209

Table 3 Average camera location error of archeological site (X-Longitude, Y-Latitude, Z-Altitude)

X error (m)	Y error (m)	Z error (m)	XY error (m)	Total error (m)
0.536976	0.388449	0.360594	0.662749	0.754496

have subcentimeter accuracy. But study of village has meter accuracy. XY errors of the campus area has been generated in centimeter accuracy and Z error has been generated in meter accuracy (Tables 1, 2 and 3; Fig. 1 and 2).

4 Discussion

We used three different methods for three different sites. Naturally we obtained different results. Setting up GCPs provide a highly accurate product but it is quite hard in the

Fig. 1 Orthophoto of the settlement areas; village (left), archeological site (right)

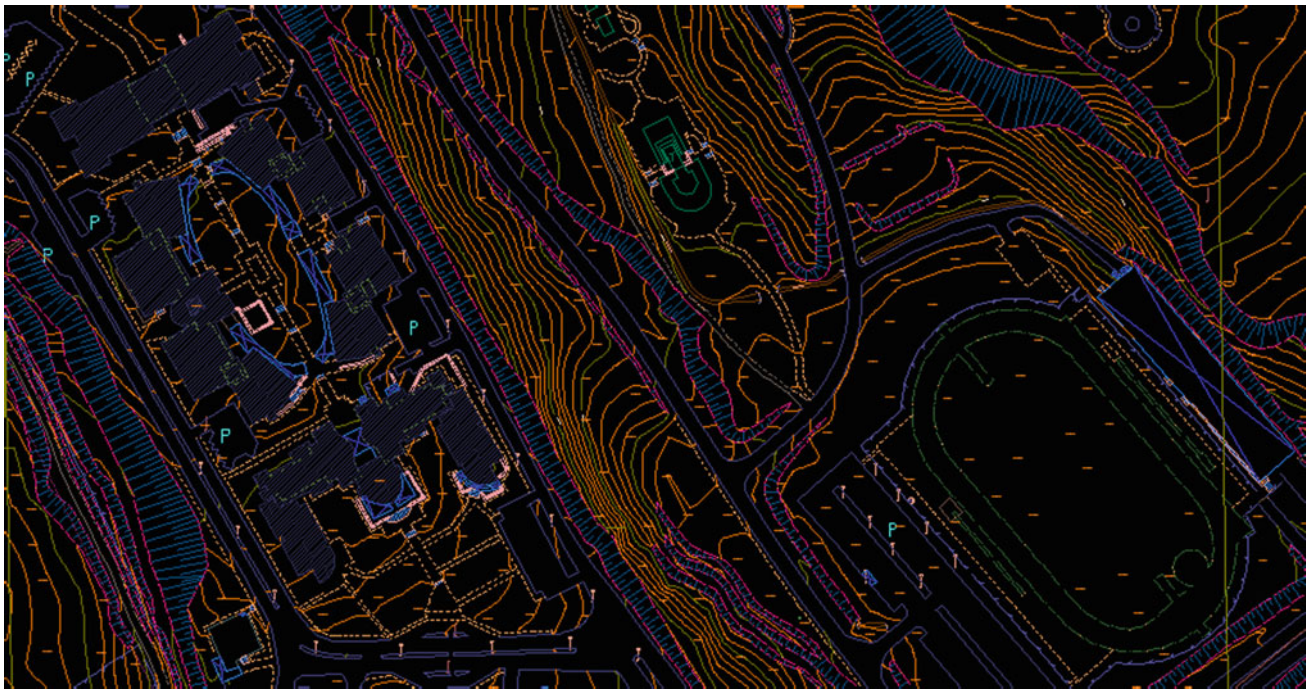

Fig. 2 Topographic map of the university campus area

challenging field (rugged, large and frequently vegetated etc.) Therefore the RTK method was more useful for this challenging field. Although the RTK integrating the UAV system is useful, it is expensive. In this case, the data collected without RTK and GCP can be used in cases where there is no need for high sensitivity and accuracy.

5 Conclusion

In this study, we observed that SfM photogrammetry provides fast and accurate 3D reconstruction. Precision and accuracy of the products depend on the used methods. UAVs are the most useful tool for 3D reconstruction nowadays. The SfM photogrammetry allows using uncalibrated, portable and light non-metric cameras carried by UAVs. Therefore, residential sites can easily be modeled with SfM photogrammetry. This study proved that the ideal method for producing a 3D reconstruction and mapping with more precision and accuracy is that applied using the GCP.

References

1. Peterson, E., Klein, M., Stewart, R.L.: Whitepaper on Structure from Motion (SfM) Photogrammetry: Constructing Three Dimensional Models from Photography. U.S. Department of the Interior Bureau of Reclamation Research and Development Office, USA (2015)
2. Micheletti, N., Chandler, J.H., Lane, S.N.: Structure from Motion (SfM) Photogrammetry. British Society for Geomorphology (2015)
3. Irschara, A., Kaufmann, V., Klopschitz, M., Bischof, H., Leberl, F.: Towards Fully Automatic Photogrammetric Reconstruction Using Digital Images Taken from UAVs (2010)
4. Yamazaki, F., Matsuda, T., Denda, S., Liu, W.: Construction of 3D models of buildings damaged by earthquakes using UAV aerial images. In Proceedings of the Tenth Pacific Conference Earthquake Engineering Building an Earthquake-Resilient Pacific, pp. 6–8 (2015)

Logistic Regression-based Geomorphological Mapping in the Arabian Platform: Implications for the Paleohydrology and the Paleoclimate of the Arabian Desert

Racha Elkadiri, Abotalib Z. Abotalib, and Mohamed Sultan

Abstract

Throughout the Quaternary, the Arabian Peninsula witnessed alternation between dry and wet periods. During the wet periods, annual precipitation significantly increased leading to recharging the fossil aquifers, elevation of the groundwater table and development of drainage systems and waterfalls along the Central Arabian Arch (CAA). Landforms that were left behind these periods provide valuable clues for deciphering the paleohydrology and paleoclimate of the Arabian Desert. Herein we used logistic regression modeling with topographic analysis to delineate theater-headed valleys (THV) along the CAA. These valleys have peculiar morphometry (e.g. theater-like heads, stubby-looking geometry, U-shaped profiles, occurrence along escarpments and propagation along fractures) and are largely attributed to groundwater sapping and/or megaflooding and water fall erosion. The model uses different topographic datasets including stream power index, plan and profile curvatures, stream density and slope gradient. The model results show that THV are abundant along the plateau escarpments and deep fluvially-incised valleys in the CAA. Additional geological, hydrological and field assessments are required to further characterize the origin of THV and examine the respective roles of groundwater processes and surface water activities in shaping the CAA landscape. This paper presents a novel mapping approach of landforms on a regional scale.

Keywords

Machine learning • Mapping • Theater-headed valleys Central Arabian arch • Groundwater sapping Paleohydrology

1 Introduction

Theater-Headed Valleys (THV) have been considered by default as groundwater sapping–related landforms in many areas worldwide [1]. However, the groundwater sapping origin of these landforms has been challenged recently by the bedrock strength of rocky materials and the difficulty of producing large-sized THV in massive rocks by spring discharge arguments. Alternative hypotheses for the origin of THV were suggested including megaflooding, waterfall erosion and landslides [2]. These arguments did not consider the role of salt weathering in the disintegration of rocky materials. Such processes ease the removal of the weathered material through an extended time-scale (e.g. several hundred thousand of years) [1]. Understanding the origin of these features could be facilitated by their detailed mapping and correlating their distribution with that of relevant hydrological (e.g. aquifer extent, confining versus water table conditions, locations of springs), geological (e.g. rock materials along THV locales, soil expansiveness, compressive strength along rock outcrops and strong-over-weak stratigraphy), structural (e.g. fault distribution, density and dip angles) and geomorphological features (e.g. salt weathering, denudational landforms, well developed streams, upslope contributing areas). In this study we develop a logistic regression model using topographic parameters, which were derived from the Shuttle Radar Topography Mission (SRTM) mosaic including stream power index, plan and profile curvatures, stream density and slope gradient.

R. Elkadiri (✉)
Middle Tennessee State University, Murfreesboro, TN 37132, USA
e-mail: racha.elkadiri@mtsu.edu

A. Z. Abotalib
Viterbi School of Engineering, University of Southern California, Los Angeles, CA 90089, USA

A. Z. Abotalib
Department of Geological Applications, NARSS, Cairo, 1564, Egypt

M. Sultan
Western Michigan University, Kalamazoo, MI 49008, USA

© Springer Nature Switzerland AG 2019

H. M. El-Askary et al. (eds.), *Advances in Remote Sensing and Geo Informatics Applications*, Advances in Science, Technology & Innovation, https://doi.org/10.1007/978-3-030-01440-7_19

Additionally, we used a geologic mask to exclude areas with thick dunes and crystalline rocks. The outputs of the model could be used to conduct spatial analysis of different hydrological, geological, structural and geomorphological features to better constrain the origin of THV in the Central Arabian Arch, which in turn would contribute to a better understanding of the paleohydrology and paleoclimate of the Arabian Desert.

2 Geomorphological Characteristics of THV in the CAA

THV in the CAA as well as in the Sahara are characterized by the theater-like heads, occurrence along scalloped-shaped escarpments, stubby-looking geometry, U-shaped profiles and high structural control (Fig. 1b). Inspection of high resolution imagery (e.g. Geoeye-1 and Quickbird) viewable from the Google Earth database show that two populations of THV occur in the CAA. The first group is located along the scarp faces of the CAA plateaus (e.g. Gebel Al-Tuwaiq); these THVs have limited upslope contributing areas and are characterized by absence of well-developed streams draining toward the location of the THV. The second group occurs in deeply incised fluvial valleys developed along the regional gradient of the CAA plateaus; these are characterized by large upslope contributing areas.

3 Description of the Logistic Regression (LR) Model Inputs and Structure

We used an SRTM mosaic over the CAA to generate five predictor variables (slope angle, plan curvature, profile curvature, drainage density, and stream power index [SPI] images).

Slope angle refers to the change in elevation over vertical distance. Plane curvature measures the surface curvature in a direction orthogonal to the slope, whereas profile curvature measures the rate of change of slope along a profile. Drainage density refers to the total length of all the streams and rivers within an area. These indices are useful for modelling the hydrodynamic behavior of water flow in connection with hillslope morphology and investigating the effects of terrain erodibility conditions [3].

The LR model is a logarithmic model that generates a multivariate regression relation between one or more predictor variables and a response variable [3]. It gives each variable a coefficient that measures its contribution to variations in the response variable. For this study, the response variable was a binary variable describing the presence and absence of THV. The logistic function equation is expressed as follows:

$$p = \frac{1}{1 + \exp(a_0 + a_1x_1 + a_2x_2 + \cdots + a_nx_n)}$$

where p is the probability of THV occurrence; a_0 is the equation intercept; x_1, x_2 to x_n denote the predictor variables; and a_1, a_2 to a_n refer to the coefficients that need to be estimated for the predictor variables using a maximum likelihood optimization method [3]. In our model, the significant variables and coefficients were determined as follows: x_1 = Slope, a_1 = 6.53795, x_2 = plan curvature, a_2 = −33.56780, x_3 = profile curvature, a_3 = 9.64728, x_4 = stream density, a_4 = −12.91560 and a_0 = −13.6842.

4 Model Outputs

The LR-delineated distribution for the THV across the CAA is an occurrence probability map ranging from 0 to 1. Figure 1 shows the distribution of the THV at probabilities equal to, or exceeding, a threshold value of 0.9. A closer look at Fig. 1 and other data sets (e.g., DEM) indicates that abundant distribution of the THV are located along the edges of the carbonate plateau in addition to deeply incised valleys. Because we targeted the onset of these valleys in the model input, the LR-delineated distribution includes the topmost locations of the THV (alcoves), whereas the main channels of the valleys were not incorporated (Fig. 1). The accuracy assessment of the model is 88.2%, which indicates a high accuracy in the detection of THV.

5 Discussion and Summary

Delineating the spatial distribution of THV in a widely extended area such as the CAA is essential to constrain the origin of THV and decipher the roles of groundwater processes versus surface floods and waterfall erosion in modifying the Arabian Desert landscape through time. Such conclusion could help to understand groundwater dynamics and paleoclimate variability in these areas. Further field, hydrological and geological investigations will be conducted to assess the origin of these features and better derive the paleohydrological and paleoclimatic patterns of the region. This paper presented a novel mapping approach to delineate geomorphological landforms on a regional scale. This approach is particularly valuable in rugged and inaccessible terrains, as a preliminary step for traditional mapping

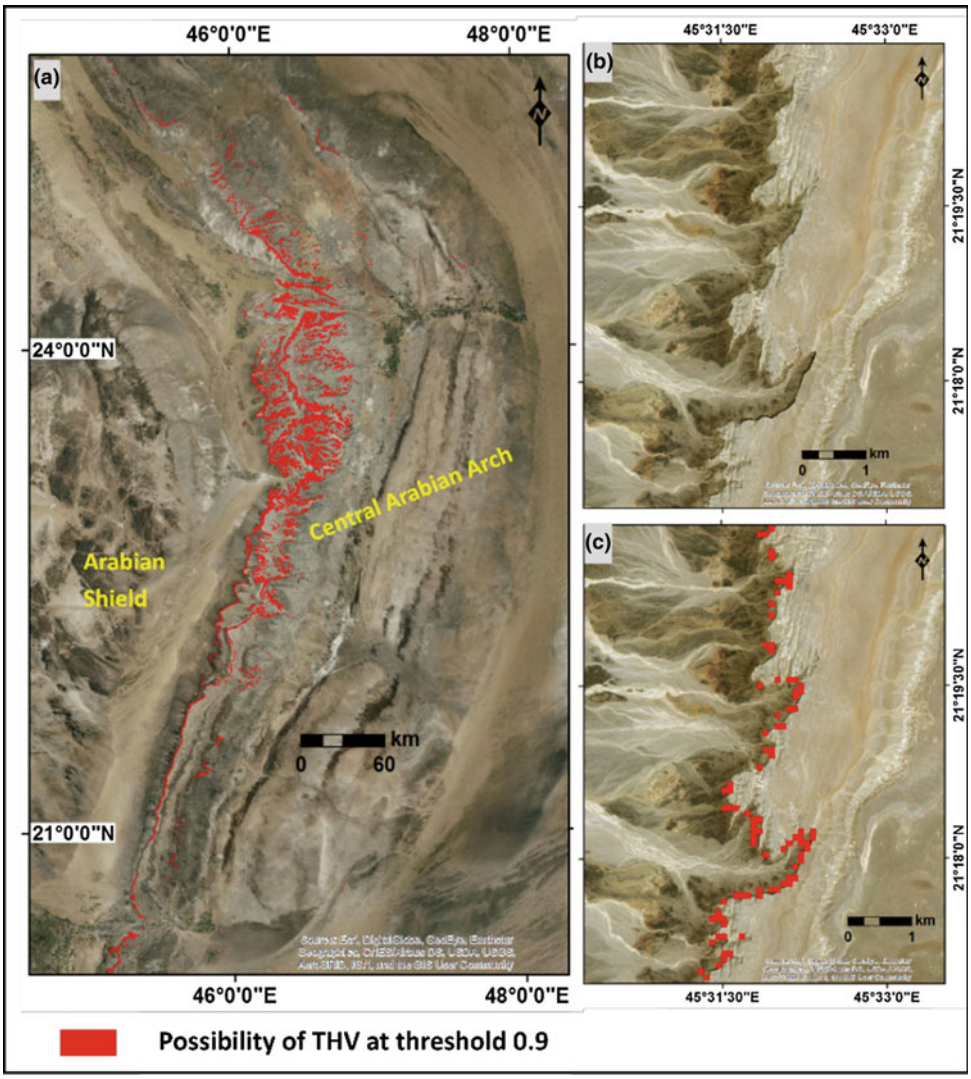

Fig. 1 Logistic regression model output showing the distribution of modeled THV in the CAA at threshold 0.9 (the model results are possibilities of THV occurrence from 0 to 1)

techniques or a substitute of the latter in case of regional studies to assess regional paleohydrological and paleoclimatic patterns.

References

1. Abotalib, A., Sultan, M., Elkadiri, R.: Groundwater processes in Saharan Africa: implications for landscape evolution in arid environments. Earth-Sci. Rev. **156**, 108–136 (2016)
2. Lamb, M.P., Dietrich, W.E., Aciego, S.M., DePaolo, D.J., Manga, M.: Formation of box canyon, idaho, by megaflood: implications for seepage erosion on earth and mars. Science **320**, 1067–1070 (2008)
3. Elkadiri, R., Sultan, M., Youssef, A.M., Elbayoumi, T., Chase, R., Bulkhi, A.B., Al-Katheeri, M.M.: A remote sensing-based approach for debris-flow susceptibility assessment using artificial neural networks and logistic regression modeling. IEEE J. Sel. Top. Appl. Earth Observations Remote Sens. **7**, 4818–4835 (2014)

Validation of TRMM Satellite Rainfall Algorithm for Forest Basins in Northern Tunisia

Saoussen Dhib, Zoubeida Bargaoui, and Chris M. Mannaerts

Abstract

At present, a number of newly satellite-derived precipitation estimates are freely available for exploration and could benefit the hydrological community. This study aimed to evaluate the Tropical Rainfall Measuring Mission TRMM 3B42 rainfall estimate algorithm in forest basins in Northern Tunisia. We selected 77 events, with 50 mm/day heavy rainfall as selection criteria, for at least one station of the study area observed during 2007, 2008 and 2009. Rainfall stations were interpolated using the inverse distance method. Results were discussed in terms of the TRMM product accuracy in comparison with rain gauges over the forestry zone (169 stations). The Pearson's correlation coefficient between satellite estimations and ground maps reached 0.7 for some events and were weak for others. The comparison results of TRMM algorithm over forestry zone within Northern Tunisia shows a weak difference in terms of false alarm ratio (FAR), and bias. However, it shows a better detection for the whole of Northern Tunisia in terms of correlation coefficient and the probability of detection (POD). Some uncertainties have been found, across the TRMM algorithm over forestry region. Thus, the evaluation of satellite algorithms before use as input for other models is recommended.

Keywords

Rainfall • Extremes • Tunisia • Forest • Validation • TRMM 3B42

S. Dhib (✉) · Z. Bargaoui
ENIT, Université de Tunis El Manar, Ecole Nationale d'ingénieurs de Tunis, Tunis, Tunisia
e-mail: Dhib_saoussen@hotmail.fr

C. M. Mannaerts
Faculty of Geo-information Science and Earth Observation, ITC: University of Twente, Enschede, The Netherlands

1 Introduction

For most Tunisians, heavy rainfall means more accidents, traffic jams. One of the main causes of the shortcomings of flood monitoring is the cruel lack of observations that hinders the characterization of the hazard. To this end, it is clear that a great effort remains to be achieved in forecasting and especially alerting. In the past two decades, satellite-derived products provided a cost-effective way to estimate precipitation. However, as mentioned by Tian et al. [1] satellite data have an inherent uncertainty. Therefore, one can see the importance of evaluation. Thus the problem can be formulated as follows: Do TRMMs 3B42 detect well extreme events over the Tunisian forestry region? And is there a difference between the rainfall detection over forestry region and the whole Northern of Tunisia?

2 Data and Methods

2.1 Regional (In Situ) Rainfall and Satellite Data

The daily rainfall network covers a zone from 36′N to 37° 2′ N and from 8°E to 9° 2′E. It is included as a part of the Medjerda River watershed (W-5), and a part of the northern coastal watersheds (W-3). The network size consists of 169 operational stations. An extreme daily event is assumed when at least 50 mm/day are recorded at least in one single station in the whole domain (Northern Tunisia).

TRMM product 3B42 V 7 was used with a resolution of 0.25° and 3 h. This product was a combination of TIR from geostationary satellites and microwave sensors [2].

2.2 Methodology

The moving average using an inverse distance weighting was adopted for interpolating the rainfall for the two seasons [3]. The spatial verification methods included visual verification,

© Springer Nature Switzerland AG 2019

H. M. El-Askary et al. (eds.), *Advances in Remote Sensing and Geo Informatics Applications*, Advances in Science, Technology & Innovation, https://doi.org/10.1007/978-3-030-01440-7_20

statistical verification (correlation coefficient (r), and ratio bias coefficient), and categorical statistics (POD, FAR, and Bias). POD, FAR and Bias range from 0 to 1, with 1 being a perfect POD, and Bias and 0 being a perfect FAR.

3 Results

3.1 Evaluation of TRMM over the Forestry Zone

Figure 1 illustrates the averaged values of the correlation coefficient (R), POD, FAR, and Bias, for all the selected heavy events during dry and wet seasons.

Figure 1 shows a weak difference between the correlation average and POD coefficients of the wet and dry seasons. However, the TRMM during the wet season shows a better performance in the estimation of the FAR and the bias coefficients.

Figure 2 presents maps 10 events as estimated by TRMM and ground observations during wet and dry seasons.

We notice that TRMM yielded a good estimation for some events such as 24/09/2007 and 18/04/2007, an underestimation of other events such as 23/02/2009 and overestimated some events such as 08/03/2007 and 12/01/2009.

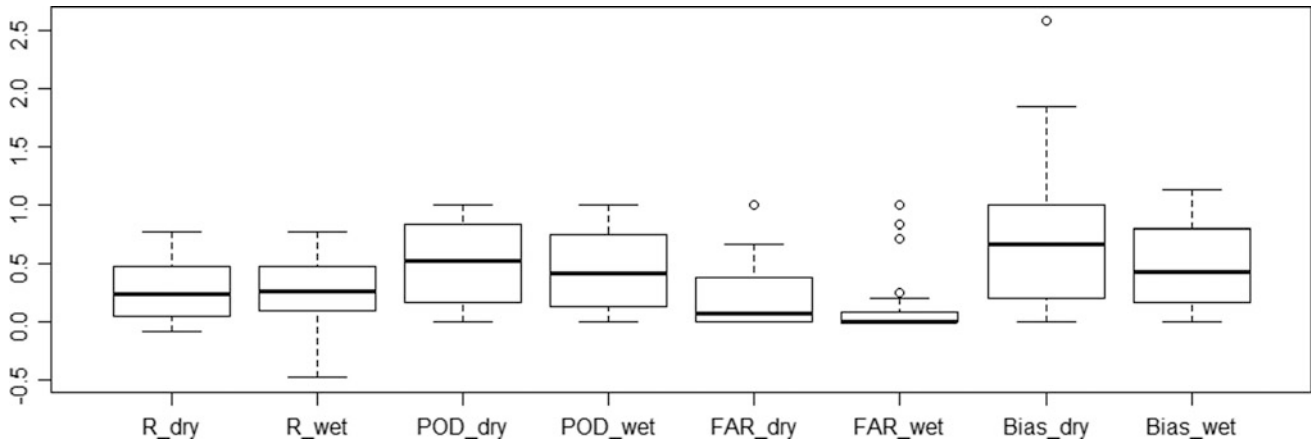

Fig. 1 Box plots of the averaged coefficients for the dry and the wet season over the forestry zone

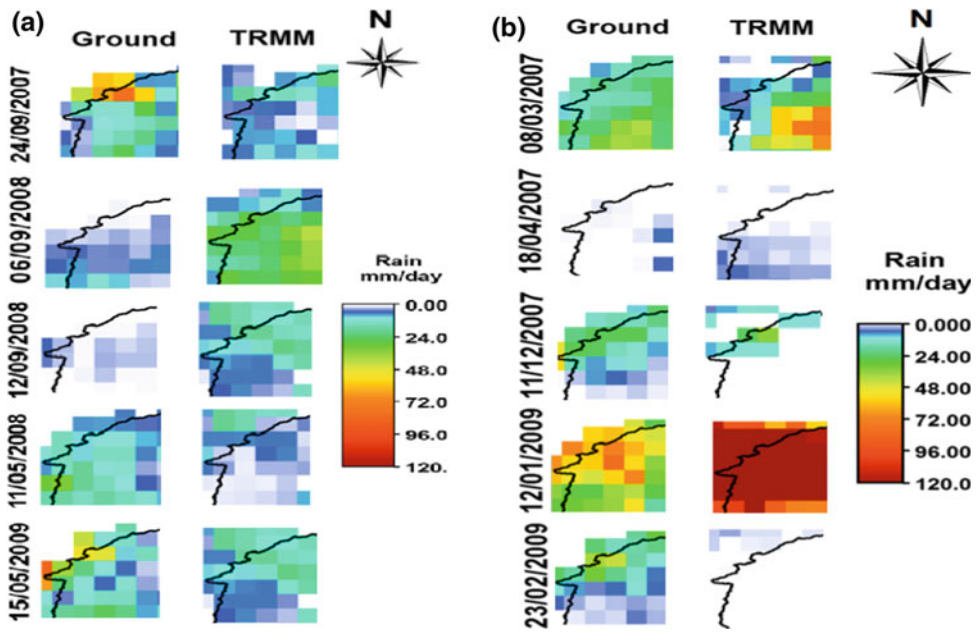

Fig. 2 Some maps examples for the dry season (**a**) the wet season (**b**)

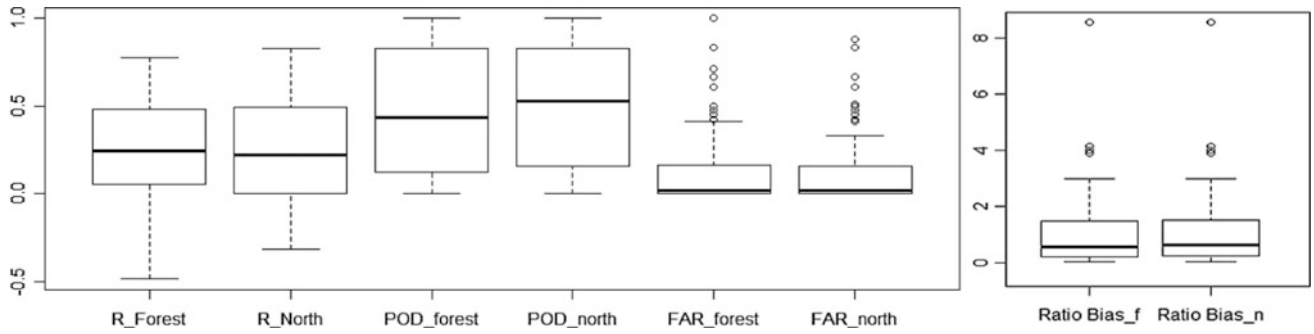

Fig. 3 Box plots of the averaged correlation coefficients (R), POD, FAR, and ratio bias over the forestry zone (f) and the whole of Northern Tunisia (n)

3.2 Comparison of TRMM algorithm performance over the forestry zone and Northern Tunisia

To compare the performance of TRMM over the forestry zone and Northern Tunisia, we performed some statistics (Fig. 3). We notice a weak difference of the average of all the evaluation coefficients (R, POD, FAR, and Ratio Bias) over the forestry zone and Northern Tunisia.

4 Discussion

The oscillation of TRMM rainfall estimation between an overestimation and an underestimation against in situ data confirms the findings of many worldwide previous studies. For example in the Iberia case study, [4] found that TRMM-3B42 tends to overestimate rainfall across the whole domain in most seasons but gives an overall underestimation in the orographic area.

5 Conclusion

This study evaluated TRMM 3B42 data version 7 using 169 ground rainfall observation stations in the Northern Tunisia forestry zone for extreme events recorded from January 2007 to August 2009. The TRMM showed a good occurrence compared with the rainy ground days where 96% were captured rainy by the satellite. 20% of the studied events were well estimated by TRMM with a correlation coefficient of about 0.5. The spatial average comparison showed a similar correlation and probability of detection during the wet and dry seasons while false alarms and bias coefficients are smaller during the wet season. As we saw in this work, monthly GPCC correction for TRMM 3B42 didn't correct well the extreme events. That is why we are planning to use some bias correction methods to ameliorate the TRMM algorithm performance over Tunisia.

References

1. Tian, Y., Liu, Y., Arsenault, K.R., Behrangi, A.: A new approach to satellite-based estimation of precipitation over snow cover. Int. J. Remote Sens. **35**, 4940–4951 (2014). https://doi.org/10.1080/01431161.2014.930208.2
2. Ouma, Y.O., Owiti, T., Kipkorir, E., KibIy, J., Ryutaro, T.: Multitemporal comparative analysis of TRMM-3B42 satellite-estimated rainfall with surface gauge data at basin scales: daily, decadal and monthly evaluations. Int. J. Remote Sens. **33**, 7662–7684 (2012)
3. Ilwis Help.: ILWIS version 2.22 (1999)
4. El Kenawy, A.M., Lopez, J.I., McCabe M.F., Vicente, S.M.: Evaluation of the TMPA-3B42 precipitation product using a high-density rain gauge network over complex terrain in northeastern Iberia. Global Planet. Change **133**, 188–200

Contribution of Remote Sensing to Cartography (Application in the Djanet Area, East Hoggar, Algeria)

Dalila Nemmour-Zekiri, Yamina Mahdjoub, Fatiha Oulebsir, and Zakaria Hamimi

Abstract

The application of space techniques to geological studies is an important source of information for geological mapping. The optimal exploitation of high spatial resolution satellite imagery can contribute to the improvement of the geological map, particularly when it comes to mapping in arid and desert areas where outcrops are often inaccessible. Indeed, the region of Djanet, main object of our study, is characterized by rather important reliefs and this made the access difficult or sometimes even impossible in certain zones. The study area is located at the northeastern end of East Hoggar. It covers the terrane of Djanet and part of the terrane of Edembo. In addition, this region is probably one of the least explored areas of the Hoggar. This is why different remote sensing techniques have been used to make geological mapping faster and more efficient. The obtained images were subject to various treatments ranging from contrast enhancements to spectral enhancements, and using images in 742 RGB color compositions and calculation processing of bands (3/1, 5/4, 7/5) and the (5/7, 2/1, 4/2), Thus, the analysis of the processed Landsat-7 ETM + images from the Djanet area allowed us to establish a tele-analytical lithological map. The correlation of this map with the field data allowed us to check the validity and the correspondence of the different facies and especially to clarify the lithological contours derived from the analysis of Landsat satellite data.

Keywords

Djanet area • Eastern Hoggar • Remote sensing • Cartography

1 Introduction

The present work is a study of the Djanet area carried out mainly in the Neoproterozoic basement. The development of the geological map is based on (1) classical field methods combined with (2) application of different remote sensing techniques. The mere use of conventional methods (field data and photo-interpretation analysis) for geological mapping remains insufficient, particularly because of the important landforms that made access, in some areas, difficult or sometimes impossible. On the other hand, the satellite imagery with high spectral and spatial resolution allowed us to identify even the different lithological units in order to improve the map and to make it relatively more complete [1–3].

The Djanet area is located at the northeastern end of East Hoggar (Fig. 1). It covers the Djanet terrane and part of the Edembo terrane [4].

The studied domain consists of a Neoproterozoic basement itself consisting of two sets: (1) a first granito-gneissic ensemble that outcrops in the West in the Edembo terrane, (2) a second set of meta-sedimentary épizonal Neoproterozoic which is intersected by post-orogenic granitoids of ages varying between 571 + 16 Ma and 558 + 6 Ma. It is topped to the north and to the east by the Paleozoic Cambro-Ordovician sandstones of Tassili n'Ajjer [5].

2 Materials and Methods

2.1 Data Used

The images we used for this study are Landsat 7ETM + scenes acquired on November 29th 2000 and

D. Nemmour-Zekiri (✉) · Y. Mahdjoub
Laboratory of Geodynamics, Geology of the Engineer and Planetology, Algiers, Algeria
e-mail: dnemmour@usthb.dz

F. Oulebsir
Laboratory of Metallogeny, Magmatism of Algeria, Algiers, Algeria

Z. Hamimi
Benha University, Benha, Egypt

© Springer Nature Switzerland AG 2019

H. M. El-Askary et al. (eds.), *Advances in Remote Sensing and Geo Informatics Applications*, Advances in Science, Technology & Innovation, https://doi.org/10.1007/978-3-030-01440-7_21

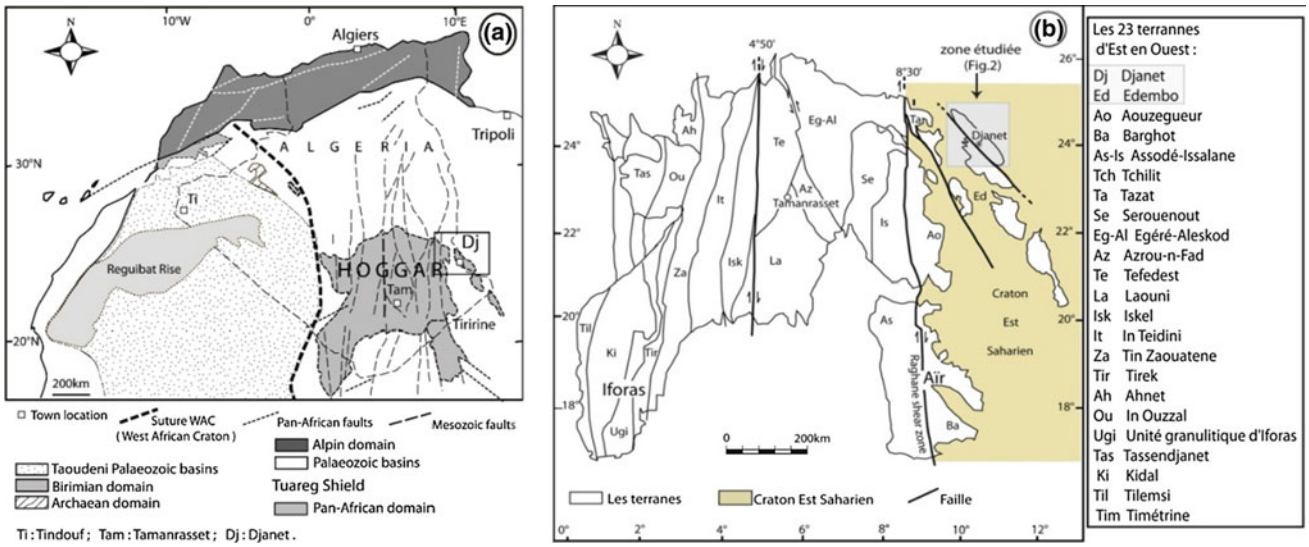

Fig. 1 Maps of the geological situation: **a** of Hoggar, [8]; **b** of the study area from the terrane map of the Touareg Shield [4, 9]

geo-referenced in UTM-32-N, WGS 84 (Scenes 190-043 and 189-043). These high-resolution images were chosen for their spectral and spatial characteristics allowing a good mapping [6]. These bands are ETM + 1 (blue), ETM + 2 (green) ETM + 3 (red), ETM + 4 (near infrared), ETM + 5 (medium infrared), ETM + 7 (far infrared) all with 30 m pixels and the ETM + 6 (thermal infrared) band with 60 m pixels.

2.2 Image Processing

The image processing of the study area, extracted from two mosaics (Fig. 2), focused on the search for specific treatments allowing maximum lithological discrimination. Thus, the identification of the lithological assemblages of the Djanet region was carried out thanks to.

2.2.1 Color Composite

The color composite of the channels 742 (red, green and blue are respectively assigned to the strips 7, 4 and 2). This combination is often used for geological applications.

2.2.2 Principal Components Analysis (PCA)

The Principal Component Analysis (CP1, CP2, CP3) allowed merging most of the variance (information) contained in the original image files into a single optimized to 90% image, thus providing a clean colored composition [7].

2.2.3 Band Reports

The analysis of the band ratios produced from the generated neo-bands makes it possible to produce new colored compositions whose best results are: (3/1, 5/4, 7/5) and the (5/7, 2/1, 4/2).

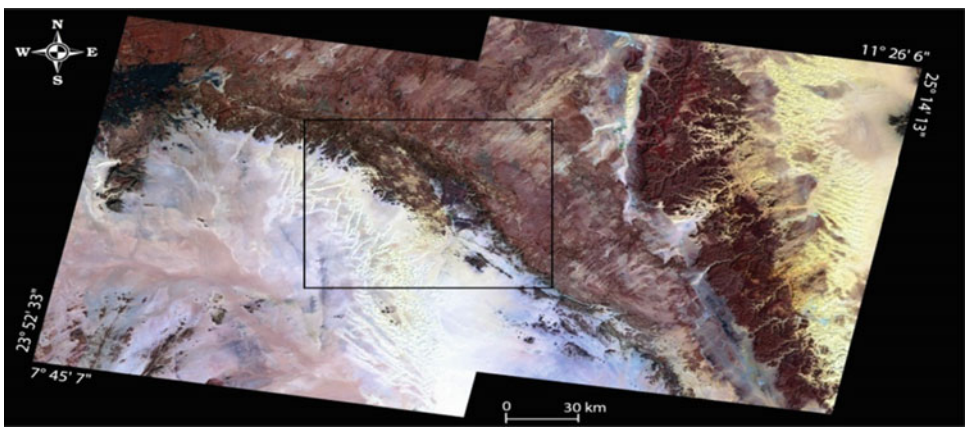

Fig. 2 Mosaic of the two scenes 190-043 and 189-043 in colored composition 742. The black rectangle indicates the treated area

2.3 Results Analysis and Interpretation

The different color compositions of the raw or transformed strips were used to bring out the homogeneous units in order to interpret the lithology of the Djanet region. All the image processing was achieved on smaller windows to specify details missing on the map, especially in inaccessible areas.

In addition, out of the nine neo-bands from the band reports, ETM+3/ETM+1, ETM+5/ETM+4, ETM+7/ETM +5, ETM+5/ETM+3, ETM+3/ETM+2, ETM+7/ETM+4, ETM+5/ETM+7, ETM+2/ETM+1, ETM+4/ETM+2, four RGB color compositions were made. These colored compositions have the particularity of highlighting the different contours and make it possible to obtain an interesting maximum lithological discrimination.

Indeed, the first type of color composition treatment of the three ETM+3/ETM+1, ETM+5/ETM+4, ETM+7/ETM +5 neo-bands was applied in two distinct regions (position and dimension). This treatment brings out all the intrusive granitic massifs in the Djanet series:

In the North of the city of Djanet, we can easily notice the outline of all the granites of the region (purplish hue). The formations of the Djanet series (in orange) are distinct from the Palaeozoic formations of Tassili n'Ajjer (in blue). The diorite veins are strongly colored in dark brown while the gabbro veins appear in mauve (Fig. 3).

The second type of color composition treatment is related to the last three neo-bands ETM+5/ETM+7, ETM+2/ETM +1, ETM+4/ETM+2. The visual interpretation of these images makes it possible to identify homogeneous ranges comparable to rhyolite dykes with a bluish tint and granites with a rather purplish hue (Fig. 4).

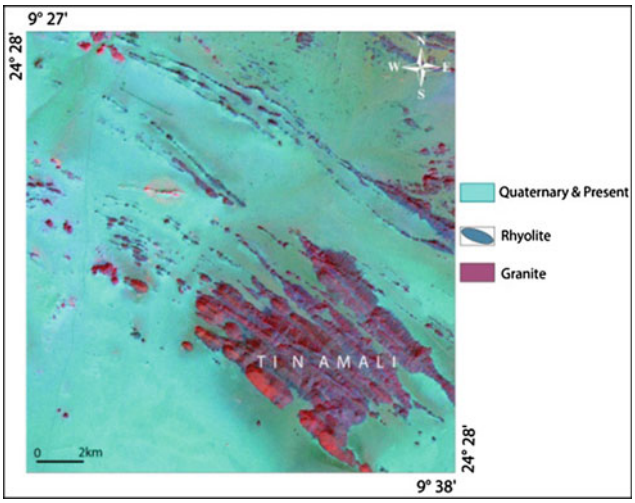

Fig. 4 2nd example of a colored composition established from the band reports ETM+5/ETM+7, ETM+2/ETM+1 and ETM+4/ETM+2

2.4 Contribution of Remote Sensing to Cartography

The interpretation of all of satellite images made it possible to draw a map of the geological units of the study area (Fig. 5). The comparison of this map with that made by classical methods shows that all major geological units in the region were distinguished. The discrimination of these lithological limits is based on the variation of the hues observed on the various image treatments. As a result, the different lithological units are well identified and appear under facies of distinct hue.

The contours of the different granite of the study area as well as the limits of the Djanet series are specified. In

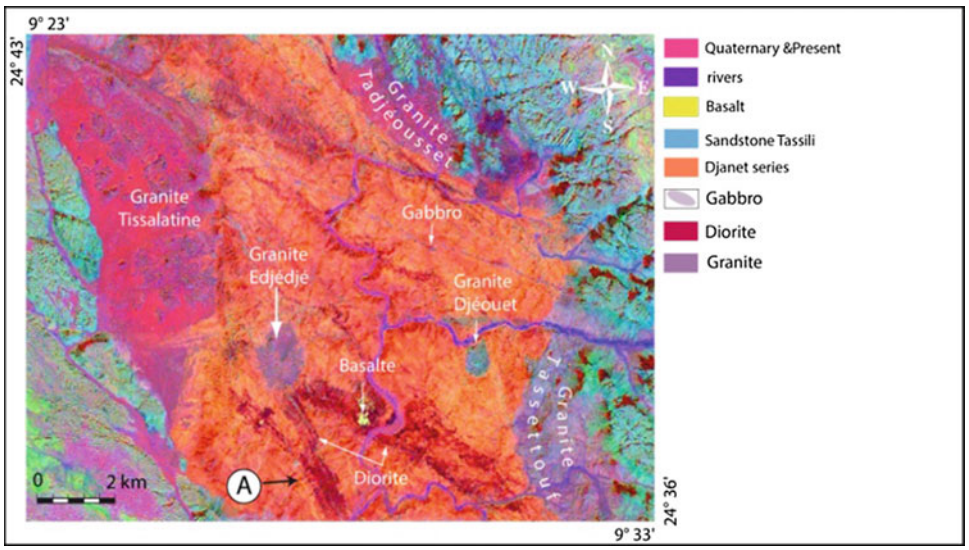

Fig. 3 1st example of a colored composition established from the bands reports. ETM+3/ETM+1, ETM+5/ETM+4 & ETM+7/ETM +5 (A) panoramic view of a diorite vein

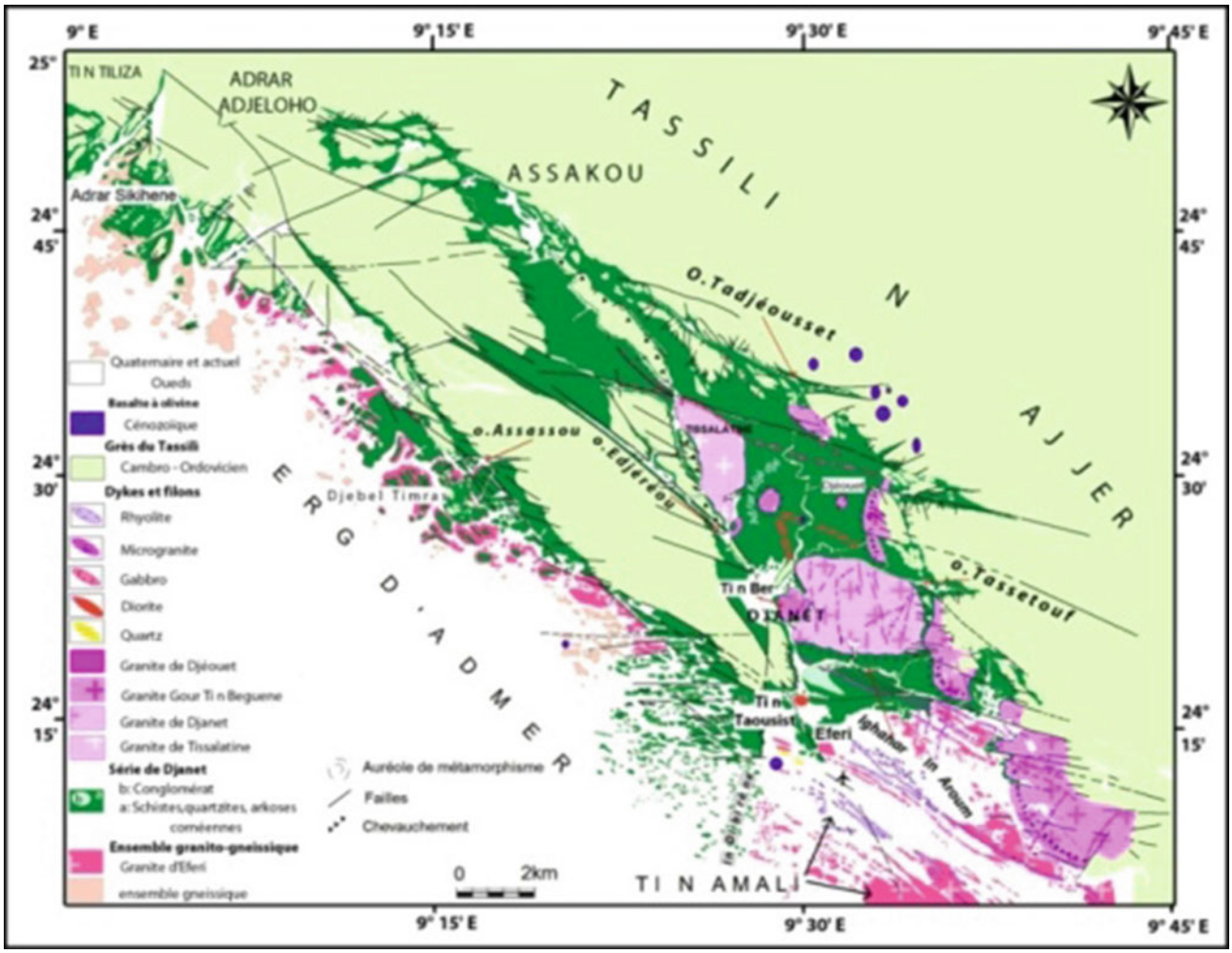

Fig. 5 Geological map based on field data and complemented by ETM + Landsat images analysis

addition, there are gabbro veins and diorite intersecting the shale formations of the Djanet series in the north and north-east of the town of Djanet. Although these veins are not mentioned on the previous geological maps, these results are in line with the field data.

3 Conclusion

The present work is a contribution to geological mapping from classical methods combined with the application of spatial remote sensing. The latter shows the contribution of satellite imagery in mapping geological contours, especially in inaccessible areas. The geological results obtained were correlated with the various works already carried out in the region. The geological map thus obtained constitutes a detailed and efficient basic document (Fig. 5). It provides more information because of the new clarifications it brings. The geological survey and the study of the formations of the Djanet region led us to draw the following conclusions:

The Neoproterozoic basement of the Djanet area consists of two sets that extend in a NW-SE global direction: (1) a granito-gneissic ensemble (shear zone of Ti n Amali), materialized by an eyed or banded gneiss locally migmatitic and sometimes intersected by other generations of porphyroid granites. (2) an epizonal meta-sedimentary set (Djanet series). The formations of the study area are mainly represented by the Neoproterozoic Djanet series consisting essentially of schists, silts and pelites, with lenticular intercalations of quartzites, conglomerates, microconglomerates and arkoses. The set is topped by PalaeozoicTassili sandstones. All these formations are crossed by isolated volcanic cones and quite preserved from the Cenozoic.

References

1. Bonn, F.: Précis de télédétection. Volume 2: Applications thématiques. Presses de l'université du Québec/AUPELF, Sainte-Foy, p. 633 (1996)
2. Bonn, F., Rochon, G.: Précis de télédétection. Vol. 1: Principes et Méthodes. Presses de l'université du Québec/AUPELF, Sainte-Foy, p. 485 (1992)
3. Girard, M.C., Girard C. M.: Traitement des données de télédétection. Éditions Dunod. Paris, p. 529 (1999)
4. Black, R., Latouche, L., Liegeois, J.P., Caby, R., Bertrand, J.M.: Pan-African displaced terranes in the Tuareg Shield (Central Sahara). Geology **22**, 641–644 (1994)
5. Beuf, S., Biju-Duval, B., Charpal, O., Rognon, P., Gariel, O., Bennacef, A.: Les grès du paléozoïque inférieur au Sahara. Sédimentation et discontinuités. Évolution structurale d'un craton. Editions Technip, p. 464 (1971)
6. Sabins, F.F.Jr.': Remote Sensing: Principles and Interpretation, . 2nd edn., p. 426. W.H. Freeman, New York (1987)
7. Rakotoniaina, S.: Analyse en composantes principales d'une image multispectrale de télédétection. J des sciences de la terre **2**, 3–5 (1998)
8. Ennih, H., Liegeois, J.P.: The moroccan Anti-Atlas: the west African craton passive margin with limited Pan-African activity. Implications for the northern limit of the craton. Precambr. Res. **112**, 289–302 (2001)
9. Liégeois, J.P., Latouche, L., Boughrara, M., Navez, J., Guiraud, M.: The Latea metacraton (Central Hoggar, Tuareg shield, Algeria): behaviour of an old passive margin during the Pan- African orogeny. J. Afr. Earth Sc. **37**, 161–190 (2003)

Part III

Land Use Land Cover Mapping and Urban Form Assessment

Producing of Land Cover Map for Marshes Areas in the South of Iraq Using GIS and Remote Sensing Techniques

Hussein Sabah Jaber

Keywords
Satellite image • Marshes • Remote sensing • GIS • Land cover

1 Introduction

Iraq's southern marshes are among the world's most affluent ecosystems and the surrounding areas with water availability and climatic viability for growing economic crops and vegetables [1, 2].

The areas of the marshes vary and change naturally along the seasons and years, depending on the levels of water in the rivers, which depend on the amount of precipitation in their springs and basins [3]. GIS and remote sensing are excellent tools to monitor, detect, and analyze changes in land use and land cover [4]. Recently, various studies have been published [4, 5]. Marshes in Iraq suffered from drought for decades ago, changes in climatic conditions and war affected the land cover, and there was no modern techniques to monitor and analyze the changes in land cover, hence this research aimed to produce a land cover map for marshes area in the south of Iraq by integrating GIS and remote sensing techniques.

2 Study Area, Materials and Methods

Figure 1 shows the map of the study area. The area is covered with four scenes of Landsat as shown in Fig. 2. Therefore, mosaics image of this area was produced for satellite scenes images using the Erdas Imagine program as shown in Fig. 3.

This study adopted the descriptive and analytical method of the Landsat satellite data where digital data and maps were processed using the Erdas Imagine program and Arc GIS. After deducing the study area from the image resulting from the digital mosaic, Transformed Normalized Difference Vegetation Index (TNDVI) and Normalized Difference Water Index (NDWI) were calculated for the study area using the below equations respectively [1, 2].

$$TNDVI = ((IR - R)\backslash(IR + R) + 0.5))^{0.5} \quad (1)$$

$$NDWI = (Band(Green) - Band(NIR))/(Band(Green) + Band(NIR)) \quad (2)$$

These indices are based on spectral behavior for water and vegetation in visible and infrared region of satellite images for the study area.

In addition, a supervised classification was performed to produce a land cover map for the study area.

3 Results and Discussion

Transformed Normalized Difference Vegetation Index (TNDVI) values ranged from 0.23 to 0.55 and vegetation appears in white color for the study area as shown in Fig. 4.

Also, Normalized Difference Water Index (NDWI) values ranged from 0.02 to 0.37 showing that there are lakes and water bodies in this study area because these values larger than zero as shown in Fig. 5.

In addition, a supervised classification using the Maximum likelihood method was achieved to produce the land cover maps for the study area where there are six types of land cover as shown in Fig. 6. The overall accuracy and kappa coefficient of the Maximum likelihood method are 92.6016% and 0.8903 respectively.

H. S. Jaber (✉)
University of Baghdad, Baghdad, Iraq
e-mail: husseinsabah00@gmail.com

© Springer Nature Switzerland AG 2019

H. M. El-Askary et al. (eds.), *Advances in Remote Sensing and Geo Informatics Applications*,
Advances in Science, Technology & Innovation, https://doi.org/10.1007/978-3-030-01440-7_22

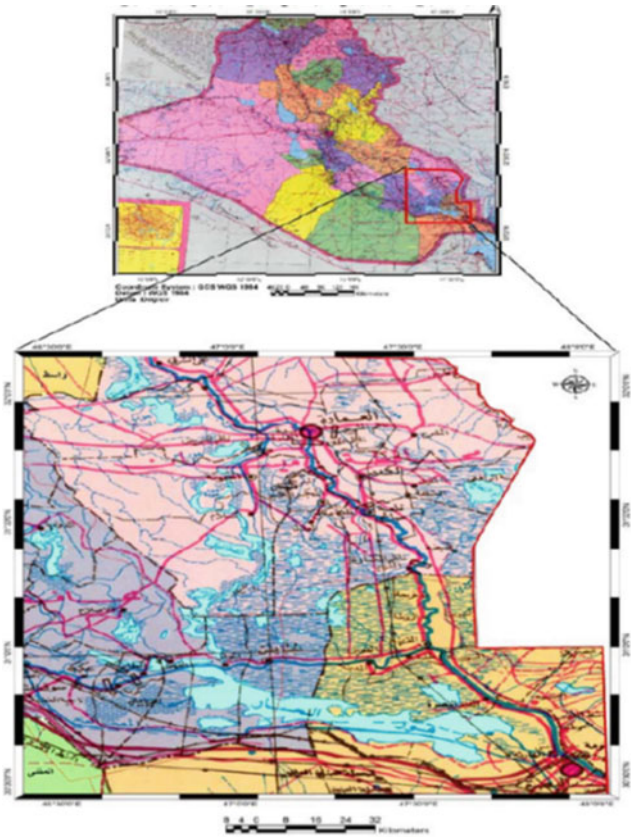

Fig. 1 Study area map

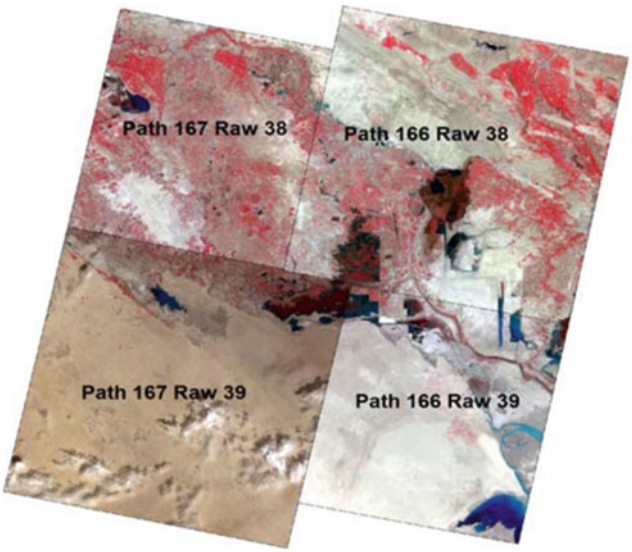

Fig. 2 Four scenes of Landsat covering the study area

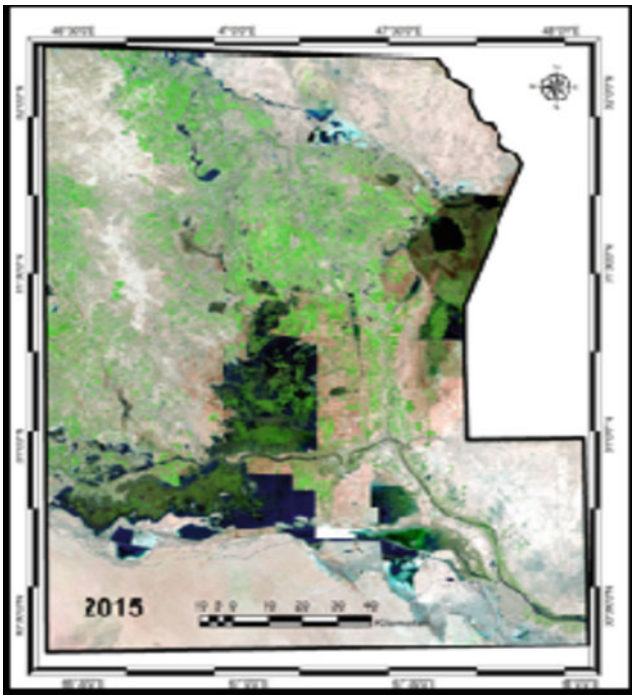

Fig. 3 Mosaic image of the study area

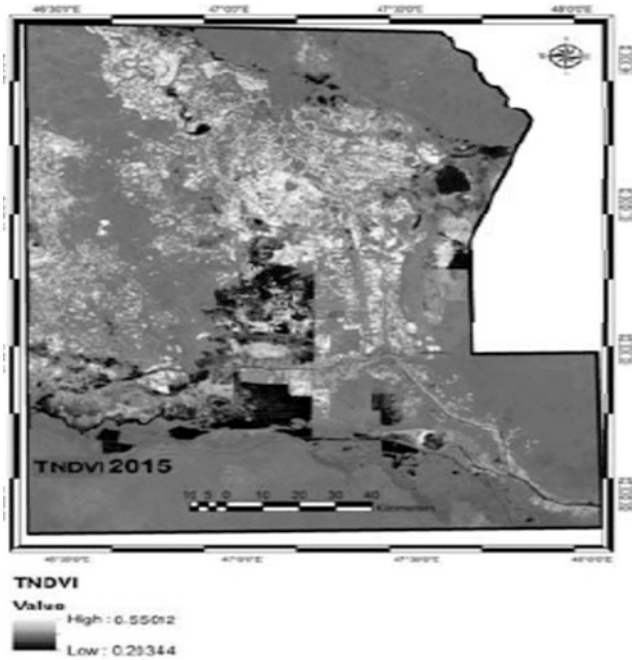

Fig. 4 TNDVI map of the study area

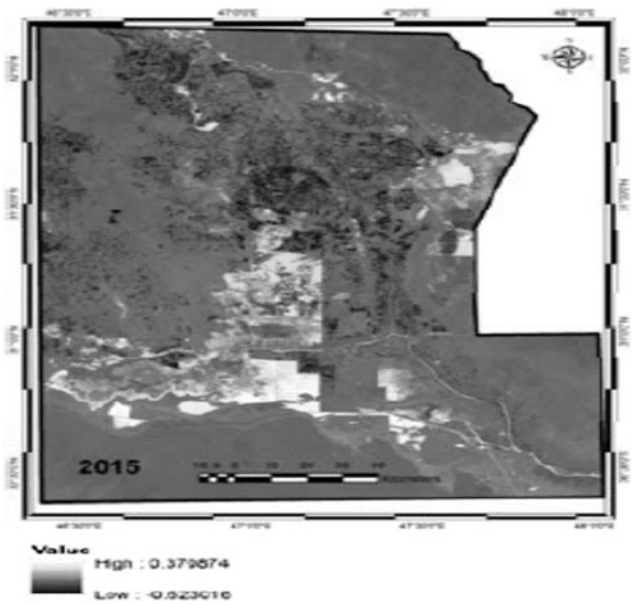

Fig. 5 NDWI map of the study area

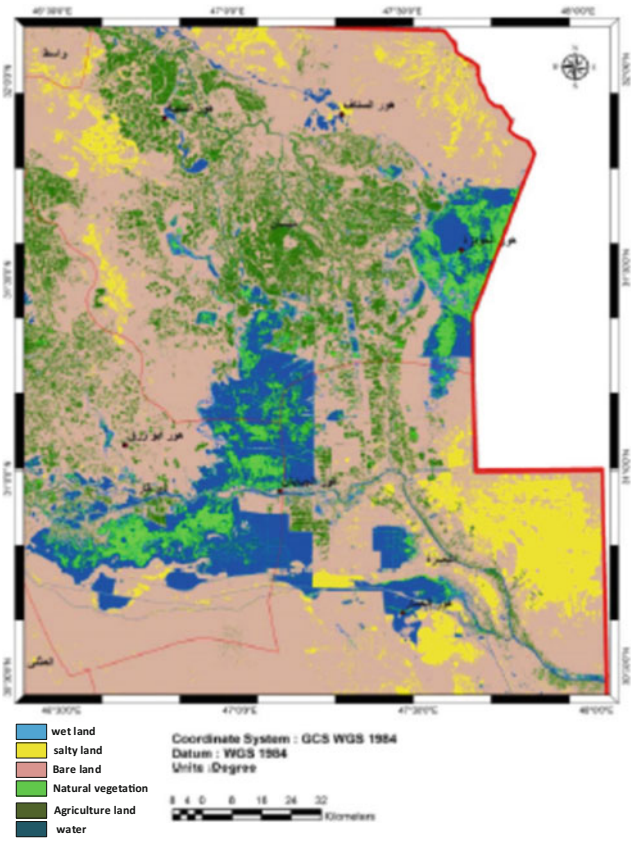

Fig. 6 Land cover map of the study area

4 Conclusion

Landsat images were utilized to monitor and analyze changes in land cover for marshes. The Maximum likelihood algorithm was used to classify the images in six main classes: wet land, vegetation, water, salty land, bare land and agriculture, under Anderson Scheme Level 1. Hence, remote sensing can be used for monitoring land cover. GIS is an effective technique for producing the land cover in marshes areas. The processing involves several factors such as TNDVI and NDWI. Also, the results showed that there is an increase in the surface area of the Marshlands and natural vegetation based on TNDVI and NDWI values. Although this study achieved its objectives, its results suffered a number of limitations. First, the satellite imagery sensors did not have high spatial resolution, making it necessary to use the open source Landsat data. Second, the classification of land cover results were affected by the data resolution, which affected the change detection analysis results.

References

1. Elachi, C., van Zyl, J.: Introduction to the physics and techniques of remote sensing. John Wiley & Sons, Inc., Hoboken, New Jersey, Canada (2006)
2. Lille sand, T.M., Kiefer, R.W.: Remote Sensing and Image Interpretation, 4th edn. John Wiley & Sons, New York (2000)
3. Mfeeters, S.K.: The use of Normalized Difference Water Index (NDWI) in the delineation of open water features. Int. Remote Sens. **17**, 1425–1432 (1996)
4. Pradhan, B., Ajaj, Q.M., Noori, A.M., Jebur, M.N.: Spatial monitoring of desertification extent in western iraq using landsat images and GIS. Land Degrad Dev. (2017) https://doi.org/10.1002/ldr.2775 (John Wiley & Sons, Ltd)
5. Ministry of Irrigation (MOI).: General Report, Iraq, p. 18 (2017)

A Modified Triangle with SAR Target Parameters for Soil Texture Categorization Mapping

Shoba Periasamy, Divya Senthil, and Ramakrishnan S. Shanmugam

Abstract

This research investigated soil texture information extraction in agricultural soil using SAR imagery of C band (5.36 GHz) frequency. The soil backscattering coefficient (σ^o_{soil}) could act as an effective estimator to the relative percentage of sand, silt, and clay when the influence of vegetation is considerably reduced from the total backscattering energy (σ^o_{total}). The contribution of vegetation in the SAR imageries of VV (σ^o_{vv}) and VH (σ^o_{vh}) polarization has been significantly reduced by Water Cloud Model, and Dual polarized SAR Vegetation Index. One of the target parameters, namely roughness (h_{rms}), was derived from the cross-polarization ratio between $\sigma^o_{vh-soil}$, and $\sigma^o_{vv-soil}$ and Dielectric Constant (ε'_{soil}) was obtained from the modified Dubois model. The extracted target parameter such as h_{rms} is adequately correlated with in situ Sand texture measurements ($R^2 = 0.81$) and, ε'_{soil} was sufficiently correlated with in situ Clay measurements ($R^2 = 0.78$). The positively correlated regions of the correlation coefficient (CC) analysis between h_{rms} and ε'_{soil} were extracted and thus represented the percentage of silt with reasonable accuracy ($R^2 = 0.77$). From the soil triangle formed with three estimated parameters, we found that the Clay category shared around 36% of the total area followed by Sandy loam (24%) and loamy sand (19%).

Keywords

Soil texture • Soil backscattering • Roughness • Dielectric constant • Correlation coefficient • Soil triangle

S. Periasamy (✉) · D. Senthil
SRM Institute of Science and Technology, Kancheepuram, India
e-mail: shoba84.geog@gmail.com

R. S. Shanmugam
Institute of Remote Sensing, Anna University, Chennai, India

1 Introduction

The investigation of spatial variability of soil texture is essential for many applications like agricultural and environmental management. Optical and hyperspectral sensing have proved their applicability in estimating the relative percentages of sand, silt and clay in the soil, yet with some reported uncertainties [1]. This is due to the fact of neglecting the physical connection between the spectral reflectance and soil samples. On the other hand, the microwave sensing provides an excellent opportunity for analyzing soil and its textural variation using monochromatic wave characteristics [2]. The backscattering values of SAR imagery are highly influenced by target parameters namely surface roughness and dielectric constant that is directly related to coarseness and the soil moisture holding capacity. The present research investigated the possibility of extracting target parameters representing the relative percentage of sand, silt, and clay from SAR imagery to form the modified soil triangle to identify the soil textural categories.

2 Materials and Methods

The research took place in Perambular district, Tamil Nadu, India that lies in a tropical wet-dry climate region. The modified form of the *Water Cloud Model* (*WCM*) was proposed [3] with the hypothesis that the total backscattering coefficient ($\sigma^0_{vv-total}$) of the like polarized SAR imagery (*VV* or *HH*) is a function of vegetation and soil. The backscattering coefficient of the soil ($\sigma^0_{vv-soil}$) was obtained by inverting the *WCM* model with the estimated σ^0_{vv-veg}. Since the *WCM* strictly ignores the second order contribution from multiple scattering returns, the Dual polarized SAR Vegetation Index (*DPSVI*) was proposed as a physical scattering model, which represents the presence of terrestrial vegetation in cross-polarized imagery (VH or HV), based on the central concept of Degree of Depolarization. Hence, the

© Springer Nature Switzerland AG 2019

H. M. El-Askary et al. (eds.), *Advances in Remote Sensing and Geo Informatics Applications*,
Advances in Science, Technology & Innovation, https://doi.org/10.1007/978-3-030-01440-7_23

$\sigma^0_{vh-soil}$ was obtained by reducing the influence of terrestrial vegetation in $\sigma^0_{vh-total}$ using *DPSVI*.

The applicability of the cross-polarization ratio was investigated for the vertically polarized SAR imageries and employed to determine the surface roughness after eliminating the effect of vegetation from both $\sigma^0_{vv-total}$ and $\sigma^0_{vh-total}$. With the estimated parameters, the Dubois model [4] was reversed to obtain the Dielectric Constant (ε'_{soil}), which is directly related to the percentage of water content held in the soil. The relative percentage of silt was identified and extracted by the novel idea of performing correlation coefficient (*CC*) analysis between h_{rms} and ε'_{soil}. Since the h_{rms} represents sand by roughness and ε'_{soil} indicates the clay by the water holding capacity of the soil, the two parameters are inversely correlated at the lower and higher range. However, the distribution of the pixels representing silt is found in the mid-range of the h_{rms} and ε'_{soil} (Fig. 1e). Hence, the negatively correlated places represented by clay or sand distribution and the positively correlated region starts representing the relative percentage of silt in the soil. The potential of the logic behind correlation was also investigated from the measures namely *Homogeneity* (*clay*) and *Entropy* (*Sand*) of Gray level occurrence matrix (*GLCM*) of h_{rms}. The spatially estimated target parameters such as h_{rms}, *CC*, and ε'_{soil} were considered to represent the soil textural triangle of USDA.

3 Results

During the validation with the Percent Ground Biomass Cover (*PGBC*), we found that WCM could adequately represent the terrestrial vegetation with the R^2 value of 0.72 and *DPSVI* model with the R^2 value of 0.75. The values of ε'_{soil} have shown good agreement with in situ soil moisture measurements ($R^2 = 0.73$). The extracted target parameter such as h_{rms} has shown sufficient linear fit with in situ Sand texture measurements ($R^2 = 0.81$) and, ε'_{soil} has shown good correlation with field observed Clay measurements ($R^2 = 0.78$) which demonstrated the suitability of those two parameters to represent the relative proportion of sand and clay in the soil. The negatively correlated places of *CC* analysis represented by the distribution of clay or sand at a higher magnitude. The positively correlated region from *CC* (value from 0 to 1) indicated the relative percentage of silt in the soil (Fig. 1e).

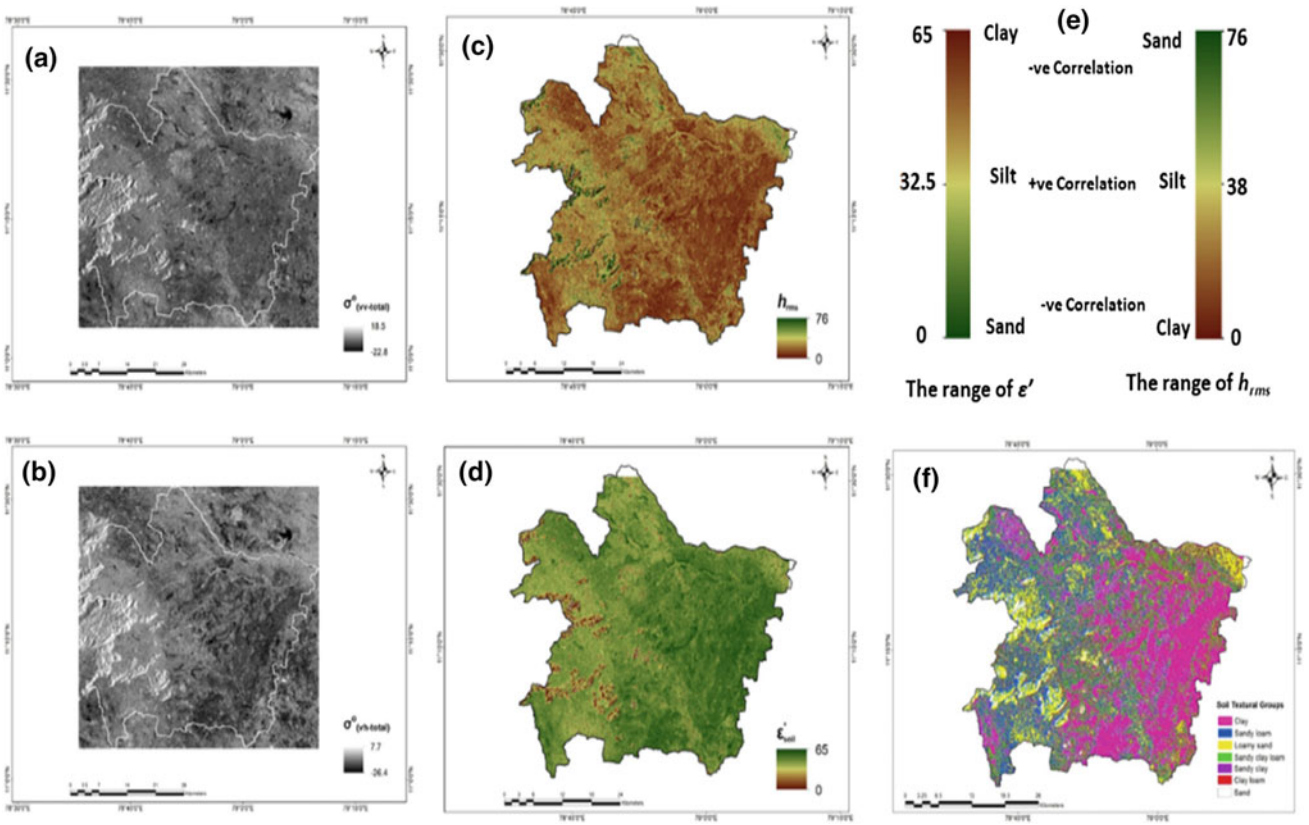

Fig. 1 **a** Sentinel 1 SAR product of VV pol. **b** Sentinel 1 SAR product of VH pol. **c** The imagery of h_{rms}. **d** The imagery of ε'_{soil}. **e** The value ranges in the resultant product of h_{rms} and ε'_{soil}. **f** A map showing the different soil textural categories in the study region

Table 1 The statistical results for the target parameters namely roughness (h_{rms}), Dielectric constant (ε'_{soil}), and resulting product of correlation coefficient (CC) in situ measurements

R^2	Sand	Silt	Clay	Min	Max	SD	RMSE	Significance level
h_{rms}	**0.81**	0.11	−0.83	0	76	19.6	5.8	$\rho = 0.011$
CC	0.11	**0.77**	0.01	0	48	11.5	7.9	$\rho = 0.014$
ε'_{soil}	−0.82	0.01	**0.78**	0	65	4.5	7.3	$\rho = 0.017$

The resultant products of target parameters were analyzed with the statistical measures namely Correlation Coefficient (R^2), Standard Deviation (SD), Root Mean Square Error (RMSE) and Minimum (Min) and Maximum (Max) values ranges.

The diagonal (Table 1) represents a good correlation between the SAR derived target parameters, and ground observed soil types. There is a strong negative correlation observed between sand and clay category ($R^2 = -0.8$). There is no sufficient correlation explained between sand and silt ($R^2 = 0.11$), and clay and silt ($R^2 = 0.01$) category at the lower range and upper range of the values. However, when the values of ground observed silt regressed against the values of h_{rms} and ε'_{soil} at the mid-range, we found a significant positive correlation ($R^2 = 0.77$). The soil triangle with the axis of *hrms*, *CC*, and ε'_{soil} have yielded seven different sub-categories of soil namely Clay (36%), Sandy loam (24%), Loamy sand (19%), Sandy Clay loam (11%), Sandy clay (4%), Clay loam (3%) and Sand (3%) according to the positions of the pixels in a triangle (Fig. 1f). According to the USCS classification, the ex-situ soil porosity estimation was used to examine the reliability of the resulting soil categories where the porosity values range from 0.27 and 0.62.

4 Discussion

Since the influence of vegetation has been reduced from $\sigma^o_{vv-total}$ and $\sigma^o_{vh-total}$, the estimated target parameters h_{rms} and ε'_{soil} have shown higher potential to represent the relative percentage of sand and clay in the soil. The strong negative correlation observed between sand and clay was well explained by spatial standard deviation of the sand (19.6) and clay (4.5) due to the nature of coarseness or roughness and water holding capacity (Table 1). The resulting *CC* product exhibited high potential to explain the distribution of silt in the soil according to its size and distribution. The soil sub-categories were observed with a high degree of sand and clay percentage (Fig. 1f). Since the resultant CC product attains the maximum value of 48, the soil categories with sand and clay combinations were observed more in the study region (Table 1).

5 Conclusions

The research intended to demonstrate that the target parameters namely roughness and dielectric constant of SAR imagery could act as an adequate indicator of significant soil groups when the influence of the overlying vegetation is reduced. The vegetation influence from both the polarization has been removed by employing modified *WCM* and by proposing *DPSVI* model. The h_{rms} and ε'_{soil} has been estimated from cross-polarization ratio and modified Dubois model. The possible places of silt in h_{rms} and ε'_{soil} were extracted through *CC* analysis. The soil triangle was formed with three-axes each representing the estimated target parameters from which the different soil categories were extracted. The proposed models and methods have provided new insight into the soil texture classification from SAR imagery.

References

1. Wang, D.-C., Zhang, G.-L., Zhao, M.-S., Pan, X.-Z., Zhao, Y.-G., Li, D.-C., Macmillan, B.: Retrieval and mapping of soil texture based on land surface diurnal temperature range data from MODIS. PLoS One **10**(6), 1–14 (2007)
2. Zhang, X., Zhang, X., Li, G.: The effect of texture and irrigation on the soil moisture vertical-temporal variability in an urban artificial landscape: A case study of Olympic Forest Park in Beijing. Front. Environ. Sci. Eng. **9**, 269–278 (2015)
3. Prevot, L., Dechambre, M., Taconet, O., Vidal-Madjar, D., Normand, M., Gallej, S.: Estimating the characteristics of vegetation canopies with airborne radar measurements. Int. J. Remote Sens. **14** (15), 2803–2818 (1993)
4. Dubois, P.C., Van Zyl, J., Engman, T.: Measuring soil moisture with imaging radar. IEEE Trans. Geosci. Remote Sens. **33**(4), 915–926 (1995)

Multitemporal Remote Sensing for Monitoring Highly Dynamic Phenomena: Case of the Ephemeral Lakes in the Chott El Jerid, Tunisia

Khairat Abbas, Jean-Paul Deroin, and Samir Bouaziz

Abstract

In the last 20 years, a number of Earth observation satellite missions has been launched, resulting in a considerable improvement in the spatiotemporal capabilities of applied remote sensing. In order to survey the main recent flooding events in Chott El Jerid, Tunisia, dated to April 2007, September 2009, June 2014 and February 2015, time-series of MODIS-Terra data have been used. The maximum surface area of the water bodies reached 660 km^2 in 2007 and 2014. The flooding event of September 2009 was the longest event (88 days) compared to only 35 days for the exceptional June event in 2014. The daily acquisition of images, the spectral range and the large swath of the sensor are well-adapted to estimate the extent of the ephemeral lake in an area that is difficult to investigate in the field. It remains difficult to decipher the part of water from direct precipitation, runoff from the reliefs and aquifer resurgence.

Keywords

Time-series • Repetitivity • MODIS • Pre-Saharan

1 Introduction

The Zone of Chotts of Tunisia and Algeria is located in a region of tectonically controlled depressions that extend from the Saharan Platform to the south to the Atlas Mountains to the north (Fig. 1). The elevation of the chotts ranges from about +25 m in Chott El Fedjaj to −40 m in Chott Melrhir, with values of +5 m in Chott El Jerid and −20 m in Chott El Rharsa. The main chott known as Chott El Jerid is also one of the largest endorheic playa basin in the world (4600 km^2) [1–3] (see [3] for recent literature review). The climate of the pre-Saharan area is typically arid as defined by the Köppen classification. The mean annual rainfall for the area is around 100 mm with a high monthly, seasonal and interannual irregularity. The evaporation is at a maximum in July and August, reaching 1700–1800 mm when the temperature is also at the maximum (48 °C). The mean annual temperature is about 21 °C.

Although saline crusts have been recently studied [3, 4], the present work focused on the extent of the ephemeral saline lake during the wet periods. The survey was carried out using large-scale remote sensing data with daily revisit time from the MODIS instrument. Water was characterized by total absorption in the near infrared range. Thus, it was easy to distinguish free water from mineral surfaces (Fig. 1).

During the rainy season (September–April), the extreme rainfall events (Table 1) have been associated with occasional desert depressions [2]. During the spring of 2007, an exceptional event of precipitation on April 24th (98 mm) affected the Chott El Jerid and its surroundings. The monthly precipitation in April 2007 (50 mm) was three times the monthly average (15 mm). During the winter of 2009, several rainfall events were recorded between January and March (49 mm on January 21 and 20 mm on March 29). For February 20th–21st, 2015, 46 mm was recorded by the meteorological station of Tozeur. During the last 30 years, only one major rainfall event was recorded in the dry season on June 2nd, 2014.

2 Materials and Methods

The Terra spacecraft was launched on December 18th, 1999. It carried the first MODIS flight instrument providing high radiometric sensitivity in 36 spectral bands ranging from 0.4 to 14.4 µm. The second MODIS flight instrument is on-board the Aqua spacecraft launched on May 4th, 2002.

K. Abbas · J.-P. Deroin (✉)
Université de Reims, EA 3795 GEGENAA and FR CNRS 3417 Condorcet, 51100 Reims, France
e-mail: jean-paul.deroin@univ-reims.fr

S. Bouaziz
Ecole Nationale d'Ingénieurs de Sfax, Laboratoire 3E, BP, 3038 Sfax, Tunisia

© Springer Nature Switzerland AG 2019

H. M. El-Askary et al. (eds.), *Advances in Remote Sensing and Geo Informatics Applications*, Advances in Science, Technology & Innovation, https://doi.org/10.1007/978-3-030-01440-7_24

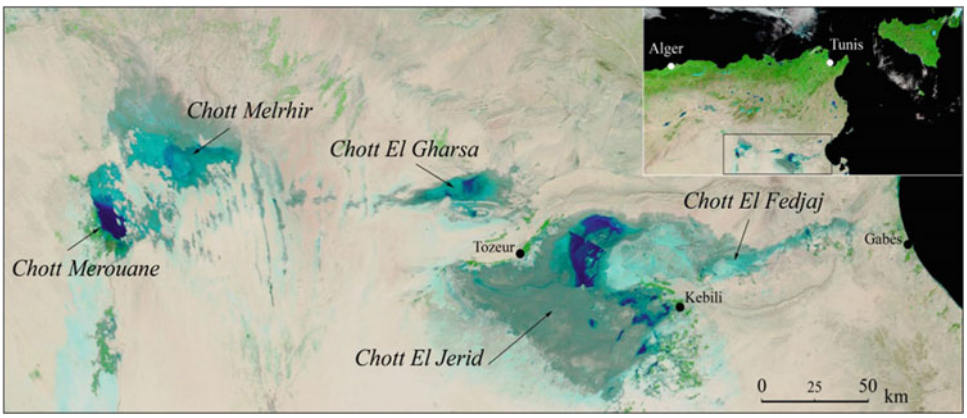

Fig. 1 The Zone of Chotts in Algeria (west) and Tunisia (east). MODIS false color composite acquired on March 3, 2015, after the main precipitation events of late February. Coding: red is band 7 (2105–2155 nm, i.e. SWIR range), green is band 2 (841–876 nm, i.e. near infrared range), blue is band 1 (620–670 nm, i.e. red range). Interpretation. Water bodies: dark blue (ephemeral lakes) or black (sea). Sand (erg) and rocky (reg) surfaces: light yellow or orange-red. Other mineral surfaces related to the chotts (evaporites): blue or cyan. Vegetation: green

Table 1 Main flooding events in the Chott El Jerid from 1995 onward

Year	1995	2003	2004	2006	2007	2009	2010	2011	2014	2015
Month										
January		X				X		X		
February			X	X		X		X		X
March										
April					X					
May										
June									X	
July										
August										
September										
October	X									
November	X		X				X			
December										

The MODIS instrument with its large swath (2330 km) offers an unprecedented look at terrestrial and oceanic phenomenology with two acquisitions per day. The spatial resolution of 250–500 m is suitable for the survey of a vast area such as the Chott el Jerid. The spectral range 1.5–2.5 µm (Bands 6 and 7 of MODIS) was adapted to evaluate the surface moisture. Band 6 (1628–1652 nm) is inversely correlated to the moisture level of the surface, but less sensitive to the mineralogy of the surface in comparison with band 7 (2105–2155 nm). For the present study we used the 7-2-1 MODIS color composite (Terra or Aqua), which is relevant to calculate the extent of the water bodies corresponding to the ephemeral lakes set up during the flooding events (Fig. 1, caption). A supervised classification is appropriate. Note that 16 MODIS-pixels (250 m × 250 m) correspond to 1 km^2.

3 Results

The comparison between the winter flooding events (2009 and 2015), the spring flooding event (2007), and the summer flooding event (2014) allows us to define three different flooding and desiccation behaviors (Fig. 2). The flood period (the time between the heavy rains and the complete desiccation of the surface) was the longest in 2009 with 88 days from January 15th to April 10th. This period was shorter in 2015 with 67 days from February 20th to April 28th, and also in 2007 with only 55 days from April 24th to June 15th. During the exceptional flood in June 2014, the behavior of flooding and desiccation has been distinguished by three characteristics: the shortest time between the flooding and the complete desiccation of

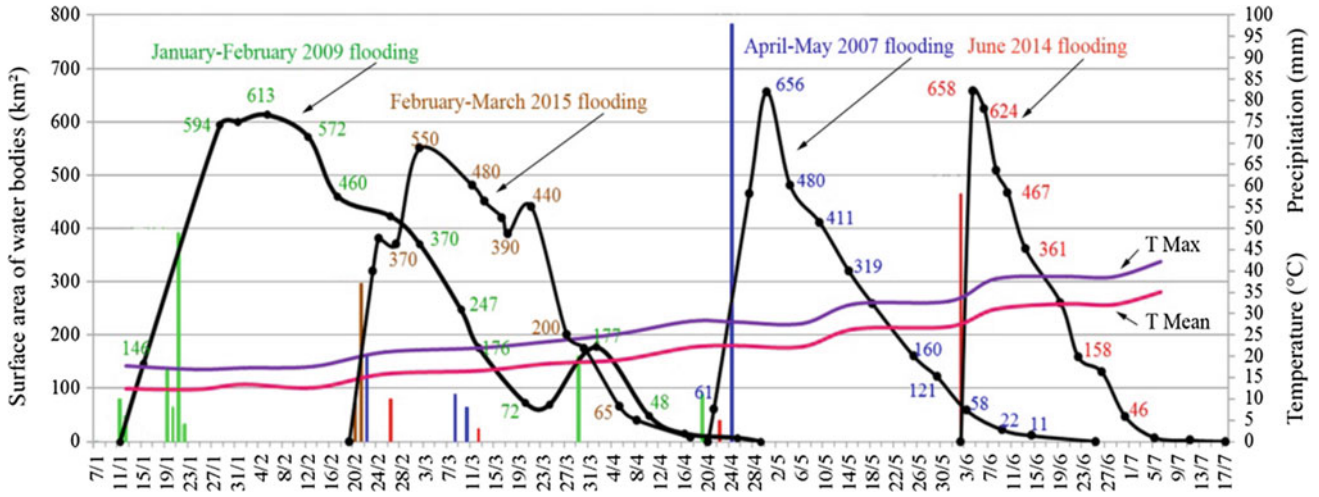

Fig. 2 The extent of the ephemeral lakes during the 2007, 2009, 2014 and 2015 floods. Colored numbers indicate the surface area of the water bodies as detected in MODIS images. Colored vertical lines indicate the main precipitation events. T Max and T Mean are the maximum temperature and the mean temperature, respectively, calculated for the period 2004–2014

the surface of Chott (30–35 days), the fastest flooding and the fastest desiccation.

Both the floods in 2007 and 2014 are characterized by a similarity in their desiccation behavior, especially when we compare with the flood in 2009. Although the total rainfall in January 2009 and in April 2007 (95–100 mm) was higher than in June 2014 (55–60 mm), the maximum area of the lake was similar and the formation of the lake in June 2014 was faster. Thus, the desiccation period of the ephemeral lake appeared directly proportional to the thermal behavior.

4 Discussion-Conclusion

Four different stages were observed in the Chott El Jerid from the flooding stage to the complete desiccation of the ephemeral lake using the MODIS time-series images: Stage I (flooding), Stage II (evaporative concentration), Stage III (brine pool) and stage IV (desiccation). From the stage I to the stage IV (April to August) a gradual increase in values of temperature and evapotranspiration, gradual desiccation of the ephemeral lake, progressive precipitation of evaporites and gradual increase in reflectance values have been recorded by MODIS in the MIR range [3].

Remote sensing data are essential for surveying changing environments such as large endorheic basins [2–5] suffering occasional precipitation events. For mapping water bodies, very high space resolution is not absolutely necessary, while high temporal resolution is needed for identifying morphological features related to phenomena that occur at the hour-scale: rainfall, runoff, resurgence, etc. Thus, the MODIS sensor is a very useful tool, although the satellite system (Terra-Aqua) is a bit old. The new generation of satellites such as Sentinel 2A or 2B is characterized by an improved temporal resolution compared to Landsat or Spot (revisiting time of 5 days for the pair), but remains not fully adapted to the daily survey of highly dynamic phenomena such as the flooding of endorheic depressions.

Moreover, it is possible to distinguish isolated resurgences related to the surficial aquifer, which is very dependent upon the season. Additional analyses can be carried out, especially using the short time between Terra and Aqua acquisitions (3 h), to quantify the respective part of water from precipitation, runoff and aquifer resurgence.

References

1. Coque, R.: La Tunisie présaharienne, étude géomorphologique. Ed. Armand Colin, Paris, 476 pp (1962)
2. Bryant, R.G., Rainey, M.P.: Investigation of flood inundation on playas within the Zone of Chotts, using a time-series of AVHRR. Remote Sens. Environ. **82**, 360–375 (2002)
3. Abbas, K.: Suivi par télédétection multi-source du bassin endoréique du Chott El Djérid (Tunisie) entre 1985 et 2015. PhD Thesis, Université de Reims, France, 281 pp (2016)
4. Abbas, K., Deroin, J.-P., Bouaziz, S.: Monitoring of playa evaporites as seen with optical remote sensing sensors: case of Chott El Jerid, Tunisia, from 2003 to present. Arab. J. Geosci. **11** (92), 1–14 (2018)
5. Li, J., Menenti, M., Mouvisand, A., Luthi, S.M.: Non-vegetated playa morphodynamics using multi-temporal Landsat imagery in a semi-arid endorheic basin: Salar de Uyuni. Bolivia. Remote Sens. **6**, 10131–10151 (2014)

Land Use Land Cover Diachronic Change Detection Between 1996 and 2016 of Region of Gabes, Tunisia

Wided Batita

Abstract

Remote Sensing Change Detection is designed to detect stand-replacing disturbances such as land cover, harvest and wildfire. Digital change detection essentially jnvolves the quantification of temporal phenomena from multi-date imagery. The main purpose of this study was to distinguish change in land cover within each land cover type (class), and to find the real changes on the land cover features between 1996 and 2016 in the region of Gabes, Tunisia. Two images were downloaded from Google Earth and then georeferenced and masked out the study area, which is imported since Kml File from Google Earth is too. The two images were also enhanced and then classified using the Maximum Likelihood algorithm. Five classes were identified: water, settlements, vegetated area, bare soil and zone under development. The supervised classification was assessed with 94% for 1996 imagery and 95.5% for 2016. The result showed a decrease in bare soil class (from 115 to 94 km^2) and an important increase in zone under development (from 96 to 834 km^2). Regarding the water, the vegetated area and settlement classes, a slight increase was noted.

Keywords

Remote sensing • Change detection • Multi-date imagery • Maximum likelihood • Supervised classification

1 Introduction

Information about change is necessary for updating land cover maps and managing the natural resources [1]. Change detected from different temporal images usually reflects natural and human activity impacts. Gabes region is known for its different geology and climate conditions, which makes the area susceptible to change. Monitoring the land cover change using multi temporal images will, therefore, provide an indication on the rate and the magnitude of change.

LULC detection is important to provide valuable information with regard to natural resources degradation and utilization.

The integration of remote sensing and GIS technologies is an effective approach for analyzing the land use and cover changes including [2, 3]:

(a) Detecting the geographical location of change found when comparing two (or more) dates of imagery.
(b) Identifying the type of change if possible.
(c) Quantifying the amount of change [4].

The main objective of this present study was to model the land-use change using remote sensing and GIS applications between 1996 and 2016.

There are many other methodological approaches to investigate land-use/land-cover (LULC) change and climate variability such as Markov chain and cellular automata [5] and [6], the Land Transformation Model (LTM), which couples geographic information systems (GIS) with artificial neural networks (ANNs) [7].

2 Materials and Methods

2.1 Study Area

Gabes is located at latitude 33.88145 and longitude 10.09819 in the northern hemisphere (Fig. 1). It is located on the coast of the Gulf of Gabes [8].

Gabès has a semi-arid climate, characterized by a hot and dry season and a cool and arid season [9].

W. Batita (✉)
Département de Géomatique Appliquée, Université de Sherbrooke`, J1K 2R1 2500 Boulevard de l'Université, Immeuble K1, Sherbrooke, QC, Canada
e-mail: widedbatita@gmail.com

© Springer Nature Switzerland AG 2019

H. M. El-Askary et al. (eds.), *Advances in Remote Sensing and Geo Informatics Applications*, Advances in Science, Technology & Innovation, https://doi.org/10.1007/978-3-030-01440-7_25

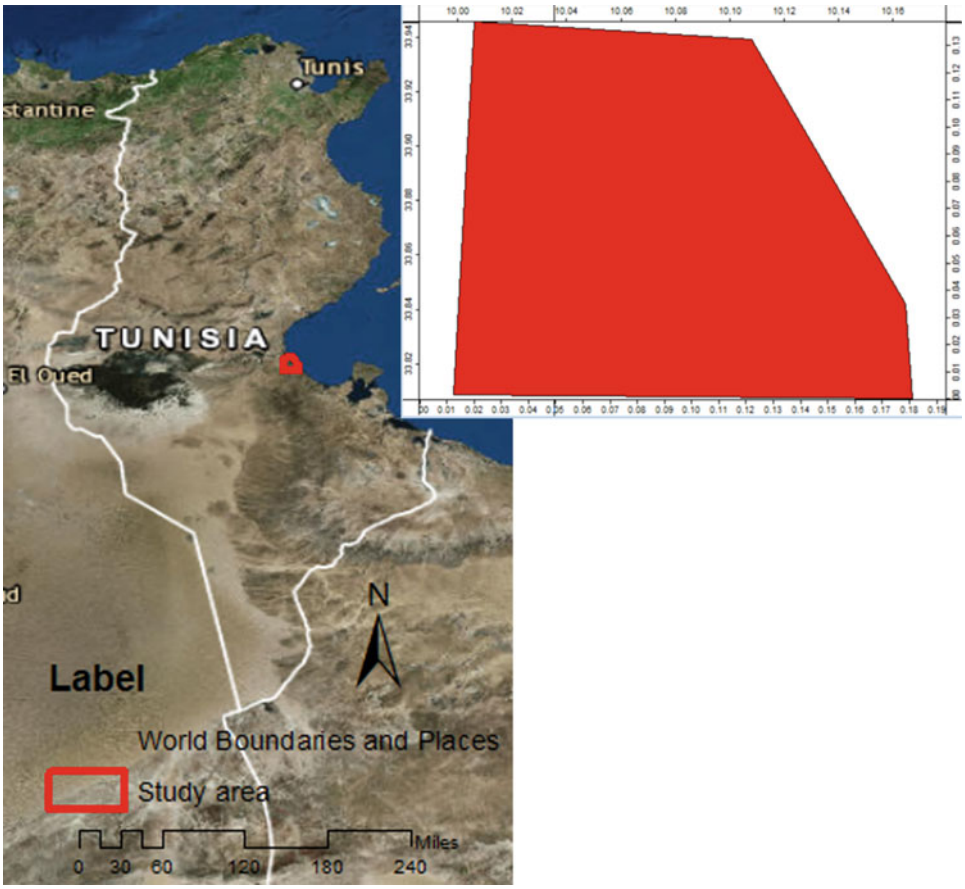

Fig. 1 Location of the study area (in red)

2.2 Methodology

Two satellite images were used to perform the analysis. These two images cover the same area of Gabes city and its surroundings, and they were taken at different dates: the first was in 1996, and the second was in 2016. Both of them within the middle spatial resolution (30 m). In order to achieve the objective of this study, many steps were performed to provide the required data as shown in the following flowchart (Fig. 2).

The downloaded images were georeferenced, masked out and then enhanced for a better interpretation. The maximum Likelihood classification was then implemented. Hence, the 2 images were split into five classes: water, settlements, vegetated area, bare soil and zone under construction. After classification, an accuracy assessment of classification was necessary to compare the classified images to ground truth data. Based on the thematic maps resulting from the classification, a single histogram was generated to perform the comparison.

3 Results and Discussion

Figures 3 and 4 show two classified images created by the maximum likelihood method. This classifier is based on Bayesian probability theory. It assigns each pixel in the image to its class belonging to the maximum likelihood [10].

The above thematic maps gave the change location and the individual transitions of 5 classes: water class in blue that includes sea, rivers, ponds and reservoirs; settlements class in magenta that includes residential, commercial, industrial, transportation, roads, mixed urban; vegetated area in green, bare soil in pink and zone under development in orange. The classification was assessed by creating a confusion matrix for each image. This step is mandatory to determine if the classification is correct or not. The images were successfully classified as the overall classification accuracies were above 90% (94% for 1996 imagery and 95% for 2016).

The histogram in Fig. 5 shows the increase or decrease in area of each class over 20 years.

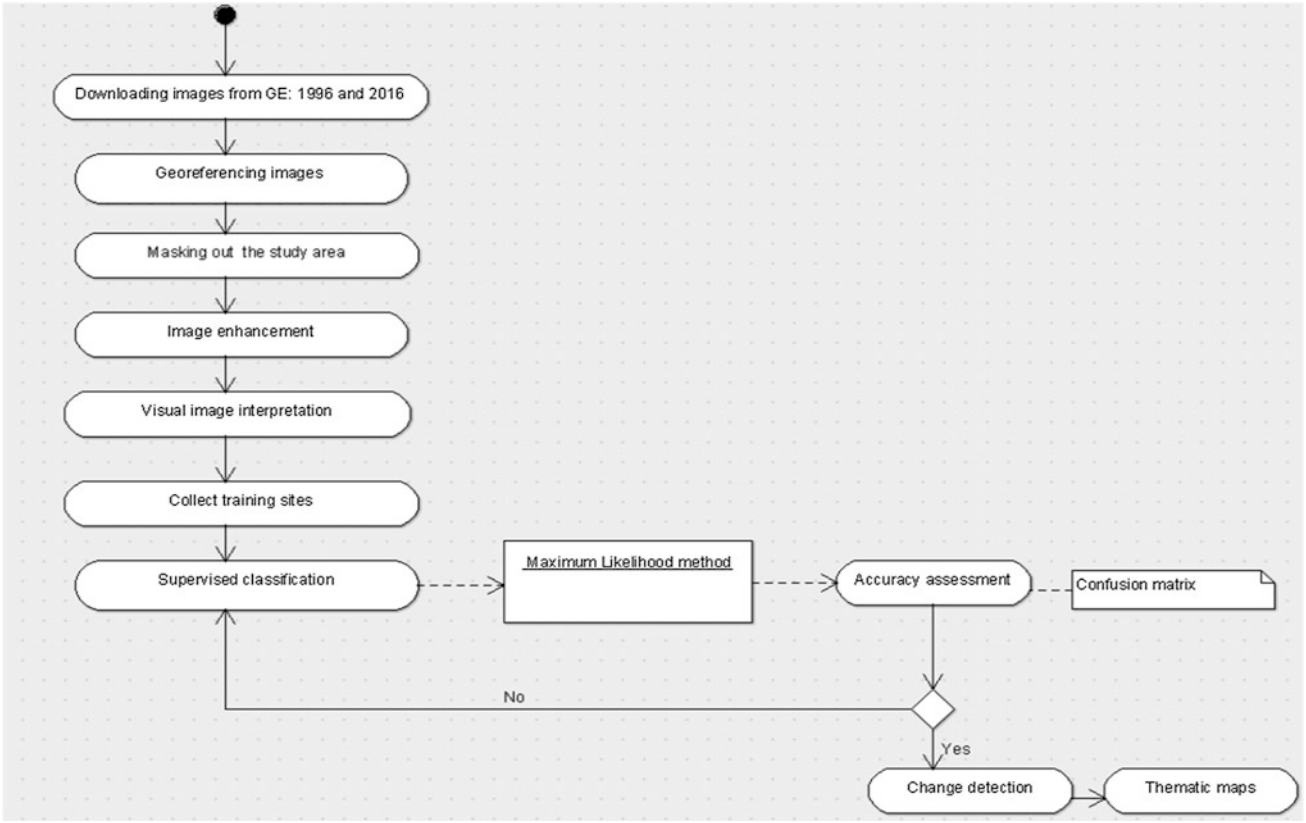

Fig. 2 Methodology

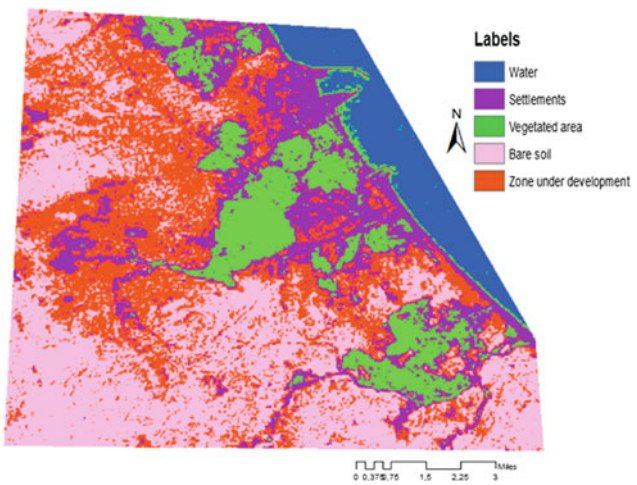

Fig. 3 Classified image (1996)

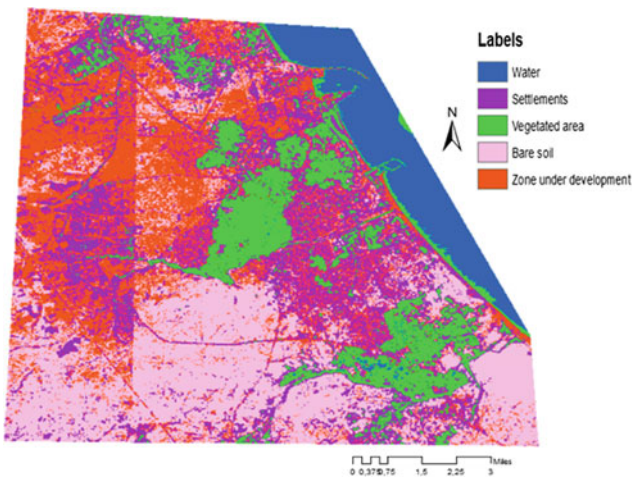

Fig. 4 Classified image (2016)

This visual interpretation gives a good idea about the changes in the land cover in terms of quantitative values. There is an increase in all the classes except for the bare soil class where which decreased from 114 km^2 in 1996 to 94 m^2 in 2016. The most important increase is noted in zone under development class from 9690 km^2 in 1996 to 83444 km^2 in 2016.

The change detection results reveal an important increase in zone under development and settlement classes, but a decrease in bare soil. Many new settlements (Fig. 3) were built in the south east of the study area near the rivers. The stakeholders should intervene by prohibiting building, especially the illegal constructions in order to avoid economic and social losses in case of flood as the case that

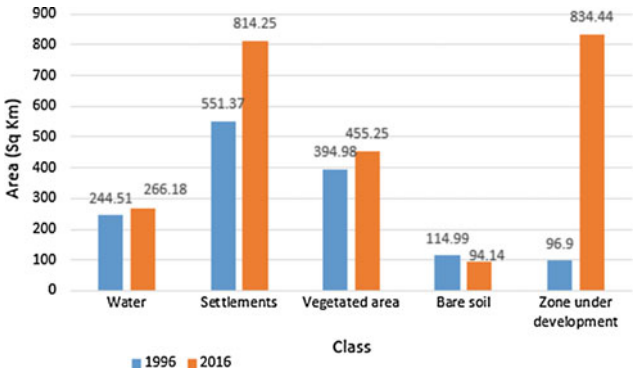

Fig. 5 Histogram of land classes distribution

occurred last November in Gabes and the result was 5 dead and 117 evacuations [11].

The same study was conducted in Abu Dhabi, UAE and the result showed a radical transformation from bare soil to settlements between 1990 and 2014. This city is more urbanized than Gabes city because of the social, economic and political differences.

4 Conclusions

Remote sensing and GIS have become powerful tools to assess natural phenomena and human activity processes nowadays. Change detection analysis of land cover features is important to qualify and quantify the human-environment relationships that help stakeholders for decision-making. In this study, land use land cover change detection was conducted. The result showed an important increase in settlements and zone under development classes. Stakeholders should intervene in controlling construction especially the illegal ones.

Modelling and predicting LULC provides valuable information with regard to natural resources degradation and utilization [12].

References

1. XiaoMei, Y., RongQing, Y.: Change Detection Based on Remote Sensing Information Model and its Application on Coastal Line of Yellow River Delta. Earth Observation Center, NASDA, China (1999)
2. Bradley, B., Mustard, J.F.: Characterizing the landscape dynamics of an invsive plant and risk of invasion using remote sensing. Ecol. Appl. **16**(3), 1132–1147 (2006)
3. Chaudhry, A., Sharma, S.: Remote sensing and GIS based approaches for LULC change detection—a review. Int. J. Curr. Eng. Technol. (2015)
4. Jungho, I., Jensen, J.R.: A change detection model based on neighborhood correlation image analysis and decision tree classification. Remote Sens. Environ. **99**, 326–340 (2005)
5. Hyandye, C., Martz, L.W.: A Markovian and cellular automata land-use change predictive model of the Usangu Catchment. Int. J. Remote Sens. (2016)
6. Wang, M.R, Murayama, Y.: Change of land use/cover in tianjin city based on the markov and cellular automata models. Int. J. Geoinf. (2017)
7. Pijanowskia, B.C., Brownb, D.G., Shellitoc, B.A, Manikd, G.A.: Using neural networks and GIS to forecast land use changes: a land transformation model. Comput. Environ. Urban Syst. J. (2002)
8. GeoDatos. https://www.geodatos.net/en/coordinates/tunisia/qabis/gabes. Last accessed 20 Apr 2018
9. Wikipedia. https://en.wikipedia.org/wiki/Gab%C3%A8s. Last accessed 15 Apr 2018
10. Akgün, A., Eronat, A.H., Türk, N.: Comparing different satellite image classification methods: an application in Ayvalik District, Western Turkey. In: 20th ISPRS Congress Technical Commission IV, Istanbul, pp. 12–23; 1091–1097 (2004)
11. Kapitalis homepage. http://kapitalis.com/tunisie/2017/11/13/inondations-a-gabes-cinq-deces-117-evacuations/. Last accessed 1 May 2018
12. Pandian, M., Rajagopal, N., Sakthivel, G., Amrutha, D.E: Land use and land cover change detection using remote sensing and gis in parts of Coimbatore and tiruppur districts, tamil nadu, india. Int. J. Remote Sens. Geosci. (2014)

Impact of Land-use Change on Soil Erosion in the Coonoor Watershed, Nilgiris Mountain Range, Tamil Nadu, India

Subbarayan Saravanan, J. Jennifer Jacinth, Leelambar Singh, T. Saranya, and S. Sivaranjani

Abstract

Over the past several decades, the conversion of native forest to tea plantation and crop land has accelerated across the Coonoor watershed in Nilgiris. It is notable that the present study explored the severity prevalent in the land cover changes including deforestation activities at Coonoor watershed region as a result of urbanization, recreation parks, resorts and tea plantation development. The Revised Universal Soil Loss Equation (RUSLE) is one of the most widely used soil erosion model which estimates the average soil loss over a long-term period. This paper therefore, imprinted the impact of land use changes on land degradation and the consequent vital phenomenon like the soil erosion. The change detection was carried out between the periods of 2005–2018. Landsat images of corresponding periods were classified using supervised classification technique and also Normalized Differential Vegetation Index (NDVI) was computed for the determination of C-factor (cover and management factor) for the corresponding periods. Conversion of forest land into tea plantation, wasteland and settlement significantly decreases the soil organic matter (SOM) and hydraulic conductivity (HC) of the soil, which leads to different K-factor (soil erodibility factor) for the study duration, whereas the R-factor (rainfall and runoff factor) and LS-factor (length-slope factor) are considered to be constant throughout the period. The results of this study indicates via promising results, that the total sediment yield of the study area has remarkably increased due to land use/cover changes. The most significant rise in soil erosion was found evitable in the deforested region where there has occurred a changeover from forest/orchard to infrastructure and wasteland.

Keywords

Land-use • Land-cover • Soil erosion • GIS • Remote sensing

1 Introduction

Nilgiris district of Tamil Nadu, part of the Western Ghats, is one of the four most landslide-prone zones in the country. Its climate and scenic beauty attract the tourists throughout the year. The effect of tourism is the primary reason for rapid urbanization and infrastructure development in the district. Officials from Geological Survey of India has proposed that the primary cause of landslide and soil erosion was construction and infrastructure development on the slopes. The infiltration of rainwater into the soil increases the pore water pressure, due to which the soil loses its stability and reaches a critical stage to erode [1–4].

2 Study Area Description

The Nilgiris District of Tamil Nadu lies in the latitude 11.4916°N, and longitude 76.7337°E. Doddabetta, which lies in this district is the highest peak in Southern India with an elevation of 2595 m. The other prominent hills of this district are Elk hills, Devarshola peak, Hulical hill and Cairn hill. Numerous waterfalls are also in this district. Almost between every pair of mountain either a river or stream flows. The most important among them are the Pykara streams which rises on the slopes of Mukkuruthi peak. The mean minimum Temperature was 5.0 °C and the mean maximum was 26.0 °C during 2015–16. The total rainfall during 2005–18 was 1357.7 mm.

S. Saravanan (✉) · J. Jennifer Jacinth · L. Singh · T. Saranya
National Institute of Technology, Tiruchirappalli, Tamil Nadu, India
e-mail: ssaravanan@nitt.edu

S. Sivaranjani
Bharathidasan University, Tiruchirappalli, Tamil Nadu, India

© Springer Nature Switzerland AG 2019

H. M. El-Askary et al. (eds.), *Advances in Remote Sensing and Geo Informatics Applications*, Advances in Science, Technology & Innovation, https://doi.org/10.1007/978-3-030-01440-7_26

3 Materials and Methods

3.1 Soil Erosion Estimation

The mean annual soil erosion estimation has been computed using the Universal Soil Loss Equation (USLE), because of its operating simplicity, convenient inputting availability and extensive applicability. Generally, USLE is defined as:

$$A = R * K * LS * C * P \quad (1)$$

where A is the mean annual soil erosion in t/(h/a), R is rainfall-runoff erosivity factor (MJ mm hm-2 h-1 a-1), K is soil erodibility factor (t h MJ-1 mm-1), LS is length-slope factor, C is cover and management factor, and P is the support practice factor. Each factor has been computed and laid out as maps using GIS technique.

4 Results and Discussion

4.1 Land Use Changes

All the Landsat images (TM and ETM+) are classified with Maximum likelihood algorithm using supervised image processing technique. The classification accurateness was estimated to about 82.6 and 80.8% with kappa coefficient being 0.80 and 0.778 for the years, 2002 and 2009, respectively. The prominent cause behind the dynamic change in the LULC is the rapid increase in population and tourism. The tea plantation adds on to the list as the cultivation practice is carried out by destroying the forest cover (Fig. 1).

4.2 Soil Erosion Maps

The erodibility amount during the study period was computed by deriving the product of all the factors in RUSLE [5]. The analysis was carried out using the satellite imagery of 30 m spatial resolution using ArcGIS 10.2.1 software. The K factor indicated the soil dispersion and transportation capability by an impact of a raindrop and thereby surface flow. This factor portrays the impact of storm events over the soil in the upland region. The factor K is in close association with the soil texture, structure, organic matter content, and permeability. The L S factor implicates the function of slope inclination and slope length, which depicts the effect of topography on the erosion process. It is an evident fact that the erosion phenomenon is associated with the gradient of the terrain. The presiding conservation plan is included as a factor; it is used to elaborate the management and cropping factor in the region, and it is known as the C factor. It is thus adopted to categorize and validate the influence of the various conservation management schemes. Earlier studies have emphasized that the C factor has close relation with the vegetation cover. On taking the erosion on 2018 as an illustration, the mean annual erodibility amount on the forest, wasteland, cropland, tea plantation and urban settlements are 60.19, 28.78, 26.75, 26.70 and 4.48 t/(h/a), respectively (Fig. 2).

The land use/land cover (LULC) fluctuations over ages has been influencing the soil erosion activity of the Coonoor region predominantly. The urbanization effect has modified the natural terrain condition of the region, thereby affecting the topographical properties of the area. The results prove evident that the erosion is high in the settlement region and

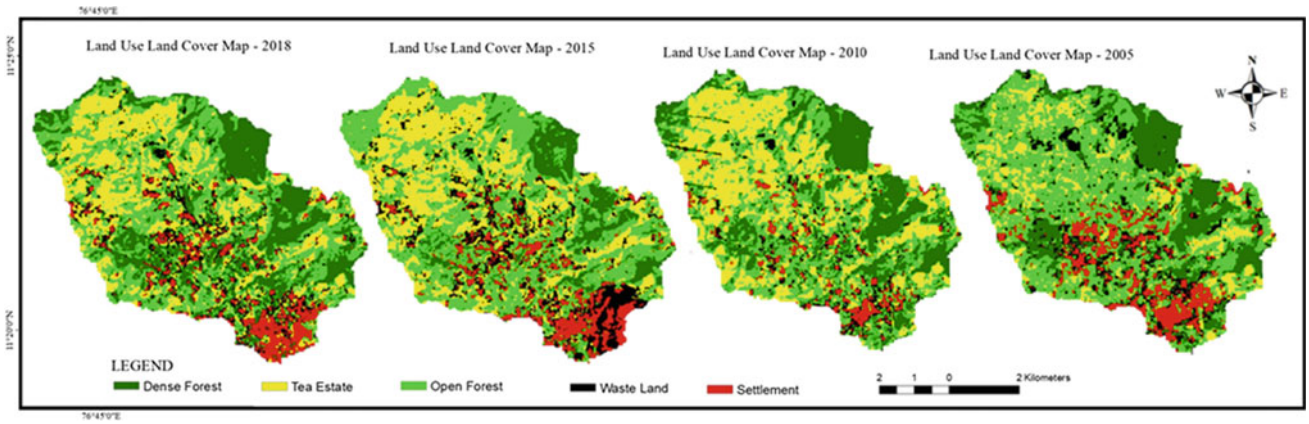

Fig. 1 Classified land use/land cover map of Coonoor watershed

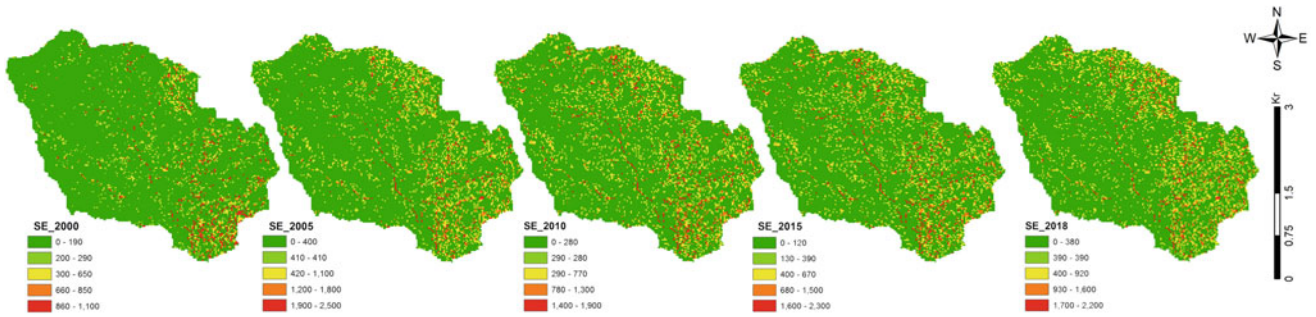

Fig. 2 Soil erosion map of Coonoor watershed

in the deforested localities, where the forest cover have been replaced by tea plantations. As the change in LULC remain persistent there seems to be a dominant change in the values of P and C factor. This portrays the reason behind the results depicting prominent changes over the years.

5 Conclusion

The study holds an evident discussion on the potential of GIS technique in the appraisal of rapid change in LULC and its effects on erosion effect in the Coonoor watershed area of the Nilgiris mountain range between 2005 and 2018. Statistical results imply that the land use type has great impact on soil erosion. Considering the year 2018 as an example, the mean annual erodibility amount of forest, wasteland, cropland, tea plantation and urban settlements are 60.19, 28.78, 26.75, 26.70 and 4.48 t/(h/a), respectively. Therefore, the research results claim the importance of the management of soil erosion with respect to the land-use pattern by adopting reasonable land use planning. Also amount of erosion has been drastically increased between 2015 and 2018, primarily due to the severe lessening in the forest cover, increase in the urban infrastructure and other relative activities. The corruption and devastation of forest owing to mining activities and intolerable human intrusion has affected the consolidation property of the soil and vegetation cover in the region, thus deepening the erosion effect. Nevertheless, the decrease in soil erosion found in Coonoor watershed has close relation with the extensive expansion of orchards. This research would serve as an eye-opener to the officials in the Nilgiris district to establish land-use planning incorporating the soil erosion effects.

References

1. Liu, B.Y., Nearing, M.A., Risse, L.M.: Slope gradient effects on soil loss for steep slopes. Am. Soc. Agric. Eng. **37**(6), 1835–1840 (1994)
2. Ustun, B.: Soil erosion modelling by using Gis and remote sensing: a case study, Ganos mountain. Int. Arch. Photogrammetry, Remote Sens. Spat. Info. Sci. **XXXVII**(B7), 1681–1684 (2008)
3. Zhang, Q.-F., Wang, L., Wu, F.-Q.: GIS-based assessment of soil erosion at Nihe Gou catchment. Agric. Sci. China **7**(6), 746–753 (2008)
4. Biswas, S.S., Pani, P.: Estimation of soil erosion using RUSLE and GIS techniques: a case study of Barakar River basin, Jharkhand, India. Model. Earth Syst. Environ. **1**(42) (2015)
5. Ganasri, B.P., Ramesh, H.: Assessment of soil erosion by RUSLE model using remote sensing and GIS—a case study of Nethravathi Basin. Geosci. Front. **7**(6), 953–961 (2016)

Exploring the Influence of Land Use Type and Population Density on Urban Heat Island Intensity

Mir I. Parvez and Yusuf A. Aina

Abstract

The urban heat island (UHI) phenomenon has gained increasing attention being an indicator of the anthropogenic activities' effects on urban areas. Moreover, the establishment of the sustainable development goals (SDGs) for urban areas underscores the need to monitor the UHI phenomenon. This paper explores the influence of land use type and population density on UHI intensity using two Saudi cities, Jeddah and Yanbu, as case studies. Landsat images from 1990 to 2015 were used to extract the land surface temperature (LST), normalized difference vegetation index (NDVI), and normalized difference built-up index (NDBI) of the study areas. Statistical measures and analysis of variance (ANOVA) were used to examine the variations in LST due to land use type. The correlations between LST and the indices (NDVI and NDBI) and population density were also computed. The results show variations in LST due to land use type (at 0.01 level of significance) and the differences in the thermal regimes of the two cities. The population density is positively correlated with LST with R^2 varying from 0.3 to 0.87 for Jeddah and Yanbu from 1991 to 2016.

Keywords

Land surface temperature • Landsat imagery • NDVI • NDBI • Urban heat island

1 Introduction

Urban heat island (UHI) is one of the indicators of the adverse effects of anthropogenic activities on the environment [1]. According to the United Nations, two-thirds of the world population will live in urban areas by 2050 [2]. The increasing level of urban growth and expansion might exacerbate the urban heat island effects. Thus, the need to monitor the thermal regimes of urban areas because UHI affects varying urban environmental sustainability issues including energy consumption. Moreover, the establishment of the sustainable development goals (SDGs) for urban areas underscores the need to monitor the UHI phenomenon. Satellite-derived thermal data allow researchers to monitor UHI at varying spatial and temporal resolution with large coverage. Bai et al. [3] asserted that earth observations and the study of climate interactions in the cities, especially in the global south, should be further developed to support cities in addressing the challenges of climate change. They emphasize the need for comparative analysis of climate interactions in different cities. Most UHI studies, especially in Saudi Arabia, have focused on large cities [4–6]. This study explores the use of Landsat images in comparing the thermal regimes of two Saudi coastal cities comparing a large urban area with a mid-size city.

2 Materials and Methods

2.1 Study Area and Data

The cities studied in this paper are Jeddah and Yanbu in Saudi Arabia. The two cities are located at the western part of Saudi Arabia on the coast of the Red Sea. Jeddah is the second most populous city in Saudi Arabia after the capital city of Riyadh. The population of Jeddah is about 3.431 million [5]. The growth of Jeddah is mainly due to economic activities (commerce and industry) and tourism (pilgrimage). Yanbu is mainly an industrial city with large petroleum refineries. The current population of the city is about 117,936 [1]. The rapid population growth and urban expansion of Jeddah city has led to notable environmental issues [5].

In this study, Landsat data between 1991 to 2016 for Jeddah and from 1991 to 2015 for Yanbu were used. The

M. I. Parvez (✉) · Y. A. Aina
Department of Geomatics Engineering Technology, Yanbu Industrial College, Yanbu, Saudi Arabia
e-mail: miri@rcyci.edu.sa

© Springer Nature Switzerland AG 2019

H. M. El-Askary et al. (eds.), *Advances in Remote Sensing and Geo Informatics Applications*, Advances in Science, Technology & Innovation, https://doi.org/10.1007/978-3-030-01440-7_27

Landsat satellites have a wide range of sensors, TM, ETM, OLI and TIRS that collect data in various regions of the electromagnetic spectrum with sensitivities to reflected and emitted radiations corresponding to visible and thermal portions of the electromagnetic spectrum. Visible, near infrared and thermal bands were used to derive NDVI, NDBI and land surface emissivity which in turn served as inputs to derive LST of the study area.

The population density data were procured from the WorldPop dataset (www.worldpop.org) as raster files with each pixel representing people per pixel (PPP). The size of each pixel is about 95 × 95 m.

2.2 Methodology

The methodology adopted in the current study to estimate LST from the above cited sensors involved a chain of processes that started with the conversion of pixel values to sensor radiances, using Digital Number (DN) conversion coefficients that are recorded within the metadata of each image file (Eq. 1), followed by converting at sensor radiances to at sensor brightness temperatures using Planks Law and Thermal band calibration constants [1].

$$Ls = \text{gain} * \text{DN} + \text{bias} \quad (1)$$

where DN is a digital number (the pixel value); and gain (the slope of the radiance) and bias (the intercept of the radiance) are the DN conversion coefficients.

Single channel algorithm [6] was implemented to derive LST from at-sensor brightness temperature using land surface emissivity along with several atmospheric parameters including atmospheric upwelling, atmospheric downwelling and atmospheric transmittance. These parameters were calculated using Atmospheric Correction Parameter Calculator (ACPC). NDVI and NDBI were calculated to decipher the influence of urbanization and vegetation on LST. Sample points of about 300 from each city were generated based on four land use classes (city center, vegetation, desert and industrial area) and the interaction of LST with the land use classes was evaluated by ANOVA. The correlations between LST and NDVI, NDBI in each land use class were computed. The population data was used to compute the correlation between LST and population density for each city.

3 Results

The results indicate positive correlations between LST and NDBI (for city center, vegetation, desert and industrial area) in both cities and negative correlations between LST and NDVI (for vegetation) in both cities especially in 2015 and 2016 (Table 1). The results of the LST analysis show a progressive increase in land surface temperature in Yanbu while the LST values in Jeddah show a reducing trend from 2000 to 2016 (Fig. 1). The temperatures of some areas, both in Yanbu and Jeddah, have decreased due to the increase in vegetation cover (Fig. 1). As for the land use classes, there are significant variations in the LST of the different land use classes at 0.01 level of significance for both Yanbu and Jeddah. The population density is also significantly positively correlated with LST for Jeddah and Yanbu. The values of R^2 varies from 0.3 to 0.87 from 1991 to 2016. The highest R^2 values were recorded in the recent years.

4 Discussion

The results are similar to what was obtained in Riyadh [7] where the LST increased generally but was moderated by vegetation cover. This is examplified by the correlations

Table 1 Correlations of LST, NDVI and NDBI

Year	Desert		Industrial area		City center		Vegetation	
	NDVI	NDBI	NDVI	NDBI	NDVI	NDBI	NDVI	NDBI
Jeddah								
1991	0.228*	0.374***	0.287**	0.357**	0.441***	0.314***	−0.904***	0.849***
2000	0.052*	0.086*	0.119*	0.378***	0.313***	0.499***	−0.822***	0.836***
2016	−0.146*	0.129*	0.039*	0.222*	0.071*	0.479***	−0.402***	0.385***
Yanbu								
1991	0.46***	0.64***	−0.60*	0.08*	−0.33***	0.66***	−0.13*	0.60***
2000	0.25***	−0.08*	0.26***	0.30***	−0.56***	0.67***	−0.37***	0.47***
2015	−0.39***	0.18**	0.29***	0.19***	−0.36***	0.58***	−0.75***	0.78***

*Not significant (p >= 0.05)
**significant at the 0.05 level (p >= 0.01 and <0.05)
***significant at 0.01 level (p < 0.01)

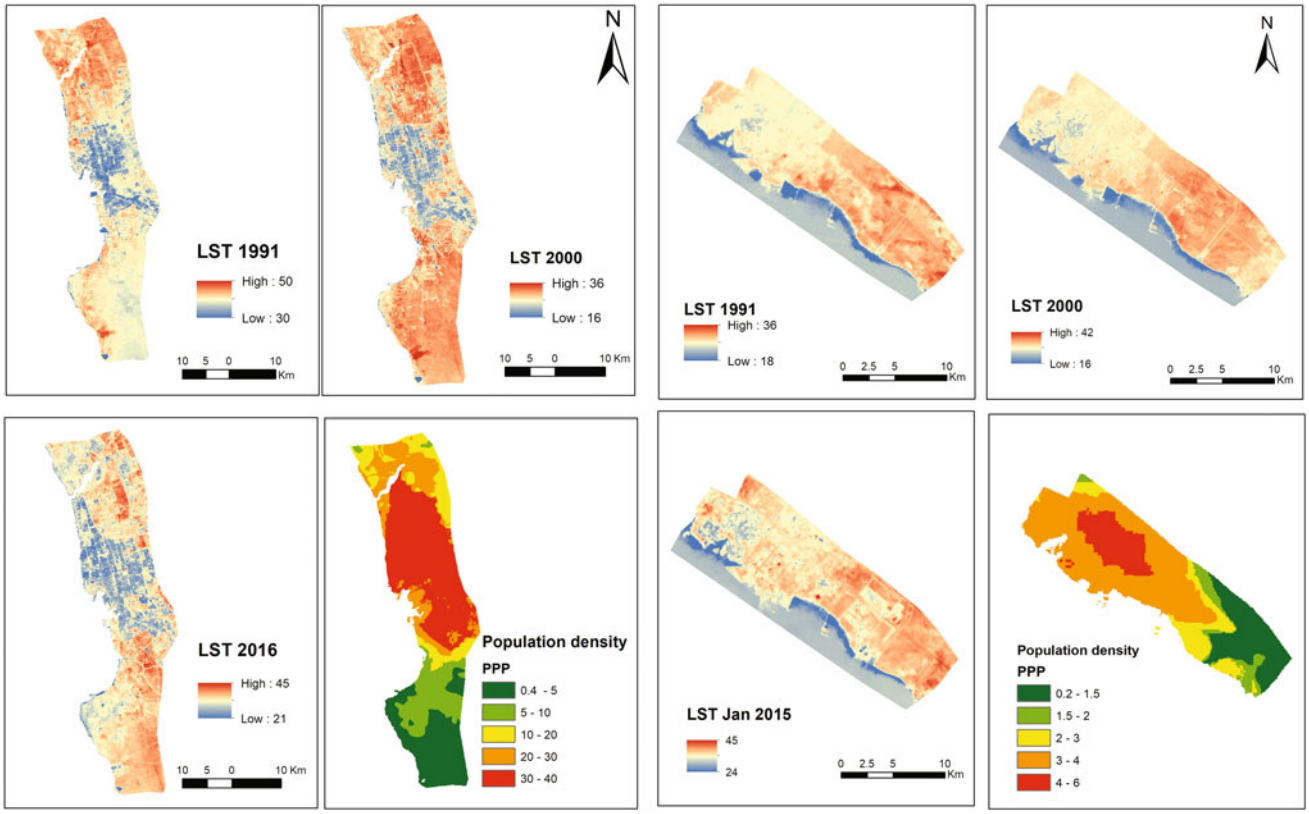

Fig. 1 LST of Jeddah and Yanbu with population density

between LST and NDVI in the city centers of the two cities. In Jeddah city center, where there is relatively sparse vegetation, the relationship between LST and NDVI is positive while in Yanbu, LST and NDVI are inversely correlated. The city center in Yanbu comprises of the residential districts with notable vegetation cover. The results contrast with the findings from tropical cities where city centers are relatively hotter than their surroundings [8]. The positive relationship between LST and population density might be due to its link with built density and surface imperviousness. A limitation of the study is the lack of data especially that are related to population, at the pixel scale, to validate the results. Some discrepancies were observed especially in Yanbu between the actual settlement area and the area where the population was allocated by WorldPop.

5 Conclusions

The study has shown the relevance of remote sensing data in monitoring urban temperature regime for environmental sustainability. It has highlighted the influence of land use types and population density on LST.

References

1. Aina, Y.A., Parvez, I.M., Balogun, A.L.: Examining the effect of land use on the spatiotemporal dynamics of urban temperature in an industrial city: a landsat analysis. In: Pirasteh, S., Li, J. (eds.) Global changes and natural disaster management: geo-information technologies, pp. 3–15. Springer, Cham (2017)
2. United Nations (UN).: World Urbanization Prospect: The 2014 Revision—Highlights. United Nations, New York, USA (2015)
3. Bai, X., Dawson, R.J., Ürge-Vorsatz, D., Delgado, G.C., Barau, A. S., Dhakal, S., Dodman, D., Leonardsen, L., Masson-Delmotte, V., Roberts, D., Schultz, S.: Six research priorities for cities and climate change. Nature **555**(7694), 23–25 (2018)
4. Alghamdi, A.S., Moore, T.W.: Detecting temporal changes in Riyadh's urban heat island. Pap. Appl. Geogr. **1**(4), 312–325 (2015)
5. Almazroui, M., Mashat, A., Assiri, M.E., Butt, M.J.: Application of landsat data for urban growth monitoring in Jeddah. Earth Syst. Environ. **1**, 25 (2017)
6. Jiménez-Muñoz, J.C., Sobrino, J.A.: A generalized single-channel method for retrieving land surface temperature from remote sensing data. J. Geophys. Res.: Atmos. **108**(D22) (2003)
7. Aina, Y.A., Adam, E.M., Ahmed, F.: Spatiotemporal variations in the impacts of urban land use types on urban heat island effects: the case of Riyadh, Saudi Arabia. Int. Arch. Photogrammetry, Remote Sens. Spat. Info. Sci. **XLII-3/W2**, 9–14 (2017)
8. Keeratikasikorn, C., Bonafoni, S.: Urban heat island analysis over the land use zoning plan of Bangkok by means of Landsat 8 imagery. Remote Sens. **10**(3), 440 (2018)

Land Use Classification and Change Detection Using Multi-temporal Landsat Imagery in Sulaimaniyah Governorate, Iraq

Karwan Alkaradaghi, Salahalddin S. Ali, Nadhir Al-Ansari, and Jan Laue

Abstract

Rapid growth in urbanized areas is a worldwide phenomenon. The rate of urban growth is very fast in developing countries like Iraq. This study illustrated urbanized area development in Sulaimaniyah Governorate from 2001 to 2017 using different Landsat imagery, Landsat Thematic Mapper (TM) and Landsat Operational Land Imager (OLI). The Environment for visualizing images ENVI 5.3 and GIS software was utilized for image pre-processing, calibration and classification. The Maximum likelihood method was used in the accurately extracted solution information from geospatial Landsat satellite imagery of different periods. The Landsat images from the study area were categorized into six different classes. These are: forest, vegetation, rock, soil, built up and water body. Land cover variation and land use change detection in the area were calculated for over a 17 year period. The Change detection Analysis shows an explosive demographic shift in the urban area with a record of +8.99% which is equivalent to 51.80 km^2 over a 17 years period and the vegetation area increased with 214 km^2. On the other hand, soil area was reduced by 257.87 km^2. This work will help urban planners in the future development of the city.

Keywords

Landsat • Land use land cover (LULC) • Maximum likelihood classification (MLC) • Change detection • ArcMap

1 Introduction

Land use land cover LULC change detection is commonly referred to as the modification of earth surface through human activities for decent urban management [1]. There is no doubt that population density growth and economic development play an important role in land cover change, thus, resulting in an observable pattern in the LULC over the time [2]. Nowadays, the rapid urbanization rate in most of developing countries is the priority of global problems; however, this mutation has a significant impact on future environment and urban planning processes [3].

Sulaimaniyah Governorate like the rest of the Kurdistan region of Iraq has faced rapid expansion in last 17 years in the urbanized area due to high population growth and economic prosperity [4]. Remote sensing and ArcMap software are the main applications applied in direct desktop mapping for temporal analysis and quantification of change in LULC with a better accuracy and low cost [5, 6].

Landsat data enhanced different imageries in the world with the ability of frequent revisits. Satellite images classification for the same area over the time affects the change in the area classes according to vegetation growth and welting on the bare soil. However, all the selected satellite images in this study refer to the same season over the years to avert detecting false changes in the land cover due to vegetation phenology [7, 8].

The Maximum likelihood is a supervised classification method that was used in this study to detect LULC change to show how land use has been changed from 2001 to 2017. Each pixel in the classified Landsat images varies according to land cover changes over the time [2].

K. Alkaradaghi · N. Al-Ansari (✉) · J. Laue
Lulea University of Technology, 97187 Lulea, Sweden
e-mail: nadhir.alansari@ltu.se

K. Alkaradaghi · S. S. Ali
Department of Geology, College of Science, Sulaimani University, Sulaimaniyah, 460013, Iraq
e-mail: salah.saeed@komar.edu.iq

K. Alkaradaghi
Kurdistan Institution for Strategic Studies and Scientific Research, Sulaimaniyah, 460013, Iraq

S. S. Ali
Komar University of Science and Technology, Sulaymaniyah, Iraq

© Springer Nature Switzerland AG 2019

H. M. El-Askary et al. (eds.), *Advances in Remote Sensing and Geo Informatics Applications*,
Advances in Science, Technology & Innovation, https://doi.org/10.1007/978-3-030-01440-7_28

Iraq witnessed successive wars in the past that affected its economic, urban and human recession all over the country including Sulaymaniyah city. According to food security and vulnerability in an in-depth survey of Sulaimaniyah Governorate after the events in 2003, Iraq witnessed a huge economic boom, Sulaimaniyah's economy today relies on tourism, agriculture, factories, trade and construction development [8].

There is no doubt that urban development affects the environment and global climate by losses in vegetation biomass, deforestation and land use change from areas with high probability of urban expansion [9].

This study is an attempt to assess the status of LULC change through the built up development in Sulaimaniyah governorate to detect the rate of land use and the changes that have occurred over the past two decades using geospatial techniques.

2 Study Area

Sulaimaniyah city is one of the three major urban cities of Kurdistan Region. Sulaimaniyah Governorate is located at the North East of Iraq (Fig. 1). Geographically, the city bounded by mountains in the northeast and situated in lower land that covers an area of around 470 km^2 with a total population of 829,245 people in early 2017 according to the data achieved from Statistical Directorate in Sulaimaniyah. The study area is characterized by a distinct continental interior climate of the Mediterranean type with the average annual precipitation ranging from 500 to 700 mm.

3 Data and Methodology

Landsat 5 Thematic Mapper (TM) of the years 2001, 2007, 2010 and 2011 were used with Landsat 8 Operational Land Imager (OLI) of 2016 and 2017 for LULC classification and all the available images were selected for the same season. The city plan collected from the Sulaimaniyah municipality as a shapefile of the study area extraction. In this study, the remote sensing software ENVI 5.3 for image processing was used. During the process, the imagery was geometrically corrected through pre-processing calibration, which consisted in atmospheric and topographic correction [10, 11]. The image-processing techniques are statistical algorithms that change the visual appearance or geometric properties of the images, These corrections are required for selected multitemporal or multisensor Landsat images to improve visibility appearance and image quality and to get more accurate results [10, 11, 12]. In Landsat Operational Land Imager (OLI), digital number values were converted to the surface reflectance with the fast line-of-sight atmospheric analysis of hypercubes (FLAASH) to remove atmospheric effects and create a surface reflectance image.

The pre-processed images were classified considering a supervised classification method. In this technique, we chose the maximum likelihood which is based on Bayesian theory in estimating parameters of a probabilistic model [13]. Each pixel is assigned to a class according to its probability. The Mean vector and covariance metrics are the key components of maximum likelihood classification that can be retrieved from a training data (signatures or region of interest ROI) [5–8, 14].

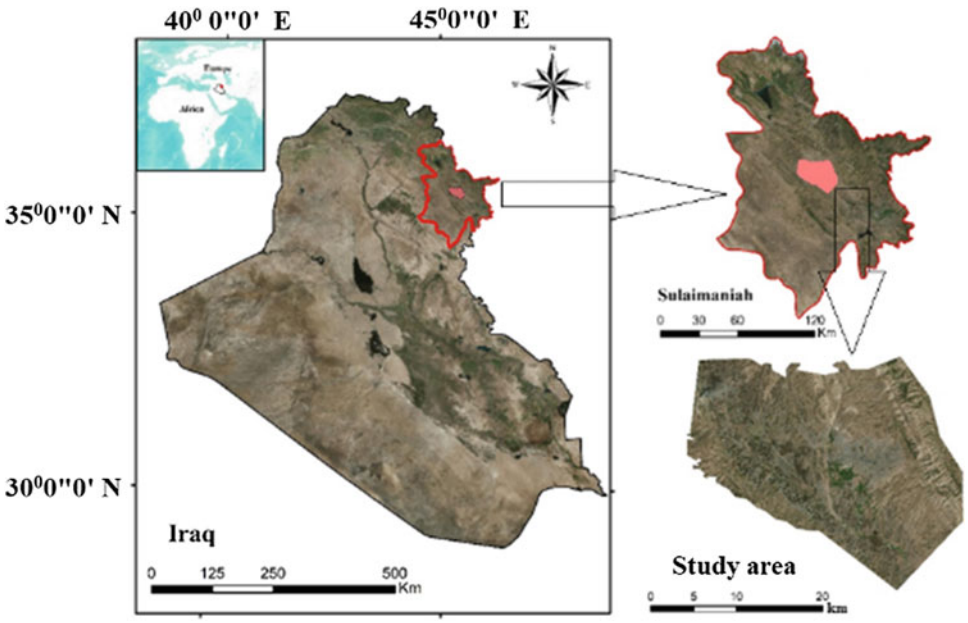

Fig. 1 Location map of the study area

Change detection in an area was calculated for each class separately according to the pixel geometry and statistical distribution of the pixels through the study area.

4 Results

4.1 Classification Results

Six land cover classes were identified from MLC. These are forests, built up area, rock, soil, vegetation and water bodies. The MLC in the Sulaimaniyah Governorate in 2001 and 2017 are shown in Fig. 2.

Change detection in the area was calculated for different LULC categories using MLC raster image and pixel geometry. The change detections in different LULC categories in the Sulaimaniyah Governorate from 2001 to 2017 are illustrated in Table 1.

4.2 Change Detection Analysis

During the 17 years (2001–2017), the built-up area has increased by 9% which represents 51.80 km^2. On the other hand, the soil area decreased by 44.77%. Rock, forest and water body recorded minimal change while vegetation increased by over 37% (Fig. 3a and Table 1). The Built-up area increased from 3.87% area in 2001 to reach 12.87% in 2017 (Fig. 3b).

5 Discussion

To produce a series of land use classification maps, all satellite images, taken in the same season, were selected over the years. The only time difference in acquisition date was that of the first image which was taken in 2001 1 month earlier. Thus, vegetation appears not to cover all the area from the

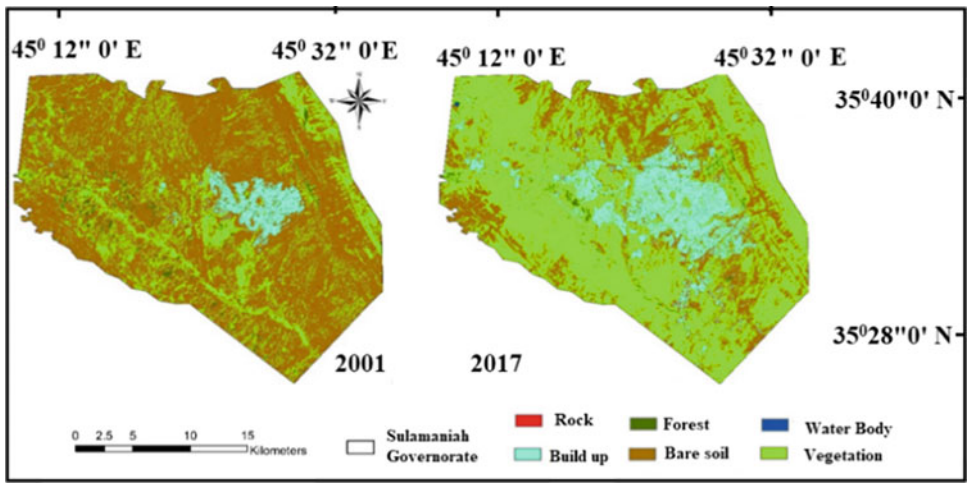

Fig. 2 Maximum likelihood classification (MLC) in the Sulaimaniyah governorate (2001 and 2017)

Table 1 Change detection in different LULC categories in the Sulaimaniyah governorate from 2001 to 2017

Classified area	% area 2001	% area 2007	% area 2010	% area 2011	% area 2016	% area 2017	Change detection in %	Change detection in km^2
Rock	0.66	0.66	0.05	0.05	0.03	0.03	−0.63	−3.61
Built up area	3.87	8.74	9.08	9.29	12.86	12.86	+8.99	+51.80
Forest	1.62	1.02	8.55	1.89	0.84	0.84	−0.78	−4.51
Soil	67.56	48.55	21.70	29.04	22.79	22.79	−44.77	−257.87
Water bodies	0.02	0.02	0.03	0.04	0.05	0.05	+0.03	+0.16
Vegetation	26.29	41.69	60.60	1.89	63.45	63.45	+37.16	+214.03

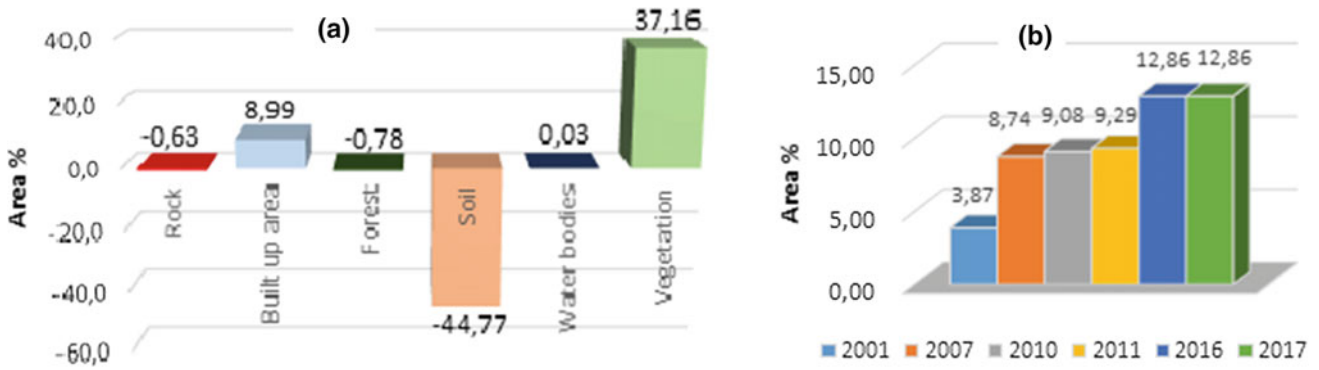

Fig. 3 **a** LULC change in area percentage from the 2001 to 2017. **b** Change in build up area percentage from 2001 to 2017

beginning which causes false changes in the land cover due to phenology [7, 8]. Classification results have shown that MLC is the robust technique and there are fewer chances of misclassification. In situations of rapid land use change, the classified images provide detailed information to understand the LULC. Observations of the earth from space provide objective crucial information to understand the influence of human activities within the urban area over time [3].

LULC studies are much salutary for future urban planners to guaratee a sustainable city development.

6 Conclusions

This study shows the LULC status for the period 2001–2017 with the view of change detection in land area. According to the results, urbanism recorded 51.80 km^2 expansion. This expansion occurs with soil, rock and forest shortage in area by 257.87, 3.61 and 4.51 km^2 respectively by the end of 2017. The water body and vegetation increased by 0.16 and 214.03 km^2 respectively.

The population density growth and economic development play an important role in land cover change. This work will help urban planners and decision makers with future plans of the city.

References

1. Comber, A.J.: Land use or land cover? J. Land Use Sci. **3**(4), 199–201 (2008)
2. Liu, J., Heiskanen, J., Aynekulu, E., Pellikka, P.K.E.: Seasonal variation of land cover classification accuracy of landsat 8 images in Burkina Faso. Int. Arch. Photogrammetry, Remote Sens. Spat. Info. Sci.—ISPRS Arch. **40**(7W3), 455–460
3. Rawat, J.S., Kumar, M.: Monitoring land use/cover change using remote sensing and GIS techniques: a case study of Hawalbagh block, district Almora, Uttarakhand, India. Egypt. J. Remote Sens. Sp. Sci. **18**(1), 77–84 (2015)
4. Eklund, L., Abdi, A., Islar, M.: From producers to consumers: the challenges and opportunities of agricultural development in Iraqi Kurdistan. Land **6**(3), 44 (2017)
5. Blaschke, T., Hay, G.J., Weng, Q., Resch, B.: Collective sensing: integrating geospatial technologies to understand urban systems-an overview. Remote Sens. **3**(8), 1743–1776 (2011)
6. Kachhwala, T.S.: Temporal monitoring of forest land for change detection and forest cover mapping through satellite remote sensing. Proc. 6th Asian Conf. Remote Sens. 77–83 (1985)
7. Weil, G., Lensky, I.M., Resheff, Y.S., Levin, N.: Optimizing the timing of unmanned aerial vehicle image acquisition for applied mapping ofwoody vegetation species using feature selection. Remote Sens. **9**(11) (2017)
8. Planning, M.O.F., Cooperation, D., Health, M.O.F.: Comprehensive food security and vulnerability analysis in Iraq. Methodology (2008)
9. Seto, K.C., Christensen, P.: Remote sensing science to inform urban climate change mitigation strategies. Urban Clim. **3**, 1–6 (2013)
10. Song, C., Woodcock, C.E., Seto, K.C., Lenney, M.P., Macomber, S.A.: Classification and change detection using Landsat TM data: when and how to correct atmospheric effects? Remote Sens. Environ. **75**(2), 230–244 (2001)
11. Schulz, J.J., Cayuela, L., Echeverria, C., Salas, J., Rey Benayas, J. M.: Monitoring land cover change of the dryland forest landscape of central Chile (1975–2008). Appl. Geogr. **30**(3), 436–447 (2010)
12. Robert, A.S.: Remote Sensing: Models and Methods for Image Processing, vol. 95, no. 1 (2012)
13. Rosenfield, G.H., Fitzpatrick-Lins, K.: A coefficient of agreement as a measure of thematic classification accuracy. Photogramm. Eng. Remote Sens. **52**(1979), 223–227 (1986)
14. Wu, C., et al.: Land surface phenology derived from normalized difference vegetation index (NDVI) at global FLUXNET sites. Agric. For. Meteorol. **233**, 171–182 (Dec 2016) (2017)

NDWI Based Change Detection Analysis of Qarun Lake Coastal Area, El-Fayoum, Egypt

Noha Donia

Abstract

Multidate satellite images have been used in this study to detect the trends of environmental changes in Qarun Lake, This study explored the applications of remote sensing and Geographical Information Systems (GIS) in the collection of information and analysis of data. NDWI index was calculated to detect and analyze the change detection of Qarun Lake coastal area. The results revealed that the overall size of the water decreased by about 5% and island area decreased by around 9% from 1972 until 2017. This could be due to the increase of the amount of drainage water to El-Rayan Depression.

Keywords

Qarun Lake • El-Fayoum • NDWI • Remote sensing • GIS

1 Introduction

Lake Qarun is located in the Western Desert of Egypt, about 130 km southwest of Cairo between latitudes 29° 02′ and 29° 35′ N and longitudes 30° 23′ and 31° 05′ E in El-Fayoum Oasis, the Fayoum Governorate. Qarun Lake suffered from various pollution types due to the industrial and agricultural waste disposal as well as domestic waste, which affect the fish and animal life in the lake with the great dangerous impact on human health [2].

2 Materials and Methods

In order to detect and monitor water bodies over the Qarun Lake Five Landsat images (path 177/row 40) acquired in 1972, 1988, 2003, 2013 and 2017 (Landsat MSS 1972, Landsat TM 1988, Landsat TM 2003, Landsat-8 2013 and Landsat-8 2017) were used (Fig. 1). Data from satellite images of Quran Lake were integrated into a geographical information system (GIS) to determine the changed area for each basin.

The Normalized Difference Water Index (NDWI) was first proposed by [3] to detect surface water in wetland environments and to allow for the measurement of surface water extent, and it produces a single grayscale image, where water is bright. (NDWI) was calculated using the equation:

$$\mathrm{NDWI} = (\mathrm{GREEN} - \mathrm{NIR})/\mathrm{GREEN} + \mathrm{NIR}),$$

the values of NDWI range between 0 and ±1, positive values or close to 1 represent surface water/deep water bodies, whereas negative values or values close to 0 represent features other than water [3].

The output image was reclassified into 2 classes (water and vegetation) and was converted into a vector layer, and then we calculated the area of each class.

After the NDWI classification of all satellite images from (1972 to 2017) and calculation of the water and vegetation areas, the image subtraction method was performed to calculate the areas decrease and/or increase. The image differencing change detection technique was performed by subtracting the digital number (DN) value of a pixel in one date for a given band from the DN value of the same pixel for the same band of another date [1].

N. Donia (✉)
Environmental Engineering Department, Institute of Environmental Studies and Researches, Ain Shams University, Cairo, Egypt
e-mail: Noha.samir@iesr.asu.edu.eg

© Springer Nature Switzerland AG 2019

H. M. El-Askary et al. (eds.), *Advances in Remote Sensing and Geo Informatics Applications*, Advances in Science, Technology & Innovation, https://doi.org/10.1007/978-3-030-01440-7_29

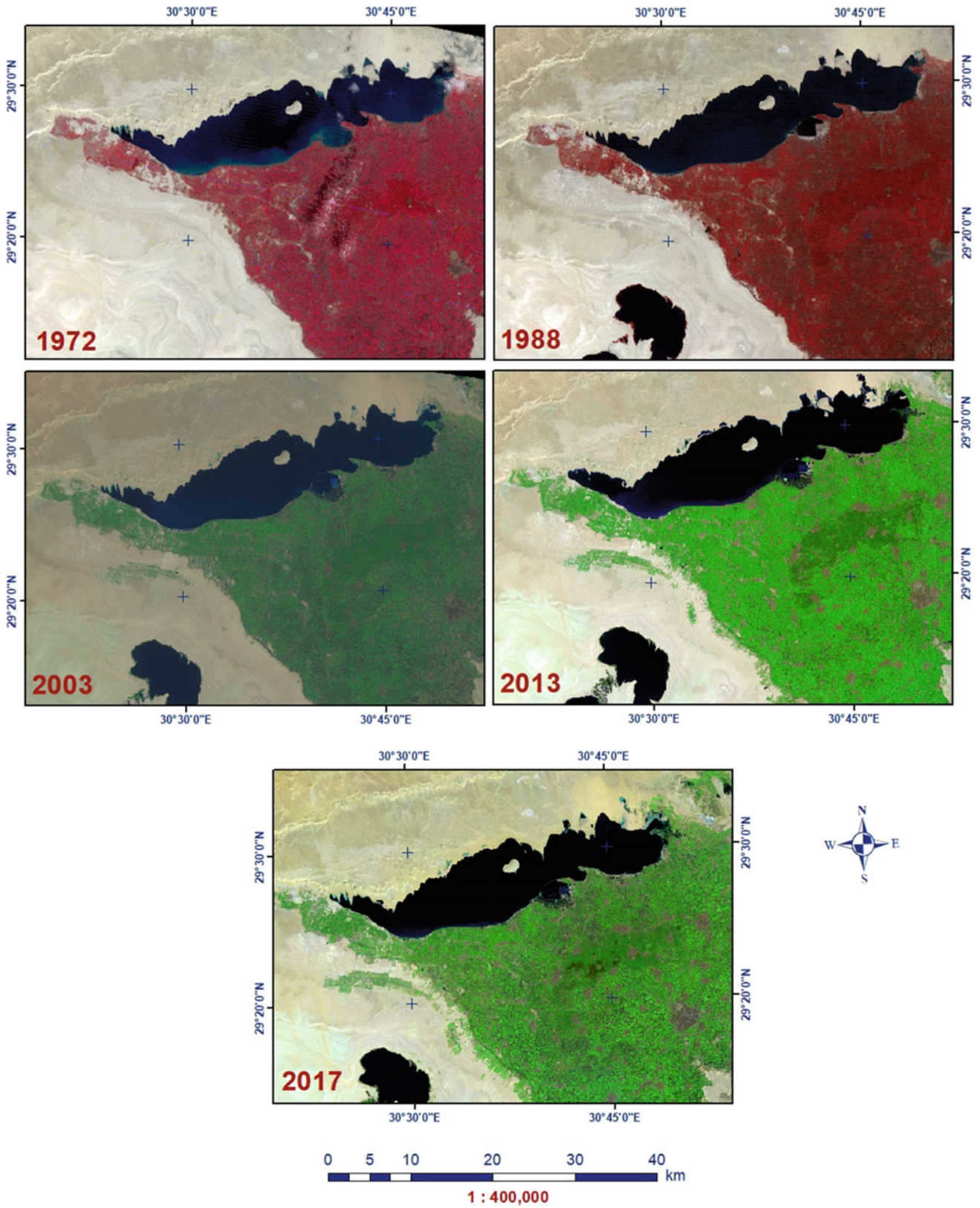

Fig. 1 Qarun Lake satellite images from 1972 to 2017

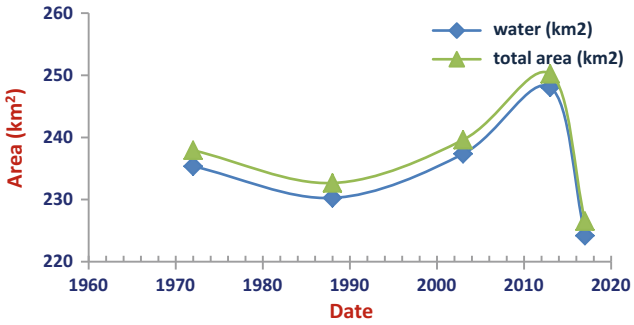

Fig. 2 Environmental changes in Quran Lake from satellite imagery during the last four decades (1972–2017)

3 Results

3.1 Normalized Difference Water Index (NDWI)

The total water area of the lake decreased by 11.17 km^2 and the island decreased by 0.23 km^2 as shown in Fig. 2.

3.2 Change Detection

The area decrease and/or increase during the last five decades (1972–2017) was calculated using the change detection technique as shown in Fig. 3.

4 Discussion

Change on the surface area of Qarun Lake was assessed by calculating the NDWI index from Landsat multi-temporal images. The environmental changes over the five decades for the lake were identified; this was undertaken using satellite images to employ historical remotely sensed data to reveal the long-term changes of the Lake The results revealed that the overall size of the water decreased by about 5% and island area decreased by around 9% from 1972 until 2017.

5 Conclusion

Remote sensing proved to be very successful in monitoring the ecological changes along the Qarun Lake. The study observed NDWI based change detection of Qarun Lake, El-Fayoum, Egypt using Landsat time series data from 1972 to 2017. It was observed that there are significant island and water cover areas changes from 1972 to 2017. It was found that index provided accurate results of change detection of the study area. Finally, the entire study was found very effective using remote sensing and GIS techniques.

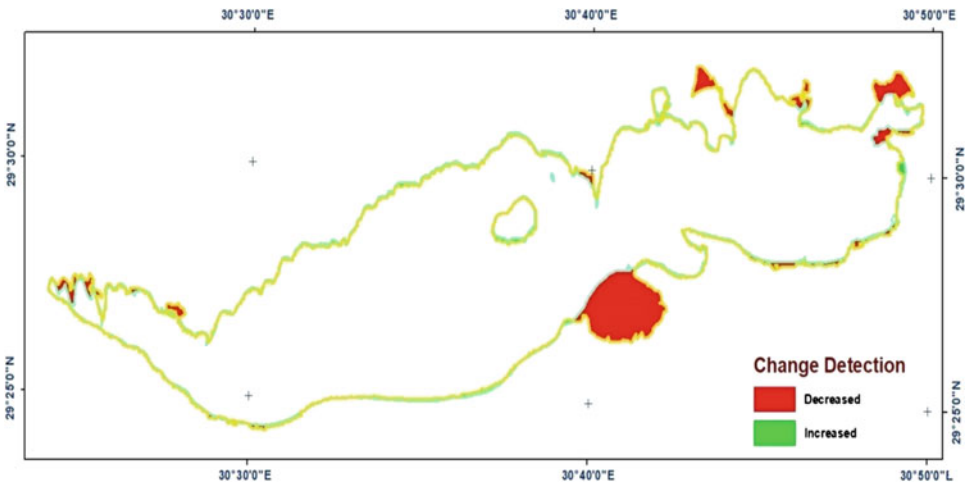

Fig. 3 Change detection in Quran Lake between satellite imagery (1972, 2017)

References

1. Afify, H.A.: Evaluation of change detection techniques for monitoring land-cover changes: a case study in new Burg El-Arab area. Alexandria Eng. J. **50**(2), 187–195 (2011)
2. Hussein, H., Amer, R., Gaballah, A., Refaat, Y., Abdel-Wahab, A.: Pollution monitoring for Lake Qarun. Adv. Environ. Biol. **2**(2), 70–80 (2008)
3. McFeeters, S.K.: The use of the normalized difference water index (NDWI) in the delineation of open water features. Int. J. Remote Sens. **17**(7), 1425–1432 (1996)

Effects of Land Use on the Chemical Characterization of Imo River Basin and Its Catchments (Nigeria): A GIS Approach

Chukwudi Nwaogu, Olutoyin Fashae, Onyedikachi J. Okeke, and Vilém Pechanec

Abstract

Water sources have been severely contaminated by heavy metals (HM) in Imo river basin due to different land uses including industrialization and intensive agriculture. Six land use types were identified using GIS and water samples were collected from both surface and underground water sources to test the HM concentrations in different land uses. Geostatistical tools such as interpolation (Kriging) and regressions were used to determine the extent of chemical concentrations, and their relationships with the land use types. Higher concentrations of the heavy metals (NO_3, Cr, and Pb) were observed in the center (middle stream watershed) around the urban built and grassland areas. Downstream watershed (wetlands areas) had low concentrations of the HM except Fe. The water quality in the built-up industrial areas were found to be of poor quality relative to other parts in the study area. The findings of this work will support the Federal Ministries of Water resources, Agriculture, Environment in sustainable decision making towards reducing pollutants and restoring the river basin and its catchments.

Keywords

Heavy metals • GIS • Land use • Water pollution • Nigeria

1 Introduction

Water is crucial for the development of organism within all spheres, biomes and ecosystems. Ground water (GW) and surface water (SW) are the most valuable natural resources serving as major sources of water to communities for domestic, commercial, agricultural and industrial purposes. Groundwater can be defined as water in saturated zone [1] which fills the cracks in rock mass or pore spaces among mineral grains, whereas surface water includes all waters found on the Earth's surface. Groundwater (GW) and surface water (SW) are not isolated components of the hydrological cycle which interact in response to land use, topographic, soil, geological, and climatic factors. The components are one single resource and impacts on either of these components will inevitably affect the quantity or quality of the other. However, the growing demands on water resources and increasing uncertainties in water supply associated with climate change created the awareness for the need to manage GW and SW as a single resource especially with GIS tools. Recently, many countries have developed new legal frameworks to regulate the sustainable use of GW and SW as a single resource [2].

The significant relationship of groundwater occurrence and conditioning factors has been indicated by many researchers [3]. For instance, the effects of groundwater extractions on river flow have been highlighted in a comprehensive study of water resources in the Murraye Darling Basin, Australia [4]. Specifically, water quality degradation often occurs because of land use and changes in landscapes causing an increase in flash runoff and nutrient loading [5]. However, the quantification of human impacts on the interactions between GW and SW is challenging because of their complexity. The adoption of the geoinformatics technologies has made it easier to analyze the interactions among human disturbances, land use changes, GW and SW [6]. Land use changes due to anthropogenic factors (especially agricultural and industrial) have had a large effect on

C. Nwaogu (✉) · V. Pechanec
Department of Geoinformatics, Palacký University Olomouc, 17, Listopadu 50, 771 46 Olomouc, Czech Republic
e-mail: chukwudi.nwaogu01@upol.cz

O. Fashae
Department of Geography, University of Ibadan, 200284 Ibadan, Oyo State, Nigeria

O. J. Okeke
Sambus Geospatial Limited, 5th Floor Elizade/Toyota House Oppo Bolingo Hotel, CBD, Abuja, Nigeria

© Springer Nature Switzerland AG 2019

H. M. El-Askary et al. (eds.), *Advances in Remote Sensing and Geo Informatics Applications*, Advances in Science, Technology & Innovation, https://doi.org/10.1007/978-3-030-01440-7_30

terrestrial and aquatic environments in tropical and subtropical regions. The changes have long-term history which are attributed to increase population, human activity, rapid urbanization, agricultural development, wide climatic and topographic differences [7]. Changes in land use have significant effect on the quality and quantity of SW and GW due to increased surface runoff, reduced groundwater discharge, and distribution of pollutants. Land use information at the watershed and catchments is crucial for identifying, planning, monitoring, and managing water resources so that the changes in land use satisfies the growing human needs with a sustainable environment [8]. Therefore, this work aimed at examining the interactions between the land use types and the measured water chemical properties. The Imo River Basin Development Authority (IRBDA) in Nigeria has been faced with the problems of ameliorating the cases of increased water pollutants from the human activities. Therefore, the findings of this work will support the Federal Ministries of Water resources, Agriculture, Environment, and the IRBDA in sustainable decision making towards reducing pollutants and restoring the river basin and its catchments.

2 Materials and Methods

To meet the study objective, the bio-physiochemical analyses of water samples for 31 randomly selected dug wells, boreholes and streams were sampled in Imo river basin and its catchments covered by different land use types (Fig. 1). A physical survey was carried out to determine the types of facilities in term of technology available in the selected locations, before the samples were taken. The collected water samples were taken to the laboratory at Obafemi Awolowo University, Ile-Ife, Osun State to determine the concentrations of Nitrates, Iron, Lead, Chromium, E-coli and water quality index. The samples for microbiological analysis were stored in refrigerated compartment within 24 h after collection. The map required for this study was acquired with the use of GIS; the available analogue base map of Imo river basin was converted into digital format to choose the major towns within the local government area. Instruments and materials used for field data collection were: a map of Imo River Basin showing the States and Local Government Areas, hand-held GPS, measuring rope, mercury-in-glass thermometer, litmus paper and

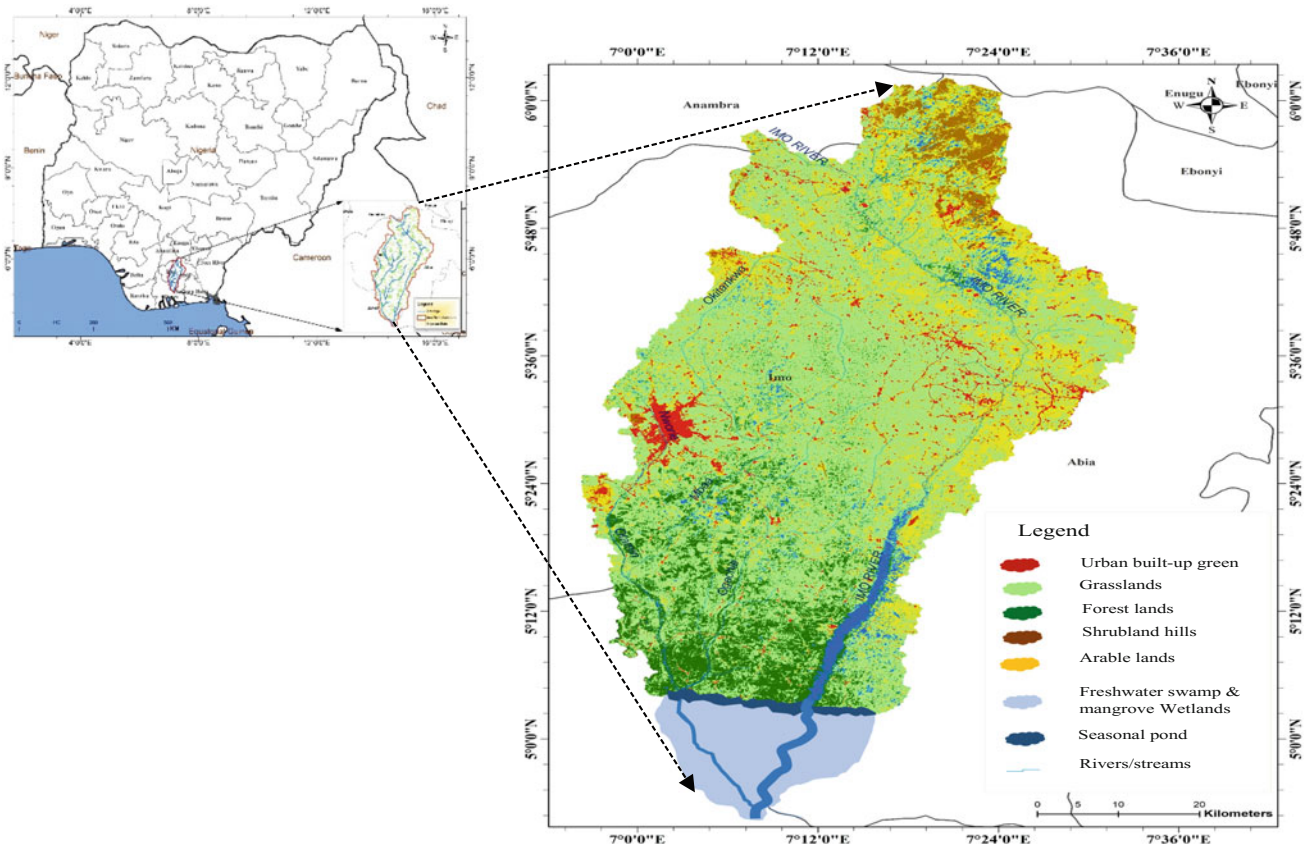

Fig. 1 Study area (Imo river basin and catchments) and the land use types-arable land (AL), forest land (FL), grassland (GL), Shrubland hills (SL), urban built-up green (UL), and freshwater swamp and mangrove wetland (WL)

questionnaires. The GPS model MAP 76CSx GARMIN was used to obtain coordinates of each facility while the measuring rope made of flexible cable and 5 kg stainless steel weight attached to it was used to determine the depths of wells. The users of water supply and sanitation facilities were interviewed using semi structured questionnaires to obtain relevant information and entered into the data forms. Water samples from motorized and hand pump fitted wells and boreholes were collected from the stand pipes provided. The streams were sampled with hand held IL plastic bottles at a depth of about 10 cm below the water surface. Geostatistical analyses including interpolations and regressions were performed to determine the extent of chemical concentrations, and their relationships with the land use types.

3 Results

Higher concentrations of the heavy metals (NO_3, Cr, and Pb) but with low Fe were observed in the center (middle stream watershed) around the urban built and grassland areas

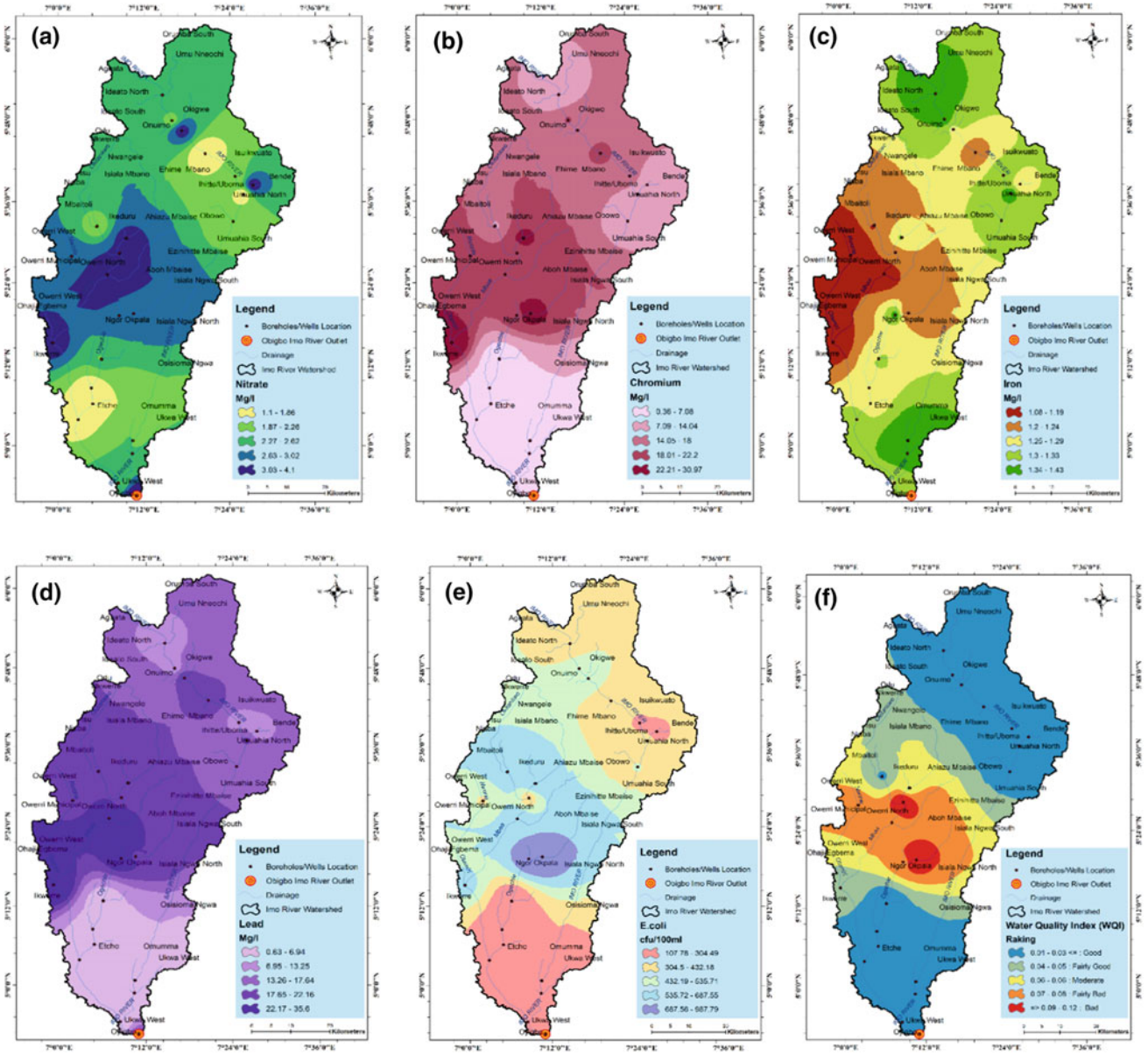

Fig. 2 Concentrations and distribution of **a** NO_3, **b** Cr, **c** Fe, **d** Pb, **e** E. coli, **f** water quality index ranking

(Fig. 2). In this part of the study area, the mean concentrations of NO_3 was 3.5 Mg/l, Cr recorded 26.59 Mg/l, Fe was 1.20 Mg/l and Pb was 28.89 Mg/l. Similarly, Escherichia coli (E. coli) was found to be high near the urban built and grassland areas with values ranging between 432.19–987.79 cfu/100 ml, and mean water quality index (WQI) ranked 0.10. On the other hand, the downstream watershed which is covered by wetlands recorded 1.34 Mg/l, 3.72 Mg/l, 1.31 Mg/l, 3.79 Mg/l, 206.14 cfu/100 ml and 0.02 as mean concentrations/values for NO_3, Cr, Fe, Pb, E. coli and WQI respectively. However, the upper stream watershed (i.e. the upper section) of the study area covering the hills showed the same Fe concentration level and WQI as the lower part, but the concentrations for NO_3, Cr, and Pb were intermediate.

4 Discussion

The heavy metals (NO_3, Cr, and Pb) were found in higher concentrations in the center around the urban built and grassland areas and this might probably be related to the types of socioeconomic activities operated in this part of the study area. For example, many manufacturing industries were located in the center of the study forming urban built-up, and the wastes and activities of these industries might have contaminated the surface and sub-surface waters through seepages from the soil. This finding is consistent with other authors working on similar issue in Nigeria [9] and other countries [10]. Besides, the activities from intensive grazing could have contributed to the high concentrations of the heavy metals in this region [11]. The downstream watershed (wetlands area) was expected to have high heavy metals because of the crude oil exploitation but on the contrary, only Fe concentration was observed to be at high concentration. This might be explained by the recent precautions taken by the miners not to pollute the land or water sources and to remediate the case immediately should there be any oil spill. However, this finding contrasts the results from many other previous studies conducted in Nigeria and other regions on this issue [12, 13]. where the concentrations of heavy metals were reportedly high because of acute human activities without sustainable management. Other reasons for this discrepancy in results could be because of differences in soil and availability of phytoremediation plants [14]. The water quality in the built-up industrial areas was found to be of poor quality relative to other parts in the study area.

5 Conclusion

Conclusively, the land use significantly affected the sources of water (surface and underground) in the study area especially in the urban-industrial and intensive grazing areas. GIS technologies have proved to be effective and successful in assessing the relationships between land use types and water quality in Imo river basin and its catchments. Our results could be used to develop strategies for more efficient stream (SW) and subsurface water restoration and management, which would enhance water quality based on the level of land use.

References

1. Berhanu, B., Seleshi, Y., Melesse, A.M.: Surface Water and Groundwater Resources of Ethiopia: potentials and Challenges of Water Resources Development, pp. 97–117. Springer, Netherlands (2014)
2. Martin, S.L., Hayes, D.B., Kendall, A.D., Hyndman, D.W.: The land-use legacy effect: towards a mechanistic understanding of time-lagged water quality responses to land use/cover. Sci. Tot. Environ. **579**, 1794–1803 (2017)
3. Eniolorunda, N.B., Mashi, S.A., Nsofor, G.N.: Toward achieving a sustainable management: characterization of land use/land cover in Sokoto Rima floodplain, Nigeria. Environ Dev. Sustain. **19**, 1855–1878 (2017)
4. Adiat, K.A.N., Nawawi, M.N.M., Abdullah, K.: Assessing the accuracy of GIS-based elementary multi criteria decision analysis as a spatial prediction tool—a case of predicting potential zones of sustainable groundwater resources. J Hydrolog. **440**, 75–89 (2012)
5. Hua K.A.: Land use land cover changes in detection of water quality: a study based on remote sensing and multivariate statistics. J. Environ. Public Health. Article ID 7515130 (2017)
6. WFD (Water Framework Directive): Establishing a framework for community action in the field of water policy. Directive 2008/105/EC of the European Parliament and of the Council. In: E. Comission (ed.) Directive 2008/105/EC, Brussels. Brussels, EU (2008)
7. CSIRO: Water availability in the Namoi. A Report to the Australian Government from the CSIRO Murray-Darling Basin Sustainable Yields Project, p. 154. CSIRO, Australia (2007)
8. Sangani, M.H., Amiri, B.J., Shabani, A., Sakieh, Y., Ashrafi, S.: Modeling relationships between catchment attributes and river water quality in southern catchments of the Caspian Sea. Environ. Sci. Poll. Res. **22**, 4985–5002 (2015)
9. Adeniji, A.E., Omonona, O.V., Obiora, D.N. Chukudebe, U.: Evaluation of soil corrosivity and aquifer protective capacity using geoelectrical investigation in Bwari basement complex area, Abuja. J. Earth Syst. Sci. **123**, 491 (2014)
10. Islam, S.M., Hossain, M.B., Matin, A., Sarker, S.I.: Assessment of heavy metal pollution, distribution and source apportionment in the sediment from Feni River estuary. Bangladesh Chemosphere **202**, 25–32 (2018)

11. Dimelu, M.U., Danjuma, S.E., Igbokwe, E.M.: Resource use conflict in agrarian communities, management and challenges: a case of farmer-herdsmen conflict in Kogi State, Nigeria. J. Rural Stud. **46**, 147–154 (2016)
12. Iwegbue, C.M.A., Lari, B., Osakwe, S.A., Tesi, G.O., Nwajei, E.G., Martincigh, B.S.: Distribution, sources and ecological risks of metals in surficial sediments of the Forcados River and its Estuary, Niger Delta, Nigeria. Environ. Earth Sci. **77**, 227 (2018)
13. Su, H., Kang, W., Xu, Y., Wang, J.: Assessing groundwater quality and health risks of nitrogen pollution in the Shenfu mining area of Shaanxi Province, Northwest China. Expo. Health **10**(2), 77–97 (2018)
14. Sumiahadi, A., Acar, R.: A review of phytoremediation technology: heavy metals uptake by plants. IOP Conf. Ser. Earth Environ. Sci. **142**, 012023 (2018)

Toward Satellite-Based Estimation of Growing Season Framing Dates in Conditions of Unstable Weather

Evgeny Panidi, Ivan Rykin, Giovanni Nico, and Valery Tsepelev

Abstract

This paper described an experiment of developing a complex technique for satellite imagery time series processing when estimating spatial distribution of framing (or changing) calendar dates of the growing seasons. Particularly, we reflected on allocation of growing season framing dates in conditions of unstable weather. As surface air temperature may fluctuate in many cases around bordering values during some days or weeks, the allocation of stable crossing of temperature through the control values (that marks time frames of growing seasons) is a fundamental problem in the case of ground observations. We compared some results of the growing season frames allocation based on ground data observations of the temperature (needed for the verification and calibration purposes), and the estimation results made relying on the data of remotely observed Normalized Difference Water Index (NDWI).

Keywords

Growing seasons • Ground meteorological observations • Remote sensing data • NDWI

1 Introduction

Ground observation and data reanalysis are widely used in climate change monitoring, modeling and forecasting. In many cases (e.g., in the case of Russian Subarctic) these data cannot ensure producing quality and detailed models (particularly digital maps) on regional and local scales. For example, the ground network of meteorological stations is too sparse in Russian Subarctic (as well as in some other regions), and interpolation of climate parameters onto big areas leads to significant local errors in modeling. A number of studies including ours in 2013–2016 [3, 4] show the applicability of satellite-based vegetation dynamics monitoring as an enabling technology for the monitoring of regional (and possibly local) climate change. We also discovered that data analyses have to be provided separately for three growing seasons, which are spring, summer and autumn, separated by the level of surface air temperature (consequently, from +5 to +10 °C, above +10 °C, and from +10 to +5 °C). The remaining issue is how to allocate time frames in conditions of sparse ground observation network, while the air temperature (as well as other weather parameters) may additionally fluctuate with high frequency around the marker value during long periods, in other words – while the weather can be unstable [6, 7].

Some authors [1, 5] propose to estimate full (surface air temperature above +5 °C) growing season time frames using the analysis of an annual graph of the Normalized Difference Water Index (NDWI) proposed by Gao [2]. Such an approach allows using satellite imagery time series to produce NDWI maps and to estimate spatial distribution of growing season framing dates without the need of interpolation of the ground observations. We used this approach and implemented additionally technique for the summer season framing and algorithm for the computations automation.

2 Data and Methods

To produce the NDWI maps we used Version 6 of the MODIS MOD9A1 V006 product (8-day averaged surface reflectance data).

E. Panidi (✉) · I. Rykin · G. Nico
Saint Petersburg State University, St. Petersburg, Russia
e-mail: panidi@ya.ru; ; e.panidi@spbu.ru

G. Nico
Consiglio Nazionale delle Ricerche, Istituto per le Applicazioni del Calcolo, Bari, Italy

V. Tsepelev
Russian State Hydrometeorological University, St. Petersburg, Russia

© Springer Nature Switzerland AG 2019

H. M. El-Askary et al. (eds.), *Advances in Remote Sensing and Geo Informatics Applications*, Advances in Science, Technology & Innovation, https://doi.org/10.1007/978-3-030-01440-7_31

The NDWI was computed using Gao's original formula:

$$NDWI = \frac{\rho_{0.86} - \rho_{1.24}}{\rho_{0.86} + \rho_{1.24}} \quad (1)$$

Where the ρ values are the radiances in corresponding spectral bands presented in reflectance units.

As a benchmark data, we used surface air temperature observations collected at the weather stations of Roshydromet (Russian meteorological agency).

3 Results

The NDWI dynamics reflect the processes of liquid water amount change in plant tissue [2], leaves greening and yellowing, and snow melt/accumulation [1]. We allocated frames of full growing season as spring and autumn minima (Fig. 1). The frames of the summer season were allocated using the linear trend of NDWI graph for the full growing season (Fig. 1). The trend separates spring and autumn parts of the graph that have high gradient with the summer plateau.

This technique of growing season frames allocation was estimated on the example of 8-day averaged MODIS imagery and was used to explore the possibility of pixel-by-pixel mapping of the spatial distribution of growing seasons' change [3].

One of the used techniques to eliminate surface air temperature (SAT) fluctuations when allocating crossing of some marker value is the averaging temperature graphs for a couple of years [6]. We used it to produce benchmark frames of the growing seasons. To ensure comparison of ground-based and satellite-based estimations, we produced averaged NDWI graphs for the same periods. Table 1 shows the example of growing season frames allocation using 5-year averaged data, and Table 2 displays the estimation example produced using 1-year data.

The currently obtained results and examples presented in Tables 1 and 2 show compliance between 1-year and multiyear averaged estimations of growing season framing dates produced using NDWI with the data of ground observations. The NDWI fluctuated in a smaller degree than SAT. In the case of high temporal resolution of NDWI time series

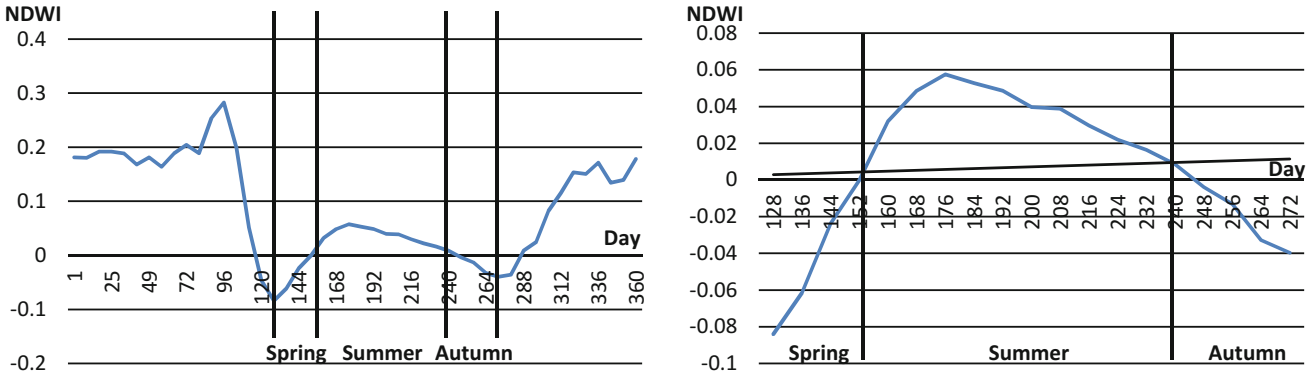

Fig. 1 Framing dates of growing seasons estimated using the mean (for the period of 2001–2015) NDWI graph (left image); allocation of summer framing dates using linear trend of NDWI graph of the full growing season (for the period of 2001–2015)

Table 1 Beginning dates of growing seasons estimated as mean values of 2001–2015, days' numbers are in parentheses

	Spring	Autumn	Summer	Winter
SAT	April 30 (120)	May 17 (137)	September 10 (253)	October 1 (274)
NDWI	May 8 (128)	June 2 (153)	August 28 (240)	September 30 (273)

Table 2 Beginning dates of growing seasons of 2015, days' numbers are in parentheses

	Spring	Autumn	Summer	Winter
SAT	April 29 (119)	May 11 (131)	September 29 (272)	October 3 (276)
NDWI	May 9 (129)	May 26 (146)	August 28 (240)	September 23 (266)

(while measurement aberrations take place and additional fluctuations occur), the averaging technique can be applied to the NDWI (in a moving window way).

4 Discussion

Some differences occur in the case of use of these two data sources. Most significant is that the NDWI-based estimations in a general case highlight shorter growing seasons than the SAT-based ones. This can be explained by the spring delay of vegetation greening in comparison to the temperature regime as well as autumn ahead of yellowing.

To increase the temporal resolution of estimations to one day, the MODIS Level 1B datasets can be used. This is the current direction of our study. Currently we are developing an automation toolset in Python programming language and working on data processing for the test area in the European part of Russia.

5 Conclusion

We found that NDWI can be an applicable instrument for the estimation of the growing season time frames. In comparison to the surface air temperature, the NDWI has a smaller number of fluctuations and allows estimating growing season frames directly through the vegetation growth, in an automated mode. However, further studies are needed to collect more statistics and find out about the technique applicability in different geographical regions.

Acknowledgements The MOD9A1 V006 datasets were retrieved from the online LP DAAC2Disk download manager, courtesy of the NASA EOSDIS Land Processes Distributed Active Archive Center (LP DAAC), USGS/Earth Resources Observation and Science (EROS) Center, Sioux Falls, South Dakota (https://lpdaac.usgs.gov/data_access/daac2disk).The MODIS Level 1B datasets were acquired from the Atmosphere Archive & Distribution System (LAADS) Distributed Active Archive Center (DAAC), located in the Goddard Space Flight Center in Greenbelt, Maryland (https://ladsweb.nascom.nasa.gov/). Ground observations data were retrieved from Waisori Web interface, courtesy of the RIHMI-WDC of Roshydromet, Veselov V.M., Pribylskaya I.R., Mirzeabasov O.A. (http://aisori-m.meteo.ru/waisori/).

References

1. Delbart, N.J.-P., Kergoats, L., Le Toan, T., Lhermitte, J., Picard, G.: Determination of phenological dates in boreal regions using normalized difference water index. Remote Sens. Environ. **97**(1), 26–38 (2005). https://doi.org/10.1016/j.rse.2005.03.011
2. Gao, B.C.: NDWI a normalized difference water index for remote sensing of vegetation liquid water from space. Remote Sens. Env. **58**(3), 257–266 (1996)
3. Panidi, E., Tsepelev, V.: NDWI-based technique for detection of change dates of the growing seasons in Russian Subarctic. Int. Arch. Photogramm. Remote Sens. Spatial Inf. Sci., **XLII-3/W2**, 179–182 (2017). https://doi.org/10.5194/isprs-archives-xlii-3-w2-179-2017
4. Panidi, E., Tsepelev, V., Torlopova, N., Bobkov, A.: Mapping of the land cover spatiotemporal characteristics in Northern Russia caused by climate change. Int. Arch. Photogramm. Remote Sens. Spatial Inf. Sci., **XLI-B8**, 997–1002 (2016). https://doi.org/10.5194/isprs-archives-xli-b8-997-2016
5. Sekhon, N.S., Hassan, Q.K., Sleep, R.W.: A remote sensing based system to predict early spring phenology over boreal forest. Int. Arch. Photogramm. Remote Sens. Spatial Inf. Sci. **XXXVIII**, 5, Part 1 (2010)
6. Skrynyk, O.A., Snizhko, S.I.: The issue of determining of the surface air temperature stable transition dates through a certain fixed value (analysis of methods). Ukrai'ns'kyj gidrometeorologichnyj zhurnal **3**, 56–66 (2008). in Ukrainian
7. Skrynnik, O.Y., Skrynnik, O.A.: Climatological method for determining of the date of average daily air temperature steady transition through a given threshold. Meteorologiya i gidrologiya **10**, 90–99 (2009). in Russian

Investigating Land Surface Temperature (LST) Change Using the LST Change Detection Technique (Gomishan District, Iran)

Maliheh Arekhi

Abstract

Monitoring variations in the spectral reflectance of thermal bands of Landsat data provide land surface temperature information of earth's surface features. This research tried to examine the variations of Land surface temperature (LST) from 1987 to 2017 at the Gomishan district and its soundings in Iran. Images preprocessing was conducted including the geo-shifting and atmospheric correction. NDVI and LST maps and their change map using a change detection technique were generated. Basic inferential statistics and spatial analysis were performed. The results show that LST mean reached approximately 42.5 °C with 9 °C increase, while it was 33.8 °C in 1987. However, comparing the statistical analysis of NDVI data did not show any differences between the two study dates. Land cover classes include water, urban, and rural covered areas had the lowest LST shifts between the two study periods. The LST of rangelands, wetlands, and bare lands with more than 10 °C increase have experienced considerable LST shifts between during the study periods. Interestingly, some parts of wetland areas had the highest increase approximately 13 °C from 1987 to 2017. This study emphasized that LST change detection approach and spatial analysis can be used successfully in LST monitoring investigations. The results can be used to identify regions that experienced LST shifts (change or no change) and also to identify the most critical and impacted areas. The obtained results can be used effectively in sustainable natural disaster management plans.

Keywords

LST • Landsat • NDVI • Rangelands

1 Introduction

Investigating LST variations is critical especially in areas which are facing various ecological disasters such as drought, climate change, etc. In fact, all the ecosystem components will be impacted if LST continues to rise in this way [1, 2, 3] as the human population and their needs are rising. Remote sensing data cover large areas and provide LST information through thermal bands [4, 3]. In addition, they provide information of plants on earth's surface by various vegetation indices such as NDVI (Normalized Difference Vegetation Index), EVI (Enhanced Vegetation Index), SAVI (Soil Adjusted Vegetation Index) etc. which can be used to evaluate plants health and production [5, 6]. Indeed, the feasibility of using LST data in regions which suffer from a lack of meteorological gauges has been emphasized in a great deal of research to explore temperature variations [7, 8]. Iran is one of the most sensitive places on earth which are facing serious challenges such as drought and climate change [9]. Moreover, most people's livelihood depends on fishing, livestock-animal husbandry, and traditional farming in the research area. Therefore, increasing LST is likely to become a real challenge for people who are living in the study area and become a serious critical problem (immigration, low income). The present study aimed to monitor LST shifts from 1987 to 2017 using the LST change detection technique and spatial analysis to identify areas which had experienced LST shifts.

2 Materials and Methods

2.1 Study Area

Research area is located in northeast Iran between 54° 4′ 16″–54° 24′ 30″E and 36° 53′ 30″–37° 22′ 11″N. The research area covers approximately 136.331 hectares, and covers more than 10 villages. The climate of the study area is arid and

M. Arekhi (✉)
Forest Engineering, Institute of Science, Graduate Education Institute, Istanbul University-Cerrahpaşa, 34452 Istanbul, Turkey
e-mail: maliheh.arekhi@ogr.iu.edu.tr

© Springer Nature Switzerland AG 2019

H. M. El-Askary et al. (eds.), *Advances in Remote Sensing and Geo Informatics Applications*,
Advances in Science, Technology & Innovation, https://doi.org/10.1007/978-3-030-01440-7_32

semi-arid (Fig. 1a). However, the Gulf of Caspian Sea in the study area is the place of breeding fish, which is drying up and most fishermen are complaining about the decrease in fishing compared to the past. Most people depend on fishing will be unemployed and they have to immigrate to other cities to meet their needs.

2.2 Landsat Data Processing and Data Analysis

Landsat 8 OLI (18 July 2017) and TM5 (16 July 1987) were used. We acquired data from the EarthExplorer (http://glovis.usgs.gov/) with Level 1T process level. After the image preprocessing, NDVI and LST maps were generated for both dates. All statistical parameters (min, max, SD, variance, mean, median, mode) were calculated for NDVI and LST [10] maps for each study date. NDVI and LST box plots were produced for each date. Additionally, the change detection technique and spatial analysis were performed to determine the areas that have experienced the highest and lowest LST changes between the two study periods. All the statistical and GIS analyses were processed in the R environment [11] and Qgis environment [12]. Research methodology is described in Fig. 1b.

3 Results and Discussion

Overall, LST mean in 2017 has increased significantly in comparison with 1987 (Table 1). As can be seen clearly, in 2017, the LST mean reached approximately to 42.5 °C with 9 °C increase, while in 1987, it was 33.8 °C. According to Table 1, the median and mode have increased with at least 10 °C in 2017 in most cases while both were approximately 34 °C in 1987. However, comparing the statistical analysis of NDVI data did not show any differences between the two study dates. All descriptive parameters of NDVI variable was nearly similar in both periods. As can be seen clearly in Fig. 1. in 1987, the LST study area was 36 °C compared to 2017, it reached to 42 °C. Yet, it can be clearly observed in the histogram frequency graph (Fig. 2). The LST box plots depict 36 °C to 49 °C range variations in 2017. In contrast, LST ranges were between 36 °C to 38 °C in 1987 (Fig. 2). Evaluating and monitoring the LST change detection map and performing spatial analysis showed that the wetland class had the highest rise with approximately 13 °C and rangeland areas is the second land cover class which has increased significantly between the two study dates with approximately 10 °C. Water covered areas had the smallest rise with roughly 4 °C increase between two study periods (Fig. 3). Landsat data provide great opportunity to investigate LST variations on Earth's surface features, which can be used in various studies such as climate change, environmental monitoring disaster management studies, and environmentally sustainable management. Performing LST change detection analysis and spatial analysis technique provide the LST shift anomalies to recognize regions which experienced the highest or lowest LST changes, which can be used for recognizing most sensitive areas between two study periods. The maximum, minimum, mean temperature was lower in 1987 in comparison to 2017 [13, 14]. In most conducted studies the main focus has been on evaluating LST spatial and temporal change and the shift in urban areas with LU/LC investigations, NDVI values range were almost similar in both study periods. However, in the present study, the research area covers various land use types mainly

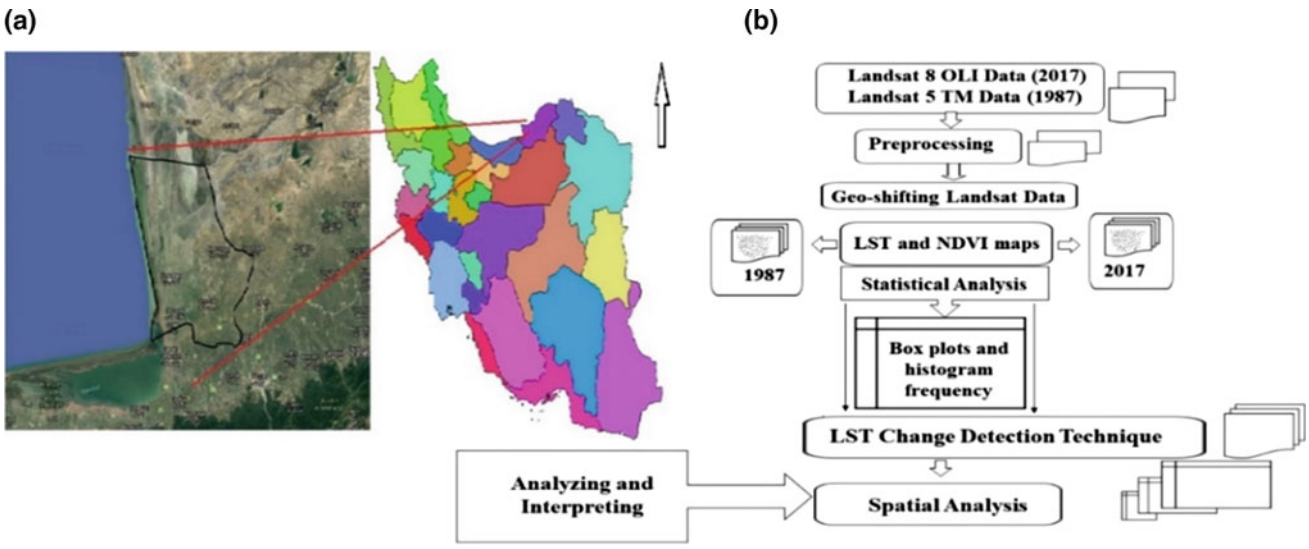

Fig. 1 Location of the study area (Path: 163, Row = 34) in Iran (**a**) and research methodology (**b**)

Table 1 LST and NDVI statistics for each study period

Variables	Min	Max	Mean	Std.	Var.	Median	Mode
2017 LST	26.546	48.544	42.484	3.301	10.899	43.183	44.497
1987 LST	24.544	50.285	33.817	2.893	8.373	34.461	34.461
2017 NDVI	−0.681	0.879	0.186	0.086	0.007	0.184	0.173
1987 NDVI	−0.553	0.754	0.154	0.117	0.013	0.158	0.162

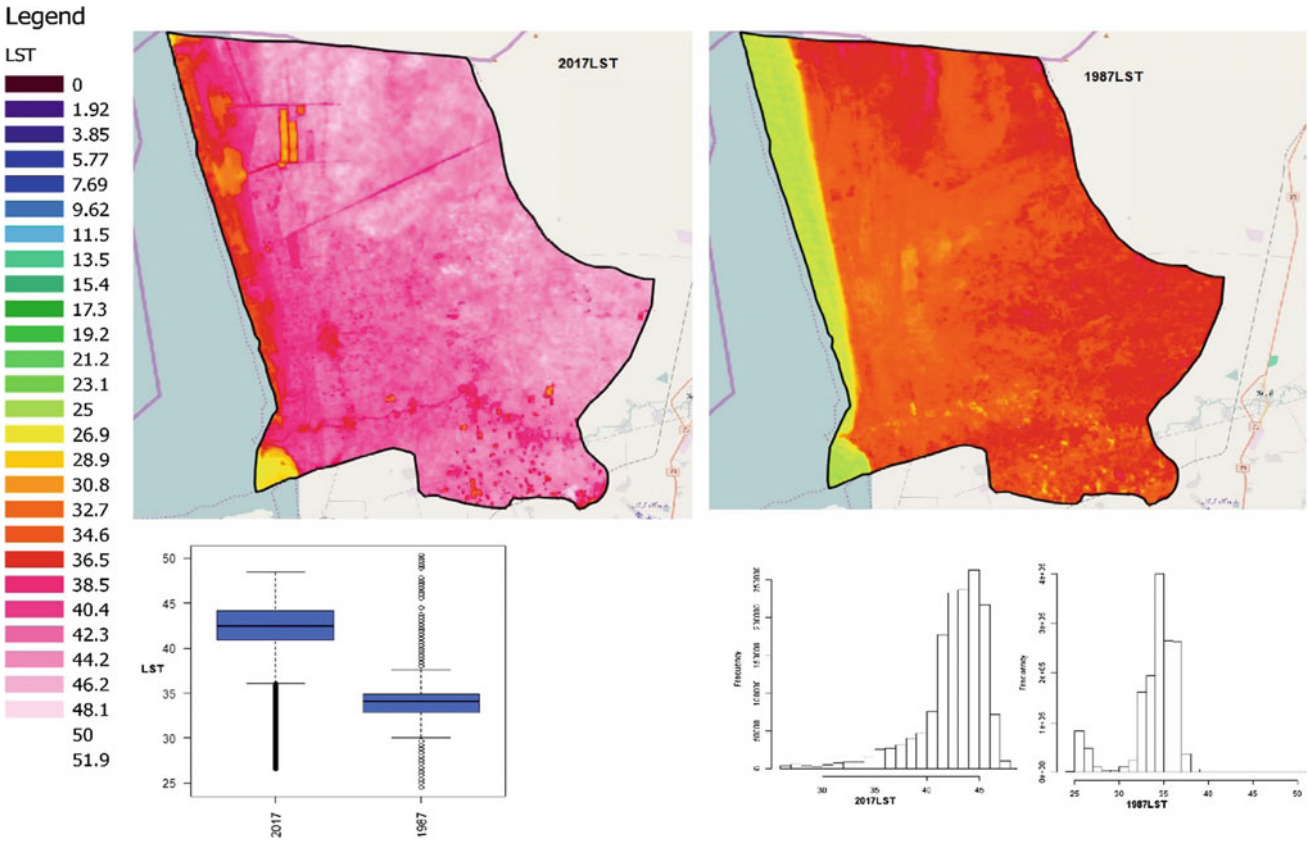

Fig. 2 LST map for 1987 and 2017 and its range values variations in °C

wetlands, bare lands, rangelands, and agricultural lands. The results showed that the highest LST changes were experienced in rangeland, wetland, and bare land areas with more than 10 °C rise which is consistent with the conducted studies [1, 9, 15].

Interestingly, urban and rural covered areas had least LST shifts which are not in agreement with other conducted studies which emphasized that urban areas had most increase in LST change between the two study periods [15–17]. However, agricultural lands had lower LST change in comparison with bare lands [9]. A number of studies have estimated the highest LST shifts in both bare lands and build up areas [2]. Using extracted LST from Landsat data can be effectively used especially in developing countries where a sufficient number of meteorological stations is not available.

4 Conclusion

Landsat LST data provide an extraordinary opportunity to monitor the thermal properties of the earth's surface, which is recognized as one of the most significant environmental factors in arid and semi-arid regions. In this paper, the importance of LST data in identifying regions that experienced thermal variations has been investigated using LST change detection technique and spatial analysis from 1987 to 2017. The current investigation proved that it is possible to determine and identify the most and least impacted areas by increased temperature applying the spatial analysis. The results showed that LST of rangelands, wetlands, and bare lands experienced more than 10 °C which can be critical in a

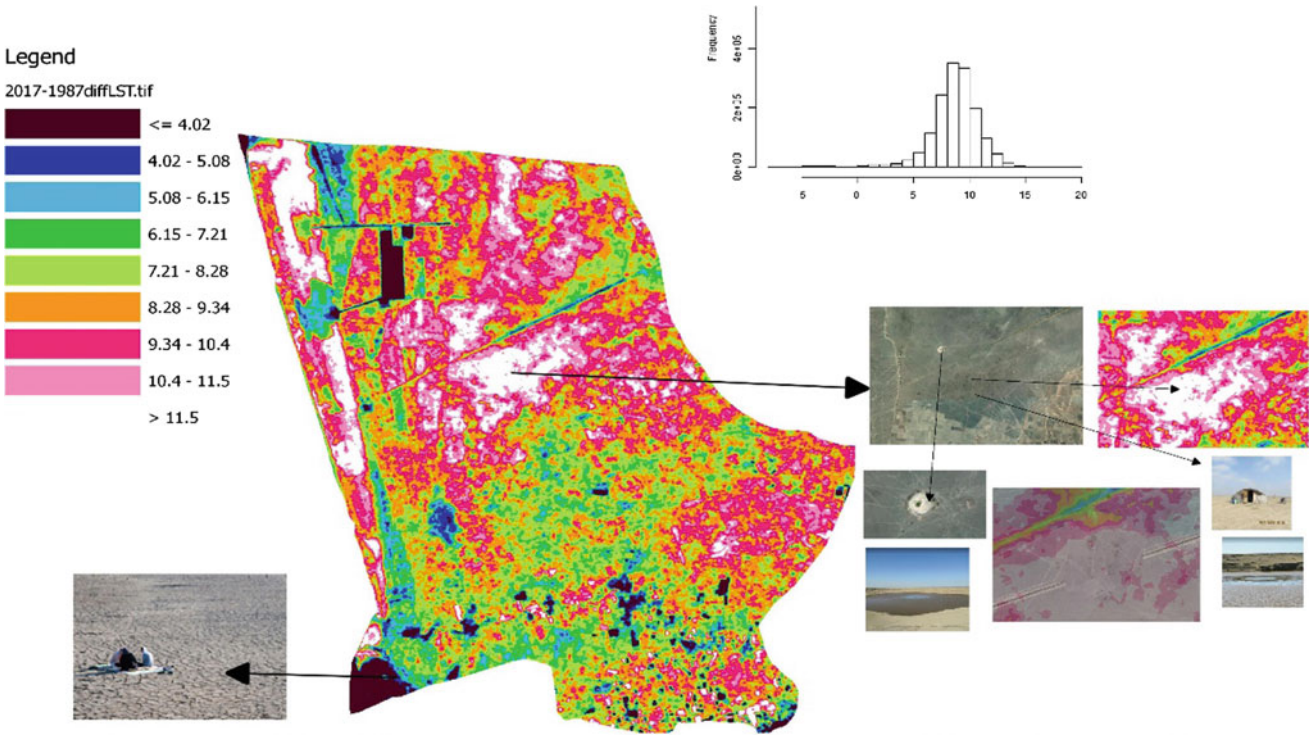

Fig. 3 LST change map between 1987 and 2017 and its change in °C

region that depends on livestock-animal husbandry and livestock. Additionally, the rising wetlands LST is likely to impact wildlife which immigrates annually from various parts of the world and the study area ecosystem. Moreover, another finding of the current study needs to be highlighted. The water class cover LST was enhanced with between 0 and 4 °C; this is likely to impact the living beings in the sea. We recommend that this approach can be taken into account especially in environmental monitoring studies which try to monitor the Earth features temperatures shifts. In future studies, we will consider LST change detection approach to identify the areas that had LST changes integrating socioeconomic data. These data include, but are not limited to, cropland products productivity, the number of livestock, fishing range shifts, population income, population health, landscape metrics, and the unemployment rate among young people to evaluate the correlation between LST and other variables in more than two periods. This research has a potential for mapping temperature variability using remotely sensed thermal infrared data. Findings are likely to contribute to understanding the variability in biomass distribution which can be investigated by available vegetation indices in various periods. Conducting similar research in different climates and other regions using different satellite data is recommended. Also, comparison of satellite-based LST data and ground-measured LST data has been suggested.

References

1. El-Zeiny, A.M., Effat, H.A.: Environmental monitoring of spatiotemporal change in land use/land cover and its impact on land surface temperature in El-Fayoum governorate Egypt. Remote Sens. Appl.: Soc. Environ. **8**, 266–277 (2017)
2. Zhou, X., Wang, Y.: Dynamics of land surface temperature in response to land-use/cover change. Geogr. Res. **49**(1), 23–36 (2011)
3. Arekhi, M., Yesil, A., Ozkan, U.Y., Sanli, F.B.: Detecting treeline dynamics in response to climate warming using forest stand maps and Landsat data in a temperate forest. For. Ecosyst. **5**(1), (2018)
4. Wang, S., Ma, Q., Ding, H., Liang, H.: Detection of urban expansion and land surface temperature change using multi-temporal landsat images. Resour. Conserv. Recycl. **128**, 526–534 (2018)
5. Xue, J., Su, B.: Significant remote sensing vegetation indices: a review of developments and applications. J. Sens. (2017)
6. Arekhi, M., Yılmaz, O.Y., Yılmaz, H. and Akyüz, Y.F.: Can tree species diversity be assessed with Landsat data in a temperate forest?. Environ. Monit. Assess. **189**(11), (2017)
7. Shuman, C.A., Comiso, J.C.: In situ and satellite surface temperature records in Antarctica. Ann. Glaciol. **34**, 113–120 (2002)
8. Brabyn, L., et al.: Accuracy assessment of land surface temperature retrievals from Landsat 7 ETM+ in the dry valleys of Antarctica using iButton temperature loggers and weather station data. Environ. Monit. Assess. **186**, 2619–2628 (2014)
9. Fathizad, H., Tazeh, M., Kalantari, S., Shojaei, S.: The investigation of spatiotemporal variations of land surface temperature based on land use changes using NDVI in southwest of Iran. J. Afr. Earth Sc. **134**, 249–256 (2017)

10. Weng, Q., Lu, D., Schubring, J.: Estimation of land surface temperature–vegetation abundance relationship for urban heat island studies. Remote Sens. Environ. **89**, 467–483 (2004)
11. RDevelopment Core Team, R. and Others R: A Language and Environment for Statistical Computing (2008)
12. Team, Q.D. and Others: Quantum GIS Geographic Information System. Open Source Geospatial Foundation Project (2014)
13. Zhang, F., et al.: Dynamics of land surface temperature (LST) in response to land use and land cover (LULC) changes in the Weigan and Kuqa river oasis, Xinjiang China. Arab. J. Geosci. **9**, 499 (2016)
14. Pal, S., Ziaul, S.: Detection of land use and land cover change and land surface temperature in English Bazar urban centre. Egypt. J. Remote Sens. Space Sci. **20**, 125–145 (2017)
15. Adeyeri, O., Akinsanola, A., Ishola, K.: Investigating surface urban heat island characteristics over Abuja, Nigeria: relationship between land surface temperature and multiple vegetation indices. Remote Sens. Appl.: Soc. Environ. **7**, 57–68 (2017)
16. Zhao, Z.-Q., He, B.-J., Li, L.-G., Wang, H.-B., Darko, A.: Profile and concentric zonal analysis of relationships between land use/land cover and land surface temperature: case study of Shenyang China. Energy Buildings **155**, 282–295 (2017)
17. Hereher, M.E.: Effect of land use/cover change on land surface temperatures-The Nile Delta Egypt. J. Afr. Earth Sci. **126**, 75–83 (2017)

Part IV

Lidar Drone and Emerging Technologies Applications

Remote Spectral Imaging Using a Low Cost sUAV System for Monitoring Rangelands

Mounir Louhaichi, Steven L. Petersen, Teresa Gomez, Ryan R. Jensen, Grayson R. Morgan, Chuck Butterfield, Russell Burton, and Chandrashekhar Biradar

Abstract

The recent introduction of low cost small unmanned aircraft systems (sUAS) to remote sensing has provided a significant improvement in the quantity and quality of high resolution imagery. The purpose of this research was to describe the acquisition of very high resolution imagery using sUAS (drones) and assess the effectiveness of spectral-based classification for distinguishing vegetation (species, total cover), percent bare ground, litter, and rock from this data. Images were obtained from a semiarid rangeland site in central Nevada, USA. Flight missions were flown 15 m above ground level using automated flight paths, and individual images were processed into orthomosaics using the Pix4D software. Features were classified using a spectral unsupervised classification. Ground-based measurements were collected in the field to compare rangeland structure with generated classification output. Results indicate that very high resolution imagery can be effectively used to assess rangeland ecosystems that can aid in rangeland assessment and monitoring. The ability to use sUAS to monitor ecosystem structure and condition can be an important resource for rangeland managers, as they improve their ability to access high quality data for making informed management decisions within and across multiple years.

Keywords

Vegetation indices • Trend • Unsupervised classification • Drone

1 Introduction

Monitoring changes in rangeland vegetation structure and understanding the dynamics of rangeland resources is becoming increasingly important for their sustainable management [1]. Monitoring rangeland dynamics can provide important information and inputs to the modelling of biogeochemical cycles, quantifying vegetation characteristics, and feedback on the effects of disturbances and resource availability [4]. The use of remote sensing, and in particular low cost small unmanned aircraft systems (sUAS) in rangeland management to monitor vegetation health and detect change in rangeland ecosystems has gained recent attention [4]. Scientists have increasingly turned to sUAS for use in research due to their accessibility, relatively low cost, and high quality data acquisition [3]. Current sUAS prices can be affordable ($800 US for DJI Mavik, $1500 US for DJI Phantom 4, $5700 for US DJI Inspire 2), compared to upper-end sUAS or more traditional aerial platforms ($12,000 US for Free fly Alta 6, $15,000 US for DJI Matrice, $42,000 US for DJI Matrice 600, and relatively high costs (thousands) for orthocorrected high resolution aerial surveys).

The low cost, wide availability, and high flexibility associated with the use of sUAS suggests that this technology can be easily deployed to work in a wide range of conditions including challenging weather conditions that are often faced by satellites and traditional airborne platforms [5]. As such, sUAS are uniquely positioned to address

M. Louhaichi (✉)
Department of Animal and Rangeland Sciences, Oregon State University, Corvallis, OR, USA
e-mail: m.louhaichi@cgiar.org

M. Louhaichi
International Center for Agricultural Research in the Dry Areas (ICARDA), Amman, Jordan

S. L. Petersen · T. Gomez
Department of Plant and Wildlife Science, Brigham Young University, Provo, UT, USA

R. R. Jensen · G. R. Morgan
Department of Geography, Brigham Young University, Provo, UT, USA

C. Butterfield · R. Burton
Y2 Consultants, Elko, NV, USA

C. Biradar
ICARDA, Cairo, Egypt

© Springer Nature Switzerland AG 2019

H. M. El-Askary et al. (eds.), *Advances in Remote Sensing and Geo Informatics Applications*, Advances in Science, Technology & Innovation, https://doi.org/10.1007/978-3-030-01440-7_33

critical environmental management-related questions, in ways that traditional remote sensing may not have been able to in the past [4]. Therefore, sUASs are establishing their place in the remote sensing toolkit, and users and regulators alike need to take steps to accommodate their use [2]. While the use of UAVs in developed countries has made considerable progress, their use in developing countries is still limited by security concerns, such as permission to fly and invasion of privacy [3]. Thus, the main objective of this research was to evaluate the capability and effectiveness of sUAS in obtaining accurate, high resolution aerial images that can be classified to determine rangeland structure. This information can then be used as a primary application in rangeland monitoring and assessment.

2 Method

Remote sensing imagery was collected along survey flight paths, flown 15 m above ground-level using an automated flight path that was established pre-flight using programmed mission planning software (i.e. Mission Planner, Drone Deploy) (Fig. 1).

Following sUAS flights, all images (RGB and CIR) and their associated log files (sUAS records GPS locations during the flight) were downloaded. Each image was geo-tagged to ensure proper alignment and overlap. A single georeferenced orthomosaic (composite image) was created for each research plot by compiling all images using Pix4D software. In cases where flight elevation was below 35 m, photoshop was used to mosaic images due to limited stitching capabilities at very high resolution in Pix4D. ESRI ArcGIS was used to display, manage and analyze each image.

Using ESRI ArcGIS Software, point and line features were created by digitizing along ground-based transect lines that could be observed within each orthomosaic. Set points were created along each line spaced 50 cm apart, resulting in a sample layout similar for both ground and remotely sensed data. Surface properties and species were determined using experience from data collected both ways. ENVI software was used to create an unsupervised classification. Using an Isodata algorithm, surface feature classes were created that included perennial vegetation, annual vegetation, and bare ground. An Accuracy Assessment and Kappa Statistic were calculated for each image for assesing reliabiltiy of the classificed imagery.

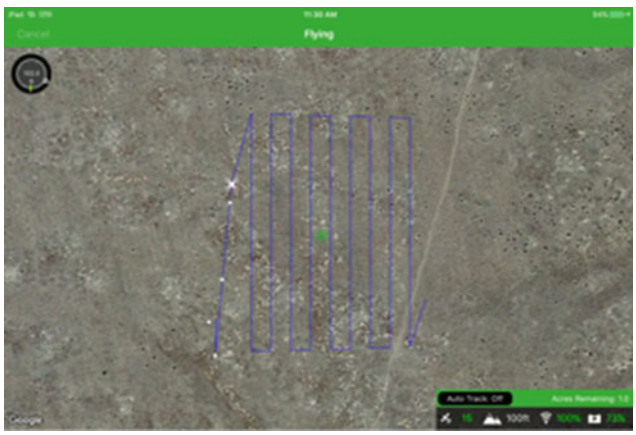

Fig. 1 Drone deploy software of the automated flight path flown by the DJI Phantom 4

3 Preliminary Results and Discussion

Preliminary results suggest that the use of UASs is effective in gathering high resolution (< 5 mm) data over heterogeneous rangeland landscapes producing clear, high quality imagery. These images can be accurately georeferenced and orthomosaiced producing reliable information for image classification and image analysis. For example, rangeland surface features were effectively classified into perennial vegetation (shrubs, perennial grasses and forbs), annual vegetation (annual grasses and forbs), litter, and bare ground (Fig. 2). Differences include healthy perennial vegetation (red patches in Fig. 2 right), bare ground (blue patches), and annual species/litter portion (yellow portion, Fig. 2 right). The Accuracy Assessment reflects high reliability in the ability to separate vegetation classes from each other and bare ground. This information demonstrates the efficacy of implementing sUAS linked with quality software to produce useful information for rangeland managers for improving rangeland assessment, health, and condition over time. These are also important in applications for grazing management. The next step of the project will determine the efficacy of using a drone to either supplement and/or replace detailed field measurements.

4 Conclusions

The use of sUAS is gaining increased attention in rangeland management and ecology, with application in land monitoring and site assessment. The research preliminary results demonstrate the utility of sUAS in generating high resolution and precise data with relatively low costs. Repeated data collection over seasons or years can provide a monitoring strategy useful in assessing variability and change in rangeland structure such as characterizing a decrease in rangeland resource availability or assessing the effectiveness of management intervention practices (i.e. rotational grazing). The use of sUAS will thus facilitate adaptive management of natural resources by providing an objective monitoring tool. Future research will include comparing field monitoring

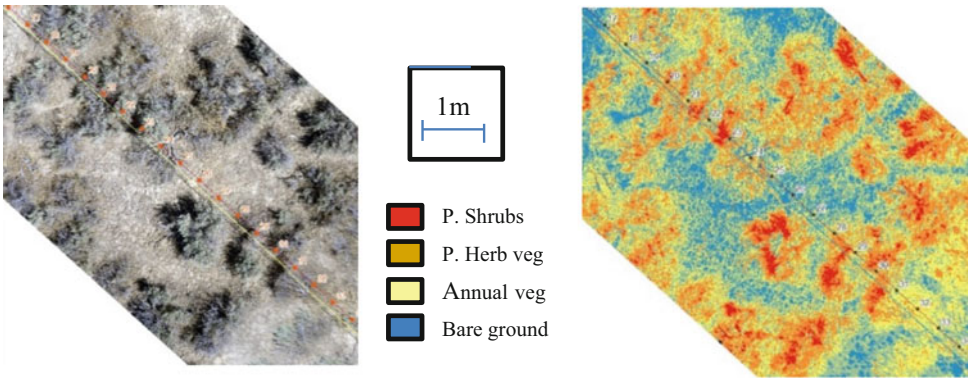

Fig. 2 Imagery taken from 15 m above ground level (left) and drone deploy Software of the automated flight path flown by the DJI Phantom 4 (right)

measurements with spectral classification results using UAS imagery. We expect this imagery to provide accurate estimates that will improve the monitoring of rangelands by enhancing a more efficient use of time, and other resources.

References

1. Breckenridge, R.P., Dakins, M., Bunting, S., Harbour, J.L., White, S.: Comparison of unmanned aerial vehicle platforms for assessing vegetation cover in sagebrush steppe ecosystems. Rangeland Ecol. Manage. **64**(5), 521–532 (2001)
2. Colomina, I., Molina, P.: Unmanned aerial systems for photogrammetry and remote sensing: A review. ISPRS J. Photogrammetry Remote Sens. **92**, 79–97 (2014)
3. Cummings, A.R., McKee, A., Kulkarni, K., Markandey, N.: The rise of UAVs. Photogrammetric Eng. Remote Sens. **83**(4), 317–325 (2017)
4. Rango, A., Laliberte, A., Steele, C., Herrick, J.E., Bestelmeyer, B., Schmugge, T., Jenkins, V.: Using unmanned aerial vehicles for rangelands: Current applications and future potentials. Environ. Pract. **8**(3), 159–168 (2006)
5. Vega, F.A., Ramírez, F.C., Saiz, M.P., Rosúa, F.O.: Multitemporal imaging using an unmanned aerial vehicle for monitoring a sunflower crop. Biosys. Eng. **132**, 19–27 (2015)

Correlation Between Surface Modeling and Pulse Width of FWF-Lidar

Fanar M. Abed

Abstract

Surface modeling is the process of creating a 3D representation of any surface by manipulating polygons, vertices, and edges in three dimensions. The 3D model represents a physical body using a collection of 3D points in space and connected by several geometric entities. These processes mainly depend on the scenario used to generate the 3D points and the filtering methodology. Lidar is an active remote sensing technique, which has rapidly developed over the last decades to remotely determine the geometry of the Earth's surface in a rapid and accurate way. However, the FWF-lidar system provides extra information for better 3D digital representation of the features and further improves the modelling for different applications. This paper discussed the correlation between FWF-lidar physical information and the potential to improve the quality of surface modeling. It also discusses the improvements in geometric point quality when integrating pulse width value in the filtering process based on a developed filtering scenario. In this scenario the pulse width value is used as an index to distinguish surface features and improve geometric filtering process. The scenario was tested and analyzed in vegetated and urban areas to show the improvements. The results show decreasing discrepancies between overlapping flight lines in terms of mean and STD values after integrating the pulse width values following Gaussian modeling.

Keywords

Remote sensing • Lidar • FWF • Filtering • Pulse width • 3D modeling

1 Introduction

Lidar is often favored for the collection of accurate information in a 3D space. FWF-lidar can capture the complete waveform of the backscatter signal thus enables distinguishing between echoes of a range smaller than the pulse length [3]. Complex and weak laser echoes can be detected towards improving modelling products [4]. It may increase the accuracy and resolution of the range measurements by providing users with a chance to interpret the physical backscatter signals of the individual pulses. This is achievable through pulse detection methods which give the user a significant opportunity to select the function which best fits the signal [1].

Waveforms are popularly modeled by a mathematical function such as the Gaussian distribution. Several studies have observed that the pulse width of the vegetation points is generally larger than that of terrain points [7]. Numerous approaches have been developed to achieve a more efficient pulse detection technique to serve wide applications. The Riegl LMS Q560 waveform system, used in this research, is highly similar to ideal Gaussian distributions and behavior. However, Gaussian models still suffer from limitations in range accuracy and resolution and thus limitations in pulse width parameter computations especially in vegetated areas where complex and weak pulses are acquired. The pulse width of the FWF echo delivers information about surface roughness, slope, scan angle, and the depth of the volumetric object [7]. This provides a promising source of information to better identify surface features [6]. Therefore integrating this information in filtering routines alongside the standard geometric information can enhance the results and provide a stronger solution than relying on the geometric information alone [5].

F. M. Abed (✉)
University of Baghdad, College of Engineering, Baghdad, Iraq
e-mail: fanar.mansour@coeng.uobaghdad.edu.iq

© Springer Nature Switzerland AG 2019

H. M. El-Askary et al. (eds.), *Advances in Remote Sensing and Geo Informatics Applications*,
Advances in Science, Technology & Innovation, https://doi.org/10.1007/978-3-030-01440-7_34

2 Case Study and Methodology

In this research, FWF—Lidar data of aerial platform used and manipulated over urban and rural areas above Raleigh Peak, Colorado, USA which were captured in May 2010 and consisted of multiple strips using Riegl LMS-Q560 scanner. Fractal Based Lidar Detection method, was designed and tested to deal with FWF—Lidar signals in this research [2]. Thereafter, a developed filtering scenario emerged to integrate pulse width value generated by the above routine to improve traditional filtering strategies. Lidar points were classified into ground and off ground points depending on their height difference to the local terrain estimate plus their pulse width value and number of returns. A post-processing step was performed to detect under-terrain outliers. Such points mainly come from under-ground erroneous echoes that were extracted during waveform processing. The filter is based on a robust local plane estimation of ground points. Points located above a given threshold were removed. This stage was performed to improve the potential and deliver classified points based on geometric information for first instance. However, as mentioned in the literature, there is a relationship between the shape of the waveform and the pulse width and amplitude parameters. This relation could improve erroneous results delivered from first stage of the filtering process. This successfully distinguishes among different Earth target features and discriminate smooth surfaces from rough surfaces. Therefore, a developed filtering strategy was applied on the results of the first stage. It was based on using a threshold value for the pulse width parameter of individual FWF echoes to differentiate rough and smooth surfaces using the number of returns as an additional constraint.

3 Results and Discussion

The developed filtering method can detect any non-ground points and remove them from the ground class successfully. The method was implemented and tested over different land cover areas and shows improved results. Figure 1 shows the results of the developed routine over vegetated and urban areas. It can be observed that filtering the vegetated and building points from ground points was successfully improved after integrating the pulse width values for individual echoes.

Further, a cross section from another interest area was selected to hold the statistics and show the performance of the developed strategy by comparing, matching and differencing between overlapping strips before and after pulse

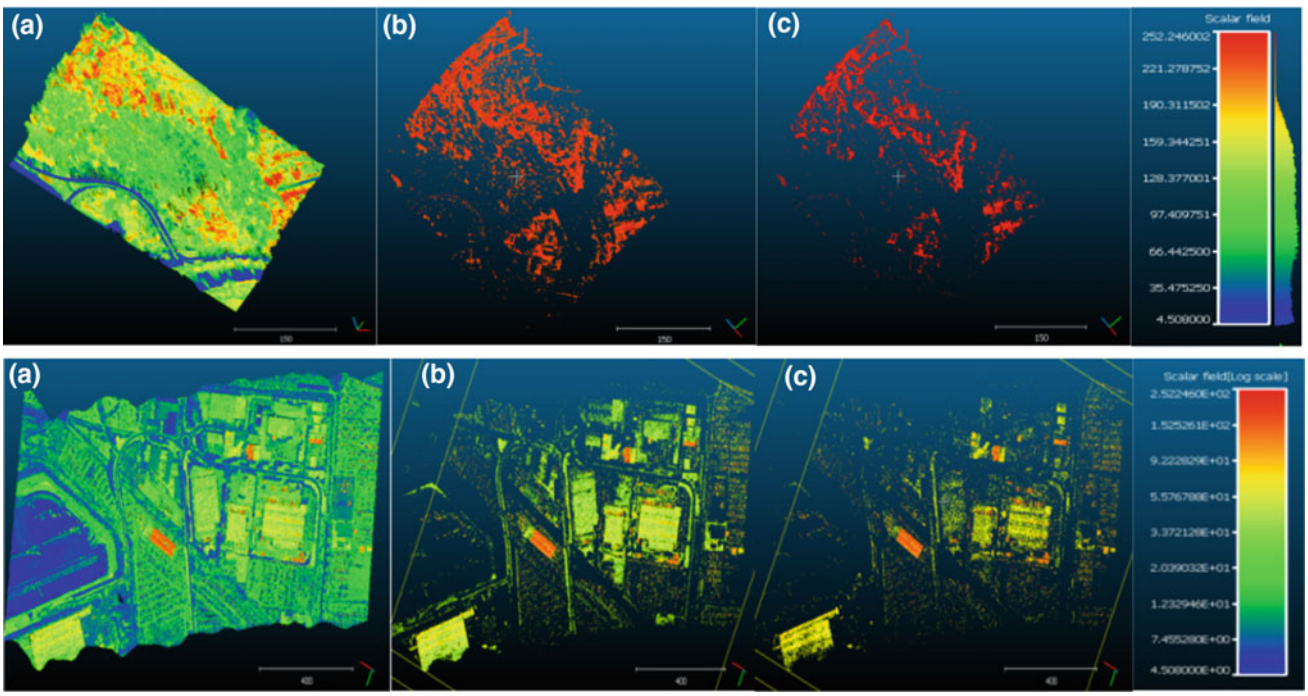

Fig. 1 Filtering results over (Top) vegetated area and (Bottom) urban area; **a** 3D point model **b** filtered 3D points without pulse width integration **c** filtered 3D points with pulse width integration

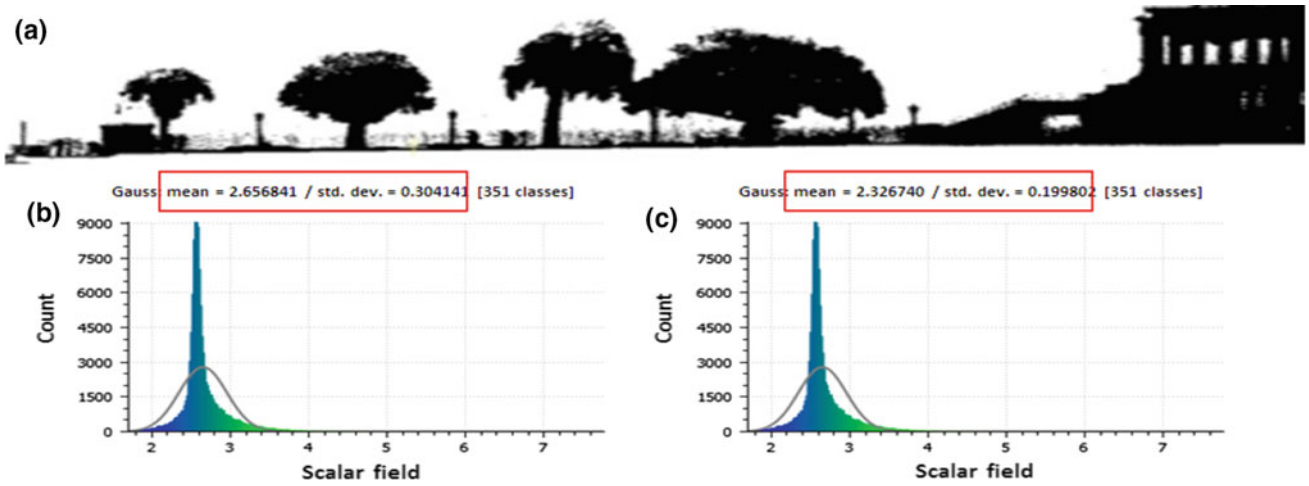

Fig. 2 Statistical analysis of a selected area showing decreasing discrepancies between two overlapping strips after pulse width integration in the filtering process; **a** cross section of 3D points model of the selected area **b** before pulse width integration **c** after pulse width integration

width integration. The statistical differences between two overlapping strips are shown in Fig. 2. It demonstrates that the standard deviation of differences between strips decreased dramatically after the pulse width integration.

4 Conclusion

The paper presented a filtering workflow of FWF-lidar data based on integrating a pulse width value to improve the distinguishing process between ground and non-ground points towards the improvement of 3D surface modeling applications. The pulse width value of FWF data was delivered by adopting a developed signal processing strategy based on fractal geometry algorithm. The filtering results show improvements against traditional filtering process which were based on pure geometric information. It also delivers more accurate 3D point clouds modeling following pulse width integration. Future works will focus on validating these results with reference ground targets to prove the efficiency of the suggested technique.

References

1. Abed, F., Mills, J., Miller, P.: Calibrated full-waveform airborne laser scanning for 3D object segmentation. Remote Sens. **6**(5), 4109–4132 (2014)
2. Abed, F., Altaie, M., Kzar, M.: Fractal theory based pulse detection analysis of ALS data. The Egypt. J. Remote Sens. Space Sci. (Submitted) (2018)
3. Jutzi, B., Stilla, U.: Range determination with waveform recording laser systems using a Wiener filter. ISPRS J. Photogram. Remote Sens. **61**(2), 95–107 (2006)
4. Lin, Y.-C., Mills, J., Smith-Voysey, S.: Rigorous pulse detection from full-waveform airborne laser scanning data. Int. J. Remote Sens. **31**(5), 1303–1324 (2010)
5. Mallet, C., Bretar, F., Roux, M., Soergel, U., Heipke, C.: Relevance assessment of full-waveform Lidar data for urban area classification. ISPRS J. Photogram. Remote Sens. **66**(6), S71–S84 (2011)
6. Shanoer, M., Abed, F.: Evaluate 3D laser point clouds registration for cultural heritage documentation. The Egypt. J. Remote Sens. Space Sci. (2017). https://doi.org/10.1016/j.ejrs.2017.11.007
7. Wagner, W., Ullrich, A., Ducic, V., Melzer, T., Studnicka, N.: Gaussian decomposition and calibration of a novel small-footprint full-waveform digitising airborne laser scanner. ISPRS J. Photogram. Remote Sens. **60**(2), 100–112 (2006)

An Innovative Technique for Estimating the Radius of Buried Cylindrical Targets Using GPR

Rim Ghozzi, Samer Lahouar, and Chokri Souani

1 Introduction

Geophysical prospecting methods are the most preferred, Non-Destructive Testing (NDT) techniques, for the detection of underground objects. Compared to other tools, these techniques are mainly characterized by their simplicity of implementation, measurement reliability and aptitude for geometric recognition. Ground Penetrating Radar (GPR) systems are commonly used as one of the NDT methods. They use electromagnetic (EM) waves to locate targets or interfaces buried within a medium. This technique has been, widely used in several fields such as geophysics [1, 2], environmental work [3] and engineering [4–6].

A particular application of GPR is the detection and radius estimation of buried utilities such as water and sewage pipes, natural gas conduits, cables, etc. The accuracy of the radius estimation of a buried object is important for urban underground engineering projects. Several solutions were, therefore, proposed in the literature to estimate the radius of buried cylindrical objects.

Among the published studies, radius information is determined in [7] using the hyperbola apex from radargram with the biases of human interaction. The authors in [8] have presented one model that relates the two-way travel time 't' to the horizontal position 'x' and the velocity of propagation 'v'. This model is based on the parabolic signature resulting from point reflectors at the top edge of buried reinforcing bars (rebar). The aim of this study was to determine the rebar cover-depth but the radius was not estimated. A new model was developed in [9] based on the hyperbolic signature that includes the radius R. Two basic techniques were used; an image processing technique to detect the hyperbolic shape based on edge-extraction techniques and a curve-fitting technique (a hyperbola-specific fitting algorithm). The adopted method showed its ability of radius estimation within 10%. Recently, in [10] a new method has been proposed to predict the diameter of underground pipeline filled with lossy medium. This method is based on a geometric association of the point reflectors at the top edge of the buried pipe and the probe positions using the shapes of semi-circles determined by the coordinates of three points. From these coordinates, a nonlinear system of three parameters (radius and x-y-coordinates of the underground pipe) is determined and solved.

The approach adopted in our work might be considered as an improvement to the technique presented in [10] allowing this method more accuracy and simplicity. In fact, the necessary steps in our work are: (i) the detection of the signature resulting from a buried cylindrical object, and (ii) the estimation of its radius using a special geometric model. The data used to validate our technique were obtained using the EM simulation software gprMax.

2 Method

It is known that when a moving, GPR receives EM signals reflected by a transversally buried cylindrical object, the resulting radargram contains a signature. This signature is obtained from the reflected signals at the top interface of the cylinder. The radius of the latter can thus be determined using the shape of the signature as measured from the radargram. To estimate this radius certain steps should be carried out.

R. Ghozzi (✉) · S. Lahouar · C. Souani
Microelectronic and Instrumentation Laboratory, Faculty of Sciences Monastir, University of Monastir, Monastir, 5019, Tunisia
e-mail: ghozzi.rym@gmail.com

R. Ghozzi
National School of Engineers of Sousse, University of Sousse, Sousse, 4023, Tunisia

S. Lahouar
Center for Research in Microelectronics and Nanotechnology, Technopole of Sousse, Sousse, 4054, Tunisia

C. Souani
Higher Institute of Applied Sciences and Technology of Sousse, University of Sousse, Sousse, 4003, Tunisia

© Springer Nature Switzerland AG 2019

H. M. El-Askary et al. (eds.), *Advances in Remote Sensing and Geo Informatics Applications*,
Advances in Science, Technology & Innovation, https://doi.org/10.1007/978-3-030-01440-7_35

The first step consists in determining the envelope of each reflected signal in the radargram using a Hilbert Transform as detailed in [11]. The peaks of this envelope will then be detected during the second step. The shapes of the curves formed by the peaks of adjacent reflected signals are an indication of the presence of a buried object. The final step consists in estimating the radius of the cylinder by fitting the detected peaks to a mathematical model obtained by applying the Pythagorean Theorem as explained in [12]. The model is given by the following equation:

$$t = \frac{2\sqrt{\varepsilon_r}}{c}\left[\sqrt{x^2 + (d_0 + R)^2} - R\right] \quad (1)$$

where: t is the peak two-way travel time, 'X' is measurement position, 'R' is the radius, 'd_0' is the depth of the cylinder, 'ε_r' is the relative permittivity of the medium, and 'c' is the speed of light in free space (c = 0.3 m/ns). The cylinder depth and relative permittivity of the medium are considered known in our model.

The previous steps were tested on a 2D structure containing multiple buried cylindrical objects as shown in Fig. 1a. This model is similar to the one used in [10]. The model contains four water-filled cylinders buried at different depths. The simulation domain has a height of 5 m and a width of almost 10 m and is made up of two layers. The first layer (air) has a thickness of 0.5 m. It contains the transmit/receive antennas. The second layer consists of clay of a relative permittivity $\varepsilon_r = 8$ and an electrical conductivity $\sigma = 0.01$ mS/m. This layer contains the four buried cylinders. Figure 1b shows the radargram obtained by gprMax on the tested structure with a highlight of the cylinders signatures.

3 Data Analysis and Results

The application of the first two processing steps, as described in the previous section, to simulated data obtained from gprMax allows detecting the peaks corresponding to the signature of each cylinder as shown in Fig. 2.

The final step consists in estimating the radius of the cylinder using nonlinear curve fitting of the detected peaks to the mathematical model in Eq. (1). The estimated radius results obtained by our technique are reported in Table 1 along with the results reported by [10].

The performance of our technique was evaluated by computing the Mean Absolute Percentage Error (MAPE) defined as follows:

$$\text{Relative Error (RE)} = \frac{|\text{estimated radius} - \text{true radius}|}{\text{true radius}} \times 100 \quad (2)$$

The MAPE is then calculated as the mean of all RE:

$$\text{MAPE} = \frac{1}{n}\sum \text{RE} \quad (3)$$

As it can be seen in Table 1, our proposed technique could estimate the radius of buried cylinders with a mean

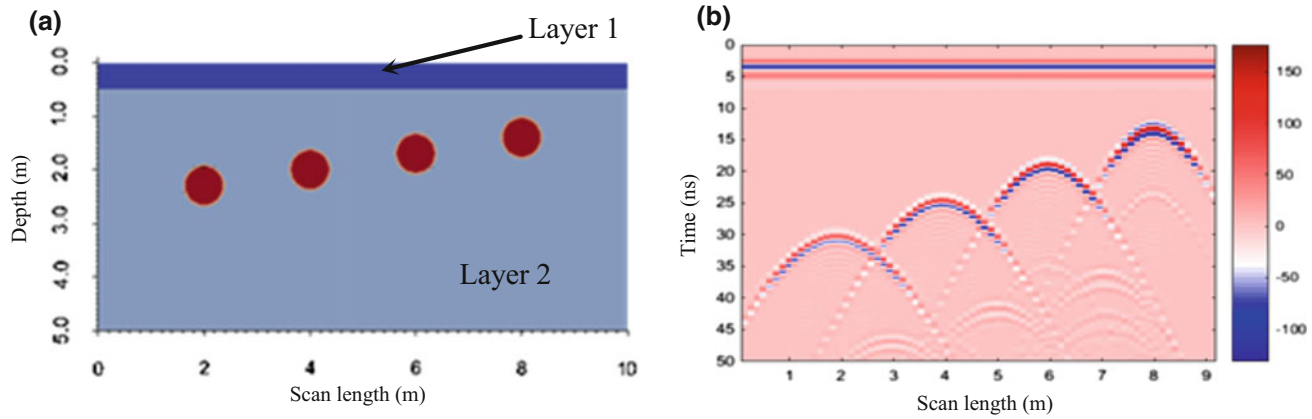

Fig. 1 **a** 2D simulated structure. **b** Radargram obtained by gprMax and showing the signatures of water-filled cylinders buried at different depths

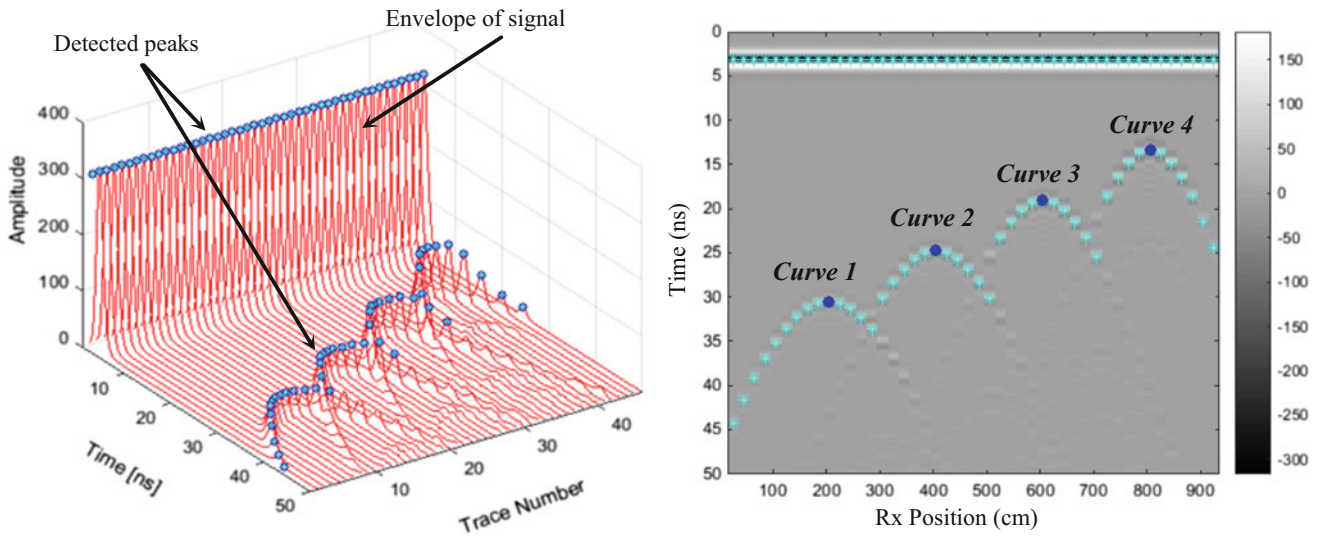

Fig. 2 Envelope determination and detection of the GPR signature of each cylinder

Table 1 Relative radius estimation error for cylinders buried at different depths

Cylinder depth (m)	True radius (cm)	Estimated radius (cm)		Relative error (%)	
		[10]	Our model	[10]	Our model
1.4	40	41.5	40.3	3.75	0.75
1.1	40	41.2	40.4	3.00	1.00
0.8	40	40.8	40.1	2.00	0.25
0.5	40	40.6	40.0	1.50	0.00
			MAPE (%)	2.56	0.50

error of 0.5% whereas the technique proposed in [10] could estimate the same parameter with a mean error of 2.56%.

4 Discussion

The technique developed in this work for estimating the radius of buried cylinders from GPR data, showed that it outperforms the technique described in [10] for different cylinder depths. This is mainly due to the fact that our method uses multiple points selected from the cylinder GPR signature to estimate the radius whereas [10] uses only 3 points. It is also noted that for both techniques the relative error in radius estimation increases with depth. This is primarily caused by the reduction of the reflections amplitudes of deeper cylinders, which deteriorates the peak detection procedure accuracy and thus increases radius estimation errors.

It should be noted that since the performance evaluation of the proposed technique was carried out on noiseless simulated GPR data, more work should be carried out to study the effects of added noise on the radius estimation accuracy. The technique should also be evaluated on real GPR data collected on buried cylinders with known radii.

5 Conclusion

In this paper, we developed a new technique to solve the problem of radius estimation of buried cylindrical objects from GPR data. This technique is based on: (i) accurately detecting and locating the peaks of the envelope of each reflected signal, which form the cylinder signature, and (ii) fitting the detected peaks to a developed mathematical model. This curve fitting procedure allows the estimation of the radius, which is a parameter in the model.

A performance evaluation of the proposed technique on simulated GPR data generated by the software gprMax showed that it has a MAPE of 0.5%, which is much lower than what was reported in a previous study for the same test conditions (2.56%). Further investigation of the developed technique performance should be carried out using real GPR data.

References

1. Ardekani, M.R.M.: Off- and on-ground GPR techniques for field-scale soil moisture mapping. Geoderma **200–201**, 55–66 (2013). https://doi.org/10.1016/j.geoderma.2013.02.010
2. Gomez-Ortiz, D., Montesinos, F.G., Martin-Crespo, T., Solla, M., Arnoso, J., Velez, E.: Combination of geophysical prospecting techniques into areas of high protection value: Identification of shallow volcanic structures. J. Appl. Geophys. **109**, 15–26 (2014). https://doi.org/10.1016/j.jappgeo.2014.07.009
3. Ma, C.G., Zhao, Q., Huo, J.J., Chang, X.H., Ran, L.M.: Single Borehole radar for well logging in a limestone formation: experiments and simulations. J. Environ. Eng. Geophys. **21**, 201–213 (2016). https://doi.org/10.2113/jeeg21.4.20
4. Arosio, D., Munda, S., Zanzi, L., Longoni, L., Papini, M.: GPR investigations to assess the state of damage of a concrete water tunnel. J. Environ. Eng. Geophys. **17**, 159–169 (2012). https://doi.org/10.2113/JEEG17.3.159
5. Oliveira, D.B., Vieira, D.A.G., Lisboa, A.C., Goulart, F.: A well posed inverse problem for automatic pavement parameter estimation based on GPR data. NDT E Int. **65**, 22–27 (2014). https://doi.org/10.1016/j.ndteint.2014.03.008
6. Solla, M., Asorey-Cacheda, R., Nunez-Nieto, X., Conde-Carnero, B.: Evaluation of historical bridges through recreation of GPR models with the FDTD algorithm. NDT E Int. **77**, 19–27 (2016). https://doi.org/10.1016/j.ndteint.2015.09.003
7. Olhoeft, G.R.: Maximizing the information return from ground penetrating radar. J. Appl. Geophys. **43**, 175–187 (2000). https://doi.org/10.1016/s0926-9851(99)00057-9
8. Al-Qadi, I.L., Lahouar, S.: Measuring rebar cover depth in rigid pavements with ground-penetrating radar. Construction **1907**, 81–85 (2005). https://doi.org/10.3141/1907-09
9. Shihab, S.: Radius estimation for cylindrical objects detected by ground penetrating radar. Sens. Imaging **6**, 151–166 (2005). https://doi.org/10.1007/s11220-005-0004-1
10. Zhang, P., Guo, X.X., Muhammat, N., Wang, X.D.: Research on probing and predicting the diameter of an underground pipeline by GPR during an operation period. Tunn. Undergr. Space Technol. **58**, 99–108 (2016). https://doi.org/10.1016/j.tust.2016.04.005
11. Ghozzi, R., Lahouar, S., Achmad Louis, S., Souani, C., Besbes, K.: Extraction of geometric parameters of underground tube using GPR. In: International Conference on Control, Automation and Diagnosis (ICCAD), Hammamet-Tunisia (2017). https://doi.org/10.1109/cadiag.2017.8075631
12. Ghozzi, R., Lahouar, S., Souani, C.: The estimation of buried empty cylindrical tubes characteristics using GPR. In: Advanced Technologies for Signal & Image Processing (ATSIP'2018), Sousse, Tunisia (2018). https://doi.org/10.1109/atsip.2018.8364486

Classification of Landslide Features Using a LiDAR DEM and Back-Propagation Neural Network

Jee-Cheng Wu and Chia-Hao Chang

Abstract

The purpose of this research was to detect landslide features using a light detection and ranging (LiDAR)-based digital elevation model (DEM) and back-propagation neural network (BPNN). The study area is in north-east of Taiwan. A high-resolution LiDAR-based DEM was used. Six training and four testing data sets were selected and manually digitized on landslide features were used as ground truth data. The relationship between landslide features and six trigger factors (slope angle, area solar radiation, roughness, profile curvature, plan curvature, and topographic wetness index) was computed from the LiDAR-based DEM. The experimental results indicated that the overall accuracy and kappa accuracy of the classification of landslide features using the BPNN algorithm were 0.950 and 0.772, respectively.

Keywords:

Back-propagation neural network • Gradient descent learning algorithm • Landslide feature

1 Introduction

Sudden and rapid landslide events are often associated with catastrophic effects on human lives, environmental degradation and different types of property damage. A cluster of triggering factors, such as geology, landscape age, intense rainfall and earthquakes, can significantly influence the geomorphic expression of landslides in the landscape. Currently interferometric synthetic aperture radar (InSAR) and light detection and ranging (LiDAR) are widely used for landslides investigations [1] because these techniques can identify useful topographical features.

J.-C. Wu (✉) · C.-H. Chang
National I-lan University, Yi-lan City, 260, Taiwan, ROC
e-mail: wujc@niu.edu.tw

Furthermore, back-propagation neural network (BPNN)-based classifiers have been successfully used in remote sensing applications because they can adapt to different types of data and inputs, overcome mixed pixel problems by providing a fuzzy output, and handle multi-source data [2].

In this study landslide triggering factors were computed using a 1 × 1 m high-resolution LiDAR-based DEM, and a BPNN classifier was trained and predicated to classify landslide features from the trigger factors and ground truth.

2 Methodology

The methodology followed in this study can be divided into three steps. In the first, six geomorphic factors are computed from the LiDAR-based DEM as input data for the BPNN classifier. In the second step, a three-layer BPNN is selected to classify the landslide features. The BPNN consists of (a) one input layer that contains six input variables, (b) one hidden layer with seven nodes, (c) one output layer that contains one output variable, and (d) connection weights that connect all the layers. The six geomorphic input variables are input to the BPNN classifier via a supervised approach as shown in Fig. 1. In the last step, the classification accuracy is evaluated as an overall accuracy and kappa accuracy.

3 Results and Discussion

3.1 Data Used

The LiDAR-based DEM data for the Provincial Highway Route 8 was collected by the Fourth Maintenance Office, Directorate General of Highways, Ministry of Transportation and Communications (MOTC), Taiwan as shown in Fig. 2. Auxiliary data such as landslide locations and types of landslide features that left discernable traces in an area were compiled by the Central Geological Survey of the Ministry of Economic Affairs (MOEA).

© Springer Nature Switzerland AG 2019

H. M. El-Askary et al. (eds.), *Advances in Remote Sensing and Geo Informatics Applications*,
Advances in Science, Technology & Innovation, https://doi.org/10.1007/978-3-030-01440-7_36

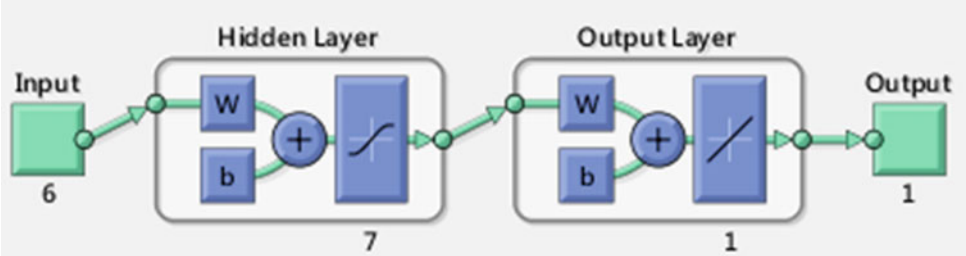

Fig. 1 Schematic diagram of the BPNN classifier used in this study

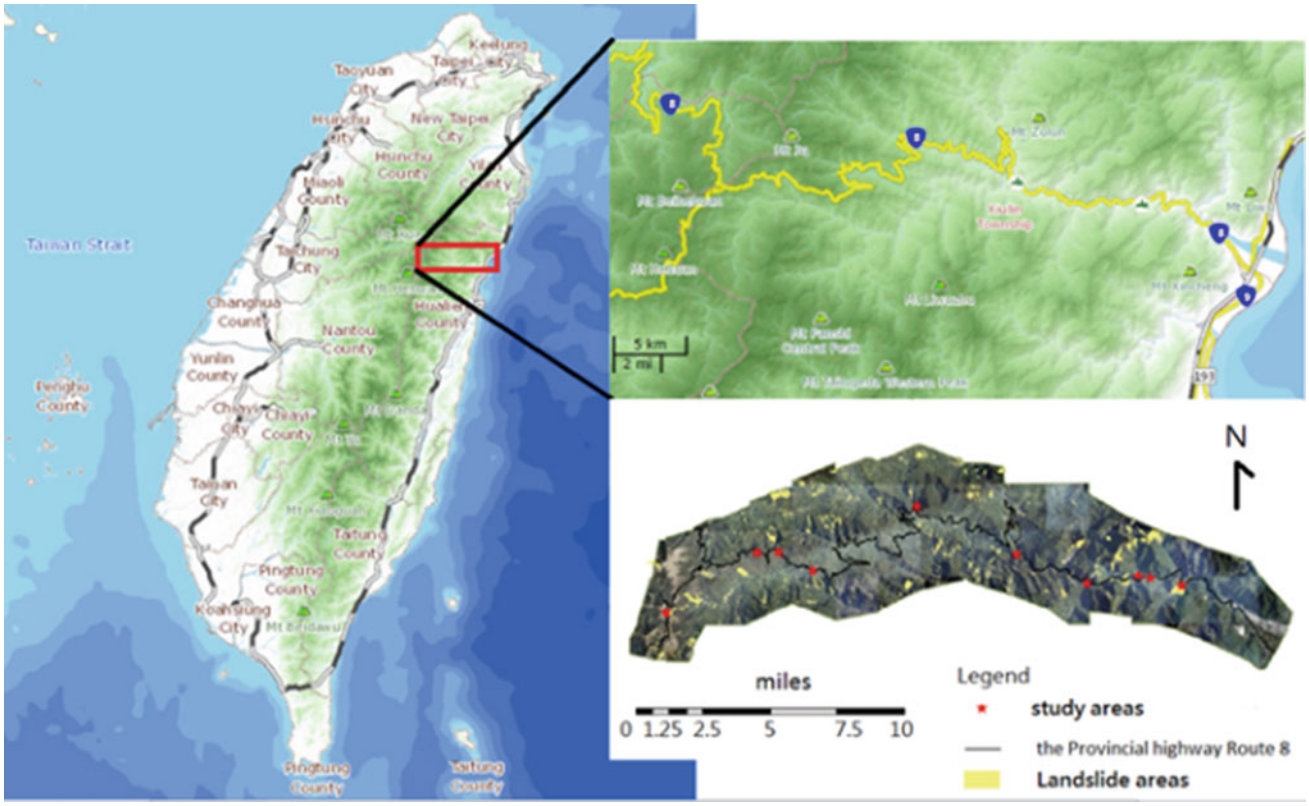

Fig. 2 Map of the study area, Hualien County, Taiwan, R.O.C

3.2 Data Generated

Ten landslide sites were selected, and for each site, six trigger factors (slope angle, area solar radiation, roughness, profile curvature, plan curvature and topographic wetness Index) were determined from the LiDAR-based DEM.

3.3 The BPNN Classifier

The gradient descent with momentum (GDM) of BPNN was used. The BPNN was trained using six randomly selected site examples that were associated with the input trigger factors of landslides to predict the output landslide features. Through trial and error, the learning rate was set at 0.5, and the initial weights were randomly selected. The momentum factor was set at 0.5. The learning process and training performance of the BPNN are shown in Fig. 3.

3.4 Classification Map

The classification map of landslide features was acquired by calculating the weights determined through back propagation and from a randomly selected testing data set as shown in Fig. 4.

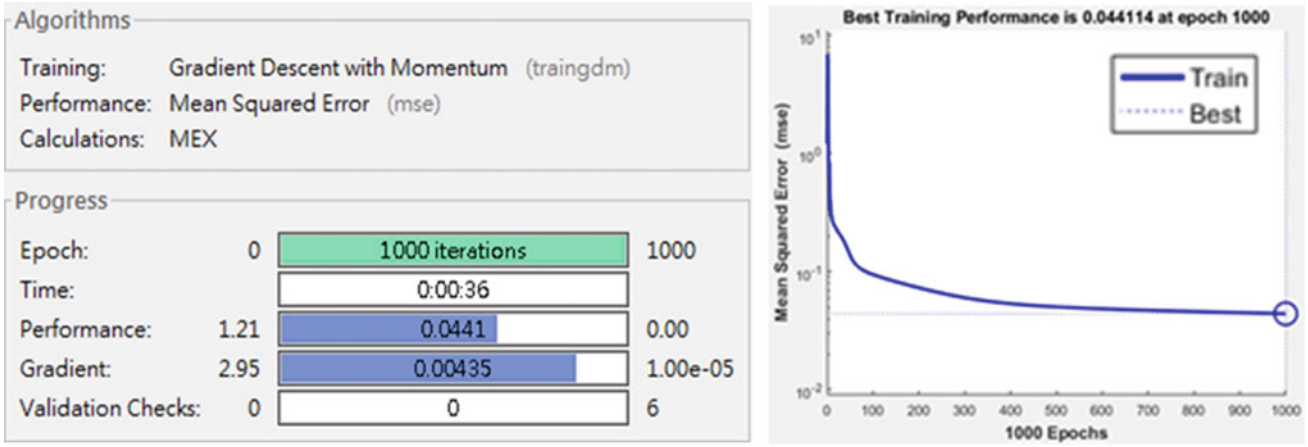

Fig. 3 The learning process of the BPNN (left) and its training performance (right)

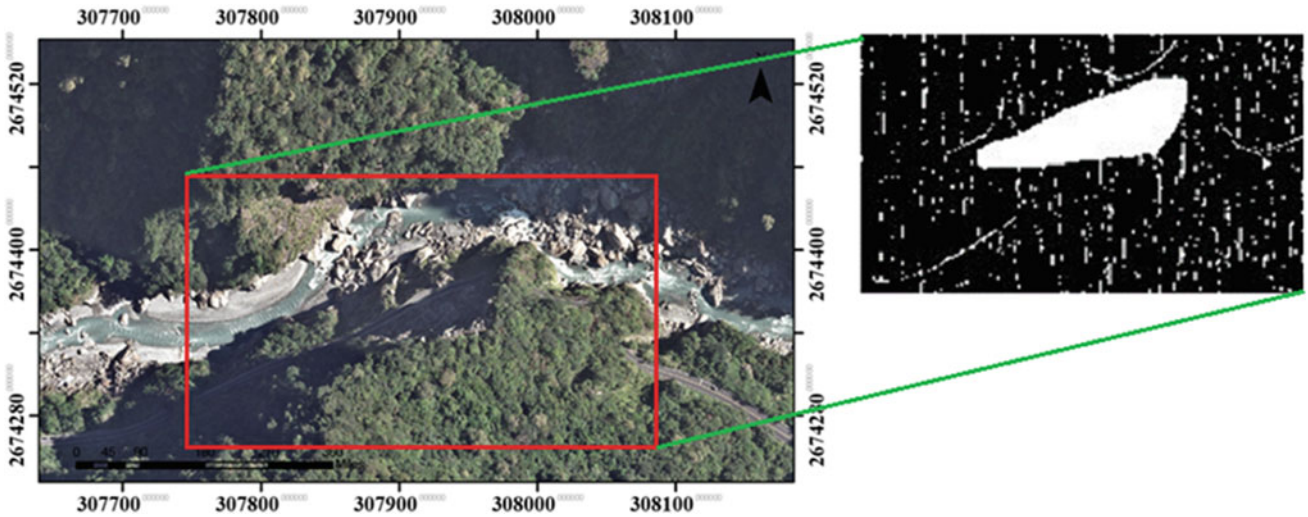

Fig. 4 Location of the testing site (left) and the classification map of the testing set (right)

Table 1 Confusion matrix of the testing site

		Reference data				
		Scarp	Landslide main body	Non-landslide area	Total	Users acc.
Classified data	Scarp	84	58	0	142	59.2%
	Landslide main body	0	2080	0	2080	100%
	Non-landslide area	4	1048	19098	20150	94.8%
	Total	88	3186	19098	22372	
	Prod. acc.	95.5%	65.3%	100%		
	Overall accuracy: 95.0%					
	Kappa accuracy: 77.2%					

3.5 Evaluation of the Classification Map Accuracy

The obtained classification map consists of three landslide features, landslide main body, non-landslide area, and scarp. The confusion matrix shows that the classification map overall accuracy and kappa accuracy were 95.0% and 77.2%, respectively, as shown in Table 1.

3.6 Discussion

This research demonstrates that a high classification accuracy can be achieved with the GDM-BPNN. However, we need to follow a trial and error method at the training stage because the classification accuracy varies with the BPNN structure, input and training data preparation methods, and selected parameters.

4 Conclusion

In this study, a GDM-BPNN consisting of six input variables (input layer), seven nodes (hidden layer), and one variable (output layer) was applied using the MATLAB software package. The input landslide trigger factors were computed from a LiDAR-based DEM. The obtained results show that the proposed approach is a useful tool for the classification of landslide features in landslide prone areas.

References

1. Zhao, C., Lu, Z.: Remote Sensing of Landslides—A Review. Remote Sensing **10**, 279 (2018)
2. Mezaal, M.R., Pradhan, B., Sameen, M.I., Shafri, H.Z.M., Yusoff, Z.M.: Optimized Neural Architecture for Automatic Landslide Detection from High-Resolution Airborne Laser Scanning Data. Applied Science **7**, 730 (2017)

Building Hights and Floor Estimation Using 3D Maps, Central Part of Kucukcekmece, Istanbul, Turkey

Arzu Erener, Gulcan Sarp, and Muhammet İbrahim Karaca

Abstract

The estimation of accurate, fast and up-to-date building and building floor data is inevitable for 3D urban map projects. These maps mostly required for tracking building construction speed, monitoring horizontal and vertical urban growth and illegal constructions, updating building inventories, preparing feasible urban plans, assessment of hazard and risk and creating infrastructure plans. Up-To-Date the passive remote sensing technologies are to detect and map urban features and to obtain land use and land cover maps. They can record large and continuous land cover information in urban areas. The buildings can be perceived as different from each other in urban areas by using high-resolution remote sensing images. For this reason, high-resolution satellite imagery is very useful for obtaining areas and locations of buildings that are difficult to identify compared to medium resolution satellite imagery. However, these systems have several constraints in creating 3D maps of urban features and detecting urban building heights. Active sensors can overcome some of these constraints when used together with passive systems. These systems create highly accurate 3D height maps for buildings, therefore, can be used to estimate an accurate floor value for each building in urban areas. 3D building detection studies have shown that the Lidar technique is promising and suitable for 3D object detection. In this study, a combination of aerial photograph and Lidar data were used to produce individual building heights and then estimate building floor in the urban central part of Kucukcekmece, Istanbul. The accuracy of the proposed algorithm was evaluated for each building floor using ground truth data and has proved an overall accuracy of 79% and a kappa equal to 0.74 which is a promising result.

Keywords

Lidar technique • Building floor estimation
3D maps • Urban areas

1 Introduction

In recent years, the three-dimensional (3D) city modeling in a Geographic Information Systems (GIS) environment has attracted more attention in engineering and non-engineering applications. The 3D modeling and visualization of buildings in a computer environment have become more convenient with the large memory, processing, handling and graphics power of today's hardware [4]. These methods play a crucial role in the creation, analysis, and visualization of 3D [3].

In fact, airborne and terrestrial LIDAR has a quite significant data source for producing more detailed Digital Surface Model (DSM) [6]. This technique offers an accurate, useful, and cost-effective means to generate wide area elevation information. There are various research projects carried out to make detailed 3D virtual scenes of building models by using laser, LIDAR [1, 2, 5] In this study, a combination of aerial photographs and LIDAR data was used to produce individual building heights and then estimate building floor in the urban central part of Kucukcekmece, Istanbul—Turkey.

2 Data Used in the Study

In the study, 30 cm sampling range of the LIDAR point cloud data, aerial photograph with a spatial resolution of 10 cm, building trace map and building height data in Excel format were used for the analysis (Fig. 1).

A. Erener (✉) · M. İ. Karaca
Department of Geomatic Engineering, Kocaeli University, 41380 Kocaeli, Turkey
e-mail: arzu.erener@kocaeli.edu.tr

G. Sarp
Department of Geography, Süleyman Demirel University, 32260 Isparta, Turkey

© Springer Nature Switzerland AG 2019

H. M. El-Askary et al. (eds.), *Advances in Remote Sensing and Geo Informatics Applications*,
Advances in Science, Technology & Innovation, https://doi.org/10.1007/978-3-030-01440-7_37

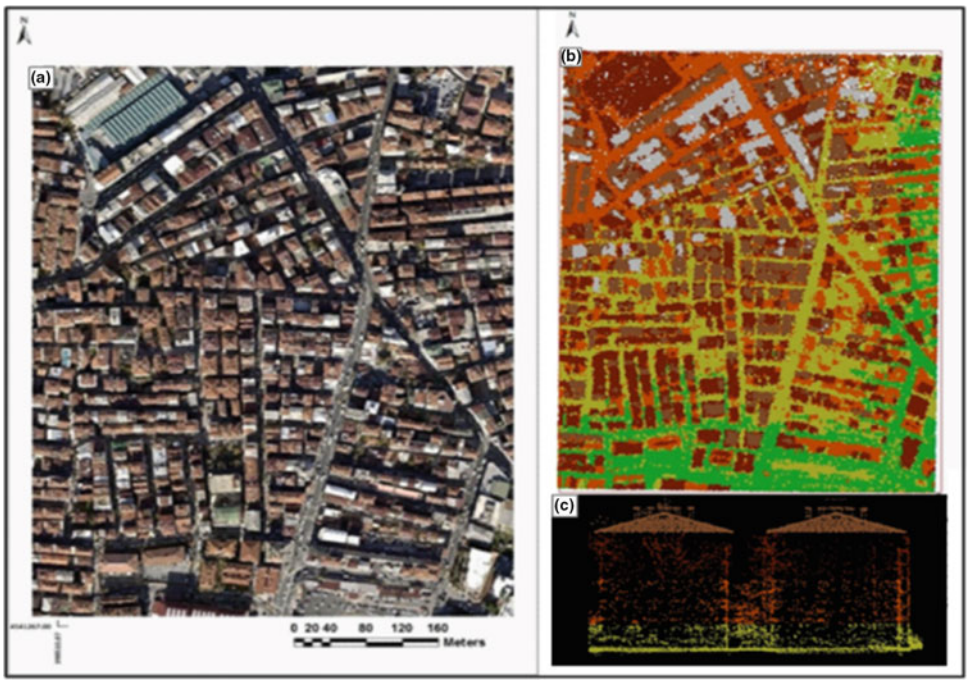

Fig. 1 Data used in the study. The aerial photo in (**a**), Point cloud in (**b**), and **c** 3D representation of the LIDAR data

3 Method of the Study

The applied methodology for the building height determination is summarized in the Fig. 2.

In the first step of the study, building and bare land surface point clouds data were determined by integrating orthophoto and LIDAR data. According to this, the points on the building were eliminated by comparing them on orthophoto. In the second step, DSM including the objects with their heights above the ground as well as the topography and Digital Terrain Model (DTM), including the earth surface without buildings, artificial man-made objects, and vegetation were determined using the TIN algorithm (Fig. 3a, b). Then normalized Digital Surface Model (nDSM) was calculated by subtracting DTM from the DSM. The nDSM data obtained within the scope of the study represent the height information of the building (Fig. 3c).

In the third stage, building floor value collected from the area was used for the accuracy of this height information. For building floor estimation, the nDSM height information of each building under the building trace map has been transferred to building trace map database. The map will best represent the height of the midpoint of each building on the building. For this reason, the point of each building on the building trace map has been shifted to the middle point. Here, each point can represent different floors belonging to the same building (roof, terrace, porch, etc.). The points representing each building are then overlaid with nDSM and the height data in the raster cell value is assigned to the building track database in dot form (Fig. 4).

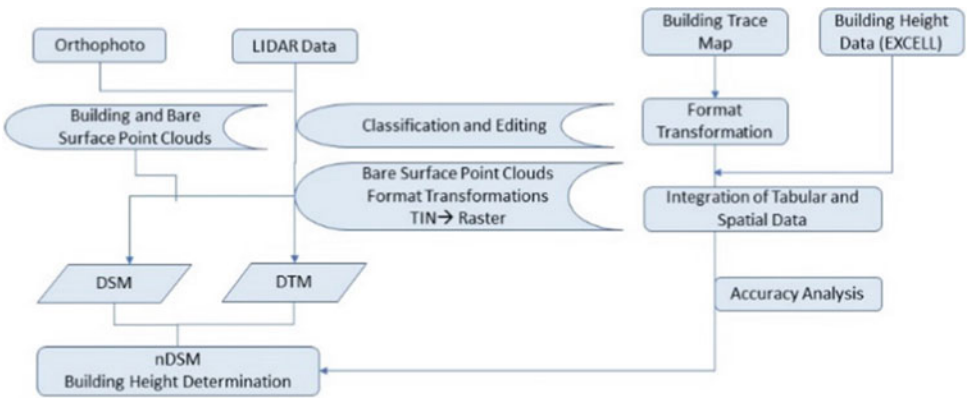

Fig. 2 Method of the study

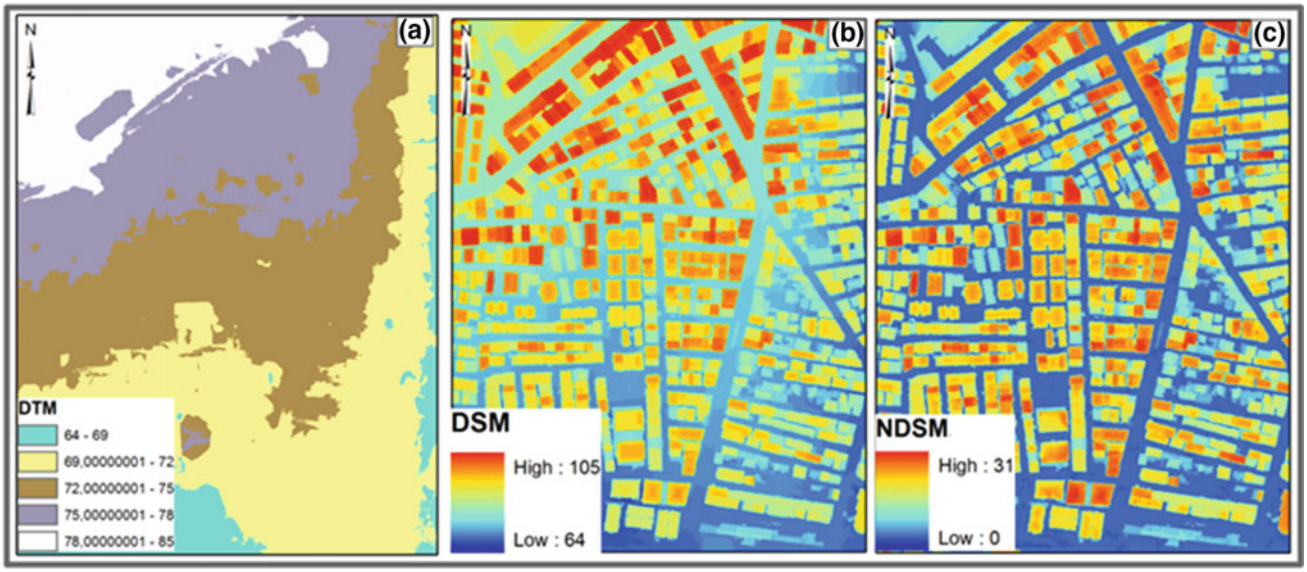

Fig. 3 Digital terrain model (DTM) in (**a**), Digital Surface Model (DSM) in (**b**), and Normalized difference surface model (nDSM) in (**c**)

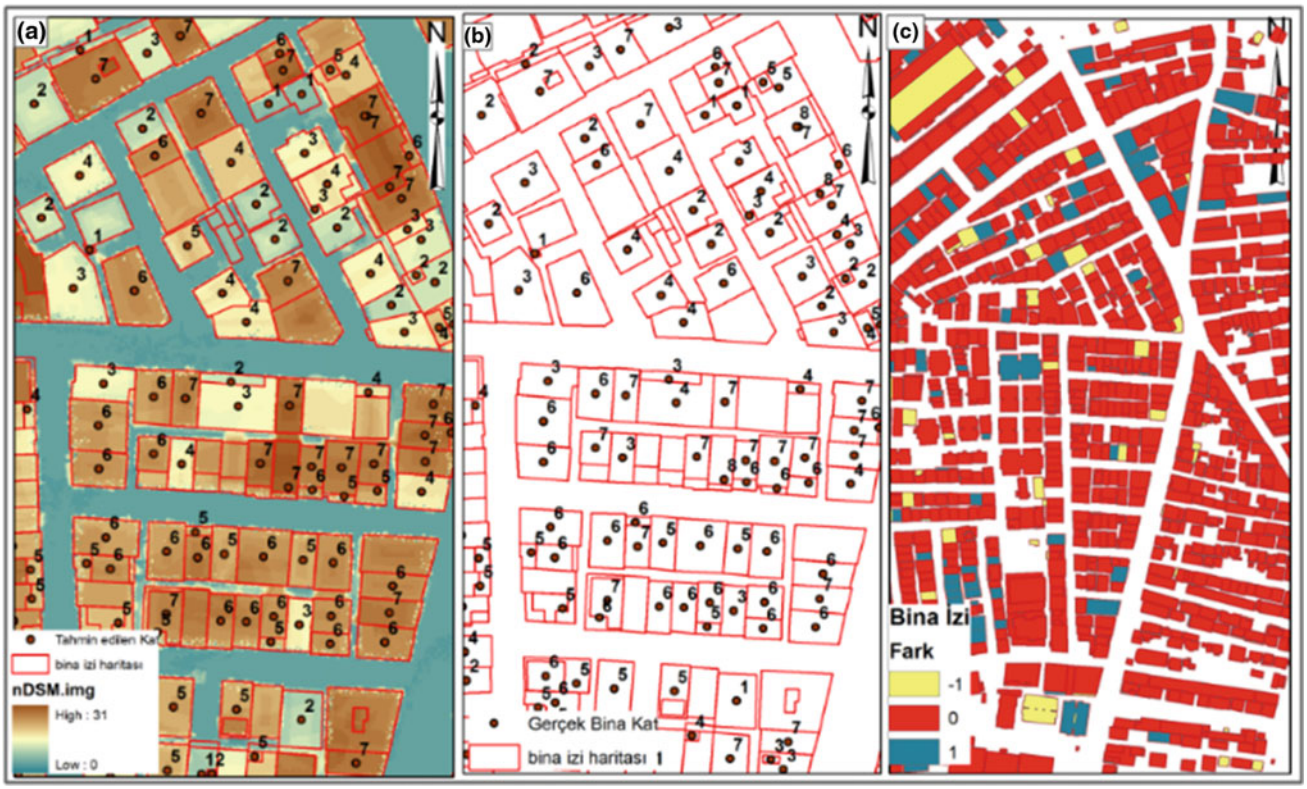

Fig. 4 Estimated building heights obtained from nDSM (**a**), real building floor data (**b**), difference map of the estimated and real building floor map (**c**)

Table 1 Accuracy of estimated floors

	Total	Matched (Difference = 0)	Matched (Difference = ±1)	Accuracy (%)
Building number	853	673	180	79
Overall accuracy	1108	862	246	78
Kappa statics				74
Not evaluated	247			

4 Results

In this study, integrated aerial photograph and LIDAR data were used to produce individual building heights in the urban central part of Kucukcekmece, Istanbul. The accuracy of the building heights was evaluated using building floor maps for the region. According to obtained results, about 79% of the building heights were correctly determined from the LIDAR data which is a promising result (Table 1).

The effects that add negativity to the operation can be listed as the fact that the city is a metropolitan structure, the control data cannot be inspected, the building roofs do not have a smooth surface and the inner ceiling heights of different buildings are different. Besides, the presence of different types of buildings has added value to the fact that they have a more general and realistic perspective to the study.

References

1. Haala, N., Kada, M.: An update on automatic 3D building reconstruction. ISPRS J. Photogrammetry Remote Sens. **65**, 570–580 (2010)
2. Kim, K., Shan, J.: Building roof modeling from airborne laser scanning data based on level set approach. ISPRS J. Photogrammetry Remote Sens. **66**, 484–497 (2011)
3. Kiran, S.S.: Three-Dimensional City Planning Using Photogrammetry and GIS, Available at: http://www.directionsmag.com/entry/three-dimensional-city-planning-using-photogrammetry-and-gis/428780 (2015)
4. Parish, Y.I., Muller, P.: Procedural Modeling of Cities, In: Proceedings of the 28th Annual Conference on Computer Graphics and Interactive Techniques, Los Angeles, CA. 301–308 (2001)
5. Sampath, A., Shan, J.: Segmentation and reconstruction of polyhedral building roofs from aerial Lidar point clouds. IEEE Trans. Geosci. Remote Sens. **48**, 1554–1567 (2010)
6. Zhu, Q., et al.: Research and practice in three-dimensional city modeling. Geo-spat. Inf. Sci. **12**(1), 18–24 (2009). https://doi.org/10.1007/s11806-009-0195-z

Automatic Building and Height Determination from Unmanned Aerial Vehicle Data

Efdal Kaya and Arzu Erener

Abstract

Determination of up to date 3D maps of urban areas and estimation of building height has crucial importance for variety of disciplines such as: city regional planning, architecture, construction industry, population directorates and planning units. In order to track information for building construction speed and illegal constructions, updating building inventories, preparing feasible urban plans 3D maps of urban areas is important to get. Unmanned aerial vehicle (UAV) is promising and suitable for 3D objects detection. These systems create high accurate 3D height maps for buildings and, therefore, can be used to estimate accurate building boundaries in urban areas. In this study, SenseFly eBee RTK Unmanned aerial vehicle (UAV) was used to obtain 3D data. The aerial photographs obtained with the UAV were processed in order to create a three-dimensional point cloud. By processing the point cloud data Digital surface model (DSM) and digital elevation model (DEM), were created. In order to determine the buildings' height, Normalized Digital Surface Model (nDSM) was formed by removing DSM from DEM. In order to determine building boundaries, high resolution aerial photographs obtained from the unmanned aerial vehicle (UAV) were classified using machine learning algorithms and support vector machines. After classification, we obtained 160 buildings. Then we estimated the buildings floor height for the selected ten buildings.

Keywords

UAV • DSM • DEM • nDSM • Building detection

E. Kaya (✉)
Aksaray Validity, Aksaray Private Administration, Geographic Information Systems Unit, Aksaray, 68200, Turkey
e-mail: kayaefdal@gmail.com

A. Erener
Department of Geomatic Engineering, Kocaeli University, 41380 Kocaeli, Turkey

1 Introduction

Remote sensing (RS) data was used to obtain fast thematic maps for large regions. However, these systems have several constraints in creating 3D maps of urban features and detecting urban building heights. Active sensors can overcome some of these constraints when they are used by passive systems. Unmanned aerial vehicle (UAV) is a promising and suitable tool for 3D objects detection. These systems create high accurate 3D maps for buildings therefore can be used to estimate accurate height value for each building in urban areas.

Feature selection is considered an important step within a classification process because it improves the performance of the classifier and reduces the complexity of the computation by removing redundant information [8]. Feature selection has been widely applied in remote sensing image classification in general [6], and for hyperspectral data in particular [5, 7]. With the extended feature space derived from segmented objects (e.g., extended spectral feature sets per object, shape properties, or textural features) [1, 3], object-based classification may increase the complexity of the classification and the demand for computing power.

Previous investigations have increasingly applied several advanced feature selection methods to object-based image analysis. Duro et al. [2] implemented feature selection by calculating the variable importance score using the Random Forest method. Stumpf and Kerle [11] and Puissant et al. [10] implemented an iterative backward elimination, whereby the least important 20% of variables, according to the variable ranking derived from the Random Forest method, were eliminated at each iteration to determine the optimal feature subset. The image segmentation processes for the delineation of agriculture from Unmanned Aerial Vehicle (UAV) images have been in operational use for several years, e.g., for precision agriculture [4, 9]. UAV images are usually different to other images (typically only RGB bands, very high spatial resolution, radiometric

© Springer Nature Switzerland AG 2019

H. M. El-Askary et al. (eds.), *Advances in Remote Sensing and Geo Informatics Applications*, Advances in Science, Technology & Innovation, https://doi.org/10.1007/978-3-030-01440-7_38

differences). Furthermore, due to laws and regulations, UAVs are mostly flown in areas without human presence (no urban areas) and where visual control is possible (open areas)—this results in an abundance of applications in agricultural areas compared to others. Subsequently, the ability to map agricultural areas at high spatial resolution encourages agriculture monitoring, combining UAV images with object-based methods, which contributes with a fundamental understanding to the available object-based classification methods.

2 Materials and Methods

2.1 Study Area

The study area is located in Dogantarla, Aksaray, Turkey, between 38°22′11.48″ North Latitude and 34°12′39.89″ East Longitude. In this study, it was aimed to create high accurate 3D height maps for buildings and obtain building boundaries. In this study, SenseFly eBee RTK Unmanned aerial vehicle (UAV) was used to obtain 3D data. The aerial photographs obtained with the UAV were processed in order to create a three-dimensional point cloud. By processing the point cloud data a Digital surface model (DSM) and digital elevation model (DEM) were created. In order to determine the buildings' height, Normalized Digital Surface Model (nDSM) was formed by removing DSM from DEM. In order to determine building boundaries, high resolution aerial photographs obtained from the unmanned aerial vehicle (UAV) were classified using machine learning algorithms and support vector machines. The flow chart of the study is presented in Fig. 1.

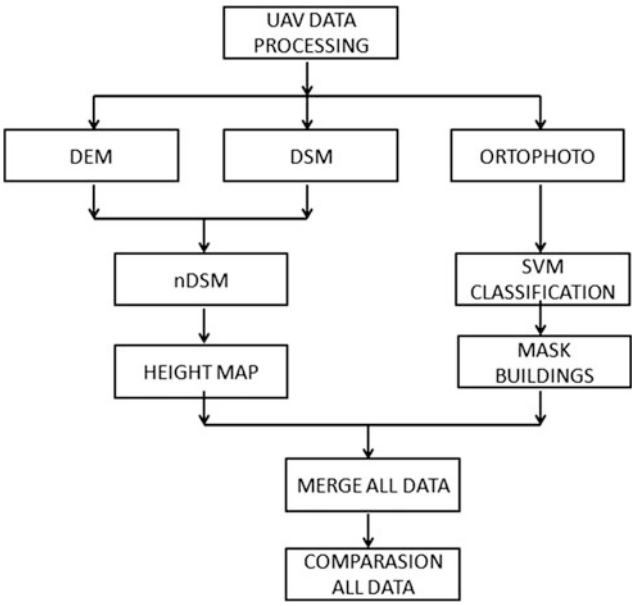

Fig. 1 Flow chart of the study

3 Results

3.1 Results of Point Cloud Analysis

The 3D point cloud includes coordinates of the objects on the earth along with the land coordinates. After the UAV data process, the obtained average ground sampling distance (GSD) was 5.56 cm. The point cloud was obtained for UAV. The point cloud was used to create the Digital Terrain Model (DTM) and Digital Elevation Model (DEM) of the land in a short time. The creation of these models makes use of the first and last return reflection measurements of the point cloud data. The first return did not belong to the ground layer of the oblate but was the reflection of the oblate that hits the surface of the edge. The last return was mostly the reflection belonging to the ground layer.

The point cloud was divided into classes such as topography, vegetation, building, energy transmission lines by applying the filter process. Using the topography class, DEM was created and presented by equilibrium curves and represent the height on land (Fig. 2a). The rest of the point cloud data was used to obtain the DSM that identifies all objects such as the building, vegetation, etc. present on the land (Fig. 2b). The normalized digital surface model (nDSM) was formed by removing SAM from SYM (Fig. 2c). nDSM represents the data of all objects on the ground. nDSM was used in order to determine the buildings' height. The height values accuracy was controlled by using the buildings map obtained from Municipalities.

3.2 Results of Building Boundary Detection

In order to determine buildings high resolution aerial photographs obtained from the unmanned aerial vehicle (UAV) were classified using machine learning algorithms, support vector machines (SVM). SVM is based on a statistical learning theory and it was founded on the concept of decision planes that define decision boundaries [12]. A decision plane is one that separates between a set of objects having different class memberships. Most classification tasks, however, are not that simple, and often more complex structures are needed in order to make an optimal separation, i.e., correctly classify new objects (test cases) on the basis of the examples that are available (train cases). Classification tasks based on drawing separating lines to distinguish

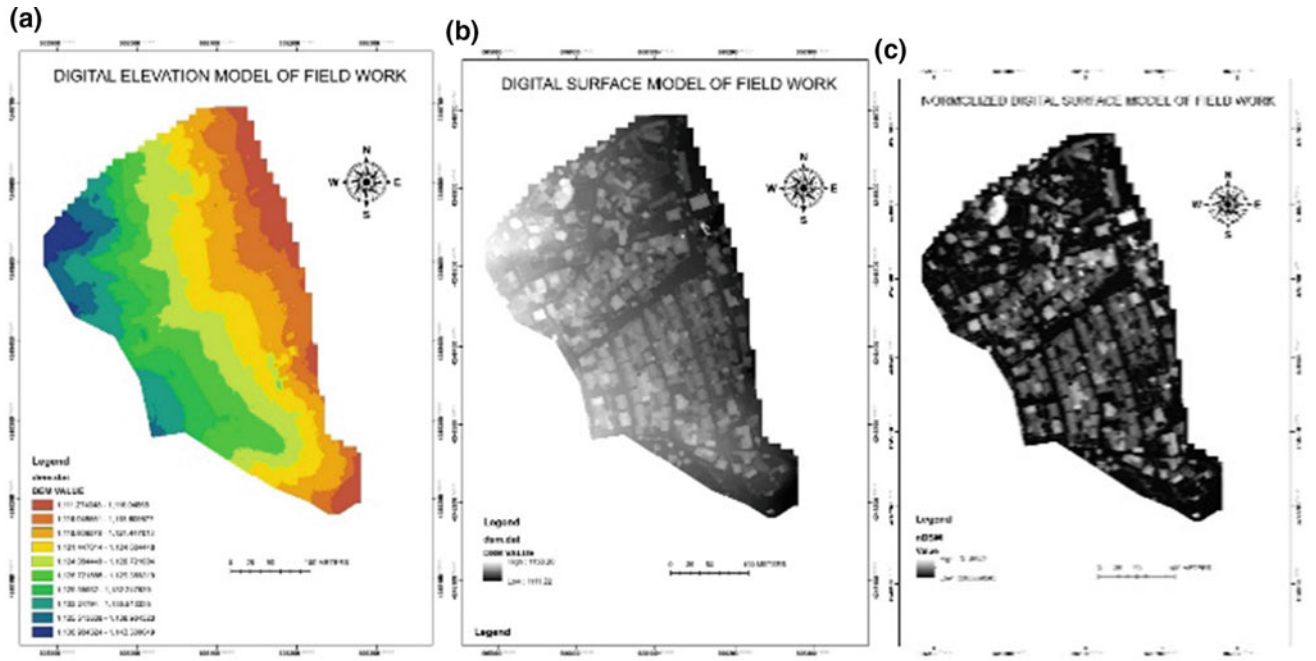

Fig. 2 **a** DEM (5 cm), **b** DSM (5 cm), **c** nDSM

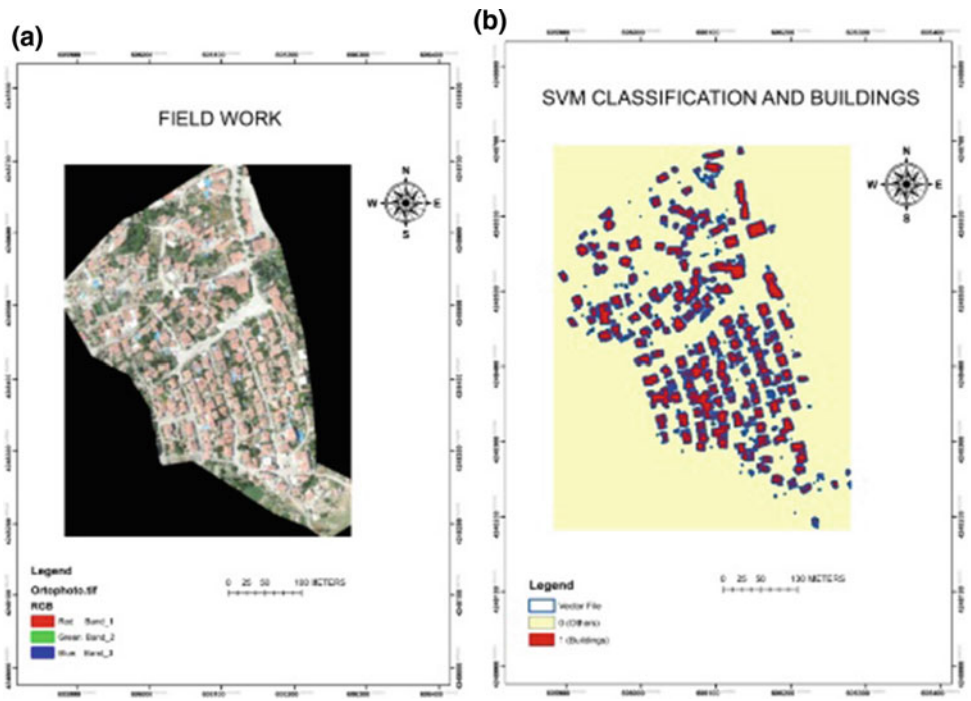

Fig. 3 **a** Field work, **b** SVM classification results

between objects of different class memberships are known as hyper plane classifiers. Support Vector Machines are particularly suited to handle such tasks. A classification map, obtained after the classification process, was reclassified to focus on building classes. One (1) is the value assigned to the building class and 0 is assigned to the other classes. The field work (Fig. 3a) and classification result map (Fig. 3b).

4 Conclusions

In this study the aerial photographs obtained with the UAV were processed in order to create a three-dimensional point cloud. In order to determine the height of buildings, Normalized Digital Surface Model (nDSM) was formed by removing DSM from DEM. In order to determine a building boundaries, high resolution aerial photographs obtained from the unmanned aerial vehicle (UAV) were classified using machine learning algorithms, support vector machines. The results indicate that the UHV provide high accurate data set to obtain building heights and building boundaries in a short time period.

References

1. Cheng, G., Han, J.: A survey on object detection in optical remote sensing images. ISPRS J. Photogrammetry Remote Sens. **117**, 11–28 (2016)
2. Duro, D.C., Franklin, S.E., Dubé, M.G.: Multi-scale object-based image analysis and feature selection of multi-sensor earth observation imagery using random forests. Int. J. Remote Sens. **33**, 4502–4526 (2012)
3. Laliberte, A.S., Browning, D., Rango, A.A.: Comparison of three feature selection methods for object-based classification of sub-decimeter resolution ultracam-l imagery. Int. J. Appl. Earth Obs. Geoinf. **15**, 70–78 (2012)
4. Ma, L., Cheng, L., Han, W., Zhong, L., Li, M.: Cultivated land information extraction from high-resolution unmanned aerial vehicle imagery data. J. Appl. Remote Sens. **8**, 1–25 (2014)
5. Melgani, F., Bruzzone, L.: Classification of hyperspectral remote sensing images with support vector machines. IEEE Trans. Geosci. Remote Sens. **42**, 1778–1790 (2004)
6. Novack, T., Esch, T., Kux, H., Stilla, U.: Machine learning comparison between worldview-2 and quickbird-2-simulated imagery regarding object-based urban land cover classification. Remote Sens. **3**, 2263–2282 (2011)
7. Pal, M., Foody, G.M.: Feature selection for classification of hyperspectral data by SVM. IEEE Trans. Geosci. Remote Sens. **48**, 2297–2307 (2010)
8. Pedergnana, M., Marpu, P.R., Dalla Mura, M., Benediktsson, J.A., Bruzzone, L.A.: novel technique for optimal feature selection in attribute profiles based on genetic algorithms. IEEE Trans. Geosci. Remote Sens. **51**, 3514–3528 (2013)
9. Peña, J.M., Torres-Sánchez, J., de Castro, A.I., Kelly, M., López-Granados, F.: Weed mapping in early-season maize fields using object-based analysis of unmanned aerial vehicle (UAV) images. PLoS ONE **8**, e77151 (2013)
10. Puissant, A., Rougier, S., Stumpf, A.: Object-oriented mapping of urban trees using random forest classifiers. Int. J. Appl. Earth Obs. Geoinf. **26**, 235–245 (2014)
11. Stumpf, A., Kerle, N.: Object-oriented mapping of landslides using random forests. Remote Sens. Environ. **115**, 2564–2577 (2011)
12. Vapnik, V.N.: The Nature of Statistical Learning Theory. Springer, New York (1995)

Estimating Crown Biomass of Oak Trees Using Terrestrial Photogrammetry in Zagros Forests

Zahra Azizi

Abstract

Accurate methods for biomass estimation is necessary for numerous topics related to global warming. Amongst different component of trees, crown biomass is the most difficult to measure. In this study, we tested a simple approach using a hand-held consumer grade camera to estimate the biomass of different components of crown including large and small branches and leaves. Two perpendicular images were taken from 36 Oak trees and the trees were cut down and fresh weight of components was measured in the field. Biomass was calculated for each component by multiplying fresh weight and density of each component. For the estimation of biomass using terrestrial photogrammetric method, pixels of each component were separated and used as predictor in regression equations. Biomass of each component were estimated and bias and RMSE were calculated. Based on the result, this approach provided the most accurate results for medium size trees. In general, the bias and RMSE of total crown biomass estimation were 1.45 and 4.64, respectively. Also, the accuracy of biomass estimation of large branches was the highest while that of leaves biomass was the lowest. However, the density of the stands and the size of trees are two important factors that limit the applicability of this approach.

Keywords

Hand-held camera • Oak trees • Non-destructive estimation • Terrestrial photogrammetry

1 Introduction

Tree crown structure is one the most important aspects of trees, since it depicts the different tree physiological functions [1]. Tree crown is not easily reachable, therefore new methods are needed to quantify tree crown structure. During the last two decades, the rapid development of digital cameras and laser scanners has provided a reliable source for tree measurements [2].

Terrestrial laser scanning (TLS) has been largely used for quantifying different variables of forest stands [3–5]. In recent years, LIDAR systems have advanced and have been used to reconstruct tree canopies [6]. However, LIDAR systems are still very expensive and for non-commercial forests, it is not possible to afford data collection using such high-tech instruments. On the other hand, using terrestrial imagery with close-range photogrammetry application can offer an applicable alternative.

Compared to TLS, camera-based methods offer potentially cheaper hardware, and reduced field time [2]. The feasibility of terrestrial images as an alternative source for estimation of individual tree attributes has not been well studied yet [7]. There are only a few studies on the estimation of tree attributes using terrestrial photogrammetry [2]. Also, most of these works have been carried out in artificial ecosystems such as orchards, parks, gardens, and plantations. Therefore, there is a gap in knowledge for applicability of terrestrial photogrammetry on forest parameters estimation.

In this study, we aimed to quantify crown parameters of individual Oak trees using a hand-held camera as a terrestrial photogrammetry method (TFM). We tested the accuracy and precision of this method to estimate different tree components in different diameter classes in comparison to field measurements (FM). Hand-held consumer cameras can be very interesting due to their low-cost and ease of operation.

Z. Azizi (✉)
Department of Remote Sensing and GIS, Science and Research Branch, Islamic Azad University, Tehran, Iran
e-mail: zazizi@srbiau.ac.ir

© Springer Nature Switzerland AG 2019

H. M. El-Askary et al. (eds.), *Advances in Remote Sensing and Geo Informatics Applications*, Advances in Science, Technology & Innovation, https://doi.org/10.1007/978-3-030-01440-7_39

2 Materials and Methods

The experience was conducted in an Oak natural forest in Lordegan, Chaharmahal and Bakhtiari province, Iran. The latitude and longitude of the study area is 50° 38′ E and 31° 28′ N, respectively. In this area, 36 trees of *Quercus brantii* were selected to cover the entire diameter range. The trees were cut down and three components including large and small branches and leaves were separated and a representative sample from each component was collected and transported to the laboratory for further analysis. The dry weight was measured by drying the samples using an Oven to reach a constant weight. Then, the biomass of each component was calculated.

The image data were acquired in January 2014. A Sony Cyber-shot DSC-H55 with 14.1 mega pixel resolution was used for imagery. The operational parameters were set to an F 7.1 aperture, a 1/125 s shutter speed, and a 400 ISO value. Two perpendicular images were taken for each tree. In each photo, the frame was set in such a way that all tree parts from collar to tree top were photographed. Distance from the photographer position to tree center was also measured. We used a pixel based approach for estimations. In this approach, the number of pixels of tree crown were used as predictor in the models. The number of pixels were regressed against the field biomass using ordinary linear regression. Precision and accuracy of the estimation were assessed using relative bias (*rB*) and relative root mean square error (*rRMSE*).

$$RMSE = \frac{\sqrt{\sum_{i=1}^{n}\left(\widehat{yi} - yi\right)^2}}{\sqrt{n}},$$

$$rRMSE = \frac{\mathrm{RMSE}}{\bar{y}},$$

$$Bias = \frac{\sum_{i=1}^{n}\widehat{yi} - yi}{n},$$

$$rB = \frac{\mathrm{Bias}}{\bar{y}} \times 100.$$

where $\widehat{yi}$ is the actual biomass of ith tree, $\widehat{yi}$ is the predicted biomass of ith tree, and $\bar{y}$ is the average of actual biomass

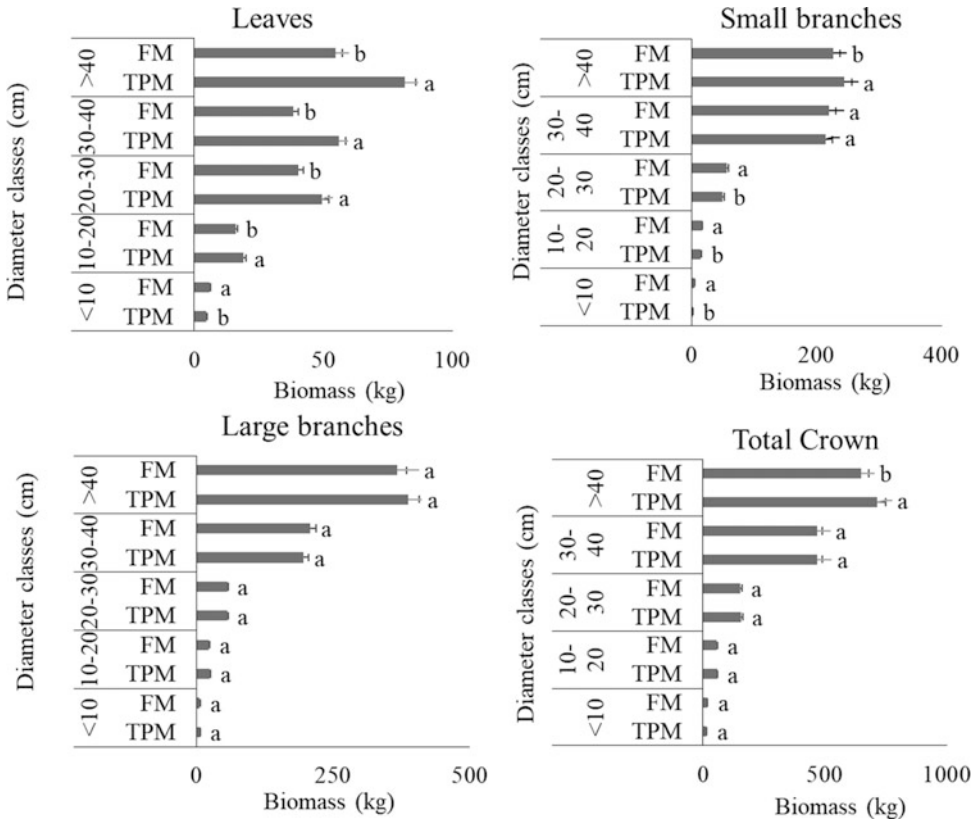

Fig. 1 Comparison of leaves biomass, small branches, large branches, and total crown by terrestrial photogrammetry (TPM) and field measurements (FM). Different letters in each diameter class shows significant statistical difference as 95% confidence level

Table 1 Relative bias (%) and relative RMSE (%) of estimation of biomass of different components of *Quercus brantii* trees based on terrestrial photogrammetry

	Relative Bias (%)				Relative RMSE (%)			
Diameter class (cm)	Large branch	Small branch	Leaves	Total	Large branch	Small branch	Leaves	Total
<10	2.59	−55.11	−22.13	−23.14	1.81	53.79	17.59	18.50
10–20	4.87	−11.02	18.99	4.11	3.36	8.24	12.26	2.85
20–30	−0.31	−11.99	22.86	1.46	0.22	9.02	14.51	1.02
30–40	−6.11	−2.04	45.59	0.07	4.46	1.46	26.25	0.05
40–50	5.71	8.07	49.61	10.24	3.93	5.48	28.11	6.88

3 Results

The estimated biomass of different components was compared to the measured biomass using paired t-test at 95% confidence. Based on the results (Fig. 1), for small branches and leaves, there were significant differences between the measured and estimated values in all diameter classes except for those smaller than 10 cm, the photogrammetry method had higher values for biomass. The estimated biomass and actual biomass of large branches and total crown were identical statistically.

The result of rB and rRMSE varied for different component as well as different diameter classes. rB and rRMSE of TPM were always high for leaves followed by small branches. The smallest values were observed for large branches and total. Furthermore, the sign of bias also varied for different components and different diameter classes. But all in one, the biomass of small branches was mostly overestimated while other components as well as total biomass were mostly underestimated (Table 1).

4 Discussion

There are several attempts for quantifying individual tree attributes using images of different cameras. Forsman et al. [2] presented different methods for profiling tree stem based on digital photogrammetry. The authors estimated tree stem attributes using terrestrial photogrammetry with a camera rig [2]. Liang et al. [7] compared terrestrial image-based point clouds from a handheld camera compared and terrestrial laser scanning for forest data collection. The authors' result showed that the accuracy of tree attribute estimates was close to an acceptable level for a forest field inventory. However, compared to TLS, the accuracy was considerably low.

5 Conclusion

Although this method is quick, non-destructive, simple, and low cost, there are some drawbacks in its application. First, it is suitable for isolated trees and its accuracy depends on the stand density. Second, it is difficult to balance the tradeoff between resolution and distance needed to outline the whole tree in the image frame. For large trees, one needs to distance more from the tree which results in lower image resolution and as a consequence, lower precision.

References

1. Shahrokhzadeh, U., Sohrabi, H., Copenheaver, C.A.: Aboveground biomass and leaf area equations for three common tree species of Hyrcanian temperate forests in Northern Iran. Botany **93**, 663–670 (2015)
2. Forsman, M., Börlin, N., Holmgren, J.: Estimation of tree stem attributes using terrestrial photogrammetry with a camera rig. In: XXII ISPRS Congress. Melbourne, 7 Aus, pp. 261–265 (2012)
3. Mikita, T., Janata, P., Surovỳ, P.: Forest stand inventory based on combined aerial and terrestrial close-range photogrammetry. Forests **7**, 1–14 (2016)
4. Polewski, P., Erickson, A., Yao, W., Coops, N., Krzystek, P., Stilla, U.: Object-based coregistration of terrestrial photogrammetric and Als point clouds in forested areas. ISPRS Ann. Photogramm. Remote Sens. Spat. Inf. Sci. **III-3**, 347–354 (2016)
5. Yang, B., Dai, W., Dong, Z., Liu, Y.: Automatic forest mapping at individual tree levels from terrestrial laser scanning point clouds with a hierarchical minimum cut method. Remote Sens. **8**, 372 (2016)
6. Biskup, B., Scharr, H., Schurr, U., Rascher, U.: A stereo imaging system for measuring structural parameters of plant canopies. Plant Cell Environ. **30**, 1299–1308 (2007)
7. Liang, X., Jaakkola, A., Wang, Y., Hyyppä, J., Honkavaara, E., Liu, J., Kaartinen, H.: The use of a hand-held camera for individual tree 3D mapping in forest sample plots. Remote Sens. **6**, 6587–6603 (2014)

Estimation of Available Canopy Fuel of Coppice Oak Stands Using Low-Density Airborne Laser Scanning (LiDAR) Data

Farzad Yavari and Hormoz Sohrabi

Abstract

Predicting fire hazards and simulating fire intensity require knowledge of fuel conditions. Many aspects of wildfire behavior including the rate of spread and intensity are influenced by the amount of vegetation that fuels the fire. Coppice Oak Forests (COF) are strongly influenced by wildfires. In the present study, we examined the ability of airborne LiDAR data to retrieve available canopy fuel (ACF) of coppice Oak forest in Zagros Mountains, Iran. Two different oak-dominated stands were selected based on the stand density including sparse and dense forests. Systematically, 127 plots were established in the field and ACF was calculated using species-specific allometric equations. An outlier filter was used to remove any outlier pulse from the point clouds. Canopy Height Models (CHM) were generated by subtracting DSM and DTM. Different metrics were calculated from CHMs at the plot locations. Linear regression (LR), Artificial Neural Networks (ANN), Boosted Random Forest (BRF), and K-Nearest Neighbor (KNN) were used for modeling. The result showed that there is a strong correlation between ACF and LIDAR-derived metrics ($r^2 = 0.74 - 0.79$). BRF was the best modeling technique. ACF was estimated more accurately in the sparse stand ($r^2 = 0.79$). LIDAR-based predictions can be used to map ACF over coppice oak forests.

Keywords

Low density LiDAR • Stepwise regression • Zagros • Canopy fuel parameters • Canopy height model

1 Introduction

One of the most hazardous natural disasters is wild-fire [1]. Due to climate change and human-related factors, the rate of forest fires has increased over recent years [2, 3]. Although, forest fires in coppice oak forests can be considered as a natural process (common plants of these stands exhibit fire-adapted traits such as thick bark and sprouting), the increase in their frequency, size and severity has led to fires being considered as a natural hazard both, for the environment and society [4]. Anthropogenic disturbances and the decrease in annual precipitation as well as hotter and drier summers, have led to more frequent and more intense fires, and as a result, a dramatic loss of forests. Amongst the Middle East and North African countries, Iran ranks fourth in forest fires. More than 150,000 ha of Iran's forests have been affected by fire over the last decade.

Many aspects of wildfire behavior, including the rate of spread, size, and severity are strongly influenced by the amount of the vegetation that fuels the fire. Available canopy fuel (ACF) is defined as fuel capable of burning in a crown fire and includes foliage and small branches [5]. Regression models can be developed to estimate the ACF based on stand characteristics [2], but field data collection is costly and time consuming. Previous studies have demonstrated the capability of multispectral, airborne LiDAR, space-borne LiDAR, and the combination of airborne LiDAR and multispectral data to estimate ACF [5]. Studies predicting ACF fuels from airborne LiDAR are numerous, but, to our knowledge, no previous study has characterized the ability of low-density LiDAR data to predict ACF in low-height stands of a coppice forest.

In this study we aimed to: (1) assess the potential of low-density LiDAR data to estimate available canopy fuel, (2) examine the effect of stand density on the accuracy and precision of the estimates, and (3) compare different parametric and non-parametric modeling techniques for ACF estimation.

F. Yavari · H. Sohrabi (✉)
Tarbiat Modares University, Tehran, Jalal AleAhmad, Nasr, Iran
e-mail: hsohrabi@modares.ac.ir

© Springer Nature Switzerland AG 2019

H. M. El-Askary et al. (eds.), *Advances in Remote Sensing and Geo Informatics Applications*,
Advances in Science, Technology & Innovation, https://doi.org/10.1007/978-3-030-01440-7_40

2 Materials and Methods

The study areas are located in coppice oak forests of Dorood, Lorestan province, with an area of 140 ha (33° 19′ 53″ E, 48° 52′ 26″) dominated by Persian oak (*Quercus brantii*). Flying height above ground was 1600 m. In September 2012, two different stands were selected based on canopy closure and 127 plots (76 and 51 plots in dense and sparse stands, respectively) with the dimension of 30 m × 30 m were established in the field and the total height and the crown width of trees were measured. Using species-specific equations [6], the biomass of leaves, twigs, and small branched were calculated and their summation was considered as ACF.

LiDAR data were acquired in August 2011 by Rayan Naghshe Inc., form 1000 m above the ground with 0.7 pulse m^{-2} density. The point cloud data were processed using FUSION software to remove obvious outlier points. To obtain normalized difference surface model representing the above ground features and bare earth surface have been extracted and the Digital Terrain Model (DTM) was produced with a pixel size of 1 m. First pulses were considered as Digital Surface Model (DSM) and Canopy Height Model (CHM) values were extracted by subtracting DSM and DTM [7]. LiDAR metrics were extracted from CHM in each plot. Different metrics including min, max, mean, standard deviation, the coefficient of variation, skewness, kurtosis, and different percentiles (5, 10, 20, 30, 40, 50, 60, 70, 80, 90, and 95%) were calculated as explanatory variables for the ACF estimation.

Different modeling techniques including linear regression (LR), artificial neural networks (ANN), boosted random forest (BRF), and k-nearest neighbor (KNN) were used to model ACF versus the metrics derived from CHM [6]. For the model comparison and selection, R-square, RASE (square root of the mean squared prediction error), and AAE (average absolute error) were calculated.

3 Results

Modelling an ACF based on different metrics derived from CHM using four different modeling techniques including LR, ANN, BRF, and KNN is shown in Table 1. Values of r^2, RASE, and AAE ranged from 0.58–0.79, 1.61–2.41, and 1.18–1.45, respectively.

For site 1 with dense canopy closure, BF and ANN had similar results and were better than LR and KNN. KNN had the worst fitting parameters in all cases. In site 2 with sparse canopy closure, BF was the best method followed by ANN, and LR. By simultaneously analyzing all data from both sites, a result similar to site 1 was observed.

The models resulted in better fitting parameters in a dense forest (max r^2 was for ANN 0.74) rather than a sparse forest (max r^2 was for BRF 0.74). Also, analyzing all data as one set resulted in models with better fitting parameters. Figure 1 shows the predicted value of ACF versus the actual data using BF algorithm for total data. The scatter plot shows that predictions are well dispersed around the bisection line indicating proper estimates resulted from BRF for all data.

4 Discussion

The results of this study indicated that LiDAR can be used to estimate of available canopy fuel. Since LiDAR data can capture structural information related to quantitative canopy

Table 1 Model comparison for ACF estimation from LiDAR derived metrics using different modeling algorithms

Site	Predictor	Creator	R-square	RASE	AAE
Dense stand	Regression	Least squares	0.6563	2.1887	1.6838
	ANN	Neural	0.7396	1.9051	1.5305
	Boosted forest	Bootstrap forest	0.7401	1.9033	1.4446
	KNN	K nearest neighbors	0.5846	2.4063	1.8787
Sparse stand	Regression	Least squares	0.6892	1.9382	1.5287
	ANN	Neural	0.6765	1.9775	1.4977
	Boosted forest	Bootstrap forest	0.7861	1.6079	1.1803
	KNN	K nearest neighbors	0.6289	2.1179	1.6481
Total	Regression	Least squares	0.6892	1.9382	1.5287
	ANN	Neural	0.6765	1.9775	1.4977
	Boosted forest	Bootstrap forest	0.7861	1.6079	1.1803
	KNN	K nearest neighbors	0.6289	2.1179	1.6481

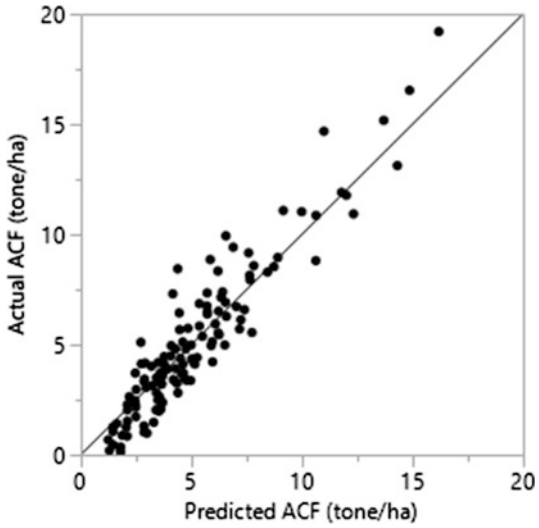

Fig. 1 Actual available canopy fuel (ACF) versus predicted ACF using boosted random forest in the total area

fuel characteristics, which was expected. Many studies in different vegetation types reported the ability of this data for ACF estimation. For canopy fuel estimation, [8] reported strong relationship in coniferous Douglas-fir and western hemlock, [9] reported an r^2 of 0.82 in dense mixed-conifer forests, [5] reported 0.59 in coniferous montane forests.

5 Conclusion

LiDAR-derived metrics can predict and map available fuel content of coppice oak forest stands with high precision and accuracy. The prediction results of depend on modeling algorithm. However, the availability of LiDAR data is a serious restriction.

References

1. Eskandari, S.: A new approach for forest fire risk modeling using fuzzy AHP and GIS in Hyrcanian forests of Iran. Arab. J. Geosci. **10**, 190 (2017)
2. Inan, M., Bilici, E., Akay, A.E.: Using airborne lidar data for assessment of forest fire fuel load potential. In: ISPRS annals of the photogrammetry, remote sensing and spatial information sciences, pp. 255–258 (2017)
3. Mutlu, M., Popescu, S.C., Stripling, C., Spencer, T.: Mapping surface fuel models using lidar and multispectral data fusion for fire behavior. Remote Sens. Environ. **112**, 274–285 (2008)
4. García, M., Riaño, D., Chuvieco, E., Salas, J., Danson, F.M.: Multispectral and LiDAR data fusion for fuel type mapping using support vector machine and decision rules. Remote Sens. Environ. **115**, 1369–1379 (2011)
5. Bright, B.C., Hudak, A.T., Meddens, A.J.H., Hawbaker, T.J., Briggs, J.S., Kennedy, R.E.: Prediction of forest canopy and surface fuels from lidar and satellite time series data in a bark beetle-affected forest. Forests **8**, 1–22 (2017)
6. Safari, A., Sohrabi, H., Powell, S., Shataee, S.: A comparative assessment of multi-temporal Landsat 8 and machine learning algorithms for estimating aboveground carbon stock in coppice oak forests. Int. J. Remote Sens. **38**, 6407–6432 (2017)
7. Sohrabi, H.: Estimating mixed broadleaves forest stand volume using DSM extracted from digital aerial images. In: International archives of the photogrammetry, remote sensing and spatial information sciences—ISPRS Archives (2012)
8. Andersen, H.E., McGaughey, R.J., Reutebuch, S.E.: Estimating forest canopy fuel parameters using LIDAR data. Remote Sens. Environ. **94**, 441–449 (2005)
9. Jakubowksi, M.K., Guo, Q., Collins, B., Stephens, S., Kelly, M.: Predicting surface fuel models and fuel metrics using lidar and CIR imagery in a dense, Mountainous Forest. Photogramm. Eng. Remote Sens. **79**, 37–49 (2013)

Part V
Rock Formations and Soil Lithology Mapping

Nile Delta Sedimentary Basin—A Big Data Guided Digital Petroleum Ecosystem

Nimmagadda L. Shastri, Said Hanafy, and Torsten Reiners

Abstract

Volumes of geological and geophysical (G & G) data sources exist in the Nile Delta basin, covering approximately 60,000 km^2 in both onshore and offshore areas. Although several varieties of data continue to support the exploration and field development activities in the basin, the Big Data sources are largely unstructured, heterogeneous and multidimensional. Connecting various G & G events of onshore-transition-offshore zones and integrating them into a single repository is a complicated process. The authors proposed a holistic data warehousing and mining methodology that can support logical and physical data organization, easing the data integration process in the warehouse repository. In addition, an implementable framework, the Nile Delta Digital Petroleum Ecosystem (NDDPE) was articulated, assessing its usability and interoperability with associated data artefacts. The NDDPE can deliver Big Data guided digital ecosystem solutions that can minimize the risk of exploration.

Keywords

Nile delta sedimentary basin • Digital petroleum ecosystem • Big data • Geo-informatics

1 Introduction

In the current basin research, we described the Nile Delta as an ecosystem [3], which is a communion of elements and processes of petroleum systems and their *chains* (conceptualized and contextualized attributes) in a spatial domain, where they constantly interact and communicate through digital media [4]. The digital data are in Big Data scale, characterized by different volumes and varieties. With a quest of acquiring new knowledge in the oil/gas producing basins, the authors proposed an integrated framework for exploring the data patterns among Big Data sources of petroleum systems. Various data relationships were interpreted to build schemas, interconnected systems and integrated with warehouse metadata structures. Metadata models were analyzed for meta-knowledge in Big Data scale.

The Nile Delta covers thousands of square kilometers area in Egypt. The geology, geography and morphology associated with the basin are well known [1, 2]. The basin covers an onshore area of about 30,000 km^2 with an equal size in offshore down to the 200 m isobath. We could identify various geological, geophysical and geomorphic data entities and interpret them as multiple dimensions for multidimensional modelling. We examined the data sources of elements and processes of petroleum systems, and whether G & G data attribute dimensions were connectable in the integration process. In the modelling process, the conceptualization and contextualization attributes emerged at the generalization and specialization levels. We made good use of these concepts, easing the complexities of large scale multidimensional schemas.

2 Contribution and Significance

The sedimentary basin, being geologically complex and multidimensional, the upstream business captures the attention of Big Data concepts and tools. The multidimensional warehouse repository can be adaptable and compatible with the NDDPE framework. To resolve complexity and heterogeneity of data representation in different basins and petroleum systems, the Big Data invades the stage of data exploration and interpretation. Flexibility is an important criterion of the dimensional modelling, in which the data structures are interoperable based on data types and sizes. Using and reusing of ontologically described data structures

N. L. Shastri (✉) · T. Reiners
School of Management, Information Systems, CBS, Curtin University, Perth, WA, Australia
e-mail: shastri.nimmagadda@curtin.edu.au

S. Hanafy
Tharwa Petroleum, Cairo, Egypt

© Springer Nature Switzerland AG 2019

H. M. El-Askary et al. (eds.), *Advances in Remote Sensing and Geo Informatics Applications*, Advances in Science, Technology & Innovation, https://doi.org/10.1007/978-3-030-01440-7_41

(depending upon rapidly changing geological situations, including drilling and production scenarios) has significance in measuring the data complexities. The study can minimize the risk of exploration plans.

3 Issues and Problem Statement

Largely, the data sources in the basin are unstructured in Big Data scale. Managing the volumes and such data sources variety is challenging including data integration and connectivity between data volumes. The data-overload, duplication and redundancy may be causative to inconsistencies in data modelling and presentations. The sedimentary basin has different domains, dimensions and volumes of fact instances with a variety of exploration data. For understanding the G & G anomalies associated with complex petroleum systems, a robust and holistic data modelling methodology is needed for generating metadata and an unknown geological knowledge.

4 Modelling Methodology

Volumes of data are routinely collected, processed and stored in the archives of many companies. Various logical and physical data schemas are considered in modelling the Big Data sources. Decomposition of dimensions, redefinition of data relationships, mapping constraints, high-level abstractions (e.g. conceptualization, generalization or specialization) based on semantics and contexts are the modelling stages [4]. In addition, an attempt was made to define data through digital clouds for a group and groups of sedimentary basins that are geographically scattered in the basin. The constructs and logical schemas used digital clouds that involved the multifaceted exploration data. As described in [4], domain- and data-modelling, schema and warehouse design—for integration; data mining schemes—for exploring data views; data visualization—for presentation; data interpretation—for building new knowledge, are various artefacts of the framework as illustrated in Fig. 1. The ontological descriptions focus on the interpretation of taxonomy of data sources [3, 4] in various domains.

The logical schemas are drawn from several attribute dimensions of petroleum systems in geographically enumerated Big Data scale. Typically the multidimensional data stored in different media are in the form of domain ontologies, as integrated in warehouse repositories and described in Fig. 1.

5 Results and Discussion

Quantitatively, all the existing data that involve gravity, magnetic, electrical and seismic volumes and their instances are considered in the modelling and generating the metadata models. The data mining extracts useful data views for quantitative interpretation of different geological features. Statistical mining is done for ascertaining the correlations and trends of the integrated geophysical data patterns. Couple of scenarios typically include, integrated geophysical responses on a salt-body and the other is an interpretation of transfer zones, describing the fault dip directions, deformation style and convergent or divergent data events, making connections among different fault systems.

Different geophysical data instances were integrated into a multidimensional warehouse repository and in various cuboid metadata structures. Slicing and dicing were performed on the metadata, providing data views for visualization and interpretation. Map and plot views were mined for geological interpretation and how best the artefacts used in the NDDPE could deliver the exploration data solutions and evaluate the prospectivity. In another scenario, the metadata established links between local fault systems and the major faults in the rifted basins. The domain ontologies search for intersections of two or more fault strands, the cross faults, the links between border fault segments characterized by strike-slip to oblique-slip faults, orientated roughly parallel to the extensional direction. The transfer zones were interpreted in extensional settings in rift systems in the central Nile Delta. It included North African and East African basins, where transfer zones played key role in trapping hydrocarbons [1–3] on commercial scale.

The processed data were loaded into Oracle databases. Cluster, association rule and decision tree mining schemes [4] were deployed for extracting the connectivity between petroleum systems at different geographic dimensions. To demonstrate the connectivity, different types of data associated with transfer zones were brought together in a single repository as illustrated in Fig. 2.

6 Conclusion and Future Scope

Systematic modelling of Big Data volumes and variety of data existing in the Nile Delta basin facilitates perceiving the heterogeneity, multidimensionality and the connectivity between G & G attribute dimensions, in particular, the structure and reservoir connections in multiple petroleum

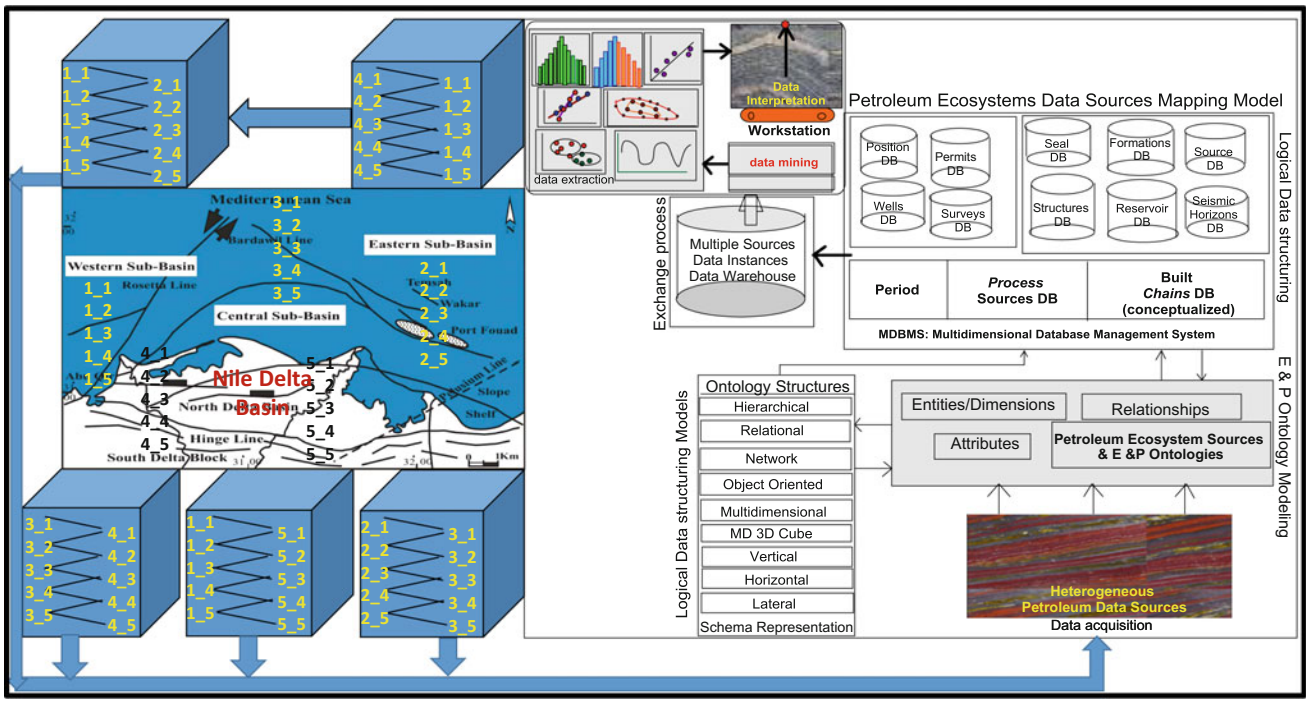

Fig. 1 The Nile Delta digital petroleum ecosystem (NDDPE) framework

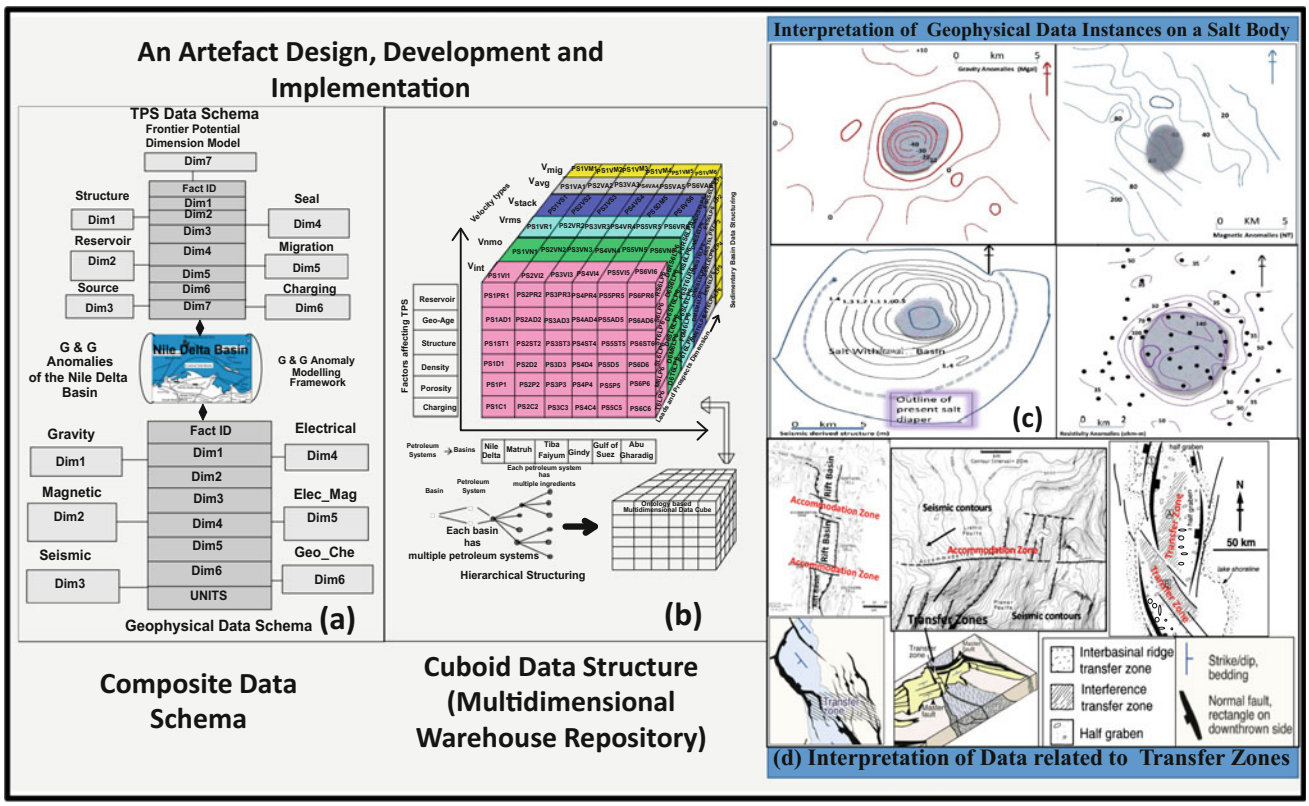

Fig. 2 Data schemas—integrating G & G data of petroleum systems in the Nile Delta

systems. The metadata are made available to explorers for detailed exploration & production. The future scope and opportunity of Big Data implementation in larger contexts of digital petroleum ecosystems are being explored.

References

1. Abdel Aal, A., El Barkooky, A., Gerrits, M., Meyer, H., Schwander, M., Zaki, H.: Tectonic Evolution of the Eastern Mediterranean Basin and Its Significance for Hydrocarbon Prospectivity of the Nile Delta Ultra-Deep water area, MOC 2000, Alex., Egypt (2000)
2. Egyptian General Petroleum Corporation: Nile Delta North Sinai Fields, Discoveries and Hydrocarbon Potentialities (as comprehensive overview). EGPC-Cairo, Egypt. 387 pp (1994)
3. Nimmagadda, S.L., Dreher, H.V.: On new emerging concepts of petroleum digital ecosystem (PDE). J. WIREs Data Min. Knowl. Disc. **2012**(2), 457–475 (2012). https://doi.org/10.1002/widm.1070
4. Nimmagadda, S.L., Reiners, T., Wood, L.: On big-data guided upstream business research and its knowledge management. J. Bus. Res. **89**, 143–158, Elsevier, USA, https://doi.org/10.1016/j.jbusres.2018.04.029 (2018)

Toward Lithological Mapping of Arabian Peninsula Using ASTER Multispectral Thermal Infrared Data

Yoshiki Ninomiya

Abstract

ASTER observes the thermal infrared (TIR; 7–14 μm) spectral radiation from the Earth at five bands where the major terrestrial minerals exhibit characteristic spectral properties. The lithological and mineralogical indices for ASTER-TIR proposed by the author have been proved to be quite effective and robust in detecting silica, carbonate, sulfate and mafic-ultramafic minerals as well as delineating silicate rocks. High quality mapping results with the indices have been supplied in the scales of local to regional with the developed procedures for efficient selection of well-conditioning scenes in the vast and expanding archive of ASTER data for mosaicking. However, the procedures are not efficient enough for global mapping. On the other hand, the global emissivity dataset version 3 (GEDv3) are developed and recently supplied to the public by one of the ASTER data providers. In this study, the global map generated with applying the indices to the GEDv3 was shown. It is compared with the regional map covering a part of Arabian Peninsula produced with the procedures developed by the author. The result indicates the GED-based map revealing the rough trend of lithology and mineralogy on Earth, however, the quality is much lower compared to the regional map produced with the author's procedures.

Keywords

ASTER • Thermal infrared spectra • Geology • Global mapping • Regional mapping • Arabian peninsula

1 Introduction

The ASTER sensor, developed by the Japanese government, was launched into orbit onboard NASA's Terra satellite in December 1999. It multi-spectrally observes the Earth in the Visible and Near Infrared (VNIR; 0.56–0.81 μm), Shortwave Infrared (SWIR; 1.65–2.395 μm) and Thermal Infrared (TIR; 8.30–11.30 μm) regions of the spectrum. The primary objective of ASTER is for geological applications. The ASTER-TIR has five spectral bands, central wavelengths of which are located at 8.30, 8.65, 9.10, 10.60 and 11.30 μm, respectively. The spatial and the radiometric resolutions are 90 m and ≤ 0.3 K, respectively. It continuously keeps observation for more than 18 years till present, far exceeding its original lifespan of five years. The data is basically provided as radiance at the sensor in units of $Wm^{-2}\ sr^{-1}\ \mu m^{-1}$. It is converted to radiance at the surface with the procedure of atmospheric corrections, and then converted to emissivity with the procedure of temperature—emissivity separation.

Concerning geological applications using ASTER multi-spectral data, the spectral absorption features are utilized for detecting minerals. For example, ASTER-VNIR is useful for detecting ferrous and ferric minerals, and ASTER-SWIR for discriminating hydroxyl minerals. Silica and silicate minerals, which are the major terrestrial minerals without any strong spectral features in VNIR and SWIR, are discriminable with ASTER-TIR. Several spectral indices for ASTER-TIR, e.g., Quartz Index (QI), Carbonate Index (CI) and Mafic Index (MI), applicable to the most available radiance at the sensor data are proposed [1] by emphasizing the features extracted from the spectral emissivity properties of typical rocks and minerals (Fig. 1). The indices are improved with careful analysis on the characteristics of the indices against the surface temperature and atmospheric parameters [2, 3]. The confirmed robustness of the indices guided the successful high quality mapping of mineralogy with the indices for quite wide regions by mosaicking a lot

Y. Ninomiya (✉)
Geological Survey of Japan, AIST, Tsukuba, 3058567, Japan
e-mail: yoshiki.ninomiya@aist.go.jp

© Springer Nature Switzerland AG 2019

H. M. El-Askary et al. (eds.), *Advances in Remote Sensing and Geo Informatics Applications*,
Advances in Science, Technology & Innovation, https://doi.org/10.1007/978-3-030-01440-7_42

of ASTER images [4]. On the other hand, the global emissivity dataset (GED) [5] generated averaging the observed ASTER data with basic cloud mask are provided to the public.

2 Study Area, Materials and Methods

The study area is the Arabian Peninsula. Especially, the border region between Oman and United Arab Emirates (UAE), the north-western corner of which is at 25°N in latitude and 55°E in longitude, and the south-eastern corner of which is at 23°N in latitude and 57°E in longitude, is the core study area for analyzing in detail.

1 km resolution version of GEDv3 [5] is applied with the indices (i.e., QI, CI and MI) [1–4] to create ASTER global map of mineralogy. 100 m resolution version of GEDv3 is applied for the core study area. Both the GED products are available at the web site of one of the ASTER data distributors (e.g., https://e4ftl01.cr.usgs.gov/ASTT/). Also, more than 400 scenes of ASTER data covering the core study area are selected with the browsing images and downloaded, and the regional map of the mineralogical indices (i.e., QI, CI and MI) is created with the selected well-conditioning 25 scenes of orthorectified ASTER Level-1T radiance at the sensor data (available at the same url shown above) using the software developed by the author [3, 4].

Based on the spectral properties of typical terrestrial rocks and minerals (Fig. 1), the mineralogical indices are defined for the ASTER-TIR data (Di; i=10 to 14) [1–4] as:

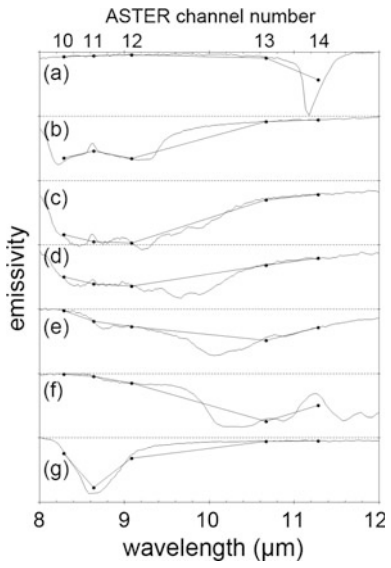

Fig. 1 Emissivity spectra of typical rocks and minerals **a** limestone (calcite), **b** quartz, **c** granite, **d** diorite, **e** gabbro, **f** peridotite, **g** gypsum. Convolved data to ASTER responsivities are also shown

$$\text{Quartz Index(QI)} = \frac{D_{11} \times D_{11}}{D_{10} \times D_{12}} \quad (1)$$

$$\text{Carbonate Index(CI)} = \frac{D_{13}}{D_{14}} \quad (2)$$

$$\text{Mafic Index (MI)} = \frac{D_{12}}{D_{13}} \Big/ CI^3 = \frac{D_{12} \times D_{14} \times D_{14} \times D_{14}}{D_{13} \times D_{13} \times D_{13} \times D_{13}} \quad (3)$$

To diminish the effect of the temperature, normalizing processing [2–4] to the radiance at the sensor data of Level-1T is applied before calculating the indices.

3 Results

Figure 2 shows the ASTER global map of mineralogy, represented as the RGB color composite image assigning the histogram regions: 0.965 to 1.045 of QI as red, 0.97 to 1.025 of CI as green, and 0.865 to 1.045 of MI as blue, respectively. Figure 3 shows the enlarged map for the Arabian Peninsula. Figure 4a, b show the regional map of mineralogy for the core study area created using the GED products [5] and mosaicking the Level-1T products with the protocol defined by the author [3, 4], respectively.

4 Discussion

The ASTER global map of mineralogy (Fig. 2) indicates the general trend of mineral distributions on Earth. Especially, it suggests the deserts of North Africa and Arabian Peninsula (Sahara, Nafud, etc.) are mainly composed of quartz with minor content of other minerals according to the pure reddish color denoted in the map. Also, the very thick layer of limestone extending the East-West direction located at the southernmost region of the Arabian Peninsula is clearly detected.

The color balancing of the global map of mineralogy (i.e., assigning 0.965 to 1.045 of QI as red, 0.97 to 1.025 of CI as green, and 0.865 to 1.045 of MI as blue) is determined to denote identical colors as much as possible with the map for Tibetan Plateau region created on the protocol proposed by the author [4] mosaicking finely selected well-conditioning ASTER Level-1T data (assigned 0.97 to 1.055 of QI as red, 1.005 to 1.055 of CI as green, and 0.79 to 0.95 of MI as blue). Comparing the global map (Fig. 2) with the map created with the author's protocol [4], especially in the high latitude region, there are many null pixels (see Fig. 2) although well-conditioning data are found with the author's procedure. This is due to the malfunction in the cloud detection processing with VNIR and SWIR data for

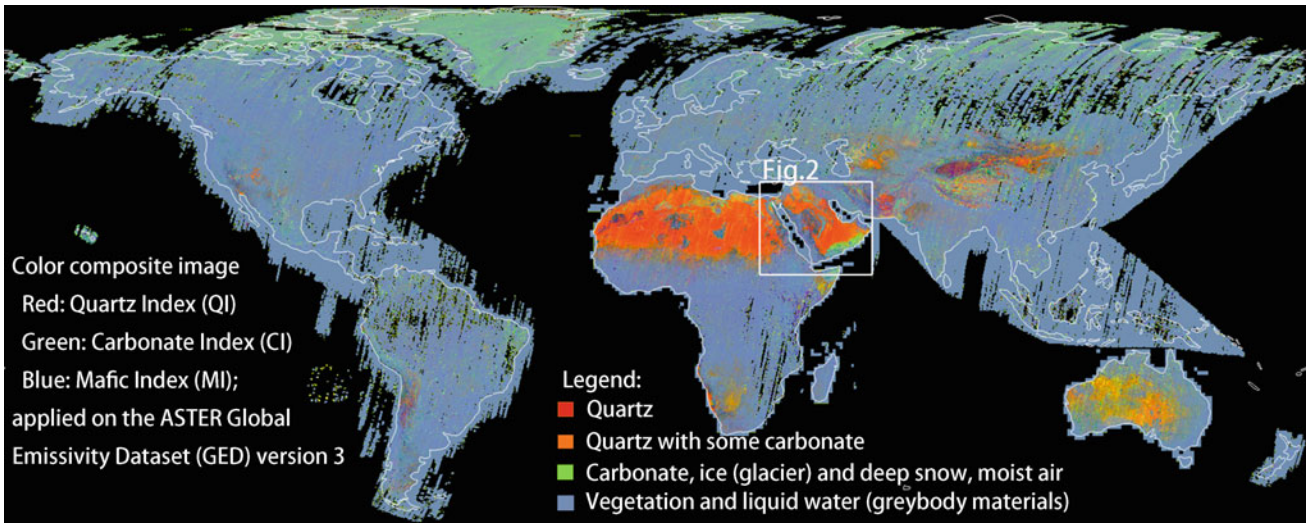

Fig. 2 Global map of mineralogical indices created with Global Emissivity Dataset (GED) of 1 km resolution. The relationship between the color and the material as shown in the legend: Red; quartz. Yellowish red; quartz with some carbonates. Light green; carbonates (calcite and dolomite), ice, snow and moist air (including cloud)

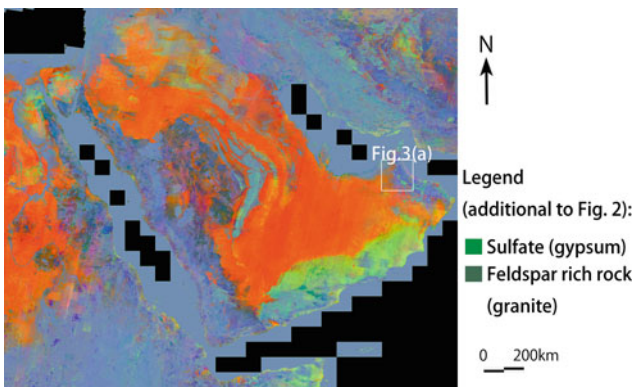

Fig. 3 Global map of mineralogical indices (Fig. 2) enlarged for the Arabian Peninsula and surrounding region. Additional legend to the one in Fig. 2 is: Deep green; sulfate (typically gypsum). Dark bluish green; feldspar rich silicate rock (typically granite)

generating GED. On the other hand, it seems atmospherically moisture-rich pixels including thin clouds, where CI is heavily biased higher, is not detected in generating GED. As a result, many pixels in the CI image created with GED (Fig. 2) are anomalously biased to higher values. These moisture-rich pixels are difficult to detect with VNIR and SWIR data, but detectable by comparing the CI multi-temporal images as in the procedures proposed by the author [2–4].

For the Arabian Peninsula region, the mineralogical map derived with GED (Fig. 3) reasonably shows reddish for quartz, deep greenish for sulfates, light greenish for carbonates, bluish for silicates and dark bluish green for feldspar-rich.

Watching in details for the core study area (Fig. 4a), most of the region seems to be often affected by atmospheric moisture, and therefore, CI based on GED seems generally biased higher. The ultramafic bodies normally denote light magenta by the properties of quite low CI and quite high MI [3, 4], however, anomalous color of bright cyanic blue is denoted in Fig. 4a by the effect of the biased CI. On the other hand, high moisture scenes are eliminated with the procedures proposed by the author (Fig. 4b), and the ultramafic rocks are detected as light magenta, which is quite a consistent color feature with the cases for the same kind of ultramafic rocks in Tibet and the adjacent regions [2–4].

5 Conclusion

ASTER global map of mineralogy using Quartz Index (QI), carbonate Index (CI) and Mafic Index (MI) is created with Global Emissivity Dataset (GED). Although it roughly presents the distribution of the major terrestrial minerals, malfunctions in detecting high moisture pixels are suggested affecting the data quality. On the other hand, the detailed and higher accuracy regional mapping of mineralogy with QI, CI and MI is proposed on the protocol defined by the author with the procedures of selecting well-conditioning scenes and eliminating high moisture scenes. However, as the procedures need to check CI image for all the scenes manually, expanding it to global is not realistic. The combined GED-based and the author's protocol based mapping of mineralogy, that is, applying the author's approach to the selected region with GED, will provide efficient and high-quality mapping of mineralogy with ASTER data for the Arabian Peninsula and the other regions.

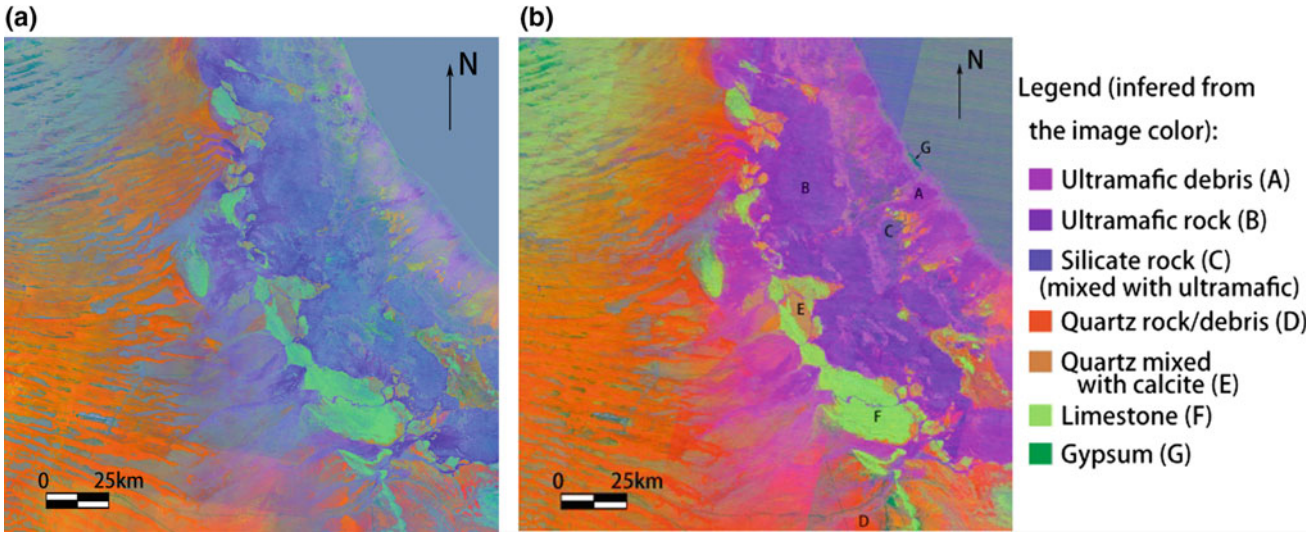

Fig. 4 Color composite image map of mineralogical indices (red: QI, green: CI and blue: MI) for the core study area in Oman-UAE border region, the north-western corner of which is at 25°N in latitude and 55° E in longitude, and the south-eastern corner of which is at 23°N in latitude and 57°E in longitude, created with: **a** ASTER GED of 100 m resolution; **b** the protocol proposed by the author [4] mosaicking well-conditioning ASTER Level-1T data. The legend shows the relationship between the image color and the inferred material for (b). The typical location of each material is pointed in the image with the character "A" to "G", respectively

Acknowledgements Pilong Shi of Institute of Remote Sensing and Digital Earth (RADI), Chinese Academy of Sciences (CAS) has compiled all the files of 1 km GED version 3 into one file. The author would like to thank him for his effort, and appreciate his letting me use the compiled file.

References

1. Ninomiya, Y., Fu, B.: Spectral indices for lithologic mapping with ASTER thermal infrared data applying to a part of Beishan Mountains, Gansu, China. Proc. IGARSS **2001**, 2988–2990 (2001)
2. Ninomiya, Y.: Mapping quartz, carbonate minerals, and mafic-ultramafic rocks using remotely sensed multispectral thermal infrared ASTER data. Proc. SPIE **4710**, 191–203 (2003)
3. Ninomiya, Y., Fu, B.: Thermal infrared multispectral remote sensing of lithology and mineralogy based on spectral properties of materials. Ore Geology Reviews (in press)
4. Ninomiya, Y., Fu, B.: Regional lithological mapping using ASTER-TIR data: case study for the Tibetan Plateau and the surrounding area. Geosciences **6**, 39 (2016)
5. NASA JPL: ASTER Global Emissivity Dataset, 100-meter and 1-km, HDF5 [Data set]. NASA EOSDIS Land Processes DAAC (2014)

Research Issues on Geovisual Analytics for Petroleum Data Management

Rifaat Abdalla

Abstract

The visual and interaction tools are useful in providing decision-makers with a comprehensive overview of multifaceted information gathered from multiple sources. Petroleum Data Management (PDM) is getting more complex due to the diversity in data providers as well as multiple sources, such as well logs, seismic sections, GIS databases, subsurface 3D cross-sections and other forms of technical reports. This research attempts to introduce Geovisual Analytics as a suitable interactive approach for petroleum exploration decision support. The paper will overview research issues and provide implicit insight on research agenda in this important earth science domain.

Keywords

Web-Mapping • Big data • Petroleum • Exploration and production • Geovisual analytics

1 Introduction

Since the explosion of the Internet, there is a huge interest in designing websites which allow users to easily find what they are seeking and to help web analysts in the decision making process. Web Analytic tools facilitate understanding and the discovery of patterns that lay beneath a website, but they are cumbersome to understand since they do not make extensive use of Information Visualization (InfoVis) techniques. The mechanisms provided by current visualization systems allow for the support required for data recovery that is needed for providing archiving of data and provide ease of data recovery, data recall as well as interesting visualizations and reusing archived visualizations [1]. However, visualization systems do not provide support for the conceptualization process related creating and maintaining awareness during the visual exploration process. The process of visual exploration help analyst with specifics for purpose-based visualization of data, i.e., exploration data or development data.

Traditional maps present geospatial data and can deliver understanding into location-based trends and patterns. However, maps can now be used to motivate deeper conceptualization and location-based geospatial patterns, relationships, and trends. A new role of maps in science, decision-making, policy formulation and as a visual thinking/decision-support tool is being adopted widely. Geovisualization as it relates to the new dimension of using maps, through addressing the visual investigation, visual analysis, in addition to the synthesis and presentation of geospatial data through integrating interdisciplinary approaches [2] (e.g. cartography, image analysis, information visualization, visual analytics, and GIScience).

2 Methods

A contemporary approach to dealing with various, complex information is that of Geovisual analytics. It is the combination of human intuition and abstract visual metaphors. Visual analytics stems from scientific and information visualization but also includes technologies from other fields such as, management, statistical analysis, cognitive science, decision science, it allows for. This research attempts to address some basic issues as they relate to geovisual analytics for Petroleum Data Management (PDM). This is through multi-dimensional models, as a standalone models or as a web-based information visualization and search context. This can allow for effective digital archiving of fields and operations zones are active from the historical documents and reports that can be used on ad hoc basis. It allows category-based or field-based search to address short-term and long-term interests based on the task level and to represent it according to the enterprise level

R. Abdalla (✉)
Department of Earth Sciences, College of Science, Sultan Qaboos University, P.O. Box 471 PC. 123, Al-Khoudh, Oman
e-mail: rabdalla@squ.edu.om

© Springer Nature Switzerland AG 2019

H. M. El-Askary et al. (eds.), *Advances in Remote Sensing and Geo Informatics Applications*,
Advances in Science, Technology & Innovation, https://doi.org/10.1007/978-3-030-01440-7_43

Fig. 1 Petroleum data examples

requirements [3]. Geospatial visualization capabilities expand the 1-dimensional information space to 2- or 3-dimensional representations of retrieved results and it can provide combination of user modelling and visualization to develop an approach to assist human users in their search process. The scope of this research attempts to link the traditional geovisual analytics approaches to application specific domain, as it relates to Petroleum Data Management (PDM), and provide strategic agenda for potential research issues that are domain specific, as they relate to petroleum exploration and production, "Fig. 1" is showing petroleum data requirements.

3 Results

3.1 Petroleum Big Data Management (PDM)

Petroleum data management attempts to provide GIS-based system for archiving, and indexing all relevant data with reference to their ground coordinates. This provides extensive database for well logs, seismic sections, technical reports, production reports, maintenance, and follow-up data in addition to various additional sources of data that can be stored, and recalled and visualized to provide specific knowledge about specific location, as it relates to:

1. Spatiotemporal discovery systems that allow for multiple scenario visualization.
2. Tagging and annotation systems that display detailed attributes.
3. Web-based annotation, tagging and annotation capabilities.

3.2 Visual Analytics Capabilities

Traditional GIS systems are to some extent are incapable of coping with the size and complexity data, which requires reduction of the map layer or data for effective use [4], this has triggered the need for new cross-disciplinary methods (e.g. geovisualization, information visualization, data mining, and cartography). 'Geovisual Analytics for Spatial Decision Support' is the name that is adopted for this interdisciplinary approach that address providing computer support to solving geospatial decision issues through enhancing human computer integration to visualize, analyses, and interpret information. Table 1 is showing these challenges.

The distinction between Geovisual Analytics for Spatial Decision Support and Visual Analytics: 1. Complexity of spatiotemporal space, 2. The interdisciplinary scope, and 3. Level of date exploration and knowledge generation. These distinction are relatively addressed by traditional GIS. However, they require sizeable reduction in size and complexity of data, which justifies the need to find a way out of this forced simplification.

4 Discussion

Normally, decision-making process involves various stakeholders with different roles, interests, levels of knowledge of the problem domain and the territory, and experiences in using visualization and analytical tools. The three main players are [5]:

1. Top management decision-makers (administrators/executives)—who often have constraints to gather data, analyze information, and thoroughly evaluate options.
2. Analysts—They normally present results of their analysis to the decision-maker, informing the decision-maker about why they chose a certain option over others. Visual representations and/or 'what-if' scenario, and comparison of options can be valuable for effective communication of information
3. Stakeholders (decision-makers and organizations that can be affected by the decisions made)—they need to be included in the analysis process. They also need an

Table 1 Challenges for geovisual analytics decision support

Common issues that impact usability and user acceptance	Decision-making utilization issues
System and technology utilization issues	Availability
Implementation	Usability
Capabilities	Scalability
Cost	Robustness
Complexity	Agility
Fusion	Standardization
Dynamic visualization	Mature policies
Data communication	Procurement and deployment
Transparent systems	Availability
Interoperability	Usability
System and technology utilization issues	Scalability

effortlessly clear demonstration of information and simply practical information display facilities [6]; in some situations, more tailored visualization might be necessary.

5 Conclusion

Although some research issues have been mentioned, there is progressive need for convincing comprehensive solutions that address the significant advances in creating tools as well as in developing the theory of geovisual analysis. This is a multidisciplinary team's effort. The research in this paper cover a spectrum of the research themes that conceptually necessary for the discussions to highlight how Geovisual Analysis can be integrated as effective interdisciplinary tool for Decision-makers in petroleum industry.

References

1. Shrinivasan, B.Y.: Supporting exploration awareness for visual analytics. In: 2008 IEEE Symposium on Visual Analytics Science and Technology, Columbus, Ohio, USA (2008)
2. Kraak, M.-J.: Geovisualization, International Encyclopedia of Human Geography. Elsevier, New York (2009)
3. www.geoanalytics.net, Internet. Accessed 23 Apr 2018
4. www.infovis.uni-konstanz.de, Internet. Accessed 23 Apr 2018
5. Ecceles, R., Kapler, T., Harper, R., Wright, W.: Stories in GeoTime. In: 2007 IEEE Symposium on Visual Analytics Science and Technology, Sacramento, CA, USA (2007)
6. Ahn, J-W., Brusilovsky, P.: Envisioning user models for adaptive visualization. In: 2008 IEEE Symposium on Visual Analytics Science and Technology, Columbus, Ohio, USA (2008)

Spatial Variations Prediction in Carbonate Porosity Using Artificial Neural Network: Subis Limestones, Sarawak, Malaysia

Yasir Ali, Eswaran Padmanabhan, S. Andriamihaja, and A. Faisal

Abstract

The estimation and modeling of carbonate porosity is of increasing interest in different aspects of geology. Several models have been developed to visualize the pore network systems of carbonate rocks. However, no modeling tools have been designed to predict changes in pore system resulting from dissolution. Therefore, this paper introduced an algorithm for predicting spatial variations in pore network. Carbonate outcropped samples representing different facies from Subis limestone, Sarawak, of Miocene age were used for this study. Continuous imagery along a 10 cm rock chip was conducted using Micro Computer Tomography (CT) scan imagery. The Artificial Neural Network (ANN) predictive code receives images which were read as a matrix. The images were processed using the Image Analysis, coded before use as a training and input data set for ANN. The ANN produced a predicted image with the same properties (such as bits, scalar or raster …etc.) as the input images and at the same interval. The predicted image was compared to the original one to estimate the prediction accuracy. The method proved to give good results in terms of the predicted images accuracy. The method can be applied to study the dissolution phenomenon in carbonates as well as siliciclastic rocks to predict spatial variations and development in a pore network system.

Keywords

Artificial neural network • Spatial variations • Carbonate rocks • Porosity • Subis limestone

Y. Ali (✉)
Red Sea University, Port Sudan, Sudan
e-mail: yasir_earth@rsu.edu.sd

E. Padmanabhan · S. Andriamihaja · A. Faisal
University Teknologi PETRONAS, Perak Darulridzuan, 31750 Tronoh, Malaysia

1 Introduction

Carbonate rocks represent an integral part of hydrocarbon reservoirs, given that they contribute with 60 and 40% of the world gas and oil, respectively [1]. Porosity is one of the most crucial properties of rocks in different geological fields as it determines the content of different fluids in rocks. Porosity of carbonate rocks is an interesting field of research because it varies over a wide range comprising depositional, digenetic, and fracture porosity [2–5]. Moreover, carbonate rocks are characterized with a less stable porosity compared to siliciclastic rocks because carbonate minerals are less stable, soluble, and more sensitive to diagenesis [4] and [6]. Several attempts have been made to model pore systems and pore networks of carbonate rocks [7–12]. The generated models, however, are able only to visualize the existing pore network systems, particularly in sandstone reservoirs because the reservoir has a relatively stable pore network system. The problem with carbonate reservoirs is that their pore systems are susceptible to change [13]. There is no proper modeling of a carbonate pore system that considers the dynamic nature of the pore network system. The available models can only visualize the existing pore systems. Also, there is no predictive tool that can predict the development of such pore network system. Therefore, the main objective of this paper was to construct a predictive tool for spatial variations in pore systems of rocks with depth to be used later for pore system variations induced by dissolution.

2 Materials and Methods

Two samples of limestone from different outcrops were selected for this study, they are of Miocene age formed as a result of uplift processes [14]. Carbonate outcropped samples representing different facies from Subis limestone, Sarawak, of Miocene age were used for this study. The used methods included thin section, CT scan [15]. Both 2D and

© Springer Nature Switzerland AG 2019

H. M. El-Askary et al. (eds.), *Advances in Remote Sensing and Geo Informatics Applications*,
Advances in Science, Technology & Innovation, https://doi.org/10.1007/978-3-030-01440-7_44

3D images for both samples were taken. A Matlab code was written combining the image processing with an artificial neural network (ANN). The ANN used an image dataset as a training data set. The input runs through different iterations from three hidden layers other than the input and output layers. The output is a matrix finally converted into an image of the same properties of the original data set. A code was written to estimate the original image porosity as well as that of the predicted image. The estimation was based on counting the area of pores (blacks ==zeros) to the total number of elements of the image.

3 Results and Discussion

3.1 CT Scanning Imagery

Initially, variations in a pore system with depth were evaluated for both samples, visualized via CT scan imagery (Fig. 1).

The estimation of porosity can provide a supportive evidence for the prediction quality. Porosity of the original sample was found to range from 0.0212 to 0.025% whereas that of the predicted samples varied from 0.0235 to 0.026%. For each sample porosity the predicted sample was slightly higher than that of original sample.

3.2 Prediction from Short-Spaced Constant Interval

The image dataset A was used with a number of four images for a supervised prediction. Comparison between the last item of the input images and the output images is shown in Fig. 2. Visually, the two images show good matching, indicating that the prediction precision is high for both samples. This precision is also confirmed when computing the RSME. The error is calculated based on the comparison between the output/predicted images with the input image. Because the input images consist of a set of four images, all in one continuous series, the comparison was achieved with the distal member (first image ("spari.000") and the nearest member (fourth image "spari.0003"). The same thing was carried out in terms of interval and space selection, training, and ANN applied for both samples I and II.

The prediction based on short-spacing constant interval achieved for the other sample showed a good matching between predicted and original images. It is clear that applying closer intervals of input data reduces the error in prediction and enhances the functionality of the algorithm. Comparison between predicted and original images is shown in Fig. 3.

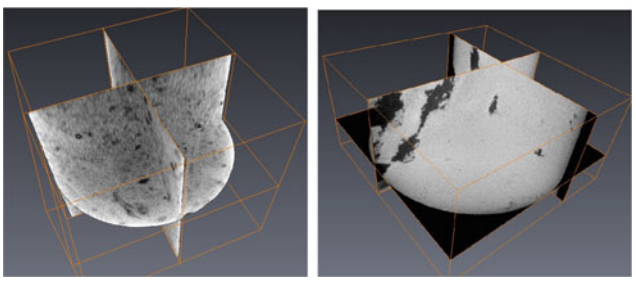

Fig. 1 **a** and **b** 3D visualization showing Pore distribution in the X-, Y-, and Z-axes for samples I and II respectively

3.3 Prediction from Large Constant Intervals

An interval of 50 images was selected for a larger interval prediction. The preliminary results showed that the error slightly increased from 4.4% for the proximal member to 14.8 for the distal member of image series. The same was performed for Group II.

3.4 Prediction from Varying Intervals

Prediction was achieved while varying the used interval with relatively much more data. A number of seven input images were used as a training dataset (images spari000-spari0006). The prediction precision for both samples is evidently very high.

4 Conclusion and Recommendations

The combination of image processing and ANN Matlab code provided a means for predicting spatial variations of pore network systems of carbonate rocks. The precision of the prediction was enhanced by increasing the number of input images. Prediction using constant short intervals showed high accuracy in both samples, while, prediction from constant interval using wide spacing resulted in the reduction of accuracy for sample 1 which has a relatively similar intensity in the pore network. For sample II, which showed a decrease in the pore network intensity with depth, large-interval prediction was different when compared to the original. Prediction while varying intervals showed good results. The method can be applied to study the dissolution phenomenon in carbonates as well as siliciclastic rocks to predict variations in a pore network system.

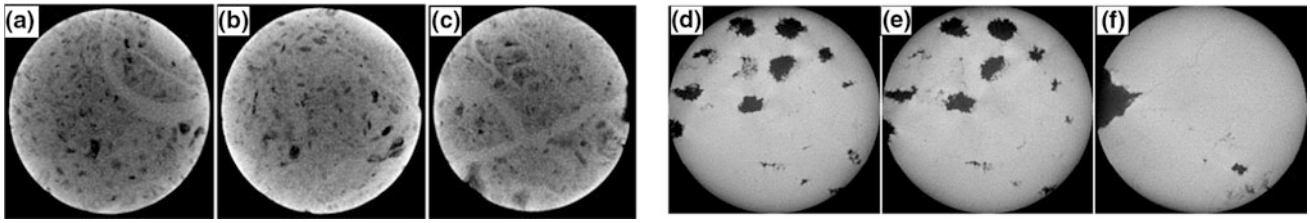

Fig. 2 Variation in pore system of the carbonate rocks for sample I (**a**-**c**), and sample II (**d**-**f**): images (**a**), (**b**), and (**c**) represent top, middle, and bottom of the sample respectively

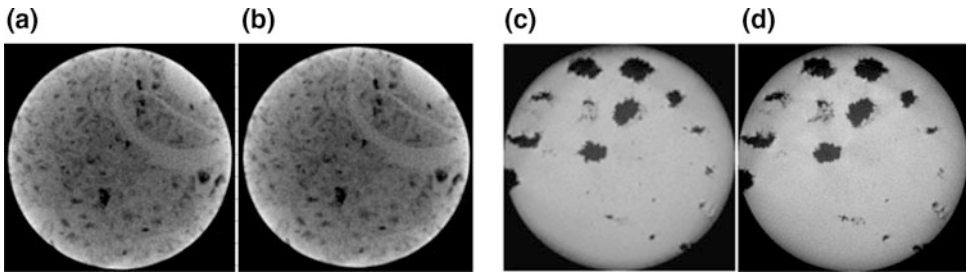

Fig. 3 Shows comparison between the last member of input images (**a**) and (**c**); and the output image (**b**) and (**d**) for sample I and II, respectively

References

1. Schlumberger: Carbonate Reservoir, Meeting Unique Challenges to Maximize Recovery, pp. 1–16 (2008)
2. Chilingar, G.V. (ed.): Fairbridge: Carbonate Rocks: Origin, Occurrence and Classification, p. 471. Elsevier, Amsterdam, London, New York (1967)
3. Mackenzie, J.W.: Geochemistry of Sedimentary Carbonates, p. 706. Elsevier, Amsterdam (1990)
4. Clyde, M.: Carbonate Reservoirs: Porosity Evaluation and Diagenesis in a Sequence Stratigraphic Framework (Developments in sedimentology 5), p. 444 (2001)
5. Fliigel, E.: Microfacies of Carbonate Rocks: Analysis, Interpretation, p. 669. Springer, Berlin, Heidelberg, New York (1967)
6. Ahr, W.M.: Geology of Carbonates: The Identification, Description, and Characterization of Hydrocarbon Reservoirs in Carbonate Rocks, p. 296. Wiley, Canada (2008)
7. Nurgalieva, N.D.: Porosity estimation of carbonate rocks with. ARPN J. Eng. Appl. Sci., 20–24 (2014)
8. Srivastava, R.M.: An Overview of Stochastic Methods for Reservoir Characterization, Stochastic Modeling and Geostatistics Principles, Methods, and Case Studies, 2nd edn, p. 370. The American Association of Petroleum Geologists, Tulsa, Oklahoma, USA (1994)
9. Wang, X., Ghassemi, A.: A three-dimensional stochastic fracture network model for geothermal reservoir stimulation. In: Proceedings, Thirty-Sixth Workshop on Geothermal Reservoir Engineering, (p. 11). California (1982)
10. Petrel. Petrel Homepage: http://websitedhoome.com/getthefile/?tr=2512&affiliate_id=2512&q=petrel. Accessed 2017
11. Zinszer, A.: A Geoscientist guide to Petrophysics, p. 363. Editions Technip, Paris (2007)
12. Bohling, G.: Stochastic Simulation and Reservoir Model Framework, p. 20. Kansas Geological Survey, Kansas (2005)
13. Noel, P., et al.: Origin of Carbonate Rocks, p. 464. Wiley, Canada (2015)
14. Sleumer, B.H.: The Subis Limestone Complex—Sarawak, Malaysia: Abstract-Proceedings of the Carbonate Seminar. In: AAPG Indonesian Petroleum Association, pp. 120–121 (1976)
15. Hartmann et.al.: CT Scanning–Techniques and Applications, p. 358 (Subburaj, K., ed.) Croatia: Janeza Trdine 9, 51000 Rijeka (2011)

Potential Artisanal to Small Scale Cement Production Site Determination Using Qualitative Site Multifactor Analysis: Case Study—South Africa

Freeman Senzani and Antoine Mulaba-Bafubiandi

Abstract

This study reviewed, captured, analyzed and synthesized all geochemical data of carbonate rocks in South Africa. It then applied the information to determine targets for small-scale cement manufacturing. So far, the geochemical data and the samples locations were not indicated in any open electronic database. In this investigation, the geographic locations were determined and coordinates entered into an electronic database, in which they were linked to the tables of geochemical data. Comparison with the oxide levels necessary for cement manufacture i.e., CaO ($\geq 42\%$), MgO ($\leq 4\%$), SiO_2 ($\leq 15\%$), Al_2O_3 + Fe_2O_3 ($\leq 16\%$), silica ratio ($SiO_2/(Al_2O_3 + Fe_2O_3)$) and $Na_2O + K_2O$ ($\leq 0.6\%$) were then conducted. Sites passing the geochemical tests were considered further after eliminating those locations further than 10 km from vital infrastructure namely roads, rail, electric power, water sources and human population clusters. Of the 709 sites identified, only four met the foregoing criteria used. These fall on the farms Wieduow 309DH, Syferfontein 457KR, Rietfontein 736KS and Rooikop 1590HR. The assessment has also revealed many deposits with inadequate geochemical information. Some of them fall close to the above infrastructural features, and thus warrant the sampling and chemical analyses.

Keywords

Cement • Limestone • Carbonate • Database • GIS

1 Introduction

There has been an attempt to open up the mining and mineral beneficiation industry in South Africa to individuals and entities that could not access it before 1994, the year which marked the beginning of the country's new political dispensation [1]. This is especially relevant in the country, as it has the greatest Gini Coefficient in the world, and an unemployment rate of 40% in general, but 60% among the youth. One of the sectors being considered is the artisanal and small-scale manufacture of Portland cement [1]. To this end, two parallel lines of investigation have been launched by the authors. The first involves the identification of sites of carbonate rock around the country using geochemical criteria [2]. The second involves research in the development of technology that is suitable for operation by the artisanal producers. The success of the approach will also prove useful in countries where large scale operations are not feasible due to the absence of high-tonnage limestone deposits [2]. It also models the investigation necessary to identify and assess industrial mineral deposits that may be developed for the benefit of the rural communities living in their proximity [2].

To this end, this study has reviewed, captured, analyzed and synthesized all geochemical data of carbonate rocks in South Africa. So far, the information has not been deposited in any open-access electronic database, but in various paper documents and maps, spanning several decades of disjointed field sampling and chemical assaying [3–6]. The data situation also applies to the geographic location information, thus this assessment also involved the determination and electronic capture of geographic coordinates of the different sites from which the historical samples were collected. Another innovation of this exercise was the linking of the assay and the location within a geographic information system (GIS) database which is now available on request.

F. Senzani (✉) · A. Mulaba-Bafubiandi
Department of Metallurgy, Faculty of Engineering and the Built Environment, School of Mining Metallurgy and Chemical Engineering, Mineral Processing Technology Research Centre, University of Johannesburg, P. O. Box 17911 2028 Doornfontein, South Africa
e-mail: fsenzani@uj.ac.za

© Springer Nature Switzerland AG 2019

H. M. El-Askary et al. (eds.), *Advances in Remote Sensing and Geo Informatics Applications*, Advances in Science, Technology & Innovation, https://doi.org/10.1007/978-3-030-01440-7_45

2 Methods

In this review and target generation study, the first step was to find, manually, all sites with carbonate in the country. The second was to capture, electronically, their coordinates in a GIS.

The third task of this study followed from the recognition that carbonate rocks are considered to be suitable for the manufacture of cement if the oxide contents are such that CaO ($\geq 42\%$), MgO ($\leq 4\%$), SiO_2 ($\leq 15\%$), Al_2O_3 + Fe_2O_3 ($\leq 16\%$), silica ratio ($SiO_2/(Al_2O_3 + Fe_2O_3)$) between 1 and 4, but also $Na_2O + K_2O$ ($\leq 0.6\%$) [5, 7–9]. Thus, in the third undertaking of this assessment, sites with deposits with these oxide levels were determined for further consideration as below.

The fourth and final test of this evaluation effort involved the determination of the proximity to infrastructure and clusters of human populations using GIS. Only carbonate locations falling within 10 km were considered suitable. The infrastructure features considered were roads, rail, electric power, and water sources. The sites had also to lie within the same distance of a human population cluster with $\geq 1000\ km^{-2}$.

3 Results

The study has identified 709 deposits and deposit clusters in South Africa (Fig. 1) from various hard copy sources. Associated with some of the deposits are 365 assays which this assessment linked with the individual sites, thereby showing that of the 709 sites and site clusters, only 169 have, in addition to the CaO assays, the results of analyses of the other oxides, namely MgO, SiO_2, Al_2O_3, Fe_2O_3, K_2O and Na_2O. Of the 169 sites and site clusters, 69 returned CaO > 42% and MgO $\leq$ 4%, 14 have the suitable levels of the rest of the oxides, while only 4 met the infrastructural, water resources and population node criteria (Fig. 2).

4 Discussion and Conclusion

Carbonates are suitable for Portland cement production if they contain at least 42% CaO, up to 4% MgO, up to 15% SiO_2, up to 16% $Fe_2O_3 + Al_2O_{3\%}$, silica ratio ($SiO_2/(Al_2O_3 + Fe_2O_{3\%})$) between 1 and 4, and up to 0.6% $Na_2O + K_2O$ [5, 7–9]. Sampling and analyses were carried out by various workers over decades in the country [3–6]. In this study, the data were captured and used to produce new findings. This enabled the determination of sites where the oxide levels were suitable for cement manufacture. Using GIS, the data were linked to the sample geographic locations, infrastructure and human population clusters. In turn, this facilitated the identification of sites with material passing the geochemical tests. Such sites were further assessed in order to find out if they fell within 10 km of a road and a rail track, an electric power line, surface water sources and centers of high human population densities $\geq 1000\ km^{-2}$.

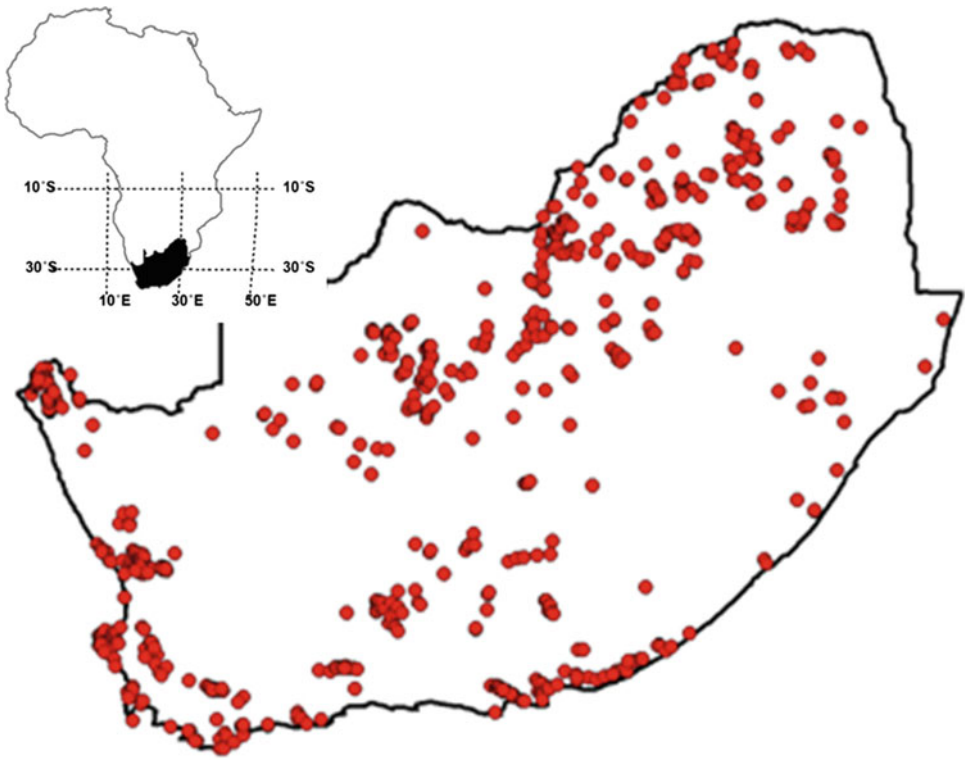

Fig. 1 Locations of carbonate deposits in South Africa (red dots)

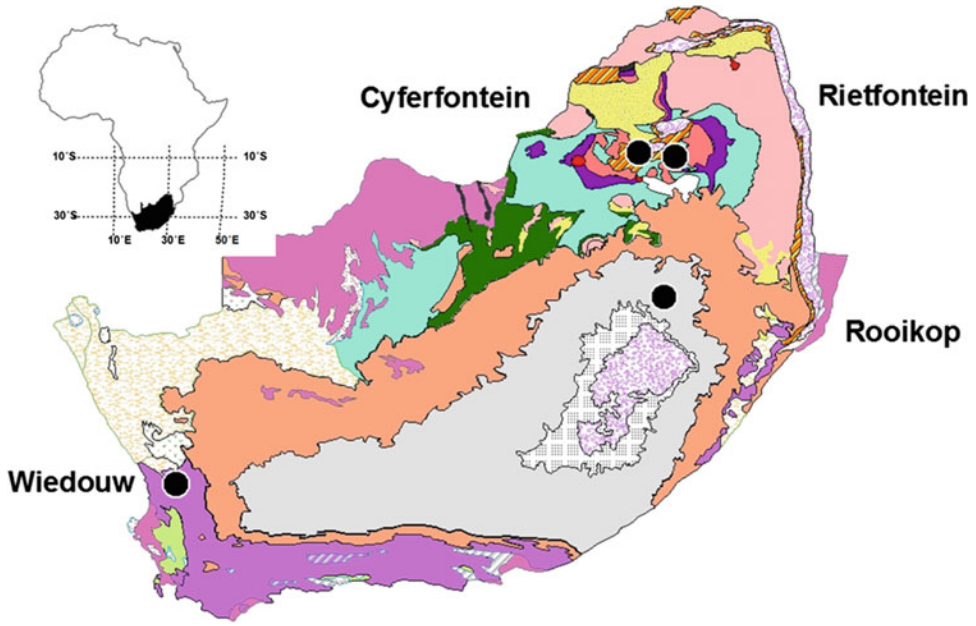

Fig. 2 Locations of carbonate targets for small-scale Portland cement production in South Africa (black dots)

Table 1 Carbonate deposits of South Africa satisfying chemical criteria for artisanal to small-scale Portland cement manufacture

Site no.	Site name	Province	WGS-Clarke 1880 coordinates in degrees	
			X	Y
1	Wieduow 309DH	Western Cape	18.734328	−31.729248
2	Rooikop 1590HR	Free State	28.980000	−27.828400
3	Syferfontein 457KR	Limpopo	28.461161	−24.811364
4	Rietfontein 736KS	Limpopo	29.196800	−24.906100

This review identified and located the 709 sites or site clusters of carbonate deposits in South Africa. It further determined the 4 sites suitable for location of small-scale Portland cement production. The sites fall on farms Wieduow 309DH in the Western Cape Province, Syferfontein 457KR and Rietfontein 736KS in the Limpopo Province, and Rooikop 1590HR in the Free State Province (Table 1). They should be investigated further for potential exploitation by local producers of lime and cement.

References

1. Tongu, E.L.: Limestone Report. Council for Geoscience, Pretoria, South Africa (2007)
2. Senzani, F.E.D., Mulaba-Bafubiandi, A.F.: Small scale processing economic potential of Malawian carbonate resources for cement production. In: Proceedings of the 35th International Geological Congress, Cape Town, 27 Aug–4 Sep (2016)
3. Wybergh, W., Du Toit, A.L.: The limestone resources of the union. Vol. 1—The Limestone Resources of the Transvaal and Portions of Bechuanaland and Zululand: Memoir of the Geological Survey of South Africa, **2**, 122p (1918)
4. Wybergh, W.: The Limestone Resources of the Union. Vol. 2—The Limestone Resources of Natal, Cape and Orange Free State Provinces: Memoir of the Geological Survey of South Africa, **11** (2), 149p (1920)
5. Martini, J.E.J.: Limestone and Dolomite Resources of the Republics of South Africa, Bophuthatswana, Ciskei, Transkei and Venda. Geological Survey, Department of Mineral an Energy Affairs, Handbook 9. Government Printer, Pretoria, 112p (1987)
6. Vorster, C.J.: Limestone and Dolomite Deposits: South Africa, Lesotho and Swaziland. Council for Geoscience—SAMINDABA map. Pretoria (2003)
7. Eckel, E.C.: Cement Materials of the United States, United States Geological Survey, United States Department of the Interior (1905)
8. Taylor, H.F.W.: Cement Chemistry. Academic Press, London (1990)
9. British Geological Survey (BGS), Mineral Profile, Cement Raw Materials. Office of the Deputy Prime Minister (2005)

Lineament Mapping Using RS and GIS Techniques at Mbateka, SE Cameroon: Implication for Mineralization

Melvin Tamnta Nforba, Linus Api, Nelvice Berinyuy, and Salomon César Nguemhe Fils

Abstract

The application of remote sensing and GIS technology has shown a great promise, over the years, and offered opportunities for improving identification of areas that are likely to be locations of lineament and mapping. Based on the ability to identify geological features, Landsat ETM-7 satellite data images were used and band-5 was found as the most suitable for lineament delineation. Parameters such as drainage patterns, previously mapped faults, lineaments, and lithological contact layers were used in this study, to produce a fault potential prediction map using the overlay model technique. The generated fault density map classifies the study area into 5 potential zones, thus, very low, low, moderate, high, and very high potential zones. 33 faults, which may represent new faults in the area of investigation were obtained from the correlation between fault segments and faults data collected from field work. NW–SE is the general orientation of the fractures and N100-1100E was the major trend obtained from fault analyses. Poly-phase ductile-brittle structures such as shear zone and faults in the study area were confirmed by our findings. Iron mineralization in the area is controlled by those structures since they form pathways for mineralizing fluids.

Keywords

Landsat ETM-7 images • Lineaments • Mineralisation • Mbetaka

1 Introduction

In the field of structural, economic and environmental geology, fault detection is an essential element. Faults are defined as weakness zones in the brittle part of the lithosphere, along which movements can take place in response to induced stresses. When faults undergo displacement, depending on geological and structural conditions, strain markers can be formed on the fault surface [1, 2]. The presence of faults in any area is based on displacement of rock layers. Also, within an area, most faults are represented by some geological features such as drainage patterns, lineaments (linear features), and lithological contacts between rock units.

Geological features are any alignment of features on satellite images such as topographic, drainage patterns, vegetative cover, and color alignments that can be recognized. Patterns such as faults, folds, joints and other structures found in rocks are geological structures or features from a natural deformation. Digital elevation models (DEMs) are very useful in aiding with the classification of landforms for many purposes [3]. Faults are often shown as linear or curvilinear traces on satellite images [1] and may extend from a few meters to tens of kilometers in length [2].

Traditional methods of fault mapping require fieldwork investigations [3]. This is usually time consuming and may take up years to complete, depending primarily on the extension and/or the accessibility of the area under investigation [3, 4]. Topography, erosion, vegetation overgrowth, scale, experience of geologists and other factors control fault determination in the field. Remote sensing has the advantage of providing synoptic overviews of the region; thus it may directly pinpoint the characteristics of structural geological

M. T. Nforba (✉)
School of Geology and Mining Engineering, University of Ngaoundere, P.O. Box 115 Meiganga, Cameroon
e-mail: nforbamel@gmail.com

L. Api
Department of Geology and Mining, Saint Monica University Institute, P.O Box 132 Buea, Cameroon

N. Berinyuy
Economic Geology Unit, Department of Geology, University of Buea, P.O. Box 63 Buea, Cameroon

S. C. N. Fils
Institute of Geological and Mining Research (IRGM), P.O Box 4110 Yaounde, Cameroon

© Springer Nature Switzerland AG 2019

H. M. El-Askary et al. (eds.), *Advances in Remote Sensing and Geo Informatics Applications*, Advances in Science, Technology & Innovation, https://doi.org/10.1007/978-3-030-01440-7_46

features extending over large areas [1, 3]. As opposed to fieldwork investigations, remote sensing together with image processing techniques are less time-consuming [4] and more cost-effective methods for fault detection [5]. Nonetheless, such techniques in no way replace field investigations, but on the contrary complement it.

Several studies [1–7] have been carried out to enhance geological knowledge, mineralization and revise existing geological maps using optical remotely sensed data and discovered new faults (mineralized and non-mineralized).

In this paper, remote sensing data processing and GIS modeling techniques were used to map and locate new faults in the study area. The objective of this study is to test the ability of GIS for fault detection over the study area and investigate its capacity in giving real results on mineralization as compared to the previous data with respect to the ground truth (field work). The approach used as well as the data obtained would make an important guide for the mineral (iron ore) exploration in the area.

2 Geological Settings, Materials and Methods

Mbateka is located in the southeastern part of Cameroon and extends between latitudes 2° 15′ 46.8″ and 2° 02′ 9.6″N and longitudes 15° 14′ 38.4″ and 15° 09′ 3.6″E (Fig. 1) with a typical equatorial climate. The geomorphology of the area falls within the Southern Cameroonian plateau, characterized by tree covered rolling hills at an average elevation that ranges between 360 and 580 m.

The Congo Craton form part of the Archean Cratonic basement, covering large parts of southern Cameroon known as the Ntem Group [8]. The Mbateka area forms part of the Lower Dja Series (Fig. 1). This series consists of poorly-exposed and structurally-complex, Archean greenstones belts. It rests, by an angular unconformity on the Archean basement of the Chaillu block in the northeastern Republic of Congo and on the Ntem Complex in Cameroon [9]. The rock types in this area are metapelites and sandstones, dated to Palaeoproterozoic [10], quartzites, amphibolites, gneisses.

All of the lithological contact, fault, drainage, and lineament factors as well as DEM data were used for fault identification and mapping (potential fault zones mapping) in the study area. The other data used in this study were topographic and geological maps. ArcGIS 10.3®, Surfer 11®, and Global Mapper 12® were used for data processing. Structural measurements were performed on the field and the processed data were plotted using rose diagram. The ranking classification system was used to determine the spatial distribution of buffering zones based on equal area classes. Table 1 outlines the classes and their weight layers used in this study. Each class gives a weight to express the occurrence of fault.

LandSat images were used for lineament processing. A band 5 was used due to its ability to delineate lineaments. A Laplachian 3 × 3 filter was applied to the images to enhance those using ArcGIS 10.3 with a Sobel Kernel (Table 2), which convolved over band-5 in four principal directions and the filtered image was added back to the original one.

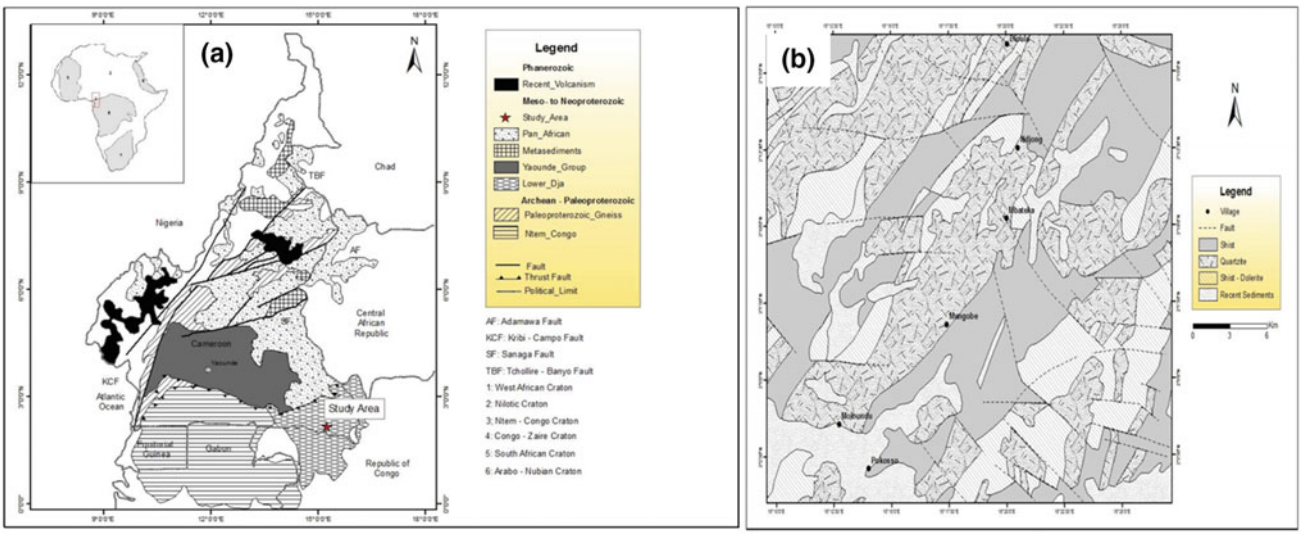

Fig. 1 **a**. Geologic map of Cameroon [11], showing the location of Mbetaka area and the main lithotectonic domains: (1) southern domain; (2) central domain; (3) northern domain; BOSZ: Bétaré-Oya Shear Zone; SF: Sanaga Fault; TBF: Tibati-Banyo Fault; NT: Ntem complex; DS: Dja Series; NS: Nyong Series. **b**. Geologic Map of Mbateka area extracted from [9]

Table 1 Parameters and weight values given to different factors in study area

Classes	Weight value
≤ 30	5
30–60	4
60–90	3
90–120	2
≥ 100	1

Color adjustments were carried out to the approximate pixels suitable intensities by increasing the levels of brightness and contrast of the image. This map was further processed to produce a point spread filtered map. The four enhanced filtered images were combined together to produce one threshold filtered image, which was subjected to pixel reduction. The lineaments detected during the interpretation process were manually traced and stored as vector file. The lineament map was then prepared and converted into lineament buffer layer and into slicing layer with five classes and finally to weight layers.

Contour line data was obtained from SRTM images with a 90 m resolution. The contour data were then used to create the DEM data with 30 m resolution of the study area. Interpolation and rescaling processing was used to convert contour line data into 30 m grid layer. The drainage pattern was then extracted automatically from the DEM data using ArcGIS 10.3 transforming it into a vector layer and then converting it into a buffer layer with 5 classes.

Few contacts between different rock types were observed in the study area due to poor accessibility. The lithological contact layer and the faults of the study area were digitized from the geological map of Mbateka. The lithological contact layer was converted into a lithological buffer layer and finally into a weight layer using the values in Table 1. The fault layer was converted into a fault buffer and then converted into weights layer.

The spatial multilayers analysis (overlay layers model) was used by combining and aggregating the maps generated. The fault segment model was produced using the modified drastic linear model equation given by:

$$Potential\ Map : DRN_W + DEM\ filter\ (shaded) + FLTw + LINw + LCTw$$

where, DRN_W is the drainage weight layer, FLT_W the fault weight layer, LIN_W the weight layer, and LCT_W the lithological contact weight layer.

3 Results

3.1 Lineament Features Structural Mapping and Characterization

Both automatic extraction and visual interpretation which help to highlight the tectonic lineaments of the area after the images were transformed, enhanced and filtered. This analysis identified 33 new linear elements. Figure 2a shows the

Table 2 Sobel kernel filters in four main directions

Four main principal directions											
NW–SE			E–W			NW–SE			N–S		
−2	−1	0	−1	−2	−1	0	1	2	1	0	−1
−1	0	1	0	0	0	−1	0	1	2	0	−2
0	1	2	1	2	1	−2	−1	0	1	0	−2

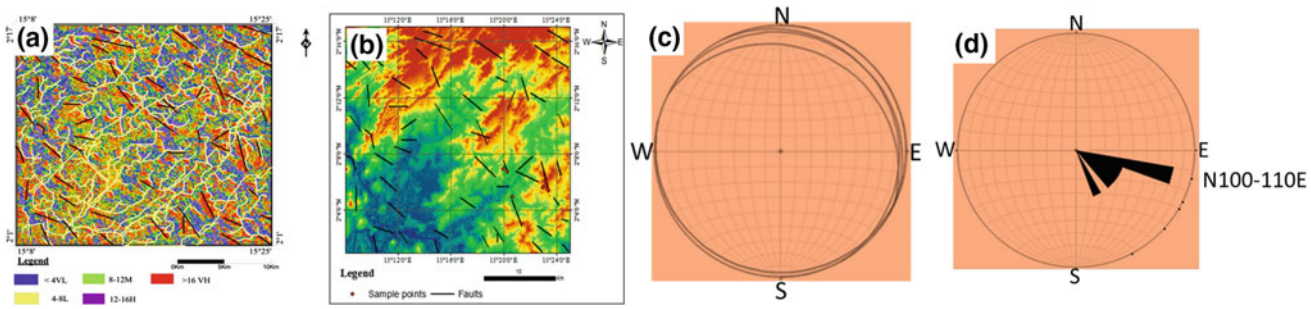

Fig. 2 **a**. Density map of fault zones over the study area, **b**. The 55 fault segments (fault lines) as extracted from the susceptibility map over the study area, **c**. Stereoplot and **d**. Rose diagram of faults from field mapping

results of the filtering and manual digitalized transformation of the lineaments. The resulting model map was classified into different zones using the ranking values into very low, low, moderate (medium), high and very high fault zones or equal area classes (Fig. 2). All the red zones were delineated for potential fault segments (Fig. 2b). There were some very high and high potential fault segments that did not match previously mapped faults. The structural (strike/dip of faults) measurements obtained during field work, were plotted on the fault model map to check if any correlation exists between the modelled and measured faults. This interpretation is confirmed by field data which have surfaced with NW–SE-trends.

3.2 Relationship Between Field Data and Satellite Image Data

The structural reading (strike/dip) of faults from fieldwork stations were analyzed to compare with the results from the remote sensing method. The strike-dip readings of the shear joints from different rock units of the area were analyzed with the stereographic plot (Fig. 2c) and Rose diagram (Fig. 2d). According to the fractures analysis result, compressional principal stress (α_1) was measured to be in the NW–SE direction. The major trend obtained from the analysis is N100-110E. There is a tendency for certain faults to turn toward NW–SE.

4 Discussion

The results indicate a similarity [1, 2, 12, 13] between faults morphology and the shearing events based on satellite data interpretation and field observation/ground truth. There is positive correlation between previously mapped faults and fault segments delineated from GIS modelling. The area presents varying degrees of susceptibility or high lineament (fault) density zones. The very low, low, medium, high and very high potential fault have total areas of 7, 15, 22, 26 and 30% respectively (Fig. 2b). The high and very high zones dominate and cover most of the faults. According to [1, 5], the zones of relatively high lineament density are identified as zones of high degree of rock fracturing, which are possible conduits for the hydrothermal fluid. At Mbetaka, iron mineralization is closely related to the dense lineament areas. The lineament intersection map provides interpretation of hidden subsurface tectonic configuration in the form of linear feature intersection/cross cutting geological structures [1, 5], which are indicators of deep seated fracture/fault medium.

From observations, the fault segments obtained from this model were relatively shorter in length compared to previous faults [1, 14, 15] in the area. The strike-dip readings of the shear joints from different rock units of the area were analyzed with the stereographic plot (Fig. 2c) and Rose diagram (Fig. 2d). The major trend obtained from the analysis is N100-110E. There is a tendency for certain faults to turn toward NW–SE. This correlates with the direction of subduction of the Ntem complex of the Congo cratonic plate under the Pan-African mobile belt [15] with two shear senses (dextral and sinistral) with prominent NW–SE and NE–SW directions.

According to [14] three deformational phases affected the area with D_1 not well defined structurally. However, [15] concluded that structures associated with D_1 deformation are oblique and crosscut by the D_2 deformation phase and are associated with metamorphic amphibolite facies. The D_2 is prominent regionally and is associated with granitization and intense migmatization [16] of the amphibolite and greenschist facies and this corresponds to the high fault density zones as obtained in this study. Regionally, the D_2 deformation phase also develops sinistral N–S and NW–SE direction corresponding to a period of intense and widespread deformation of the crust [14–16]. Their variations in this area from N100-110E and iron ore mineralization are directly linked to this orientation. The D_3 phase is characterized by intense mylonitic or brittle deformation and their direction generally vary from N045E to N115E, similar to lineament depicted from this study.

Overall, the linear structures obtained from the image processing correspond to the ductile-brittle structures such as shear zone and faults. These structures form pathways for both mineralizing fluids and ground water.

5 Conclusions

- This study shows that remote sensing data and GIS technique are powerful tools in identifying geological structures such as fault segments especially in area where field mapping may be hampered by thick vegetation cover.
- There is good correlation and distribution between fault segments and faults (previous fault lines) in the study area and a corresponding correlation with iron mineralization.
- There are 33 new fault zones have been identified in the area. The presence of these faults is not known from the previous literature and this study has shown that structures control mineralization in this region.

References

1. Abdullah, A., Nassr, S., Ghaleeb, A.: Remote sensing and geographic information system for fault segments mapping a study from Taiz Area, Yemen. J. Geol. Res., 1–16 (2013). http://dx.doi.org/10.1155/2013/201757
2. Karimi, B., Karimi, H.A.: An automated method for the detection of topographic patterns at tectonic boundaries. In: The Ninth International Conferences on Pervasive Patterns and Applications, pp. 72–77 (2017)
3. Papadaki, E.S., Mertikas, S.P., Apostolos, Sarris A.: Identification of lineaments with possible structural origin using ASTER images and DEM derived products in Western Crete, Greece. EARSeL eProceedings **10**, 9–26 (2011)
4. Cracknell, A.P., Hayes, L.: Introduction to Remote Sensing. Taylor & Francis Press, London (1991)
5. Edet, A.E., Teme, S.C., Okereke, C.S., Esu, E.O.: Application of remote sensing data to groundwater exploration: a case study of the cross river state, Southeastern Nigeria. Hydrogeol. J. **6**, 394–404 (1998)
6. Solomon, S., Ghebreab, W.: Lineament characterization and their tectonic significance using landsat TM data and field studies in the central highlands of Eritrea. J. Afr. Earth Sci. **46**(4), 371–378 (2006)
7. Mogaji, K.A., Aboyeji, O.S., Omosuyi, G.O.: Mapping of lineaments for groundwater targeting in the basement complex region of Ondo State, Nigeria, using remote sensing and geographic information system (GIS) techniques. Int. J. Water Resour. Environ. Eng. **3**(7), 150–160 (2011). http://www.academicjournals.org/ijwree
8. Ndéléc, A., Nsifa, E.N: Le complexe du Ntem (Sud-Cameroun): une serie tonalitique rondhematique archeene typique. In: Schandelmeier, H., Matheis, G. (eds.) Current Research African Earth Sciences, pp. 3–6. Berlin (1987)
9. Vicat, J.P., Lips, B., Pouclet, A., Léger, J.M., Willems, L.: Phénomènes pseudo-karstiques dans les roches plutoniques et métamorphiques du Sud du Cameroun. Karstologia **29**, 17–22 (1997)
10. Vicat, J.P., Gaetan, M., Pouclet, A.: Les granitoïdes de la couverture protérozoïque de la bordure nord du craton du Congo (Sud-Est du Cameroun et Sud-Ouest de la République centrafricaine), témoins d'une activité magmatique post-kibarienne à pré-panafricaine. Earth Planet. Sci. **332**, 235–242 (2001)
11. Nzenti, J.P., Abaga, B., Suh, C.E., Nzolang, C.: Petrogenesis of peraluminous magmas from the Akum-Bamenda Massif, PanAfrican Fold Belt, Cameroon. Int. Geol. Rev. **53**(10), 1121–1149 (2011)
12. Sulaksana, N., Hamdani, A.H.: The analysis of remote sensing imagery for predicting structural geology in Berau Basin East Kalimantan. Int. J. Sci. Res. **3**(4), 18–21 (2014)
13. Limaye, M.A.: Unfolding the time relationship of structural events through landsat data: a case study from Khandia formation, Champaner group, Gujarat. J. Geomatics **10**(1), 24–28 (2016)
14. Wambo, J.D.T., Ganno, S., Ngambu, A.A., Negue, N.E., Ondoa, J. M., Nzenti, J.P.: Use of landsat 7 ETM+ Data for the geological structure interpretation: case study of the Ngoura-Colomines Area, Eastern Cameroon. J. Geosci. Geomatics, **4** (3), 61–72 (2016). http://pubs.sciepub.com/jgg/4/3/3, https://doi.org/10.12691/jgg-4-3-3
15. Nzenti, J.P., Kapajika, B., Wörner, G., Lubala, R.T.: Synkinematic emplacement of granitoids in a Pan-African shear zone in Central Cameroon. J. Afr. Earth Sci. **45**, 74–86 (2006)
16. Ngako, V., Affaton, P., Nnange, J.M., Njanko, T.: Panafrican tectonic evolution in central and Southern Cameroun: transpression and transtension during sinistral shear movement. J. Afr. Earth Sci. **36**, 207–214 (2003)

Prediction of Lamination Patterns in Heterolithic Sedimentary Sequence, Offshore Sarawak (Malaysia)

Yasir Ali and Eswaran Padmanabhan

Abstract

This paper aimed at predicting spatio-temporal variations and new lamination patterns based on available core samples and core images. For this purpose, a scan line method was applied on core photographs showing heterolithic laminations to generate a signal. Then, the generated signal from the scan line was analyzed and interpreted as time series data that can be used in many applications. Samples were taken from different depths to reflect the temporal or vertical variations, and their signal data were compiled into one continuous time series. A new pattern of sedimentary structures represented by new signal data was identified and was converted back into sedimentary structures. The predicted pattern varies in space and depth, and therefore, represents variations on both spatial and temporal bases. The study is therefore significant as the prediction of different patterns can provide information on the depositional environment, paleogeography, and petrophysical properties.

Keywords

Scan line method • Signal analysis • Spatio-temporal variations • Heterolithic sequences

1 Introduction

The study of lamination is of great significance in determining reservoir properties as well as inferring the depositional environments, paleo-current direction, paleogeography, and the prediction of reservoir properties. Several methods have been applied for the purposes of lamination pattern prediction. Data of sequential nature such as sedimentary sections, stratigraphic record… etc., can be considered as signals [1]. Lamina extraction in the form of signal from core images was applied as a nondestructive, low cost method [2]. Several trials in signal extraction and analysis have recently been made. These mostly depend on Fast Fourier Transforms to produce signal from any sequential data. A time series analysis such as wavelet analysis can be applied to analyze patterns and convert depth scale into time scale. This method was used to interpret the geological records and reveal the climatic change [3]. Steps for converting image data into high-resolution data are best described in [4]. These include different steps on image processing. The current study aimed at analyzing and interpreting such patterns as time series data and predicts spatio-temporal variations in lamination patterns.

2 Materials and Methods

Core samples were selected from two wells (Well 1 and Well 2) from the Alpha Field which is located in the offshore part of Sarawak where 70% of the province is located in the offshore Sarawak [5, 6]. The cores were studied, described and photographed. Dominant lamination types were identified for each well. Light images (in RGB colors stored as JPEG format) were taken using a digital camera set at the same distance from the core and the same illumination intensity to avoid errors in signal acquisition. Colors were assigned for each lithotype by mapping core images versus core samples. Signals were extracted using time Signal-Strata software in longitudinal scan lines across the lamination. Normally, converting image data into high-resolution data involves different steps in image processing [4].

Y. Ali (✉)
Red Sea University, Port Sudan, Sudan
e-mail: Yasir_earth@rsu.edu.sd

E. Padmanabhan
University Teknologi Petronas, 31750 Tronoh, Perak Darulridzuan, Malaysia

© Springer Nature Switzerland AG 2019

H. M. El-Askary et al. (eds.), *Advances in Remote Sensing and Geo Informatics Applications*,
Advances in Science, Technology & Innovation, https://doi.org/10.1007/978-3-030-01440-7_47

3 New Patterns Prediction

To achieve this type of prediction, a free statistical-based package, GMDH (Shell) [7] was used, with the capability of receiving time series data as XLS, SVG and TXT format, analyze them, and predict different patterns. This format is received as output from the strati-signal software [8] used for image scan line. Conversion from depth series to time series and the prediction process are designed to estimate the spatio-temporal variations. Scanned data from Well 2 (lower in depth) were compiled with data of Well 1 (deeper than well two) to form a continuous time series.

4 Results and Discussion

The core description showed that Well 1 is dominated by dark, massive or lenticular brown shale. The massive shale exhibited some degree of coloration and fracturing, and is bioturbated in many instances. The lenticular shale showed sediment deformation structures such as convoluted lamination, pillows and microfaults. Sandstone is interbedded and is rarely massive, showing mud-flasers, mud-clasts and microfaults. Coal-bearing beds are more frequent and differentiated, and still reflect the yellow color and odor of sulfer. Coaliferous mud is shown in this section underlying the coal facies, where the top part of coal is in sharp contact. In Well 2, an interbedding of sand ripples and mud flasers of different sizes occurs; with coal seams of less abundance. Massive sandstone is rarely interbedded, and predominantly shows mud flasers. Soft sediment deformation structures are identified in the form of balls and pillows, and microfaults. Laminations in shale at the center of core and below, are thinner and of limited lateral extent. Bioturbation also characterized the laminated shale, generally in the form of vertical and horizontal burrows. Sandstone at the bottom of the section is almost loose with some coal fragments which might have inhibited the cementation in sandstone. Contacts between shale and interbedded sandstone are sharp wavy in all cases.

A quick analysis of photographs was performed through the image histogram which reflected the distribution of dark and light pixels in the grey scale. In this 256 gray scale the low values are assigned for the dark parts of the image and vice versa.

Therefore, the overall sand-mud ratio can be easily inferred from this histogram (Fig. 1) and we can now judge that sample two has a higher sand content (laminated).

Intensity ranges for each Lithotype are shown in Table 1. The extracted signal from scan line of sample 1showed that the scale of color intensity is almost the same as in sample 2, ranging from 0 to 224. A cutoff line can be constructed to show signal limit for each lithology.

The prediction was extended from the end of the time unit to 750 units (highlighted in red). The spectrum shows that there is a general declining trend in the pixel value, indicating an increasing pattern of fine-textured materials, with some local intervals of increase in sand content (increasing values of color scale) (Fig. 2).

Based on the color cut-off shown in Table 1, variations from coaliferous mud, through mudrock to sand can be reconstructed. Based on this predicted signal, the new lamination patterns can be reconstructed. Initially, the signal was segmented and converted into corresponding succession of

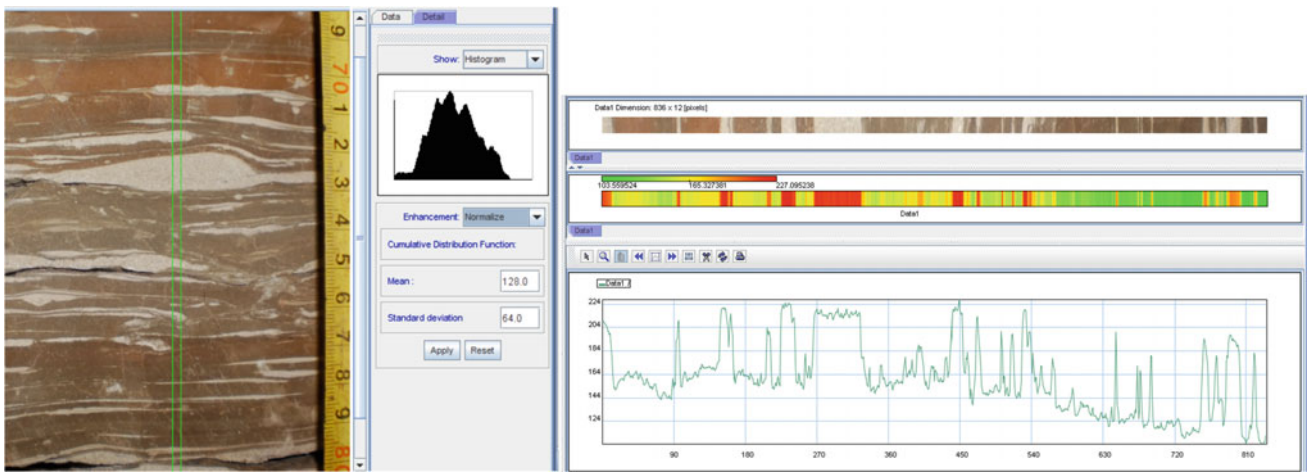

Fig. 1 **a**. Lamination from well 1, **b**. histogram generated using a grey scale of 256 bits. **c**. Signal extraction from scan line method of sample 1. Sand, shale, and coaliferous mud could be identified by mapping the signal values obtained versus the core image

Table 1 Color cut-off and ranges in pixels for each lithotype

Facies	Lower limit (pixels)	Upper limit (pixels)
Coaliferous mud	0	124
Mudrock	125	164
Sandstone	165	256

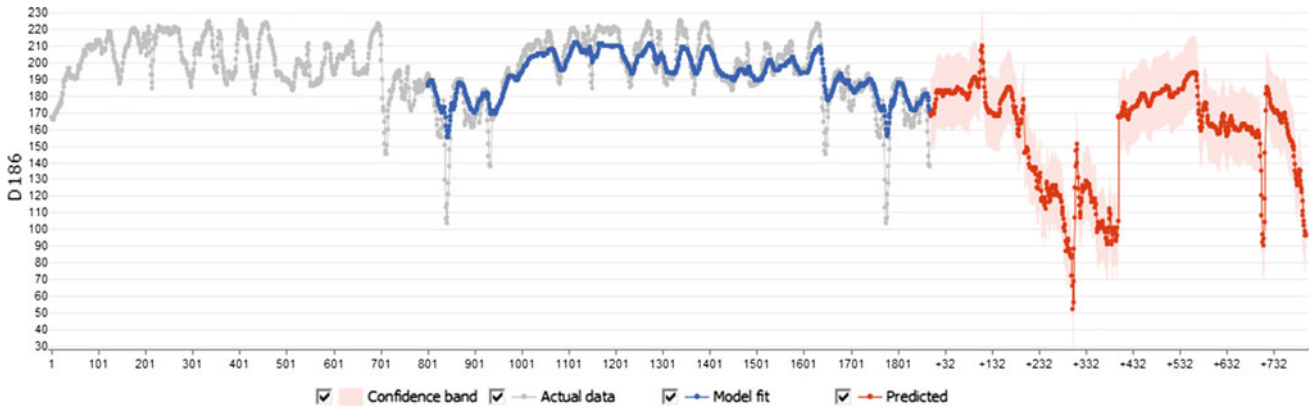

Fig. 2 Extracted signals from scan line of well 1 and predicted signal

coaliferous mud, mudrock, and sand using softwares. A similar scheme for heterolithic sequence was adopted to demonstrate the spatio-temporal variations. The signal should have been converted into an image using microstructure-reconstruction software. This was not achieved because of the lack of suitable data.

5 Conclusions

Lamination patterns in heterolithic sequences have been converted into a signal using signal an extraction software. Although the pattern seemed cyclic, the autocorrelation was always negative reflecting the heterogeneity of the sequence where each new lamina set shows some variation degree from the previous one. Further, the prediction of new pattern was achieved by compiling signal data from both wells. The prediction represented the trend from both patterns in terms of sand-mud distribution and intensity. This prediction can provide good information on the spatio-temporal variations of the reservoir quality and depositional environments from given patterns.

References

1. Ndiaye, M.: A Multipurpose Software for Stratigraphic Signal Analysis (2007). Retrieved 2014, from http://archive-ouverte.unige.ch/unige:717
2. Francus, P.: Image Analysis, Sediments and Paleoenvironments. Springer Science + Business Media, Inc. (2005)
3. Prokoph, A., Patterson, R.T.: From depth scale to time scale: transforming sediment image color data into a high-resolution time series. In: Image Analysis, Sediments and Paleoenvironments, vol. 7, pp. 143–164 (2004)
4. Prokoph, A.: From depth scale to time scale: transforming sediment image color data into a high-resolution time series. In: Prokoph, A. (ed.) Image Analysis, Sediments and Aleoenvironments, p. 340 (2004)
5. Hutchison, C.S.: Geology of North–West Borneo: Sarawak, p. 404. Brunei and Sabah (2005)
6. Dronamraju, S.V., Koraini, A.M., Zakaria, A.A., Finol, J.J.: Constraining geological heterogeneity in complex reservoirs: implications for stochastic modeling and reservoir management. In: Proceedings of SPE Asia Pacific Oil and Gas Conference and Exhibition (2005)
7. Shell, GMDH.: GMDH Shell. Available at https://www.gmdhshell.com. Last accessed (2015)
8. Ndiaye, M., Davaud, E.J., Ariztegui, D., Fall, M.: Semi automated method for laminated sediments analysis. Int. J. Geosci. **3**, 206–210 (2012)

Investigation of Aqueous and Light Non-aqueous Phase Liquid in Fractured Double-Porosity Soil

Hossein Moayedi, Loke Kok Foong, Ramli Nazir, and Biswajeet Pradhan

Abstract

The issue of leakage and spillage of light non-aqueous phase liquids (LNAPLs) and aqueous phase liquids (APLs) contribute to groundwater contamination, resulting in groundwater pollution and rendering the quality of groundwater unsafe for drinking and agricultural use. This paper aimed to investigate the APL and LNAPL in the deformable double-porosity soil, which has become important for sustainability of groundwater utilization and a comprehensive understanding of the characteristics of APL and LNAPL migration into the groundwater through the use of digital image processing techniques. The results of the experiments show that the flow of the APL and LNAPL migration was not uniformly downward. Faster migration occurred at the cracked soil surface condition compared to other locations on the soil surface that were not cracked, even when not using a liquid such as toluene. It was concluded that the factors that significantly influenced the APL and LNAPL migration was the soil sample structure, soil sample fracture pattern, physical interaction bonding between the liquid and soil sample, and capillary pressure of the fluid. The output of this study indicates that digital image analysis can provide detailed information to enable researchers to have better understanding and simulating the pattern of liquids migration characteristics that influence the groundwater resources.

Keywords

Aqueous phase migration • Fracture porous media • Vibration • Digital image analysis

1 Introduction

Groundwater contamination is one of the most challenging geo-environmental issues faced in many countries, resulting in rendering the quality of groundwater unsafe for consumption and agriculture. More complicated problems arise when the surface or subsurface has experienced earthquake vibration, which is more likely to influence the migration of aqueous phase liquids (APL) and light non-aqueous phase liquids (LNAPL) into groundwater sources. Vibration leads to rearrangement of soil structure, unstable soil structure, cracked soil, and volumetric deformation of soil aggregate structures. The resulting structures generate a problem that affect the characteristics of pore sizes [1]. These problems need to be overcome to ensure the sustainability of geo-environment and groundwater resources.

According to Lewandowska et al. [2], the double-porosity characteristics in soil could be generated in the laboratory, where most studies dealing with double-porosity soil were carried out. Recently, a number of researchers like Sa'ari et al. [3] and Peng et al. [4] have conducted experiments on double-porosity soil media that have contributed to the body of knowledge with critical view point. However, the aforementioned studies were limited to common intact aggregated method and reaction such as vibration to the aggregated porous media; but these were never applied. A powerful method used in most research fields known as the image analysis method, was also applied to investigate the complicated characteristics of contaminants and determine the liquid saturation rate [5]. Therefore, this study used the digital image analysis to understand and analyze the APL and NAPL migration in fractured double-porosity soil. It attempted to bridge the gap with the objective to determine

H. Moayedi
Department of Civil Engineering, Kermanshah University of Technology, Kermanshah, Iran

L. K. Foong (✉) · R. Nazir
Faculty of Civil Engineering, Centre of Tropical Geoengineering, Universiti Teknologi Malaysia, Johor Bahru, Johor, Malaysia
e-mail: edwinloke84@yahoo.com

B. Pradhan
Faculty of Engineering and IT, School of Systems, Management and Leadership, University of Technology Sydney, Ultimo, NSW, Australia

© Springer Nature Switzerland AG 2019

H. M. El-Askary et al. (eds.), *Advances in Remote Sensing and Geo Informatics Applications*, Advances in Science, Technology & Innovation, https://doi.org/10.1007/978-3-030-01440-7_48

and differentiate the behavior of APL and LNAPL migration in fractured double-porosity soil using the image processing technique.

2 Materials and Methods

Commercially available kaolin soil type S300 was used as the soil sample to produce double-porosity. The aggregated kaolin soil was prepared based on the method suggested by Loke [1] and Bagherieh et al. [6], where the dried kaolin powder was first mixed with 25% of moisture content for sample 1 and 2, respectively to produce kaolin granules. The kaolin granules were placed in an acrylic soil column. The experiments were conducted in acrylic soil column sealed base with the dimensions of 300 mm high × 100 mm-outer diameter and 94 mm-inner diameter. The vibration frequency for the vibration table was set on the control panel to 0.98 Hz frequency and the vibration process duration was 60 s based on the method and setup [7]. The fractured double-porosity in the soil column was used to measure and monitor the liquid migration inside the whole circular column area to simulate the groundwater contamination behavior.

Both experiments began by pouring the liquid instantaneously onto the top center of the fractured aggregated soil sample in the acrylic soil column. 70 ml of dyed red distilled water (APL) and toluene (NAPL) were used in samples 1 and 2, respectively. After the dyed water and toluene were poured and covered the surface area of the fractured soil sample, the first digital image of fluid migration was taken. The subsequent digital images were taken at a specific frequency time interval to capture the fluid migration pattern for both experiments. The JPEG digital images were recorded and transferred from a digital camera to a computer for further image processing using Matlab routine and Surfer Softwares.

3 Results

The downward migration pattern of HSI contour plot of dyed distilled water and toluene in the fractured double-porosity soil sample with 25% moisture content for samples 1 and 2, respectively, are shown in Fig. 1. In both experiments, the water flow and LNAPL migration were not uniformly downward at the front boundary horizontal line due to the non-homogeneity of the fractured double-porosity soil structure.

In the soil sample 1, the selected HSI plots of dyed distilled water (APL) migration occurred at intervals of 5, 180, and 2160 s, respectively, as seen in Fig. 1a. Based on the HSI intensity contour plot result, faster migration occurred at the cracked soil surface condition compared to other locations on the soil surface that were not cracked. 5 s after initiation of the experiment, the dyed APL penetrated nearly halfway of the soil sample at the location of fractured soil surface as shown in Fig. 1a. The highest APL downward migration depth along the soil column was 92 mm out of the 100 mm soil sample column. The dyed distilled water (APL) migration stopped at 2160 s and did not fully migrate in this study because the water viscosity was 0.00089 kg/m/s, while toluene viscosity was 0.00055 kg/m/s, which means a viscosity difference of about 38%. Water has a higher viscosity compared to toluene. Thus, the dyed water caused a high resistance and friction to gradual migration. In soil sample 2, intervals of 5, 180, and 1800 s, respectively, were selected for dyed LNAPL migration HIS contour plot as shown in Fig. 1b. The LNAPL migration was similar to the results found in sample 1. At 5 s after the initiation of the experiment, the dyed LNAPL migration reached nearly halfway through the test sample at the location of fractured soil surface. The LNAPL completely receded from view on the whole top soil surface area into the fractured soil sample of the test, which took about 5 s.

This could be due to the physical bonding between toluene and soil which is weaker than water and soil. The physical bonding between toluene and soil was attributed to Van Der Waals Force, which is weaker than hydrogen bonding and has stronger physical bonding between water and soil. Indeed, this was one of the reasons why the water (APL) migration was slower than that of toluene (LNAPL). In a previous study provided by Sa'ari et al. [3], an experiment on toluene migration in double-porosity soil with 25% moisture content without vibration effect was performed. The results showed that the toluene LNAPL migration to the bottom took 2280 s compared to this study, in which LNAPL and APL migration took only about 1800 and 2160 s, respectively, to reach the soil column bottom. This could be because the fracture that occurred at the double-porosity loosened the soil structure in this study compared to previous research migration which had intact double-porosity and stronger and more compact soil structure. Thus, this study supported the previous research provided by Loke et al. [1], which stated that a fractured soil experiences faster migration compared to an intact soil.

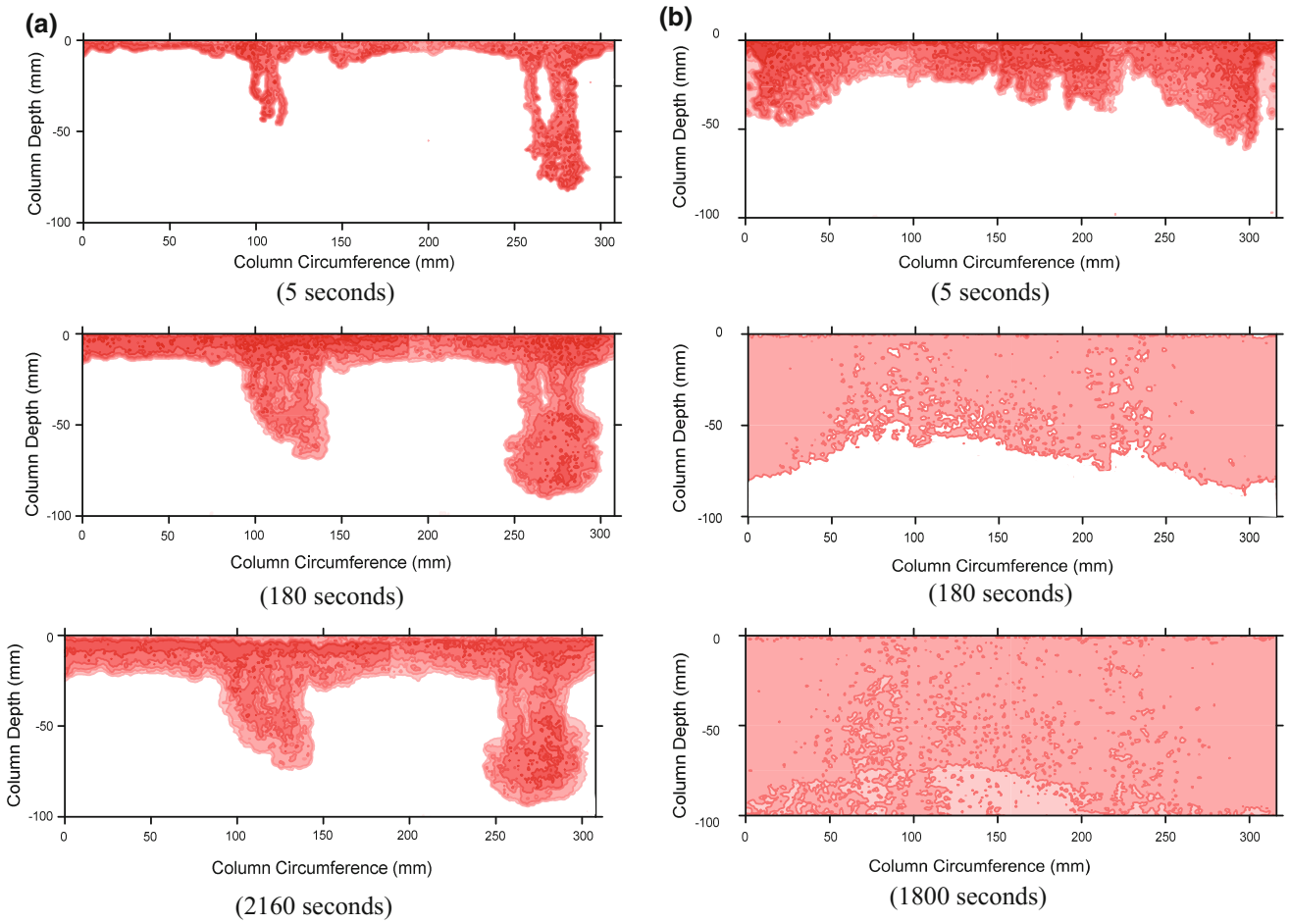

Fig. 1 **a** Sample 1 (APL). **b** Sample 2 (LNAPL) HSI plots of downward migration in fractured double-porosity soil

4 Conclusion

From the results observed, both experiments indicated that in comparison to the APL migration, the LNAPL migrated faster from top surface to the bottom of soil column. The significant finding was that the LNAPL fully migrated to the bottom (100%), but the APL migration stopped at 92% of the soil column depth. This result may help conclude that the factors that significantly influenced the APL and LNAPL migration in samples 1 and 2, respectively, was the structure of the soil sample, fractured pattern of the soil sample, liquid viscosity, physical interaction bonding between the liquid and soil sample, and the capillary pressure of the fluid. In conclusion, this study indicated that the fractured double-porosity soil under vibration effect with LNAPL migration has very bad consequences for groundwater resources. The current model provides a more practical contribution to future sustainable groundwater remediation.

References

1. Loke, K.F., Rahman, N.A., Nazir, R.: Experimental study on unsaturated double-porosity soil phenomena under vibration effect. J. Teknologi **79**(4), 65–72 (2017)
2. Lewandowska, J., Szymkiewicz, A., Gorczewska, W., Vauclin, M.: Infiltration in a double-porosity medium: experiments and comparison with a theoretical model. Water Resour. Res. **41**(2), W02022 (2005)
3. Sa`ari, R., Rahman, N.A., Latif, N.H.A, Yusof, Z.M., Ngien, S.K., Kamaruddin, S.A., Mustaffar, M., Hezmi, M.A.: Application of digital image processing technique in monitoring LNAPL migration in double porosity soil column. J. Teknologi **3**(72), 23–29 (2015)

4. Peng, Z., Duwig, C., Delmas, P., Gaudet, J.P., Strozzi, A.G., Charrier, P., Denis, H.: Visualization and characterization of heterogeneous water flow in double-porosity media by means of X-ray computed tomography. Transp. Porous Media **110**, 543–564 (2015)
5. Luciano, A., Viotti, P., Papini, M.P.: Laboratory investigation of DNAPL migration in porous media. J. Hazard. Mater. **176**, 1006–1017 (2010)
6. Bagherieh, A.R., Khalili, N., Habibagahi, G., Ghahramani, A.: Drying response and effective stress in a double porosity aggregated soil. Eng. Geol. **105**(1–2), 44–50 (2009)
7. Loke, K.F., Rahman, N.A., Nazir, R., Lewis, R.W.: Study of aqueous and non-aqueous phase liquid in fractured double-porosity soil using digital image processing. Geol. Croat. **71**(2), 55–64 (2018)

A Review on Soil Erosion Control Studies

Hossein Moayedi, Ramli Nazir, Loke Kok Foong, and Biswajeet Pradhan

Abstract

Soil erosion resulting from heavy rainfall, depends on a number of factors, such as the native soil properties (the angle of internal friction, cohesion, unit weight, etc.), hydraulic conditions (surface runoff, groundwater seepage, etc.), the removal of vegetation and change in the surrounding environment. This study investigated the preliminary factors that could cause Soil erosion and detailed the literature through an exhaustive review of the previous published materials on the field and laboratory research works dealing with the soil erosion control techniques.

Keywords

Soil erosion control • Rainfall erosion • Runoff

1 Introduction

Engineers are often confronted with problems of the prediction and estimation of the triggering factors that lead to the failure of a slope. Most of the slope failure process exhibits a high degree of uncertainty in the parameter estimates. The understanding of professionals in many areas is far from perfect, which makes empiricism play an important role in modeling studies. The detachment and movement of soil particles induced by rain splash and overland flow cause erosion, and subsequently the internal friction angle and slope stability will deteriorate [1]. A slope is generally unstable if its angle of repose is higher than the internal friction angle. Hence, to prevent the first stage of failure, engineers tried to provide rational answers to problems that arise in the design and management of slope failure remedies. Slope failure is critical to many activities, such as designing new retaining structures [2].

Erosion has always been one of the major sources of damage to both human-made structures and the natural environment [3]. Soil erosion is also a major environmental threat to the sustainability and productive capacity of agriculture [4]. Erosion is caused by different factors and can be avoided only if protection measures tailored to the specific cause are applied. Erosion on slopes can be caused by rainfall, runoff or wind. Rainfall erosion occurs mainly on bare slopes, as vegetation provides good protection [5]. Aird [6], discussed how to deal with the slope stabilization problems caused by soil erosion using mesh, soil nails, blankets, and cellular confinement systems. For example, to protect a slope from this kind of erosion, one simple way is to quickly establish dense and uniform grass cover.

2 Surface Erosion Measurement and Data Collection

Most of the artificial slopes are exposed to weather without any surface protection during the construction stage or else only supported by turf protection. This practice could create erosion that is one of the triggering factors of slope failure. The rate of erosion is based on testing either full-scale or small-scale models in various soil types [7]. In fact, the data on soil erosion and its controlling factors can be collected in the field or simulated in the laboratory. For realistic data on soil loss, field experiments are most reliable but, because conditions vary in both time and space, it is often difficult to determine the chief causes of erosion. The mechanics of

H. Moayedi (✉)
Department of Geotechnics and Transportation, School of Civil Engineering, Faculty of Engineering, Universiti Teknologi Malaysia, Skudai, Johor Bahru, Malaysia
e-mail: hossein.moayedi@gmail.com

H. Moayedi · R. Nazir · L. K. Foong
Centre of Tropical Geoengineering (Geotropik), School of Civil Engineering, Faculty of Engineering, Universiti Teknologi Malaysia, Skudai, Johor Bahru, Malaysia

B. Pradhan
Faculty of Engineering and IT, School of Systems, Management and Leadership, University of Technology Sydney, Ultimo, NSW, Australia

© Springer Nature Switzerland AG 2019

H. M. El-Askary et al. (eds.), *Advances in Remote Sensing and Geo Informatics Applications*,
Advances in Science, Technology & Innovation, https://doi.org/10.1007/978-3-030-01440-7_49

erosion are best studied in the laboratory, where the effects of many factors can be controlled. Because of the artificiality of experiments, however, some degree of confirmation of their field result is desirable.

As stated, a full-scale test would probably be the most reliable way to collect useful information for predicting erosion rates on a slope. However, a test on a small-scale model in the laboratory would involve scaling errors, since the slope configuration and rainfall are important factors determining the erosion behavior of slopes. Although a number of field tests and small-scale model tests have been carried out previously, few attempts have been made to compare the results obtained from each type of test. In a study performed by Morgan [1], small-scale models were used to obtain the overland flow and sediment with a known quantity of runoff for different soil types. However, while performing comparison studies on model runoff and sediment with the field test, the existence of a scale error between the model and the prototype was observed. They attributed this to the variation of the internal friction angle and shear strength of the soil with the detachability level.

3 Laboratory Experiments

Generally, it is usually impossible to construct a scaled down version of field conditions using a small plot to represent a large hill slope. Geotechnical characteristics and climatic conditions, such as soil particle size and raindrop size, also cannot be reduced without affecting their basic properties and behavior. It is preferable to treat laboratory experiments as representative of true-to-scale field simulations. Many laboratory studies use a rainfall simulator, which is designed to produce rainfall of a known drop size and energy which can be repeated when required. The most important design criteria of the simulator are that it should be repeatable and capable of reproducing the drop-size distribution, drop velocity at impact and intensity of natural rainfall with a uniform spatial distribution [1]. However, Bubenzer [8] reported that the need to reproduce the energy of natural rainfall for the intensity being simulated is generally regarded as being less important. According to Hall [9], many simulators are available but none can accurately recreate all the properties of natural rainfall. To minimize the discrepancies due to equipment, same rainfall simulators should be used both in the field and in the laboratory when carrying out the experiments [1, 10].

4 Surface Erosion Remediation

Agnew [11] investigated the selection of appropriate erosion control products. It was noted that many sites require the use of natural or synthetic erosion control materials to ensure a stable soil surface to accommodate seed germination. He provided generic designs and installation guidelines for three erosion control product types, specifically: mats and blankets, and soil confinement systems. As defined by Agnew [11], the soil confinement systems generally consisted of a series of honeycomb-like cells formed into a spreadable sheet or blanket. Theisen [12], gave an overview of the role of geosynthetics in erosion and sediment control. In his research, a brief overview of the materials and concepts involved is provided. The geosynthetic components are an integral part of erosion and sedimentary materials, ranging from temporary products such as hydraulic mulch geofibers, plastic erosion control meshes and nettings, erosion control blankets and silt fences, to high performance turf reinforcement mats, geocellular confinement systems, erosion control geotextiles and fabric-formed revetments. Cancelli et al. [13], used geocells to confine the soil placed on steep slopes to prevent severe erosion. They also provided specific testing procedures appropriate for geocells. Gruver [14], stated that practices that increase infiltration, such as tile drainage and cover cropping, reduce run-off and thus limit the transport of detached particles. Practices that slow run-off, such as buffer strips and terraces, promote the deposition of suspended sediment before it leaves the field.

5 Challenges to Experimental Modelling

Field runoff plots are most effectively used for the demonstration of how serious the erosion that takes place is and its comparison. Another valid use is to obtain data which are to be used to construct or validate a model or equation to predict runoff or soil loss [10, 15]. Rainfall simulation in a laboratory or in the field can never simulate natural rainfall. The effects of wind on rainfall are difficult to simulate, since the wind speed and duration varies as it occurs in reality. Therefore, simulators are designed for individual experimental objectives with certain rainfall characteristics to be eliminated. Moreover, systematic errors can be built into an experiment [1]. For instance, a specific procedure for a laboratory study on slope steepness results in a gentle slope, however the same procedure may result in increasing the slope steepness. Therefore, in studying the slope steepness effects involving simulated rainfall of several intensities, it is expedient to complete all the runs at one intensity before proceeding to the next because of the problems encountered in altering the operation of the simulator. The performance of a cellular confinement system for a selected site is compared with that of one without a confinement system. such as: (i) the preliminary factors that lead to slope failure; (ii) the effectiveness of cellular confinement systems for slope rehabilitation; (iii) improvising slope stability using

confinement systems; and (iv) developing charts for the design of confinement systems.

6 Conclusions

The aim of the present study was to simplify the engineering process for soil erosion remediation techniques and look for a better solution to protect slopes from deterioration. It also sought to assist developing easier installation methods and improving various erosion control systems.

References

1. Morgan, R.P.C.: Soil Erosion and Conservation. Wiley, USA (2009)
2. Milleer, S.: Soil Retaining Structure, A Natural Approach to Grade Separations. The Primer Magazine for the California, Nevada & Arizona Residential Building Industry, US (2003)
3. Pretty, J.N., Brett, C., Gee, D., Hine, R.E., Mason, C.F., Morison, J.I.L., Raven, H., Rayment, M.D., Van der, B.G.: An assessment of the total external costs of UK agriculture. Agric. Syst. **65**(2), 113–136 (2000)
4. Martín, F.L., Martínez, N.M.: An empirical approach to estimate soil erosion risk in Spain. Sci. Total Environ. **409**(17), 3114–3123 (2011)
5. Lim, K.L: Soil Confinement System to Prevent Slope Failure on Clayey Soil. Department of Geotechnics and Transportation, Universiti Teknologi Malaysia (2007)
6. Aird, J.: Challenges in slope stabilization: solving problems with blankets, mesh, soil nails, and cellular confinement systems. Erosion Control **17**(1), 18–25 (2010)
7. Wauchope, R.D.: Soil Resources in the Coastal Plain: Process Characterization, Management Impacts, and Assessment Tools. Southeast Watershed Research Laboratory, Tifton, Georgia (2000)
8. Bubenzer, G.D.: Inventory of rainfall simulators. In: Proceedings of the Rainfall Simulator Workshop, p. 130 (1979)
9. Hall, J.: Erosional losses of s-triazine herbicides. J. Environ. Qual. **3**(2), 174–180 (1974)
10. Nazir, R., Moayedi H.: Soil Mass Loss Reduction during Rainfalls by Reinforcing the Slopes with the Surficial Confinement. Surge (2014)
11. Agnew, W.: Erosion control product selection. Geotech. Fabr. Rep. **9**(3), 24–27 (1991)
12. Theisen, M.S.: The role of geosynthetics in erosion and sediment control: an overview. Geotext. Geomembr. **11**(4–6), 535–550 (1992)
13. Cancelli, A., Rimoldi, P., Montanelli, F.: In: Cheng, S.C.J. (ed.) Index and Performance Tests for Geocells in Different Applications, pp. 64–75. ASTM, San Antonio, TX, USA (1993)
14. Gruver, J.B.: Prediction, prevention and remediation of soil degradation by water erosion. Nat. Educ. Knowl. **4**(12), 2 (2013)
15. Nazir, R., Ghareh, S., Mosallanezhad, M., Moayedi H.: The influence of rainfall intensity on soil loss mass from cellular confined slopes. Measur. **81**, 13–25, (2016)

Spatial Estimation of Soil Organic Matter Content Using Remote Sensing Data in Southern Tunisia

Emna Medhioub, Moncef Bouaziz, and Samir Bouaziz

Abstract

Learning the spatial distribution of soil organic matter content is essential for the planning of land use and environmental protection. Because laboratory measurement of soil samples is time-consuming and costly, a good alternative is required to estimate spatial content of soil organic matter. This problem can be solved by using remote sensing and GIS techniques. In this study, soil organic matter content was estimated from remote sensing data derived from LandSat8 satellite image by generating a multi linear regression model using the backward regression technique. The multiple regression equation between SOM and remote sensing data was significant with R = 0.678. The resulting multi linear regression equation was then used for the spatial prediction for the entire study area. The predicted SOM derived from remote sensing data was used as auxiliary variable using cokriging spatial interpolation technique. Integrate remote sensing data with cokriging method improves significantly the estimates of surface soil organic matter content.

Keywords

Soil organic matter • Remote sensing • Spatial estimation • Multi linear regression • Cokriging

1 Introduction

Soil is an important natural element providing life to all kinds of living beings. Levels of soil organic matter is one of the most significant soil properties that determine soil fertility and control different chemical and biological properties of the soil system [1]. Previous studies revealed that SOM is prone to anthropogenic activities [2–4]. Understanding the relation between the land use practices and the SOM content has received considerable attention [4, 5].

Auxiliary information extracted from spatial data can be correlated to improve the prediction accuracy of soil properties [4]. Over the past few years, remote sensing (RS) data has also been used to assess the spatial variability of SOM due to multispectral features [6, 7].

The present attempt was designed to evaluate the potential of multi linear regression statistics by backward method to forecast the SOM content in the study area and use the output as an approach for estimating the soil organic matter content using cokriging spatial interpolation technique.

2 Materials and Methods

The study area is located in the southern region of Tunisia. It covers part of the coastal plain in southern Tunisia (Jeffara Northern Plain). It is bounded to the NE by the Mediterranean Sea and to the SW by the Matmata's mountains. The choice of the study area is made owing to its location in the southern exoreic watersheds of Gabes.

A total of 57 samples were taken from the top soil (0–10 cm) and analyzed to predict the organic matter content. To carry out such a task in the study area using remote sensing data as auxiliary variables, we selected a Landsat8 data acquired on 17th April 2017. 12 bands of this satellite image were obtained after preprocessing. Seven spectral indices were derived from LanSat8 bands. The equations predict different indices are presented in Table 1 using the following formula.

Multi linear regression (MLR) method using the backward technique was conducted for soil organic matter of the 57 soil samples (dependent variable) with different bands and indices extracted from LandSat8 image (independent variables).

E. Medhioub (✉) · M. Bouaziz · S. Bouaziz
Laboratoire 3E, Ecole Nationale d'Ingénieurs de Sfax, Université de Sfax, 3023 Sfax, Tunisia
e-mail: medhioub_emna@yahoo.fr

M. Bouaziz
Faculty of Environmental Sciences, Institute of Geography, TU-Dresden, Helmholtzstr. 10, 01069 Dresden, Germany

© Springer Nature Switzerland AG 2019

H. M. El-Askary et al. (eds.), *Advances in Remote Sensing and Geo Informatics Applications*, Advances in Science, Technology & Innovation, https://doi.org/10.1007/978-3-030-01440-7_50

Table 1 Spectral indices

Index	Formula	Reference
Normalized difference vegetation index: NDVI	(NIR − R)/(NIR + R)	Tian et al. [8]
Brightness index: BI	$(R^2 + G^2 + B^2)/3)^{0.5}$	Ray et al. [9]
Saturation index: SI	(R − B)/(R + B)	Ray et al. [9]
Hue index: HI	(2 * R – G − B)/(G − B)	Ray et al. [9]
Coloration index: CI	(R − G)/(R + G)	Ray et al. [9]
Redness index: RI	$R^2/(B * G^3)$	Ray et al. [9]
Grain size index: GSI	(R − B)/(R + B + G)	Xiao et al. [10]

In this study, cokriging is expected to produce a more accurate estimation since the relationship between SOM content and remote sensing data was considered in the interpolation.

The SPSS software was used for all of the statistical tests. SOM spatial distribution was extracted using the Geostatistics Analyst toolbox in ArcGIS 10.5.

3 Results

The multilinear regression equation was generated between soil sample data and spectral bands using the backward regression technique. The empirical equation generated only significant correlated parameters. The equation obtained is written as follows:

$$OM(\%) = 1.523 + 4.116 * B4 - 6.346 * B8 + 0.001 * RI - 9.480 * SI + 11.628 * GSI \quad (1)$$

The empirical relation between OM and spectral indices was highly significant with coefficient of determination R = 0.678 (R^2 = 0.459) and F = 7.147 as shown in Fig. 1.

Soil organic matter (SOM) content in this case is found to be significantly correlated (R = 0.678) with remote sensing reflectance (B4 and B8) and derived spectral indices (RI, SI and GSI).

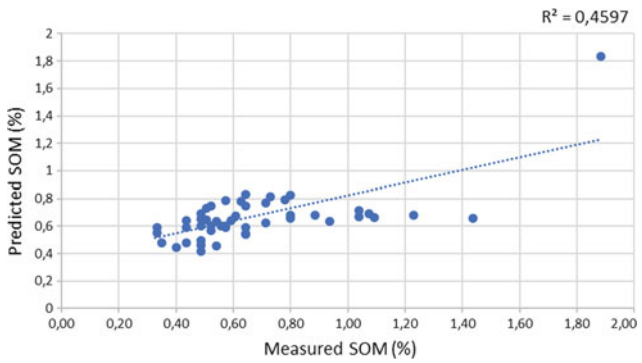

Fig. 1 Measured SOM content (%) versus predicted SOM content (%)

The predicted SOM values extracted from the statistical analyses (Fig. 2) are used as auxiliary variables by cokriging as interpolation technique to estimate SOM content. This method improves a good potential as healthy method to predict the accuracy and reliability of SOM content.

4 Discussion

In this study, the SOM content had a strong spatial dependency with a mean of 0.67% and the average bias between the predicted value and the measured one of 2.08 * 10 − 7. Spatial concentration in the study area varies between 0.4 and 1.85%. The cokriging method has a good potential to predict the soil quality and managing soil organic matter content.

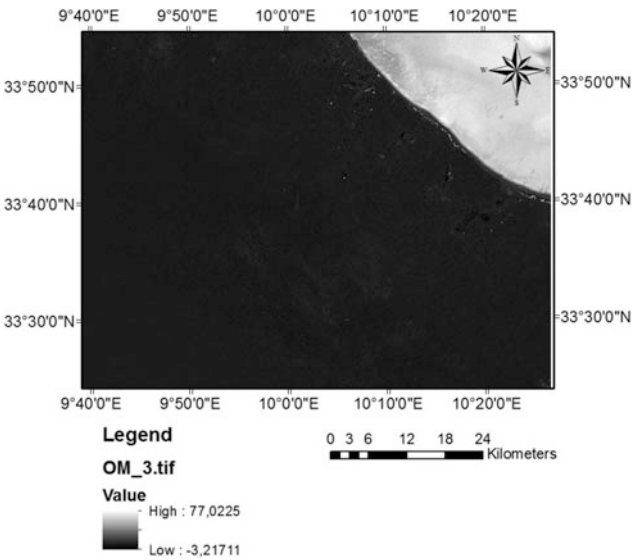

Fig. 2 Predicted SOM content (%) extracted from LandSat8 data after statistical analyses

5 Conclusion

This study has shown the relevance of using multispectral remote sensing data for the assessment of soil organic matter content related parameters and generate SOM content maps. The distribution of soil organic matter content is controlled by soil parent materials in the study area used as an auxiliary factor in cokriging. The predicted value of SOM content obtained by cokriging method achieve to an acceptable result and more precise than that obtained from the MLR method.

References

1. Sparks, D.L.: Advances Agronomy, vol. 129, pp. 1–322, Elsevier, New York (2015)
2. Huang, B., Sun, W.X., Zhao, Y.C., Zhu, J., Yang, R.Q., Zou, Z., Ding, F., Su, J.P.: Temporal and spatial variability of soil organic matter and total nitrogen in an agricultural ecosystem as affected by farming practices. Geoderma **139**(3–4), 336–345 (2007)
3. Mao, Y.M., Sang, S.X., Liu, S.Q., Jia, J.L.: Spatial distribution of pH and organic matter in urban soils and its implications on site-specific land uses in Xuzhou, China. C. R. Biol. **337**(5), 332–337 (2014)
4. Liu, S., An, N., Yang, J., Dong, S., Wang, C., Yin, Y.: Prediction of soil organic matter variability associated with different land use types in mountainous landscape in southwestern Yunnan province, China. Catena **133**, 137–144 (2015)
5. Zhu, H.H., Wu, J.H., Guo, S.L., Huang, D.Y., Zhu, Q.H., Ge, T. D., Lei, T.W.: Land use and topographic position control soil organic C and N accumulation in eroded hilly watershed of the Loess Plateau. Catena **120**, 64–72 (2014)
6. Song, Y.Q., Yang, L.A., Li, B., Hu, Y.M., Wang, A.L., Zhou, W., Cui, X.S., Liu, Y.L.: Spatial prediction of soil organic matter using a hybrid geostatistical model of an extreme learning machine and ordinary kriging. Sustainability **9**, 754 (2017). https://doi.org/10.3390/su9050754
7. Mirzaee, S., Ghorbani-Dashtaki, S., Mohammadi, J., Asadi, H., Asadzadeh, F.: Spatial variability of soil organic matter using remote sensing data. Catena **145**, 118–127 (2016)
8. Tian, Y., Wang, Y., Zhang, Y., Knyazikhin, Y., Bogaert, J., Myneni, R.B.: Radiative transfer-based scaling of LAI/FPAR retrievals from reflectance data of different resolutions. Remote Sens. Environ. **84**, 143–159 (2002)
9. Ray, S.S., Singh, J.P., Das, G., Panigrahy, S.: Use of high resolution remote sensing data for generating site specific soil management plan. The international archives of the photogrammetry, remote sensing and spatial information sciences organic matter using remote sensing data. Catena **145**, 118–127 (2004)
10. Xiao, J., Shen, Y., Tateishi, R., Bayaer, W.: Development of topsoil grain size index for monitoring desertification in arid land using remote sensing. Int. J. Remote Sens. **27**(12), 2411–2422 (2006)

Applicability of Landsat TM Images to Detect Soil Salinity of Coastal Areas in Bangladesh

Jannatul Ferdous and M. Tauhid Ur Rahman

Abstract

Soil salinity is one of the most important controlling factors in agricultural production. For an agrarian country like Bangladesh, it is vital to map the saline affected area and keep track of changes. It would be very convenient if the conventional time consuming method of detection soil salinity could be replaced with the application of remote sensing indices. So this study aimed to evaluate the applicability of Landsat 5 TM images, both level 1 and 2 for detecting saline affected areas of Coastal Bangladesh. Seventeen indices were used and compared with the field salinity data collected from SRDI. The R^2 values reveal no significant correlation between the aforementioned indices and soil data. So this study concluded that Landsat TM images cannot be used to detect soil salinity in Coastal Bangladesh.

Keywords

Landsat TM • Level 1 product • Level 2 product • Salinity indices • Soil salinity

1 Introduction

Soil salinity refers to significant concentration of mineral salts in soil layers. Soil salinity is a common phenomenon in arid regions and coastal regions of the world. Both natural and anthropogenic actions cause soil salinity. In coastal region of Bangladesh, soil salinity is one of the prominent factors of crop yield. Cyclonic storm surge, high tide and flood are the natural causes of excessive soil salinity in this region. Poor agricultural management and damaging polders from the entering saline water for shrimp culture are the anthropogenic causes which aggravate the natural phenomenon [1, 2]. Agricultural lands have been severely affected by soil salinity and this excessive salinity would result in the abandonment of these lands [3].

Considering the importance of soil salinity studies, monitoring and mapping of saline affected areas, keeping track of the changes should be promoted for sustainable agricultural practices [2, 4, 5]. Remote sensing technology with its vast time series data makes it easier to map the saline affected areas and detect the change in soil salinity levels, which has already been proved dependable and effective method in arid regions [1, 6–10]. In the case of coastal Bangladesh, there is a huge research gap in this sector. Morshed et al. [2] have tried to develop a multiple regression equation for detecting soil salinity by using Landsat 7 ETM+ images [2]. So this study aimed to evaluate the applicability of Landsat TM images, both level 1 and 2 products in soil salinity mapping of coastal Bangladesh. Level 2 products provide the surface reflectance value after proper atmospheric correction, which is missing in level 1 products. After calculating the salinity indices, the indices values were compared with the field level salinity data collected from Soil Resource Development Institute (SRDI) of Bangladesh.

2 Materials and Methods

For this study, Barisal Sadar Upazila of Barisal district was selected, which is enlisted as coastal districts in Coastal Zone Policy of Bangladesh (Fig. 1) [11].

The field level salinity data was collected from SRDI, which was in book format. Map of the Upazila (1:50000), indicating the sample collection locations, was georeferenced and a total of 93 points were digitized for analysis. Another secondary data, level 1 and 2 types images (WRS2: 137/44) of Landsat 5 TM (dated 23rd February 2007) were downloaded from the United States Geological Survey (USGS) website. The soil samples were also collected on February to March of 2007. After extracting the study area from the scene, necessary radiometric corrections were

J. Ferdous (✉) · M. T. U. Rahman
Department of Civil Engineering, Military Institute of Science and Technology, Dhaka, 1216, Bangladesh
e-mail: jannatulferdous.buet@gmail.com

© Springer Nature Switzerland AG 2019

H. M. El-Askary et al. (eds.), *Advances in Remote Sensing and Geo Informatics Applications*,
Advances in Science, Technology & Innovation, https://doi.org/10.1007/978-3-030-01440-7_51

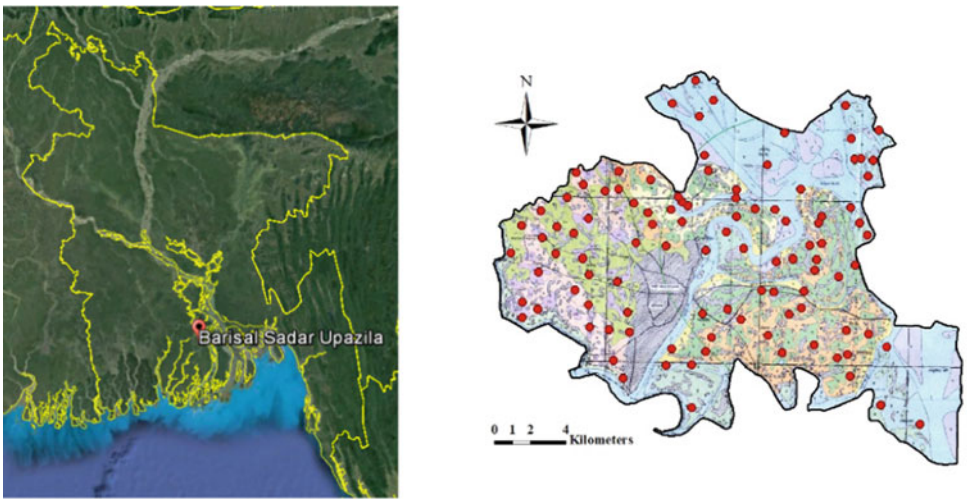

Fig. 1 Study area location with sample collection points

performed on level 1 product. Level 2 product was used without any correction. Seventeen salinity indices were selected for different literature sources and calculated using the corresponding bands. Finally, the calculated indices values were compared with the field EC values and coefficient of correlation (R^2) was computed.

3 Results and Discussion

Seventeen remote sensing indices were calculated for both level 1 and 2 products. Then the values of indices were extracted for the sample points of soil collection by SRDI. After computing the correlation value (R^2), it revealed that there is no significant relationship between these indices values and field EC values. Table 1 represents the corresponding formulas of seventeen indices with the correlation values for both level 1 and 2 products.

B, G, R and NIR are the blue (band 1), green (band 2), red (band 3) and Near infrared (band 4) bands of Landsat TM images and L is the constant which has a value of 0.5 in most of the cases [2]. From the analysis, it is clear that there is no significant correlation between the field EC and calculated indices values. Although the salinity indices showed good results for arid regions, some studies suggest that Landsat images are more capable of detecting soil salinity of arid regions than of semiarid ones [12, 13].

4 Conclusion

Both level 1 and 2 products show very low correlation values with the field EC values, which points out that Landsat TM is not applicable for detecting soil salinity in semiarid countries, more specifically, in Coastal Bangladesh. More research should focus on this issue. If soil salinity

Table 1 Correlation between field EC value and calculated salinity indices values for Barisal Sadar Upazila

Salinity indices	Formula	R^2 values for level 1 product	R^2 values for level 2 product
Normalized difference salinity index (NDSI)	(R − NIR)/(R + NIR)	0.0271	0.0285
Brightness index 1	$\sqrt{(NIR^2 + R^2)}$	0.006	0.0006
Brightness index 2	$\sqrt{(NIR^2 + G^2)}$	0.0013	0.001
Vegetation soil salinity index (VSSI)	2 * G − 5 * (R + NIR)	0.00003	0.0000003
Salinity index 1	$\sqrt{(B * R)}$	0.0355	0.0338
Salinity index 2	$\sqrt{(G * R)}$	0.0295	0.0279
Salinity index 3	$\sqrt{(NIR^2 + R^2 + G^2)}$	0.000008	0.00003
Salinity index 4	$\sqrt{(G^2 + R^2)}$	0.0277	0.0269
Salinity index 5	$\sqrt{(NIR * R)}$	0.006	0.01
Salinity index 6	(B − R)/(B + R)	0.0352	0.0225
Salinity index 7	(G * R)/B	0.0268	0.0214
Salinity index 8	(B * R)/G	0.0445	0.0385
Salinity index 9	$\sqrt{(G + R)}$	0.0294	0.0289
Salinity index 10	B/R	0.0386	0.0241
Salinity index 11	(R * NIR)/G	0.0012	0.0024
Soil adjusted vegetation index (SAVI)	(NIR − R) * (1 + L)/(NIR + R + L)	0.0163	0.0285
Normalized vegetation index (NDVI)	(NIR − R)/(NIR + R)	0.0271	0.0285

could be detected from these easily accessible data, it would be very helpful for geoscience and agriculture sector.

References

1. Ivushkin, K., Bartholomeus, H., Bregt, A.K., Pulatov, A.: Satellite thermography for soil salinity assessment of cropped areas in Uzbekistan. Land Degrad. Dev. **28**, 870–877 (2017)
2. Morshed, M.M., Islam, M.T., Jamil, R.: Soil salinity detection from satellite image analysis: an integrated approach of salinity indices and field data. Environ. Monit. Assess. **188**, 119 (2016)
3. Li, D.J., Chun, W.M., Tiyip, T.: Study on soil salinization information in arid region using remote sensing technique. Agric. Sci. China **10**(3), 404–411 (2011)
4. Al-Khaier, F.: Soil salinity detection using satellite remote sensing. M.Sc. thesis, International Institute for Geoinformation Science and Earth Observation (2003)
5. Nwer, B., Zurqani, H., Rhoma, E.: The use of remote sensing and geographic information system for soil salinity monitoring in Libya. GSTF Int. J. Geol. Sci. **1**(1), 1–5 (2013)
6. Azabdaftari, A., Sunarb, F.: Soil salinity mapping using multi-temporal landsat data. In: The International Archives of the Photogrammetry, Remote Sensing and Spatial Information Sciences XLI-B7, XXIII ISPRS Congress, Prague, Czech Republic (2016)
7. Matinfar, H.R., Panah, S.K.A., Zand, F., Khodaei, K.: Detection of soil salinity changes and mapping land cover types based upon remotely sensed data. Arab. J. Geosci. **6**(3), 913–919 (2011)
8. Elhag, M.: Evaluation of different soil salinity mapping using remote sensing techniques in arid ecosystems, Saudi Arabia. J. Sens. **2016** (2016)
9. Asfaw, E., Suryabhagavan, K.V., Argaw, M.: Soil salinity modeling and mapping using remote sensing and GIS: the case of Wonji sugar cane irrigation farm, Ethiopia. J. Saudi Soc. Agric. Sci. **17**(3), 250–258 (2018)
10. Nawar, S., Buddenbaum, H., Hill, J., Kozak, J.: Modeling and mapping of soil salinity with reflectance spectroscopy and landsat data using two quantitative methods (PLSR and MARS). Remote Sens. **6**, 10813–10834 (2014)
11. Ministry of Water Resources. Coastal Zone Policy. http://warpo.gov.bd/policy/czpo_eng.pdf. Last accessed 2018/03/20 (2005)
12. Rahmati, M., Mohammadi-Oskooei, M., Neyshabouri, M.R., Fakheri-Fard, A., Ahmadi, A., Walker, J.: ETM+ data applicability for remote sensing of soil salinity in Lighvan watershed, North-west of Iran. Curr. Opin. Agric. **3**(1), 10–13 (2014)
13. Panah, S.K.A., Pouyafar, A.M.: Potentials and constraints of soil salinity studies in two different conditions of Iran using Landsat TM data. https://www.semanticscholar.org/paper/Potentials-andconstraints-of-soil-salinity-studiePanah/5d05cbdd4b4621975dfdbeb8a2d0730561c49e12. Last accessed 2018/03/23

Part VI

Vegetation Mapping impact Assessment

Monitoring Dynamics of Date Palm Plantations from 1984 to 2013 Using Landsat Time-Series in Sahara Desert Oases of Algeria

Ali Mihi, Tarai Nacer, and Haroun Chenchouni

Abstract

This study used remote sensing tools to quantify spatial dynamics of date palm plantations (DPP) in desert oases of Ziban region (NE Algeria) over the past three decades and understand the impacts of agricultural development on land use-land cover changes. Spatiotemporal changes of DPP (*Phoenix dactylifera*) were detected using likelihood supervised classification for each of three Landsat satellite images (TM-1984, ETM+-1999 and OLI-2013). The DPP area quadrupled over the last three decades (1984–2013), accounting for about 75.46% of date palm cultivation expansion, while arid rangelands decreased with about 25,932.96 ha as result of political agricultural programs that favored the exploitation of natural habitats into DPP. This study reported the potential of remote sensing imagery processing technique for monitoring and rapidly detecting land change in landscapes of desert oases, with accuracy and a relatively low cost over a long-time period and large scale regions.

Keywords

Algeria • Date palm plantation • Ziban oases • Landsat images • Remote sensing

Abbreviations

DPP	Date palm plantations
TM-1984	Thematic Mapper-1984
ETM+-1999	Enhanced Thematic Mapper plus-1999
OLI-2013	Operational Land Imager-2013.

1 Introduction

Oasis is a fertile ecosystem in desert zones, strongly dependent on water resources, where agriculture is among the main human activities. In date palm oases, the upper canopy is occupied by date palm trees and underneath is a high biodiversity of animal and plant species [7]. Date palm (*Phoenix dactylifera* Linnaeus 1753) is a monocotyledon plant belonging to the Arecaceae family, with a great tolerance against hot climatic conditions and soil salinity. Date palm is one of the most horticultural crops cultivated in desert regions worldwide [2]. In Algeria, date palm oases are mainly distributed in the low Sahara from Biskra to Ouargla, and between Saouara depression and Tadmait foothill [5]. Actually, date palm oases in the Sahara Desert have been neglected and even completely abandoned for a long period; however, during the last three decades, DPP has experienced a significant recovery, especially in the Ziban region [9, 13].

Several studies treated the spatiotemporal changes of oases land-use/land cover based on geomatics approach [3, 10–13]. Nevertheless, only a few studies have focused on using geospatial tools and remote sensed data for monitoring the dynamics of landscapes in this specific area, which is the most important region in DPP crops in Algeria. Within this framework, this survey aimed to quantify the changes in DPP extent based on remote sensing tools using long-time series of Landsat images as a cost-efficient tool.

A. Mihi (✉) · H. Chenchouni
Department of Natural and Life Sciences, FSESNV, University of Tebessa, 12002 Tebessa, Algeria
e-mail: mihialieco@gmail.com

T. Nacer
University of Mohamed Khider, 07000 Biskra, Algeria

H. Chenchouni
Laboratory of Natural Resources and Management of Sensitive Environments 'RNAMS', University of Oum-El-Bouaghi, 04000 Oum-El-Bouaghi, Algeria

© Springer Nature Switzerland AG 2019

H. M. El-Askary et al. (eds.), *Advances in Remote Sensing and Geo Informatics Applications*, Advances in Science, Technology & Innovation, https://doi.org/10.1007/978-3-030-01440-7_52

2 Materials and Methods

Geographically, the region of Zinan is located along the southeastern foothills of Aures Mounts in northeastern Algeria. The study area includes 18 municipalities of Wilaya of Biskra (Fig. 1) and stretches over an area of 21,671 km^2. Agriculture is the main human activity in this region, where DPP prevails as the main permanent crop in the Ziban region. The region is characterized by a Saharan Mediterranean climate with hot and dry summers and mild winters.

The satellite images used in this study were collected from the USGS Landsat archive (L1T) (http://glovis.usgs.gov). They have a spatial resolution of 30 m and less than 1% cloud cover as they have been acquired in the summer season (June 30th, 1984 for Landsat 5 TM, July 2nd, 1999 for Landsat 7 ETM+, and June 30th, 2013 for Landsat 8 OLI). The two images, TM-1984 and ETM+-1999 were geometrically corrected (Nearest-neighbour resampling technique) to the image of reference (image OLI-2013), with 15 points and an acceptable error with the Root Mean Square (RMS) is less than one pixel (0.92). All images were finally re-projected to Universal Transverse Mercator (UTM) Projection zone 31 North with the datum World Geodetic System (WGS) 1984. The maximum of likelihood classifier was adopted then sample areas representing categories of land use/land cover of habitats in the study region were collected randomly using GPS for more classification accuracy estimation. In order to assess the classification accuracy, the overall accuracy and kappa coefficient were computed. One range class of land cover was distinguished and considered in our case (date palm groves). For the RGB composite selection, the three bands: short wavelength infrared, the near infrared, and the Blue bands were used. The software ENVI 4.5 was used for processing all satellite images. The following equation (Eq. 1) allowed evaluating the change rate (T) in DPP. The DPP area increase is represented by positive values whereas its decrease is indicated by negative values. Besides, the unchanged area of DPP is referred to as 0 value [6].

$$T = \left(1 - \left(\frac{S2}{S1}\right)^{\frac{1}{n}}\right) \times 100 \quad (1)$$

Where: T = Change rate (%), S1 = DPP surface at date 1 (ha), S2 = DPP surface at date 2 (ha), n = number of years between the two dates.

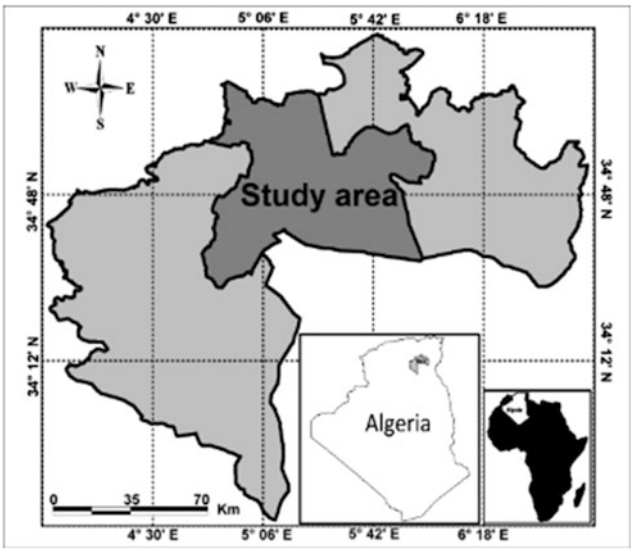

Fig. 1 Location of study area (dark grey) with the province 'wilaya' of Biskra (light grey) north of the Sahara Desert of Algeria

3 Results

Figure 2 shows the mapping results of DPP changes over the Ziban region during the past 30 years. These results were validated with more than 90% of accuracy for both Kappa coefficient and the overall accuracy (Table 1). A clear increase in DPP was recorded during the period 1984–1999, with an 8116 ha increase in the area, about 1 M newly-planted palm trees, and a change rate of −4.51%. Another expansion peak in DPP occurred from 1999 to 2013 in a cultivated area (17,816.49 ha), with 1M palm trees, and a change rate of −5.36%. Overall, a high DPP increase was observed during the last 30 years (1984–2013), in areas with 25,932.96 ha, a change rate (−5.63%), and a number of palm trees with two million newly-planted trees (Table 1).

4 Discussion

According to the results of remote sensing, the two DPP peaks, i.e. 1999 and 2013, coincide with, on the one hand the start of the new DPP established within the framework of the Accession to the Agricultural Land Ownership (APFA) in 1983, that aimed to promote the Saharan agriculture and a second ongoing cycle of DPP began in 2000, through another program called the National Plan of Agricultural and Rural Development (PNDA) on the other hand. Furthermore, the Algerian government launched the great project for oasis development in 1994, which aimed to the rehabilitation and extension of DPP in order to sustainably double the current date yield and date palms by the year 2010 [5]. The results presented in this work remain basically consistent with the government's inventory data provided by the DSA [8]. Besides, our results of DPP change are similar to the findings of Afrasinei et al. [1] and Mihi et al. [13] that reported that DPP area quadrupled in the region of Ziban

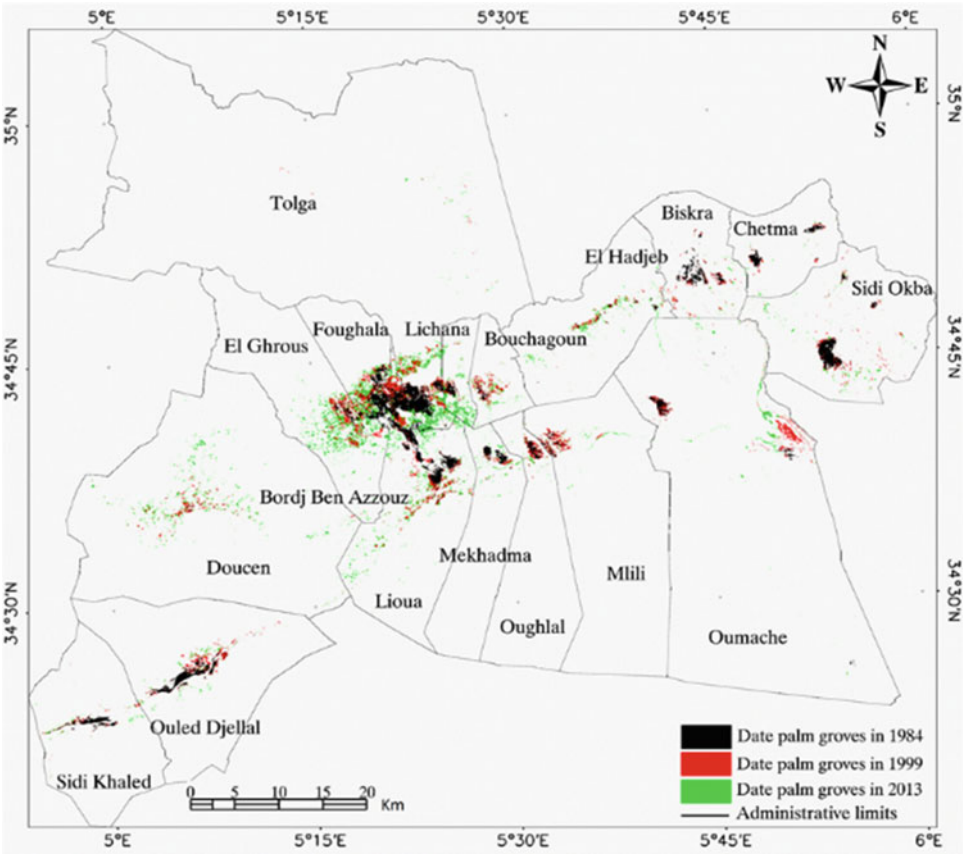

Fig. 2 Date palm plantation dynamics from 1984 to 2013 in a desert oasis (Ziban region) of the Algerian Sahara

Table 1 Summary of date palm change for 1984, 1999 and 2013 in the region of Ziban (Sahara Desert of Algeria)

DPP	1984	1999	2013	Change rate (1984–1999)	Change rate (1999–2013)	Change rate (1984–2013)
Area (ha)	8434.26	16,550.73	34,367.2	−4.51%	−5.36%	−4.96%
NPT[a]	973,976.4	2137,978.8	3,111,955.2			
PTN (DSA)	–	2,052,781	3,041,957.6			
O-A	96.43	95	94.68			
K-C	95	92	94			

DPP Date palm plantation, *NPT* Number of date palm trees, *O-A* Overall accuracy, *K-C* Kappa-Coefficient
[a]According to Bouguedoura et al. [5] (1 ha = 120 date palm trees)

over the past three decades (1984–2013). The present situation of spatial distribution of date palm trees depends on several environmental and agricultural factors, of which some may act as limiting factors such as soil conditions, drought duration and intensity and the choice of unsuitable varieties [4]. Actually, the variety Deglet-Noor dominated in the study area, mainly because of its high commercial value in local and international markets. Nevertheless, the monoculture model causes the marginalization of indigenous varieties (often with less commercial value), which increased the fragility and the vulnerability of the oasis ecosystem to biotic and abiotic stresses [13].

5 Conclusion

Date palm plantation area recorded a significant increase through a period of 30 years between 1984–2013, with 25.93 km^2 increase at the detriment of desert rangeland habitats surrounding the DPP oases. This means a loss of about 26 km^2 of the arid rangelands system. Our findings stress the significant extent of DPP area over a short period and simultaneously illustrate the potential of using the time-series of Landsat images for monitoring dynamics and detecting changes in hot desert landscapes especially oases.

References

1. Afrasinei, G.M., Melis, M., Buttau, C., Bradd, J.M., Arras, C., Ghiglieri, G.: Assessment of remote sensing-based classification methods for change detection of salt-affected areas (Biskra area, Algeria). J. Appl. Remote Sens. **11**(1), 1931–3195 (2017)
2. Al-Khayri, J.M., Jain, S.M., Johnson, D.V.: Date palm genetic resources and utilization. In: Africa and the Americas, 1st edn. Springer, Netherlands (2015)
3. Aldakheel, Y.Y.: Assessing NDVI spatial pattern as related to irrigation and soil salinity management in Al-Hassa Oasis, Saudi Arabia. J. Soc. Remote Sens. **39**, 171–180 (2011)
4. Born Bouzaher, L., Alkama, D.: Palm trees reuses as sustainable element in the Sahara. The case of Ziban, as self-sustainable urban units. Energ. Procedia **18**, 1076–1085 (2012)
5. Bouguedoura, N., Bennaceur, M., Babahani, S., Benziouche, S.E.: Date palm status and perspective in Algeria. In: Al-Khayri, J.M., Jain, S.M., Johnson, D.V. (eds.) Date Palm Genetic Resources and Utilization, pp. 125–168. Springer, Netherlands (2015)
6. Brou, T.: Variabilité climatique, déforestation et dynamique agrodémographique en Côte d'Ivoire. Sécheresse **21**(4), 327–329 (2010)
7. De Grenade, R.: Date palm as a keystone species in Baja California peninsula, Mexico oases. J. Arid Environ. **94**, 59–67 (2013)
8. Direction des Services Agricoles (DSA): Annuaire des statistiques agricoles de la wilaya de Biskra. Biskra, Algérie (2013)
9. Dubost, D., Larbi-Youcef, Y.: Mutations agricoles dans les oasis algériennes: l'exemple des Ziban. Sécheresse **9**, 103–110 (1998)
10. Kawy, W.A.M.A., El-Magd, I.H.A.: Use of satellite data and GIS for assessing the agricultural potentiality of the soils South Farafra Oasis, Western Desert, Egypt. Arab J. Geosci. **6**, 2299–2311 (2013)
11. King, C., Thomas, D.S.: Monitoring environmental change and degradation in the irrigated oases of the Northern Sahara. J. Arid Environ. **103**, 36–45 (2014)
12. Luedeling, E., Buerkert, A.: Typology of oases in northern Oman based on Landsat and SRTM imagery and geological survey data. Remote Sens. Environ. **112**, 1181–1195 (2008)
13. Mihi, A., Tarai, N., Chenchouni, H.: Can palm date plantations and oasification be used as a proxy to fight sustainably against desertification and sand encroachment in hot drylands? Ecol. Ind. (2017). https://doi.org/10.1016/j.ecolind.2017.11.027

VegMeasure: Image Processing Software for Grassland Vegetation Monitoring

Mounir Louhaichi, Sawsan Hassan, and Douglas E. Johnson

Abstract

Vegetative inventories, whether they are agronomic, ecologic, range, or forestry, often measure plant cover. Vegetation cover is a fundamental parameter in many studies of plant ecology. It is used to measure the surface of the ground exposed to the direct impact of rain drops, sunlight and it is also used to monitor changes in vegetation structure over time. VegMeasure®, an image processing software, was developed to monitor vegetation cover over a period of time, through utilizing green leaf and brightness algorithms as well as K-means classifications. This study demonstrates that digital image processing of vegetation can be fast and affordable, through creating a permanent digital record that can be revisited over time.

Keywords

Image processing • Digital camera • Central Asia • Arid environment • Rangelands

1 Introduction

Vegetation cover plays an important role in ecosystem stability, through reducing soil loss in the form of soil erosion [4]. Traditional vegetation sampling techniques are subjective, time consuming, costly, and, at times, destructive [5]. Therefore, it is important to adopt new technologies which are easy to use, cost and time effective, and also non-destructive to the vegetation [3]. With the recent advances in geoinformatics, assessing and monitoring vegetation characteristics using non-destructive techniques is becoming more widely used. For example, vegetation cover is a key variable which could be sampled in a non-destructive approach for biomass estimates in rangelands [2].

The purpose of the study was to assess rangeland health by estimating the percent vegetation cover of a selected rangeland site from Kazakhstan using computer assisted image processing.

2 Methods

VegMeasure® is a software developed by the VegMeasure Project in collaboration with the International Center for Agricultural Research in the Dry Areas (ICARDA). The program is aimed to assess and monitor rangeland vegetation in a non-destructive manner. In particular, it allows rangeland ecologists to make meaningful classes to measure the percent cover of foliage, litter and bare ground, as well as other categories of interest. The software enables hue extraction, calibrating a threshold, K-means classification, brightness algorithms, and green leaf algorithms; thus providing natural resource management agencies with an objective approach for rapidly collecting rangeland cover data to pro-mote management decisions which are based on adequate and valid field data.

The software operates by using a mathematical formula (ratio) these pixel values that indicate where green light (reflected) was most intense and red and blue light were low (used by leaves in photosynthesis). The resulting ratioed image had pixel values from a − 1 to a + 1. When displayed it shows a boolean image illustrating two main classes (soil and vegetation).

$$[(\mathbf{G}-\mathbf{R})+(\mathbf{G}-\mathbf{B})]/[\mathbf{G}+\mathbf{R}+\mathbf{G}+\mathbf{B}]$$

M. Louhaichi (✉) · S. Hassan
International Center for Agricultural Research in the Dry Areas (ICARDA), Amman, Jordan
e-mail: m.louhaichi@cgiar.org

M. Louhaichi · D. E. Johnson
Department of Animal and Rangeland Sciences, Oregon State University, Corvallis, OR, USA

© Springer Nature Switzerland AG 2019

H. M. El-Askary et al. (eds.), *Advances in Remote Sensing and Geo Informatics Applications*, Advances in Science, Technology & Innovation, https://doi.org/10.1007/978-3-030-01440-7_53

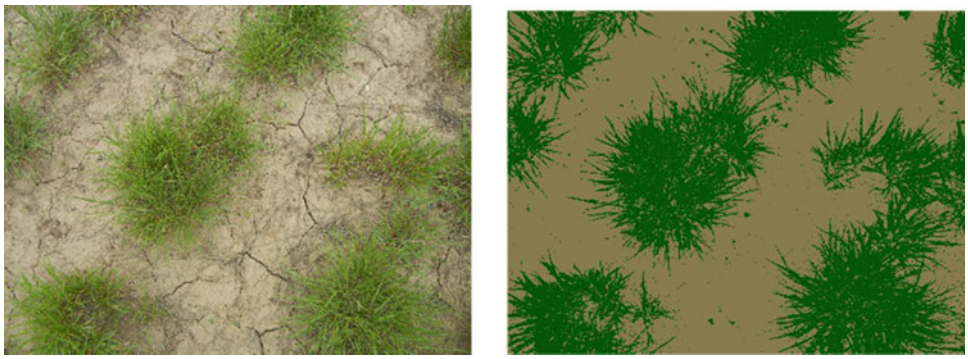

Fig. 1 Original (left) and processed (right) images using VegMeasure® software to estimate ground cover in a rangeland site in Uzbekistan

In this study, we analyzed data collected from a semi-arid grassland site in Kazakhstan. We used GPS-enabled digital camera with a 16 mega-pixel resolution and a high quality lens. For most of the surveys, we used a Nikon Cool Pix AW 110 camera with a built-in GPS, mounted on a staff or pole that held the camera at a height of 1.5 m above the ground. During the photographic sampling, the camera was maintained in an upright position so the GPS fixes are of the highest quality possible. GPS accuracy on our camera was generally within 3–5 m of true location. Classification accuracy was assessed using the accuracy assessment tool in VegMeasure® through computing the error matrix and the Kappa Index of Agreement. The error matrix permits measurement of overall accuracy, category accuracy, producer's accuracy and user's accuracy [1].

3 Results and Discussions

Grasslands cover vast areas and play an important role for the livelihood of rural communities residing in arid and semi-arid ecosystems, and their productivity is highly correlated to rainfall. Therefore, having a good estimate of their productivity is crucial, not only to local communities, but also to decision makers to maintain sustainable livestock production systems. Traditional methods of plant cover and litter estimation are labor intensive and time-consuming. VegMeasure® software allow estimation of grassland vegetation parameters and to monitor native grassland with minimum cost in a non-destructive manner. Figure 1 illustrates the use of VegMeasure® in the grasslands in Kazakhstan.

Vegetation cover has been recognized as a surrogate variable to predict biomass of grassland [6]. In the example above the percent green cover (vegetation) was estimated at 75% while the bareground (soil) was 25% while the classification accuracy was 98%. The higher the vegetation cover the more stable and healthy is the site.

4 Conclusions

The proposed technique is quick to learn and use. The VegMeasure® software is offered free of charge. Unlike other image processing software, users have to acquire expensive programs and should have a solid remote sensing background. In addition, this technique offers to land manager and researchers quantitative data in a non-destructive manner to assess grassland health. Monitored areas can be revisited each season or year to assess the spatial and temporal effect of natural and human induced factors.

Acknowledgements This study was supported by the International Center for Agricultural Research in the Dry Areas (ICARDA), the VegMeasure project and the CGIAR Research Program on Livestock (CRP Livestock).

References

1. Congalton, R.G.: A review of assessing the accuracy of classification of remotely sensed data. Remote Sens. Environ. **37**, 35–46 (1991)
2. Louhaichi, M., Hassan, S., Clifton, K., Johnson, D.E.: A reliable and non-destructive method for estimating forage shrub cover and biomass in arid environments using digital vegetation charting technique. Agrofor. Syst. (2017). https://doi.org/10.1007/s10457-017-0079-4
3. Louhaichi, M., Johnson, M.D., Woerz, A.L., Jasra, A.W., Johnson, D.E.: Digital charting technique for monitoring rangeland vegetation cover at local scale. Int. J. Agric. Biol. **12**, 406–410 (2010)
4. Royan, M., Sepehry, A., Salman Mahiny, A.: Estimating rangeland vegetation frequency & density using low-altitude aerial photographs. Iran. J. Appl. Ecol. **5**(17), 1–10 (2016)
5. Serrano, J., Sales-Baptista, E., Shahidian, S.Marques, da Silva, J., Ferraz de Oliveira, I., Lopes de Castro, J., Pereira, A., Cancela d'Abreu, M., de Carvalho, M.: Proximal sensors for monitoring seasonal changes of feeding sites selected by grazing ewes. Agrofor. Syst. **1**, 1–15 (2018)
6. Tarhouni, M., Ben Salem, F., Tlili, A., Ouled Belgacem, A., Neffati, M., Louhaichi, M.: Measurement of the aboveground biomass of some rangeland species using a digital non-destructive technique. Bot. Lett. **163**(3), 281–287 (2016)

Assessing the Impact of Vegetation Cover on Total Column Ozone Over West Africa

Samuel Ogunjo, Ibiyinka Fuwape, Babatunde Rabiu, Sunday Oluyamo, and Eunice Owoola

Abstract

This study investigated the linear relationship between the normalized difference vegetation index and total column ozone. Total Column Ozone and Normalized Difference Vegetation index data were obtained from January 2005 to November 2017 from NASA's AURA and MODIS archives respectively. The obtained results showed a predominant and significant positive linear relationship between the two variables over the West African region. The prevalent practices of bush burning, deforestation, crude oil exploration and other activities will continue to contribute to global warming through an increase in the total column ozone and its precursors.

Keywords

Total column ozone • NDVI • Global warming • Deforestation

1 Introduction

Many indices have been developed to give information about vegetation across the globe using satellite measurements. Some of the proposed indices include Normalized Difference Vegetation Index (NDVI), Perpendicular Vegetation Index (PVI), Weighted Difference Vegetation Index (WDVI) and Soil Adjusted Vegetation Index (SAVI). NDVI was obtained from satellite measurements using the amount of visible light and near-infrared light reflected from the Earth's surface [1]. NDVI was found usable for vegetation analysis, studying spatial vegetation patterns and vegetation dynamics [2].

Ozone has been shown to pose a threat to humans and vegetation in the lower atmosphere [3]. Total Column Ozone (TOC) has been shown to be influenced by ENSO [4], eclipse [5] and energetic electron precipitation events [6]. In the stratosphere, ozone acts as an absorber for the sun's biologically harmful ultraviolet rays, thereby. The impact of variations in TCO on vegetation and human health has been investigated for various regions of the world [7].

Human activities such as bush burning, and gaseous emissions tend to increase TCO values in the troposphere. Thus, a reduction in vegetation is expected to result in an increase in TCO. However, a quantitative analysis of this scenario has not been investigated. A large proportion of the population within sub-Saharan region depend on agriculture for their sustenance. It is imperative to investigate and quantify the impact of TCO on agricultural activities in the region. In this study, we aimed to investigate the linear relationship between vegetation index and total column ozone over the West African region.

2 Study Area, Data and Methods

2.1 Study Area

The study area is West Africa (between latitude 0°N and 23°N; longitude 20°W and 15°E). The region is bounded to the south and west by the Atlantic Ocean and to the north by Sahara Desert. The spatial variation of tropical rainfall is determined by the Intertropical Discontinuity (ITD). The ITD is a low-pressure system formed because of the separation between the tropical maritime air mass and the dry tropical continental air mass [8]. The West African region exhibits a bimodal rainfall which supports the agrarian lifestyle of inhabitants.

S. Ogunjo (✉) · I. Fuwape · S. Oluyamo · E. Owoola
Department of Physics, Federal University of Technology, Akure, Ondo State, Nigeria
e-mail: stogunjo@futa.edu.ng

I. Fuwape
Michael and Cecilia Ibru University, Ughelli North, Delta State, Nigeria

B. Rabiu
Centre for Atmospheric Research, National Space Research and Development Agency, Anyigba, Kogi State, Nigeria

© Springer Nature Switzerland AG 2019

H. M. El-Askary et al. (eds.), *Advances in Remote Sensing and Geo Informatics Applications*, Advances in Science, Technology & Innovation, https://doi.org/10.1007/978-3-030-01440-7_54

2.2 Data and Methods

Monthly TOC and NDVI data were obtained from NASA's AURA and MODIS respectively on Aura Satellite from January 2005 to November 2017 (https://neo.sci.gsfc.nasa.gov). NDVI was downscaled to a resolution of 0.25 by 0.25 using nearest neighbour interpolation for ease of comparison. The linear relationship between NDVI and TOC was computed using a linear regression. Trends in the data were removed by simple differencing.

3 Results

The linear relationship between NDVI and TCO were computed over the West African region using the regression analysis. The slope of the regression line for each point on the grid is presented in Fig. 1.

4 Discussion

As shown in Fig. 1, both positive and negative relationships between NDVI and TCO do exist in the Western and Northern African regions, respectively. The relationships are positive and strongest around the coastal regions. This is seen to weaken northwards where negative relationships were found beyond the 15°N latitude. This implies that an increase in NDVI will result in an increase in TCO values over the West African region but in Northern Africa (especially over the Sahara Desert), a reduction in the vegetation

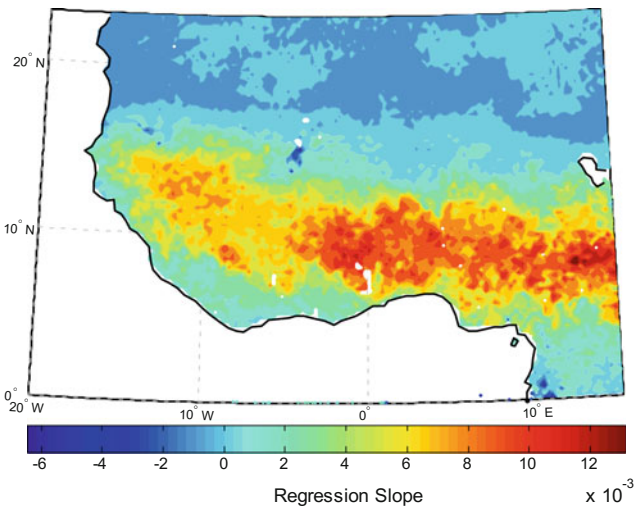

Fig. 1 Linear regression slope between NDVI and total column ozone over West Africa

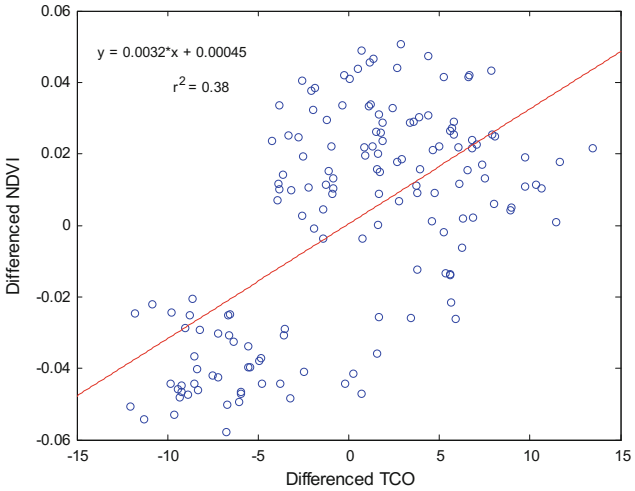

Fig. 2 Areal regression analysis over the study area

index will result in an increase of TCO. In Fig. 2, two distinct regions could be observed in the regression analysis over the region. The lower left hand corresponds to the North African region with negative relationship between TCO and NDVI while the top region represents the West African region. A linear relationship was obtained for the region with slope and intercept of 0.0032 and 0.00045 respectively. Deforestation in the region destroy the stratospheric ozone through the release of N_2O, which is the single most important ozone-depleting emission [9, 10]. Deforestation and conversion of rainforests to pastures has been shown to similar effects on ozone dynamics over the Amazonian forest [11, 12]. The continuous deforestation, desertification and urbanization of tropical forests poses a great risk, not only to the regional, but also the global climate by reducing TCO.

5 Conclusion

In this research, the linear relationship between NDVI and TCO over the West African region has was investigated using the linear regression. The obtained results show that the relationship between the two is negative around Northern Africa but positive in Western Africa. This result is positive and strong for the region where agriculture is the main occupation. Agricultural practices such as bush burning is predominant. Also, high and uncheckered population growth has led to deforestation through rapid urbanization. The continuous deforestation and other practices will lead to the depletion of the total ozone column. This will a have negative impact on humans within and beyond the region.

References

1. NASA Data Homepage. https://mynasadata.larc.nasa.gov/glossary/ndvi-2/. Last accessed 03 Apr 2018
2. Schmidt, H., Karnieli, A.: Sensitivity of vegetation indices to substrate brightness in hyper-arid environment: the Makhtesh Ramon Crater (Israel) case study. Int. J. Remote Sens. **22**(17), 3503–3520 (2001)
3. Lefohn, A.S., Malley, C.S., Simon, H., Wells, B., Xu, X., Zhang, L., Wang, T.: Responses of human health and vegetation exposure metrics to changes in ozone concentration distributions in the European Union, United States, and China. Atmos. Environ. **152**, 123–145 (2017)
4. Zhang, J., Tian, W., Xie, F., Li, Y., Wang, F., Huang, J., Tian, H.: Influence of the El Nino southern oscillation on the total ozone column and clear-sky ultraviolet radiation over China. Atmos. Environ. **120**, 205–216 (2015)
5. Mateos, D., Anton, M., Vaquero, J.M.: Influence of solar eclipse of November 3rd, 2013 on the total ozone column over Badajoz, Spain. J. Atmos. Solar Terrestrial Phys. **112**, 43–46 (2014)
6. Karagodin, A., Mironova, I., Artamonov, A., Konstantinova, N.: Response of the total ozone to energetic electron precipitation events. J. Atmos. Solar Terrestrial Phys., 1–6 (2017)
7. Mills, G., Harmens, H., Wagg, S., Sharps, K., Hayes, F., Fowler, D., Sutton, M., Davies, B.: Ozone Impacts on vegetation in a nitrogen enriched and changing climate. Environ. Pollut. **208**, 898–908 (2016)
8. Fuwape, I.A., Ogunjo, S.T., Oluyamo, S.S., Rabiu, A.B.: Spatial variation of deterministic chaos in mean daily temperature and rainfall over Nigeria. Theoret. Appl. Climatol. **130**(1–2), 119–132 (2017)
9. Houghton, R.A.: The global effects of tropical deforestation. Environ. Sci. Technol. **24**(4), 414–422 (1990)
10. Ravishankara, A.R., Daniel, J.S., Portmann, R.W.: Nitrous oxide (N2O): the dominant ozone depleting substance emitted in the 21st century. Science **326**(5949), 123–125 (2009)
11. Ganzeveld, L., Lelieveld, J.: Impact of Amazonian deforestation on atmospheric chemistry. Geophys. Res. Lett. **3**(L06105), 1–5 (2004)
12. Sigler, J.M., Fuentes, J.D., Heitz, R.C., Garstang, M., Fisch, G.: Ozone dynamics and deposition processes at a deforestation site in the Amazon basin. J. Human Environ. **31**(1), 21–27 (2002)

Contribution of Satellite Imagery to Study Salinization Effect of Agricultural Areas at Northern Eastern Oasis Algerian Region

Madina Khelifi Touhami, Seyfallah Bouraoui, and Mohamed-Chérif Berguig

Abstract

This paper summarized a new and precise spatio-morphological mapping of cultivable area located at northern-eastern oasis Algerian region affected by land salinization phenomena. We gave qualitative and quantitative views by mapping the presence of salt deposit transported by watersheds, accumulated in the same region and raised to the surface following the Albien's drainage for the irrigation of the settlements, or by tectonic movement at depth. In order to study a spacious area with a metric precision, processing optical remote sensing data were required. We processed heterogeneous data; from satellites (sentinel-2b multi-spectral) Combined with an old map of the area and field measurements to produce a new and more accurate up-to-date map. The results obtained by applying supervised classifications (Artificial Neural Network) combined with unsupervised (K-means) methods show the amount of salt on cultivable region over the areas of Touggourt. We deduced the risk that the nearest areas (not yet affected by this phenomenon) have to face. Five classes extracted from the satellite image: salt, sand, agricultural land, palm trees, and buildings Show the distribution of salinity levels as well as the cultivability trend of each class. The total salt (salinization) occupation rate of ~24%, which represents 1/4 of the area affecting almost all cultivable and palm classes.

Keywords

Agriculture area • Classification • Clustering • ANN • K-means

1 Introduction

Soil salinity is a term that includes not only saline soils but also sodic, and alkaline soils [12]. Soil salinization is one of the main causes of soil degradation, particularly in arid zones, affecting more than 100 countries, covering 932.2 Mha of land worldwide [9], of which more than 10% is caused by poorly managed irrigation. The causes inducing salinization can be natural (geological events, upwelling of salt rich groundwater towards the surface and others) or anthropogenic (irrigation with salt rich waters, discharge of salt rich wastewater, use of fertilizers, insufficient drainage, to name but a few). Salt accumulation leads to a significant reduction in soil fertility. Salt disrupts plant growth by limiting nutrient uptake, inhibiting water abstraction and reducing the quality of water available to plants, knowing that most field crops do not tolerate salt well. Thus, this leads to alterations or even disturbances of the biological [11], biochemical [3] and hydrological [6] natural cycle. Soil salinity monitoring and mapping has become an urgent objective to achieve in order to effectively manage soils and water and agricultural land sustainability.

2 Data and Methods

2.1 Study Area

Touggourt lies in the Oued Righ valley located in the northwestern margin of the Grand Erg Oriental between latitudes 32° 53′; 34° 10′ North and the longitudes 5° 47′; 6° 10′ East [2]. The bottom of the region is a long depression (150 km length, 20 km wide), oriented north south, the general shape is about 1‰ [8]. This valley is bordered by the wilaya of Biskra to the north, by the oases of Ouargla to the south-west, the valley of Oued Souf and to the east. Touggourt belongs to an arid climate area; the average annual rainfall is less than 10 mm, and the mean annual

M. Khelifi Touhami (✉) · S. Bouraoui · M.-C. Berguig
University of Sciences and Technology Houari Boumediene, Algiers, Algeria
e-mail: mkhelifitouhami@usthb.dz

© Springer Nature Switzerland AG 2019

H. M. El-Askary et al. (eds.), *Advances in Remote Sensing and Geo Informatics Applications*, Advances in Science, Technology & Innovation, https://doi.org/10.1007/978-3-030-01440-7_55

temperature is around 22 °C [2]. From a geological perspective, the study area consists of Paleozoic formations that outcrop south of the study area, Mesozoic and Cenozoic formations, which are outcrops of borders, Tertiary, and Quaternary continental deposits that occupy the center of the basin. Groundwater is the region's only water resource. Apart from the sub-surface high salinity groundwater, the region relies on the Northern Sahara aquifer system, which extends under Algeria, Libya and Tunisia. This reservoir is made up of two main entities that are Intercalary Continental (IC), and Terminal Complex.

2.2 Methods

Salt accumulation causes modifications in the soil reflectance by affecting the spectral signature (spectral response) and changing the dielectric matters properties. Remote sensing raw data is affected by different types of noises, dues to the interaction with atmospheric particles, spectral, material, topographic and orbital changes. We made an atmospheric correction to the raw image in the preprocessing phase using SEN2COR (SNAP and Sentinel Toolboxes). Then, we used a combination of several classification methods to detect salt and highlight the changes. In the processing phase, we started by calculating salinity and vegetation indices to quantify the presence of each of them and produce the ROI (region of interest) vectors. Then, we compared them to those obtained from supervised (ANN) and Unsupervised (K-means) classification methods using confusion matrix and true ground data.

2.2.1 Vegetation and Salinity Indices

We calculated the Normalized Difference Vegetation Index (NDVI) in order to analyze the quality of vegetation in the region as the presence of salt leads to degradation in soil fertility. Salinity indices were used to detect salty soils, their rates and extension. The most commonly used indices are Normalized Difference Salinity Index, Salinity Ratio, Vegetation Soil Salinity Index and others. The index formulae were initially developed for Landsat images; we adapted and converted them for the sentinel 2 images. Table 1 summarizes the calculated indices, where NIR, R, G, B, b2, b3, b4 and b8 represent respectively Near Infra Red, Red, Green, Blue, 2nd, 3rd, 4th and 8th bands of the used Sentinel 2 multispectral image.

2.2.2 Classification

One of the most common technique used to process remote sensing data is classification. It consists in dividing the image into a number of subsets (classes), based on information belonging to known classes (supervised classification), or without a learning database (unsupervised) [5]. For clustering, we chose the K-means method, which is a fast and efficient classical technique whose aim is to divide the pixels of the image into a set of homogeneous clusters based on the value of the Euclidean mean of the distance between pixels [1]. Processed with different software: SNAP, ENVI and Matlab, the best and retained number of k for this study was five centroids. Although, this method has an important disadvantage, which is the random initialization of centroids engendering different results for each iteration. In order to overcome this problem, we used different classification methods, made a comparison with ROI, on the one hand and with true ground map, on the other hand. The supervised classification was handled by the feed-forward artificial neural networks method. For this raison, we built a learning database using 1000 samples randomly chosen from the different ROI vectors of each class. The neural network topology is made of eight neurons in the input layer (B4, B8, B12, NDVI, NDSI, SR, SI,and SSI), ten hidden layers and five output neurons for the different classes. The activation function is the sigmoid (Logistic) given by:

Table 1 Vegetation and salinity indices with their respective formula used in this study

Vegetation and salinity index	Band ratios	Sentinel 2 bands	References
Normalized difference vegetation index	$NDVI = \frac{(NIR-R)}{(NIR+R)}$	$NDVI = \frac{(b8-b4)}{(b8+b4)}$	Rouse et al. [10]
Normalized difference salinity index	$NDSI = \frac{(R-NIR)}{(R+NIR)}$	$NDSI = \frac{(b4-b8)}{(b4+b8)}$	Major et al. [7]
Salinity ratio	$SR = \frac{(R-NIR)}{(G+NIR)}$	$SR = \frac{(b4-b8)}{(b3+b8)}$	Dehni and Lounis [4]
Salinity index	$SI = \sqrt{(B \times R)}$	$SI = \sqrt{(b2 \times b4)}$	Dehni and Lounis [4]
Vegetation soil salinity index	$SSI = 2 \times G - 5(R + NIR)$	$2 \times b3 - 5(b4 + b8)$	Dehni and Lounis [4]

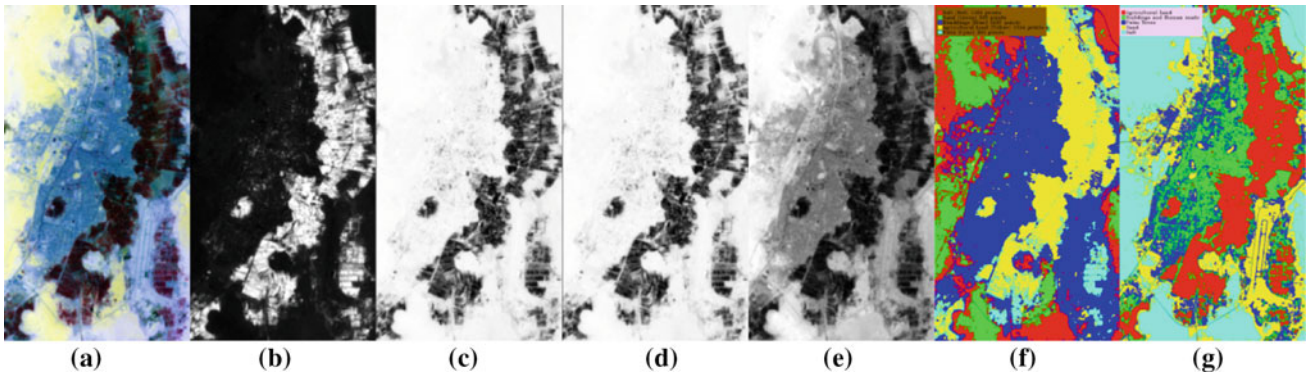

Fig. 1 Chosen results from the application of different methods. **a** Original image cropped according to Touggourt region, **b** NDVI, **c** NDSI, **d** SI1, **e** SR, **f** K-means using SNAP, **g** ANN using Matlab

$$f(x) = \frac{1}{1 + e^{-x}} \quad (1)$$

After 300 iterations, using the same learning rate and learning database, we obtained convergence with all software, and the best response for training RMS < 0.1, reached with MatLab.

3 Results and Discussion

Figure 1 below shows the chosen results obtained and retained after application of the different methods, namely, salinity and vegetation indices (Fig. 1b–d), k-means classification using SNAP (Fig. 1f), classification by artificial neural networks using Matlab (Fig. 1g). After calculating the different salinity indices (Fig. 1c–e), we noticed that salt occupies a large part of the area, it spreads over most of the terrain with a varying intensity (the white color indicates the maximum and black the minimum). The Vegetation Soil Salinity Index shows that despite the existence of vegetation in certain areas, the soil is still affected by this phenomenon.

The classification method by K-means (Fig. 1f) divides the land into 5 different classes (palm trees, agricultural land, salt, sand and buildings), the three software (SNAP, ENVI and Matlab) gave almost similar results. The K-means classification also confirms the results obtained from the salinity indices; the salt class actually occupies the same portion as in the previous results.

The classification method by Artificial Neural Networks (Fig. 1g) is much more precise, because it is assisted by a supervisor and implemented by other field data. The salt class is always present but with less extent (24.19%).

The confusion matrix which calculates the error between regions of interest and ANN yielded very good results (Overall Accuracy = (4623/4811) 96.0923% Kappa Coefficient = 0.9482).

4 Conclusion

In this article, we tried to achieve a spatial study of the extent of salty soils in the Touggourt region, south east of Algeria. This region, known for its dry climate, is experiencing a deterioration in the quality of its agricultural land. In order to achieve our objective, we performed a comparative study using different techniques for interpreting optical satellite imagery, the results are very satisfactory and complementary between the three used methods; vegetation and salinity indices, supervised and unsupervised classifications. We found a percentage of saline soils exceeding 20% of the study area.

References

1. Ahmed, R., Mourad, Z., Ahmed, B.H., Mohamed, B.: An optimal unsupervised satellite image segmentation approach based on pearson system and k-means clustering algorithm initialization. Int. Sci. Index **3**(11), 948–955 (2009)
2. Boulghorba, N., Koull, N., Benzaoui, T.: Four decades period of climatic data for assessing the aeolian hazard in the region of Touggourt (low Algerian Sahara). Geographia Technica **11**(1), 13–22 (2016)
3. Decock, C., Lee, J., Necpalova, M., Pereira, E.I.P., Tendall, D.M., Six, J.: Mitigating N_2O emissions from soil: from patching leaks to transformative action. Soil 687–694 (2015)
4. Dehni, A., Lounis, M.: Remote sensing techniques for salt affected soil mapping: application to the Oran region of Algeria. Procedia Eng. **33**, 188–198 (2012)
5. Duda, R.O., Hart, P.E.: Pattern Classification and Scene Analysis. Wiley, Hoboken, New York (1973)

6. Keesstra, S., Geissen, V., Mosse, K., Piiranen, S., Scudiero, E., Leistra, M., van Schaik, L.: Soil as a filter for groundwater quality. Curr. Opin. Environ. Sustain. **4**, 507–516 (2012)
7. Major, D.J., Baret, F., Guyot, G.: A ratio vegetation index adjusted for soil brightness. Int. J. Remote Sens. **11**(5), 727–740 (1990)
8. MohamedouOuld Baba, S.Y.: Recharge et Paléorecharge du système aquifère du Sahara septentrional. Geology doctorate thesis, University of Tunis and Manar, p. 271, Tunisia (2005)
9. Rengasamy, P.: World salinization with emphasis on Australia. J. Exp. Bot. **57**, 1017–1023 (2006)
10. Rouse J. Jr., et al.: Monitoring Vegetation Systems in the Great Plains with ERTS. NASA Special Publication, pp. 351–309 (1974)
11. Smith, P., Cotrufo, M.F., Rumpel, C., Paustian, K., Kuikman, P.J., Elliott, J.A., Mc-Dowell, R., Griffiths, R.I., Asakawa, S., Bustamante, M., House, J.I., Sobocka, J., Harper, R., Pan, G., West, P. C., Gerber, J.S., Clark, J.M., Adhya, T., Scholes, R.J., Scholes, M. C.: Biogeochemical cycles and biodiversity as key drivers of ecosystem services provided by soils. Soil **1**, 665–685 (2015)
12. Van Beek, C.L., Tóth, G.: Risk Assessment Methodologies of Soil Threats in Europe. JRC Scientific and Policy Reports EUR 24097 (2012)

Monitoring of Grasslands Management Practices Using Interferometric Products Sentinel-1

Ons Chiboub, Amjad Kallel, Pierre-Louis Frison, and Maïlys Lopes

Abstract

Grasslands are globally important for their economic and environmental services, for these reasons their conservation and their mode of exploitation must be monitored. In this work we wanted to study the relationship between temporal interferometric coherence, radar backscattered coefficient and types of agricultural practices associated with grasslands such as grazing, mowing, and the mixed exploitation of these two practices. High coherence values due to backscattering from the ground were linked to ploughed bare fields and low vegetation height and the backscattering coefficient σ^o increases with the biomass up to a saturation level. Results revealed that grazing actions are easily detectable especially with the coherence values while mowing date cannot be clearly detected whether by coherence or by backscattered coefficient.

Keywords

Grasslands • Mowing • Grazing • Sentinel-1 • Times series • Interferometric coherence • Radar backscattered coefficient

1 Introduction

Grasslands which cover a great diversity now, occupy around 40% of terrestrial surfaces. In Europe permanent and temporary grasslands still cover respectively 33 and 6% of the total Useful Agricultural Area (UAA) in 2007 [1].

Grasslands play an important role for both economic and environmental services. This biodiversity supports many ecosystem benefits such as carbon regulation, food production [2], crop pollination, pest regulation and water quality regulation. The functional role of grasslands depends, on their management methods (fertilization, mowing, and/or grazing) as well as on their nature. However, the areas of the grasslands are in decrease because of agriculture escalation, neglect and urbanization. Therefore, prompt survey/interventions have become urgent for their future preservation.

Remote sensing is particularly well suited to monitoring terrestrial surfaces, especially vegetation as it allows the estimation of land use over large areas. In the case of forests, remote sensing data are mainly used for the monitoring of deforestation, plantations and their certification or for applications in agro-forestry [3]. In recent years, several studies have been conducted to retrieve grassland biophysical parameters (classification, biodiversity, biomass estimation, yield) based on satellite data-acquisition [4–6]. Tamm et al. [7] analyzed Sentinel-1 interferometric coherence in relation to mowing events recorded to evaluate management practices of grasslands in Estonia.

In this context the current work presented a preliminary assessment of possible correlation between the management practices of grasslands located in the South of France and inter-ferometric coherence extracted from Sentinel-1A and 1B (when available) acquisitions.

O. Chiboub (✉) · A. Kallel
Sfax National School of Engineering, University of Sfax, Sfax, Tunisia
e-mail: onschiboub94@gmail.com

P.-L. Frison
LaSTIG, University of Paris-Est Marne-la-Vallée/IGN, 5 boulevard Descartes, 77454 Marne la Vallée, France

M. Lopes
DYNAFOR, INRA, University of Toulouse, Castanet-Tolosan, France

© Springer Nature Switzerland AG 2019

H. M. El-Askary et al. (eds.), *Advances in Remote Sensing and Geo Informatics Applications*, Advances in Science, Technology & Innovation, https://doi.org/10.1007/978-3-030-01440-7_56

2 General Characteristics of the Study Area

The study area (Fig. 1) is located on the ecological research site «coteaux et vallées de Gascogne» which is part of the European network LTER (European Long-Term Ecological Research). The study site lies in Gascony 80 km south-west of Toulouse and covers a total area of 35 km^2. It is highly anthropized, the surfaces being mainly dedicated to agricultural activities, 56.8% of the surfaces are allocated to seasonal crops, with 32.1%, for grasslands, 7.9% of the land is occupied by forests, and 2.4% by urban areas [8]. Most grasslands are under mixed management, used for mowing and grazing. Grasslands are represented on steep slopes while annual crops are in the valleys on the most productive lands. The climate is sub-Atlantic with sub-Mediterranean and mountain influences (mean annual temperature, 12.5 °C; mean annual precipitation, 750 mm) [9].

3 Data and Methods

The study period extends throughout 2016 during which Sentinel-1A and Sentinel-1B data are available. The acquisition mode is the Interferometric Wide mode that allows the acquisition of data in VV and VH polarizations. The coherence parameter is extracted from the data in SLC format (Single Look Complex) while the radar backscattered coefficient was extracted from the data in GRDH format (Ground Range Detected High resolution).

The data processing was performed using the SNAP software; GRDH data are calibrated then ortho-rectified as per the following steps.

- Co-registration: this step ensures that each ground target contributes to the same (range, azimuth) pixel in master and slave images.
- Coherence: the interferometric coherence ρ, which estimates the complex correlation in amplitude and in phase on a local neighborhood of N pixels of 2 different acquisitions to evaluate the temporal stability of the diffusers, is calculated by Eq. (1).

$$\rho = \frac{\sum \mathrm{Mi} * \mathrm{Ei}}{\sqrt{(\mathrm{Mi}^2 * \mathrm{Ei}^2)}} \quad (1)$$

With Mi and Ei denote the complex radar responses of the pixel i for the master and the slave image, respectively.

- Deburst: this operation consists in removing black bands that are the result of the acquisition mode of the radar image.
- Terrain correction: this step allows correcting Geometric distortions and then moving on to a flat geometry.

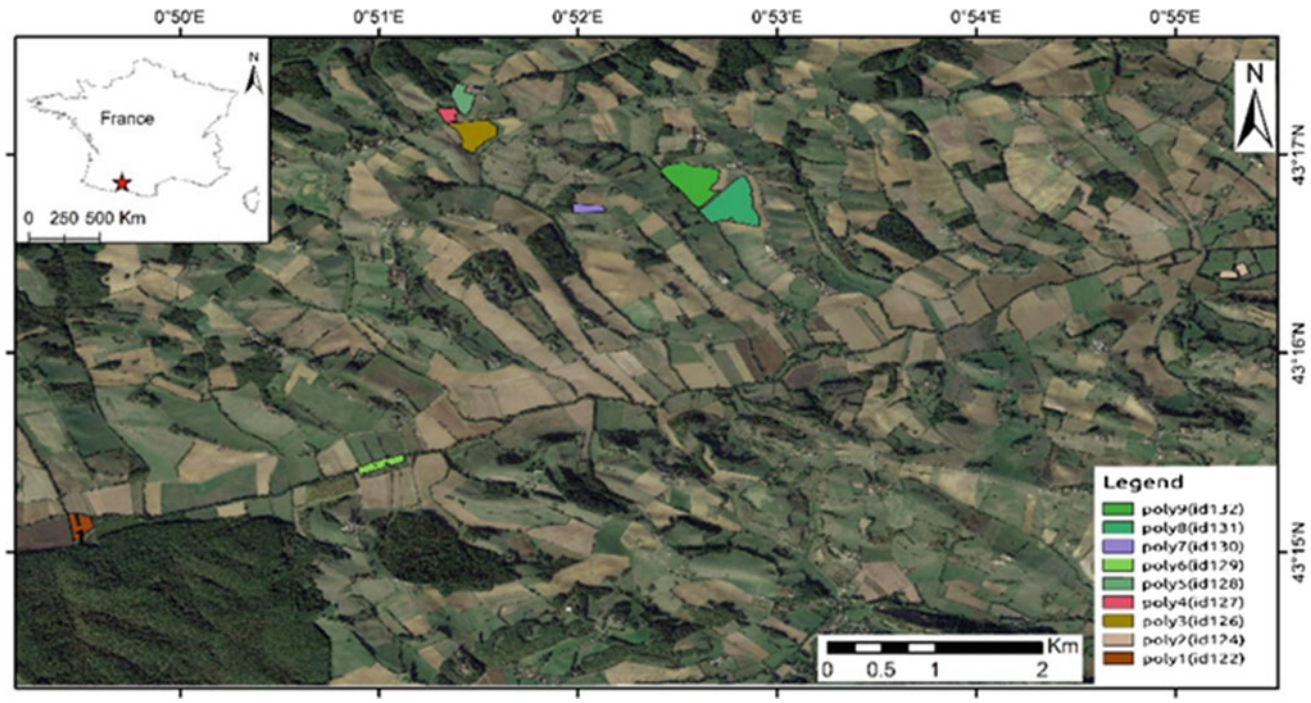

Fig. 1 The location of the study area (red color indicates the grasslands of interests)

It is worth noting that the management practices and their intensity (i.e., number of mowings, intensity of grazing) are known for the studied parcel owing to field survey and monitoring during 2016.

4 Results and Discussion

In order to analyze the behavior of the values of the backscattering coefficient (σ^o) and the coherence with the seasonality of the vegetation and the meteorological data, it is important to draw a temporal profile which joins the mean values of the σ^o/the values of coherence (Fig. 2), the values of annual precipitations and the seasons in Julian days. The interpretation of the obtained results was achieved using historical land data about grassland exploitation.

Mowing event was occasionally characterized by a complete removal of herbs, and grass with a height of 20 cm was often left on the field. For these reason we only noticed the increase of coherence that could be linked to the mowing event for both grassland shown in Fig. 2a, b and that is especially with VH polarization. For other parcels coherence values fluctuated, which makes the correlation between coherence and mowing event hard to detect. While for a grazing event, the time series illustrate a clear relationship between this event and coherence. Figure 2a, b show the increase of coherence in October which means just after the grazing event that happened in late August, early September. The parcel shown in Fig. 2d has never been grazed and this is why the coherence values remain constant. Fluctuations observed in Fig. 2e return to the fact that this grassland presents a lot of slope effect and that it was operated in mixed management (pasture mown in the same period).

A higher response could be observed in Fig. 2c; an increase of coherence value was recorded in mid-July after the grazing event to reach a value that exceeds 0.5. For the same parcel a second grazing event on 4th August was followed by an increase of coherence to attain a value of 0.4. For most time series a drop of coherence was noticed in November, and this is related to the autumn regrowth of herbs.

Figure 2f shows that backscattered coefficient has no response whether towards mowing or grazing.

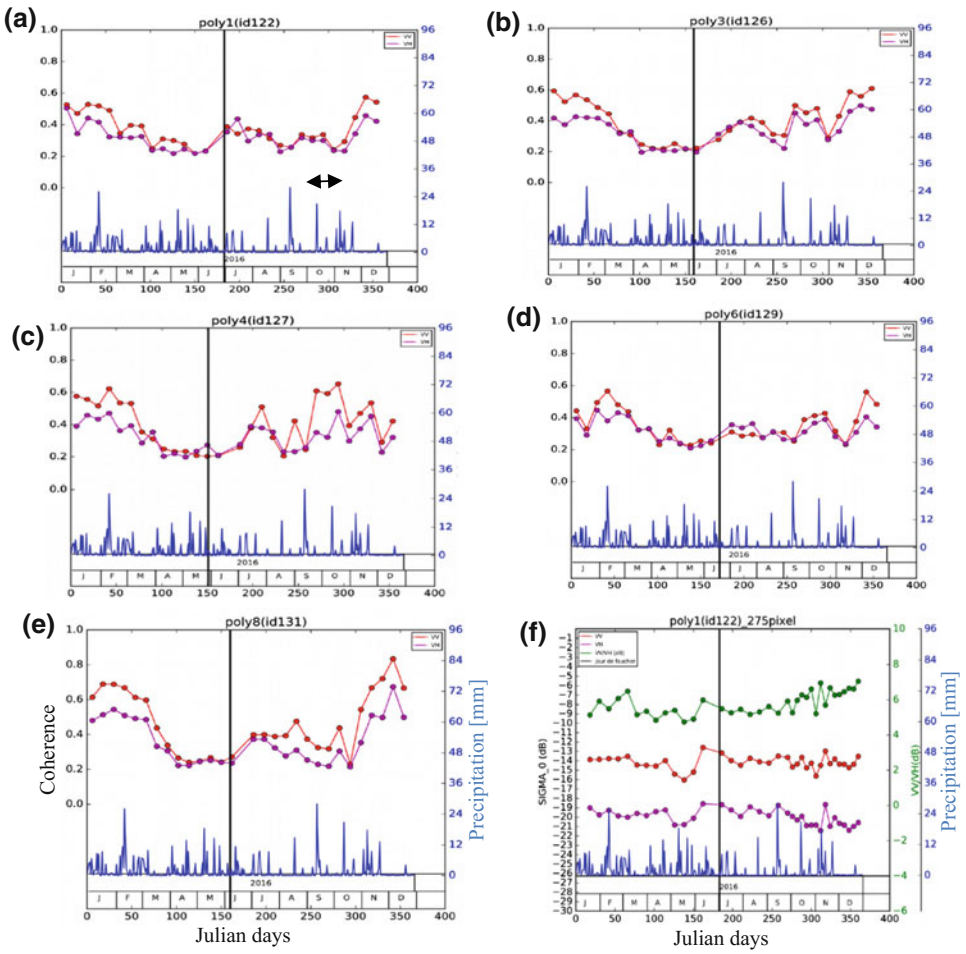

Fig. 2 **a–e** Temporal profile for interferometric coherence (red color is for VV polarization, purple color is for VH polarization, black vertical line indicate mowing date); **f** temporal profile for backscattered coefficient (red color is for VV polarization, purple color is for VH polarization, green color is for VV/VH polarization, black color is for mowing date)

For all figures, the recorded precipitation does not show a significant influence on the spectral response while Tamm et al. [7] found that precipitation causes coherence to drop. Mowing date is not clearly detected either by coherence or by backscattered coefficient while grazing dates are easily detectable especially with the coherence values and precipitation does not have a significant influence on the spectral response.

5 Conclusion

The objective of this study was to evaluate the relationship between grassland agricultural practices and time series of sentinel-1 measurements.

A systematic behavior in VH and VV polarimetric coherence was identified. For most of the observed fields, VH and VV coherence values increase after the action of pasture while for mowing, the date was not easily detectable which can be related either to the mowing mode (half mowed, entirely mowed, etc.), or the practice speed.

References

1. Huyghe, C., Vliegher, A., Gils, B., Peeters, A. (coordinators).: Grasslands and herbivore production in Europe and effects on common policies. Versailles, France: Editions Quae (2014)
2. O'Mara FP.: The role of grasslands in food security and climate change. Ann. Bot **110**, 1263–1270 (2012). https://doi.org/10.1093/aob/mcs209doi:
3. Frison, P., Lardeux, C.: Vegetation cartography from sentinel-1 radar images. In: Baghdadi, N., Mallet, C., Zribi, M. (eds.) QGIS and Applications in Agriculture and Forest (2018). https://doi.org/10.1002/9781119457107.ch6
4. Ali, I.: Retrieval of grassland biophysical parameters using multi-temporal optical and radar satellite data. Ph.D. thesis, University College Cork, Cork, Ireland, 299 pages (2016)
5. Lopes, M., Fauvel, M., Ouin, A., Girard, S.: Potential of Sentinel-2 and SPOT5 (Take5) time series for the estimation of grasslands biodiversity indices. In: IEEE MultiTemp 2017—9th International Workshop on the Analysis of Multitemporal Remote Sensing Images, Jun 2017, Bruges, Belgium, pp. 1–4 (2017)
6. Grant, K., Siegmund, R., Wagner, M., Hartmann, S.: Satellite based assessment of grassland yields. In: The International Archives of the Photogrammetry, Remote Sensing and Spatial in formation Sciences, vol. XL-7/W3 (2015)
7. Tamm, T., Zalite, K., Voormansik, K., Talgre, L.: Relating sentinel-1 interferometric coherence to mowing events on grasslands. Remote Sens. **8**(10), 802 (2016). https://doi.org/10.3390/rs8100802
8. Fieuzal, R.: Apports des données radar pour l'estimation des paramètres biophysiques des surfaces agricoles. Sciences de la Terre. Université Toulouse III - Paul Sabatier. Français (classification réalisée par Marais-Sicre en 2010) (2013)
9. Carrié, R., Andrieu, E., Cunningham, S.A., Lentini, P.E., Loreau, M, Ouin, A.: Relationships among ecological traits of wild bee communities along gradients of habitat amount and fragmentation. Ecography. **40**, 85–97 (2016). https://doi.org/10.1111/ecog.02632

On the Drying Trends Over the MENA Countries Using Harmonic Analysis of the Enhanced Vegetation Index

Wenzhao Li, Hesham M. El-Askary, Mohamed Qurban, Mohamed Allali, and K. P. Manikandan

Abstract

Arid and semi-arid environments characterize the Middle East and North Africa (MENA) region. Climate change posed significant effects in these regions making them drier and suffer water scarcity especially in recent years. In this research, we used the enhanced vegetation index (EVI) as an indicator of this drying trend over the MENA region the past 20 years. We used harmonic analysis model for comparison with observation data to reveal trends in some capital cities within the MENA region, namely, Tunisia, Egypt, Iraq, Saudi Arabia and Iran. The models performed well and different vegetation changes among these countries were observed. The results revealed a changing behavior over different areas among the MENA region. For instance regions such as Iraq and middle Saudi Arabia suffer drier climate, whereas parts of Iran is more humid.

Keywords

EVI • Vegetation • MENA • Global warming • Cloud platform

1 Introduction

Studies have shown that global warming exacerbates a dry weather. Climate in arid/semi-arid regions has also undergone significant changes making them increasingly drier over the past 100 years [1–3]. Temperature analysis of the main arid regions worldwide from 1900 to 1994 showed that they have experienced a warming trend [4]. By the end of this century, arid/semi-arid regions will increase in area by about 10% [5]. Meanwhile, different changes in arid areas might react differently to climate change, i.e., humid areas will become more humid and dry areas will become drier [6–10].

The MENA region is amongst the most arid/semi-arid areas globally, because of the lack of precipitation and prolonged drought events in the 1970s and 1980s [4]. The MENA region has a dry climate, scarce rainfall, lack of water resources, and an extremely fragile ecological environment. It is sensitive to human activities and global climate change [11–13]. To obtain the spatial distribution of vegetation changes in the MENA region, EVI as a vegetation index can minimize canopy background and atmospheric noise [14]. In this research, we aimed to assess EVI's predictive power for the ecosystems in this region in coherence with the prolonged observed drought conditions. The 2000–2017 MODIS EVI data with Harmonic analysis was to further model the changes of capital city area of five MENA countries (Tunisia, Egypt, Iraq, Saudi Arabia and Iran).

2 Methods

The harmonic analysis is a method that involves the representation of functions or signals as a superposition of elementary waves. In this study, to estimate the variation of EVI, the harmonic model was built with elements of a constant band ($\beta 0$), a linear term of slope ($\beta 1$) and harmonic terms of amplitudes ($\beta 2$, $\beta 3$, $\beta 4$ and $\beta 5$).

$$EVI(t) = \beta_0 + \beta_1 t + \beta_2 \cos(2\pi ft) + \beta_3 \sin(2\pi ft) + \beta_4 \cos(4\pi ft) + \beta_5 \sin(4\pi ft) \quad (1)$$

The term β_1, associated with the linear part of EVI, represents the increasing/decreasing trend, whereas a constant band β_0 represents the extent of consistency of the time series; f represents the fundamental frequency.

W. Li · H. M. El-Askary (✉) · M. Allali
Chapman University, Orange, CA 92866, USA
e-mail: elaskary@chapman.edu

H. M. El-Askary
Alexandria University, Moharem Bek, Alexandria, 21522, Egypt

M. Qurban · K. P. Manikandan
King Fahd University of Petroleum and Minerals (KFUPM), Dhahran, 31261, Saudi Arabia

© Springer Nature Switzerland AG 2019

H. M. El-Askary et al. (eds.), *Advances in Remote Sensing and Geo Informatics Applications*,
Advances in Science, Technology & Innovation, https://doi.org/10.1007/978-3-030-01440-7_57

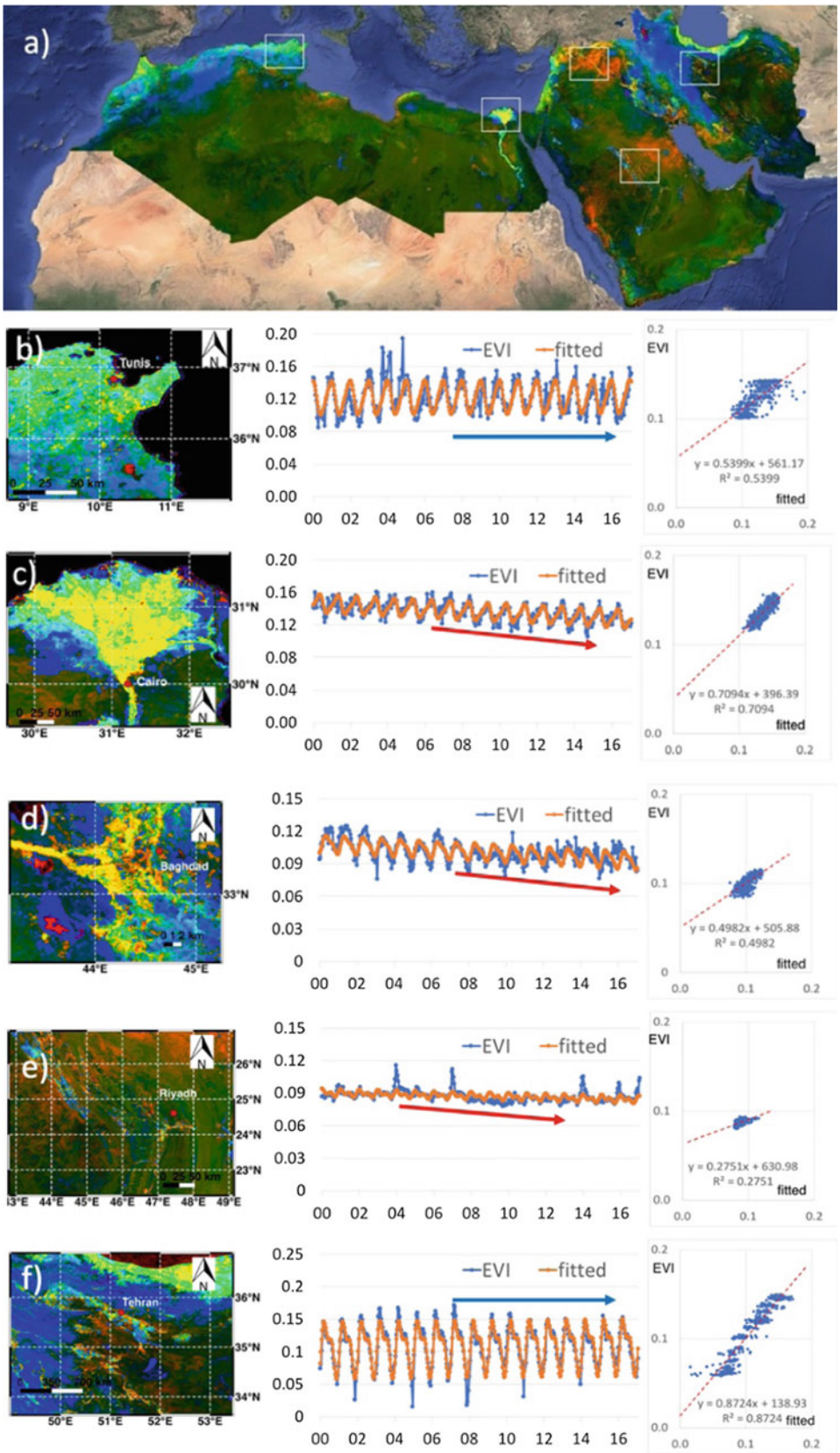

Fig. 1 **a** EVI changing trend among MENA countries, red indicates decrease, blue indicates increase, and green indicates no change. **b**–**f** EVI trend (left), harmonic analysis (middle), regression analysis (right) for **b** Tunis, Tunisia; **c** Cairo, Egypt; **d** Baghdad, Iraq; **e** Riyadh, Saudi Arabia and **f** Tehran, Iran

3 Results

EVI trends and harmonic analysis for the MENA area are presented in the Fig. 1a–e.

Figure 1a shows that regions among the MENA area changes differently: regions such as Iraq and middle Saudi Arabia suffer a drier climate, whereas dotted areas and parts of Iran will be more humid. As seen in Fig. 1b, the EVI trend in the surrounding area of Tunis stays stable, but the southern region increases, except for a dotted red area. The Harmonic model fits EVI data well (except for high records during 2004–2005), showing the same stable trend. In Fig. 1c, the Nile delta of Egypt trends slightly decrease (yellow), whereas the two wings of the delta show an obvious increase. Again the Harmonic model fits the data perfectly, showing the declining trend in Cairo region. A slight decrease (yellow) is also observed along the river near Baghdad (Fig. 1d), but areas of southwest show an increase. The Harmonic model shows the declining trend but misses some of the anomalous changes during 2014–2017. The Riyadh area (Fig. 1e) is an extremely dry region with low EVI values. The model shows the slow decrease trend in general. In Fig. 1f, the western part of Tehran area trends show very strong increase of vegetation. The model shows the overall stable trend and depicts the strong seasonal variations.

4 Discussion

This research supports the idea that some humid areas will become more humid and dry areas will become drier. Also, the regression analysis indicates that models in relatively humid regions (Tunis, Cairo and Tehran) matches better (R-square > 0.5) than the arid regions (Baghdad and Riyadh), since the arid regions are more influenced by anomalous records, i.e., Figure 1e misses several higher records in 2004 and 2007. The harmonic analysis excelled in modeling the inter-annual variability of the EVI index. Harmonic amplitudes $\beta 2$ and $\beta 3$ construct the seasonal changes within the year, whereas $\beta 4$ and $\beta 5$ focus more on the small scale within the season, i.e., an increase after the summer peak value represented in Fig. 1f. In general, the more the harmonic components are used, the more variation details will be denoted in the model. However, regardless of computational resources, introducing too many components could cause the overfitting problem, especially with some anomalous or missing records, i.e. high biases in modeling aerosol optical depth in a desert area where summer records are usually absent.

5 Conclusion

In this research, with the support from cloud-based platform to high scale of scientific data, the drying trend was assessed over the past 20 years for selected MENA areas using EVI. The EVI images exhibited varying spatial patterns of vegetation conditions with varying magnitudes in the different areas. Owing to the presence of some anomalous records in drier areas, the harmonic models showed less correlation over Riyadh and Bagdad compared to Cairo, Tunisia and Tehran. Generally, EVI tends to exhibit a level of uncertainty in sparsely vegetated lands due to the disturbance of blue band reflectance affected by aerosols. It is noteworthy to mention that the EVI time-series captured the largest inter-annual variability for the different locations.

References

1. Narisma, G.T., Foley, J.A., Licker, R., Ramankutty, N.: Abrupt changes in rainfall during the twentieth century. Geophys. Res. Lett. **34** (2007)
2. Nicholson, S.: Climatic and environmental change in Africa during the last two centuries. Clim. Res. **17**, 123–144 (2001)
3. Nicholson, S.E., Tucker, C.J., Ba, M.B.: Desertification, drought, and surface vegetation: an example from the west African Sahel. Bull. Am. Meteorol. Soc. **79**, 815–829 (1998)
4. Hulme, M.: Recent climatic change in the world's drylands. Geophys. Res. Lett. **23**, 61–64 (1996)
5. Feng, S., Fu, Q.: Expansion of global drylands under a warming climate. Atmos. Chem. Phys. **13**, 10081–10094 (2013)
6. Chou, C., Neelin, J.D., Chen, C.-A., Tu, J.-Y.: Evaluating the "Rich-Get-Richer" mechanism in tropical precipitation change under global warming. J. Clim. **22**, 1982–2005 (2009)
7. Held, I.M., Soden, B.J.: Robust responses of the hydrological cycle to global warming. J. Clim. **19**, 5686–5699 (2006)
8. Neelin, J.D., Chou, C., Su, H.: Tropical drought regions in global warming and El Niño teleconnections: tropical drought in global warming and ENSO. Geophys. Res. Lett. **30** (2003)
9. Seager, R., Naik, N.H., Vecchi, G.A.: Thermodynamic and dynamic mechanisms for large-scale changes in the hydrological cycle in response to global warming. J. Clim. **23**(17), 4651–4668 (2010)
10. Trenberth, K.E., Dai, A., Rasmussen, R.M., Parsons, D.B.: The changing character of precipitation. Bull. Am. Meteorol. Soc. **84**, 1205–1218 (2003). https://doi.org/10.1175/BAMS-84-9-1205
11. Reed, S.C., Coe, K.K., Sparks, J.P., et al.: Changes to dryland rainfall result in rapid moss mortality and altered soil fertility. Nat. Clim. Change **2**, 752–755 (2012)
12. Reynolds, J.F., Smith, D.M.S., Lambin, E.F., et al.: Global desertification: building a science for dryland development. Science **316**, 847–851 (2007)
13. Rotenberg, E., Yakir, D.: Contribution of semi-arid forests to the climate system. Science **327**, 451–454 (2010)
14. Liu, H.Q., Huete, A.: A feedback based modification of the NDVI to minimize canopy background and atmospheric noise. IEEE Trans. Geosci. Remote Sens. **33**, 457–465 (1995)

Part VII
Natural Hazards Monitoring and Mapping

Case Study of Debris-Flow Alluvial Fan at Dabaini Catchment, Yunnan Province, China

Yanji Li and Kaiheng Hu

Abstract

People in mountainous regions are likely to settle on alluvial fans that are primarily composed of accumulated debris flow sediment. Despite their many agricultural benefits, these areas are also highly vulnerable to debris flow hazards. Dabaini catchment, in the Xiaojiang basin, Yunnan province, was chosen as a study area to monitor the long-term change of alluvial fans as well as the corresponding influencing factors. Landsat images of the area from 1987 to 2013 and an object-oriented classification method were used to interpret the debris flow fans in each of these years. Their evolution characteristics revealed that (1) the hazard area of debris flow fans has shrunk during the recent 30 years; (2) the debris flow alluvial fans in Dabaini are affected by the size of the debris flows; (3) less precipitation, sediment source, human activities and higher vegetation are the main factors that contribute to the changes of volume in the alluvial fan in recent years.

Keywords

Debris flow • Alluvial fan • Risk assessment • Remote sensing

1 Introduction

Debris-flow alluvial fans are major areas for people living in mountainous regions. The fertile soil is highly suitable for farming and can thus provide means for sustainable living. However, these areas are also highly prone to debris flow hazards which can result in massive losses in life and property. Many scientists have investigated the relationships between the geometric characteristics and the geographic parameters of alluvial fans [1–6]. In recent years, indoor experiments and numerical simulations were used to study the accumulation process of debris flow on the fans [7–11]. Lately, spatial information technologies (including GPS, GIS, RS and LIDAR) have been used to monitor the evolution of debris flows, allowing for more detailed and accurate risk assessments [12–14].

In large debris flow basins (such as the Xiaojiang basin), geological and geographical factors dominate the evolution of debris flow fans. Only a few studies, however, have focused on the relationships between the evolution of debris flow fans and the different influence factors [15]. Although remote sensing and LIDAR images have high spatial resolution, the geometric-characteristics still cannot be expressed very well. In this paper, TM/OLI satellite images of debris flow catchment area, from 1987 to 2013 were used to study the evolution of alluvial fans.

2 Study Area

The Dabaini catchment has an 18.05 km^2 drainage area situated on the left bank of Xiaojiang River which is a tributary to Yangtze River (latitude 26° 02′, longitude 103° 05′) (Fig. 1). The elevation of the Dabaini gully is from 1440 to 3100 m. In the debris flow fan, the average slope of the left bank is 36°, and 47° on the right bank. Dabaini lies in Dabaihe fracture which is the east branch of Xiaojiang fault. The climate of Dabaini is typical plateau monsoon,

Y. Li · K. Hu (✉)
Key Laboratory of Mountain Hazards and Earth Surface Processes, Chinese Academy of Sciences, Chengdu, 610041, China
e-mail: khhu@imde.ac.cn

Y. Li · K. Hu
Institute of Mountain Hazards and Environment, Chinese Academy of Sciences, Chengdu, 610041, China

Y. Li
University of Chinese Academy of Sciences, Beijing, 100049, China

© Springer Nature Switzerland AG 2019

H. M. El-Askary et al. (eds.), *Advances in Remote Sensing and Geo Informatics Applications*, Advances in Science, Technology & Innovation, https://doi.org/10.1007/978-3-030-01440-7_58

Fig. 1 Location map of the study site in Xiaojiang basin

with an annual precipitation range of 600–800 mm. 88% of which occur during the wet season which lasts from May to October. The annual average temperature is 20.1 °C.

Debris flows in Dabaini have repeatedly blocked the Dabaini River all throughout history. For example, a debris flow had jammed the river for a day in 1902, for 2 h in 1933, 3 h in 1957, 1 h in 1959, 3 h in 1963, 12 h in 1968 and 2 h in 1980. Most of the debris flows in Dabaini have high solid concentrations, and transport tremendous amounts of sediment into Xiaojiang River. According to long-term monitoring data, Dabaini is still active, and therefore has great value for debris flow research.

3 Materials and Methods

The TM of Landsat 4/5 and the OLI of Landsat 8 were used in this paper. Images were collected from 1st May, 1988 to 13th October, 2013. Only the clear images were chosen. The spatial resolutions of TM and OLI images have been found to meet the experimental needs.

ENVI5.0 was used for image pre-processing. TM and OLI images can show debris flow fans clearly after geometric correction, radiation correction, and image cutting. An object-oriented classification method was used to look for the information of debris flow-fans. Based on the spatial and spectral information of the images, debris flow fans were identified using ENVI5.0. The results were then amended into 1:50000 topographic maps through manual digitizing (Fig. 2). The characteristics of the debris flow fans were analyzed according to their shapes and sizes.

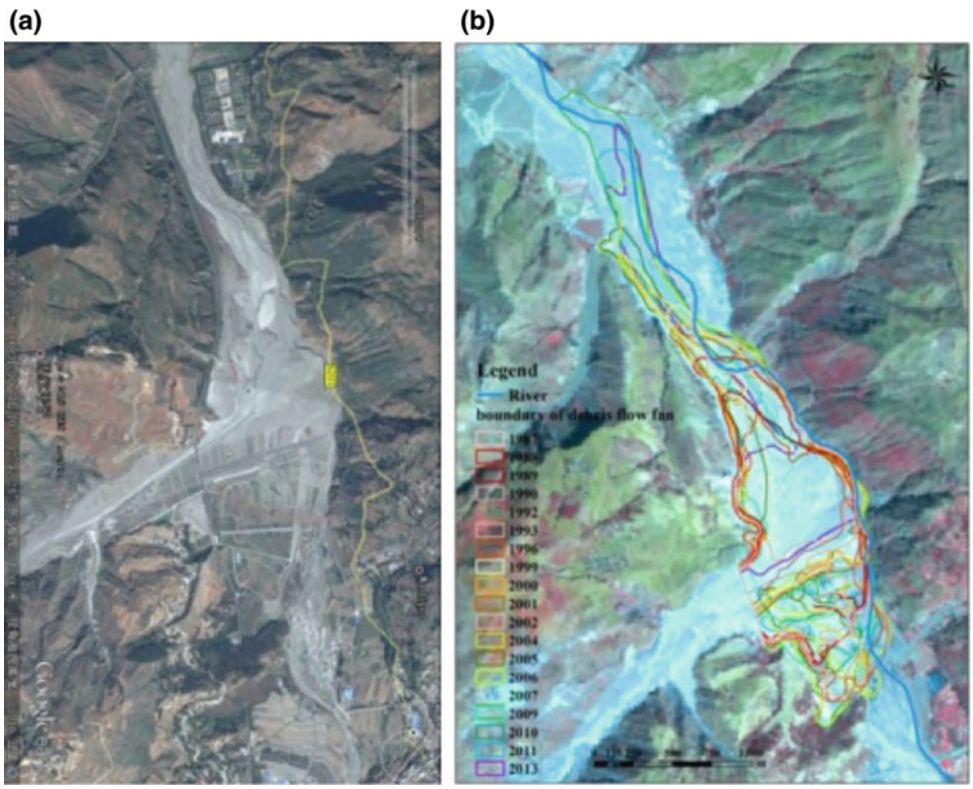

Fig. 2 The interpretation results of hazard areas at the alluvial fans in the Dabaini catchment. **a** Google Earth image of the Dabaini debris flow fan and the **b** debris flow fans of Dabaini from 1987 to 2013

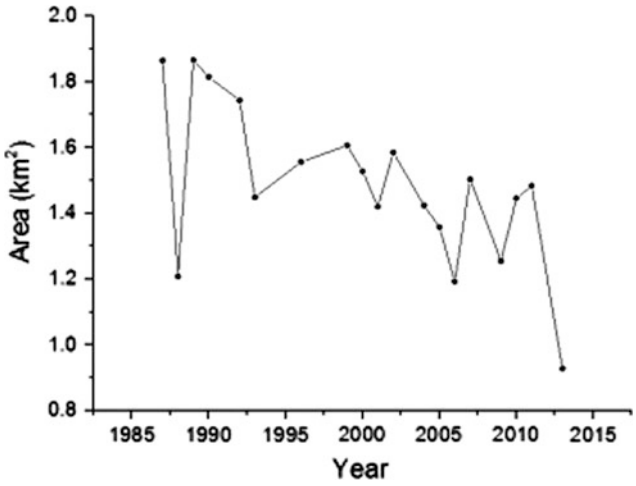

Fig. 3 The hazard areas at the alluvial fans in the Dabaini catchment

4 Results

In recent years, the debris flows in Dabaini are still frequent but have been decreasing in terms of hazard area range. Their hazard range has decreased to about 50.24% between the observation periods of 1987 and 2013 (Figs. 2 and 3). The area in 1987 was estimated to be 1.865 km^2, but has been reduced to 0.928 km^2 in 2013. Annually, within the said time period, the total hazard area was fluctuating with minor expansions such as those in 1996. Overall, the largest area of damage was 1.988 km^2, which occurred in 1989. The minimum was 0.928 km^2, measured in 2013.

5 Conclusions

Based on the remote sensing images, the characteristics and development of the debris flow fans in Dabaini can be summarized as follows:

(1) According to the investigation and interpretation of images, although the hazard range area is decreasing, debris flow activity in Dabaini is still high.
(2) Debris flow fans can reflect the activities of debris flow. When debris flows break out frequently, the area of debris flow—fan is increasing. On the other hand, the less the debris flows, the smaller the debris flow fan.
(3) Water, sediment provenance, human activities and lack of plants are the most important factors that cause debris flows. If we want to reduce the risk of debris flow, we should take measures to reduce water and sediment provenance, and implement disaster prevention engineering and bioengineering measures.

References

1. Bull, W.B.: Geomorphology of segmented alluvial fans in western Fresno County, California. USGS Professional Report, Pos52E, pp. 89–128 (1964)
2. Chen, J., Wei, F.Q., Cui, P.: Restricting conditions and their characteristics for debris flow fans in Xiaojiang river valley. J. Geosci. **12**(5), 704–708 (2005)
3. Franzi, L., Bianco, G.: A statistical method to predict debris flow deposited volumes on a debris fan. Phys. Chem. Earth **26**(9), 683–688 (2001)
4. Liu, X.L., Tang, C.: Debris Flow Hazard Analysis. Science Press, Beijing, pp. 35–61 (1995)
5. Tang, C.: Study on debris flow fan. Yunnan Geol. **9**(3), 239–246 (1990)
6. Zhang, J.S., Shen, X.J., Wei, J.L.: Observational study on the characteristics of development and evolvement of debris flow deposit fan. Resour. Environ. Yangtze Basin **19**(12), 1479–1483 (2010)
7. Liu, X.L., Ni, H.Y.: Variation property of annual sediment yield of debris flow along Jiangjia ravine and catastrophe forecast. J. Mt. Sci. **24**(5), 550–554 (2005)
8. Liu, J.F., Ou, G.Q., You, Y.: Experimental research on velocity and deposition mode of debris flow. Res. Soil Water Conserv. **13**(1), 120–121 (2006)
9. Takahashi, T.: Estimation of potential debris flows and their hazardous zones: soft countermeasures for a disaster. J. Nat. Disaster Sci. **3**, 57–89 (1981)
10. Wang, Y.Y., Zou, R.Y., Yan, B.Y., et al.: Experimental research on prediction model of debris flow deposition. J. Nat. Disaster Sci. **9**(2), 81–86 (2000)
11. Wei, F.Q., Hu, K.H., Lopez, J.L., et al.: Method and its application of the momentum model for debris flow risk zoning. Chin. Sci. Bull. **48**(6), 298–301 (2003)
12. Dubayah, R., Knox, R., Hofton, M., et al.: Land surface characterization using lidar remote sensing. Spat. Inf. Land Use Manage. 25–38 (2000)
13. Li, F.B., Cui, P., Zhou, A.X.: Application of remote sensing and GIS in the prevention and mitigation of hazard caused by landslide and debris flow. J. Catastrophology **19**, 18–24 (2004)
14. Qi, X., Tang, C.: Study on risk evaluation of geological disaster. J. Nat. Disasters (5), 34 (2012)
15. Tang, C., Zhou, J.Q., Zhu, J., et al.: A study on the risk zoning of debris flow on alluvial fans by applying technology of numerical simulation. J. Catastrophology **9**(4), 7–13 (1994)

Spatial Modeling of Gully Erosion Using Different Scenarios and Evidential Belief Function in Maharloo Watershed, Iran

Mahdis Amiri, Hamid Reza Pourghasemi, Gholam Abbas Ghanbarian, and Sayed Fakhreddin Afzali

Abstract

The main purpose of the present study was to model gully erosion susceptibility by Evidential Belief Function (EBF) data-driven technique via different scenarios in Maharloo Watershed, Fars Province, Iran. So, according to extensive field surveys, the locations of the head cut, end cut, and also the boundary of the gully locations were identified and the gully inventory map was prepared. Then, different spatial layers such as: elevation, slope degree, plan curvature, TWI, distance from rivers, distance from roads, drainage density, slope aspect, lithology, annual mean rainfall, NDVI, land use, and soil characteristics (pH, clay percent, electrical conductivity (EC), and silt percentage), were identified as effective factors on the occurrence of gullies and their maps were prepared and classified in the GIS software. In the next stage, the correlation among each agent and gully erosion positions was considered using the EBF algorithm. Finally, gully erosion spatial maps were prepared and evaluated using ROC curve. The accuracy of the maps prepared using EBF algorithm by three scenarios was 0.833, 0.756, and 0.809 for the head cut, end cut, and polygon of gully locations, respectively.

Keywords

Evidential belief function • Gully erosion • Spatial modeling • Iran

1 Introduction

Gully erosion is one of the different surface erosion types. A gully has been defined as a steep sided channel, sometimes with a steeply and actively eroding head scarp, caused by erosion due to intermittent surface current or water [9]. Several GIS-based models have been applied for the gully erosion susceptibility mapping such as the frequency ratio (FR) [8], weights of evidence (WofE) [4], logistic regression [3], linear regression [2], the analytical hierarchy process [15], machine learning model like the Support vector machine (SVM) with different kernel types, Artificial neural network (ANN), Random forest (RF), Boosted regression trees (BRT) [12, 13], and index of entropy (IofE) [16]. So, the aim of the current study was to introduce the effective factors, prepare a map and a spatial modeling of the gully erosion using different scenarios (using head cut points, end points, and polygon format), and EBF data-driven technique in Maharloo watershed, Fars Province, Iran.

2 Materials and Methods

2.1 Study Area

The area of Maharloo watershed in Fars Province is 4274 km^2. It has an average altitude of 1500 m above sea level and is located in the southwestern part of Iran (29° 1′ to 29° 58′ N and 53° 12′ to 53° 28′ E); Fig. 1 shows a map of the case study in Fars Province and Iran.

2.2 Methodology

2.2.1 Gully Erosion Mapping and Data Set Preparation

In the present study, using extensive field studies, the gully erosion sensitive areas were recorded by Global Positioning System (GPS) and mapped in the ArcGIS software 10.2.2. In total, 100 gullies were identified in the mentioned region. Among these, 70% of the gullies were randomly [6, 14] selected for training and the remaining 30% were applied for the validation of maps produced using an EBF algorithm and three different scenarios. In the following, sixteen spatial

M. Amiri · H. R. Pourghasemi (✉) · G. A. Ghanbarian · S. F. Afzali
Department of Natural Resources and Environmental Engineering, College of Agriculture, Shiraz University, Shiraz, Iran
e-mail: hr.pourghasemi@shirazu.ac.ir

© Springer Nature Switzerland AG 2019

H. M. El-Askary et al. (eds.), *Advances in Remote Sensing and Geo Informatics Applications*, Advances in Science, Technology & Innovation, https://doi.org/10.1007/978-3-030-01440-7_59

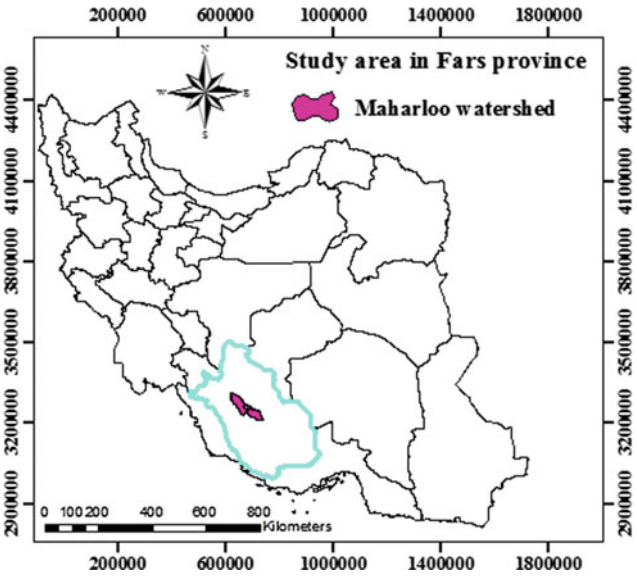

Fig. 1 Location of the study area in Fras Province, Iran

thematic layers including, elevation, slope degree, plan curvature, TWI, distance from rivers, distance from roads, drainage density, slope aspect, lithology, annual mean rainfall, NDVI, land use, and soil characteristics (pH, clay percent, EC, and silt percent), are considered as effective factors on gully erosion occurrence. The effective factors were prepared using different maps and data using topography and geology maps, satellite images, soil sampling in the field and collecting rainfall data from the Regional Water Organization of Fars Province.

2.2.2 Evidential Belief Function (EBF) Algorithm

According to Shafer [13], The EBF theory consists of four sub-functions: degrees of belief (Bel), disbelief (Dis), uncertainty (Unc), and plausibility (Pls). Dempster [5] indicated that Bel and Pls are lower and upper probabilities, respectively. In the mentioned algorithm, the sum of Bel, Unc, and Dis is 1 [7]. Details of the model are presented in the research of Caranza and Hale [1], Pourghasemi and Beheshtirad [10].

2.2.3 Evaluation of Gully Erosion Maps Using the EBF Model

To determine the accuracy of the final gully erosion maps, the ROC curve and the AUC were used. In general, AUC values vary from 0.5 to 1 [12]. For the ROC curve drawing and AUC value calculation, SPSS 17 software was used.

3 Results and Discussion

The results obtained from the effective factors and gully erosion locations correlation based on the EBF theory by three different scenarios are presented in Table 1. For example, in the mentioned research, the Bel functions results in the different scenarios for elevation/altitude factor were calculated (see Table 1).

Also, the final maps of gully erosion susceptibility by EBF model was prepared and classified into 4 categories including, low, moderate, high, and very high (Fig. 2) susceptibility based on Natural Break [16]. The results of the

Table 1 Spatial correlation between elevation and gully erosion places using the EBF model in three scenarios

Factor	Factor classification	Bel (polygon locations)	Bel (head cut locations)	Bel (end cut locations)
Elevation (m)	0–1632	0.025	0.198	0.188
	1632–1844	0.128	0.433	0.336
	1844–2069	0.041	0.212	0.274
	2069–2348	0.025	0.157	0.148
	2348–3003	0.781	0.000	0.054

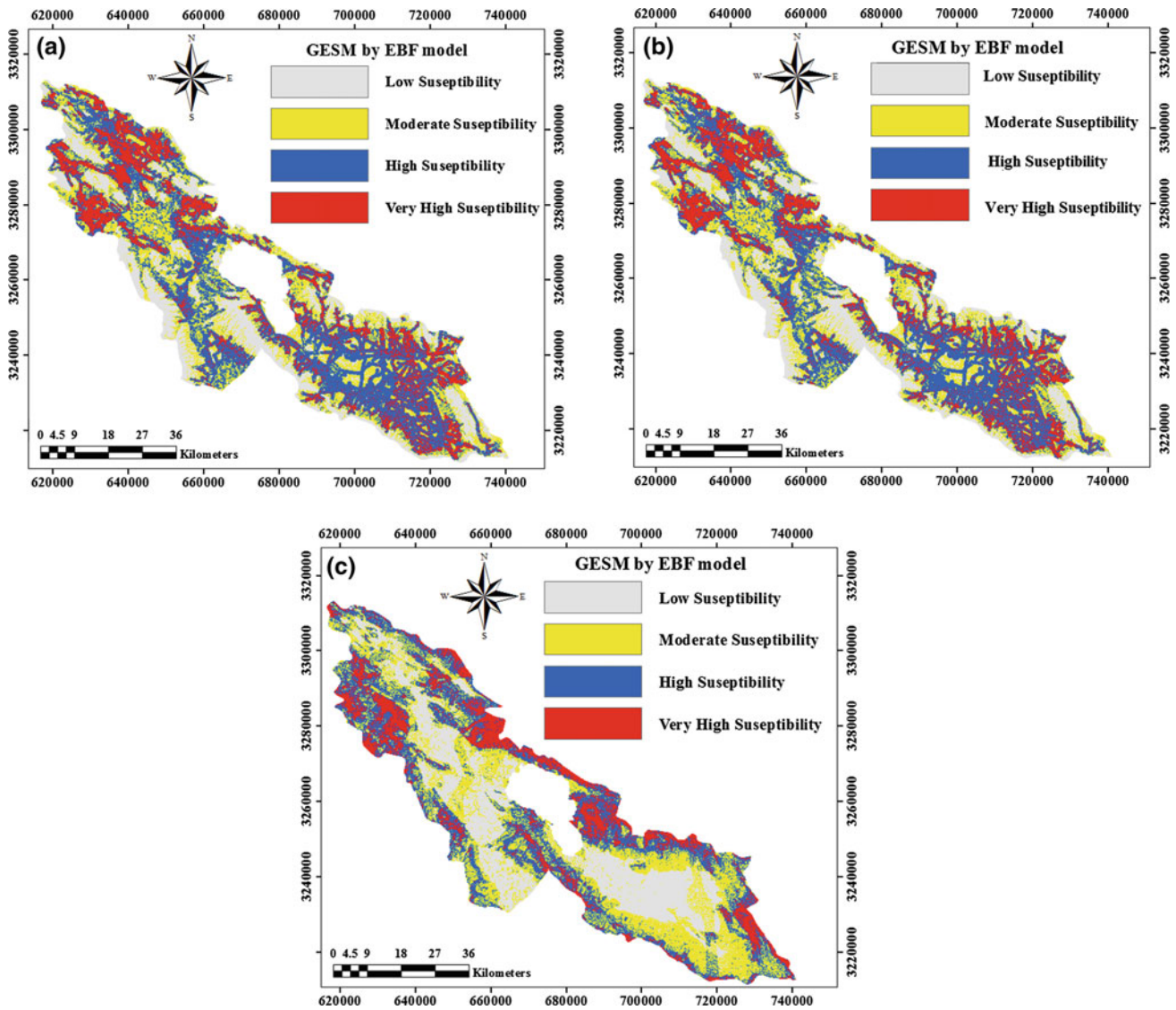

Fig. 2 Gully erosion susceptibility map produced using EBF model: **a** head cut locations, **b** end cut locations, and **c** polygon locations

model evaluation indicated that AUC values of three built scenarios are 0.833, 0.756, and 0.809 for head cut, end cut, and polygon of gullies. Also, the results showed that efficiency of modeling the head cut of gullies in the EBF model was higher than the two other scenarios. Meanwhile all three models have good and very good accuracy.

4 Conclusion

The goal of this study was to model the gully erosion susceptibility using the EBF theory by three scenarios in Maharloo watershed, Fars Province, Iran. The validation of

results showed that the EBF model with AUC value of (head of gullies = 0.833) has very good precision. The layer weighting results using the same model also indicated that: rainfall increase, high drainage density high silt percentage, low altitudes, south direction, low distances from roads and rivers, Asmari, Razak, Aghajari, Gachsaran geological formations and bare lands as well, have all played an effective role in the occurrence of the gully erosion in the study area.

References

1. Carranza, E.J.M., Hale, M.: Evidential belief functions for data-driven geologically constrained mapping of gold potential, Baguio district, Philippines. Ore Geol. Rev. **22**, 117–132 (2002)
2. Chaplot, V., Giboire, G., Marchand, P., Valentin, C.: Dynamic modeling for linear erosion initiation and development under climate and land-use changes in northern Laos. Catena **63**(2), 318–328 (2005)
3. Conoscenti, C., Angileri, S., Cappadonia, C., Rotigliano, E., Agnesi, V., Märker, M.: Gully erosion susceptibility assessment by means of GIS-based logistic regression: a case of Sicily (Italy). Geomorphology **204**, 399–411 (2014)
4. Conforti, M., Aucelli, P.P.C., Robustelli, G., Scarciglia, F.: Geomorphology and GIS analysis for mapping gully erosion susceptibility in the Turbolo stream catchment (Northern Calabria, Italy). Nat. Hazards **56**, 881–898 (2011)
5. Dempster, A.P.: Upper and lower probabilities induced by a multivalued mapping. Ann. Math. Stat. **38**, 325–339 (1967)
6. Hussin, H.Y., Zumpano, V., Reichenbach, P., Sterlacchini, S., Micu, M., van Westen, C., Bălteanu, D.: Different landslide sampling strategies in a grid-based bi-variate statistical susceptibility model. Geomorphology **253**, 508–523 (2016)
7. Lee, S., Hwang, J., Park, I.: Application of data-driven evidential belief functions to landslide susceptibility mapping in Jinbu, Korea. Catena **100**, 15–307 (2012)
8. Lucà, F., Conforti, M., Robustelli, G.: Comparison of GIS based gullying susceptibility mapping using bivariate and multivariate statistics: Northern Calabria, South Italy. Geomorphology **134**, 297–308 (2011)
9. Poesen, J.: Conditions for gully formation in the Belgian loam belt and some ways to control them. Soil Technol. Ser. **1**, 39–52 (1989)
10. Pourghasemi, H.R., Beheshtirad, M.: Assessment of a data driven evidential belief function model and GIS for groundwater potential mapping in the Koohrang Watershed, Iran. Geocarto Int. **30**(6), 662–685 (2015)
11. Pourghasemi, H.R., Rahmati, O.: Prediction of the landslide susceptibility: which algorithm, which precision? Catena **162**, 177–192 (2018)
12. Rahmati, O., Haghizadeh, A., Pourghasemi, H.R., Noormohamadi, F.: Gully erosion susceptibility mapping: the role of GIS-based bivariate statistical models and their comparison. Nat. Hazards **82** (2), 1231–1258 (2016)
13. Shafer, G.A.: Mathematical Theory of Evidence. Princeton University Press, Princeton (1976)
14. Youssef, A.M., Al-Kathery, M., Pradhan, B.: Landslide susceptibility mapping at Al-Hasher area, Jizan (Saudi Arabia) using GIS-based frequency ratio and index of entropy models. Geosci. J. **19**(1), 113–134 (2015)
15. Zakerinejad, R., Maerker, M.: Prediction of Gully erosion susceptibilities using detailed terrain analysis and maximum entropy modeling: a case study in the Mazayejan Plain, Southwest Iran. Geogr. Fis. Din. Quat. **37**(1), 67–76 (2014)
16. Zabihi, M., Mirchooli, F., Motevalli, A.R., Khaledi Darvishan, A., Pourghasemi, H.R., Zakeri, M.A., Sadighi, F.: GIS-based gully erosion spatial modeling in northern Iran. Catena **161**, 1–13 (2018)

Mapping Information of Fire Events, from VGI Source (Twitter), for Effective Disaster Management (in Greece); The Fire of North-East Attica, August 2017, (Greece) Case Study

Stathis G. Arapostathis and Marianthi Karantzia

Abstract

This article introduced a novel method for mapping information related to fire events, from a source of Volunteered Geographic Information (VGI) and from Twitter, in particular. As a case study, the fire of North East Attica (August 2017, Greece), was used. The fire event resulted in the burn of 15,000 decares of woodland. Moreover, state of emergency was declared in the region and thousands of citizens who were in the middle of summer vacations were incited to leave from the area of Kalamos, even if they were located at the coastal part. Regarding the methodology, as a first step, all the tweets that were published within 168 h of the fire event and contain relevant information, were collected. Next, they were classified into certain groups the most important of which are: (i) to information regarding fire event tracking, (ii) to the tracking of the consequences and (iii) to the simple identification of the fire event. The geo-referencing of the classified information is performed by using a script written in R. The final output consisted of thematic maps that visualize the classified information.

Keywords

Disaster management • Fire events • Twitter Tweets • Volunteered geographic information VGI

1 Introduction

Greece, as a Mediterranean country, with extensive and long summer periods is confronting a plethora of fire events each year. As a result, disaster management has emerged as an important research field that contributes to minimizing the negative consequences and even preventing the occurrence of related events.

An important tool that aspires to acquire disaster management initiatives is Volunteered Geographic Information (VGI) which is the act of having volunteers produce geographic data usually through a web service [6]. Many researchers consider VGI an effective way of sharing information, extremely accurate, rapid and complete, for disaster management purposes [5, 7, 8]. Moreover, various methods that employ VGI for monitoring areas and preventing fire events are introduced in the scientific literature [4].

The main purpose of this research was to present some initial methods and techniques, applied in a source of Volunteered Geographic Information (VGI), and twitter data particularly, for contributing effectively and drastically to the management of fire events in Greece. As a case study, a recent fire event that occurred in North East Attica, Greece (2017) was considered. About 80,000 tweets that contain specific words related to the case study were analyzed, and thus, extracting and mapping information that can be important for managing similar emergency situations effectively.

2 Methods and Materials Used

The general methodology consisted of few basic steps. The first step was the selection, acquisition of the data that would be analyzed. For this specific case study, we selected twitter data that have been published within 168 h (a week) from the starting point of the fire event. Moreover, we selected tweets in Greek and English. The second step was related to classifying the data in various categories. This led to a conceptual classification structure that can make all the needed information emerge to contribute effectively to disaster management. The tweets were classified according to the following 1–5 classes: 1. tweets related to the identification of fire events in general. 2. tweets related to identifying other emergencies, 3. tweets related to tracking the fire

S. G. Arapostathis (✉)
Department of Geography, Harokopio University, 176 71 Athens, Greece
e-mail: sarapos@hua.gr

M. Karantzia
National Technical University of Athens, 105 80, Athens, Greece

© Springer Nature Switzerland AG 2019

H. M. El-Askary et al. (eds.), *Advances in Remote Sensing and Geo Informatics Applications*, Advances in Science, Technology & Innovation, https://doi.org/10.1007/978-3-030-01440-7_60

event of North East Attica, 4. emergency management of the fire event of North East Attica, 5. events related to the consequences of the fire event. Moreover, the information classified as related to the consequences was further classified to certain score values according to the impact of each reported consequence. The score values range from I to V; I is the simple identification of a fire event and V is the loss of human life. Table 1 describes each score value.

The next step of the used methodology was about geo-referencing the tweets. The method follows the standards of other published works of the authors [1, 3]. Specifically, each tweet was replicated N times where N is the number of geographic entities that are contained within the text of each tweet, creating thus point observations with x, y coordinates from simple tweets. Next, each observation point (from the replicated or original tweet) was matched with the geographic coordinates of each one of the corresponding geographic entities, mentioned within the text, in such a way that all the geographic entities would be matched with the corresponding coordinates once. Moreover, a precision score value was added to each observation point according to the size of the geographic area it represents. Table 2 describes the precision score values for each geographic entity. Finally, according to the needs of the map creation the observations point were randomized geographically within the polygon area that represents the geographic area as described within the text of each observation. The whole procedure was performed automatically by running a script, developed by the authors [2] in R programming language.

The final step of the methodology is about creating various maps that visualize the information in a way that can be really useful to a range of scientists, authorities, citizens and other people that are responsible for managing the disaster event. Within this framework, various maps were developed using various classified and sub-classified groups of observation points. The timestamp in which an observation point was published in twitter was highly considered in order to assess the proposed method in terms of rapidness, a really factor important for effective response during the occurrence of a natural hazardous event.

3 Data and Materials Used

As already stated, the used dataset was acquired from discover text and consisted of 81,000 tweets. This is the total number of tweets that were published from 13th of August 2017 at 00:00:01 GMT time until 19th of August at 23:59:59 GMT time and contained one of the following keywords: fire, firestorm, kalamos, attica, panic, north east attica, damages in Greek or “fire Greece”, “fire Kalamos” and “fire attica” in English.

We used a spreadsheet software (MS-Excel) for classifying the appropriate information, R-studio for developing and running the script for geo-referencing the tweets in R-programming language and for creating various graphs. Finally, we used ArcGIS Desktop for developing and sharing the final maps on-line.

4 Results

Map I: Point density map of consequence score values, extracted from a sample of about 25% of total dataset

Table 1 Conceptual description of consequence score values for each point observation extracted from twitter

Consequence score values	Description
I	Simple fire event identification
II	Small areas consisted of trees are burnt
III	Emergency situation, large areas are burnt, property in danger
IV	Danger of human life, property is burnt, extremely large areas are burnt
V	Human life loss

Table 2 Conceptual description of geographic precision score values

Geographic precision score values	Description
I	Street name and number or specific POIS
II	Street name
III	Neighborhood or hamlet
IV	Municipality
V	Prefecture and above

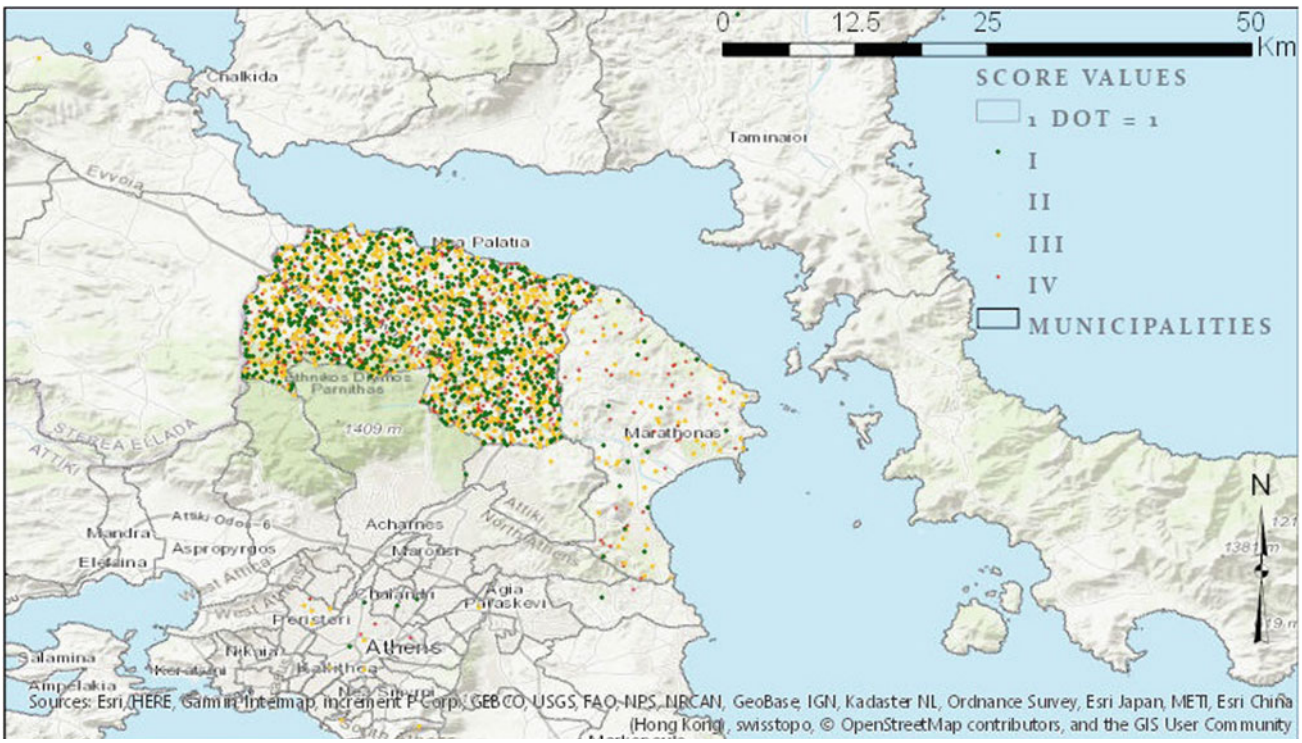

Map II: Simple Fire event identification (after analyzing 25% of the total dataset)

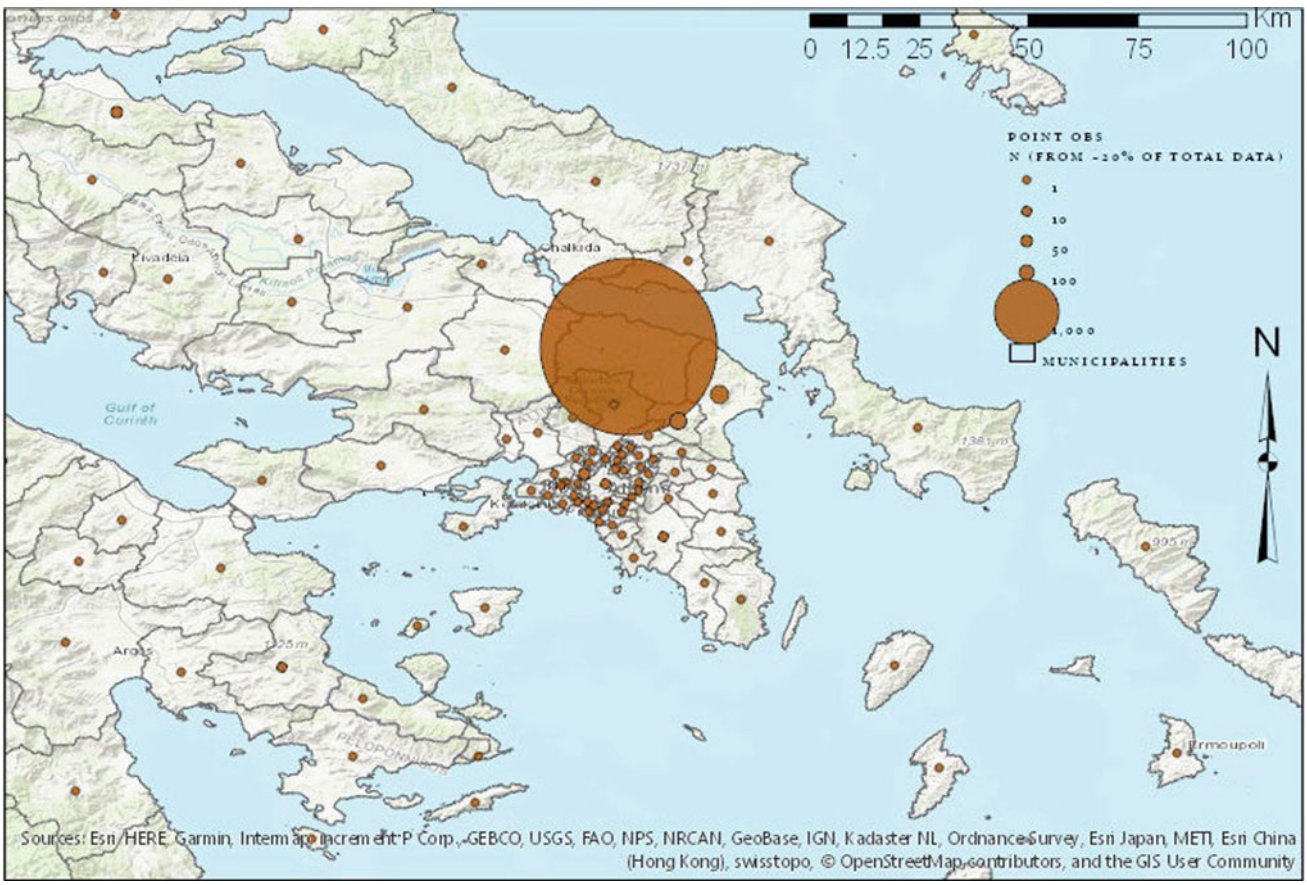

5 Discussion

According to the results of this initial analysis, VGI from social media, can contribute significantly to face fire events that might occur in Greece. After analyzing about 25% of the total dataset that is related to the fire event of North East Attica (August 2017, Greece), 13,708, observation points have been extracted from the entire dataset of tweets. The volume of information is so big and was rapidly produced that it can be safely assessed that the effective mapping of this information can really assist the authorities in responding to emergencies more effectively. Various challenges need to be considered though; as Zhong et al. [9] declare, the appropriate formalization of social media data is still a challenging field, as it is difficult to produce automated methods that will lead to the generation of accurate and credible related maps in real time. Perhaps the trends of classifying information with the use of support vector machine (SVM) algorithms is an approach that can overcome the problems created through the conventional procedures. Moreover, even the geo-referencing process, which is automated as it is performed through an R script, takes some time to be applied, especially if it is performed on an old PC.

References

1. Arapostathis, S.G., Parcharidis, I., Stefanakis, E., Drakatos, G., Kalogeras, I.: A method for creating seismic intensity maps from twitter data. J. Civ. Eng. Archit. (2016). https://doi.org/10.17265/1934-7359/2016.07.013
2. Arapostathis, S.G.: Automated methods for effective geo-referencing of tweets related to disaster management. In: Proceedings of GeoMapplica International Conference 2k18, 23–29 June, Syros, Mykonos (2018)
3. Arapostathis, S.G., Lekkas, E., Kalabokidis, K., Drakatos, G., Xanthopoulos, G., Spyroy, N., Kalogeras, I.: Developing seismic intensity maps from twitter data; The case study of Lesvos Greece 2017 earthquake: assessments, improvements and enrichments on the methodology. In: Proceedings of the GI4DM 2018 Congress, Istanbul, Mar 2018
4. Connors, J.P., Lei, S., Kelly, M.: Citizen science in the age of neogeography: utilizing volunteered geographic information for environmental monitoring. Ann. Assoc. Am. Geogr. (2011). https://doi.org/10.1080/00045608.2011.627058
5. Dashti, S., Palen, L., Heris, M.P., Anderson, K.M., Anderson, S., Anderson, T.J.: Supporting disaster reconnaissance with social media data: a design-oriented case study of the 2013 Colorado floods. In: Proceedings of the 11th International ISCRAM Conference, University Park, Pennsylvania, USA (2013)
6. Goodchild M. F.: Citizens as sensors: The world of volunteered geography. GeoJournal 69 (4):211-221 (2007)
7. McDougall, K.: Using volunteered information to map the Queensland floods. In: Proceedings of the Surveying & Spatial Sciences Biennial Conference 2011. 21–25 Nov 2011, Wellington, New Zealand (2011)
8. Yin, J., Lampert, A., Cameron, M., Robinson, B., Power, R.: Using social media to enhance emergency situation awareness. IEEE Comput. Soc. 1541–1672 (2012)
9. Zhong, X., Duckham, M., Chong, D., Tolhurst, K.: Real time estimation of wildfire parameters from curated crowdsourcing. Sci. Rep. (2016). https://doi.org/10.1038/srep24206

Sinkhole Susceptibility Hazard Zones Using GIS Framework and Heuristic Method

Mohd Asri Hakim Mohd Rosdi, Zulkiflee Abd Latif, Ainon Nisa Othman, and Nasyairi Mat Nasir

Abstract

Sinkhole is not named new marvel in this nation, particularly encompass Klang Valley, Malaysia. Since 1968, the expanding quantities of sinkhole occurrence have been reported in Kuala Lumpur and surrounded areas. As the outcomes, it represents a genuine danger for human lives, resources and structure especially in the capital city of Malaysia. Therefore, a Sinkhole Hazard Model (SHM) was created with incorporation of GIS system by applying Analytical Hierarchical Process (AHP) procedure in order to created sinkhole susceptibility map for the specific territory. Five successive criteria for principle criteria each classified by five sub-classes were chosen for this study which is Lithology (LT), Groundwater Level Decline (WLD), Soil Type (ST), Land Use (LU) and Proximity to Groundwater Wells (PG). An arrangement of relative weights were allotted to each instigating factor and registered through pairwise correlation framework got from expert judgment. Lithology and Groundwater Level Decline has been distinguished gives the highest effect to the sinkhole phenomenon. A sinkhole susceptibility risk zones was grouped into five inclined territories which is very low, low, moderate, high and very high zones. The outcomes acquired were approved with 33 past sinkhole inventory data. This assessment demonstrates that the model shows 61 and 15% of the sinkhole events fall inside high and very high zones respectively. In light of this result, it unmistakably shows that AHP approach is helpful to foresee catastrophic event, for example, sinkhole hazard.

Keywords

GIS • Analytical hierarchical process heuristic method • Sinkhole • Susceptibility hazard zones

1 Introduction

A disaster is an event whose timing is unexpected and whose consequences are seriously destructive. These definitions identify an event that includes three elements namely suddenness, unexpectedness and significant destruction or adverse consequences. Sinkhole or land subsidence isn't named new marvel in this country, particularly surround Klang Valley. As indicated by Meng [4], Sinkhole can be characterized as on the ground surface despondency because of the dissolving of the limestone near to the surface or the fall of an underground grotto.

GIS technology currently enables the integration of various data layers, representing physical and social data, on a spatial analysis platform [1, 2]. Based on reading, the capability of GIS framework in giving quality outcome was examined [3]. Multi-criteria decision making together with GIS is a powerful tools which can be applied to predict and mapping [5]. Thus, GIS were used to assess the potential sinkhole hazard territories utilizing Analytical Hierarchy Process (AHP) procedure [6]. The AHP approach was successfully approve as a systematic tool for site suitability assessment which integrates with GIS and can evolve the greatest innovation applications [3].

M. A. H. Mohd Rosdi · Z. Abd Latif (✉) · A. N. Othman
Applied Remote Sensing and Geospatial Research Group, Faculty of Architecture, Planning and Surveying, Centre of Studies for Surveying Science and Geomatics, Universiti Teknologi MARA, 40450 Shah Alam, Selangor, Malaysia
e-mail: zabdlatif@gmail.com

N. Mat Nasir
Faculty of Architecture, Planning and Surveying, Centre of Studies for Quantity Surveying, Universiti Teknologi MARA, 40450 Shah Alam, Selangor, Malaysia

© Springer Nature Switzerland AG 2019

H. M. El-Askary et al. (eds.), *Advances in Remote Sensing and Geo Informatics Applications*, Advances in Science, Technology & Innovation, https://doi.org/10.1007/978-3-030-01440-7_61

2 Materials and Methods

2.1 Study Area

The territory covers an entire of DBKL and MPAJ administrative regions. The region under DBKL is around 279,327 ha, while the territory for MPAJ is 14,350 ha. This zone was chosen according to topographical setting, visit issues happened, the accessibility of past sinkhole episode information and the accessibility of data (Fig. 1).

2.2 Data Acquisition

The principle source of primary information is by interviews with specialists and some literature surveys from past study. Expert sentiment is pivotal because AHP method is considered as heuristic technique which is utilized expert judging idea that diminishes the search activity in clear up issue process. Computerized lithology and soil map from Mineral and Geoscience Department considered as the fundamental source. The topography of the territory is examined utilizing computerized topographic map got from Department of Survey and Mapping Malaysia (JUPEM) and being separated for the land use information. Groundwater level also was gotten from Mineral and Geoscience Department that incorporates groundwater well areas as well.

2.3 GIS Data Processing

AHP and linear scale transformation method are utilized as a part of this study to decide estimation of relative weight for criteria and sub-criteria. The advancement of model is primarily based on the final weight of parameter and sub-parameter of the criterion. This model is named as Sinkhole Hazard Model (SHM) and comprises of five (5) criteria which shows as follows:

$$\mathrm{SHM} = (0.457 \times \mathrm{sc\_litho}) + (0.109 \times \mathrm{sc\_soil}) + (0.046 \times \mathrm{sc\_lu}) + (0.299 \times \mathrm{sc\_wld}) + (0.090 \times \mathrm{sc\_pg})$$

where sc_litho is regulated score for lithology sub criterion, sc_soil is regulated score for soil types sub criterion, sc_lu is regulated score for landuse sub criterion, sc_wld is regulated score for water level decline sub criterion and sc_pg is regulated score for proximity to groundwater sub criterion. The pairwise correlation framework is represented in Table 1.

In view of Table 2, the consequence of normalization weight, it can be resolved that lithology has biggest weight which is 0.457, while land use produces a smallest weight which is 0.046. The weightage of sub-criteria is determined by utilizing linear scale transformation. Based on previous study, the total normalized weight must be 1.

3 Results and Discussion

3.1 Sinkhole Susceptibility Map Using Heuristic Method

The sinkhole susceptibility maps produced from the SHM model by utilizing AHP strategy is represented in Fig. 2. It was discovered that the North West part can be ordered as high and very high risk zone. In this study, the majority of sinkhole hazard happened at the high value of water level decline which is −22 to −70 m^3.

Next, for Ampang zone, the moderately high and very high risk falls at the middle and western of the region. Highest urban zones plus encompassed by mined land region can be grouped indistinguishable with Kuala Lumpur.

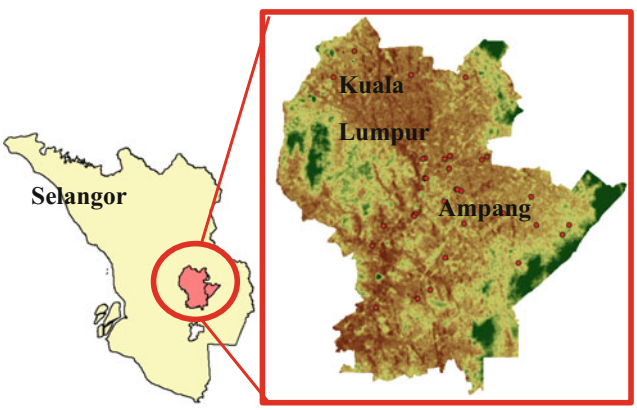

Fig. 1 Location of study area

Table 1 Pairwise correlation framework of parameters

Criteria	LT	ST	LU	WLD	PG
LT	1	5	7	2	6
ST	0.200	1	3	0.167	2
LU	0.143	0.333	1	0.200	0.333
WLD	0.500	6	5	1	3
PG	0.167	0.500	3	0.333	1

Table 2 Relative weightage value of every main parameters

Criteria	Normalized comparison matrix					Weightage
	LT	ST	LU	WLD	PG	
LT	0.498	0.390	0.368	0.541	0.486	0.457
ST	0.099	0.078	0.158	0.045	0.162	0.109
LU	0.071	0.026	0.053	0.054	0.027	0.046
WLD	0.249	0.468	0.263	0.270	0.243	0.299
PG	0.083	0.040	0.158	0.090	0.081	0.090

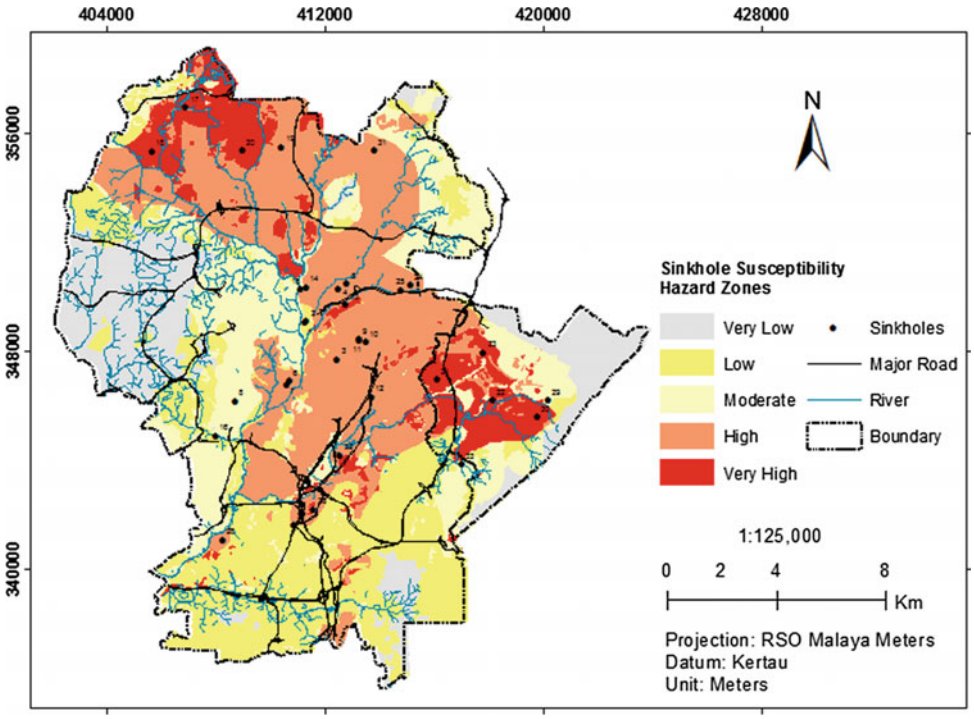

Fig. 2 Sinkhole susceptibility map and previous sinkhole location

3.2 Validation and Accuracy Assessment

To approve the SHM, the essential classes that should be incorporated are high and very high potential areas (Table 3).

From the outcome, it demonstrates that precision of the model is 76% allude to the high and very high class while the staying 24% fall inside low and moderate class. The outcomes got were approved with thirty-three (33) past sinkhole

Table 3 Accuracy percentage of the model

Hazard classes	Area (km^2)	Sinkhole number	Sink hole (%)
Very low	41.773	None	0
Low	70.212	2	6
Moderate	61.528	6	18
High	91.487	20	61
Very high	31.597	5	15
Total	296.597	33	100

inventory information. This assessment demonstrates that the model shows 61 and 15% of the sinkhole events fall inside high and very high danger zones respectively.

4 Conclusions

Sinkhole hazard has expanded dramatically since 1968 in Kuala Lumpur and Ampang regions. Precise model should be created in order to created dependable hazard maps. The model exhibited in this work has been developed by integration of GIS and AHP framework. As the impediments of the study in order to enhance this paper for the others specialist later on, it proposes to utilize the others appropriate strategies or methods to distinguish the sinkhole development instead of AHP method. From the inventory information, the size and measurement of the sinkhole is recorded for estimation the conceivable sinkhole to happen in multi-year. This data is exceptionally essential for local authority for arranging and overseeing catastrophic event in Malaysia.

References

1. Dom, N.C., Latif, Z.A., Ahmad, A.H., Ismail, R., Pradhan, B.: Manifestation of GIS tools for spatial pattern distribution analysis of dengue fever epidemic in the city of Subang Jaya, Malaysia. Environ. Asia **5**(2), 82–92 (2012)
2. Idris, R., Latif, Z.A.: GIS multi-criteria for power plant site selection. In: Proceedings—2012 IEEE Control and System Graduate Research Colloquium, ICSGRC 2012, July, pp. 203–206 (2012)
3. Latif, Z.A., Zaki, N.A.M., Salleh, S.A.: GIS-based estimation of rooftop solar photovoltaic potential using LiDAR. In: Proceedings —2012 IEEE 8th International Colloquium on Signal Processing and Its Applications, CSPA 2012, Mar, pp. 388–392 (2012)
4. Meng, T. S.: Karstic Features of Kuala Lumpur Limestone. Geol. Soc. Malays. Bull. **46**, 447– 453 (2005)
5. Othman, A.N., Naim, W.M., Noraini, S.: GIS based multi-criteria decision making for landslide hazard zonation. J. Soc. Behav. Sci. 595–602 (2012)
6. Rosdi, M.A.H.M., Othman, A.N., Zubir, M.A.M., Latif, Z.A., Yusoff, Z.M.: Sinkhole susceptibility hazard zones using GIS and analytical hierarchical process (AHP)—a case study of Kuala Lumpur and Ampang Jaya. In: International Archives of the Photogrammetry, Remote Sensing and Spatial Information Sciences —ISPRS Archives, 42(4W5), pp. 145–151 (2017)

Two Dimensional Flood Inundation Modelling in Urban Areas Using WMS, HEC-RAS and GIS (Case Study in Jeddah City, Saudi Arabia)

Kuswantoro Marko, Amro Elfeki, Nassir Alamri, and Anis Chaabani

Abstract

This research presents a two-dimensional flood inundation modelling in urbanized areas when some features such as roads, buildings, and fences have great effect on flood propagation. Wadi Qows located in Jeddah City, Saudi Arabia was chosen as case study area because of the flood occurrence of 2009 causing lots of losses either economic or loss of life. The WMS and HEC-RAS program were used for a hydraulic simulation based on channel geometry built by incorporating urban features into DEM using GIS effectively. A resampling method of DEM 90 × 90 m become 10 × 10 m grid cell sizes was conducted to produce a higher resolution DEM suitable for urban flood inundation modelling. The results show that a higher resolution leads to increasing the average flood depth and decreasing the flood extent. Although the change of the grid cell sizes does not affect its elevation values, this approach is helpful to perform flood simulations in urban areas when high resolution DEM availability is limited. In addition, the integration of WMS, HEC-RAS and GIS are powerful tools for flood modelling in rural, mountainous and urban areas.

Keywords

Two dimensional • Flood inundation • Urban areas • WMS • HEC-RAS • GIS

1 Introduction

The 2009 flooding that occurred in Jeddah Saudi Arabia has become the highlight of world society. This is due to an unexpected flash flood causing the death of many people, thousands of people were affected, and lots of economic damage [1]. The extreme weather conditions and the unplanned housing developed by people in the lower lands of the wadi streams have contributed to the occurrence of such flash flood that occurred in Wadi Qows in around Guwaizah District, Jeddah.

Flood modelling is becoming an essential tool to study the effect of floods on urbanized areas [2] and draw inundation maps. In the past, simulating a flood event required simplification of the full governing flow equations owing to the lack of computational power and inadequacy of input data as described by Thang et al. [3]. However, advances in computational power combined with larger and more extensive meteorological data monitoring and topographic data acquisition techniques have allowed for the use of simulation models which solve the full governing equations to describe the hydraulic transport processes and develop the inundation map.

The two-dimensional hydraulic model using a coupled WMS and HEC-RAS without considering the urban features was conducted by Sadrolashrafi et al. [4] to map a potential flood zonation, Kusratmoko et al. [5] to map the flood inundation in the tropical floodplain and Elfeki et al. [6] to map flood inundation in an arid region. This research presented a two dimensional flood inundation modelling using the coupled WMS and HEC-RAS in the urbanized watershed that some urban features such as roads, buildings, and, fences are considered in higher resolution DEM.

2 Materials and Methods

The flood inundation modelling was conducted using WMS River tools to construct a HEC-RAS flow model. HEC-RAS can perform a step backwater curve analysis for steady state

K. Marko (✉)
Department of Geography, Faculty Mathematics and Natural Sciences, Universitas Indonesia, 16424 Depok, Indonesia
e-mail: kuswantoro@sci.ui.ac.id

A. Elfeki · N. Alamri · A. Chaabani
Department of Hydrology and Water Resource Management, King Abdulaziz University, Jeddah, 21589, Kingdom of Saudi Arabia

© Springer Nature Switzerland AG 2019

H. M. El-Askary et al. (eds.), *Advances in Remote Sensing and Geo Informatics Applications*,
Advances in Science, Technology & Innovation, https://doi.org/10.1007/978-3-030-01440-7_62

conditions to determine water surface elevations and velocities [7]. The required data is digital elevation models (DEMs) 90 m sourced from Shuttle Radar Topographic Mission (SRTM), urban features i.e. building and fences in raster format, and the discharge used is 116.2 m^3/s according to the estimated peak discharge of a three-hour duration of the precipitation (70 mm) for Wadi Qows in normal moisture condition for the event of 25th November 2009.

The proposed method consists of five steps. The first step, modifying DEM to become a digital surface model (DSM) by resampling DEM 90 m to become 10 m then adding urban features such as building and fences to DEM 10 m using ArcGIS. The second step, DEM conversion to a triangular irregular network (TIN) on WMS. The floodplain mapping is more appropriately carried out using TIN than DEM [8]. The third step, building a geometric data such as the stream centerline, the main channel banks, the cross-section lines, and the material zones. The fourth step, defining the network schematic on HEC-RAS using Manning's roughness coefficient (n) for every land use type. The fifth step, applying a steady gradually varied flow analysis which consists of peak discharge information, boundary conditions, and flow regime. The sixth step, floodplain delineation is conducted to obtain the flood inundation area involving a flood depth and a flood extent. Water surface TINs are created as a scatter set for each cross section in the model that can be read as 2-D scatter files [9].

3 Results

Figure 1 shows the flood inundation delineation for different methods over the study area. Figure 1a shows the flood inundation based on the field observation of 301 measured locations affected by the flood event. The flood depth map can be obtained by an interpolation using the inverse distance weighting (IDW) in a 25 × 25 m grid format. A personal interviewing was conducted to the local inhabitants who live at the locations of the event and witnessed the flood event. The flood depth delineation shows patches of water in the high density residential areas such as around Guwaizah and Al Musaid District, and reach up to 3.9 m. Figure 1b shows the model result using DEM 90 m. Figure 1c shows the model result using modified DEM 10 m by adding buildings and fences. Table 1 summaries the simulations' quantitative results. Both models' results were compared to know the effect of DEM resolution and urban features on the flood depth and extent.

4 Discussion

The floodplain delineation process in two dimensional models was completely achieved for different DEM resolution for the same peak discharge Q = 116.2 m^3/s. The flood plain delineation was automatically simulated in WMS by

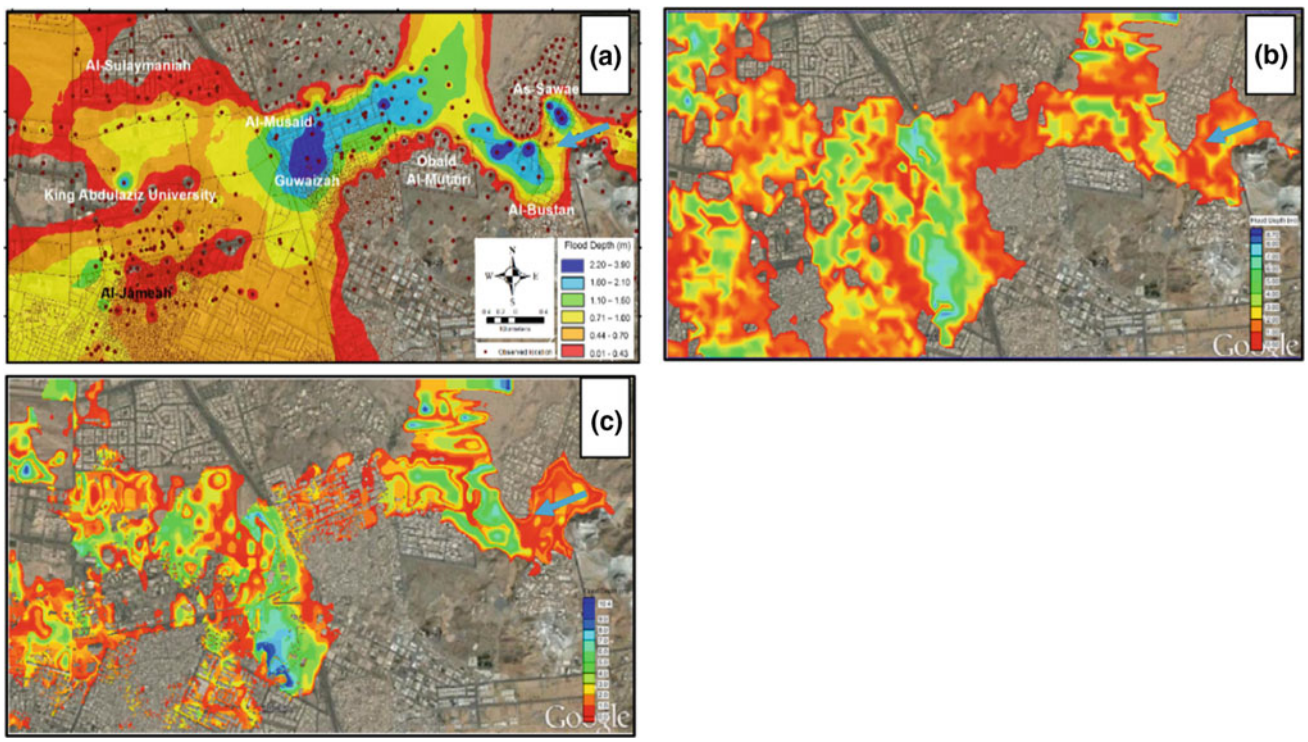

Fig. 1 Flood inundation maps of **a** field observation result, **b** model result using DEM 90 m, **c** model result using modified DEM (10 m)

Table 1 Flood depth and flood extent results based on Q = 116.2 m^3/s

Cell size (m)	Number of values (TINs)	Flood depth (m)				Flood extent (km^2)		Total flooded area percentage (%)
		Min.	Max.	Avg.	St dev.	Modeled flooded area	Observed flooded area	
90 × 90 without buildings	4608	0.01	8.72	1.72	1.52	17.07	18.90	90
10 × 10 with buildings	334,961	0.01	9.60	1.90	1.68	11.20		60

considering some options such as flow paths and quadrant. The optimum values were obtained after sensitivity analysis of the model results.

The results show that, the grid cell increasing sizes from 90 to 10 m has influenced the maximum modelled flood depth increases from 8.72 to 9.60 m, whereas the average of the flood depth increased from 1.72 to 1.90 m. Therefore, the modelled flood extent decreases from 17.07 to 11.2 km^2 or 90 to 60% of the observed flood area when the grid cell sizes are reduced from 90 to 10 m as shown in Table 1. The modified DEM 10 m which urban features were added to DEM affects the flood depth and flood extent. The flood depth increases due to the flow path of the flood is narrower causing the water depth to increase or move vertically so that the flood extent becomes narrower.

5 Conclusions

The combination of HEC-RAS, WMS and GIS have the ability to simulate flood inundation based on the both low and high resolution DEM. The modified DEM by resampling DEM 90 m and adding the buildings and fences on the DEM shows the quite significant difference of the model results based on the low resolution DEM 90 m. Although the change of the grid cell sizes does not influence the magnitude of the elevation, this approach is helpful to perform the flood simulations in urban areas when the high resolution DEM availability is limited.

References

1. Al Saud, M.: Assessment of flood hazard of Jeddah area 2009, Saudi Arabia. J. Water Resour. Prot. **2**(9), 839–847 (2010)
2. Sharif, H.O., Al-Juaidi, F.H., Al-Othman, A., Al-Dousary, I., Fadda, E., Jamal-Uddeen, S., Elhassan, A.: Flood hazards in an urbanizing watershed in Riyadh, Saudi Arabia. Geomatics Nat. Hazards Risk **7**(2), 702–720 (2016)
3. Thang, N.T., Inoue, K., Toda, K., Kawaike, K.: A Model for Flood Inundation Analysis in Urban Area: Verification and Application. Annuals of Disaster Prevention Research Institute, Kyoto University No. 47B (2004)
4. Sadrolashrafi, S.S., Mohamed, T.A., Mahmud, A.R.B., Kholghi, M. K., Samadi, A.: Integrated modeling for flood hazard mapping using watershed modeling system. Am. J. Eng. Appl. Sci. **1**(2), 149–156 (2008)
5. Kusratmoko, E., Marko, K., Elfeki, A.: Spatial modelling of flood inundation case study of Pesanggrahan floodplain, Jakarta, Indonesia. J. Geogr. Environ. Earth Sci. Int. **5**(3), 1–10 (2016)
6. Elfeki, A., Masoud, M., Niyazi, B.: Integrated rainfall–runoff and flood inundation modeling for flash flood risk assessment under data scarcity in arid regions: Wadi Fatimah basin case study, Saudi Arabia. Nat. Hazards **85**(1), 87–109 (2017)
7. Nelson, E.J.: Watershed Modeling System, Version 7.1, Tutorials. Department of Civil and Environmental Engineering, Environmental Modeling Research Laboratory, Brigham Young University, Provo, Utah, USA (2004)
8. National Research Council (NRC): Elevation Data for Floodplain Mapping. The National Academies Press, Washington DC (2007)
9. Aquaveo Homepage: https://www.xmswiki.com/wiki/WMS:Preparing_Stage_Data. Last accessed 2017/12/10

Detecting Recent Deformation Patterns Using Geomorphometric Indices and Remote Sensing: A Case Study from the Sahel of Sfax (Eastern Tunisia)

Mourad El Koundi, Radhia Mansour, and Abdessalem El Ghali

Abstract

Geomorphometric indices such as Amplitude Relief (Ar), Stream length gradient (SL), Drainage density (Dd), Stream frequency (Fu), Slope gradient (S), Aspect and Topographic Wetness Index (TWI) calculated from SRTM-DEM with hydrographic network analysis and density of lineaments (Ld) automatically extracted from Landsat ETM+ satellite image were used to extract lineaments maps of the Sahel of Sfax (eastern Tunisia). The synthesis of these lineaments allowed the establishment of morpho-structural map and understanding the structural evolution of the area. The produced lineament map was then confronted to gravimetric maps and to the previous studies carried out on this area using geophysical data. This map is in high agreement with all these works.

Keywords

Geo-morphometric indices • Remote sensing • Lineaments • Sahel of Sfax • Tunsia

1 Introduction

In the context of Africa-Eurasia convergence, tectonics has continuously shaped the landscape of Northern Africa and kept exerting a significant effect on the geomorphological properties of landscapes. Quantitative analyses of landscape using remote sensing and geo-morphometric indices are helpful in deducing the pattern and spatial variation of recent topographic deformation and neo-tectonic activity. In this paper, we evaluated the contribution of geo-morphometric indices and remote sensing to the recent deformation analysis of the Sahel of Sfax.

The study area is located in the southern part of the Tunisian Sahel (Eastern Tunisia) between longitudes (09° 55′ 27.3″ E to the West and 10° 53′ 13.0″ E to the East) and latitudes (35° 04′ 34.6″ N to the North and 34° 30′ 35.0″ N to the south). It presents a relatively flat topography which lacks significant geological discontinuities at the surface. However, using geophysics, many authors have identified a complex faulting system in the subsurface.

2 Geological Setting

The sedimentary outcropping series predominantly consist of Quaternary deposits with Upper Miocene to Pliocene rare outcrops [1, 2]. The oldest documented outcropping series is Messinian and corresponds to the continental Segui Formation [3]. Marine deposits are limited to coastal areas [4].

At surface, this domain is considered as tectonically stable compared to the Atlasic domain. It is limited at it western part by a major lineament called the "North-South Axis" [3]. This lineament acted like a buffer from the Late Cretaceous first compressive phases causing an active subsidence in the Sahel block during Mid- to Late Eocene [1, 2]. In this area, structural strain is moderate and shows large wide anticlines forming low hills and moderately high plains or plateaus separated by wadis with seasonal flow.

Many investigations used geophysical data to detect profound structures discontinuities. They revealed a very complex faulting system that dislocates the substratum in multidirectional oriented compartments [5, 6]. These previous studies also concluded that the Sahel block has been gradually affected by several subsidence phases during Mesozoic, Tertiary and Quaternary ages. During upper Miocene, several grabens where formed and filled later by thick Plio-Quaternary deposits [1]. During Lower Pleistocene, a major tectonic event occurred causing the uprising of folded zones and subsidence of atlasic endorheic basins.

M. El Koundi (✉)
Office National des Mines, Tunis, Tunisia
e-mail: mourad.elkoundi@gmail.com

R. Mansour · A. El Ghali
Faculté des Sciences de Bizerte, University of Carthage, Bizerte, Tunisia

© Springer Nature Switzerland AG 2019

H. M. El-Askary et al. (eds.), *Advances in Remote Sensing and Geo Informatics Applications*,
Advances in Science, Technology & Innovation, https://doi.org/10.1007/978-3-030-01440-7_63

3 Methodology

The developed methodology is based on the fact that the current forms of the relief result from the interaction between (1) geodynamic phenomena more or less deep linked essentially to the tectonic context of the region and (2) superficial phenomena directly related to water erosion and sedimentation [7, 8].

The adopted methodology is based on the analysis of geo-morphometric indices and remote sensing images as well as the drainage network to detect anomalies coinciding with morpho-structural features. The first step consists in generating maps of (1) Amplitude Relief (Ar), (2) Stream length gradient (SL), (3) Drainage density (Dd), (4) Stream frequency (Fu), (5) Slope gradient (S), (6) Aspect, (7) Topographic Wetness Index (TWI) and (8) Drainage anomalies maps. For each map, lineaments are extracted, analyzed and then grouped in one synthetic map. Defining the importance of the lineament regarding to neo-tectonic landscape deformation was based on evaluating these various thematic maps and by superimposing them to the satellite gravity data.

4 Results

The arrangement of the previously extracted lineaments obviously coincides with the gradients variation lines in the Bouguer anomaly map. These lineaments show the existence of extensive faults and discontinuities network that follow four preferential directions: NS, NE-SW, EW and NW-SE.

Submeridian and NE-SW faults are hardly detectable by morphometric analysis and not highly visible in field. The Bouguer anomaly map shows the normal motion for these faults that generated strong subsidence and led to the individualization of globally N-S and NE-SW trending basins. The borders of these basins are well detectable in the Bouguer anomaly map. They are represented by a negative gradient indicating subsidence. The fact that these two directions are very clear on the Bouguer anomaly map and less visible at the surface indicates that: (1) An important filling phase has followed the establishment of these basins and (2) newer orogenic movements took place subsequently thus deleting the morpho-structural features associated with these movements. N-S and E-W trending faults are therefore the oldest and the deepest (first order faults).

The NW-SE direction is more expressed at the surface than the N-S and E-W directions; related faults are thus classified as second order faults. In fact, the Bouguer anomaly map proves that these faults disrupt longitudinally the created basins; this configuration assumes that NW-SE faults are more recent than first order faults and show shearing motion.

The E-W Direction is the most frequent and the clearest at the surface. It is represented by third order faults showing active neo-tectonic activity. On the Bouguer anomaly map, they clearly appear as extensive dextral strike-slip faults with an important deepening (Fig. 1).

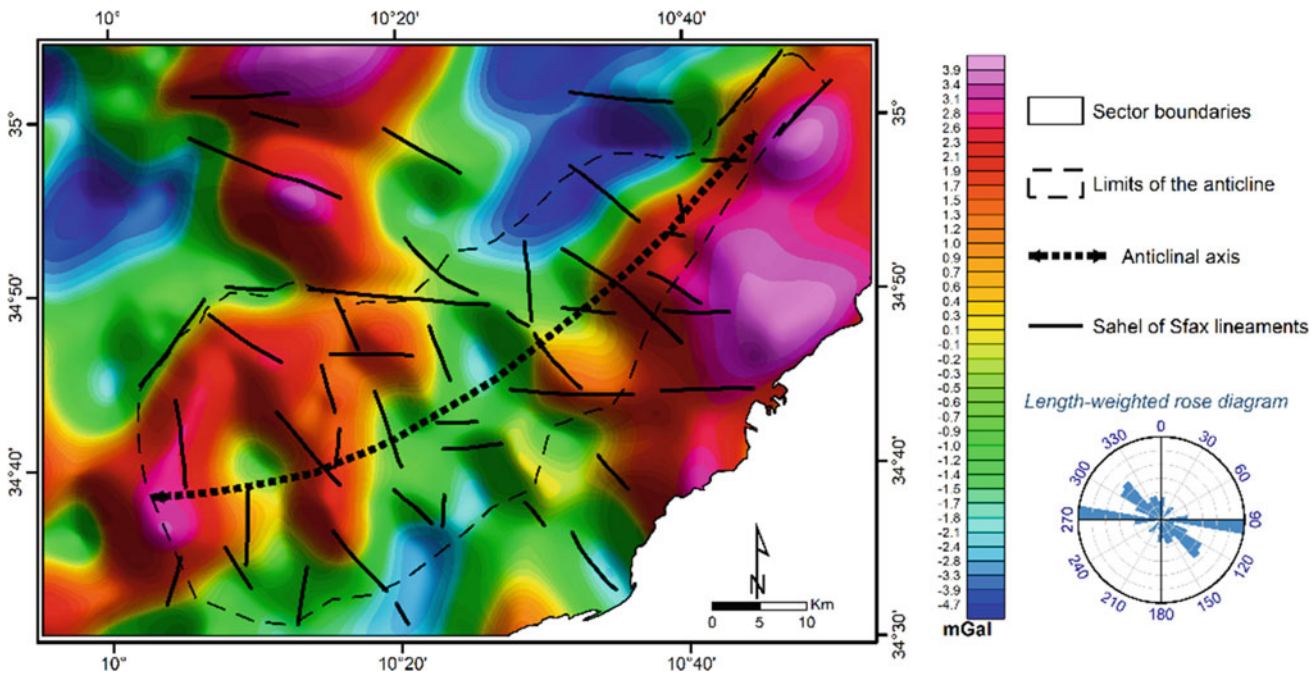

Fig. 1 Synthetic map of the lineaments superimposed to the Bouguer anomaly map

5 Discussion

The majority of the subsurface scars affecting the region propagate to the surface and generate the landscape geomorphologic features. However, some other lineaments detected in subsurface do not appear on the surface. The absence of these outcropping lineamentary structures and their existence in depth is logically explained by the effect of synsedimentary deformations and the ending of the activity of some faults in depth during the filling of the collapsed blocs at the Miocene age [6]. Also, we can explain the current architecture of the lineaments toward the surface by the simple spread of some deep discontinuities reactivated with neotectonic activity. A dialectical relationship seems to exist between the geodynamic activity of anomalic structures in depth and the lineamentary architecture at the ground level of the region.

6 Conclusion

We used geo-morphometric indices and remote sensing images to establish the synthetic map of the geological lineaments of the Sahel of Sfax. This approach allowed ranking the directions of lineaments associated with recent deformation that played a decisive and precursor role in the spatial distribution of the geomorphological envelopes and the current landscape architecture. The comparison between these results and gravimetric data shows that the arrangement of the deduced lineaments perfectly follows the gradients of variation of the gravimetric anomalies. This work confirms the importance of using such approaches in morpho-structural studies of areas with low deformation index.

References

1. Burollet, P.F., Mugniot, J.M., Sweeney, P.: The geology of the pelagian block: the margins and basins off Southern Tunisia and Tripolitania. In: Nairn, A.E.M., Kanes, W.H., Stehli, F.G. (eds.) The Ocean Basins and Margins, pp. 331–359. Springer, U.S. (1978)
2. Mejri, F., Burollet, P.F., Ben Ferjani, A.: Petroleum Geology of Tunisia a Renewed Synthesis. ETAP, Tunis, Tunisia (2006)
3. Burollet, P.F.: Contribution à l'étude stratigraphique de la Tunisie centrale. Annales des Mines et de la Géologie, vol. 18. ONM, Tunis, Tunisia (1956)
4. Bouaziz, S., Sghari, A., Ben Akacha, M.: Carte géologique de la Tunisie à 1/50.000: Feuille de Agareb (N°106). ONM, Tunis, Tunisia (2003)
5. Haller, P.: Structure profonde du Sahel tunisien. Interprétation géodynamique. Thèse de Doctorat en géologie appliquée, Faculté des Sciences et des Techniques, Université de Franche-Comté (1983)
6. Bedir, M.: Mécanismes géodynamiques des bassins associés aux couloirs de coulissements de la marge atlasique de la Tunisie séismo-stratigraphie, séismo-tectonique et implications pétrolières. Thèse de Doctorat, Faculté des Sciences de Tunis, Université de Tunis II (1995)
7. Deffontaines, B., Chorowicz, J.: Principles of drainage basin analysis from multisource data: application to the structural analysis of the Zaire Basin. Tectonophysics **194**(3), 237–263 (1991)
8. Burbank, D.W., Pinter, N.: Landscape evolution: the interactions of tectonics and surface processes. Basin Res. **11**(1), 1–6 (1999)

GIS Based Multi-criteria Analysis for Flood Risk Assessment: Case of Manouba Essijoumi Basin, NE Tunisia

Salwa Saidi, Anis Ghattassi, Brice Anselme, and Salem Bouri

Abstract

Effective flood risk management requires updated spatial information to ensure that the correct decisions are made. Therefore, developing appropriate responses to prevent surface water flooding is highly required. This paper aimed to map the spatial distribution of vulnerability of communities to flooding, the hazard and the socioeconomic factors including land use that affect people's exposure to flooding and nature of settlements. In addition, it focused on weights determination using Intelligent Decision System (IDS) by the means of pairwise comparison approach. The results reveal high risk of Manouba Essijoumi in the Northern part and particularly in Sebkhat Essijoumi, corresponding to the urban areas with high rain intensity and especially spontaneous settlements. The results of this study allow a new vision to the urban management schema of the region and propose some efficient strategies of flood risk management.

Keywords

Flood risk • GIS • Multi-criteria assessment • Management measures • Essijoumi Sebkhat

1 Introduction

With the increase of urbanization, conditions of the underlying surface and natural climate conditions have been changed by human activities [1]. This results in more frequent flood events and inundation problems in urban areas such as Mediterranean environments.

In Tunisia over the last 50 years, floods have caused a huge damage and serious socio-economic risks. In fact, between 1959 and 2015 (floods of 1959, 1962, 1969, 1973, 1979,1980, 1982, 1990, 1995, 2003, 2007, 2011, 2015), at least 815 people were killed by floods, thousands were injured, and 76,300 people were dislocated because of habitat destruction [2].

Consequently, this paper aimed to spatially analyze the vulnerability of communities to surface water flooding. It then analyzed the relation between the spatial distribution of vulnerability, exposure and hazard in order to investigate the risk to communities.

The parameters influencing risk flooding needs to be weighted in order to identify its degree of influence of each one on risk flooding in the study area. Many methods were developed to determine these weights. As an example, the AHP approach, introduced and developed by [3], was applied for solving a wide variety of problems [4]. Since in any MCDA the weights are reflective of the relative importance of each criterion, they need to be carefully selected.

Multi-criteria methods have been successfully employed in GIS environment since the early 1990s to help decision-makers make [5–9].

S. Saidi (✉) · A. Ghattassi
Faculty of Sciences of Tunis, University of Tunis
El Manar, Manar II, 2092 Tunis, Tunisia
e-mail: salwa_saidi@yahoo.fr

S. Saidi
Water Energy and Environment Laboratory, ENI-Sfax,
Sfax, Tunisia

B. Anselme
UMR 8586 PRODIG Laboratory, University of Sorbonne,
2 Rue Valette, 75005 Paris, France

S. Bouri
Faculty of Sciences of Sfax, Sfax, Tunisia

© Springer Nature Switzerland AG 2019

H. M. El-Askary et al. (eds.), *Advances in Remote Sensing and Geo Informatics Applications*,
Advances in Science, Technology & Innovation, https://doi.org/10.1007/978-3-030-01440-7_64

2 Methods

2.1 Vulnerability Assessment

Vulnerability is defined as the susceptibilities, fragilities, weaknesses, deficiencies, or lack of capacities that favor adverse effects on the exposed elements [10].

Vulnerability in the context of disaster risk management was related to the physical resistance of engineering structures [11].

The appropriate vulnerability indicators used in this study were selected based on literature review [11–14].

2.2 Hazard Assessment

Hazard refers to the possible, future occurrence of natural or human-induced physical events that may have adverse effects on vulnerable and exposed elements [10, 15].

Hazard index in this study is based on the rainfall intensity, spontaneous habitats or slums and land use parameters.

2.3 Risk Evaluation

Flood risk is the likelihood of a flood event together associated with the actual damage [9].

In general, risk as a concept that incorporates hazard {H} (initiating event of failure modes) and vulnerability {V} (specific space/time conditions). It is customary to express risk (R) as a functional relationship of hazard (H) and vulnerability (V).

$$\{R\} = \{H\} * \{V\}$$

Using GIS platform all the parameters of Vulnerability (Drainage density, permeability, topography) and Hazard (land use, rainfall intensity and spontaneous habitats parameters) were mapped. After that using the Analytical Hierarchic Process (AHP) method the weights of different parameters were calculated.

By the help of raster calculator of GIS platform risk map was generated (Fig. 1).

3 Results

3.1 Vulnerability Assessment

The vulnerability map shows an index ranging from 50.9 to 87.3 and subdivided into 3 classes (Fig. 2):

- High and very high vulnerability classes cover the zones with low permeability and correspond to urban surfaces and Sebkhat Essijoumi. Such zones are flat and have a high drainage density.
- Moderate vulnerability located in the central part of the watershed which corresponds to high permeability and moderate slope.

3.2 Hazard

High index is observed in the central part of the watershed where urbanization and rainfall intensities are high. The vicinity of the Sebkhat Essijoumi is occupied by spontaneous habitats. It is also deprived of the network of sewerage and drainage of rain water and consequently faced a high hazard.

The western part of Sebkhat Essijoumi is characterized by low hazard due to the low urbanization and low rainfall intensity (Fig. 3).

3.3 Risk

The risk map shows a high and very high index in Sebkhat Essijoumi and its vicinity and in the Northern part of the study area. This map reveals that the integrated risk is highest where spatial intensity of hazards and vulnerability coincide (Fig. 2). Despite the western part, it is characterized by moderate risk. This is the case in some constituencies of Manouba Essijoumi where vulnerability is high alongside with some medium to high hazard indices. A similar risk level is observed where lower levels of vulnerability and high hazards are encountered (Fig. 4).

The high risk zone covers 35% of the total area of Manouba Essijoumi. According to this risk map, people in the central

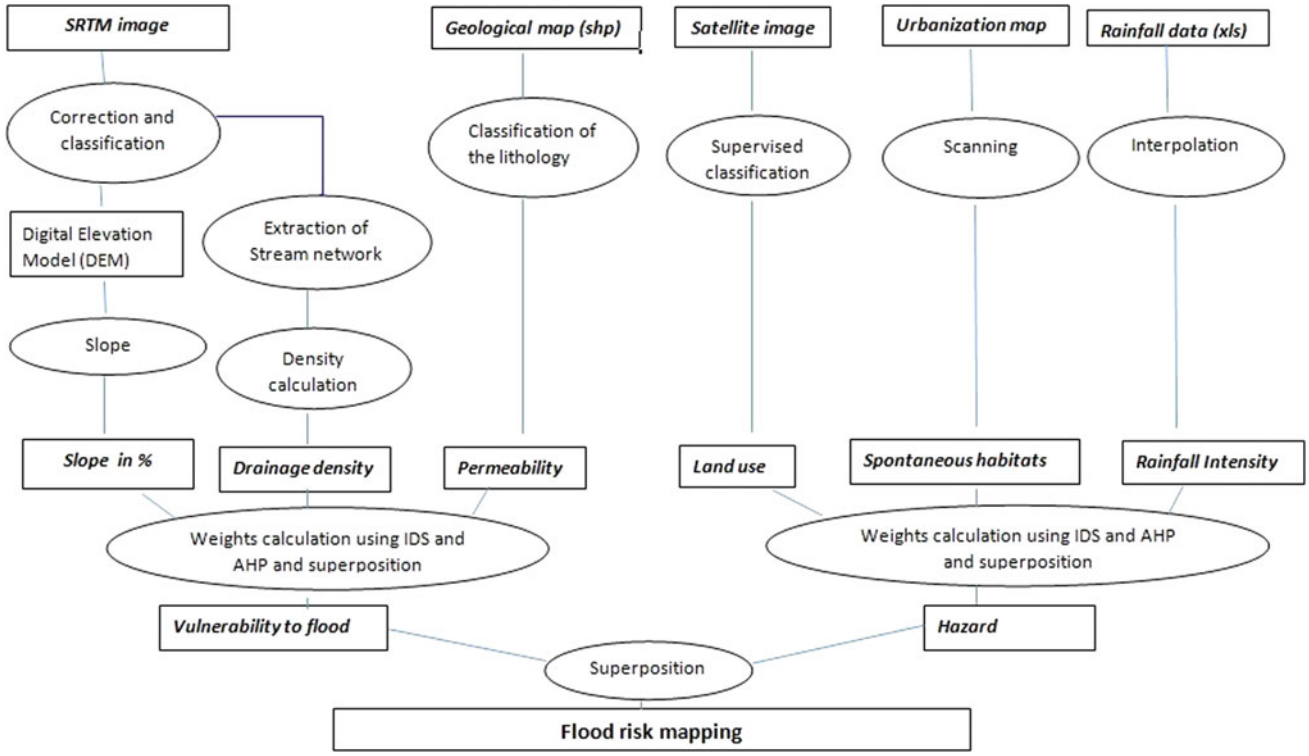

Fig. 1 Methodology chart

and the vicinity of Sebkhat Essijoumi are those who suffer the most of any other risk zone during flood events. This means that during floods in these zones, buildings, especially the spontaneous ones, and people are by far more prone to damage than in any other risk zone. On the contrary 20% of buildings are established in low risk zone.

4 Discussion

The study area has 26% of its total area with high vulnerability but the presence of hazards makes it an area of high risk. According to the Table 1, hazards in the study area especially the spontaneous one has a huge influence on the study area (Table 1).

5 Conclusion

The main objective was the delimitation of the area of risk in relation to the physical parameters and hazards of the Manouba Essijoumi region. The results show that spatial variation of composite parameters of flood risk is a powerful tool for directing future investigations and managements at risk areas. However, a detailed hydrological and urban study in the vicinity of Sebkhat Essijoumi should be undertaken in

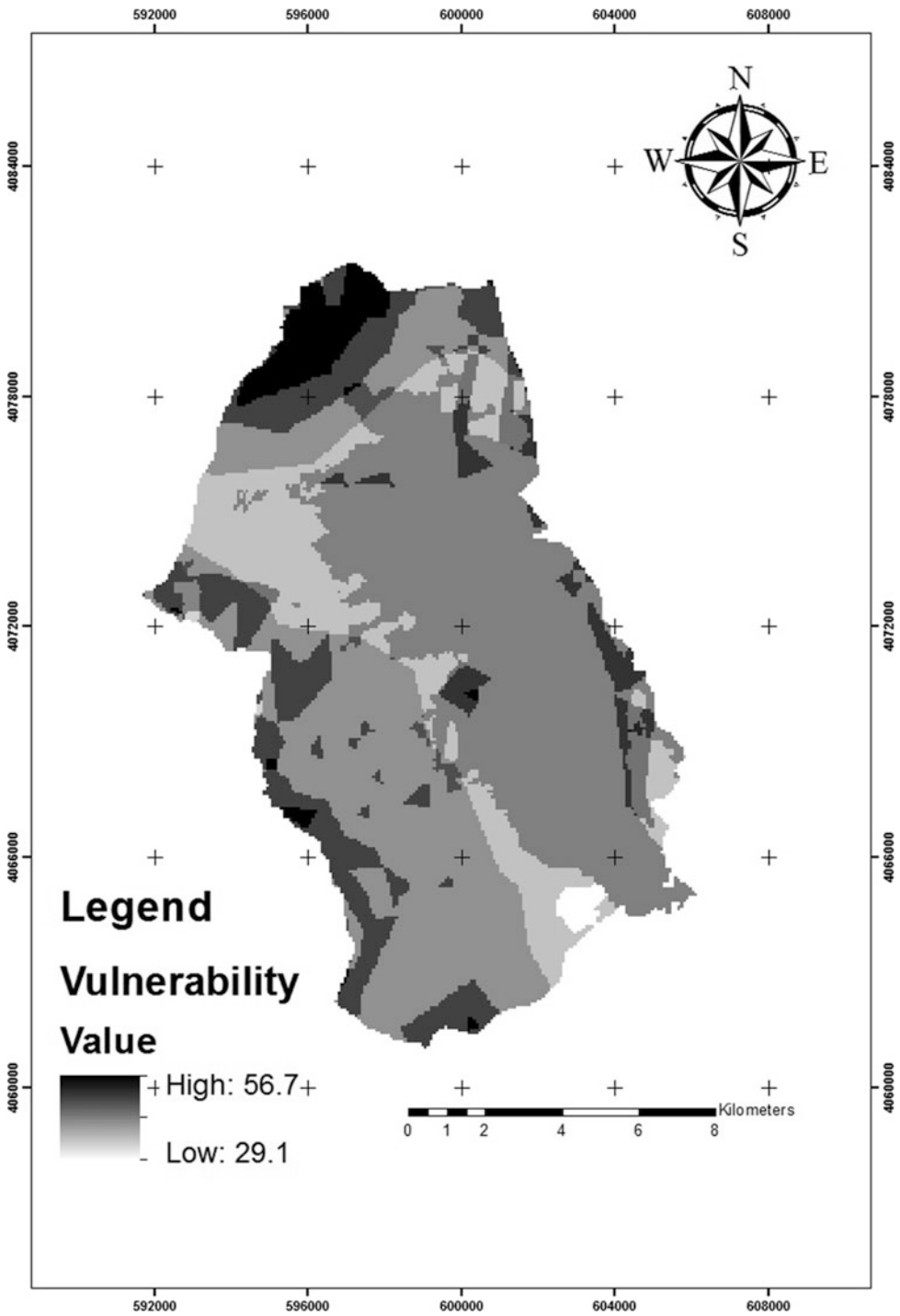

Fig. 2 Vulnerability map

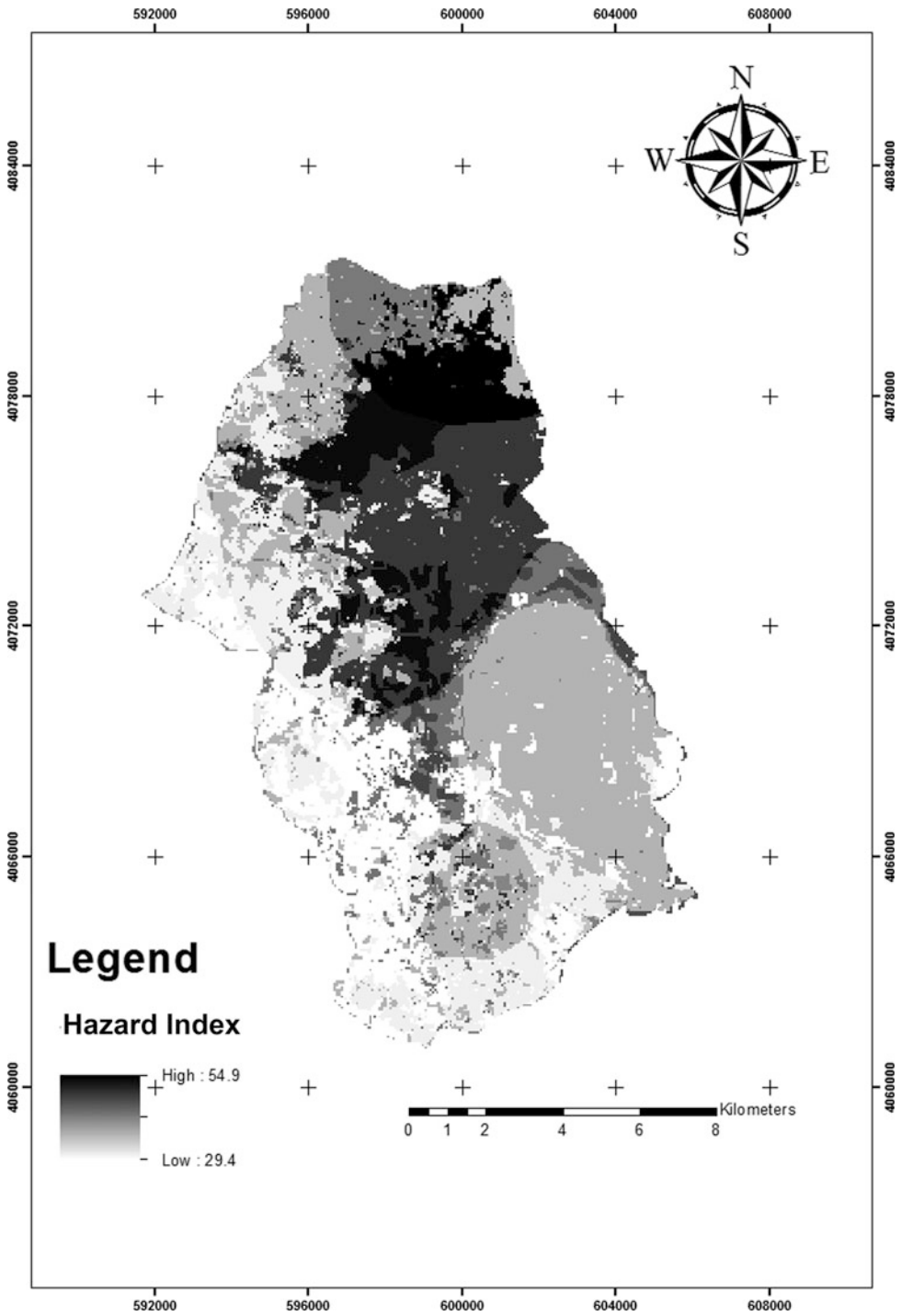

Fig. 3 Hazard map

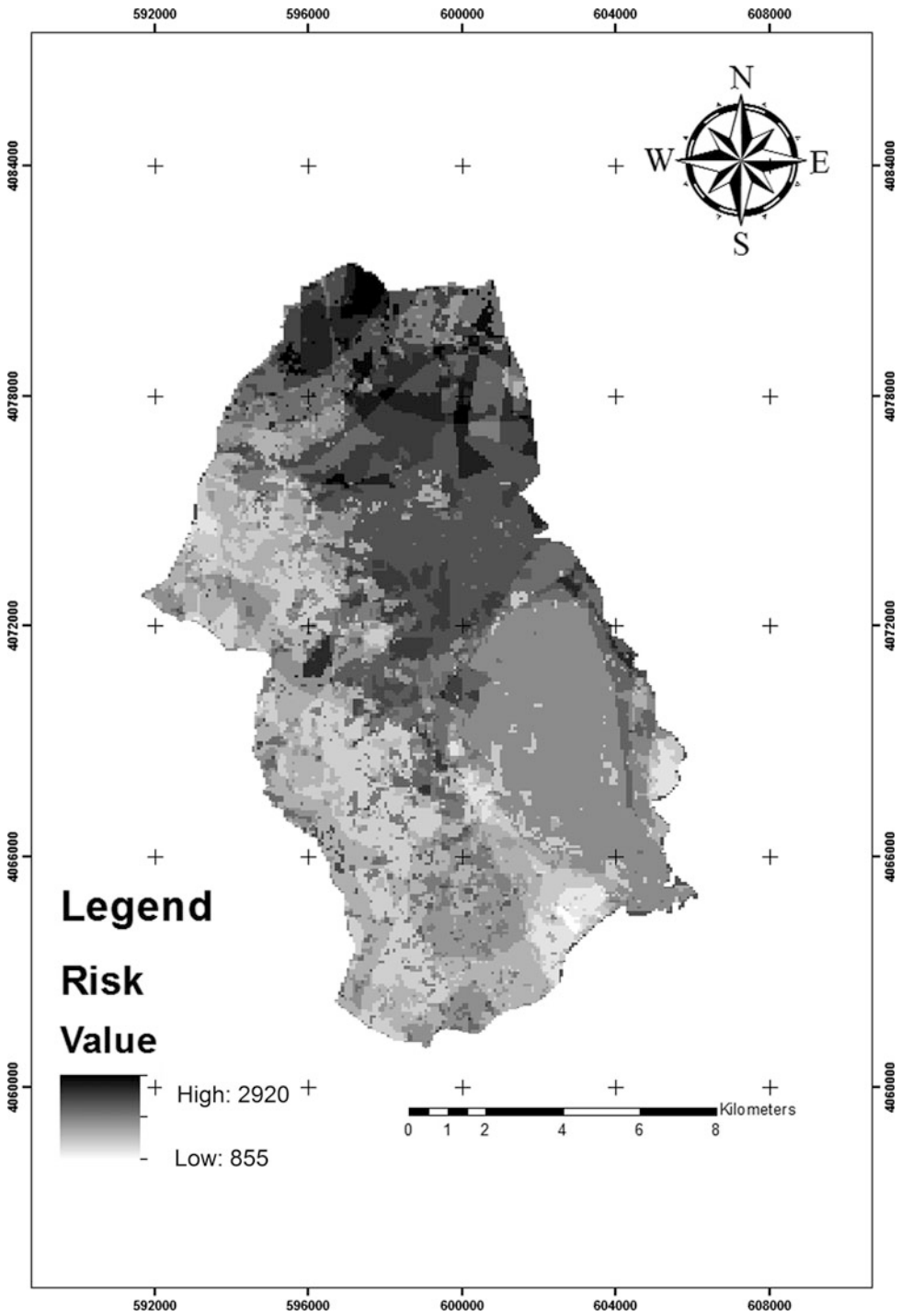

Fig. 4 Risk map

Table 1 Vulnerability, hazard and risk area (%) per classes

Classes/area (%)	Vulnerability	Hazard	Risk
High	26	33	35
Moderate	53	26	32
Low	21	41	33

order to improve the quality of the spatial distribution of vulnerability factors in this area.

References

1. Zhang, S., Pan, B.: An urban storm-inundation simulation method based on GIS. J. Hydrol. **517**, 260–268 (2014). https://doi.org/10.1016/j.jhydrol.2014.05.044
2. AUGT: L'urbanisation dans le Grand-Tunis, Tunisie, rapport inedit, p. 20 (2015)
3. Saaty, T.L.: A scaling method for priorities in hierarchical structures. J. Math. Psychol. **15**, 234–281 (1977)
4. Feizizadeh, B., Blaschke, T., Nazmfar, H.: GIS-based ordered weighted averaging and dempster Shafer methods for landslide susceptibility mapping in Urmia lake basin. Iran. Int. J. Digit. Earth (2012). https://doi.org/10.1080/17538947.2012.749950
5. Malczewski, J.: Visualization in multi-criteria spatial decision support systems. Geomatica **53**, 139–147 (1999)
6. Malczewski, J.: On the use of weighted linear combination method in GIS: common and best practice approaches. Trans. GIS **4**, 5–22 (2004)
7. Marinoni, O.: Implementation of the analytical hierarchy process with VBA in Arc GIS. Comput. Geosci. **30**(6), 637–646 (2004)
8. Marinoni, O., Higgins, A., Hajkowicz, S., Collins, K.: The multiple criteria analysis tool (MCAT): a new software tool to support environmental investment decision making. Environ. Modell. Softw. **24**(2), 153–164 (2009)
9. Rothman, D.S., Romero-Lankao, P., Schweizer, V.J., Bee, B.A.: Challenges to adaptation: a fundamental concept for the shared socio-economic pathways and beyond part of special issue "A Framework for the Development of New Socio-economic Scenarios for Climate Change Research". In: Nakicenovic, N., Lempert, R., Janetos, A. (eds.) Climatic Change (2013). https://doi.org/10.1007/s10584-013-0907-0
10. UNDHA: Internationally Agreed Glossary of Basic Terms Related to Disaster Management. DNA/93/36, United Nations, Department of Humanitarian Affairs, Geneva, Switzerland (1992)
11. Aronica, G.T., Candela, A., Fabio, P., Santoro, M.: Estimation of flood inundation probabilities using global hazard indexes based on hydrodynamic variables. Phys. Chem. Earth **42–44**, 119–129 (2012)
12. Chen, Y., Syvitski, J.P.M., Gao, S., Overeem, I., Kettner, A.J.: Socio-economic impacts on flooding: a 4000-year history of the yellow river, China. Ambio **41**, 682–698 (2012). https://doi.org/10.1007/s13280-012-0290-5
13. Marnitez-Grana, A.M., Boski, T., Goy, J.L., Zazo, C., Dabrio, C. J.: Coastal-flood risk management in central Algarve: vulnerability and flood risk indices (South Portugal). Ecol. Ind. **71**, 302–316 (2016)
14. Ciro Aucelli, P.P., Di Paola, G., Incontri, P., Rizzo, A., Vilardo, G., Benassai, G.: Coastal inundation risk assessment due to subsidence and sea level rise in a Mediterranean alluvial plain (Volturno coastal plain e southern Italy). Estuar. Costal Shelf Sci. 1–13 (2016)
15. Birkmann, J.: Measuring Vulnerability to Natural Hazards—Towards Disaster Resilient Societies. United Nations University Press, Tokyo, 450 p (2006)

Adaptation of MEDALUS Method for the Analysis Depicting Land Degradation in Oued Labiod Valley (Eastern Algeria)

Bouhata Rabah and Bensekhria Aida

Abstract

The development of arid and semi-arid climatic mountain areas is strongly affected by land conservation and the fight against land degradation, which is the consequence of a set of several processes. In this study, we applied the Mediterranean Desertification and Land Use (MEDALUS) method on a mountainous area (the Oued Labiod valley) located in the southern foothills of the Aurès in eastern Algeria. The mapping of the vulnerability of this region to land degradation was developed by crossing four thematic layers (vegetation, climate, soil and management system, and human influence). The application of this method was based on the identification of vulnerable areas by making different parameters that can affect the process of desertification. Spatial analysis is a powerful tool that allows the modeling of each indicator. The cartographic and alphanumerical data are input and structured in a basic data, and analyzed by the Geographic Information Systems GIS. The results provide a document on the spatialization of priority zones and allowed achieving an integrated management of this mountainous area.

Keywords

MEDALUS • Desertification • Oued labiod • GIS

1 Introduction

The desertification phenomenon mainly results from the interaction of environmental factors, human activity and climate variations [1]. This phenomenon is manifested by processes that lead to changes in vegetation cover, elements of the soil surface (litter, bare soil, frosting film, silting), the impoverishment of the soil and its disappearance. Today desertification is considered as a major environmental problem for the 21st century [2]. Combating drought, land degradation and desertification is an international priority. Desertification is a no less serious problem faced by many countries [3].

In Algeria, this phenomenon is the result of a series of processes in arid and semi-arid environments. The Labiod valley which is situated in the southern slope of the eastern part of the Saharan Atlas is considered as a representative sample of this situation. As such, the creation of a vulnerability map to desertification is an essential step for the development of these mountainous areas. Our work is based on the use of a Mediterranean Desertification and Land Use (MEDALUS) model [4] and geomatics tools. This model is one of the most relevant methods of assessment and mapping of desertification in the Mediterranean regions [5]. It has been tested in most Mediterranean countries and has shown good results [6, 7].

2 Geographical Settings

The watershed of Labiod valley is located in the Aurès massif (eastern part of the Saharan Atlas). It is part of the great Chott Melghir watershed and covers 1313 km^2. It is formed by the meeting of descending torrents of the steep slopes of Chelia Mount which represents the highest peak 2326 m to the Saharan plain then towards the dam of Foum EL Gherza. The hydrographic network consists of the principal course: Labiod valley which crosses alternating formations between limestone and marls of the Cretaceous

B. Rabah (✉) · B. Aida
State Key Laboratory of Natural Hazards and Regional Planning, Institute of Earth Sciences and Universe, University of Batna 2, Batna, Algeria
e-mail: r.bouhata@univ-batna2.dz

B. Aida
e-mail: a.bensekhria@univ-batna2.dz

© Springer Nature Switzerland AG 2019

H. M. El-Askary et al. (eds.), *Advances in Remote Sensing and Geo Informatics Applications*, Advances in Science, Technology & Innovation, https://doi.org/10.1007/978-3-030-01440-7_65

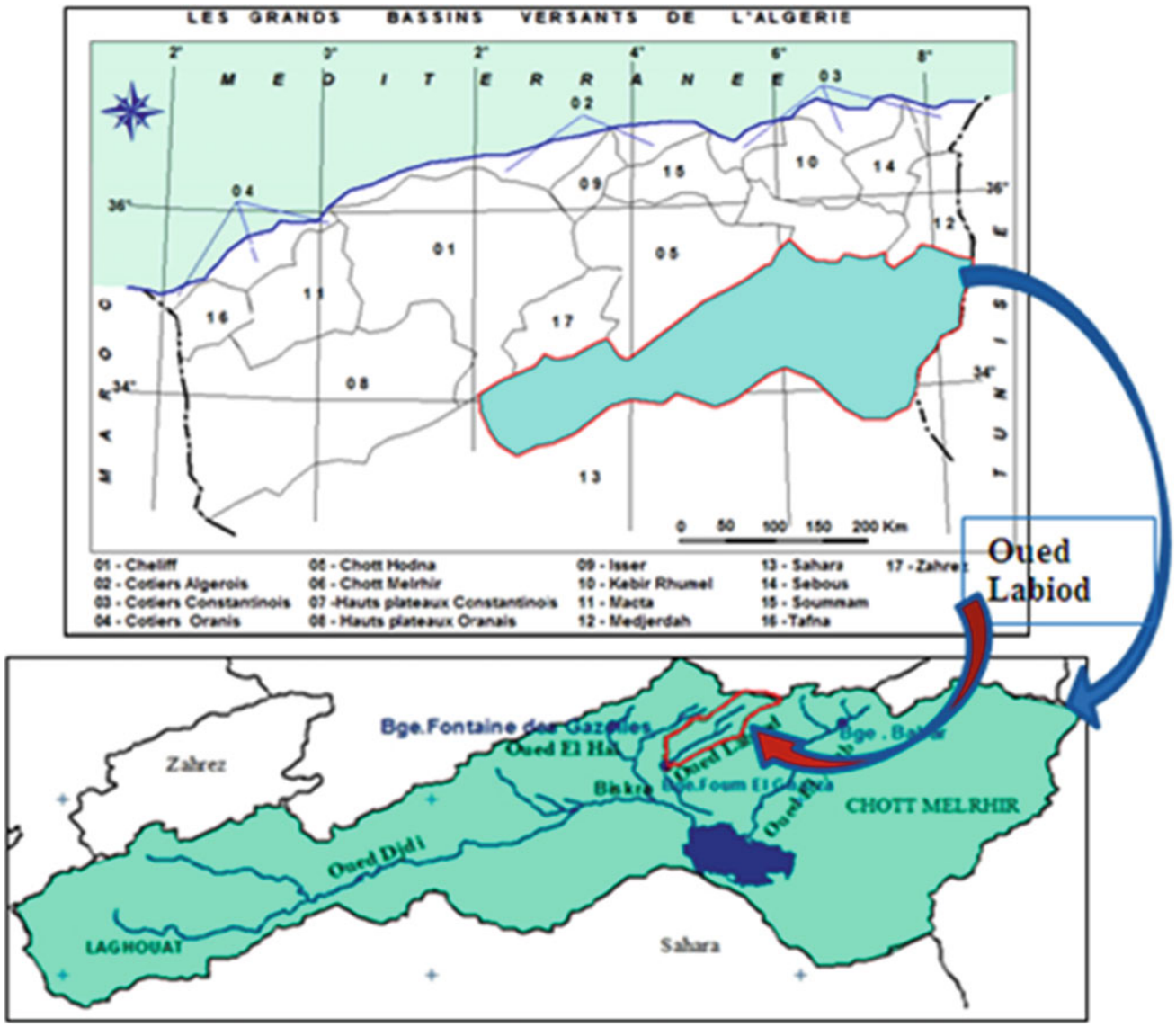

Fig. 1 Location of the study area

and Eocene ages. The BV of Labiod valley is characterized by a semi-arid cold climate in winter, hot and dry in summer, with an average annual rainfall of 276 mm and an average annual temperature ranging between 16 and 23 °C. The vegetation consists of a permanent cover of cedar forests, holm oak and Aleppo pine. The rest is occupied by maquis, Alfa and poorly protected or bare land (Fig. 1).

3 Methodology

The methodology was inspired from the one developed in the MEDALUS project, [4] identifying the vulnerability to desertification of Mediterranean ecosystems by a desertification sensitivity index (DSI), obtained from the geometric mean of four other quality indices from the environment and the man action, these indices are related to the quality of the climate (IQC), soil quality (IQS), the quality of the vegetation cover (IQV) and the quality of the Management System and Human Influence (IQSG). Each of these indices is grouped into different uniform classes with a weighting factor assigned to each class, then, four layers were evaluated. The ISD was given by the following relation: (ISD) = (IQC * IQS * IQV * IQSG) ¼.

All data defining the four main layers were introduced into a geographic region under a (GIS) [8, 9]. These layers were created in (Arcgis 10.2) using the spatial analysis tool.

4 Results and Discussion

According to the map of vulnerability to land degradation:

- Critically endangered areas (very vulnerable, critical) account for 45.69% of the total area with an index ranging between 2.71 and 4.31. They are generally superimposed on the south facing areas where the vegetation cover is almost zero, this sensitivity is also due to the rapid socialization of these areas (Figs. 2, 3, 4, 5 and 6).
- Relatively threatened areas are moderately sensitive lands occupying 33.3% of the total area. These lands are subjected to desertification with a less degree than the rest of the classes but are not immune because if these lands are poorly managed, they will suffer the consequences and will turn into deserted land in a few years.
- Low-risk areas represent 21.1% of the total area, thanks to their geographical position, isolated from any anthropic constraint, and the fact that these lands are occupied mainly by forest vegetation.

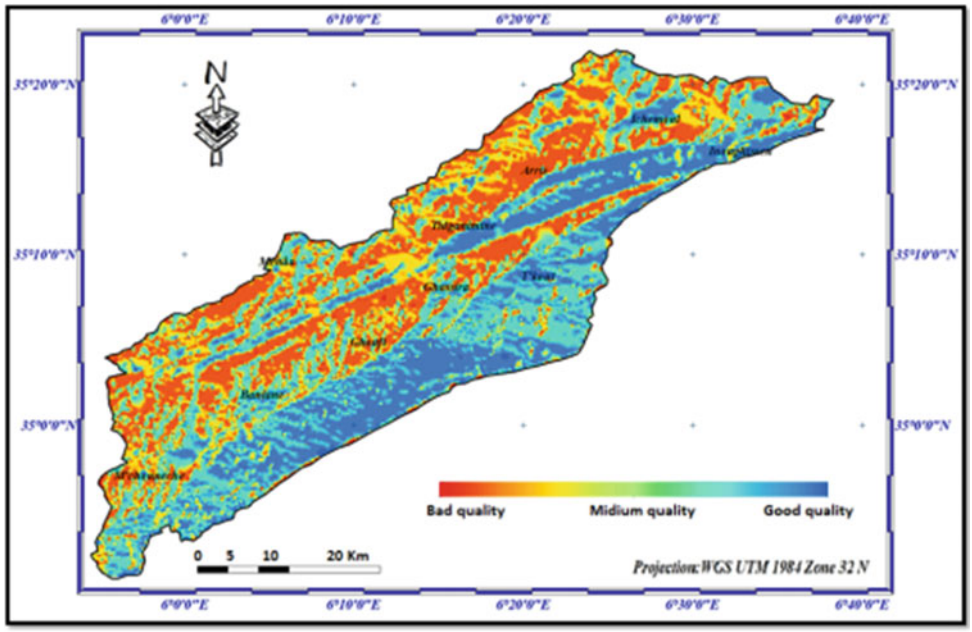

Fig. 2 Map of the climate quality index

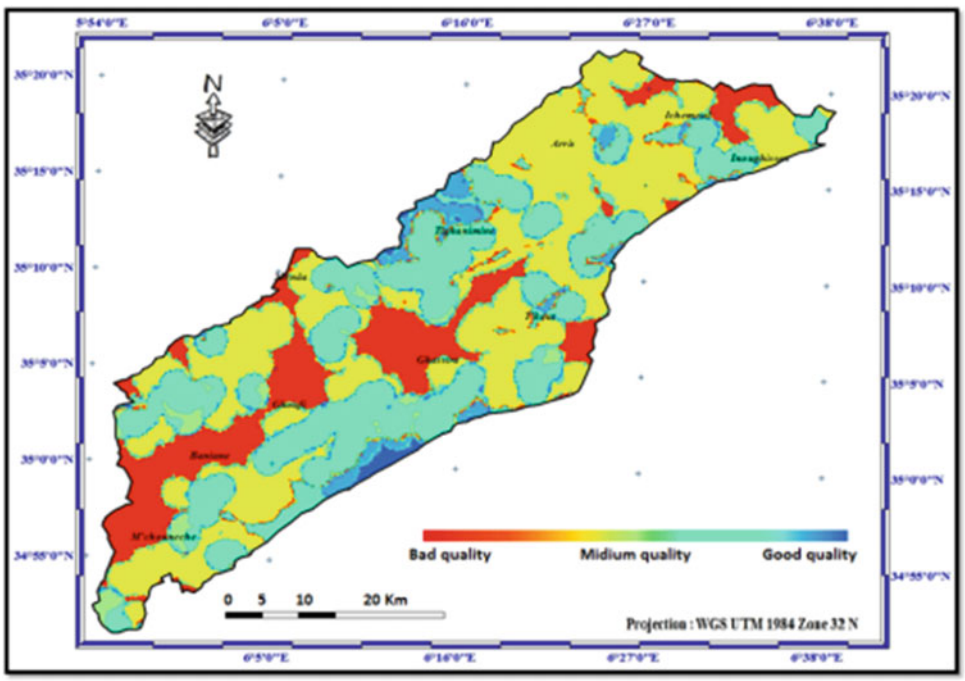

Fig. 3 Map of soil quality index

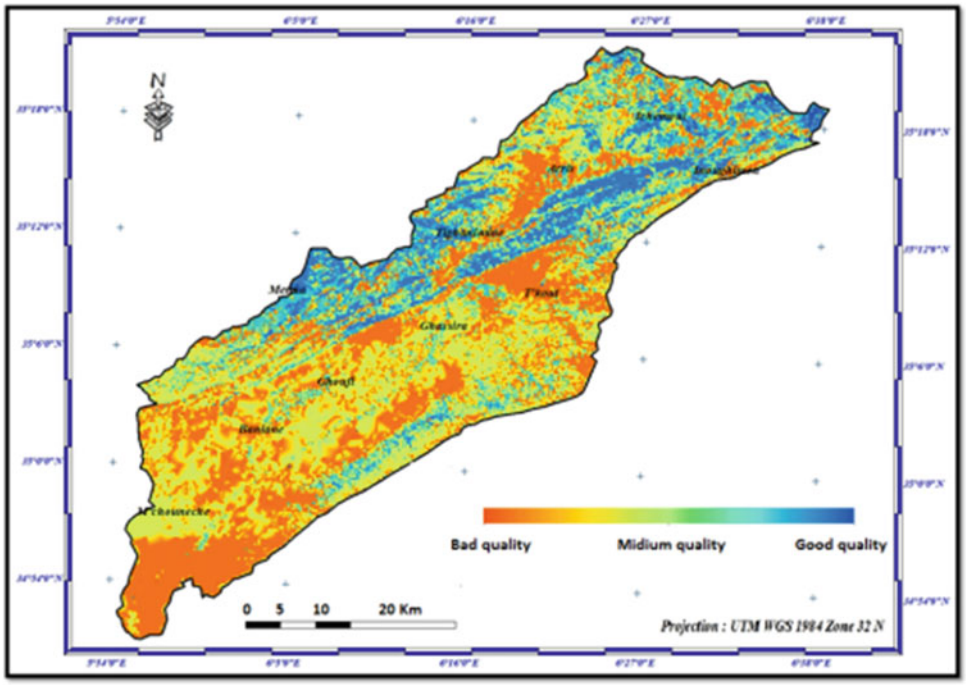

Fig. 4 Map of the vegetation cover quality index

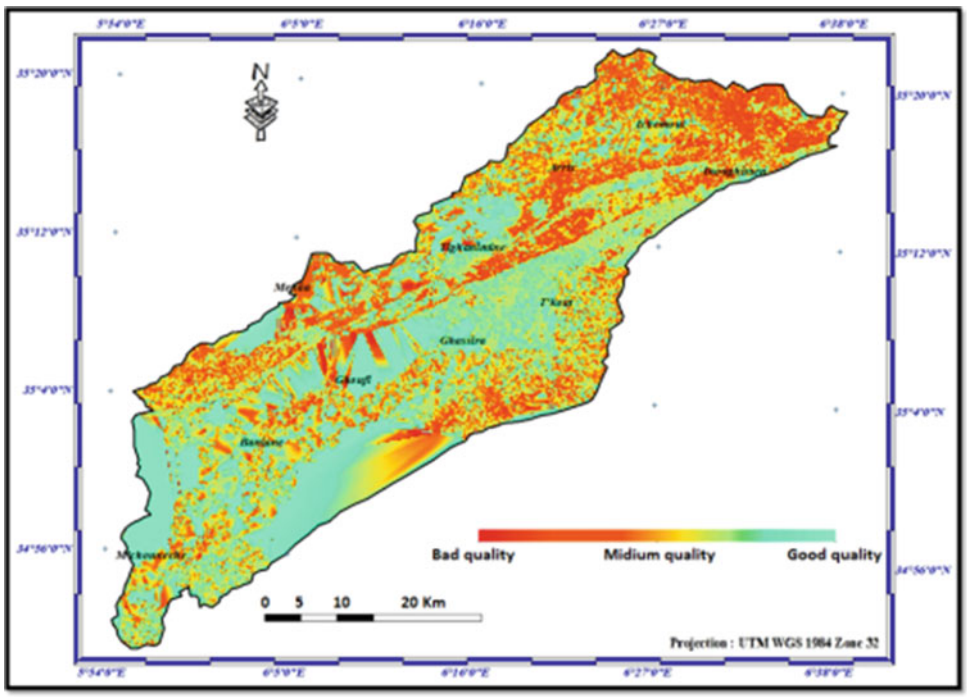

Fig. 5 Map of management system quality and human influence index

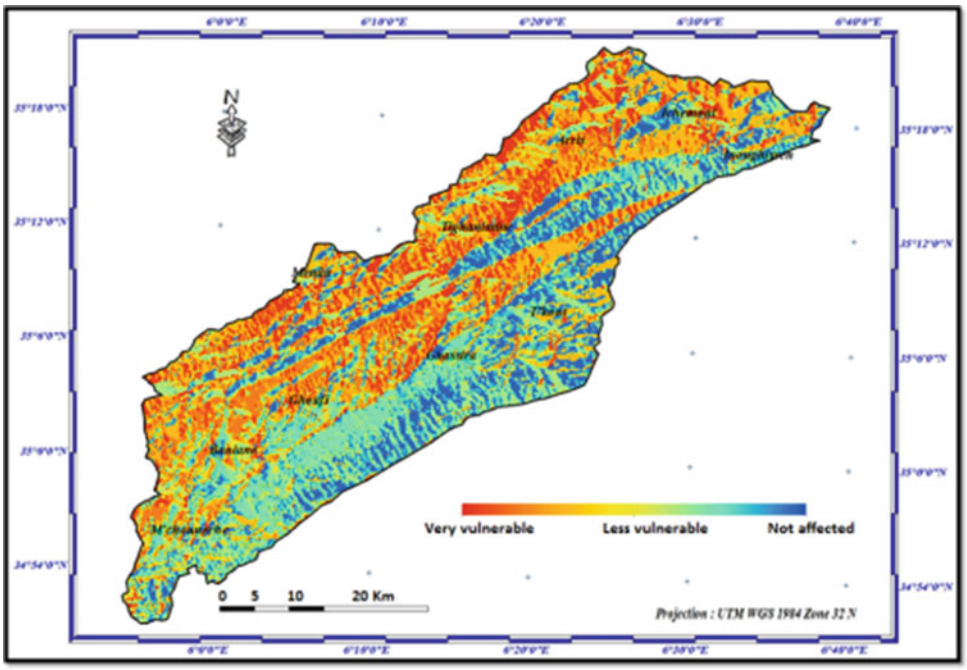

Fig. 6 Map of vulnerability to land degradation based on major contributing factors

5 Conclusion

In this study, attempts were made to map vulnerability to land degradation by adapting the MEDALUS method and using GIS tools. The analysis of the obtained results shows the importance of the desertification phenomenon which threatens practically almost half (45.69%) of the total area of the study area. Several factors and their articulations in space and time have been the causes of this state of strong sensitivity to desertification; among the most important factors, we can cite: climatic deterioration, and socialization by agricultural activity which leads to the destruction of the plant cover protecting the soil against erosion.

The results showed the intensity and severity of desertification processes in this area and gave us an insight into the evolution of ecosystems. Such an insight can be used as an essential tool to help decision-making and planning (i.e., the definition of priority areas for intervention fight against the evolution of land degradation).

References

1. United Nations Environment Programme: World Atlas of Desertification, 2nd edn. UNEP Edition, Ch. 1 (1997)
2. World Bank: World Development Report: Sustainable Development in a Dynamic World: Transforming Institutions, Growth, and Quality of Life. Oxford UniversityPress, World Bank (2002)
3. UNCCD: Desertification Coping with Today's Global Challenges in the Context of the Strategy of the United Nations Convention to Combat Desertification. Unites Nations Convention to Combat Desertification, Report on the High-Level Policy Dialogue, Bonn, Germany (2008)
4. Kosmas, C., Kirkby, M., Geeson, N.: Manual on Key Indicators of Desertification and Mapping Environmentally Sensitive Areas to Desertification. The Medalus Project on Mediterranean desertification and Land Use. Directorate-General Science, Research and Development, EUR 18882 (1999)
5. Brandt, J.C., Thornes, J.B.: Mediterranean Desertification and Land Use. Wiley, London (1996)
6. Geeson, N.A., Brandt, C.J., Thornes, J.B.: Mediterranean Desertification: A Mosaic of Processes and Responses. Ed. Wiley (2002)
7. Basso, F., Bove, E., Dumontet, S., Ferrara, A., Pisante, M., Quaranta, G., Taberner, M.: Evaluating environmental sensitivity at the basin scale through the use of geographic information systems and remotely sensed data: an example covering the Agri basin (Southern Italy). CATENA **40**, 19–35 (2002)
8. Sepehr, A., Hassanli, A.M., Ekhtesasi, M.R., Jamali, J.B.: Quantitative assessment of desertification in south of Iran using MEDALUS method. Environ. Monit. Assess. https://doi.org/10.1007/s10661-007-9613-6 (2007)
9. Bouhata, R., Kalla, M.: Mapping of environmental vulnerability of desertification by adaptation of the MEDALUS method in the Endoreic area of Gadaine (Eastern Algeria). GeographiaTechnica **09**(2), 1–8 (2014)

Measuring and Monitoring Land Subsidence and Earth Fissures in Al-Qassim Region, Saudi Arabia: Inferences from InSAR

Abdullah Othman

Abstract

Numerous land deformations (land subsidence and fissures) events have been reported from the Central part (Al Qassim) of the Kingdom of Saudi Arabia. An integrated approach (geo-informatics, geologic, and hydrogeology) is adapted to identify areas threatened and affected by land deformations, and also to evaluate the causes of these phenomena. A fourfold approach is applied in this research including; (1) Conducting field visits to collect observations, (2) Constructing spatial correlations in a GIS for the damaged locations which related to the registered spatial datasets (surface and subsurface geology) and temporal datasets (e.g., land use, groundwater extraction, distribution, depth and magnitude of earthquakes), (3) Extracting deformation rates (subsidence) using SBAS radar inter-ferometric technique using ENVISAT data sets, and (4) Correlating the extracted subsidence rates spatially and temporally with GRACE mass variations data. The SBAS investigation revealed high subsidence rates (−5 to −12 mm/yr) along a NW-SE direction, with some subsidence (−2 to −4) in the southwestern part of the study area. This subsidence is correlated with areas witnessing a huge drawdown in the fossil groundwater levels and a depletion in GRACE-derived TWS. Most earth fissures are located around the margins of the subsiding areas and are caused by bending beam activities surrounding the subsiding lands.

Keywords

Subsidence • Earth fissures • InSAR • GRACE • Groundwater

1 Introduction

Land subsidence is defined as the gradual sinking of the land's surface because of the volume reduction of subsurface materials and increasing in subsurface voids caused by anthropogenic and/or natural factors [7, 9]. This phenomenon is generally a slow operating process over relatively large areas, and traditionally have been measured by the ground based geodetic methods (e.g., differential leveling, global positioning system, tripod LiDAR) [3, 7]. Since the nineties of the last century, however, the advent of InSAR techniques has given more cost-effectiveness and very accurate tools in the measurement of land subsidence in huge areas [2]. These types of techniques have been successfully used over many places around the world such as Santa Clara and Antelope in the western part of California, Las Vegas of southern Nevada, [1, 4, 5], and recently over the area witnessing a high rate of subsidence caused by the excessive groundwater extraction in Wadi As-Sirhan Basin in Saudi Arabia [7]. In this study, I focused on and investigated the distribution and causes of the land subsidence, identified the areas threatened and affected by this phenomenon in central Saudi Arabia (Al Qassim) and used Inter-ferometric Synthetic Aperture Radar (InSAR) and Small Baseline Subset (SBAS) radar interfero-metric methods to reach these goals, with Gravity Recovery and Climate Experiment (GRACE) mass variations data to monitor and estimate aquifer depletion rates over the study area.

2 Methodology and Data Source

A fourfold approach has been applied for this research: (1) Conducted field visits to collect obser-vations from locations where subsidence incidences were reported; (2) Spatial correlation has been implemented by using GIS environment methods for the damaged deformation

A. Othman (✉)
Natural Hazards Unit, Department of Environmental and Health Research, Umm Al-Qura University, Mecca, 21955, Saudi Arabia
e-mail: agothman@uqu.edu.sa

© Springer Nature Switzerland AG 2019

H. M. El-Askary et al. (eds.), *Advances in Remote Sensing and Geo Informatics Applications*,
Advances in Science, Technology & Innovation, https://doi.org/10.1007/978-3-030-01440-7_66

(subsidence and fissures) locations to correlate co-registered spatial datasets (e.g., geo-surface materials, structures, lithologies), as well as the temporal datasets (e.g., groundwater abstraction, land use, earthquakes); (3) Subsidence rates were taken by using Small Baseline Subset (SBAS) radar inter-ferometric technique and processing ENVISAT "Environmental Satellite" data sets for a two-year period (2003–2004). (4) The extracted subsidence rates were correlated spatially (in GIS environment) and temporally (time series analysis) with the Gravity Recovery and Climate Experiment (GRACE) mass variations data. Mutual relationships were investigated to detect and quantify the land subsidence and factors causing such a phenomenon in Al Qassim Province.

3 Results

3.1 Small Baseline Subset Technique (SBAS)

The SBAS technique allows generating accurate deformation velocity maps of the study area as well as detecting the temporal evolution of the ongoing displacements [6]. The small Baseline method: performance evaluation and latest developments for surface vertical displacement analysis of super large areas [8]. A total of nine scenes (SBAS approach) of the study area were taken at different time intervals and used in the analysis. The scenes are (20031005, 20031005, 20031109, 20031128, 20031214, 20040102, 20040328, 20040521, 20040625) taken from the two tracks (49 and 278).

For the analysis of the SBAS, SRTM DEM map with 60 m resolution was used as an input. SARscape 5.2 version was used in the SBAS subsidence result generation. The resulting map (Fig. 1e) shows: (1) Both sides (East and West) in the southern part of study area show the highest rate of subsidence beside low rates in the north west and central parts. (2) The North East and some central parts of the study area show a certain stability. (3) The city of Buraydah, located in the extreme South East region of the study area, is also experiencing a subsidence event. (4) The earth fissures around the boundaries of the subsidence bowls were caused by the curving displacement beam around the subsidence bowls, the area where the horizontal extension is high.

3.2 Groundwater Datasets

Groundwater data sets were obtained from the Ministry of Environment, Water and Agriculture and used to straighten and map the regional groundwater level. For this approach, the local multimodal interpolation method was used to interpret the limited data reasonably and the result showed a groundwater level change, mapped over a 45-year span (1960–2005). The analysis results of the 45 years (1965–2005) (Fig. 1c) proved a groundwater change (drop) in the study area and the result of GRACE-derived TWS shows that the study area is experiencing significant negative TWS trends (Fig. 2a, b) strongly correlated with the subsidence map produced by the SBAS method showing that the cause of the subsidence in the region is mainly attributed to the excessive groundwater pumping.

4 Discussion

In the previous sections, we demonstrated that the identified land subsidence and earth fissures-related features were correlated spatially with features related with the highest rates of the agricultural activities and groundwater abstraction in Al Qassim Province suggesting a causal effect. The results analyzed in ArcMap and ENVI (SARscape) show that the subsidence map generated using SBAS revealing that the northwestern, central, southeastern and Southwestern parts of the study area show subsidence (Fig. 1e). The groundwater level change map (Fig. 1c) and GRACE-derived TWS result (Fig. 2a) strongly correlates with the subsidence map implying that most of the subsidence was caused by excessive pumping of the groundwater resource that resulted in unprecedented groundwater decline in the region and that contributed to the subsidence event in the study area. The subsidence in the southwestern part highly correlated with the wadi's deposits (Fig. 1d) which recently became a disorganized irrigated area. This phenomenon is highly supported by the high density of agricultural plantations (showing in the Landsat scenes (Fig. 1a, b) that extensively used groundwater are located in that part of the study area. Consequently, these observations supported the suggestion that excessive fossil groundwater abstraction was the main factor for the subsidence and earth fissures in the study area.

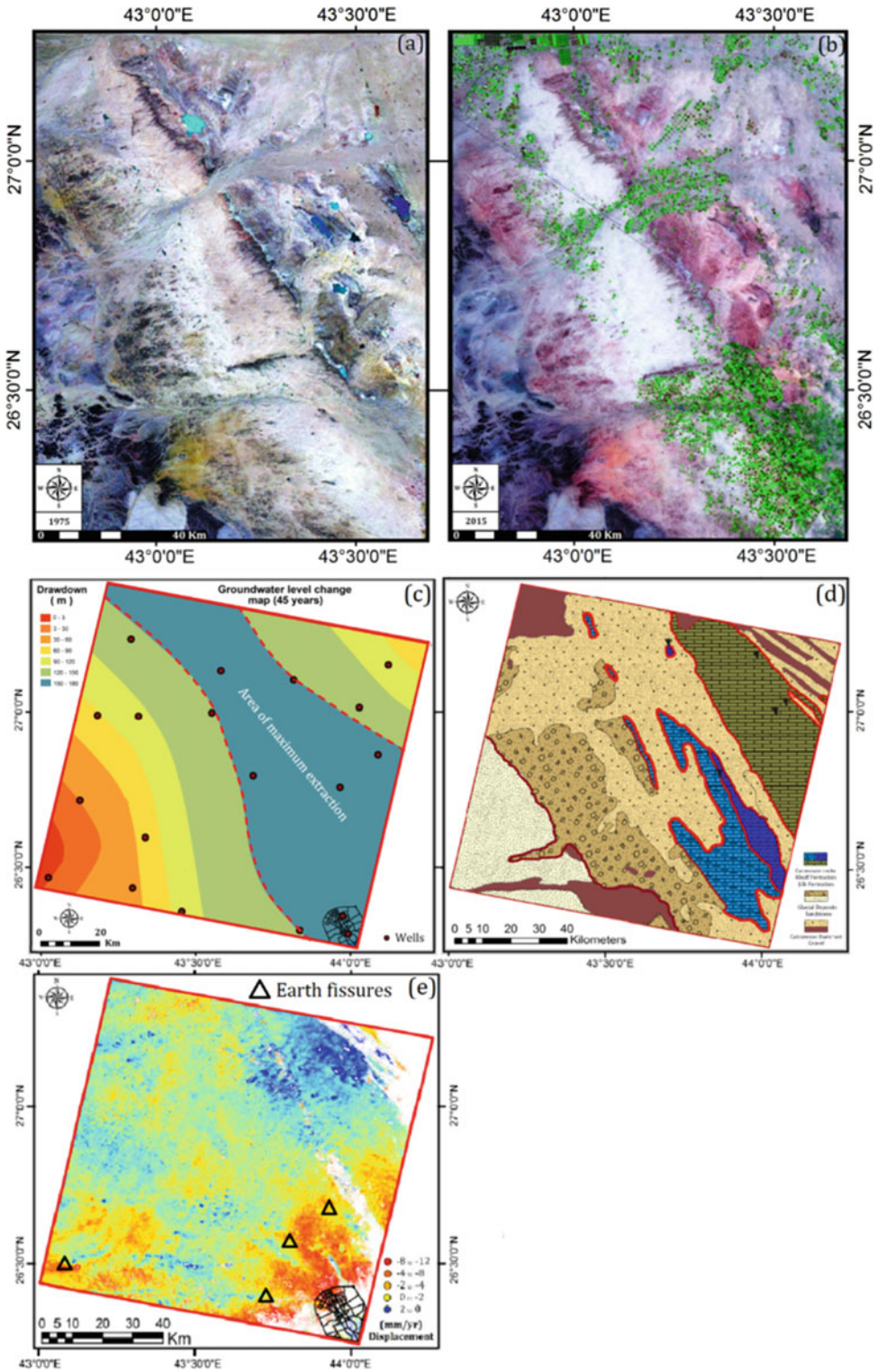

Fig. 1 **a** Landsat 2, 1975, **b** Landsat 8, 2015, **c** groundwater level change map from 1960 to 2005, **d** geological map of the study area, **e** distribution of land subsidence with SBAS results. Also shown the distribution of the earth fissures around the major subsidence lands

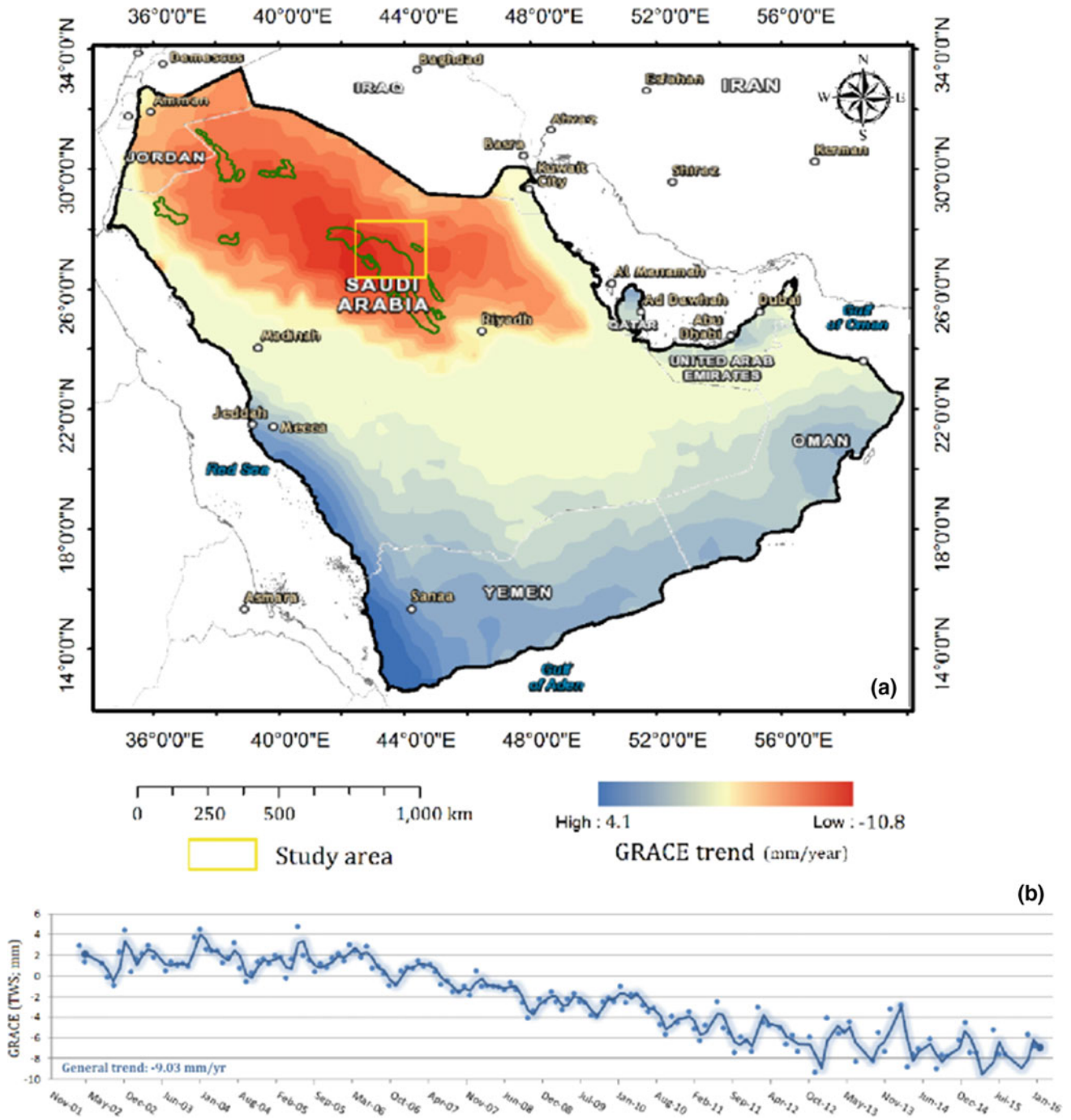

Fig. 2 **a** Trend (mm/yr) in temporal (04/2002-01/2016) GRACE-derived terrestrial water storage (TWS), **b** temporal variations in GRACE—derived TWS data during the period 04/2002–01/2016 averaged over the central parts of Saudi Arabia (Al-Qassim, study area)

5 Conclusion

The Saq aquifer, one of the most productive and highly utilized aquifers in Saudi Arabia and Jordan, is the main source of groundwater for irrigation in the study area. This sandstone formation is being excessively utilized for drinking and agricultural purposes. Consequently, the regional groundwater level has been declining for a while now. So in the light of these results, we can say that most of the subsidence event witnessed in our area is due to the excessive pumping of this aquifer which resulted in a decline in the groundwater level and hence subsidence. It is recommended that the detailed radar inter-ferometric studies,

conducted in central Saudi Arabia, be extended to cover the entire damaged areas and the irrigated regions as well as the Arabian Peninsula. These studies should take advantage of the new generations of the European Space Agency Sentinel SAR satellites. Finally, a special attention should be paid to the development of a national plan for the early geo-hazard warning system.

References

1. Fielding, E.J., Blom, R.G., Goldstein, R.M.: Rapid subsidence over oil fields measured by SAR interferometry. Geophys. Res. Lett. **25**, 3215–3218 (1998)
2. Gabriel, A.K., Goldstein, R.M., Zebker, H.A.: Mapping small elevation changes over large areas: differential radar interferometry. J. Geophys. Res.: Solid Earth **94**, 9183–9191 (1989)
3. Galloway, D.L., Burbey, T.J.: Review: regional land subsidence accompanying groundwater extraction. Hydrogeol. J. **19**, 1459–1486 (2011)
4. Galloway, D.L., Hoffmann, J.: The application of satellite differential SAR interferometry-derived ground displacements in hydrogeology. Hydrogeol. J. **15**, 133–154 (2007)
5. Galloway, D.L., et al.: Detection of aquifer system compaction and land subsidence using interferometric synthetic aperture radar, Antelope Valley, Mojave Desert, California. Water Resour. Res. **34**, 2573–2585 (1998)
6. Manunta, M., Marsella, M., Zeni, G., Sciotti, M., Atzori, S., Lanari, R.: Two-scale surface deformation analysis using the SBAS-DInSAR technique: a case study of the city of Rome, Italy. Int. J. Remote Sens. **29**(6), 1665–1684 (2008)
7. Othman, A., et al.: Use of geophysical and remote sensing data for assessment of aquifer depletion and related land deformation. Surv. Geophy., 1–24 (2018)
8. Pepe, A.: Advanced multitemporal phase unwrapping techniques for DInSAR analyses. In: Recent Interferometry Applications in Topography and Astronomy. InTech (2012)
9. Ren, G., Whittaker, B., Reddish, D.: Mining subsidence and displacement prediction using influence function methods for steep seams. Mining Sci. Technol. **8**, 235–251 (1989)

GIS and Remote Sensing-based Approach for Desert Risk Reduction

Khamis Sayl

Abstract

Combating desertification includes having an accurate knowledge on the existing land degradation status and the amount of the potential risk. The remoteness, size and harsh nature of the world's desert make it expensive and difficult to map or monitor this landscape or to determine the effect of the land use on them. Using the combination of Geographic Information system (GIS) and remote sensing (RS) techniques, this study tried to detect the changes in the land surface which may enable us to determine the existing land degradation and identify suitable sites for dams. The thematic maps extracted based on Normalized Differential Vegetation Index (NDVI) and Land Degradation Index (LDI) should be useful to identify and determine the priority of the areas with the highest potential for rainwater harvesting.

Keywords

Rainwater harvesting • Geographic information system • Desertification

1 Introduction

The west desert of Iraq is one of the most arid regions facing great problems regarding desertification. Desertification represents one of the environmental issues threatening future agricultural and environmental development. The total area of Iraq exposed to desertification is 167,000 km^2 which represents (40%) of its total area 437,500 km^2. According to the United Nations Environment Program [8], all parts of Iraq are at risk of drought in various stages. Thus, the nature of the threat facing the West Desert of Iraq in the coming years in indisputable unless effective steps to identify and face this environmental threat are taken.

Combating desertification includes having an accurate knowledge on the existing land degradation status and the magnitude of the potential risk. Therefore, there is a need for an effective solution to tackle the issue of desertification. Recently, rainwater harvesting (RWH) came out as an imperative tool for water conservation. RWH has the ability to provide safe, accessible and affordable water for many types of use such as drinking, agriculture, livestock and small-scale industries and domestic uses [1, 4].

Remote sensing techniques are considered advanced and effective tools to study natural resources, soil, water, and vegetation, and identify their characteristics and then monitor and develop plans to exploit them. The combination of GIS and Remote sensing techniques was applied in monitoring and tracking environmental phenomena such as degradation, drought, and desertification that affect agricultural development process [2, 3]. As with most remote sensing applications, a spectral index can only indicate the presence of a certain land cover type.

The Normalized Difference Vegetation Index (NDVI) is used primarily for vegetation identification, and determination of the lushness of vegetated land surfaces. Vegetation indices have been widely used to monitor biomass changes or identify processes of land degradation [6, 7]. The amount of vegetation cover in semi-arid and arid rangelands undergoes dramatic changes during the year. Sertel et al. [5] proposed a Land Degradation Index (LDI) which is another spectral approach to express land degradation and successfully implement the use of Advanced Space borne Thermal Emission and Reflection Radiometer (ASTER) images to analyze and evaluate the risks of the expansion of land degradation in Northern Morocco. This study presented an application of RS and GIS to combat desertification, in particular it aimed to (i) have an accurate knowledge on the

K. Sayl (✉)
Department of Dams and Water Resources, Engineering College, University of Anbar, Ramadi, Iraq
e-mail: khamis.naba@gmail.com

© Springer Nature Switzerland AG 2019

H. M. El-Askary et al. (eds.), *Advances in Remote Sensing and Geo Informatics Applications*, Advances in Science, Technology & Innovation, https://doi.org/10.1007/978-3-030-01440-7_67

existing land degradation status and the amount of the potential risk, and (ii) identify and determine the priority of a suitable site for rainwater harvesting in the west desert of Iraq.

2 Materials and Methods

2.1 Study area

The study area is located in the west of Iraq in Al-Anbar governorate, which is in the east of the Euphrates river located between 32° 10′ 44″ and 34° 11′ 00″ North and 39° 20′ 00″ to 42° 30′ 00″ East and with a catchment area of 13,370 km^2, as shown in Fig. 1. The catchment has an arid climate with dry summers and cool winters. It is called desert due to low precipitation. The mean annual rainfall is (100–150) mm; about 49% of the rain falls in winter; 36% in spring; 15% in autumn. The mean annual potential evaporation is 3200 mm and the monthly average evaporation varies strongly with seasons.

2.2 Methodology

The methodology consists of two main parts: in the first the decline in (LDI) and (NDVI) was studied using remote sensing tools in different periods whereas the second elucidated ideas to identify suitable sites for rainwater harvesting using the Model Builder in ArcGIS 10.2. Five criteria were considered in this model: slope, rainfall and runoff, soil texture, land use and land cover, and stream order.

To identify the potential sites for rainwater harvesting, a model was developed using Model Builder in ArcGIS 10.2. The suitable areas for rainwater harvesting were identified by rescaling layers of biophysical criteria and combining

Fig. 1 Study area

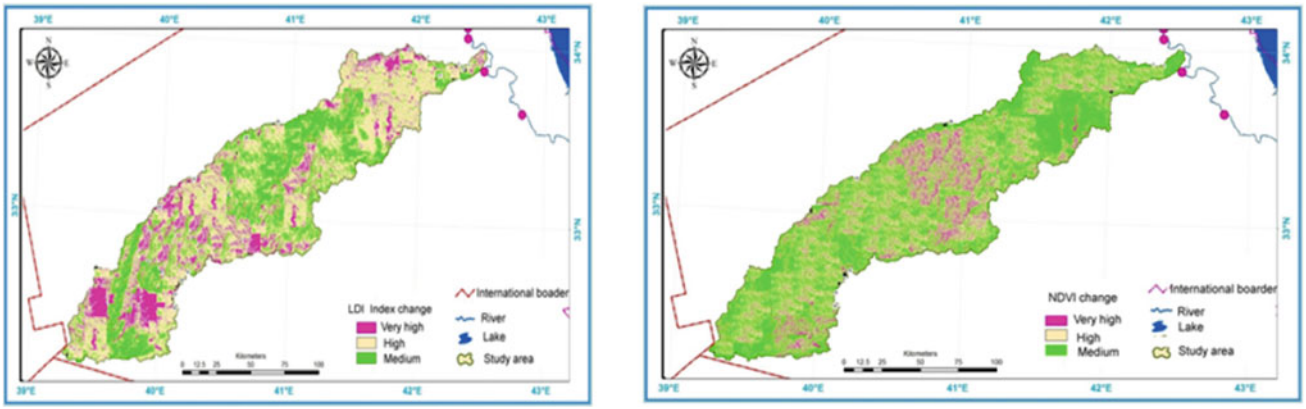

Fig. 2 LDI and NDVI change in study area (1999–2013)

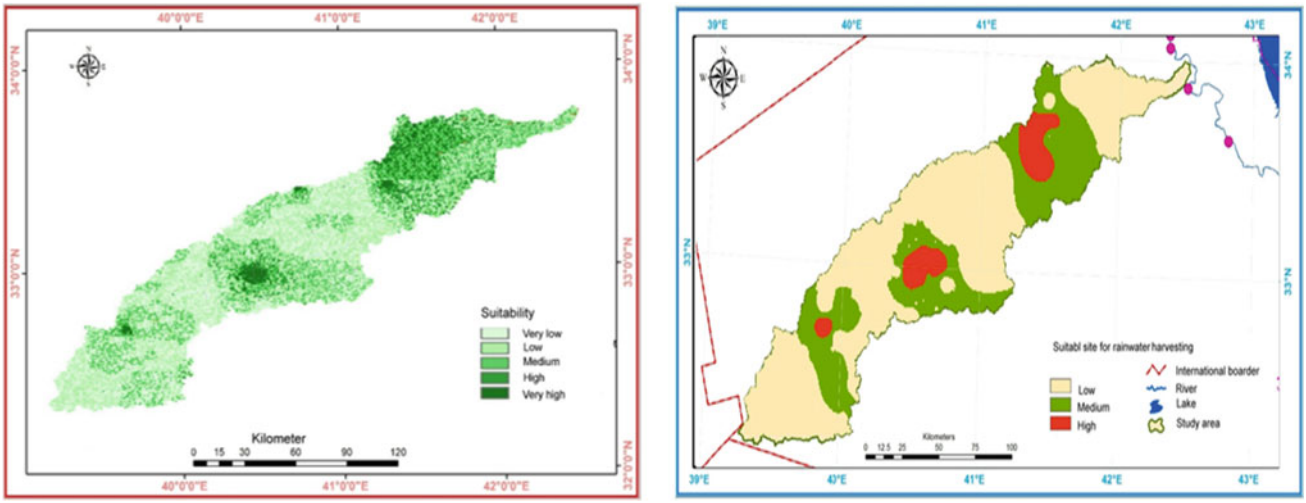

Fig. 3 Suitability and priority site for rainwater harvesting in the study area

them using spatial analyst of ArcGIS 10.2. Then, the land suitability was combined with the NDVI and LDI maps to give priority for the regions that are more affected by environmental issues.

3 Results and Discussion

As shown in the Fig. 2, the results show that the LDI changes in the areas with very high and medium degradation increased 15.5, 34.5 and 50% respectively for the period 1999–2013. The NDVI result shows that the classes decreased by 10% (between 0.0 and 0.2 representing the low vegetated area), 28.5% (between 0.2 and 0.5 representing the medium vegetated area) and 61.5% (between 0.5 and 0.8 representing high vegetated area) for very high changes, high, and medium changes, respectively as shown in the Fig. 1. The result of the integration between the rainwater harvesting suitability map with the degradation maps and vegetation changes determines the areas that must be considered first and gives the priority to determine suitable site for rainwater harvesting as shown in the Fig. 3.

4 Conclusion

The main objective of this study was the use of RS and GIS to combat desertification in the West Desert of Iraq based on the existing land degradation status and the estimated potential sites for rainwater harvesting. The results show that the LDI changes in the areas with very high, high and medium degradations increased by 15.5, 50 and 34.5%, respectively for the period 1999–2013. In addition, the NDVI changes show that the classes decreased by 10% (between 0.0 and 0.2 representing low vegetated area), 28.5% (between 0.2 and 0.5 representing the medium

vegetated area) and 61.5% (between 0.5 and 0.8 represents for the highly vegetated area) for very high changes, high, and medium changes respectively. The proposed approach was found to be efficient, cost effective, and time sparing for screening large areas.

References

1. Agarwal, A., Narain, S., Khurana, I.: Making Water Everybody's Business: Practice and Policy of Water Harvesting. Centre for Science and Environment (2001)
2. Mekonnen, M., Melesse, A.M., Keesstra, SD.: Spatial runoff estimation and mapping of potential water harvesting sites: a GIS and remote sensing perspective, Northwest Ethiopia, pp 565–584 (2016)
3. Sadrolashr, S.S., Mohamed, T.A., Mahmud, A.R.B., et al.: Integrated modeling for flood hazard mapping using watershed modeling system. Am. J. Eng. Appl. Sci. **1**, 149–156 (2008). https://doi.org/10.3844/ajeassp.2008.149.156
4. Samra, J.S., Sharda V.N., Sikka, A.K.: Water harvesting and recycling (2002)
5. Sertel, E., Ormeci, C., Robock, A.: Modelling land cover change impact on the summer climate of the Marmara Region, Turkey. Int. J. Glob. Warm. **3**, 194 (2011). https://doi.org/10.1504/IJGW.2011.038379
6. Soufflet, V., Tanré, D., Begue, A., et al.: Atmospheric effects on NOAA AVHRR data over Sahelian regions. Int. J. Remote Sens. **12**, 1189–1203 (1991). https://doi.org/10.1080/01431169108929721
7. Stafford, J., Ambler, B., Lark, R., et al.: Mapping and interpreting the yield variation in cereal crops. Comput. Electron. Agric. **14**, 101–119 (1991)
8. UNEP.: How Environmental Damage Causes Food Insecurity in IRAQ. World Environmental Day, Technical Assessment Report. Accessed June 2013, p. 32 (2013)

Part VIII
Ground Water Mapping and Assessment

Quantification of Groundwater Storage Variations and Stressed Areas Using Multi-temporal GRACE Data: A Case Study of Upper Indus Plains, Pakistan

M. Amin, M. R. Khan, and Ahsan Jamil

Abstract

Groundwater is depleting at a more rapid rate than its replenishment in Indus Basin due to increased demand attributed to urbanization, inefficient water management practices especially in the agricultural sector and increase in impervious area in the name of development that can expose the country to severe challenge in the future. Through an unregulated groundwater exploitation now farmers often meet inadequacy in surface water supplies. The concurrent use of surface water and groundwater water now takes place on more than 70% of irrigated lands. Therefore, water resources should be monitored on frequent intervals to sensitize policy makers to formulate an optimal framework for water management practices. This study assessed the competence of Gravity Recovery and Climate Experiment Satellite (GRACE)—based estimation of changes in Ground Water Storage (GWS) as a substitute approach for groundwater quantitative approximation for management of groundwater resources in the Indus basin. The GRACE satellite Total Water Storage (TWS) data from 2011 to 2015 was used to calculate GWS. A common reduction trend was seen in the Upper Indus Plain (UIP) where the average net loss of groundwater was observed to be 1701.39 km^3 of water amid 2011–2015. A net loss of around 0.34 km^3/year groundwater storage was deduced for the UIP where flooding in 2014 assumed a fundamental part in natural replenishment of groundwater aquifer of the UIP. In view of TWS varieties three out of four doabs Bari, Rachna, Thal demonstrated a decrease in groundwater capacity though Chaj doab brought about increment of 0.09 km^3. Based on this study, GRACE-Tellus satellite data is competent enough to hint for groundwater storage variations, however there is a vibrant need to calibrate GRACE-Tellus data with hydrological stations data periodically in order to take a maximum advantage for utility of GRACE to monitor groundwater variations on regional scale. Future studies should focus on this aspect.

Index Terms

Hydrology • GIS • Groundwater • GRACE • Indus • Remote sensing

1 Introduction

The imbalance between groundwater resource utilization and recharge has prompted water table to go down at an alarming rate according to past studies due to which several issues like insufficient water for agricultural use, groundwater siltation and land subsidence take place. The groundwater stressed areas need to be delineated on an optimal temporal scale to sensitize policy makers to develop strategies of water management practices on appropriate time groundwater and place. The Indus Basin has a vast groundwater aquifer that covers 16.2 million ha (hectare) [1]. Groundwater is pumped with the help of tube wells, currently numbered at 0.9 million and 87% of these are run on diesel, making groundwater pumping impractical during Pakistan's frequent periods of power shortfall [2]. Since downstream is likely to continue to increase, precise hydrological projections for the future supply are important. The water resources supplied by the Upper Indus Basin (UIB) are essential to millions of people and future changes in both demand and supply may have large impacts [3]. The UIB provides water for the world's largest continuous irrigation scheme through several large reservoirs (e.g. the Tarbela and Mangla dams. Water demands are high, primarily because of water consumption by irrigated agriculture, and hydropower generation. At the same time, the downstream part of the basin is characterized by very dry conditions, making it predominantly dependent on water supply from the upstream areas. The downstream demands exceed the supply and on an annual basis,

M. Amin (✉) · M. R. Khan · A. Jamil
Institute of Geo-Information & Earth Observation, Pir Mehr Ali Shah Arid Agriculture University, Rawalpindi, Pakistan
e-mail: m.amin@uaar.edu.pk

© Springer Nature Switzerland AG 2019

H. M. El-Askary et al. (eds.), *Advances in Remote Sensing and Geo Informatics Applications*,
Advances in Science, Technology & Innovation, https://doi.org/10.1007/978-3-030-01440-7_68

groundwater resources are depleted by an estimated 31 km^3, which makes the Indus basin aquifer the most overstressed aquifer in the world. According to recent studies the Himalayan glaciers will continue to retreat over the next 50 years and beyond because of climate change [4]. This will cause reduction of glacial mass, erratic snow patterns, unpredictable rainfall patterns, natural disasters and affected flow patterns in the Himalayan Rivers. The Indus River flows are greatly dependent on glacial and snowmelt (jointly termed melt water) and hence all the riparian's will face the impact of climate change in the future [5]. Monitoring groundwater using conventional in situ geophysical methods, i.e. resistivity survey demands extensive efforts, time, and cost. These methods further limit the data applicability and reliability to generalize on a regional scale due to lesser spatial extent and insufficiency for interpolation. Remote Sensing and GIS technology is not only capable of quantitative but also qualitative water research [6] (Fig. 1).

2 Study Area

The Indus basin extent ranges Himalayan mountains in the north and stretches to the alluvial fields of Sindh province and streams out into the Arabian sea. The potential groundwater zones where utilization or abstraction is in excess lies in Punjab province plains popularly known as 'Doabs' that cover the area lying in between the adjacent 5 rivers Indus, Jhelum, Chenab, Ravi and Sutlej. The geographic extent of Punjab plains starts from 29.04°N to 34.2°N and 70.5°E to 75.4°E.

3 Data and Methods

In 2002, GRACE satellite provided opportunity to water managers globally to accurately estimate groundwater changes over the years at the regional scale. For regions of 200,000 km^2 or more, GRACE can monitor changes in total water storage with an accuracy of 1.5 cm equivalent water thickness [7]. GRACE has the major advantage of sensing water stored at all levels, including groundwater. Unlike radars and radiometers, it is not limited to measurement of atmospheric and near-surface phenomena. In this study, we downloaded GRACE satellite product GRC Tellus JPL RL05 for the period 2010–2015. Each monthly GRC Tellus grid represents the surface mass deviation for that month relative to the baseline average over Jan 2004 to Dec 2009. A glacial isostatic adjustment (GIA) correction was applied based on the model from Geruo et al. [8]. A descripting filter was applied to the data to minimize the effect of correlated errors whose telltale signal are N-S stripes in GRACE monthly maps. A 300 km wide Gaussian filter was also applied to the data. All reported data are anomalies relative to the 2004.0–2009.999 time-mean baseline. A scaling factor of 1.26 was used in this study to recover the damped signals due to filtering. The soil moisture content (SMC), surface runoff (SR) data, canopy water storage (CWS) were derived

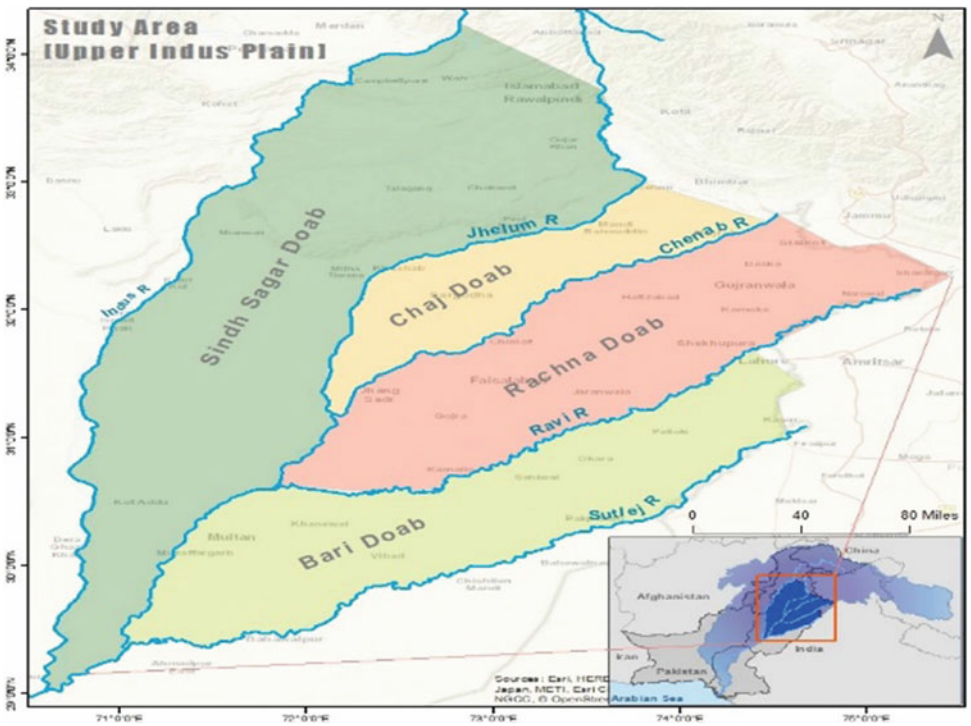

Fig. 1 Location map of upper Indus Plains, Punjab

from Global Land Data Assimilation System (GLDAS) land surface model (NOAH, CLM). The previous studies on the same area incorporated only two hydrological components and neglected canopy water storage. The GLDAS-Noah model provided soil moisture content in 4 distinct layers ranging from 0–10 cm, 10–40 cm, 40–100, and 100–200 cm. Therefore, all the layers data were stacked in ArcGIS environment to calculate cumulative soil moisture content. The spatial resolution of GLDAS-NOAH (1 * 1 Degree) was used so to match the pixel size of GRACE TWS data. The Noah model was preferred over CLM, VIC, Mosaic models because of greater accuracy in the Indus basin with slightly better precision.

3.1 Calculation of Gws

Derived outputs were added to calculate 'surface water storage' that was subtracted from TWS and thus GWS values obtained which was further plotted on graph for trend analysis and rates of variations were calculated. The areas which were below the mean value were highlighted as groundwater stressed areas. The GWS GRC Tellus JPL RL05 data units are centimeters of equivalent height of water. Therefore, it was converted to millimeters to be comparable to the rest of hydrological components. The used equation for the calculation of GWS is as below:

$$\mathrm{GWS} = \mathrm{SR} + \mathrm{SMC} + \mathrm{CWS}$$

GWS = Groundwater Storage (water equivalent height in mm)
SR = Surface runoff (kg/m^2)
SMC = Soil Moisture Content (kg/m^2)
CWS = Canopy Water Storage (kg/m^2)

The GWS was again converted to its native units (cm) for generation of maps.

3.2 Calculation of Annual Gws Variations

GWS data obtained by the previous step for each month from 2010 to 2015 (except for the missing 15 months due to data outages). The annual GWS mean raster for each year was generated at spatial resolution of 1 * 1 degrees. The annual mean of each year was then converted into GWS variations by subtracting the preceding year GWS raster with subsequent year. The equation for the GWS variation calculation is as below:

$$\Delta\mathrm{GWS\,T} \times 2 = \mathrm{Annual\ Mean\ GWS\,T} \times 2 - \mathrm{Annual\ Mean\ GWS\,T} \times 1$$

ΔGWS = GWS variation,
Annual Mean T × 2 = Proceeding Year GWS annual mean raster
Annual Mean T × 1 = Subsequent Year GWS annual mean raster

The raster's of groundwater storage variations were then downscaled to 0.0154 * 0.154 m using geo-statistical method Kriging by converting raster's into point data and applying 'Kriging' interpolation technique that tends to reduce variance (Fig. 2).

4 Results and Discussion

The mean annual groundwater storage variation data of UIP for the year 2011 showed almost similar trend for all UIP doabs with varying intensity. Bari doab showed an increase of 1.71 cm, Rachna 1.36 cm, Chaj 1.58 and Thal 0.50, respectively. Therefore, an overall increase of 5.15 cm was observed for UIP. The recharge impact could be attributed to heavy flooding in the subsequent year 2010 and a greater recharge rate due to precipitation greater than the groundwater abstraction rate. The decrease in groundwater equivalent height compared to subsequent year could be because of higher abstraction rate as compared to that of recharge. The UIP mean groundwater storage variation data for 2013 showed negative change in all UIP doabs.

Bari doab showed a decrease of 4.1 cm, Rachna 3.5 cm, Chaj 2.9 and Thal 2.6 cm respectively. In terms of volume, 17.78 km^3 of decrease in groundwater was observed for UIP. The decrease in groundwater equivalent height compared to subsequent year could be because of higher abstraction rate as compared to recharge rate.

The mean groundwater storage variation data of UIP for 2014 showed a notable rise in water equivalent height of all doabs. That is of course attributed to a heavy flooding in this year across UIP that inundated massive area of Bari doab. Bari doab showed a decrease of 4.1 cm, Rachna 3.5 cm, Chaj 2.9 and Thal 2.6 cm respectively. In terms of volume, 17.73 km^3 of increase in groundwater was observed for UIP that almost recompensed the deficit of 2013. The increase in groundwater equivalent height compared to subsequent year was due to extreme rainfalls during 2014 (Table 1).

The mean GWS variation data of UIP for year 2015 showed positive change in all doabs of UIP except for Thal doab. Bari doab showed an increase of 1.2 cm, Rachna 1.4 cm, Chaj 2.2 whereas Thal a decrease of 2.6 cm respectively. In terms of volume, 6.09 km^3 of increase in groundwater was observed for UIP. The increase in groundwater equivalent height compared to subsequent year could because of higher amounts of rainfall recorded in 2015.

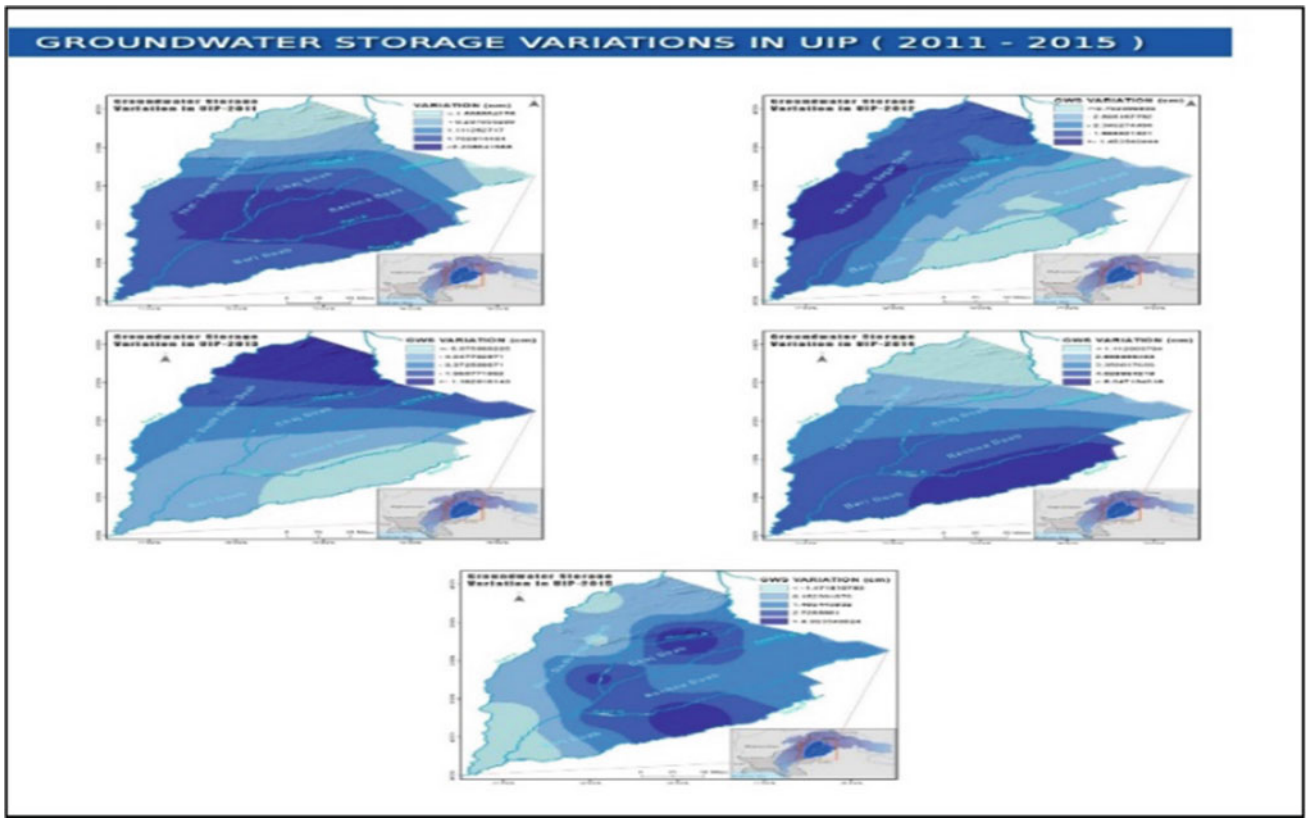

Fig. 2 Showing GWS variations in UIP for 2011–2015

Table 1 Groundwater storage variation (cm) for different UIP doabs (2011–2015)

	Groundwater storage variation (cm)				
Year	Bari	Rechna	Chaj	Thal	Net change (cm)
2011	1.71	1.36	1.58	0.50	5.15
2012	−3.10	−3.12	−3.00	−1.63	−10.85
2013	−4.1	−3.5	−2.9	−2.6	−13.09
2014	4.1	3.5	2.9	2.6	13.06
2015	1.2	1.4	2.2	−0.2	4.48
Total	−0.23	−0.37	0.73	−1.38	−1.25

The mean GWS variation UIP data for 2011–2015 showed a decrease in all doabs of UIP except for Chaj doab. Bari doab showed a decrease of 0.23 cm, Rachna 0.37 cm, Chaj an increase of 0.73 cm whereas Thal a decrease of 1.38 cm, respectively (Fig. 3).

Interestingly, if we breakdown the data in pre and post flooding time zones, from 2011 to 2013 there was a neat decrease of 18.79 cm (0.6 ft). A high jump of 13.06 cm in 2014 has replenished the groundwater aquifer of UIP to a great extent. However, the proportion increase never remained same in 2015 and a net increase of 4.48 cm was observed. The net groundwater storage variation was divided into three equal interval zones I, II and III indicating areas of high, medium and low groundwater stress respectively. Based on the findings of the study, groundwater pricing policy must be adapted as there exists no market for groundwater and ownership laws also need to be passed and implemented to curb excessive groundwater mining. A zone wise management concept must be introduced in groundwater management. Future studies should focus on formulating a credible scale/index to calculate water stress in a watershed (Table 2).

For agricultural purposes, it must be ascertained that groundwater is exploited as per crop water requirement of respective crop. Water delineation plants are the need of the hour in order to achieve water security in Pakistan.

The water reuse by industries and agriculture could be the possible solution to meet future water, agricultural and

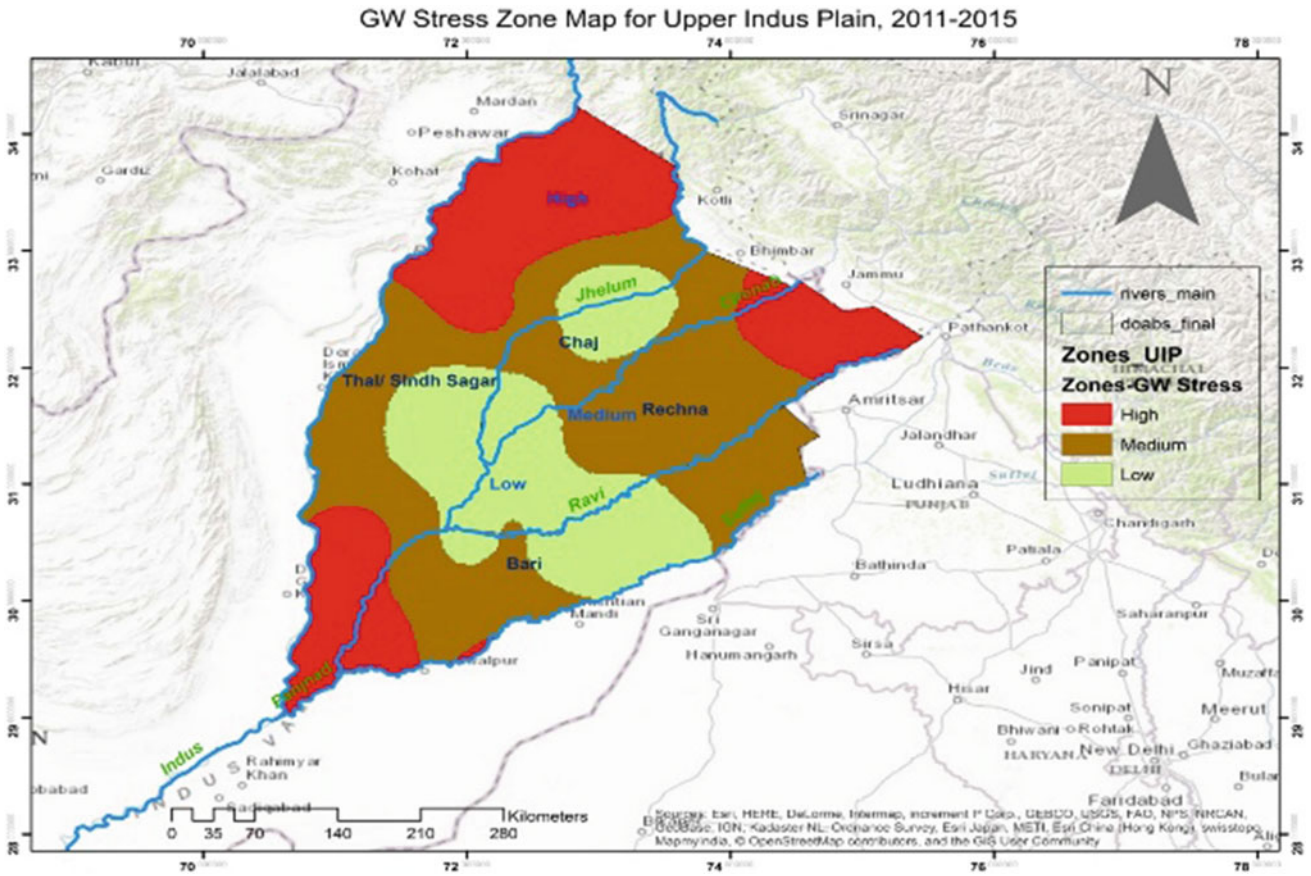

Fig. 3 Spatio-temporal GWS variations in UIP

Table 2 Groundwater storage stress characteristics for the UIP doabs

Doab	Area (km^2)	Cumulative GWS variation (cm)	Volume change (km^3)	Variation rate (cm/yr)	Variation rate (km^3/yr)
Bari	30986.6	−0.23	−0.070	−0.05	−0.014
Rachna	31177.6	−0.37	−0.11	−0.07	−0.022
Chaj	13771.2	0.73	0.09	0.15	0.019
Thal	59867.0	−1.38	−0.82	−0.28	−0.16
Total	135802.4	−1.3	−1.70	−0.25	−0.34

Table 3 Zone wise area distribution of UIP doabs

Zone wise area distribution of UIP doabs							
Doab	Area (km^2)	Zone 1 area (km^2)	Zone 1 area (%)	Zone 2 area (km^2)	Zone 2 area (%)	Zone 3 area (km^2)	Zone 3 area (%)
Bari	30986.6	3528.9	11.39	17179.8	55.44	10095.8	32.58
Rachna	31177.6	6831.2	21.91	16105.5	51.65	8150.3	26.14
Chaj	13771.2	773.47	5.62	6850.1	49.74	6116.5	44.42
Thal	59867.0	29097.8	48.60	20050.8	33.49	10438.4	17.44
Total	135802.4	40231.37	29.62	60186.2	44.31	34801	25.63

Industrial needs. Water desalination plants could play a role of game changer in such crucial stage where the country is on the brink of becoming water bankrupt.

In order to predict future water availability-demand scenarios, the socioeconomic digital data repository or geo-database generation is also required to have a better insight (Table 3).

References

1. Iqbal, N., Hossain, F., Lee, H., Akhter, G.: Satellite gravimetric estimation of groundwater storage variations over Indus Basin in Pakistan. IEEE J. Sel. Top Appl. Earth Obs. Remote Sens. **9**(8), 3524–3534 (2016). https://doi.org/10.1109/JSTARS.2016.2574378
2. Ashraf, A., Ahmad, Z.: Regional groundwater flow modelling of Upper Chaj Doab of Indus Basin, Pakistan using finite element model (Feflow) and geoinformatics. Geophys. J. Int. **173**(1), 17–24 (2008). https://doi.org/10.1111/j.1365-246X.2007.03708.x
3. Shakeel, M., Huk, S., Mirza, M.I., Ahmad, S. Monitoring water-logging and surface salinity using satellite remote sensing data. In: International Geoscience and Remote Sensing Symposium, 1993. IGARSS'93. Better Understanding of Earth Environment, vol. 4, p. 2029. https://doi.org/10.1109/igarss.1993.322360 (1993)
4. Ali, I., Shukla, A. A knowledge based approach for assessing debris cover dynamics and its linkages to glacier recession. In: 2015 IEEE International Geoscience and Remote Sensing Symposium (IGARSS), pp. 2072–2075. https://doi.org/10.1109/igarss.2015.7326209 (2015)
5. Kwak, Y., Park, J., Fukami, K.: Near real-time flood volume estimation from MODIS time-series imagery in the Indus River Basin. IEEE J. Sel. Top Appl. Earth Obs. Remote Sens. **7**(2), 578–586 (2014). https://doi.org/10.1109/JSTARS.2013.2284607
6. Barros, A.P.: Water for food production—Opportunities for sustainable land-water management using remote sensing. In: IGARSS 2008—2008 IEEE International Geoscience and Remote Sensing Symposium, vol 4, IV-271–IV-274. https://doi.org/10.1109/igarss.2008.4779710 (2008)
7. Chambers, D.P.: Calculating trends from GRACE in the presence of large changes in continental ice storage and ocean mass. Geophys. J. Int. **176**(2), 415–419 (2009). https://doi.org/10.1111/j.1365-246X.2008.04012.x
8. Geruo, A., Wahr, J., Zhong, S.: Computations of the viscoelastic response of a 3-D compressible Earth to surface loading: an application to Glacial Isostatic adjustment in Antarctica and Canada. Geophys J Int. **192**(2), 557–572. https://doi.org/10.1093/gji/ggs030 (2013)

Groundwater Productivity Potential Mapping Using Logistic Regression and Boosted Tree Models: The Case of Okcheon City in Korea

Saro Lee, Chang-Wook Lee, and Jeong-Cheon Kim

Abstract

This study analyzed Groundwater Productivity Potential (GPP) using different models in a geographic information system (GIS) in Okcheon area, Korea. These models used the relationship between groundwater-productivity data, including specific capacity (SPC) and transmissivity (T), and its related hydrogeological factors. Data about related factors, including topography, lineament, geology, forest and soil were constructed to a spatial database. Additionally, T and SPC data were collected from 86 well locations. Then, GPP were mapped using the Logistic Regression (LR) and Boosted Tree Regression (BT) models. The resulting GPP maps were validated using Area Under Curve (AUC) analysis with the well data. The GPP maps using the LR and BT models had accuracies of 85.04 and 81.66% with T value, respectively. And the GPP maps using the LR and BT models had accuracies of 82.22 and 81.53% with SPC value, respectively. These results indicate that LR and BT models can be useful for GPP mapping.

Keywords

Groundwater potential • GIS • Logistic regression • Boosted tree • Korea

1 Introduction

Groundwater is one of the important natural resources used in agriculture, industry and public water supply. In Korea, the use of groundwater increased by more than 225% between 1994 and 2014, and the current national supply of groundwater no longer meets the needs of society. Therefore, reliable analytical models predicting locations of groundwater are needed for efficient management use of groundwater. So, the purpose of the study was to develop and apply the GIS based Groundwater Productivity Potential (GPP) model using Logistic Regression (LR) and Boosted Tree (BT) models in the Okcheon country of Korea. The GPP is defined as the probability of finding out groundwater in an area. Especially, the study mainly used topographical factors among various others, because groundwater is most affected by such factors. Recently, many GPP mapping studies that have been published used new models such as Frequency Ratio (FR) [1], Artificial Neural Network (ANN) [2], Random Forest (RF) [3], Logistic Regression (LR) [4], Boosted Regression Tree (BTR) [5] and Support Vector Machine (SVM) [2].

For the GPP mapping, T (Transmissivity) and SPC (specific capacity) point data were obtained and randomly classified as either training data (50%) or validation data (50%). Geology, topography, soil texture, and land cover data were combined into a spatial database. Hydrogeological factors, including slope, aspect, slope gradient, relative slope position, hydraulic slope, valley depth, topographic wetness index (TWI), slope length (LS) factor, convergence index, depth from groundwater, distance from lineament, distance from channel network, and so forth, were extracted from spatial databases. Then T and SPC data were selected (T values ≥ 2.6, SPC values ≥ 4.875) as training data for the three models. Finally, the GPP maps were assessed using AUC techniques.

S. Lee (✉)
Korea Institute of Geoscience and Mineral Resources (KIGAM), 124 Gwahang-no, Yuseong-gu, Daejeon, 305-350, South Korea
e-mail: leesaro@kigam.re.kr

C.-W. Lee
Kangwon National University, 1 Kangwondaehak-Gil, Chuncheon-si, Gangwon-Do 200-701, South Korea

J.-C. Kim
National Institute of Ecology (NIE), 1210 Geumgang-Ro, Maseo-Myeon, Seocheon-gun, Chungcheongnam-Do 33657, South Korea

© Springer Nature Switzerland AG 2019

H. M. El-Askary et al. (eds.), *Advances in Remote Sensing and Geo Informatics Applications*, Advances in Science, Technology & Innovation, https://doi.org/10.1007/978-3-030-01440-7_69

2 Data and Method

The study area is the Okcheon country of South Korea. This area lies between 36°10′N and 36°26′N latitude and 127°29′E and 127°53′E longitude and covers 537.06 km^2. Since groundwater is associated with drinking and irrigation water supplied to communities, it is very meaningful to estimate GPP.

This study using LR and BT models are based on the relationship between groundwater productivity data (SPC and T) and hydrogeological factors (Table 1). To calculate groundwater productivity, SPC and T are set as dependent variables and various hydrogeological factors are set as independent variables. SPC is the amount of water that can be produced per unit drawdown. Also, T is the rate of flow under a unit hydraulic gradient through a unit width of aquifer of given saturated thickness. The groundwater productivities respond to a total of 86 cells (each 43 cells (including the T data of ≥ 2.6 m^2/d, SPC ≥ 4.875 m^3/d/m) for training and 43 cells for validation.

The LR model is to help find the best expression to describe the relationship between dependent variables and various independent variables. The BT model is a general calculation method of stochastic gradient amplification. Ultimately, this approach allows fitting the best estimate of the observed values to yield better results. In summary, the GPP mapping was performed as follows: (1) geospatial data were constructed and the related factors were extracted or calculated, (2) a geospatial database was founded with a grid, (3) the GPP assessment was conducted using the LR and BT models, and (4) the validation of the potential map was achieved using AUC.

3 Results

The GPP maps using the LR and BT models results are shown in Fig. 1. The AUC was recalculated since the total area used the well data that had not been used for the training the models. From the validation, the LR and BT models produced AUC values of 0.8113 and 0.8372 by T value, respectively. Also, the validation of the GPP maps, the LR and BT models produced AUC values of 0.8024 and 0.8080 by SPC value, respectively.

4 Discussion and Conclusion

This study applied and assessed the LR (statistics) and BT (data mining) models for groundwater potential. As a result, the accuracies were computed as 85.04 and 81.66% for LR and BT models with T value, 82.22 and 81.53% for LR and BT models with SPC value, respectively. Therefore, it can be concluded that LR with T value had the best performance. In addition, other models using T or SPC values in this study also showed a good accuracy of over 80% when predicting spatially groundwater potential.

From the result of calculated LR models table or predictor importance of BT model, in order of influence, the relationships between well data and the examined factors were

Table 1 Data layers of the study area

Original data	Factors	Data type	Scale
Yield	T[m^2/d/m], SPC [m^3/d/m]	Point	
Topographical map[a]	Slope [°], Aspect, Relative slope position Plan curvature, Topographic Wetness Index (TWI), Slope Length factor (LS-factor), Convergence index, Lineament density, Drainage basin, Hydraulic slope [m], Valley depth [m], Depth to groundwater[m]	Grid	1:5000
Geological map[b]	Hydrogeology	Polygon	1:50,000
Soil map[c]	Soil texture	Polygon	1:25,000
Land cover map[d]	Land cover, Distance from fault [m], Distance from lineament [m], Distance from channel network [m]	Polygon	1:5000

[a]Topographical factors were extracted by the National Geographic Information Institute (NGII)
[b]The geology map offered by the Ministry of Land, Transport and Maritime Affairs (MLTM)
[c]The soil map was offered by the National Institute of Agricultural Science and Technology
[d]The land cover map was offered by the Korean Ministry of Environment

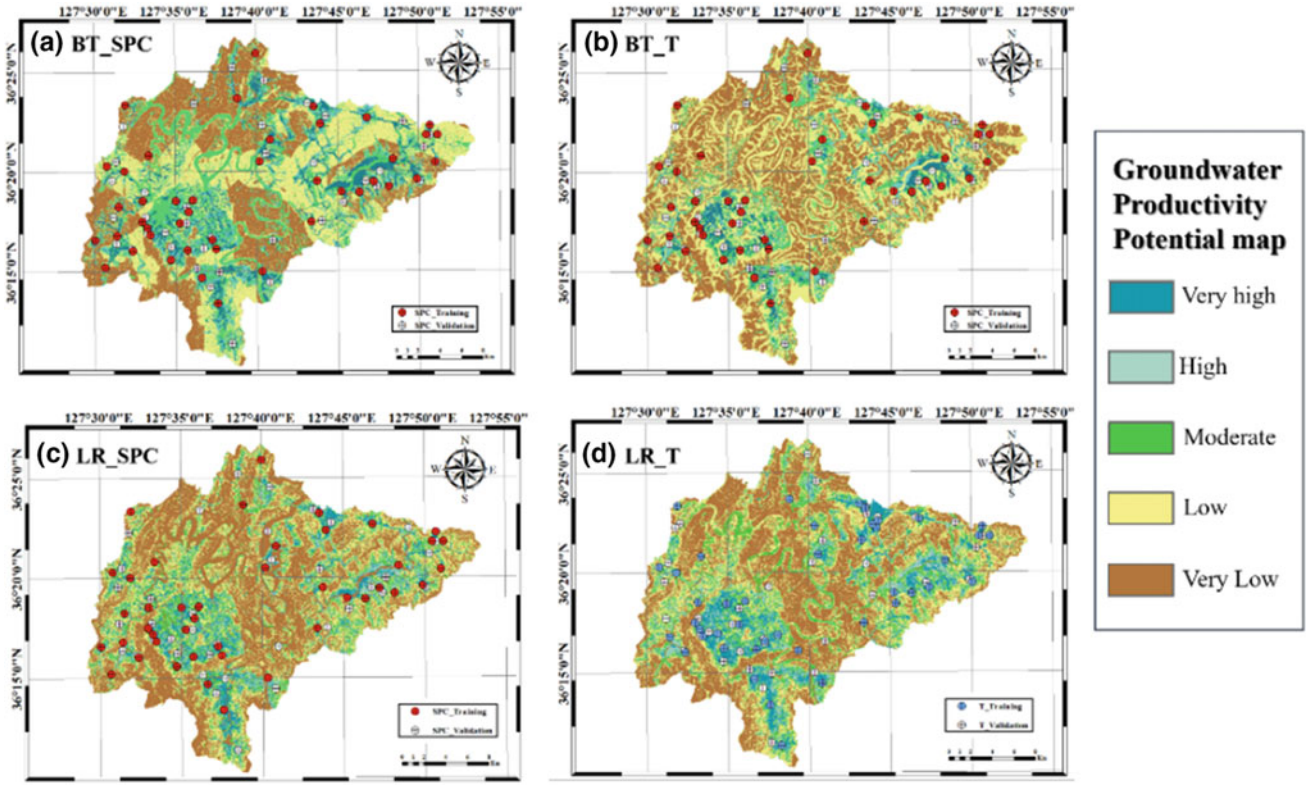

Fig. 1 GPP maps using logistic regression (LR) and boosted tree (BT) models

as follows. With gentle slope & hydraulic slope, lower relative slope position, and shorter slope length, GPP was estimated to be higher. However, with steeper slope & hydraulic slope, higher relative slope position, and longer slope length, GPP was estimated to be higher because rainfall running off in the upper region is accumulated in the lower region and influences the aquifer. On the other hand, the distance from the fault, distance from lineament, distance from channel network showed a negative correlation with GPP. The closer the channel is, the greater the GPP will be because the rivers have gotten water from the underground.

The proposed GPP mapping method can be applied to groundwater use planning and management, such as regional groundwater development planning, water system control based on systematic and objective planning. Finally, it can be deduced that new models of more recently developed statistics and data mining models could provide better results in future studies.

References

1. Jothibasu, A., Anbazhagan, S.: Spatial mapping of groundwater potential in Ponnaiyar River basin using probabilistic-based frequency ratio model. Model. Earth Syst. Environ. **3**(1), 33 (2017)
2. Lee, S., Hong, S.-M., & Jung, H.-S.: GIS-based groundwater potential mapping using artificial neural network and support vector machine models: the case of Boryeong city in Korea. Geocarto. Int., 1–15 (2017)
3. Rahmati, O., Pourghasemi, H.R., Melesse, A.M.: Application of GIS-based data driven random forest and maximum entropy models for groundwater potential mapping: a case study at Mehran Region, Iran. Catena **137**, 360–372 (2016)
4. Park, S., Hamm, S.-Y., Jeon, H.-T., Kim, J.: Evaluation of logistic regression and multivariate adaptive regression spline models for groundwater potential mapping using R and GIS. Sustainability **9** (7), 1157 (2017)
5. Mousavi, S.M., Golkarian, A., Naghibi, S.A., Kalantar, B., Pradhan, B.: GIS-based groundwater spring potential mapping using data mining boosted regression tree and probabilistic frequency ratio models in Iran. AIMS Geosci. **3**(1), 91–115 (2017)

Radar Space Measurements of the Deforming Trends at Northern Greece Resulting from Underground Water Activity

Nikos Svigkas, Ioannis Papoutsis, Constantinos Loupasakis, Paraskevas Tsangaratos, Anastasia Kiratzi, and Charalambos (Haris) Kontoes

Abstract

Two case studies, in northern Greece, that monitor surface deformation were presented. Both are related to aquifer overexploitation and its impact on the earth's surface. Using the archive of ERS and ENVISAT satellites, radar time series were performed applying the PS and SBAS techniques. For the justification of the remote sensing results and the interpretation of the physical mechanism behind the detected deformation, in situ data were also exploited. The areas of focus are: the village of Kalochori, a significant industrial hub, and the Anthemountas basin, an active tectonic region, both located in the vicinity of the metropolitan area of Thessaloniki. The Kalochori case indicated that the aquifer activity is directly affecting the surface movements. A low underground water level in the 90's caused a subsidence of more than 20 mm/year and the subsequent recharge of the aquifers in the 2000s caused a surface rebound with a rate of up to +12 mm/year. Regarding Anthemountas basin, the subsidence has a maximum rate of −18 mm/year in the 90's, and the deformation appears to exist over the whole basin. In conclusion both cases reveal that northern Greece is suffering from a hazard imposed by anthropogenic causes.

Keywords

InSAR time-series • PS • SBAS • Aquifer overexploitation

N. Svigkas (✉) · A. Kiratzi
Dept of Geophysics, Aristotle University of Thessaloniki, 54124 Thessaloniki, Greece
e-mail: svigkas@geo.auth.gr

N. Svigkas · I. Papoutsis · C. (Haris)Kontoes
National Observatory of Athens, Metaxa & Vas. Pavlou, 15236 Athens, Greece

C. Loupasakis · P. Tsangaratos
National Technical University of Athens, Heroon Polytechniou 9, 15780 Athens, Greece

1 Introduction

The case studies presented are shown in figure (Fig. 1a). The broader area of interest is at the proximity of the city of Thessaloniki, the second largest city in Greece, besides Athens, the capital. The tectonic regime of the broader area is characterized by extensional tectonics (approximately N-S) [1, and references therein] and the main part of seismicity is concentrated to the northeast of the city (Fig. 1b). During the instrumental era the seismicity in both study areas is sparse and of moderate magnitude (Fig. 1b).

The Kalochori village, the first case study presented here, is located western of Thessaloniki. Over the previous years, many unauthorized drills were established—a result of the industrial development that occurred in the area. In the 50's, the aquifers used to be artesian; however, this changed in the next decades, when a lowering of the piezometric surface [2] was observed. The area was under a subsiding trend during the 90's [2–4], something that caused infrastructure damage. This subsidence was in accordance with the lowering of the underground water level and was attributed to aquifer over-pumping [2, 4].

The second area of focus, the Anthemountas basin, is located a few kilometers from the center of Thessaloniki and was subjected to a rapid industrial development. The recent years have been characterized by the establishment of various industries and a significant increase in the population of the basin. The water demand caused the aquifer overexploitation that reduced the groundwater level in the 90's [5]. Anthemountas hosts the longest known tectonic structures close to the metropolitan area of Thessaloniki (structures F1 and F2, Fig. 1b). F2 is considered to be active. Moreover, close to the coastal front lies the Thessaloniki International Airport (Fig. 1a).

The goal of this study was to present a summary of previous and new on-going works held at northern Greece related to groundwater activity and thus highlighting the environmental effects that arise for the area. More

© Springer Nature Switzerland AG 2019

H. M. El-Askary et al. (eds.), *Advances in Remote Sensing and Geo Informatics Applications*, Advances in Science, Technology & Innovation, https://doi.org/10.1007/978-3-030-01440-7_70

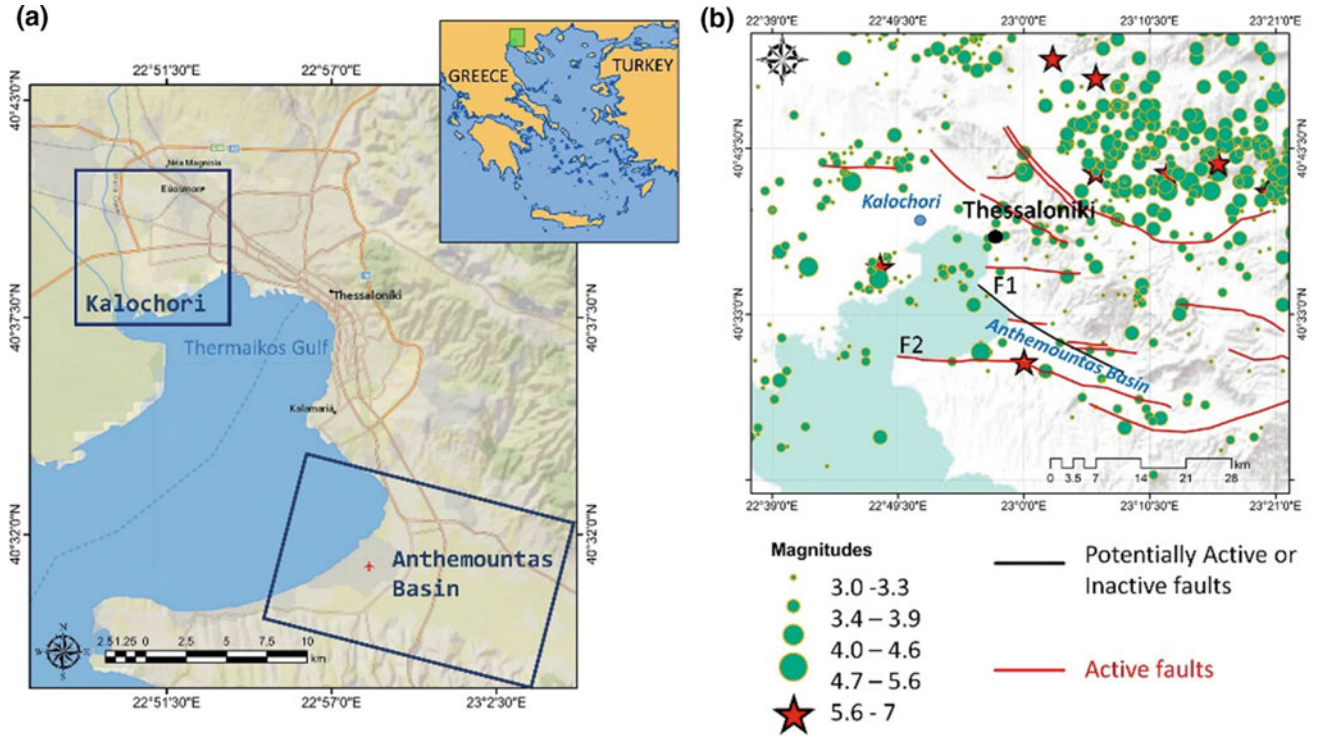

Fig. 1 **a** Map showing the regions of the case studies presented: Kalochori village (Sect. 3.1) and Anthemountas basin (Sect. 3.2). Upper right inset map indicates the study areas (green rectangle) in the Greek territory. **b** Seismicity (green circles) at the broader area and active faults (red lines). The red asterisks denote strong (M.6) earthquakes. (Maps are in the World Geodetic System 1984—WGS84)

specifically, the aim was to detect and measure the surface deformation, analyze its extent and finally identify the main driving mechanism, both for scientific merit but also for defining whether the cause is natural or anthropogenic.

2 Radar Satellite Methods & Data

SAR interferometry was the basic tool of this study and more specifically the Persistent Scatterer Interferometry (PS) and Small Baseline Subset (SBAS) time series methods. A single Differential interferograms was created by combining two radar images and showing the displacement that occurred during the two passes of a radar satellite. Using the PS and SBAS methods, the surface deformation velocities that occurred during numerous years at the areas of study, can be measured. Both techniques make use of multiple number of interferograms. In the case of PS, one radar image was selected to participate in all images' combinations. In the case of SBAS, a network of all the radar images was created based on specific criteria. In general, SBAS is suitable for tectonic studies and PS is more convenient for monitoring urban areas.

Satellite imagery from the European Space Agency (ESA) was exploited: the two-decade archive of ERS and EVISAT. For the topographic corrections, the SRTM DEM was used, orbital data were collected from Delft University of Technology and VOR data from ESA. SARscape and StaMPS [6] software were used to perform SAR time-series. In the case of StaMPS, the focus on the raw images was achieved with the ROI_PAC code [7] and the interferogram generation with DORIS [8].

3 Results

3.1 The Kalochori Case Study

In Kalochori, during the late 90's the underground water level was 40 m below the surface, while in 2012 there was a recovery to 1–8 m [2]. After the detected subsidence of the past (90's) [2, 3], the recent remote sensing results show that the subsidence reversed to uplift [4], after 2000 (Fig. 2a). This is in accordance with the uprising of the underground water level at the area. A comparison between the surface deformation of the two decades as a whole and a drill's water level (Fig. 2b) showed that the aquifer's level change was directly affecting the surface by causing a subsequent change in the deformation trend.

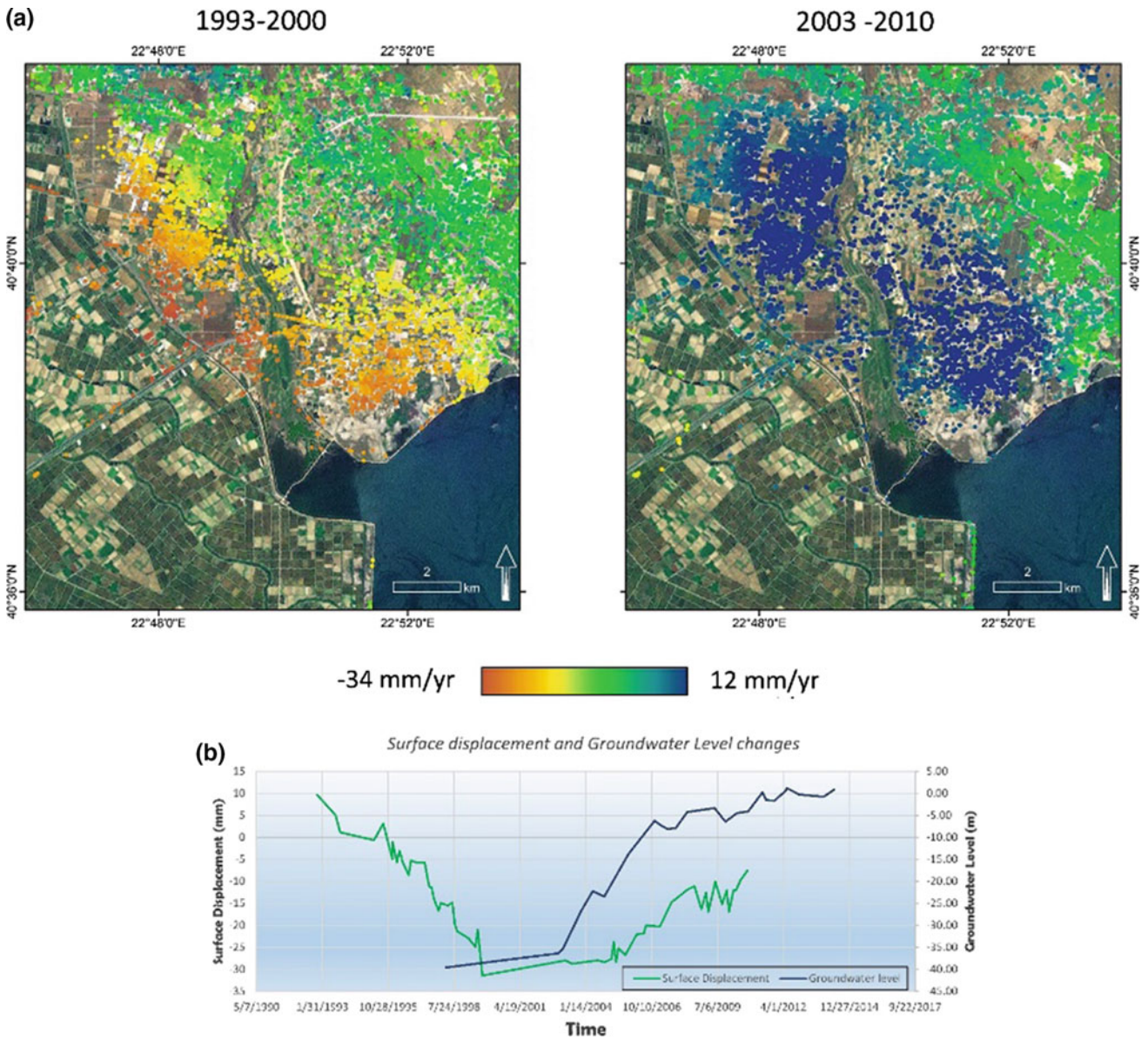

Fig. 2 **a** Deformation pattern (velocities) during the ERS (left) and ENVISAT (right) eras. During 1993–2000 the subsidence was more than 20 mm/year whereas, the detected uplifting trend of the 00's was up to 12 mm/year. **b** Graph showing the underground water level measurements at a drill of the study area (blue line) together with the temporal evolution of surface deformation (green line) at the specific drill site (data from [4]) (Maps are in the World Geodetic System 1984 - WGS84)

3.2 The Anthemountas Case Study

The Anthemountas basin (Fig. 1) hosts a number of critical facilities, such as the Thessaloniki International Airport (Fig. 1a) and many densely populated and rapidly developing suburbs. The two fault segments F1 and F2 are both optimally oriented to the present N-S extensional stress field. Previous studies showed that the area was subsiding in the 90's [3, 5] due to acquirer overexploitation [5]. SBAS surface deformation results of this study for the 90's, indicated a maximum subsidence of −18 mm/year, in accordance with [3]. It was presented here (Fig. 3) and for the first time, that not only were the edges and the forefront of the basin deforming, but the subsidence also occurred throughout the entire basin to the far East.

4 Conclusion

Two case studies were presented here for the area of northern Greece. In the case of Kalochori, the comparison of in situ data and remote sensing results fully agree and

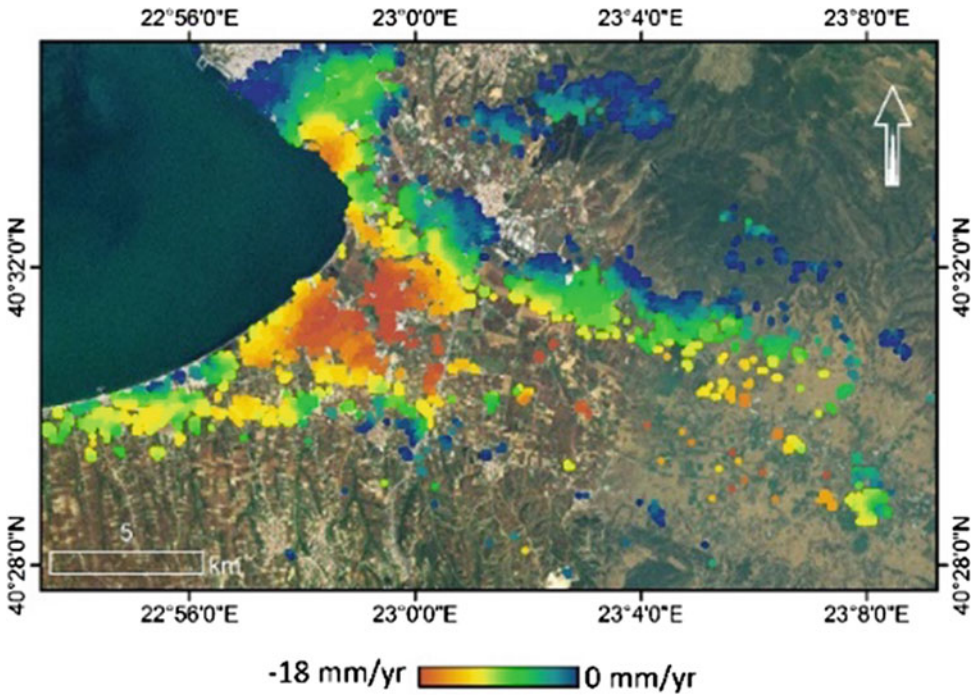

Fig. 3 SBAS velocity result from SARscape using the ERS satellites for Anthemountas basin. (Map is in the World Geodetic System 1984 -WGS84)

indicate a direct relationship between them. The low groundwater level during 1993–2000 caused a subsiding trend (more than 20 mm/year) and the 2003–2010 uplift (12 mm/year) was the surface response to the underground water recharge. It is notable that the time between the initiation of the water recharge and the initiation of the surface rebound there was a time-lag of 1.3–2 years.

During the monitoring period of the present study, Anthemountas was under a subsiding regime. The maximum detected value (−18 mm/year) was detected at the proximity of the Thessaloniki International Airport. This subsiding environment could cause infrastructure failures. Evidence from remote sensing presented in this study indicated that the displacement occurs over a broader area than previously believed. It is not known whether in Anthemountas the phenomenon stopped after the 90's.

Overall, this summary of studies in Northern Greece indicate that there are strongly deforming signals in the vicinity of Thessaloniki city caused by human intervention (i.e. acquirer over-pumping). A water management plan is suggested to avoid the continuation of the hazard in the years to come.

The type of study presented here is applicable to cases of surface deformation worldwide: (a) for the detection of areas that are not known to deform (b) for defining the type of deformation, its spatial extent and quantifying the magnitude of displacement and (c) by benefitting from additional data (in situ) the driving mechanism can be identified and in consequence the proper anti-measures can be taken.

Acknowledgements We thank ESA for the provision of the radar data (ESA-Greece AO project 1489OD/11-2003/72). EC for establishing the Center of Excellence BEYOND (GA 316,210) under FP7-REGPOT-2012-2013-1 providing support to this research. AK acknowledges support of the project HELPOS (MIS 5,002,697) (NSRF 2014-2020).

References

1. Kiratzi, A.: Mechanisms of earthquakes in Aegean. In: Encyclopedia of Earthquake Engineering, pp. 1–22. Springer, Berlin Heidelberg. https://doi.org/10.1007/978-3-642-36197-5_299-1 (2014)
2. Raspini, F., Loupasakis, C., Rozos, D., Adam, N., Moretti, S.: Ground subsidence phenomena in the delta municipality region (Northern Greece): geotechnical modeling and validation with persistent scatterer interferometry. Int. J. Appl. Earth Obs. Geoinf. **28**, 78–89 (2014)
3. Raucoules, D., Parcharidis, I., Feurer, D., Novali, F., Ferretti, A., Carnec, C., Lagios, E., Sakkas, V., Le Mouelic, S., Cooksley, G., Hosford, S.: Ground deformation detection of the greater area of Thessaloniki (Northern Greece) using radar interferometry techniques. Nat. Hazards Earth Syst. Sci. **8**, 779–788 (2008)
4. Svigkas, N., Papoutsis, I., Loupasakis, C., Tsangaratos, P., Kiratzi, A., Kontoes, H.: Land subsidence rebound detected via multitemporal InSAR and ground truth data in Kalochori and Sindos regions. Northern Greece. Eng Geol. (2016). https://doi.org/10.1016/j.enggeo.2016.05.017

5. Raspini, F., Loupasakis, C., Rozos, D., Moretti, S.: Advanced interpretation of land subsidence by validating multi-interferometric SAR data: the case study of Anthemountas basin (Northern Greece). Nat. Hazards Earth Syst. Sci. **13**, 2425–2440 (2013)
6. Hooper, A., Segall, P., Zebker, H.: Persistent scatterer interferometric synthetic aperture radar for crustal deformation analysis, with application to Volcán Alcedo. Galápagos. J. Geophys. Res. **112**, B07407 (2007). https://doi.org/10.1029/2006JB004763
7. Rosen, P., Hensley, S., Peltzer, G., Simons, M.: Updated repeat orbit interferometry package released. EOS Trans. AGU **85**(5), 47 (2004)
8. Kampes, B., Hanssen, R., Perski, Z.: Radar Interferometry with Public Domain Tools. In: Proceedings of Fringe 2003, Dec. 1–5, Frascati, Italy (2003)

Delineation of Groundwater Potential Zones for Hard Rock Region in Karnataka Using AHP and GIS

Mohit Aggarwal, Subbarayan Saravanan, J. Jacinth Jennifer, and D. Abijith

Abstract

The satellite based technology adopting the efficacy of Geographical Information System (GIS) plays a dynamic role in groundwater exploration, assessment and management. The current study investigated the demarcation of groundwater potential zones by integrating RS, GIS and Multi-Criteria Analysis for the hard rock terrain of Gundihalla watershed which lies in Bellary district of Karnataka, India. The thematic layers incorporated in this research includes the Geomorphology, Soil, Drainage Density, Lineament Density, Rainfall, and Slope. Saaty's Analytical Hierarchy Process was used to determine the weights and ranks of all the thematic layers and the significant classes within each layer. All the thematic layers were then integrated to create the groundwater potential zonation map for the study area. The resulting map was categorized into five different groundwater potential zones, viz., 'very good,' 'good,' 'moderate,' 'poor' and 'very poor.' The area coverage of these zones in the study region are: 263 km^2 (18.76%), 332.3 km^2 (23.7%), 327 km^2 (23.3%), 238 km^2 (17%) and 229 km^2 (16.3%) respectively.

Keywords

Groundwater potential zone • AHP • Hard rock basin • GIS • Remote sensing

1 Introduction

Groundwater is considered to be the most significant freshwater reserve in the world. In India, nearly 90% of the country residents depend on groundwater for their elementary needs. Perhaps, shortage and overuse of groundwater resources with improper planning prevails in India [1]. The term groundwater potential indicates the availability of groundwater in a region. Numerous conventional techniques have been used to provide statistics about the potential of groundwater in various localities. However, Remote sensing and GIS technology have become a vibrant tool in defining the groundwater potential zones [2].

There are no previous studies associated with the demarcation of potential groundwater resource in Gundihalla watershed. Therefore, the core objective of the present study focused on the demarcation of the Ground Water Potential (GWP) zones in Gundihalla watershed by combining AHP with RS and GIS techniques.

2 Study Area

Gundihalla watershed covers an area of 1401 km^2 in the Bellary district of Karnataka state in Southern India (Fig. 1). It lies between the latitude 15°27′10.14″ to 14°52′37.36″ N and longitude 76°26′3.30″ to 76°48′46.36″ E. The watershed is south facing and drains into Gundihalla River which is the main tributary of the river Krishna. The catchment is located in the Lower Tungabhadra river. The maximum and minimum temperatures of the area are 41 and 11 °C respectively with the average being 25.3 °C.

Six thematic layers of geomorphology, drainage density, slope, lineament density, soil, and rainfall were converted into a raster layer and were then integrated by weighted overlay analysis. The analysis incorporated the weights for each layer according to Saaty's AHP technique. In this technique, the nine points mentioned in the Saaty's scale were assigned to each map in accordance with the hierarchy of their impact on the groundwater potential assessment [3]. Groundwater potential zones were finally obtained as a resulting map by AHP method.

M. Aggarwal · S. Saravanan (✉) · J. Jacinth Jennifer · D. Abijith
National Institute of Technology, Tiruchirappalli, Tamil Nadu, India
e-mail: ssaravanan@nitt.edu

© Springer Nature Switzerland AG 2019

H. M. El-Askary et al. (eds.), *Advances in Remote Sensing and Geo Informatics Applications*, Advances in Science, Technology & Innovation, https://doi.org/10.1007/978-3-030-01440-7_71

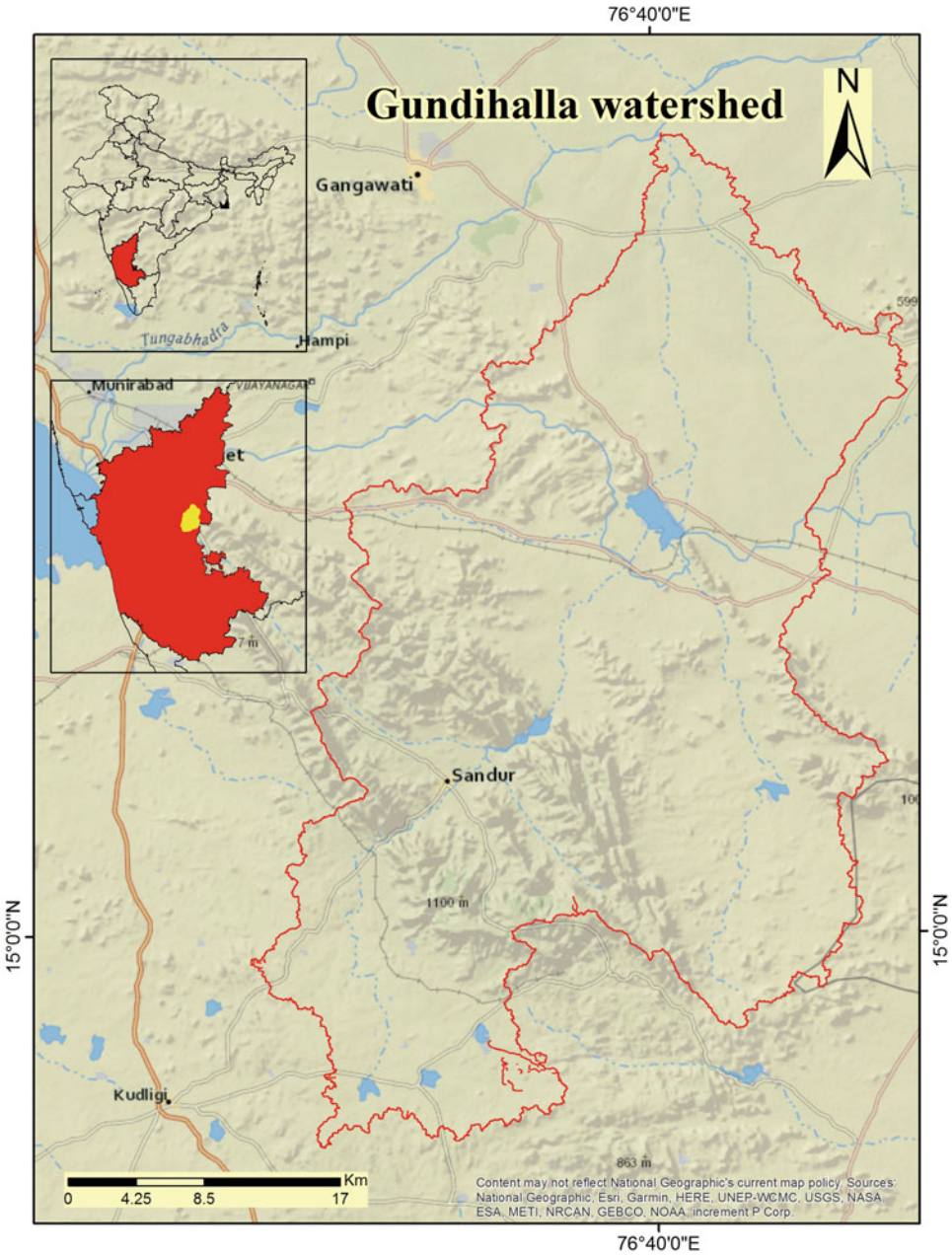

Fig. 1 Study area map of Gundihalla watershed, Karnataka, India

3 Results and Discussion

Suitable weightage were allotted to the thematic layers and their classes according to the Saaty's Analytical Hierarchy Process. Then the value of consistency ratio was calculated and came out to be 2%, knowing that it is claimed to be well if it is below the maximum limit of 10%. The value of the 'consistency ratio' confirmed the accuracy of the weights assigned to the layers and their classes. After the computation of the normal weightage for all the six thematic layers and the ranks of their classes, the layers were then integrated with one another using ArcGIS 10.2.1 software to delineate the groundwater potential map of the entire watershed as presented in Fig. 2.

The geomorphological study of the watershed was carried out since topography impacts the distribution of the groundwater. The Gundihalla watershed holds eight types of geomorphologic features, and it has been understood that a large portion of the district consists of pediplains, which have a good infiltration capacity when compared to structural and residual hills. The drainage pattern of the study area reflects the typical nature of the subsurface formation. The drainage density is defined as the total length of streams per unit area. High drainage density indicates the formation of springs in the lower order streams and eventually increasing its contribution and prevailing prominent base flow from the catchment; thus it complements the streams of different order thereby rejuvenating the main stream [4].

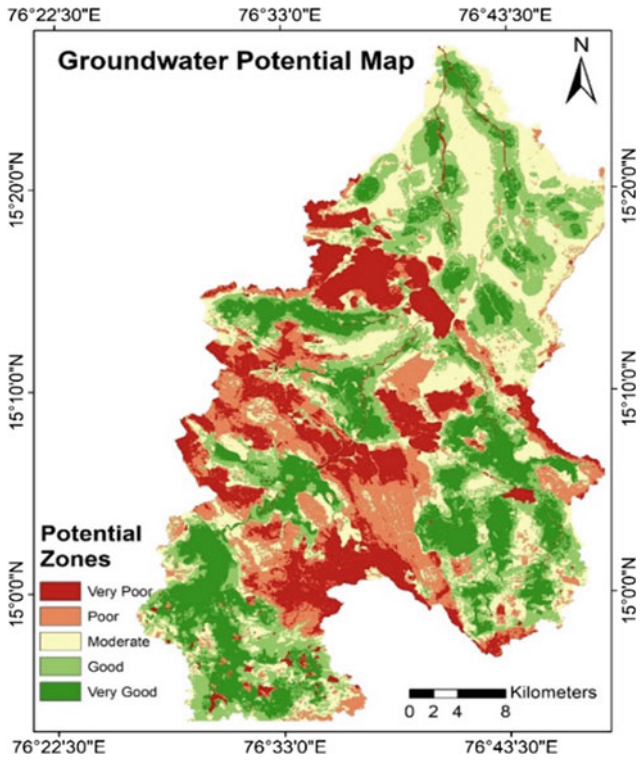

Fig. 2 Groundwater Potential map of the study area

The surface drainage density in the hilly terrains directly influences permeability, and hence a higher drainage density indicates greater permeability. Drainage density varies from 0.01 to 3.11 km/km^2 in the study area, thereby dividing the drainage density layer into five classes. Slopes have a strong hold on groundwater infiltration. The class possessing minimal slope range was given with the highest weight, it was due to the reason that the gentle slope surfaces have the capacity to give ample dwelling time for the surface runoff to percolate; however, the range having the maximal slope is given with the lowest rank due to the fairly high run-off which specifies poor groundwater availability. Rainfall is the key input to the recharge of a groundwater resource, as it regulates the volume of water that would infiltrate inside the surface. The area that receives the highest rainfall is assigned the highest rank. Lineaments also play a vital part in the groundwater prospect in hard rock terrains [5]. The lineament density varies from 0–1.88 km/km^2. The highest ranking was assigned to the lineament density with the highest interval, this is due to the fact that the groundwater potential prevails high near the high interval lineament zones. The study area consists of eleven soil classes based on their texture, namely clayey over sandy, clayey skeletal, coarse-loamy, fine, fine loamy, loamy, loamy-skeletal, dyke ridges, habitational mask, rock outcrops and water body mask. The penetration of water is highly restricted in the fine soil region as it consists of tiny clay particles and dyke ridges. The fine loamy soil is ranked very high due to its high porosity. Whereas clayey soils have a low infiltration rate due to their higher water holding capacity, and hence have been assigned the least values. Fine soil was dominant in the watershed. Based on the weightage of each parameters influencing the groundwater potential, the resultant grondwater potential zonation map was obtained from the weighted-overlay process in GIS environment.

4 Conclusion

This study has validated the efficacy of remote sensing and GIS techniques to be a great tool in the distinction of groundwater potential zones for Gundihalla watershed. Six thematic maps were assigned weights and ranks according to Saaty's Analytical Hierarchy process. The resulting map was divided into five zones namely: 'very good,' 'good,' 'moderate,' 'poor' and 'very poor' covering 18.76, 23.7, 23.3, 17, 16.3% of the study area, respectively. 'Very good' GWP zones cover the southern and eastern portions, which is mainly due to the presence of pediplains in that region. 'Moderate' zone are located in the northern side of the watershed; which is due to the high drainage density in the region. The region including structural hills fall in the 'poor' and 'very poor' zones. The data served well in validation of the results.

The resulting map will be of great help to the government authorities as well as the concerned planners in assessing the given watershed for groundwater exploration.

References

1. Agarwal, R., Garg, P.K.: Remote sensing and GIS-based groundwater potential & recharge zones mapping using multi-criteria decision-making technique. Water Resour. Manage **30**(1), 243–260 (2016)
2. Pinto, D., Shrestha, S., Babel, M.S., Ninsawat, S.: Delineation of groundwater potential zones in the Comoro watershed, Timor Leste using GIS, remote sensing, and analytic hierarchy process (AHP) technique. Appl. Water Sci. **7**(1), 503–519 (2017)
3. Saaty, T.L.: The analytic hierarchy process. McGraw-Hill, New York (1980)
4. Sahoo, S., Dhar, A., Kar, A.: Ram P: Grey analytic hierarchy process applied to effectiveness evaluation for groundwater potential zone delineation. Geocarto Int. **32**(11), 1188–1205 (2017)
5. Koch, M., Mather, P.M.: Lineament mapping for groundwater resource assessment: a comparison of digital Synthetic Aperture Radar (SAR) imagery and stereoscopic Large Format Camera (LFC) photographs in the Red Sea Hills, Sudan. Int. J. Remote Sens. **18**(7), 1465–1482 (1997)

Part IX
Coastal Management and Marine Environment

Evaluating and Predicting Changes Occuring on Coastal Borders of the Jeddah City Using Satellite Images

Hamdy Aboulela, Rashad Bantan, and Ramadan Zeineldin

Abstract

The current study highlighted the usefulness of satellite images in monitoring and predicting changes occurring on the shorelines through a bi-dimensional data based and situational based strategy. Three coastal areas of the Jeddah city were selected as Salman Bay, Sharm Abhar and Jeddah Port. For the data-based dimension, data collected through satellite images were used in the analysis covering the period 1972–2016. Four regression models were used to study the variation in the coastal borders of the study area. Predictions for the next 9 years (up to 2025) were carried out using the four Regression models. The results of the findings revealed that shrinkage has been witnessed in all areas under study. Another fact came to the limelight is the proximity of the objective results with expectations of the experts thus providing credence to the appropriateness of the used statistical models. For the situational based dimension, the effect of various anthropogenic activities and geo-environmental natural processes in the study area were identified. Based on the study findings, a continuous monitoring of the coastal areas is suggested along with maintaining a concrete database. The proposed techniques can be extended to study the coastal shrinkage and extension in other regions as well.

Keywords

Shoreline • Shrinkage • Prediction • Anthropogenic • Geo-environmental

1 Introduction

Monitoring and predicting changes in coastal borders are significant predictors to support improvement and safety of the environment. The western coastal zone margins of Saudi Arabia i.e., Red, Sea has resulted in land use changes by anthropogenic activities and due to the development of ongoing mitigation plans [1]. Therefore, the prediction statistical techniques for the future analysis rate of coastal borders change of the study area are suitable tools for recognizing temporal and spatial trends of beach erosion and accretion activated by natural processes and various anthropogenic activities.

The present study area lies in the middle of the eastern coastal margin of Red Sea and the west of Saudi Arabia (Fig. 1a) at the latitudes 20°:50′:57″–22°:18′:35″ and longitudes 38°:55′:42″–39°:25′:12″. It stretches over areas bordered by Salman Bay, Sharm Abhar and Jeddah Port to the north and the south of the city respectively. The city of Jeddah, situated lengthwise on the shoreline plain is approximately 10 km wide and restricted eastwardly by the number of highland chains with an altitude of approximately 200 m [2, 3].

The present study aimed to delineate the rate of coastal borders changes of the study area from satellite images from 1972 to 2016. In addition, a database was generated on the changes occurring in the study area and an actionable plan of sustainable management was envisaged to analyze the local changes that occurred on the coastal borders of Jeddah and its surrounding areas due to the effects of geo-environmental natural processes and various anthropogenic activities. Moreover, the statistical techniques analysis of the rate of coastal borders was applied change to predict the future

H. Aboulela (✉) · R. Bantan
Department of Marine Geology, Faculty of Marine Sciences, King Abdulaziz University, Jeddah, Kingdom of Saudi Arabia
e-mail: haaboualolaa@kau.edu.sa

H. Aboulela
Department of Marine Sciences, Faculty of Science, Suez Canal University, Ismailia, 41522, Egypt

R. Zeineldin
Deanship of Scientific Research, King Abdulaziz University, Jeddah, Kingdom of Saudi Arabia

R. Zeineldin
ISSR, Cairo University, Giza, Egypt

© Springer Nature Switzerland AG 2019

H. M. El-Askary et al. (eds.), *Advances in Remote Sensing and Geo Informatics Applications*, Advances in Science, Technology & Innovation, https://doi.org/10.1007/978-3-030-01440-7_72

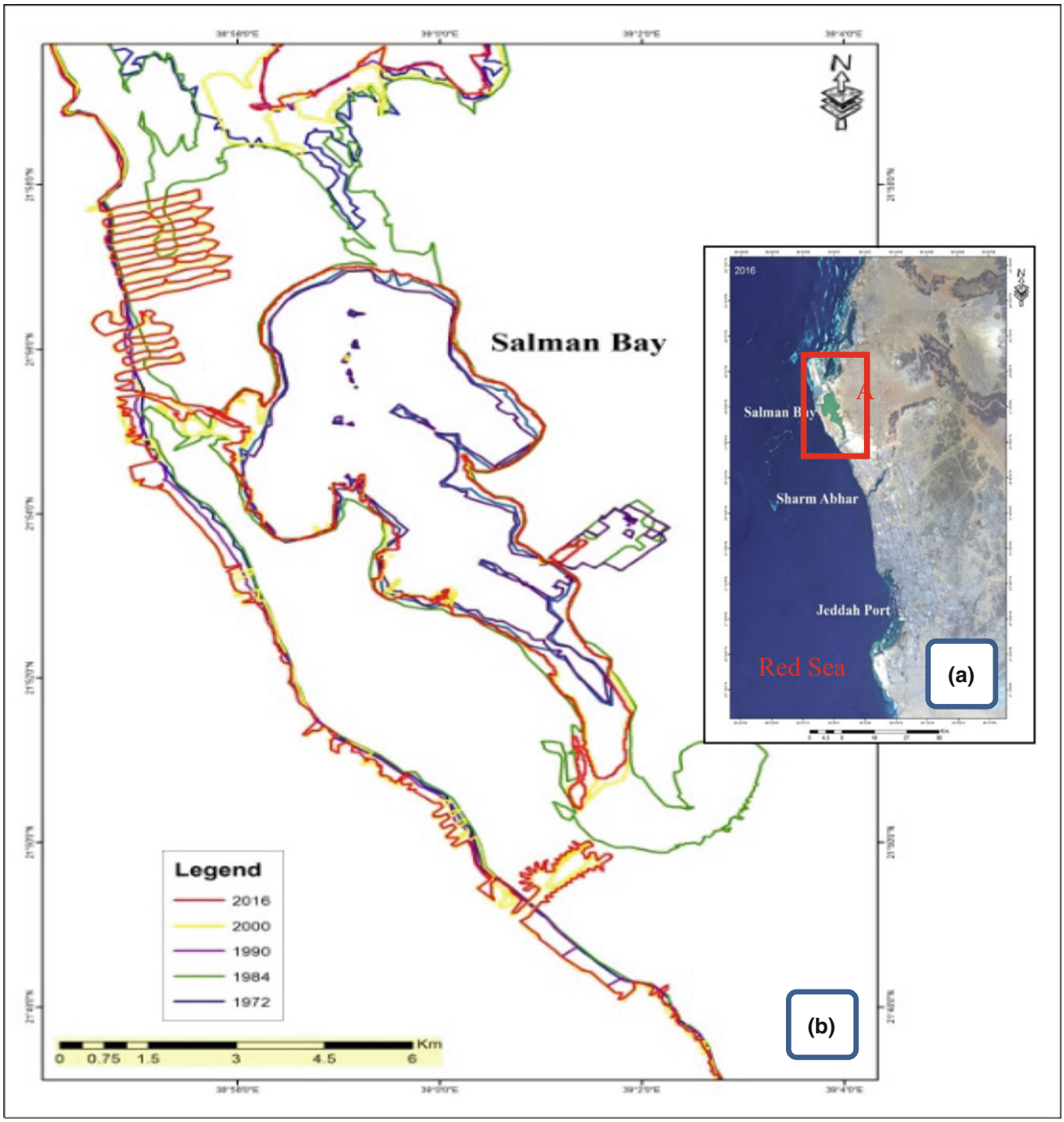

Fig. 1 **a** Location of the study area, and **b** Comparison of spatial changes of areas bordered by Salman Bay area

changes on coastal borders in the study area over both short-(1972) and long-terms (2025).

2 Materials and Methods

For the present study, satellite images for the period between 1972 and 2016, obtained from Landsat; MSS, TM, ETM+, and Landsat_8_images, were analyzed. Additionally, geological maps [4], field surveys and ancillary data were collected. The collection of these materials and documents depended on their accessibility as well as their availability to the related issues. Additionally, statistical techniques such as the Linear Regression, Logarithmic, Inverse and Power techniques were used to predict the future rate of coastal borders change of the study area especially along three areas as Salman Bay, Sharm Abhar and Jeddah Port from 1972 to 2025.

The change in coastal borders areas is affected by a variety of different anthropogenic activities such as industrial development, random projects and filling processes. The simulation approach was also used in the prediction process for the three areas. The prediction results were compared with the actual data and evaluated using the mean square error and mean absolute deviation methods.

3 Results

To monitor and predict changes in coastal borders, it is essential to compare changes on coastal borders to the extracted coastline from reliable and accurate maps. In order to monitor and predict changes, an image-driven reference data was used [5]. The accurate image was provided by fusing Landsat/ETM+ multispectral bands with Landsat/ETM+ panchromatic bands. The changes on coastal borders from truth images were extracted via visual interpretation. Figure 1b shows changes in images of the study area of coastal borders of Salman Bay (Fig. 1b), Sharm Abhar (Fig. 2), and Jeddah Port (Fig. 3) in 1972, 1984, 1990, 2000, and 2016 respectively. When changes occurring in areas of Salman Bay (Fig. 1b), Sharm Abhar (Fig. 2) and Jeddah Port (Fig. 3) were compared, it was found that natural processes and anthropogenic activities during the period of 1972–2016 were responsible (Table 1). There were significant changes in the coastal borderline area of 30.66 km^2 in 2016 as compared to 25.97 km^2 recorded in 1972, especially at Salman Bay area.

The changes revealed that the area of this region increased with approximately 4.69 km^2 from 1972 to 2016. These changes in Salman Bay area were attributed to initiate random projects and filling processes (Table 1). The changes in the coastal borderline area of Sharm Abhar in 1972 were 6.42 km^2 as compared to 5.18 km^2 in 2016, revealing a decrease in the area of 1.24 km^2 from 1972 to 2016. These changes were also attributed to anthropogenic activities, such as dredging operations (Table 1). In the case of Jeddah Port, the area of 58.98 km^2 in 1972 was found to be decreased to 42.20 km^2 in 2016, a reduction of 16, 78 km^2 from 1972 to 2016. These changes were also attributed to anthropogenic activities, establishing random projects and filling processes (Table 1). Applying statistical techniques, the results produced from the prediction methods were compared with the actual data, the Mean Square Error (MSE) and Mean Absolute Deviation (MAD) were calculated to compare the two methods. IBM SPSS 25 Package was used in the prediction of the three areas depending on the collected real data. A curve estimation was performed to select the methods with the highest determination factor (R^2). Arena Simulation Package Version: 14.70.00 was used to develop simulation models. The models with the least square error were adopted. Figure 4 shows the results of predication methods for a salman Bay, b Sharm Abhar and c Jeddah port.

4 Discussion

The statistic Geometric mean was calculated to find an average percentage change over a period of time (Table 2). The rate of increase/decrease is determined by the following formula:

$$G.M = \sqrt[n]{\frac{value\ at\ the\ end\ of\ period}{value\ at\ the\ start\ of\ period}} - 1$$

where the $G.M$, unlike an arithmetic mean, tends to reduce the effect of very high or low values, which might bias the mean if a straight average (arithmetic mean) were calculated. Geometric mean is often used to evaluate data covering several orders of magnitude, and sometimes for evaluating ratios, percentages, or other data sets.

As far as the average percentage change in the area is concerned Table 2 shows a mixture of increases and decreases. For Salman Bay the largest decrease is witnessed from 1984 to 1990 (almost 12%). But the highest increase is also witnessed in Salman Bay from 1990 to 2000 (almost 10.50%). Sharm Abhar decreased till 2000 but then it shows an increase of 0.76% in 2016. Jeddah port, on the other hand, has intermittent increases and decreases but the amount of decrease has gone down from −2.74% in 1984 to −0.46% in 2000.

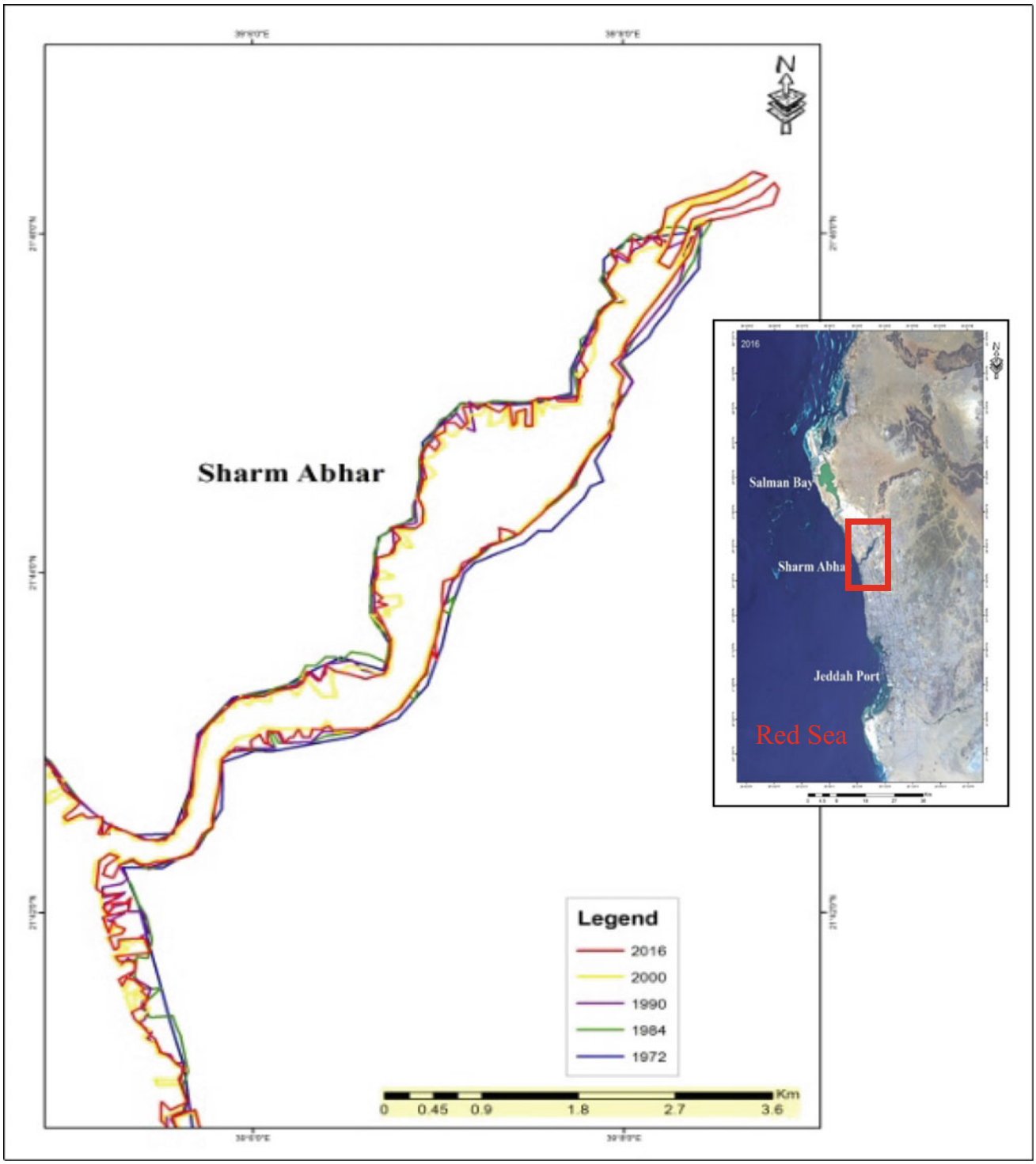

Fig. 2 Comparison of spatial changes of areas bordered by Sharm Abhar

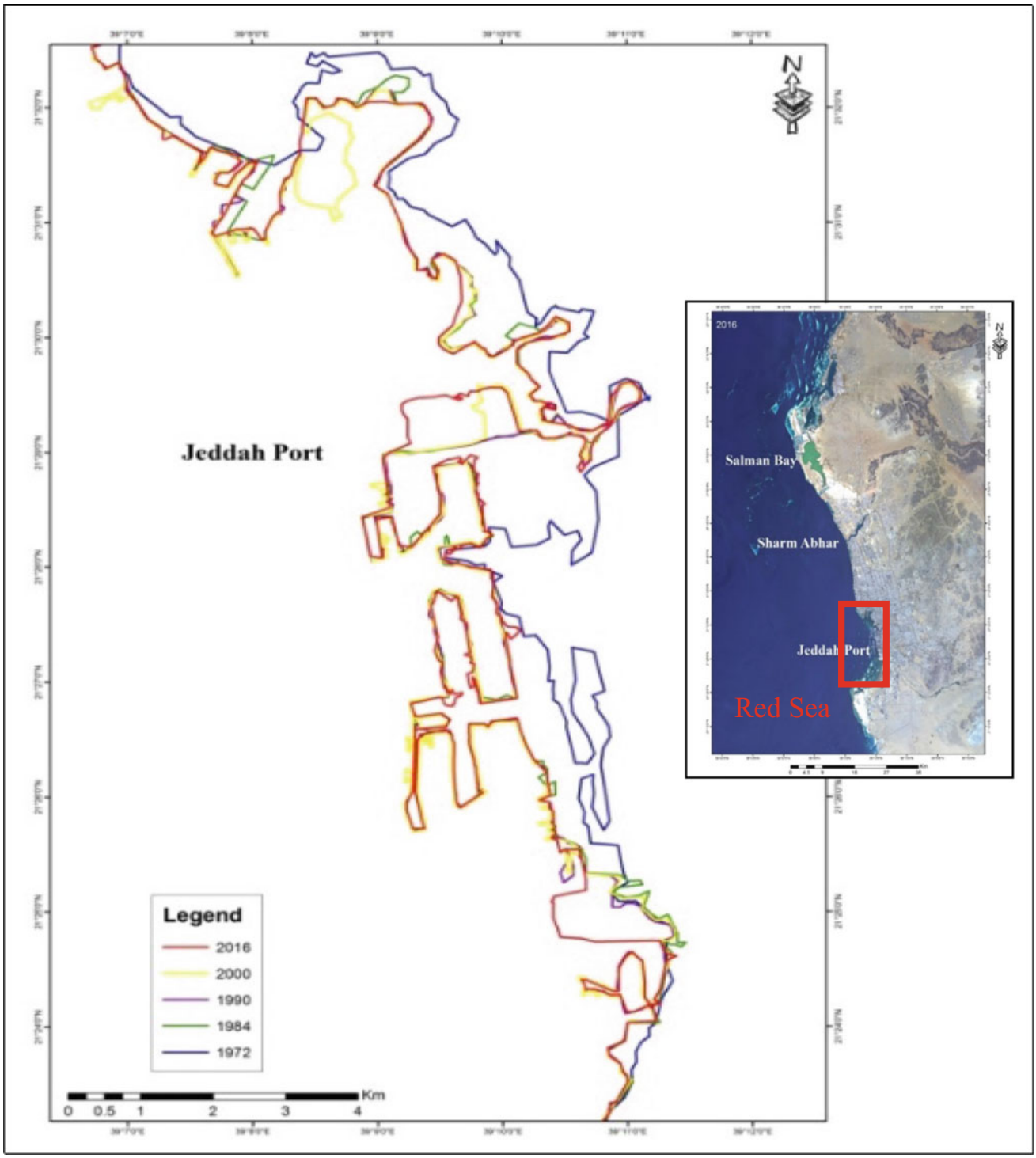

Fig. 3 Comparison of spatial changes of areas bordered by Jeddah Port

Table 1 Changes of spatial bordered areas attributed to anthropogenic activities, in Salman Bay area, Sharm Abhar and Jeddah Port during 1972–2016 classified images

Year	Change of spatial bordered area in km^2		
	Salman Bay (Area in km^2)	Sharm Abhar (Area in km^2)	Jeddah Port (Area in km^2)
1972	25.97	6.42	58.98
1984	42.64	5.93	42.25
1990	23.89	5.35	43.86
2000	30.99	4.59	41.87
2016	30.66	5.18	42.20

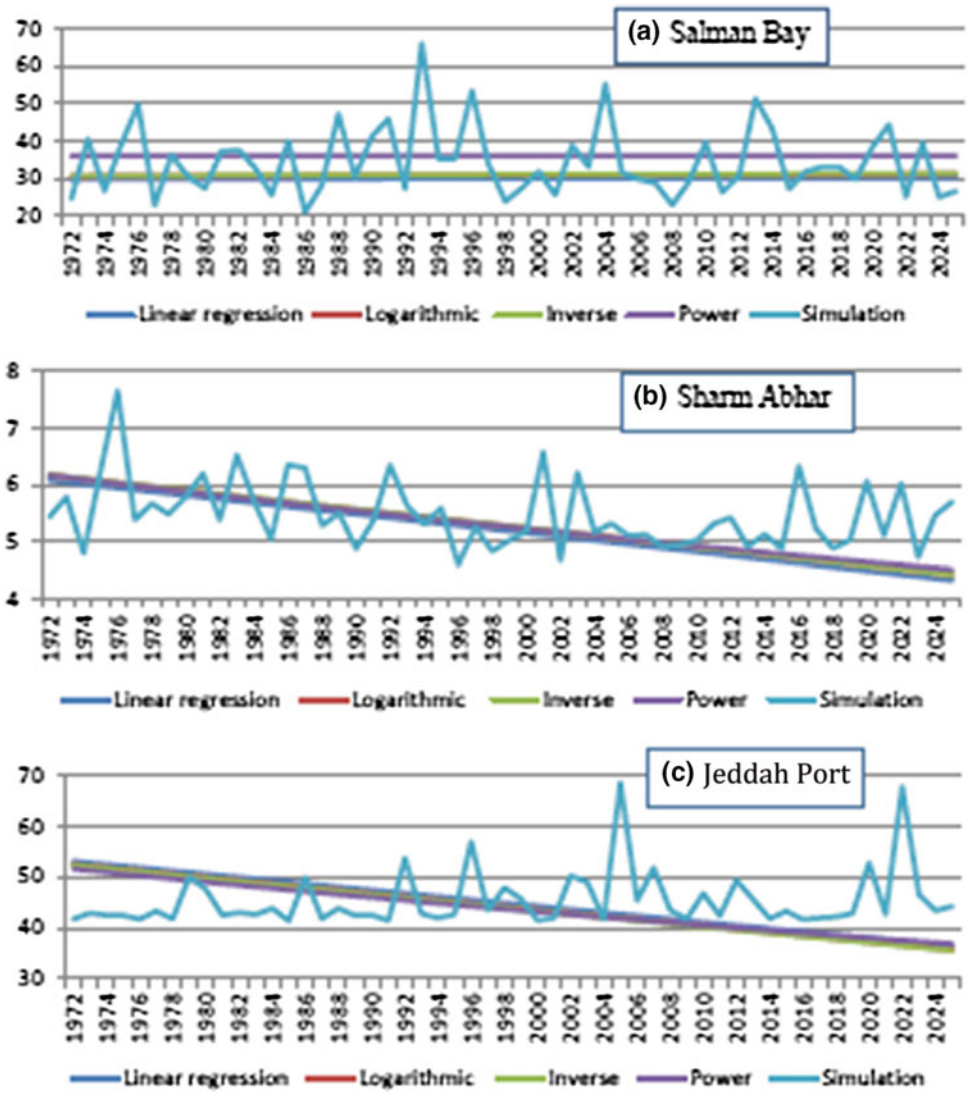

Fig. 4 The prediction methods results for **a** Salman Bay, **b** Sharm Abhar and **c** Jeddah Port

Table 2 Average percentage change in Spatial Borders using Geometric Mean

Year	Average percent change of spatial bordered area in km^2 over the years		
	Salman Bay (%)	Sharm Abhar (%)	Jeddah Port (%)
1972	–	–	–
1984	4.21	−0.66	−2.74
1990	−7.94	−1.46	0.54
2000	2.63	−1.52	−0.46
2016	−0.07	0.76	0.05

5 Conclusion

- The changes occurring from 1972 to 2016 on coastal borders of the study area have resulted from the extensive establishment of random projects. The accreted processes of coastline areas were due to the effects of geo-environmental natural processes and anthropogenic activities.
- Frequent assessments of geo-environmental impacts and ancillary geological studies have continue on existing construction projects.
- Statistical techniques used for forecasting the areas can be interacted with the decision makers and not only depending on the highest R^2 but also incorporating the least squared error; the decision maker can then, on the basis of the results, select the suitable model for the forecast.
- The prediction methods used in this study can be updated and merged with other techniques such as Genetic Algorithm (GA), Particle Swarm (PS) and Ant Colony (AC) tools. As a future perspective, it is suggested that Artificial Neural Networks (ANN) be used to predict the study area.

Acknowledgements This work was supported by the Deanship of Scientific Research (DSR), King Abdulaziz University, Jeddah, under Grant no. (D-146-150-1437). The authors, therefore, gratefully acknowledge the DSR technical and financial support.

References

1. Abdullah, F., Lalit, K.: Land use and land cover change detection in the Saudi Arabian Desert Cities of Makkah and Al-Taif using satellite data. Adv. Remote Sens. **3**, 106–119 (2014). https://doi.org/10.4236/ars.2014.33009
2. Amal, Al-Sheikh: Management of environmental degradation of Jeddah coastal zone, Saudi Arabia, using remote sensing and geographic information systems. J. Am. Sci. **7**, 665–673 (2011)
3. Al Saud, M.: Assessment of Flood Hazard of Jeddah Area 2009, Saudi Arabia. Journal of Water Resource and Protection **2**, 839–847 (2010). Available on: https://doi.org/10.4236/jwarp.2010.29099
4. Moore, T., AI-Rehaili, H.: Geologic Map of the Makkah Quadrangle, sheet 21D, Kingdom of Saudi Arabia, Saudi Arabian Directorate General of Mineral Resources. Geoscience Map GM-107C, scale 1:250,000 (1989)
5. Alesheikh, A., Blais, J., Chapman, M., Karimi, H.: Rigorous geospatial data uncertainty models for GIS in spatial accuracy assessment: land information uncertainty in natural resources, Chapter 24. Ann Arbor Press, Ann Arbor (1999)

Quantification of Phytoplanktonic Algae Density in Algiers Bay (Algeria) by Combining In Situ Measurements and Landsat Satellite Images

Redouane Boufeniza, Fouzia Bachari Houma, Mohammad Alsahli, and Nour el Islam Bachari

Abstract

Satellite remote sensing is considered a promising technique for studying some phytoplanktonic algae because of such advantages as large-scale, real-time and long-term monitoring. The application of statistical models in the field of remote sensing is a crucial tool. The main objective of this study was to quantify the spatial distribution, and develop an empirical model, to detect phytoplankton algal density (diatoms and dinoflagellate). We used ratios of transformed reflectance values (REF) from Landsat Operational Land Imager (OLI) data to establish statistical relationships to dinoflagellate and diatoms densities cells, in the coastal area of Algiers Bay in Algeria. Another additional advantage of our study is that in situ measurements, it coincides with the passage of the satellite at the same time. The result shows that the proliferation prediction model could predict diatoms algae with an accuracy of 77%. The results of this research provided the possibility for the development of an appropriate methodology for remote monitoring of this phytoplankton types in coastal water.

Keywords

Remote sensing • Dinoflagellate • Diatom • Correlation • Algiers bay

R. Boufeniza (✉) · F. B. Houma
Higher National School of Marine Science and Coastal Management, University Campus Dely Ibrahim, Bois des cars, PB 19, 16320 Algers, Algeria
e-mail: boufenizaredouane@gmail.com

M. Alsahli
Geography Department, Kuwait University, P.O.Box 6496(b) 70460 Shuwaikh, Kuwait

N. el Islam Bachari
Department of Biology, University of Sciences and Technology Houari Boumedienne, BP 32 El Alia, 16111 Bab Ezzouar Algiers, Algeria

1 Introduction

Algeria has a coast of 1300 km in length. Almost 60–70% of the population lives in coastal areas. These are rapidly changing in land use that have direct consequences on the quality of marine waters under the natural effects and human actions [1]. The bay of Algiers is unique not only because of its semicircular shape and bathymetry but also its socio-economic activity. Several development projects of the bay of Algiers have been made in the last two years to make it cleaner, and unpolluted. These water characteristics influence the productivity of marine organisms and explain their behaviors [2]. Remote sensing is one of the techniques that allows for satellite images to study the marine phenomena, and follow their evolution at relatively low costs and a very good coverage of space. It has become relatively essential to observe different environmental changes, and it is this remote sensing technique that provide a potential tool for the identification of dominant phytoplankton groups and monitoring spatial and temporal changes in biodiversity in oceans [3]. Satellite measurements are the only way to obtain a repetitive description of phytoplankton biomass and its temporal evolution.

As a consequence, the spatial and temporal variability of important seawater characteristics [2], such as diatoms and dinoflagellates phytoplankton algae, in this region remains unknown, or at least, their estimation remains scientifically insufficient. To the authors knowledge, empirical remotely sensed models quantifying phytoplankton repartition in the Algiers coast waters have not been established [4]. Based on limitations in estimating spatial repartition of phytoplankton densities described above, the goals of this study are to: (1) Develop empirical models to estimate and quantify the spatial distribution of phytoplankton algae in Algiers seawater; (2) map the spatial and temporal distributions of algal phytolanktonic bloom; (3) Assess the interrelationships between satellite parameters and biological density.

© Springer Nature Switzerland AG 2019

H. M. El-Askary et al. (eds.), *Advances in Remote Sensing and Geo Informatics Applications*, Advances in Science, Technology & Innovation, https://doi.org/10.1007/978-3-030-01440-7_73

These goals could be achieved by addressing the following questions:

- What is the relationship between remotely sensed spectral measurements and the density of diatoms and dinoflagellates algae?
- What is the spectral behavior of these planktonic algae?
- Is the distribution of the spectral parameters of the OLI satellite heterogeneous?
- What mathematical relationship is there between satellite parameters and biological density? Can it be presented in a mathematical form?

To answer these questions we were interested in synchronized spatial information (satellite) and in situ measurements taken in real time and at the same time.

2 Materials and Methods

The bay of Algiers is located in the heart of the Algerian coast, it is located in the hollow of the plain of Mitidja (South), characterized by its semi-circular shape, delimited to the North by the Mediterranean Sea, to the West by the Pescade Point (RAIS HAMIDOU) and Cape Matifou (EL MARSA) to the East (Fig. 1).

The coastal zone of Algiers is mainly contaminated by different sources of pollution and subject to several types of urban, industrial and petroleum waste. It is the receptacle of several types of pollution and its wastewater is loaded with organic matter, suspended solids, detergents and lubricating oils generating organic and chemical pollution. This situation is aggravated by the lack of water treatment scheme [5].

2.1 In Situ Measurement

The sampling campaign was conducted on: 04/04/2017, it was taken from the surface water (1 m in depth) and included 16 stations across the bay, most of which were affected by pollution zones and human activity in the Bay of Algiers. Phytoplankton samples were taken using a bottle of (Niskin of 5 L) mounted on a graduated rope. They were taken in transparent and clean polypropylene (PP) bottle with a volume of 500 ml; the filling of the bottle was achieved with the help of a technique of the pipe in order to have a sample of a large, homogeneous and representative volume. The phytoplankton samples are then fixed in the field with an alkaline Lugol solution, approximately 2.5 ml for a 500 ml flask. This final concentration was appreciated by the light brown, orange (whiskey) color.

The samples were stored at 4 °C in coolers filled with cold accumulators and then sent to the laboratory for the physicochemical analysis. The sea trips were made in favorable weather conditions clear sky and calm sea.

2.2 Enumeration of Phytoplankton

The method involves counting and identifying diodes and dinoflagellates under reverse microscopy in a prepared sedimentation chamber. The identification was carried out with maximum precision. The results were then expressed in numbers of individuals per unit volume [6]. The technique adopted for the identification and counting of microplankton is that of Uthermol.

2.3 Image Processing

Radiometric calibration and atmospheric calibration were predicted to analyze the radiance, reflectance and digital number (DN) of each pixel was calculated from the original image OLI by CSRSR.

These images were correlated and therefore posed the problem of information redundancy. Ratios of reflectance values were used to improve spectral differences between bands and reduce soil effects. The division of a spectral band by another produces an image that provides band intensities relating to the quality of the studied environment.

The principal component analysis (PCA) was applied to determine the optimal relationship between numerical count, radiance, reflectance, and planktonic cell densities.

3 Results

The results obtained were classified into four parts:

The 1st part deals with the In Situ results whereas the 2nd contains the laboratory results The 3rd part includes the image processing results including the reflectance values, reflectance ratios relative to the coordinates of the measured stations as well as the correlative analysis between In Situ measurements and satellite measurements. Finally the 4th presents the cartographies of the various studied parameters.

The choice of the reflectance ratios is such that the correlation coefficients were more significant than the reflectance values. A strong correlation was recorded and the correlative study yielded better correlation results. Figure 2 is presented by an adjustment relation which is a linear function characterized by a correlation coefficient $R = 0.7776$. It can be deduced that the diatoms are strongly

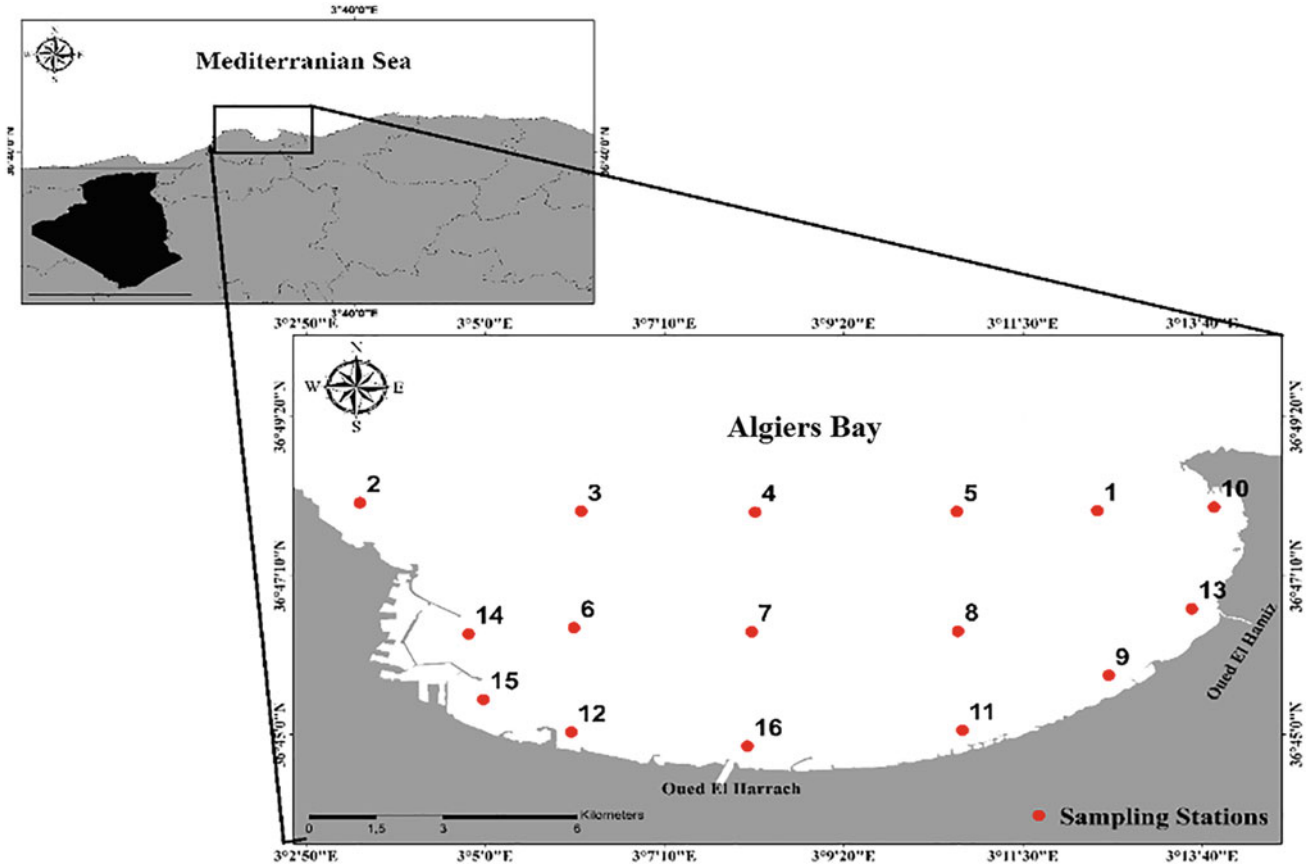

Fig. 1 Algiers Bay and sampling stations

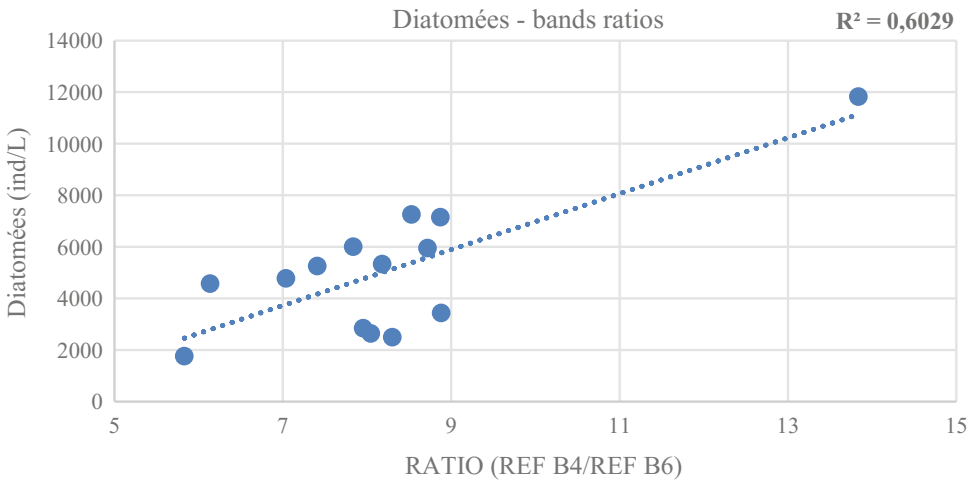

Fig. 2 Correlation between diatoms and (REF b4/REF b6) ratio. **Diatoms (cells/L) = 10,844 * (REF B4/REF B6) – 38,682**

correlated with the ratio (B4/B6). Knowing that one of the characteristics of the band is the determination of vegetation. Unlike diatoms, dinoflagellates are independent of reflectance values. In our work, we found that the number of cells of dinoflagellates present in the bay of Algiers is very high. This can be explained by the values of reflectance

more or less significant, we note that the highest correlation is 0.478 represented by the ratio b6/b5. This is interpreted by the fact that band 4 (red) and band 6 (near infrared) indicate the presence of vegetation and mainly photosynthetic pigments. In addition, band 5 is connected directly to the biomass, which explains the results obtained.

4 Conclusion

We can say that dinoflagellates and diatoms have a heterogeneity of spatial distribution that can be explained by an inverse behavior and therefore a different spectral response. It is assumed that dinoflagellates and diatoms do not have the same pigments responsible for the reflectance of electromagnetic radiation. Also the diatoms are observed in large quantities in the zones which present some anomalies of pollution (Oued el Harrache). This might explain the fact that these algae present a certain resistance to the marine pollution.

References

1. Houma, F.B: Modélisation et cartographie de la pollution marine et de la bathymétrie à partir de l'imagerie satellitaire. HALL, Paris Est, 2009. Doctoral dissertation (2009)
2. Alsahli, M.M., et al.: Modeling kuwait seawater clarity a spatial-temporal study using remote sensing and gis. Appl. Remote Sens. J. **2**(2), 17–34 (2012)
3. Torrecilla, E., et al.: Cluster analysis of hyperspectral optical data for discriminating phytoplankton pigment assemblages in the open ocean. Remote Sens. Environ. **115**, 2578–2593 (2011)
4. Boufeniza, R.L., et al.: Estimation of dinoflagellate and diatoms Algae in Algiers bay from landsat satellite data. In: Euro-Mediterranean Conference for Environmental Integration, Springer, Cham, Algiers (2017)
5. Houma, F., et al.: Correlative study of physico-chemical parameters and satellite data to characterize IRS1C water pollution. Appl Bay Oran Algeria, Oran: Water Sci **17**(4), 429–446 (2004)
6. Druart, J.C., Rimet, F.: *Phytoplankton analysis protocols INRA: sampling, counting and biovolumes.* s.l.: INRA-Thonon, 2008. Rapport SHL (2008)

Active-Fault Controlled Fluvial Geomorphology Along the Coastal Plain of Odisha: East Coast of India

Chinmay Dash and Pitambar Pati

Abstract

In response to the sub-surface basement fault reactivation, few coast-parallel shallow-depth normal faults have been nucleated in the Quaternary cover sediments along the coastal plain of Odisha. Lack of exposure, extreme flatness of the plain, intense fluvio-aeolian and anthropogenic activities makes mapping of these faults difficult. Therefore, fluvial response to faulting like stream convergence, channel offset, variation in sinuosity, initiation of new streams recognized by remote sensing have been used for marking the position of these faults. The Jajpur fault offsets the Baitarani and Kharsuan rivers ~1.4 km to NE and ~4 km to SW, respectively. The Gop fault offsets the Kushabhadra River ~4 km to SW. Channel sinuosity varies from 1.3 to 1.5 on the up-thrown and down-thrown blocks across the Jajpur fault and that of the Gop fault is 1.8 and 2.1, respectively. Exaggerated DEM around these faults shows significant relief break. GPR imaging across these faults confirms their subsurface continuity with wide zones of displacement consisting of several synthetic normal faults.

Keywords

Subsurface fault • GPR • Quaternary sediment • East coast of India

1 Introduction

Eastern coastal alluvial tract of Odisha (along east coast of India) is extremely flat and frequently being modified by intense fluvial and eolian activities. In addition, recent surface faulting activities triggered by the sub-surface basement fault reactivations have contributed to the geographic modification of the plain to certain extent. However, lack of exposure, extreme flatness of the plain, intense fluvio-aeolian and anthropogenic activities makes mapping of these faults difficult. Therefore, for such terrains like the Ganga plain in north India, indirect methods and integrated approaches have been used in mapping such active faults (Fig. 1) [1, 2]. Geomorphic markers especially the fluvial geomorphic indicators are increasing being used in such studies due to their high sensitivity to even very weak tectonic movement [2]. The response of fluvial systems to active faulting includes stream beheading and diversion [3, 4], convergence of few streams at certain point, sudden change in channel sinuosity, generation of new streams, along a linear zone. Though such fluvial geomorphic indicators are available at places but association of such characteristics changes with other geological environments such as natural slope breaks, closeness to basin, inputs certain uncertainties in applying such fluvial geomorphic parameters independently. Therefore, subsurface geophysical evidences in association with the fluvial geomorphic markers makes the methodology robust in mapping active faults in flat terrains [5, 6, 1]. In the present study an integrated approach has been adopted using fluvial geomorphic response studied from remote sensing image, to map the active faults in this extremely flat terrain and has been validated through the Ground Penetrating Radar (GPR). In addition exaggerated digital elevation model (DEM) clearly displays a linear slope break across the fault.

The geographical position and alignment of these faults coincide with the sub-surface basement faults of the region (Fig. 2). Therefore, it is believed that these faults have been developed due to nucleation of new faults within the sediment cover due to the basement fault reactivation. As these secondary faults create a fault zone of several kilometers, fluvial anomaly along the fault zone provides the signature of the position of the faults.

C. Dash (✉) · P. Pati
Indian Institute of Technology Roorkee, Roorkee, Uttarakhand 247667, India
e-mail: dash1des@iitr.ac.in

P. Pati
e-mail: ppatifes@iitr.ac.in

© Springer Nature Switzerland AG 2019

H. M. El-Askary et al. (eds.), *Advances in Remote Sensing and Geo Informatics Applications*, Advances in Science, Technology & Innovation, https://doi.org/10.1007/978-3-030-01440-7_74

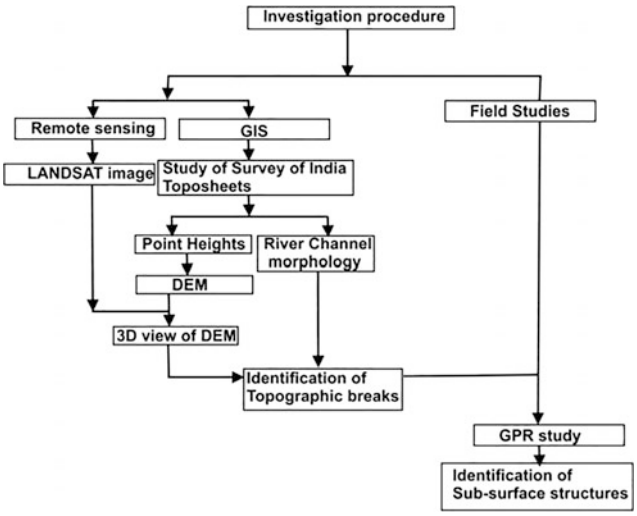

Fig. 1 Flow chart showing investigation procedure

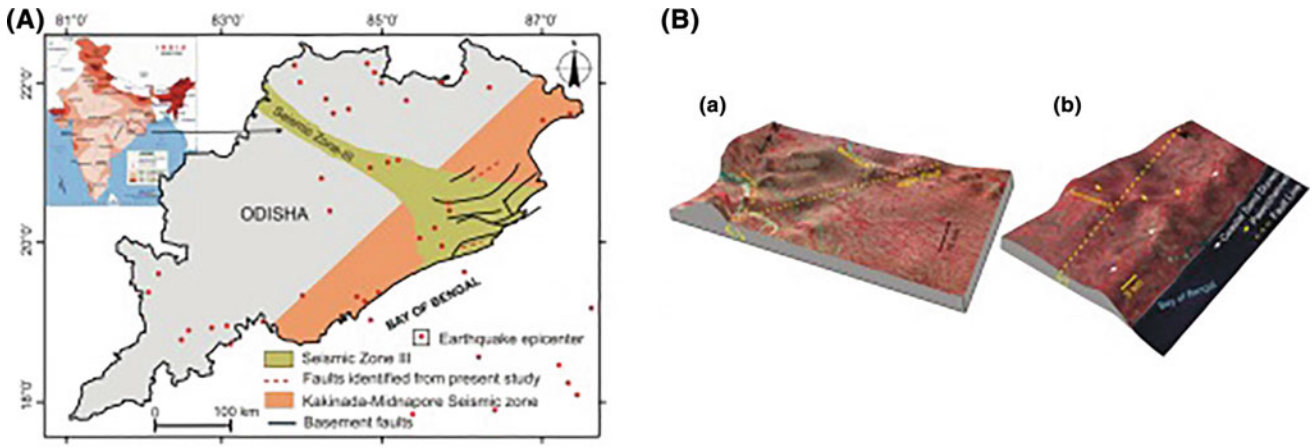

Fig. 2 **A** Study area showing location of basement and surface faults. **B** 3D perspective view of the study area (a) Jajpur Fault (b) Gop fault

2 Materials and Methods

As the area is almost flat, the techniques adopted for identifying faults in topographically flat plains such as the Ganga plains in north India and elsewhere in the world have been preferably adopted here. The thematic Mapper (TM) image was used to map the fluvial geomorphic responses of the region. Few parameters such as channel sinuosity and offset were calculated from this image. SRTM data with (height resolution of ±6 m) is not useful for studying low topographic surfaces like flat alluvial plains [6, 1]. Therefore, for generating DEM spot heights (Point heights from the Survey of Indian topographic maps of 1:50,000 scales) with an accuracy of greater than ±2 m were manually digitized. Spot height density of 2–3 points/10 km^2 was adequate for regional studies [7]. In the present study 6–7 points/10 km^2 are available for preparing the DEM (Fig. 2b). Depth contours obtained from the Seismo-tectonic Atlas of India [8] have been used to map the geographical position of the basement faults buried under 500–2400 m sediment cover. Thalweg profiles along the rivers across the faults were prepared from the DEMs (Fig. 4a, b). the GPR study was carried out across the mapped fault with 100 MHz antennae

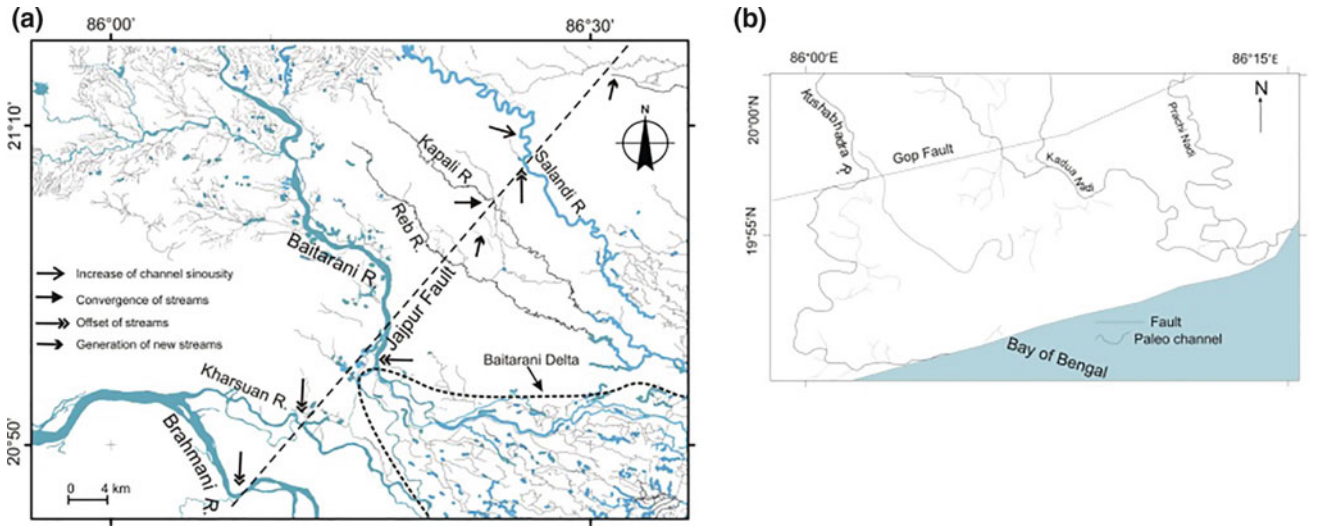

Fig. 3 Drainage morphology along Jajpur and Gop fault. **a** Drainage morphology changes across Jajpur fault. **b** Drainage morphology changes across Gop fault

in distance mode. The obtained data were processed by RADAN-5 software with optimal use of the processing parameters as the data warranted.

2.1 Results

The geomorphic elements respond to even very weak tectonic movements in low relief flat plains, which is well established in the northern Indian plains by Pati et al. [1], Bhosle et al. [2]. Drainage patterns like convergent streams, offsetting drainages, change in channel sinuosity and generation of new streams etc. are observed along the study area (Fig. 3). The Jajpur fault offsets the Baitarani and Kharsuan rivers ~1.4 km to NE and ~4 km to SW, respectively. The Gop fault offsets the Kushabhadra River ~4 km to SW. The channel sinuosity varies from 1.3 to 1.5 on the up-thrown and down-thrown blocks across the Jajpur fault and that of the Gop fault is 1.8 and 2.1. DEMs show topographic breaks across the faults (Fig. 2b). GPR imaging across these faults confirms their subsurface continuity with wide displacement zones consisting of several synthetic normal faults (Figs. 4c, d).

3 Discussion

In this paper we presented a case study on the effect of active faults on fluvial geomorphology in an extremely flat alluvial landscape. Due to unavailability of exposure, an integrated approach was adopted using remote sensing, GIS and GPR along with field studies to confirm the presence of faults. The effect of faults on fluvial geomorphology and landscape modification was discussed. As this region is tectonically less active, the development of active faults and their influence on a wide spectrum of geological problems required a seismo-tectonic re-evaluation. This study was of academic interest for mapping active faults in terrains with negligible relief, and for the planners working in infrastructure development in highly populated coastal plains. How the fluvial system responds to even very feeble tectonic movement was discussed in the present study.

The coastal plain has buried basement faults which reactivated during Tertiary and Quaternary periods as evident from gravity, magnetic and seismic refraction studies [10]. At present (Late Holocene) these faults are active in many places and trigger small magnitude earthquakes along the coastal plains. Twelve historical earthquakes were recorded since 1837–1992 due to the activities of these faults [11]. The geographical position of basement and surface faults shows a close link between the two (Fig. 2). The mechanism of sub-surface fault propagation to surface have been documented in many previous studies [9, 12]. However, due to frequent reworking of surface sediments by fluvio-aeolian and anthropogenic activities, these faults are not recognized directly on the surface. Therefore, the fluvial geomorphic responses as discussed here were successfully used for demarcating the fault zone on the surface. Though, due to closeness to the sea and old stage of the rivers, drainage convergence, sinuosity change issues could be argued, but subsurface continuity and nature of studied the faults by GPR clearly rules out the former. Therefore, the observed fluvial geomorphic changes were well correlated with the activity of the subsurface faults.

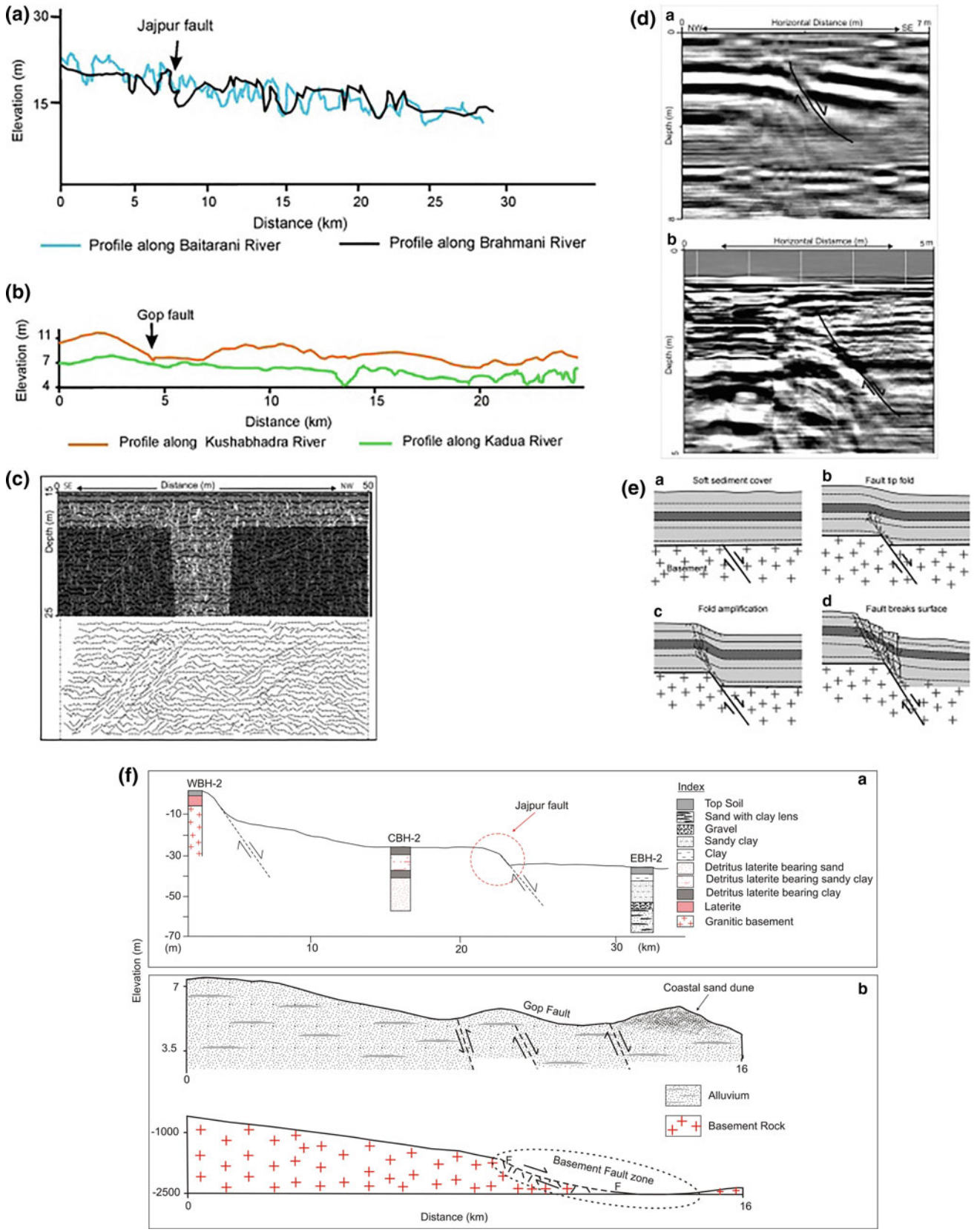

Fig. 4 **a** River thalweg profile along Brahmani River and Baitarani River across Jajpur Fault. **b** River thalweg profile of Kushabhadra Riveraross Gop fault. **c** GPR profile across Gop fault. **d** GPR profile across Jajpur fault. **e** Basement fault propagation to surface (after [9]). **f** Relationship between surface faults and basement faults in the study area

4 Conclusion

The present study leads us to draw the following conclusions:

a. In terrains with lower relief and negligible slope where faults are not exposed to the surface, an integrated approach using the remote sensing, GIS and GPR are very much useful in mapping active faults. A further detailed study using seismic and other geophysical methods will be more informative about depth continuity of these faults and their relation to basement faults.
b. Fluvial geomorphology in flat plain responds to even weak tectonic movements and influences the channel parameters.
c. This study is also useful for geotechnical investigation before infrastructure development in highly populated coastal plains.

References

1. Pati, P., Parkash, B., Awasthi, A.K., Acharya, V.: Holocene tectonogeomorphic evolution of parts of the Upper and Middle Gangetic plains, India. Geomorphology **128**, 148–170 (2011)
2. Bhosle, B., Parkash, B., Awasthi, A.K., Pati, P.: Use of digital elevation models and drainage patterns for locating active faults in the Upper Gangetic Plain, India. Int. J. Remote Sens. 30, 673–691 (2009). https://doi.org/10.1080/01431160802392604
3. Bishop, P.: Drainage rearrangement by river capture, beheading and diversion. Progress Phys. Geogr. **19**, 449–473 (1995) Bolivian Amazon. Journal of South American Earth Science 47, 230–242
4. Clark, M.K., Schoenbohm, L.M., Royden, L.H., Whipple, K.X., Burchfiel, B.C., Zhang, X., Tang, W., Wang, E., Chen, L.: Surface uplift, tectonics, and erosion of eastern Tibet from large-scale drainage patterns. Tectonics 23, TC1006 (2004)
5. Anderson, K.B., Spotila, J.A., Hole, J.A.: Application of geomorphic analysis and ground-penetrating radar to characterization of paleoseismic sites in dynamic alluvial environments: an example from southern California. Tectono Phys **1**, 25–32 (2003)
6. Bhosle, B., Parkash, B., Awasthi, A.K., Singh, S., Khan, M.S.H.: Role of extensional tectonics and climatic changes in geomorphological, pedological and sedimentary evolution of the Western Gangetic Plain (Himalayan Foreland Basin), India. Himalayan Geol **29**(1), 1–24 (2008)
7. Badura, J., Przybyski, B.: Application of digital elevation models to geological and geomorphological studies-some examples. Przegld Geologiczny **53**, 977–983 (2005)
8. GSI: Seismotectonic Atlas of India and Its Environs. Geological Survey of India, Bangalore (2000)
9. Gawthorpe, R.L., Leeder, M.R.: Tectono-sedimentary evolution of active extensional basins. Basin Res. **12**(3–4), 195–218 (2000)
10. Bharali, B., Rath, S., Sarma, R.: A brief review of Mahanadi Delta and the deltaic sediments in Mahanadi Basin. Memoirs Geological Society of India, No. 22, Bangalore, India, pp. 31–49 (1991)
11. Anon, 1998.: Geological map of India, 1:2 million. In: Narula, P. L., Acharya, S.K., Benajee, J. (eds), 2000. Seismotectonic Atlas of India and its Environs, Geo logical Survey of India, Kolkata
12. Robson, A.G., King, R.C., Holford, S.P.: 3D seismic analysis of gravity-driven and basement influenced normal fault growth in the deepwater Otway Basin, Australia. J. Struct. Geol. **89**, 74–87 (2016)

Evaluation of Coastal Vulnerability and Exposure to the Risk of Erosion and Submersion in the Coasts of Bou Ismail Bay

Walid Chaib, Mokhtar Guerfi, and Yacine Hemdane

Abstract

Coastal areas are likely to be eroded or submerged and this can be accentuated by the effect of global warming; yet some coasts are more vulnerable than others to natural or man-made hazards. The improvement of knowledge on coastal risks inevitably involves a better cartographic coverage conveying and locating the different dynamic themes directly or indirectly affecting the coastline. The coastal vulnerability and exposure Index is one of these themes and it aims to move from the general detail to a holistic model so as to allow decision-makers to take the right decision in terms of optimizing the intervention procedures provided by the regulations in force, especially the rationalization of expenses when renting classified sites vulnerable by the coastal vulnerability and exposure Index.

Keywords

Assessment • Coastal vulnerability index • Exposure • Vulnerability • Mapping • Sensitivity • Resilience

1 Introduction

Vulnerability is the condition of weakness of the elements exposed (which represent the exposure) to a hazard [4], which exposes them to suffer from damage [6]. Vulnerability depends on two factors which are sensitivity and resilience (or adaptability) [4].

Sensitivity is defined according to the IPCC as the physical susceptibility of humans, infrastructure and the environment to be affected by a dangerous phenomenon because of the lack of resilience and/or the predisposition of society and ecosystems to undergo [3]. Resilience can be described as the amount of disturbance that a system can absorb while remaining in the same state or maintaining its functions [1]. The improvement of knowledge on coastal risks inevitably involves a better cartographic coverage conveying and locating the different dynamic themes directly or indirectly affecting the coastline.

This study aimed to set up a coastal vulnerability and exposure assessment plan specific to the Algerian coasts and more specifically for BouIsmail Bay (Eastern Tipaza, western Algiers). Also, it is necessary to map the coastal vulnerability and exposure indicators and index. This is to say that identified and localized areas as such will consequently require, according to the degree of fragility of the coasts in question to erosion and marine submersion hazards, a risk management plan and very adapted measures to human and economic issues.

2 Methods

Bou Ismail Bay is located west of Algiers (2° 20′E and 2° 55′E). It covers an area of 350 km^2, it is oriented south east-northeast. It has an agricultural and touristic vocation (Fig. 1).

For our study, we adopted a coastal vulnerability and exposure index specific to the Algerian coasts by integrating indicators from previous studies as well as data actually available. The contribution of satellite imagery is important in the calculation of vulnerability and exposure to fill the lack of information on pointed topics that can be extracted from this imagery. The coverage of the area and the topographic data (which is one of the indicators of vulnerability) were downloaded from the USGS data [8]. As for the citizenship indicator, a survey was produced.

W. Chaib (✉)
Ecole Nationale Supérieure des Sciences de la Mer et de l'Aménagement du Littoral (ENSSMAL), Alger, Algérie
e-mail: walid.chaib16@gmail.com

M. Guerfi · Y. Hemdane
Université des Sciences et de la Technologie Houari Boumediene (USTHB), Alger, Algérie

© Springer Nature Switzerland AG 2019

H. M. El-Askary et al. (eds.), *Advances in Remote Sensing and Geo Informatics Applications*,
Advances in Science, Technology & Innovation, https://doi.org/10.1007/978-3-030-01440-7_75

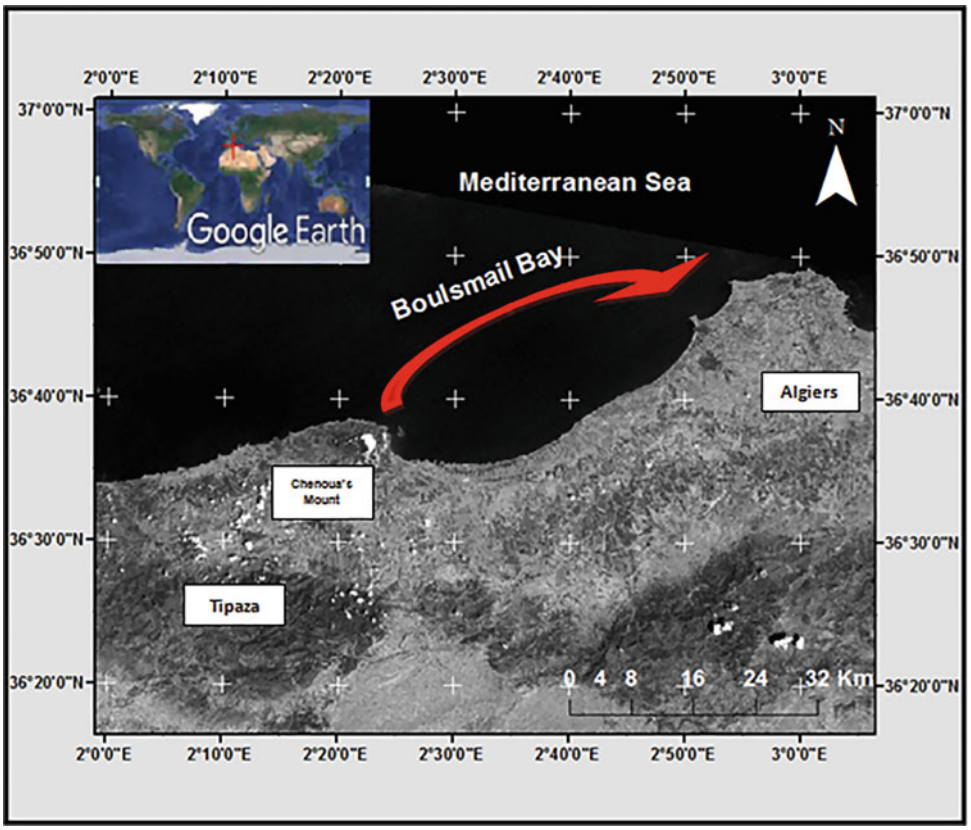

Fig. 1 Geographical location of BouIsmail Bay using USGS satellite image as coverage

The chosen indicators for our study are: coast type, altitude, Posidonia herbarium, and terrestrial sediment supply (Rivers) for sensitivity, and laws and citizenship for resilience. The indicators of exposure are: Population, land use, historical sites and Roads.

A map of the coastal vulnerability and exposure indicators that were selected after the creation of a geographical database will be obtained. The scores attributed to the indicators vary from 1 to 5:

1. very little vulnerable
2. not very vulnerable
3. moderately vulnerable
4. highly vulnerable
5. very highly vulnerable (Table 1).

3 Results

By filling the database according to the data in possession, we obtained a sensitivity map and a resilience map; the sum of the values obtained in the two maps gives us the global map of coastal vulnerability. We have also obtained a map of exposure by the sum of values of exposure indicators, cartographic format is adequate to show vulnerability and exposure by geographical area (Figs. 2 and 3).

4 Discussion

The mapping of the coastal vulnerability of Bouismail Bay shows us that most of this zone is of low to medium vulnerability and this is due to the fact that most of the indicators show very low to very high vulnerability values, as is the case for the low indicator, which shows a very low vulnerability, whereas citizenship shows a very high degree of vulnerability. The same result was achieved for exposure; it is generally low to moderate because of the absence of roads and historical sites in large area of the bay.

5 Conclusion

The vulnerability and exposure mapping of the Algerian coasts shows that the BouIsmail bay is moderately vulnerable. More precise results can be obtained by adding other indicators of vulnerability. Moreover, the study of vulnerability informs us about the fragility of the coast but does not inform us about the impact that an area can suffer in the case

Table 1 Assignment of vulnerability and exposure scores [2, 5, 7] modified

Indicators/scores	1	2	3	4	5
Coast type	Cliff	Rocky beach	Coast protected by coastal protection structure	–	Sand beach
Altitude (m)	More than 30	20–30	10–20	5–10	Less than 5
Rivers	Presence	–	–	–	Absence
Posidonia herbarium	Presence	–	–	–	Absence
Laws	Presence	–	–	–	Absence
Citizenship (awareness ratio)	More than 80%	60–80%	40–60%	20–40%	Less than 20%
Population (per/km^2)	Less than 51	51–100	101–200	201–400	More than 400
Landuse	Wet area	Natural coastal zone	Forest	Agriculture area	Urban and/or industrial area
Historical sites	Absence	–	–	–	Presence
Roads	Absence of roads	Secondary roads	Departmental road	National road	Highway

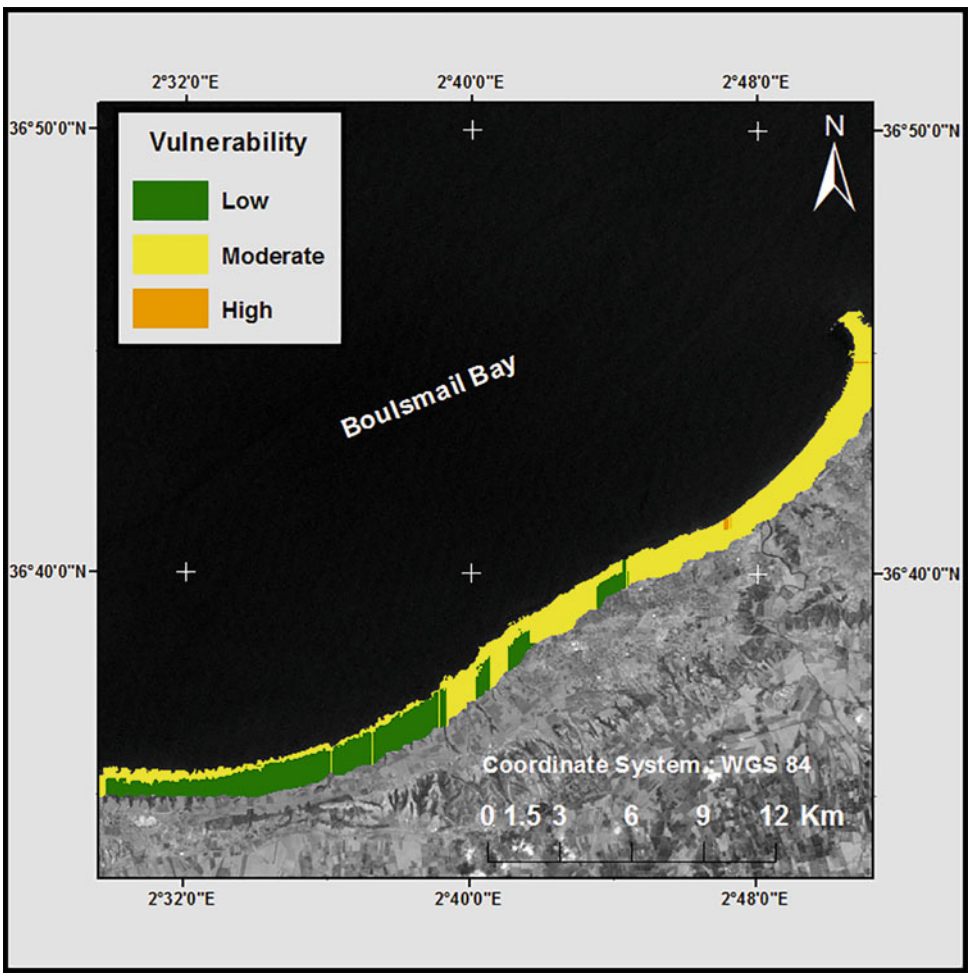

Fig. 2 Map of coastal vulnerability in BouIsmail Bay

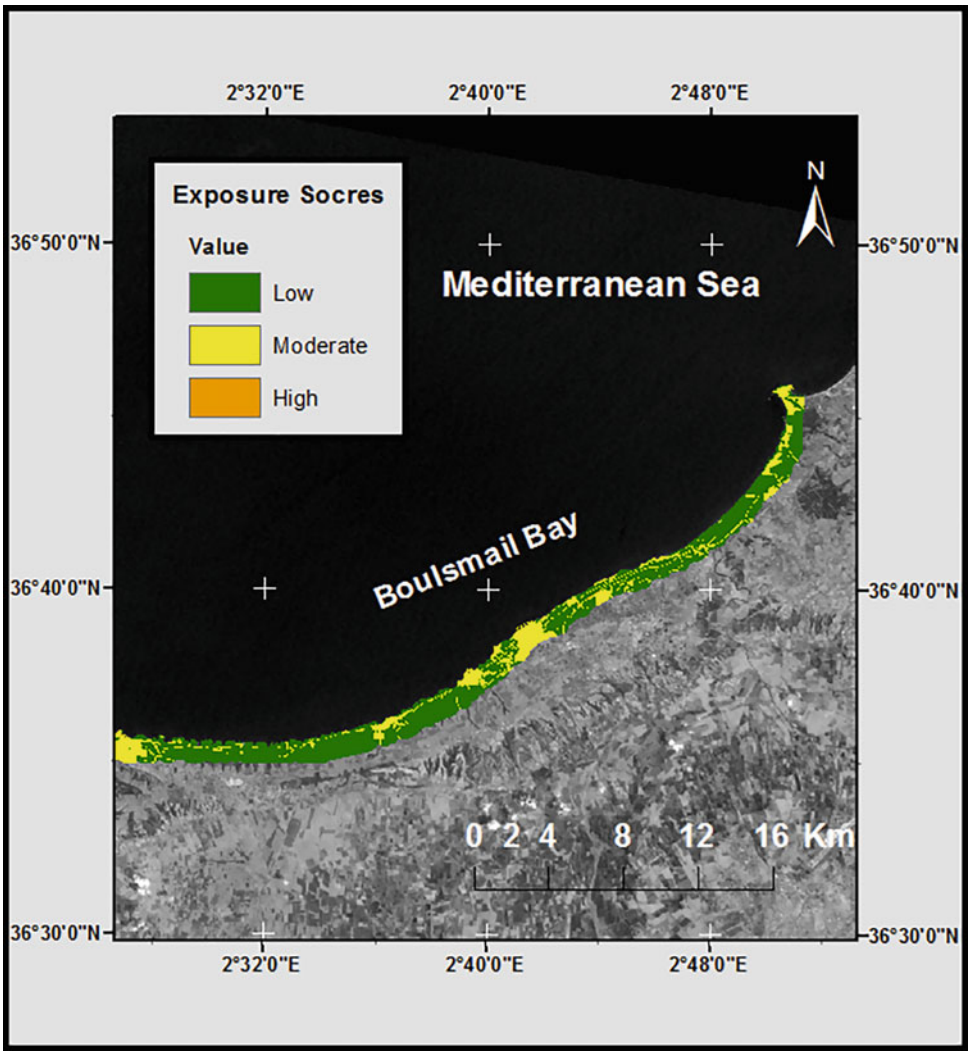

Fig. 3 Map of coastal exposure in BouIsmail Bay

of a natural disaster and to fill this information deficit, specific indicators of coastal hazards can be added.

References

1. ETC-CCA.: Climate change vulnerability and adaptation, pp. 1–8 (2008)
2. Gornitz, V., Global coastal hazards from future sea level rise. In: Palaeogeography, Palaeoclimatology, Palaeoecology (Global and Planertary Change Section), vol. 89, Elsevier Science Publishers B.V, pp. 379–398 (1991)
3. IPCC.: Managing the risks of extreme events and disasters to advance climate change adaptation (2012)
4. IPCC.: Climate change Synthesis report (2014)
5. McLaughlin, S., Cooper, J.A.G.: A multi scale vulnerability index: a tool for coastal managers? Environ. Hazards Human Policy Dimensions 234–248 (2010)
6. Morin, M.: Concepts de base en sécurité civile, p. 4 (2008)
7. Satta, A., Venturini, S., Puddu, M., Firth, J., Lafitte, A.: Application of a multi-scale coastal risk index at regional and local scale in the Mediterranean (2015)
8. USGS: https://earthexplorer.usgs.gov/. Last Accessed10 Mar 2018

Oil Pollution in the Persian Gulf: Satellite-Monitoring Results in 2017

Natalia Evtushenko, Andrey Ivanov, and Vyacheslav Evtushenko

Abstract

Oil extraction and transportation practices have turned the Gulf region into one of the most polluted sea areas in the world. In this context, monitoring oil related pollution as persistent in the Persian Gulf was implemented through application of the interactive classification method on the SAR images. The achieved findings appear to reveal that no less than 5000 oil spills were detected and identified to prevail in the Gulf area.

Keywords

Satellite monitoring • Oil pollution • Persian gulf • SAR • Geoinformation

1 Introduction

The following research was conducted in a bid to help solve the actual ecological problems persisting in the Persian Gulf, by estimating the state of the environmental and overall pollution predominant there [1]. In effect, Oil extraction and transportation activities have turned the region into one of the most polluted sea areas worldwide. According to the experts' released estimations, the annual quantities of oil spilled into the Gulf waters prove to range from tens to thousands tons [2, 3]. It is in this context that the present work could be set, with the aim of providing a rather accurate estimation of the number of oil spill outs poured into the Gulf region over the years.

N. Evtushenko (✉) · A. Ivanov
P.P. Shirshov Institute of Oceanology of the Russian Academy of Sciences, 36 Nahimovskiy pr., Moscow, 117997, Russia
e-mail: slav133@yandex.ru

N. Evtushenko · V. Evtushenko
SCANEX Group, Kiev highway p.1., 108811 Moscow, Russia

2 Technologies and Methods for Locating and Identifying Oil Spills as Detected on SAR Images

The "ScanEx" corporate group relating technologies and methods were applied for the purpose of observing the Gulf sea waters. The geoinformatical approach was used to identify the oil spills as detected by means of SAR images. In effect, an SAR based image, appearing in the form of a grayscale image, stands as an input datum for the oil spills' detection algorithm. The algorithm involves the following major steps: image preprocessing, detection of dark segments [4], parameter extraction and classification of the detected dark segments. The speckle noise is an integral component of the SAR image that could significantly well affect the processing results. Hence, we can use mean, median, adaptive Lee, Frost filters or other filters to reduce the images associated noise. As the area of interest is water surface, the second preprocessing relevant step consists in masking the land areas. This preprocessing step helps in avoiding false detections, usually associated with relief roughness, and other land surface features. To this end, the coastlines' vector database was implemented. An integral step of the algorithm lies in detecting the dark spots prevailing in the image processing stage. At this level, segmentation is performed in order to pick out the dark areas, which generally correspond to oil pollution. In this respect, the dark segments' classification process represents an important step of the oil spill detection algorithm, entailing a complex estimation of each segment. At this stage, the set of slicks, likely oil spills, are formed. To note, a major feature characterizing oil pollution is the related geometric shape, as determined through the relating circularity and eccentricity [5, 6]. Other important parameters distinguishing the oil slick is its size. Segments with noticeably small areas are likely to be formed due mainly to the strong sea surface disturbance and interference effects. As for the remarkably large segments, they are usually slicks of

© Springer Nature Switzerland AG 2019

H. M. El-Askary et al. (eds.), *Advances in Remote Sensing and Geo Informatics Applications*,
Advances in Science, Technology & Innovation, https://doi.org/10.1007/978-3-030-01440-7_76

natural origin (colonies of algae) or calm areas. Edge detection of the polluted areas plays an important role, as oil spills typically have a well-defined smooth contour. Moreover, the distinctive feature characterizing the oil slicks from natural pollution lies in the homogeneity of their texture. The detailed nautical charts (Figs. 1 and 2), as drawn with the help of the offshore tools and devices of the oil and gas industry helped greatly in implementing the analysis, as they allowed us to estimate the ship traffic and identify the most densely used ship navigation routes [6]. The SAR based images, as acquired in 2017 via the satellites Sentinel-1A and Sentinel-1B were applied. Additionally, we have also made use of optical images as extracted from the satellites Terra, Aqua, Suomi NPP, Sentinel-3 and Landsat-8, as well as the geographical by-products based on these images.

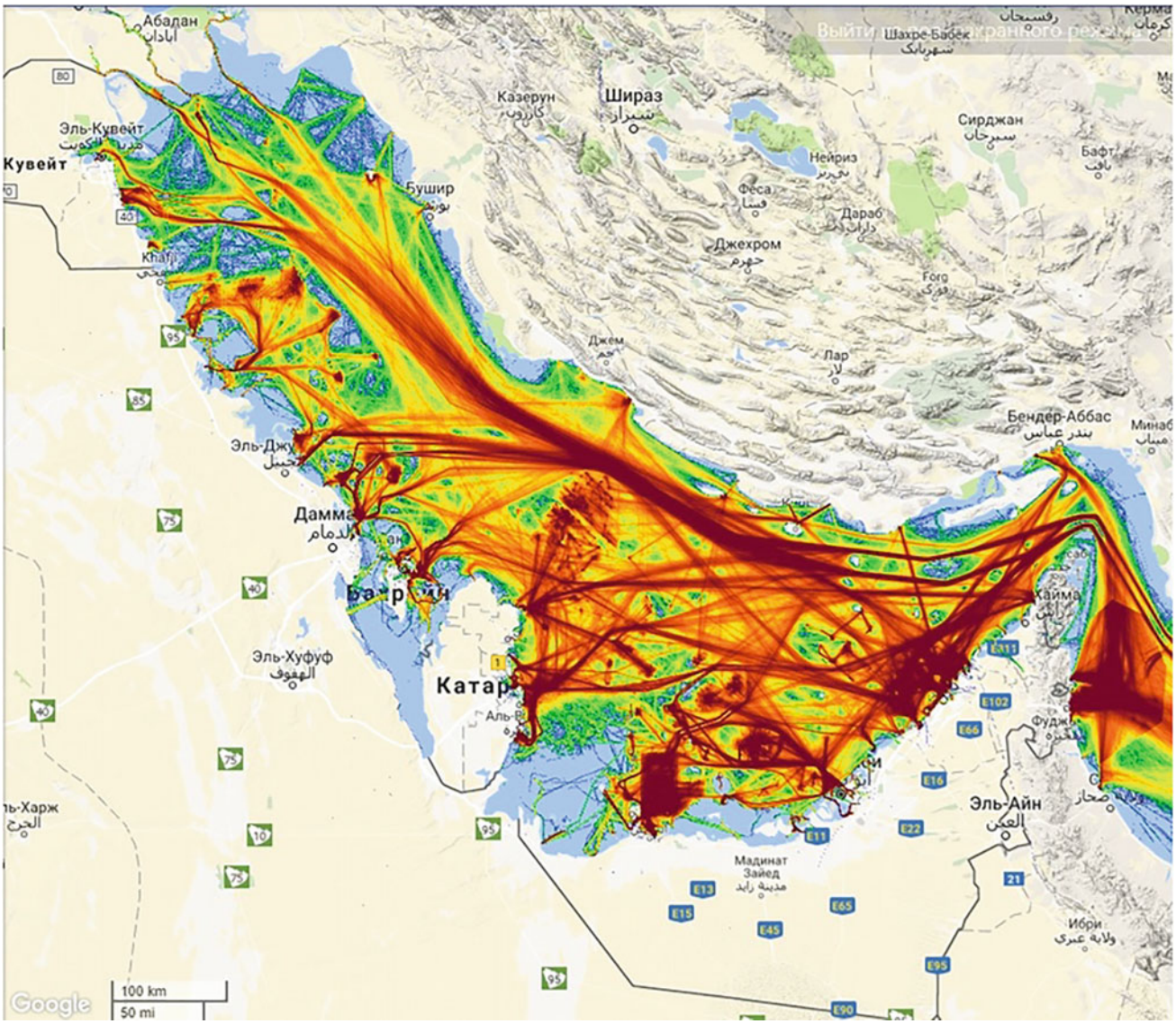

Fig. 1 Marine traffic intensity taking place in the Persian Gulf in 2016 © marinetraffic.com

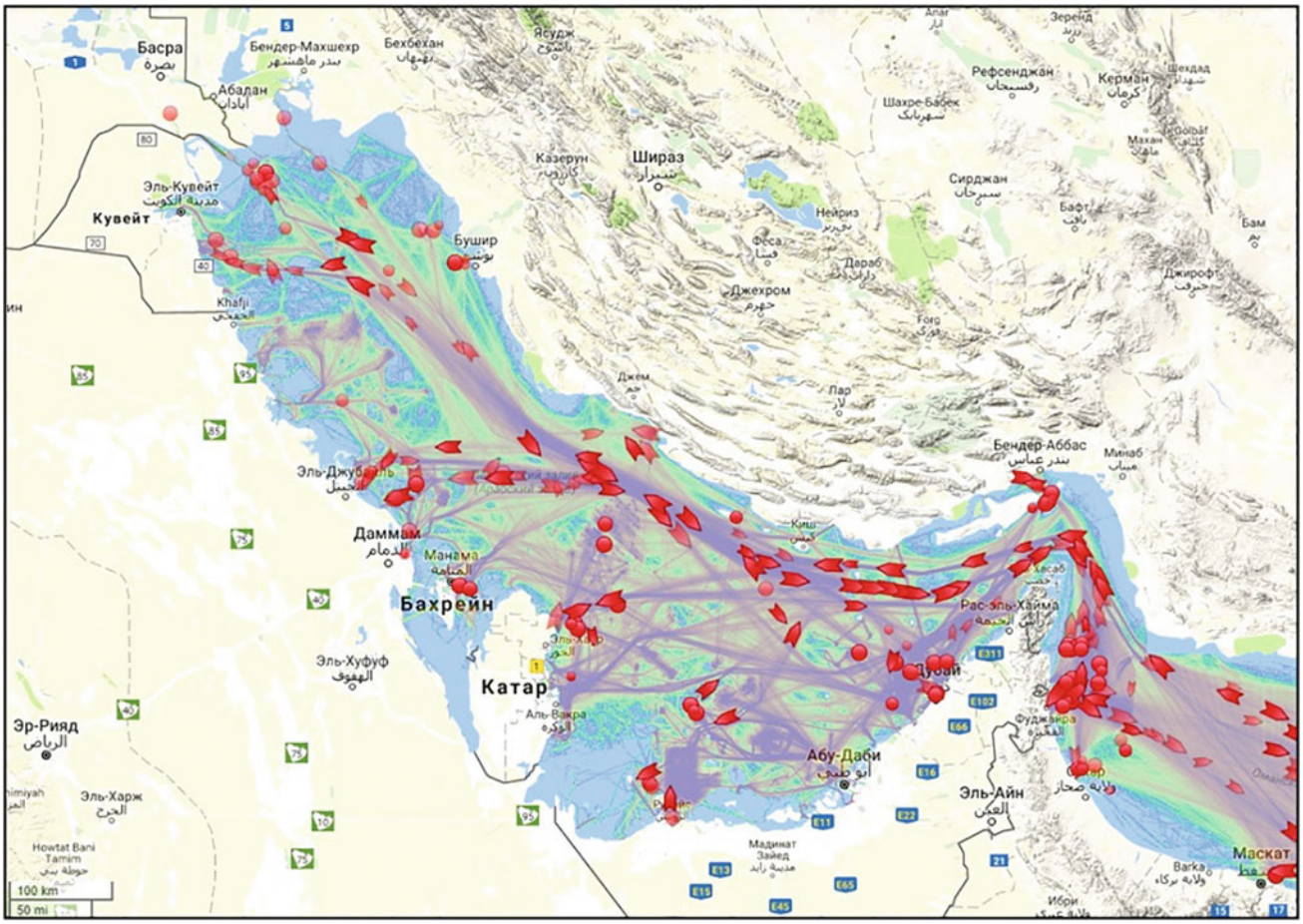

Fig. 2 The oil tankers associated locations in the Persian Gulf, on Jan. 14, 2018, according to marinetraffic.com portal

3 Results

Some 209 SAR images were analyzed, along with a total of 4905 slicks were detected to feature different areas lying across the Persian Gulf (Fig. 3). The total surface area of detected pollutions was of the size of 13,840 km^2. As for the individual spots surface area, it proved to vary between 0.5 and 600 km^2 (Table 1). The largest oil spills (of total areas ranging between 240 and 780 km^2) were detected to occur in the Irani sector of the Gulf (south Syria), as captured at the end of the first decade of March 2017, sited at the Sirri-E drilling spot.

4 Discussion

The total surface of the detected polluted area proved to cover 13,840 km^2. The area covering individual spots appeared to vary between 0.5 and 600 km^2. A large proportion of these polluted sites was identified to take place in the oil-extraction based areas, as well as alongside main ship navigation routes, some of which cross the whole gulf and connect the major oil transportation bases and ports. The largest oil spill outs (total area from 240 to 780 km^2) were detected to occur in Irani sector of the Gulf (in the south of Syria), as captured in the end of the

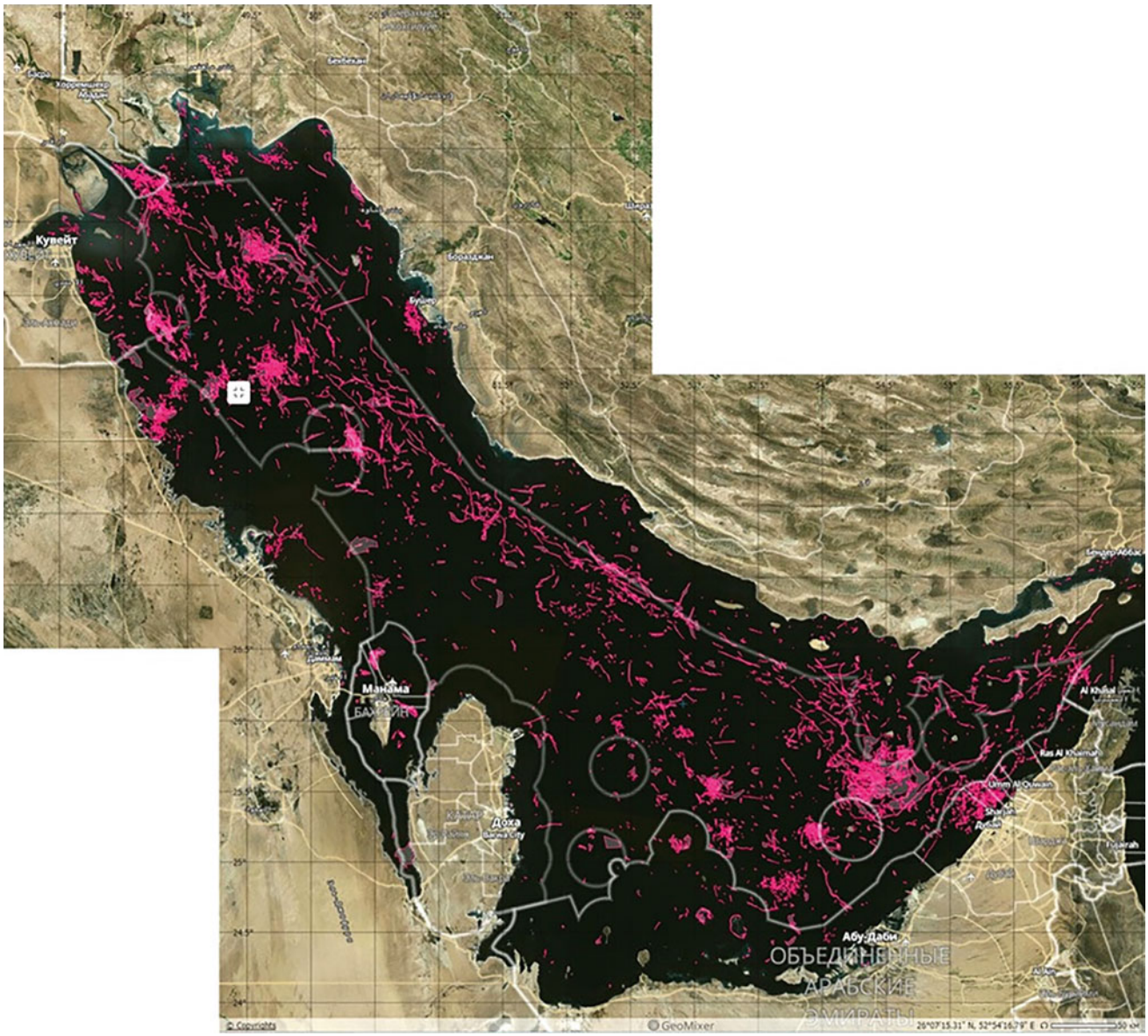

Fig. 3 Integral map of the entire oil polluted spots, located in the Persian Gulf, as captured in 2017 via Sentinel-1A and Sentinel-1B based images (with the bold grey line marking territorial waters)

first decade of March, 2017 at the site of the Sirri-E drilling spot. Indeed, an accidental release took place then at the WPE-1 platform, while a second leak release was recorded to take place in the beginning of June, at the Aboozar drilling spot and in mid-August very close to the Kuwaiti shore.

5 Conclusions

Nowadays, satellite-radar based monitoring stands as the only effective instrument whereby sea and ocean surfaces related oil pollution could be monitored. The "ScanEx"

Table 1 Quantity and area of the oil slicks, as detected during the 2017 monitoring process

Month	Quantity	Area (km)
January	176	143
February	297	246
March	399	2011
April	265	1061
May	403	775
June	306	932
July	564	2279
August	575	2612
September	773	1759
October	390	954
November	358	643
December	399	420
Total	4905	13,835

company group based approach and concept, relevant for controlling oil pollution via satellite based images helped greatly in effectively detecting and identifying almost the entirety of sea-surface associated film pollution, including the oil spills. As for the geo-informational service relating technologies, they turned out to display high functionality, in respect of the worldwide standards. The data analysis process, as achieved following the monitoring proceeding helped provide valuable information useful for understanding the quintessence of the problem.

Acknowledgements The study was supported by a grant provided by the Russian Science Foundation (project# 14-50-00095), as granted to the P.P. Shirshov Institute of Oceanology, the Russian Academy of Sciences.

References

1. Pashaei, R., Gholizadeh, M., Jodeiri, Iran K., Hanifi, A.: The effects of oil spills on ecosystem at the Persian Gulf. Int. J. Rev. Life Sci. **5** (3), 82–89 (2015)
2. Oil and Gas of the Persian Gulf (http://biofile.ru/geo/15421.html)
3. Zhao, J., Temimi, M., Al Azhar, M., Ghedira, H.: Satellite-based tracking of oil pollution in the Arabian Gulf and the Sea of Oman. Can. J. Rem. Sens. (2015). https://doi.org/10.1080/07038992.2015.1042543
4. Ivanov, AYu., Zatyagalova, V.V.: A GIS approach to mapping of oil spills in a marine environment. Int. J. Rem. Sens. **29**(21), 6297–6313 (2008)
5. Oil Spill in the Persian Gulf (https://www.skytruth.org/2017/03/oil-spill-in-the-persian-gulf/)
6. Ivanov, AYu.: The oil spill from a shipwreck in Kerch Strait: radar monitoring and numerical modeling. Int. J. Rem. Sens. **31**(17–18), 4853–4868 (2010)

Part X
Atmospheric Sensing

Aerosol Optical Depth of Dust in Urban and Desert Area of Kuwait

Noor Al-Dousari, Ali Al-Dousari, and Modhi Ahmad

Abstract

The sun photometer instrument measures atmospheric dust and aerosols distribution showing aerosol optical properties of the atmosphere. The study shows different uses of the device when used in an urban area (K) or desert area (S) investigating 339 days of collected data from August 2015 to July 2016 in the visible wavelength i.e. 870, 675, 500, 440 nm. The results show that there were 35 days of extreme dust events. Values varied from one location to another but in General, data in an urban area were always higher than those of a desert area. The objective of this study was to investigate particle distribution difference between two different locations. The obtained values for the urban area exceeded those of the desert on dusty days with a 32.21% due to wind element that is considered as a critical factor in obtaining data.

Keywords

AOD • Sun photometer • Dust • Atmosphere • Kuwait

1 Introduction

Aeolian activities including windblown dust are considered one of the main characterizations of arid regions. Since Kuwait is considered as an arid country, it faces many challenges with atmospheric dust due to its fragile ecosystem inducing the movement of the soil upper surface that eventually increases dust storms in the country especially in summer exceeding wind speeds that enhance the occurrence of dust storms in the country. Wind is the most active element that causes the initiation of dust storms by lifting the upper surface of sand, silt and clay particles from one location to another as dust and sandstorms [1, 2]. Sabbah et al. [3] measured the Aerosol Optical Thickness (AOT) in Alexandria—Egypt, for one year and steered that a powerful dry convection could have developed over the region and could have upraised the dust to a high altitude permitting southwesterly winds to move the dust northeastward over the southeastern Mediterranean region. According to Sabbah et al. [4] numerous dust stroms and increased levels of pollution are major characteristic of AOT and Arabian Peninsula. Ulanowski et al. [5] found that atmospheric mineral dust was sustained with electrical charging over Kuwait and Saudi Arabia and may attain the occurrence of great level of dust particle alignment.

The Cimel sun photometer instrument measures atmospheric dust and aerosols distributed in the atmosphere. Toledano et al. [6] studied the African dust events throughout autumn, winter with a mean value of aerosol optical depth (AOD) in the visible spectrum of 440 nm was 0.31 and less frequent episodes in April. Sabbah et al. [7] studied aerosol optical measurements of desert dust over Kuwait over a seven-year period using satellite borne terra/moderate resolution imaging spectroradiometer (MODIS) and showed a seasonal variation of Aerosol Optical Thickness (AOT) in which the low values of Ångström wavelength exponent (α) indicated the presence of large aerosol particles (dust). Yunfei et al. [8] measured heavy aerosol loading in China, for climate modeling and remote sensing.

2 Methods

There are two Cimel Sun photometer instruments in Kuwait, one is located in a desert area i.e. Shagaya that is 100 km away from Kuwait city (29.209 N, 47.060 E, 242 m sea level), the other is in Khaldia which is an urban area that is 4.8 km away from Kuwait city (29.325 N, 47.971 E, 42 m

N. Al-Dousari (✉) · A. Al-Dousari · M. Ahmad
Kuwait Institute for Scientific Research, P.O. Box 24885 Safat, 13109, Kuwait
e-mail: ndousari@kisr.edu.kw

© Springer Nature Switzerland AG 2019

H. M. El-Askary et al. (eds.), *Advances in Remote Sensing and Geo Informatics Applications*,
Advances in Science, Technology & Innovation, https://doi.org/10.1007/978-3-030-01440-7_77

sea level). The instrument measures physical optical characterization of the aerosols providing continuous monitoring through an official website of the instrument (http://aeronet.gsfc.nasa.gov/). Data for both sites of aerosol optical depth properties were retrieved for a similar period that both instruments were working i.e. from August 2015 to July 2016. Data were collected from Aeronet public online website that includes four visible wavelength bands: 870, 675, 500 and, 440 nm. Daily mean values were calculated for the AOD data using Excel. Graphs and tables were achieved to analyze the difference between both sites. The statistical analysis included maximum (max), minimum (min), mean, and difference percentage presented in tables.

3 Results and Discussion

The increased AOD values indicate a hazier or cloudy sky and if values are closer to zero, it indicates a clear sky and homogenous particle distribution in visible and that the wavelength is from 440 to 870 nm. Table 1 shows the maximum, minimum and average wavelength observed during the study period in both locations.

The values in a desert area are lower than those of an urban area most of the time. The maximum value obtained was 3.02 at 440 nm in urban area. As for the highest value, it was 1.8 in a desert area in the four visible wavelengths.

The results showed that there were 35 extreme dust events in which values exceeded 1 reaching a maximum of 3.02 in urban areas. However, the instrument did not record a reading in the desert area and this might be due to an extreme dust storm and most likely was shut down automatically in severe conditions and extreme events. The instrument failed to record 33 days in desert area and 11 days in urban area. Table 2 that shows the difference between both locations in the 35 dusty days. It shows that the average difference between the two locations of aerosol optical thickness at 870 nm wavelengths was the highest and the 675 nm wavelength was the lowest. In general, there are no significant differences between both locations when comparing the whole data. There was a significant difference among values on extreme dust storms that were recorded during this period as seen in Fig. 1. Generally, dusty days in urban areas were greater than those in the desert area by 32.21% as seen in Fig. 1.

4 Conclusion

Kuwait is featured with dust and sand storms as a major form of being an arid country as they peak in spring and summer due to the strong northwesterly winds that characterize the weather during winter to spring seasonal transition. This study measured the quantification and physical optical characterizations of aerosols in the urban and desert area of Kuwait. Data of the 339 days showed that there were 35 extreme dusty days in both locations. Data in urban area were always higher than those of the desert area by 32.21%. This is due to wind element that is considered a critical factor in obtaining data. The device is a sun tracking device. In the case of the desert area (Shagaya), it lasted for 11 months. Desert area is faced with many challenges;

Table 1 Maximum and minimum observed values in desert and urban areas

Location		Aerosol Optical Depth (AOD)			
		870 nm	675 nm	500 nm	440 nm
Desert area	Max	1.865	1.884	1.882	1.875
	Min	0.0139	0.015	0.025	0.031
	Avg	0.276	0.301	0.353	0.379
Urban area	Max	3.010	2.97	2.994	3.021
	Min	0.0341	0.040	0.062	0.077
	Avg	0.318	0.347	0.413	0.453

Table 2 The difference between desert and urban area on dusty days

Difference between desert and urban areas	Aerosol Optical Depth (AOD)			
	870 nm	675 nm	500 nm	440 nm
Max	3.0103	2.997	2.994	3.021
Min	0.0229	0.0218	0.116	0.0001

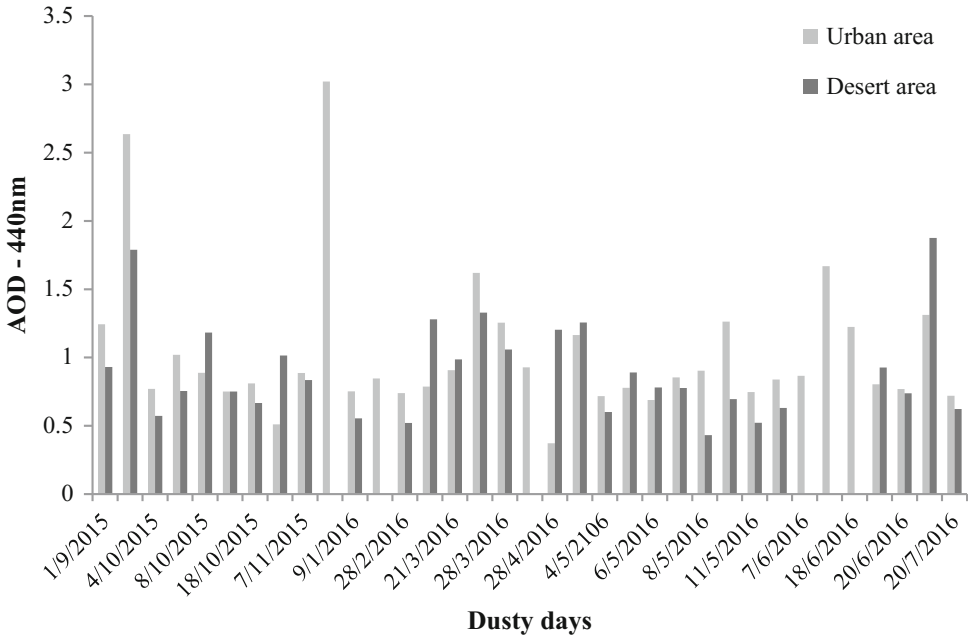

Fig. 1 Values of 35 dusty days in both locations

strong wind, sun, dust and sand encroachments. This ultimately has led to an instrument error and troubleshoot while instrument in the urban area (Khaldiya) worked correctly.

Acknowledgements We thank the PI Eng. Alaa Ismail and Dr. Hala Al-Jassar for their efforts in establishing and maintaining Shagaya park and Kuwait University sites.

References

1. Al-Awadhi, J., Al-Shuaibi, A.: Dust fallout in Kuwait City deposition and characterization. Sci. Total Environ. J. **461–462**, 139–148 (2013)
2. Al-Dousari, A.M.: Origin, characteristics and hazards of dust fallout in Kuwait. In: Conference on land degradation in dry lands. Kuwait University, 8–14 March 2009
3. Sabbah, I., Ichoku, C., Kaufman, Y.J., Remer, L.: Full year cycle of desert dust spectral optical thickness and perceptible water vapor over Alexandria, Egypt. J. Geophys. Res. Atmos. **106**, 18305–18316 (2001)
4. Sabbah, I., Saeed, T., Al-Jassar, H., Rao, K.S.: Remote sensing of desert dust in Kuwait. Kuwait J. Sci. Eng. **33**, 101–117 (2006)
5. Ulanowski, Z., Sabbah, I., Harrison, R.G., Nicoll, K.A., Hirst, E., Kaye, P.H., Al-Abbadi, N., Rogers, G.: Atmospheric dust charging vertical profiles and optical properties measured in the Arabian Peninsula during the DREAME campaign. EGU General Assembly 12, EGU2010-13473 (2010)
6. Toledano, C., Cachorro, V.E., de Frutos, A.M., Sorribas, M., Prats, N., de la Morena, B.A.: Inventory of African desert dust events over the southwestern Iberian Peninsula in 2000–2005 with an AERONET Cimel sun photometer. J. Geophys. Res. **112**(D21201), 2007 (2007). https://doi.org/10.1029/2006jd008307
7. Sabbah, I., Al-Mudhaf, H., Al-Kandari, A., Al-Sharifi, F.: Remote sensing of desert dust over Kuwait: long-term variation. Atmos. Pollut. Res. **3**, 95–104 (2012)
8. Yunfei, W., Zhu, J., Che, H., Xia, X., Zhang, R.: Column-integrated aerosol optical properties and direct radiative forcing based on sun photometer measurements at a semi-arid rural site in northeast china. J. Atmos. Res. **157**, 56–65 (2015)
9. Aeronet—NASA. 2018. Available at https://aeronet.gsfc.nasa.gov/

Seasonal Air Pollution Investigation and Relation Analysis of Air Pollution Parameters to Meteorological Data (Kocaeli/Turkey)

Arzu Erener, Gülcan Sarp, and Özge Yıldırım

Abstract

Air pollution refers to the release of harmful, excessive amounts, above the normal values, of pollutants into the atmosphere. Although, it is crucial to map and analyze the temporal distribution of pollutants, meteorological factors also have great influence on these parameters distribution and their effect on the ecosystem. Therefore, this study aimed to analyze the relationship between dispersion characteristics of air pollution with the meteorological parameters such as, wind speed, wind direction, relative humidity, air pressure and temperature for different seasons using the correlation analysis. Additionally, the seasonal distribution changes of pollutants were mapped and analyzed using GIS techniques in Kocaeli case. In this study the daily data obtained from 8 air monitoring stations including SO_2 and PM10, wind speed, wind direction, relative humidity, air pressure and temperature belonging to 2015 year were examined. Pollution and meteorological distribution maps of the study area were obtained using Kriging interpolation method using GIS. By integrating the pollution and meteorological data, the regression analyses were carried out. The results of seasonal regression analysis and pollution distribution maps were evaluated using the wind maps obtained for each seasons.

Keywords

GIS • Pollution • Kriging • Regression • Wind map • Meteorological parameters

1 Introduction

It is the atmosphere that ensures the life of the planet Earth and the human beings. The atmosphere holds oxygen and other gases which are essential for life. Even small changes in the air can cause to qualify the air as dirty. There are mainly five important pollutants in terms of primary importance. These are Particulate Matter (PM), sulfur dioxide (SO_2), carbon monoxide (CO), carbon dioxide (CO_2), ozone (O_3), nitrogen oxides (NOx) and hydrocarbons (HC) that constitute almost 90% of all contaminants. Air pollution occurs when the quantity and intensity of these pollutants adversely affect the living health. Therefore, it is crucial to monitor air pollution, understand its status and analyze its effect to ecosystems in order to take precautionary measures. The technologies such as GIS systems provide opportunity to obtain data from various sources and store them in a geographical database, after being transformed, analyzed, mapped and queried.

In the literature, [1] investigated the seasonal variation of air quality in India, and [2] obtained air quality measures for Southern China between 1981 and 2000. Tian et al. [3] studied the PM10 and PM2.5, in sampled data set in China during the period of 2006–2014. In Turkey, Erener, [4] aimed to determine the relationship between dispersion characteristics of air pollution with the density of industrial regions and topography by wind direction evaluation using GIS techniques and correlation analysis in Kocaeli. Daylan ve ark. (2002) analyzed the SO_2 and PM values in Istanbul between 1994 and 1996 with meteorological factors. Hamzaoğlu et al. [5] aimed to determine the causes and characteristics of cancer-related deaths in 2004 in Dilovası, Kocaeli considering industrial chemicals.

A. Erener (✉)
Department of Geomatic Engineering, Kocaeli University, 41380 Kocaeli, Turkey
e-mail: arzu.erener@kocaeli.edu.tr

G. Sarp
Department of Geomatics Engineering, Süleyman Demirel University, 32260 Isparta, Turkey

Ö. Yıldırım
Başaran İleri Teknoloji, Diyarbakır, Turkey

© Springer Nature Switzerland AG 2019

H. M. El-Askary et al. (eds.), *Advances in Remote Sensing and Geo Informatics Applications*, Advances in Science, Technology & Innovation, https://doi.org/10.1007/978-3-030-01440-7_78

2 Materials and Methods

This study aimed to make a spatial analysis of the SO_2 and PM10 pollutants, map and analyze their differences and display the seasonal changes of pollutants using GIS techniques in the Kocaeli case. Additionally, such meteorological data as wind speed, wind direction, relative humidity, air pressure and temperature for different seasons were associated with pollutants using the regression analysis and the results were interpreted. The flow chart of the study is presented in Fig. 1.

3 Results

3.1 Results of Kriging Analysis

The air pollution dispersion characteristics were identified by mapping the spatial distribution of pollutants. Kriging was used to map the seasonal mean values of these parameters. Ordinary Kriging was used in order to interpolate the pollution measurements to the region. In winter, autumn and spring the SO_2 values exceeded the annual pollution limits of EU and Turkey which are 20 and 52, respectively. In winter and autumn the values were higher in the south–western part of the Kocaeli city. The PM10 values almost reached the limit level (annual limit 52 for Turkey) in all seasons. In winter and autumn the values were higher in the south–western part of the city and in spring and summer the south eastern parts PM values were higher in Kocaeli city (see Fig. 2). The PM10 almost reached the limit level (annual limit 52 for Turkey) in all the seasons. In winter and autumn the values were higher in the south–western part of the city and in spring and summer the south eastern parts were higher than those of Kocaeli city.

3.2 Regression Analysis Results

The regression parameters for SO_2 and PM10 were presented for each season in Table 1. The R2 values for SO_2 in spring, summer, autumn and winter are 0.97, 0.81, 0.88 and 0.98% respectively. The R2 values for PM10 in spring, summer, autumn and winter are 0.17, 0.77, 0.86 and 0.95 respectively. The model best explains both SO_2 and PM10 for winter season with higher R2 parameter whereas it proved that the PM10 value in spring is meaningless with % 0.17.

3.3 Wind Direction Analysis Results

In ArcGIS the pollution and wind direction parameters for each season were mapped. During the winter season, Dilovasi pollution parameters were maximum for Kocaeli, and when the wind effect was examined it was evident that, the direction and speed of the wind were among the factors causing high pollution to Dilovasi (Fig. 3).

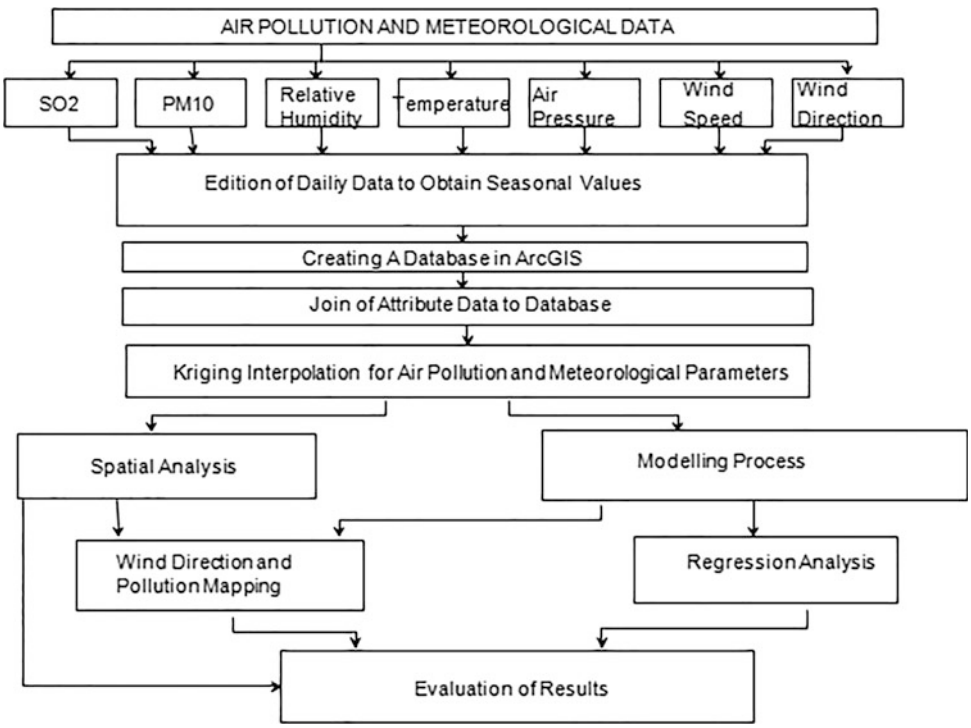

Fig. 1 Flow chart of the study

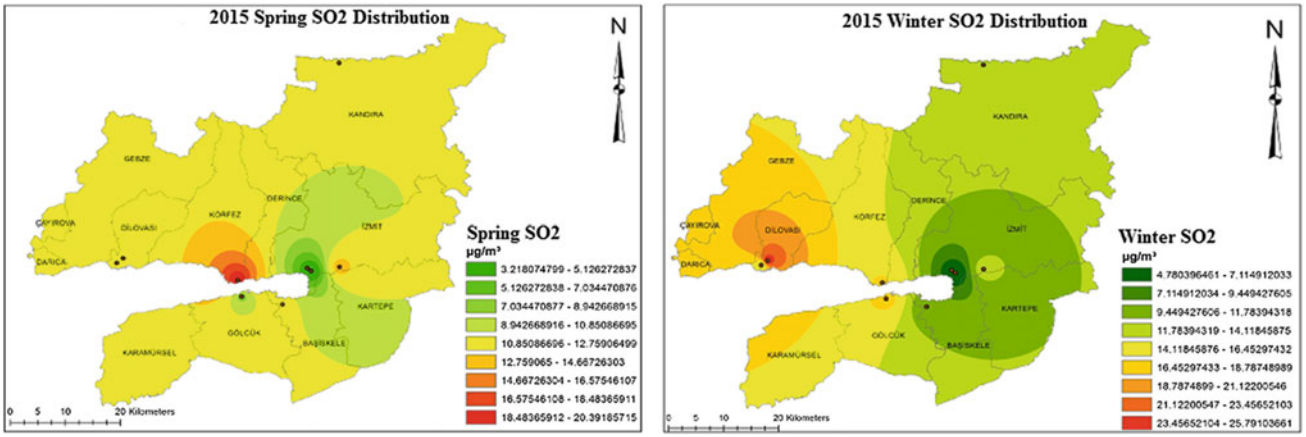

Fig. 2 Flow chart of the study

Table 1 Regression analysis for SO_2

Parameter	β-autumn	P-autumn	βwinter	P-winter
X0	47.75288	0.06119	2.30051	0.76310
Wind speed	0.48920	0.28688	0.35447	0.13410
Temperature	15.36911	0.03782	1.85480	0.01916
Pressure	−59.71561	0.05116	−2.33267	0.75349
Humidity	−2.63705	0.05245	3.24233	0.00261
PM10	−1.10125	0.06270	0.69477	0.00818

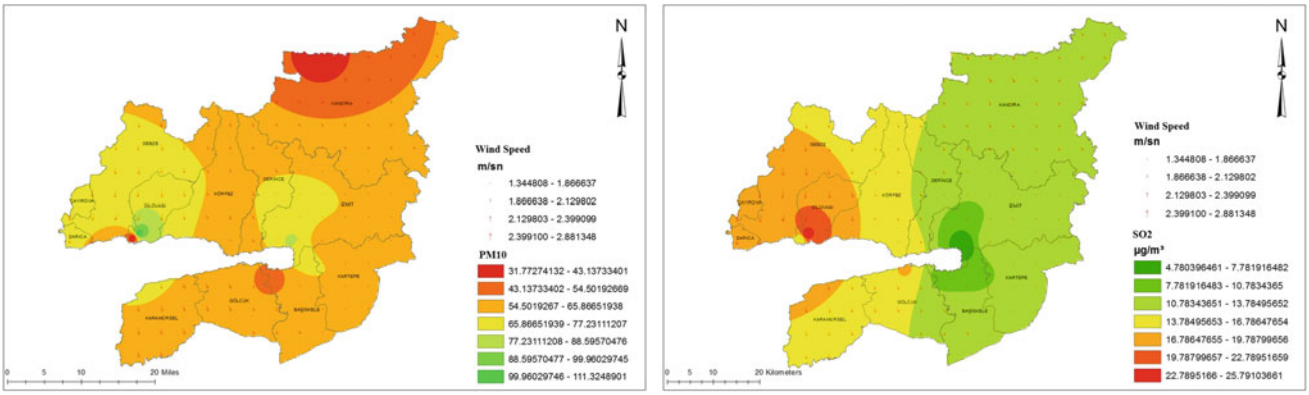

Fig. 3 The wind direction of the region for SO_2 and PM10 for the winter season

4 Discussion

The β parameters indicate that in the winter season the PM10 was positively correlated with wind speed and humidity but negatively correlated with SO_2, temperature and pressure. In the winter season the SO_2 was positively correlated with wind speed, temperature, PM10 and humidity and negatively related with pressure. In the autumn season, Dilovası station has the highest pollution values. The direction of the wind is Southeastern and affects the pollutants' distribution.

5 Conclusion

Taking into account this study, it is evident that in terms of air pollution intensity, the values exceed the limit values for PM10 especially in the winter season. The results of the regression analysis indicate that the model set up is most meaningful for winter and autumn. The PM10 is most influenced by air pressure and humidity, and their effects are positive. The results of wind direction and pollution maps indicate that the most polluted station is Dilovası when compared to the results of the 8 stations belonging to Kocaeli.

The pollution values of Dilovasi could be higher during the winter season due to the wind direction and intensity.

References

1. Chattopadhyay, S., Gupta, S., Saha, R.N.: Spatial and temporal variation of urban air quality: a GIS approach. J. Environ. Prot. **10** (1), 264–277 (2010)
2. Weng, Q., Yang, S.: Urban air pollution patterns, land use, and thermal landscape: an examination of the linkage using GIS. Environ. Monit. Assess. **117**(1–3), 463–484 (2006)
3. Tiany, Y.Z., Shi, G.L., Fu, Y., Song, D., Liu, J., Zhou, L., Feng, Y.: Seasonal and regional variations of source contributions for PM10 and PM2.5 in urban environment. Science of The Total Environment **557–558**, 697–704 (2016)
4. Erener, A.: Industrialization and pollution monitoring by using GIS. In: 37 Asian conference on remote sensing, Srilanka-Colombo, 16–21 Ekim 2016, ACRS 2016, TS32- Ab 0031, 1–7 (2016)
5. Hamzaoğlu, O., Etiler, N., Yavuz, C.I., Cağlayan, C.: The causes of deaths in an industry-dense area: example of Dilovası (Kocaeli). Turk J. Med. Sci. **41**(3), 369–375 (2011)

High Resolution Passive Microwave Sounder Observation on South Indian Region Using Megha-Tropiques Payload

M. P. Vasudha and G. Raju

Abstract

Emission techniques are generally useful over the majority of the Earth's surface. Low-frequency channels are better suited to measure the emission due to liquid associated with rain, most techniques to date rely on high-frequency, scattering-based schemes. The passive microwave satellite based data used includes the Special Sensor Microwave Imagers, SSMI Sounder, SAPHIR (Sondeur Atmosph rique du Profil d Humidit Intertropicale par Radiom trie), Advanced Microwave Sounding Units (AMSU), and Microwave Humidity Sounder (MHS), along with land surface model emissivity estimates. The analysis of SAPHIR sounder data brightness temperature data relating to selected vegetated land with different surface obtained for continuous period of 3 years from 2014 to 2016 was achieved. From our study SAPHIR sounder data is found useful for retrieving surface emissivity. This study relates 183.31 ± 11.0 GHz emissivity values, retrieved from a radiative transfer model using collocated SAPHIR sounder brightness temperature measurements. This examination is noteworthy for microwave sounder assimilation in climate conjecture models and for the usage of the information from passive microwave sensors on-board the Indo-French satellite "Megha-Tropiques," which is committed to tropical environmental studies.

Keywords

SAPHIR • Brightness temperature • Land surface emissivity • Soil moisture

1 Introduction

Measurement of land related applications on surface emissivity is useful to determine variation in i. Surface heat fluxes; ii. Soil moisture content; iii. Vegetation and vi. Climatic condition. Land surface emissivity study can be classified into bare soil emissivity, canopy emissivity (vegetation canopy) and snow emissivity. Bare soil emissivity with no or sparse vegetation of candidate study area on temporal and seasonal scale has been selected as a parameter for our observation. Observations of land surface emissivity using infrared and/or microwave images obtained by sounder onboard satellites provide most of the information relating to the surface emissivity [1, 2]. Among the various satellite missions involved in the retrieval of land surface emmissivity, brightness temperature data obtained from AMSU [3] sensor onboard NOAA and SAPHIR sensor onboard Megha-Tropiques satellite mission were selected for our study purpose [4].

The primary data used for our analysis is in the form of brightness temperature measurement of microwave sounders. The values of brightness temperature measurement for 6-layer averaged values from 0 to 12 km from the surface were processed using numerical/statistical algorithms to determine the emissivity properties [5]. The main objective of the present study was to get an estimation of microwave emissivity from satellite observations and characterization of emissivity over the Indian subcontinent and examination of its seasonality. Further an attempt was made to demonstrate the advantages of SAPHIR data related to land applications for monitoring seasonal variation, geographical variations of vegetation conditions, moisture content etc. over selected regions of South India.

2 Methodology

Emissivity is a measure of how strongly a body radiates at a given wavelength. Land Surface Emissivity (LSE) is defined as the emissivity of an element on the surface of the Earth

M. P. Vasudha (✉) · G. Raju
Department of Electronics and Communication Engineering, JAIN (Deemed-to-be-University), Bangalore, India
e-mail: mp.vasudha@gmail.com

© Springer Nature Switzerland AG 2019

H. M. El-Askary et al. (eds.), *Advances in Remote Sensing and Geo Informatics Applications*, Advances in Science, Technology & Innovation, https://doi.org/10.1007/978-3-030-01440-7_79

and includes the emissivity of the surface and land surface temperature (LST). SAPHIR TB (Brightness Temperature) data were obtained from microwave sounder for all 6 channels with a 10 km resolution at nadir and 22.9 km at edge spatial resolution. Using SAPHIR microwave TB, the estimation of land surface emissivity by any of the three popular methods which are (i) Direct observation method, (ii) Physical retrieval and (iii) Dense media radiative transfer [6] would be as follows:

(i) Direct Observation Method: estimation of LSE by using SAPHIR satellite TB observation over the vegetated land and dense forest as input parameters. The microwave radiative transfer formulation under clear cloud sky for satellite observed brightness temperature $T_B(p,f)$ is

$$T_B(p,f) = \varepsilon(p,f)T_{skin}\Gamma + (1-\varepsilon(p,f))T_{\downarrow}(f)\Gamma + T_{\uparrow}(f) \quad (1)$$

where $\varepsilon(p,f)$ is the surface emissivity at a frequency f for the polarization p,

$\Gamma = e^{-\tau(0,h)\sec(\theta)}$ where h is the height of the satellite and θ = incident angle. Thus, Land emissivity is expressed as

$$\varepsilon(p,f) = \frac{T_B(p,f) - T_{\uparrow}(f) - T_{\downarrow}(f)\Gamma}{(T_{skin} - T_{\downarrow}(f))\Gamma} \quad (2)$$

and estimated by

$$\varepsilon(p,f) = \frac{T_B(p,f)}{T_{skin}} \quad (3)$$

where T_{skin}—Skin temperature, T_B (p,f)—satellite observed brightness temperature, Γ is net atmospheric transmissivity. $T_{\uparrow}(f)$—Upwelling brightness temperatures, $T_{\downarrow}(f)$—downwelling brightness temperatures. Land surface emissivity (ε) is processed through Eq. (3). Climatic profiles of temperature, humidity, and water vapor are taken from the Japan Meteorological Agency Reanalysis (JRA).

(ii) Physical retrieval method: based on the principle of satellite observations with physical consistency among the received parameters.
(iii) Dense media radiative transfer theory with surface parameter (soil type) as input parameters.

3 Observation and Analysis

The variation of climatological seasonal changes in terms of brightness temperature variation is shown in Fig. 1 is shown to be in accordance with the gradation represented in accompanying color barcode i.e., min 220 K and max 280 K. In Fig. 1 column right to left shows the observations form SAPHIR during the year 2014, 2015, 2016. First row shows observations for the winter season on 14th Jan 2014 to 2016, second row depicts observations during the summer season 14-04-2014 to 14-04-2016, third row displays

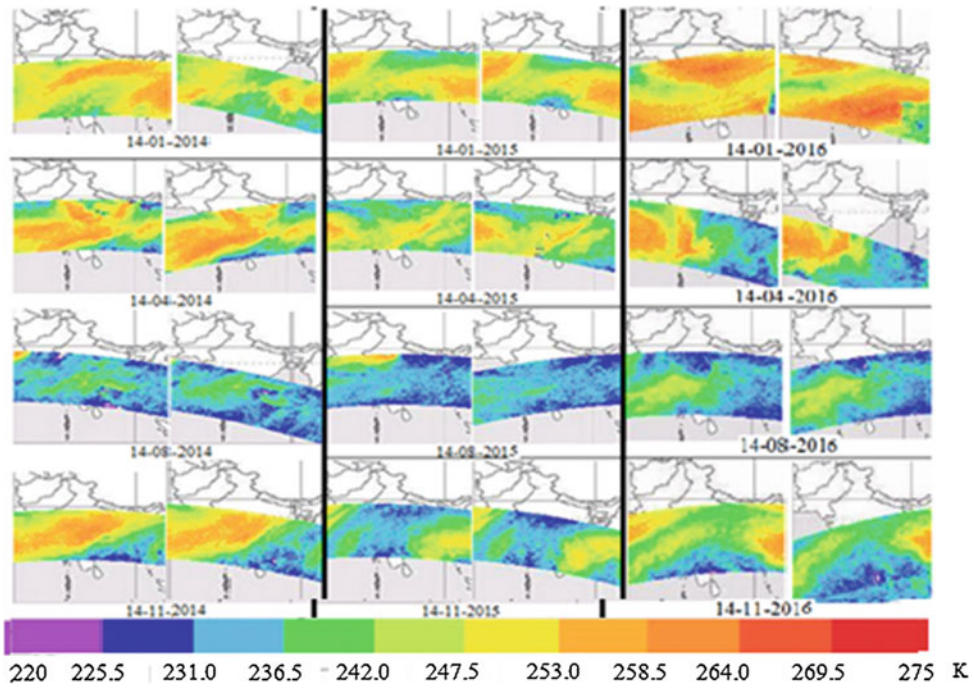

Fig. 1 Shows Seasonal variation of BT in middle and south India (2014–2016)

Table 1 Shows the variation of brightness temperature measured by SAPHIR (MT)

	Year: 2014		Year: 2015		Year: 2016	
Date	Middle Indian region (K)	South Indian region (K)	Middle Indian region (K)	South Indian region (K)	Middle Indian region (K)	South Indian region (K)
14th Jan	242–258.5	242–253	236.5–253	231–247.5	275.5–260	247.5–264
14th Apr	253–264	247–264	242–253	236–258.5	231–242	236.5–255
14th Aug	225.5–236.5	225.5–242	231–258.5	225.5–237	228–236.5	228–236.5
14 Nov	253–258.5	231–247.5	225.5–236.5	225.5–236.5	236.5–248	228–240

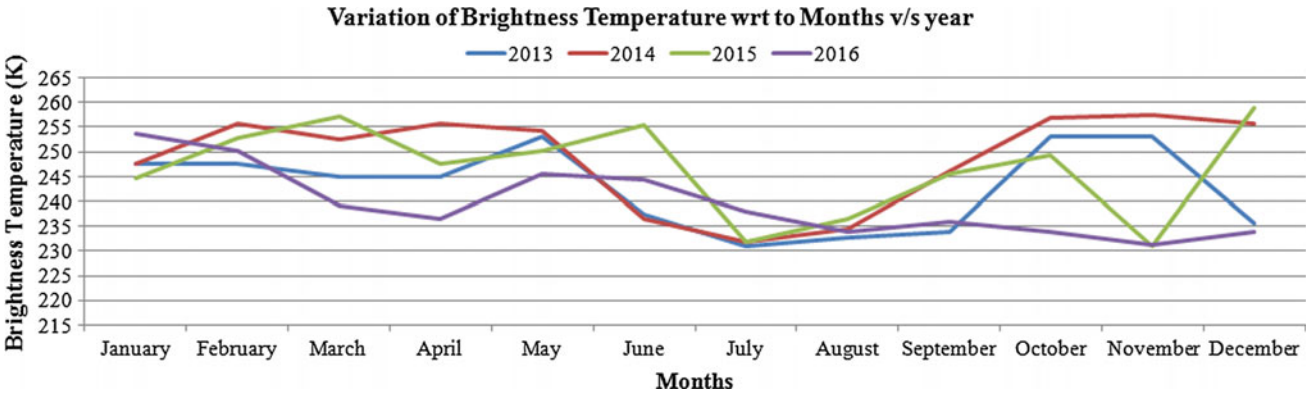

Fig. 2 Variation of TB over land from Jan 2013 to Dec 2016 by SAPHIR

observations during the monsoon/rainy season on 14th Aug 2014 to 2016 and last row is for observations during the autumn season.

The seasonal variation of brightness temperature in terms of kelvin is tabulated in Table 1. The brightness temperature variation from Jan 2013 to Dec 2016 measured by SAPHIR in South Indian region of every month was plotted as shown in Fig. 2. During the monsoon season which starts in mid of June and ends mid August of every year we can observe the lower temperature i.e., 225 K compared to the other seasons. In Fig. 2 the lower TB observed during June to Aug month might be due to the effects of rainfall and change in mean observed values of moisture content of the surface.

4 Conclusion

The observations of bare soil emissivity using microwave sounder images on seasonal and temporal scale were performed. The main objective of these observations were to find out the capabilities of MWS images to provide sufficient, frequent and accurate information regarding the parameters stated above. A study of the efficiency of the sensors clarified that MWS Images are more useful because they can be obtained in all atmospheric conditions when compared to IR Sounder images. They give the impression that the effect of precipitation upon the emissivities in the light-to-direct vegetated zone is most perceptible after direct substantial rain occasions (surpassing 10 mm in the earlier day). The LSM and physical emissivity strategies can be utilized to examine how the extent and time size of the related decrease in surface emissivity, during and after precipitation occasions.

References

1. Antony, T., Raju, C.S., Mathew, N., Saha, K., Krishna Moorthy, K.: A detailed study of land surface microwave emissivity over the indian subcontinent. IEEE Trans. Geosci. Remote Sens. **52**, 3604–3612 (2013)
2. Wang, D., et al.: Surface emissivity at microwaves to millimeter waves over polar regions: parameterization and evaluation with aircraft experiments. J Atmos. Oceanic Technol **34**(5), 1039–1059 (2017)
3. Karbou, F., et al.: Microwave land emissivity calculations using AMSU measurements. IEEE Trans. Geosci. Remote Sens. **43**(5), 948–959 (2005)
4. Raju, C.S., Antony, T., Mathew, N., Uma, K.N., Krishna Moorthy, K.: MT-MADRAS Brightness temperature analysis for terrain characterization and land surface microwave emissivity estimation. Curr. Sci. **104**(12), 1643–1649 (2013)
5. Vasudha M.P., Raju, G.: Monitoring of tropical cyclone formation, growth and dissipation by using SAPHIR sensor. MAUSAM. **69**(2), 209–218 (2018)
6. Ralph, R., et al.: An evaluation of microwave land surface emissivities over the continental United States to benefit GPM-Era precipitation algorithms. IEEE Trans. Geosci. Remote Sens. **51**, 378–398 (2013)